

The design and synthesis of novel
fluorescent coumarin-based derivatives as
chemosensors for the application of toxic
metal ion detection

By

Stiaan Schoeman

Submitted in fulfilment of the requirements for the
Doctoral degree in the Faculty of Science to be awarded
at the Nelson Mandela University

April 2023

Supervisor: Dr N. Mama

Declaration

In accordance with Rule G5.6.3, I, Stiaan Schoeman (student number: 212259954), hereby declare that the dissertation for the Doctoral degree in the Faculty of Science is my own work and that it has not previously been submitted for assessment or completion of any postgraduate qualification to another University or for another qualification.

Signed: 

Printed name: Stiaan Schoeman

Date: 06 April 2023



**PERMISSION TO SUBMIT FINAL COPIES
OF TREATISE/DISSERTATION/THESIS TO THE EXAMINATION OFFICE**

Please type or complete in black ink

FACULTY: Science _____

SCHOOL/DEPARTMENT: Chemistry _____

I, (surname and initials of supervisor) Mama, N _____

and (surname and initials of co-supervisor) _____

the supervisor and co-supervisor respectively for (surname and initials of
candidate) Schoeman S _____

(student number) 212259954 _____ a candidate for the (full description of qualification)
Doctor of Philosophy (Chemistry) _____

with a treatise/dissertation/thesis entitled (full title of treatise/dissertation/thesis):

The design and synthesis of novel fluorescent coumarin-based derivatives as chemosensors
for the application of toxic metal ion detection. _____

It is hereby certified that the proposed amendments to the treatise/dissertation/thesis have been effected and that **permission is granted to the candidate to submit** the final copies of his/her treatise/dissertation/thesis to the examination office.

A handwritten signature in black ink, appearing to be "A. S.", written over a horizontal line.

SUPERVISOR

06/04/2023

DATE

And

CO-SUPERVISOR

DATE

“The researcher in this field has the privilege of literally seeing the outcome of molecular experiments, i.e. molecular fluorescence is a natural interface between human and molecular domains via the intermediacy of the photon.”

- Richard A. Bissell et al., 1992

Abstract

The rise of humankind has caused pollution, increasing damage to the environment. The actions of humans over hundreds of years have led to an increase in the release of heavy metal cations in concentrations that are toxic to plants, animals and humans. These toxic metals can find their way into humans' diets through water sources or bioaccumulation in plants and animals such as fish. Heavy metals such as lead and mercury are known to cause serious health issues when consumed, affecting the functioning of the circulatory and nervous systems and causing developmental disorders. Other metal cations, such as iron and copper, can be found in the human body. However, detrimental health issues can occur when normal concentrations are disturbed (either too high or too low). Iron, for example, can be toxic if in excess in the human body, causing damage to the liver and heart and can cause neuroinflammation and Alzheimer's disease.

Many methods have been employed to detect and measure the concentrations of toxic metal cations. However, these methods are performed in a laboratory and need skilled operators using expensive equipment. This results in long and tedious sample collection, long feedback time and costly analysis.

Chemosensors have been researched and proposed as a cost-effective, on-site, real-time alternative for use as metal detectors. Chemosensors can selectively detect specific metal cations and can be sensitive up to the nanomolar range. Various chemosensors have been synthesised and screened for their colourimetric and fluorometric abilities. Colourimetric chemosensors can be used to visually detect cationic and anionic analytes, whereas fluorometric chemosensors are used to detect anions using their emission properties which handheld devices can measure.

Herein several novel compounds are synthesised and tested for their chemosensor abilities. Schiff base chemosensors were designed and synthesised in good yields. **S4** displayed a colour change from clear to blue in the presence of Cu^{2+} . However, this colour change needed up to 25 minutes to develop fully and thus could not be used as a real-time chemosensor. The colourimetric chemosensor **S10** can characteristically identify Cu^{2+} , Ni^{2+} , and Fe^{2+} , each inducing a different complex colour, blue-green, yellow, and red, respectively. Competition studies were performed for each cation, and it was determined that **S10** was not selective for the three cations tested. **S10** had a slight preference for Cu^{2+} followed by Ni^{2+} and least for

Fe^{2+} . Real-world studies indicated that using paper strips, **S10** could also identify Cu^{2+} and Fe^{2+} .

Investigation into mixed ligand chemosensors was conducted. Metal complexes are known to complex with a variety of solvents. In nanoscience, mixed-ligand magnetic nanoparticles can be used for different applications, such as enhanced sensing, binding multiple analytes, and system stability. **E2** was compared to the mix-ligand solution **E6**, which contains **E2** and o-anisaldehyde. Absorbance studies indicated that **E6** was more selective than **E2**, but fluorescence studies indicated that o-anisaldehyde affected the emission spectrum. Further studies into **E2** showed that **E2** was highly selective for the 1:1 **E2**- Fe^{2+} complex. Reversibility studies revealed that the **E2**- Fe^{2+} was partially reversible using EDTA and H_2O_2 . However, real-world application studies, unfortunately, showed that analytes present in the water samples interfered with complexation, and the concentrations could not be determined.

Two novel coumarin-based dimers were designed and synthesised. **D1** and **D2** were investigated for their fluorometric chemosensor abilities for the detection of cations. **D1** had a maximum absorption band at 487 nm, whereas **D2** had no absorbance spectra. Cation screening was performed in acetonitrile for both **D1** and **D2**. **D1** functioned as an “on-off” chemosensor in the presence of Cu^{2+} . **D2** was examined for its “off-on” chemosensor abilities, and no significant change in the emission spectra was observed. Competition studies showed that **D1** was not selective towards Cu^{2+} in the presence of competing metals. Reversibility studies indicate that **D1**- Cu^{2+} was not reversible in the presence of EDTA, sodium ascorbate, and cyanide. Real-world application studies, unfortunately, showed that impurities in the water samples interfered with the complexation of **D1**- Cu^{2+} , and the concentrations could not be accurately determined.

Lastly, thionation reactions were attempted on ethyl-8-ethoxy-2-oxo-2H-chromene-3-carboxylate, **T1**. The thio analogue ethyl-8-ethoxy-2-thioxo-2H-chromene-3-carboxylate, **T2**, was successfully synthesised using Lawesson’s reagent. The substitution was observed in the ^1H and ^{13}C NMR. Molecular modelling was employed to illustrate the electrostatic changes that transpired due to thiocarbonyl’s presence. Furthermore, cationic screening studies indicated that **T1** and **T2** interacted with Fe^{2+} . Additionally, **T2** uniquely interacted with Hg^{2+} , leading to the possibility of using **T2** for the detection of Hg^{2+} in the presence of other metal ions.

Acknowledgements

Dr Neliswa Mama, the best mentor and pillar, is **specially thanked** for her constant support, guidance and enthusiasm in this project, as well as her valuable and constructive suggestions.

To Liesl, my Love, thank you for your encouragement, devotion and endless meals you prepared for us while I was busy with research. Thank you for assisting me in the lab and pulling me through the hard times. Thank you for all the coffees you continuously brought me. Thank you for believing in me. I love you.

To my parents, thank you for supporting me, in every way possible, to follow my passion and pursue a degree I have little to no experience in the sciences. You believed in me, encouraged me to do my postgraduate studies, and supported me through this long journey.

I am grateful to Dr Aidan Battison for her valuable discussions, input, support, and well wishes throughout my postgraduate studies.

To my in-laws, thank you for the support and, yes, the early phone calls to make sure I reached my goals. Thank you for the meals and for giving me time to breathe and become human again between long study sessions.

Thanks to my friends and lab collages for the moral support and the chemicals I borrowed.

Mr Eric Bashman and Mr Henk Schalekamp are thanked for their technical and chemical assistance in the lab.

Dr Eric Hosten is thanked for conducting the Single Crystal X-Ray Diffraction experiments and for the technical assistance.

Dr Richard Betz for providing the Lawesson's reagent.

Nelson Mandela University (NMU) is thanked for the financial support they provided, as well as for providing the opportunity and facilities to carry out this project.

National Research Foundation (NRF) is thanked for the financial support they provide.

Lastly, but just as importantly, to God for giving me the capacity, endurance and potential to come this far.

Selected Abbreviations

AcOH – Acetic acid
CDCl₃ – Chloroform-D₁
CH₃CN – Acetonitrile
CHQF – Chelation Quenched Fluorescent
DMF – Dimethylformamide
DMSO – Dimethyl sulfoxide-D₆
EDG – Electron Donating Group
EDTA – Ethylenediaminetetraacetic Acid
EtOH – Ethanol
EWG – Electron Withdrawing Group
FRET – Förster Resonance Energy Transfer
FT-IR – Fourier Transform Infrared
GAA – Glacial Acetic Acid
H₂O – Water
HOMO – Highest Occupied Molecular Orbital
LOD – Limit of Detection
LOQ – Limit of Quantification
LR – Lawesson's Reagent
LUMO – Lowest Unoccupied Molecular Orbital
MetOH – Methanol
MNP – Magnetic Nanoparticle
NMR – Nuclear Magnetic Resonance
TLC – Thin Layer Chromatography
UV-vis – Ultraviolet-visible
WHO – World Health Organisation
XRD – X-ray Diffraction

General Table of Contents

Abstract	i
Acknowledgements	iii
Selected Abbreviations	iv
Published work	vi
In the process of publishing	vii
Chapter 1 – General Introduction	1
Chapter 2 – Schiff based Chemosensors	41
Chapter 3 – Mixed ligand Chemosensors	98
Chapter 4 – Dimer Chemosensors	159
Chapter 5 – Thio analogue Chemosensors	221
Chapter 6 – Hydrazone Chemosensors	251
Chapter 7 – Real-world application studies	266
Chapter 8 – Conclusion and Future work	280



A Coumarin-azo Derived Colorimetric Chemosensor for Hg²⁺ Detection in Organic and Aqueous Media and its Extended Real-world Applications

Aidan Battison¹ · Stiaan Schoeman¹ · Neliswa Mama¹

Received: 4 May 2022 / Accepted: 1 November 2022

© The Author(s), under exclusive licence to Springer Science+Business Media, LLC, part of Springer Nature 2022

Abstract

Pollution caused by the release of toxic heavy metals into the environment by industrial and farming processes has been regarded as a major problem worldwide. This has attracted a great deal of attention into restoration and remediation. Mercury is classified as a toxic heavy metal which has posed significant challenges to public and environmental health. To date, conventional methods for mercury detection rely on expensive, destructive, complex, and highly specialized methods. Evidently, there is a need to develop systems capable of easily identifying and quantifying mercury within the environment. In this way, organic-based colorimetric chemosensors are gaining increasing popularity due to their high sensitivity, selectivity, cost-effectiveness, ease of design, naked-eye, and on-site detection ability. The formation of coumarin-azo derivative **ADI** was carried out by a conventional diazotization reaction with coumarin-amine **1c** and N,N-dimethylaniline. Sensor **ADI** displayed remarkable visual colour change upon mercury addition with appreciable selectivity and sensitivity. The detection limit was calculated as 0.24 µM. Additionally, the reversible nature of **ADI** allowed for the construction of an IMPLICATION type logic gate and Molecular Keypad Lock. Chemosensor **ADI** displayed further sensing applications in real-world water samples and towards on-site assay methods. Herein, we describe a coumarin-derived chemosensor bearing an azo (N=N) functionality for the colorimetric and quantitative determination of Hg²⁺ in organic and aqueous media.

Keywords Mercury cation · Coumarin · Azo-dye · Colorimetric sensing

Introduction

The pollution caused by the release of toxic heavy metals into the environment by industrial and farming processes has been regarded as a major problem worldwide, especially in third-world countries, which has attracted a great deal of attention into restoration and remediation [1–3]. In developing countries, like South Africa, the culmination of poorly maintained waste-water treatment and disposal facilities; and increased agricultural, industrial, and mining activities have all contributed to contamination of soil and water sources [4]. This poses a potential risk to informal households where groundwater and surrounding water bodies are utilized as primary sources of drinking-water. Environmental

proliferation of heavy metals into the soil and marine/aquatic ecosystems has been shown to elicit numerous health risk to humans and organisms and also impedes on the overall functioning of the ecosystem [5, 6]. Once these heavy metals are released into the environment, they quickly alter the physical, chemical, and biological properties of soil and water bodies [7, 8]. When these metals are released into aquatic environments, particles can be absorbed via biogeochemical cycles which can be lethal to surrounding organisms and the overall health of the ecosystem. Furthermore, heavy metals can also accumulate in the sediments of aquatic and marine water bodies. As a result, seaports, river-systems, and industrial coastlines exposed to continuous influx of heavy metals display the greatest amounts of polluted sediments [9, 10]. Heavy metals and metalloids are elements possessing an atomic density greater than 4 g/cm³; this includes copper (Cu), cadmium (Cd), zinc (Zn), lead (Pb), mercury (Hg), arsenic (As), silver (Ag), chromium (Cr), iron (Fe) and platinum (Pt) group elements [11].

✉ Neliswa Mama
neliswa.mama@mandela.ac.za

¹ Department of Chemistry, Nelson Mandela University, P.O. Box 77000, Port Elizabeth 6031, South Africa



A comparison between an ester coumarin-based chemosensor and the ester 2-thiocoumarin analogue using Lawesson's reagent.

Stiaan Schoeman and Neliswa Mama*

Department of Chemistry, Nelson Mandela University, P.O Box 77000, Port Elizabeth, 6031, South Africa

Email: neliswa.mama@mandela.ac.za

Dedication (optional)

Received mm-dd-yyyy

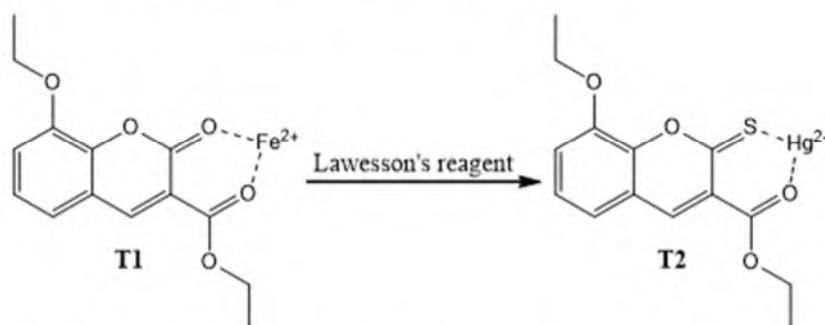
Accepted Manuscript mm-dd-yyyy

Published on line mm-dd-yyyy

Dates to be inserted by editorial office

Abstract

Lawesson's reagent is a thionating reagent that can convert a carbonyl group into the thiocarbonyl analogue. Sulphur is known to form complexes with mercury readily. Herein, an ester-functionalised coumarin compound was successfully monosubstituted into the 2-thiocoumarin analogue. In the ^{13}C NMR of **T1**, the lactone carbonyl was observed at 156.24 ppm, which, after the successful thionation, shifted to 192.13 ppm as the thiocarbonyl **T2**. The ester carbonyl peak stayed relatively constant, 163.04 ppm in **T1** and 164.97 ppm in **T2**. Molecular modelling was employed to illustrate the change in the electronic environment due to the presence of the sulphur atom. The thionation of **T1** resulted in the shift of the electron density, the HOMO and the LUMO. Lastly, cationic chemosensor screening tests were performed in which **T1** interacts strongly with Fe^{2+} , whereas **T2** resulted in a shift in selectivity towards Hg^{2+} and Fe^{2+} .



Keywords: Coumarin, chemosensor, iron(II), cyanide, fluorescence, molecular modelling.

Chapter 1

General Introduction

Table of Contents

Table of Figures	3
List of abbreviations	4
1 General introduction	6
1.1 Background	6
1.2 Definition of a chemosensor	7
1.2.1 Components of a chemosensor	8
1.3 Uses of chemosensors	11
1.3.1 Detection of anions	11
1.3.2 Detection of cations	12
1.4 Advantages of chemosensors	13
1.5 Importance of chemosensors	13
1.6 Types of chemosensors	14
1.6.1 Colourimetric sensors	14
1.6.2 Fluorescent sensors	15
1.6.3 Dual sensors	16
1.6.4 Ratiometric sensors	17
1.6.5 “On-off” and “off-on” sensors	18
1.7 Photophysical properties	19
1.7.1 Absorption properties	19
1.7.2 Emissions properties	21
Reference	33

Table of Figures

Figure 1.1: General structure of a chemosensor.	8
Figure 1.2: Structures of common chemosensor fluorophores.	9
Figure 1.3: Illustration of an electron “push-pull” system on the coumarin backbone. ¹⁷	10
Figure 1.4: The structure of a triazole ring.	10
Figure 1.5: Interaction of chemosensor 3 with F ⁻ via proton abstraction.	12
Figure 1.6: Quinoline-based fluorescent chemosensor 4 and the complex formed in the presence of PdCl ₂	13
Figure 1.7: A colourimetric chemosensor, 5 , for detecting mercury. ⁴⁵	15
Figure 1.8: A fluorescent chemosensor, 6 , used to detect mercury. The sensor has a weak orange fluorescence which changes to a bright light blue upon adding mercury. ⁴⁶	16
Figure 1.9: A chemosensor, 7 , with a colourimetric and fluorescent component. ⁴⁷	17
Figure 1.10: A graph depicting the absorbance spectrum of a) “single-signal pattern” and b) “two-signal pattern” ratiometric sensor.	18
Figure 1.11: “On-Off-On” chemosensor, 8 used for detecting Hg ²⁺ , quenched, the complex is reversed adding S ²⁻ , fluorescence regained.	19
Figure 1.12: Shifts observed in absorption spectra.	20
Figure 1.13: Chemosensor, 9 , used for naked-eye chemosensing of acetate in DMSO. ⁵⁴	21
Figure 1.14: A energy diagram depicting the non-radial relaxation of an excited electron. ..	22
Figure 1.15: A energy diagram depicting the radial relaxation of fluorescence.	22
Figure 1.16: A energy diagram depicting radial relaxation of phosphorescence.	23
Figure 1.17: PET system showing the transference of the electron between the donor site and the acceptor site. ⁵⁷	24
Figure 1.18: Fluorescent Schiff base chemosensor, 10 , showing on-off PET system. ⁶⁰	24
Figure 1.19: Dexter exchange diagram showing the double electron transfer between the excited donor and an acceptor in the ground state.	25
Figure 1.20: Illustration of the excimer and exciplex intermediates.	26
Figure 1.21: FRET system showing an excited donor site transferring energy through Coulombic interaction to an acceptor site in the ground state, resulting in a donor site and an excited acceptor site.	27
Figure 1.22: FRET a) on-off and b) off-on systems. ⁶⁴	27
Figure 1.23: The off-on FRET system in chemosensor 11 , which contains a quinoline–benzothiazole, donor site, and the rhodamine as acceptor site. ⁶⁴	28

Figure 1.24: The spectral overlap of quinoline-benzothiazole donor emission (blue line) and rhodamine acceptor absorbance (pink line) of 11 . ⁶⁴	29
Figure 1.25: Intramolecular proton transfer through hydrogen bonding in compound 12 . ⁶⁵ ..	30
Figure 1.26: Intermolecular proton transfer in the presence of F ⁻ in acetonitrile as solvent. ³⁰	30
Figure 1.27: Four-level ESIPT cycle showing the transference of a proton in the excited state and deprotonation to return to the ground state. ⁶⁶	31
Figure 1.28: Benzimidazole-based ESIPT chemosensor, 14 , capable of detecting Cu ²⁺ . The enol and keto form with the hydrogen bond for each are shown.	32

List of abbreviations

AES – Atomic Emission Spectroscopy

CE – Capillary Electrophoresis

CHEF – Chelation-Enhanced Fluorescence

DIS – Photodissociation

DMSO – Dimethyl sulfoxide

EDG – Electron Donating Group

ESIPT – Excited State Intramolecular Proton Transfer

ET – Energy Transfer

EWG – Electron Withdrawing Group

FAAS – Flame Atomic Absorption Spectrometry

FRET – Förster Resonance Energy Transfer

H-a – Hydrogen atom transfer

HOMO – Highest Occupied Molecular Orbital

IC – Internal Conversion

ICP-AES – Inductively Coupled Plasma-Atomic Emission Spectroscopy

ICP-MS – Inductively Coupled Plasma Mass Spectrometry

LOD – Limit of Detection

LUMO – Lowest Unoccupied Molecular Orbital

PET – Photo-Induced Electron Transfer

PT – Proton Transfer

sub – Photo-substitution

UV-vis – Ultraviolet-visible

VI – Valence photoisomerisation

XAS – X-ray Absorption Spectroscopy

XPS – X-ray Photoelectron Spectroscopy

XRF – X-ray Fluorescence

1 General introduction

1.1 Background

With the dawn of the industrial age, humanity has flourished and embraced the benefits associated with the rise of power-driven machines. The use of coal to power steam engines and the rise of factories was the starting point for air and water pollution. Pollution is a broad topic covering a toxic substance's presence in any ecosystem. It can be further grouped by location, such as air- and water pollution or by type of pollution, such as heavy metal pollutants.

Toxic heavy metals pollution existed even before the industrial revolution, as published by JP Candelone and his co-workers.¹ Their study used ultraclean procedures to obtain ice core samples from Greenland covering the time before and after the industrial age. In their investigations, metals such as lead (Pb) were present in the ice caps long before it was initially thought. However, with the onset of the industrial age, Pb levels increased up to 20 times previously noted.¹

Lead was commonly used during the Roman empire for water pipes, glazing of pottery, cosmetics, and sweetening wine. Its low melting point, durability, and ease with which it can be worked resulted in its broad uses as a construction material during the industrial revolution.² Presently, lead is used in lead-acid batteries, construction, bullets, weights, solder, pewter, fusible alloys, smelting, industrial emissions, and agricultural fertilisation.^{3,4} Lead can be extracted from ores containing copper, zinc and silver, resulting in co-products.⁴ Natural lead sources are lead ore, volcanic eruptions, and sea sprays.⁵

Lead pollution can be found in water, air and soil. It can be harmful to plants and animal life in elevated concentrations.⁵ In humans, lead poisoning can be deadly at higher concentrations, affecting the functioning of the circulatory and nervous systems. At low concentrations, lead poisoning can cause reduce cognitive ability and cause developmental disorders.^{2,6}

“Even today more than half of the world population depends on groundwater being a vital source for drinking as it contributes 97% of global freshwater. In several geographical regions, groundwater is a vital source for drinking since it contributes the single largest supply for serving drinking water.”⁵ This quote by R. Dongre emphasises the importance of detecting various pollutants as the vast majority of humanity depends strongly on sources such as water to survive.

Detection methods range from spectrometry (such as Flame Atomic Absorption Spectrometry (FAAS), Atomic Emission Spectroscopy (AES), Inductively Coupled Plasma-Atomic Emission Spectroscopy (ICP-AES), and Inductively Coupled Plasma Mass Spectrometry (ICP-MS)), electrochemical techniques (such as surface plasmon resonance and Capillary Electrophoresis (CE)), and X-ray spectroscopic techniques (such as X-ray Fluorescence (XRF), X-ray Photoelectron Spectroscopy (XPS), and X-ray Absorption Spectroscopy (XAS)).^{7,8}

Each of these techniques comes with its specific advantages and disadvantages. The disadvantages of these techniques include low signal-to-noise ratio, drift, sensitivity, selectivity, specificity, stability, reusability, cost of the specialised procedures, the preparation of the samples, and contaminating/clogging of instruments. In addition, to improve the results' quality and prolong the equipment's usability, a professionally trained technician is needed to prepare samples, operate (and maintain) equipment, set up procedures and methods to run different samples and interpret these results. Furthermore, the instruments required for these techniques are big and bulky, and samples must be sent back to the lab for analysis, thus, excluding the possibility of on-site analysis and limiting the availability of these techniques.⁸

However, chemosensors possess abilities not possible with current techniques without the disadvantages possessed by conventional methods. Chemosensors have more distinct advantages, such as ease to use and understand, rapid response, low cost, and real-time monitoring, allowing on-site monitoring.⁷

1.2 Definition of a chemosensor

Chemosensors fall under the field of sensor technology and host-guest chemistry. The field of sensors has seen a rapid expansion over the last few decades due to the advantages over traditional detection methods. The field of sensor technology can be categorised into two broad groups: chemical sensors (Chemosensors) and biological sensors (biosensors).⁸

Chemosensors are organic molecules that can quantitative and qualitatively identify analytes, while biosensors have a biological component (such as microorganisms, tissue, cells, organelles, nucleic acids, enzymes, or antibodies).⁸ Sensors can identify a specific analyte due to their observable interactions, which can be detected and measured.⁹

Photosensitive sensors such as photochromic, fluorescent and phosphorescent molecules change their optical properties upon interaction with the desired analyte.^{10,11} The interaction between the chemosensor and the analyte induces changes in its spectral properties (¹H NMR,

electronic, fluorescence, or absorbance spectra).^{10,12} Specific analytes can be identified by observing their characteristic changes.

1.2.1 Components of a chemosensor

A chemosensor (**Figure 1.1**) can consist of many different components with different functions. However, the two most important components are the fluorophore (the signalling unit) and the receptor (the recognition site).^{12,13} A linker or spacer unit can be added to aid in the photophysical properties by extending conjugation¹⁴. The linker can also increase the size of the preferred analyte by giving more space between the fluorophore and receptor, allowing for bigger analytes to interact due to less steric hindrance.¹⁵ Furthermore, the linker can also contribute to stabilising the complex by donating electrons to the binding site¹⁶.

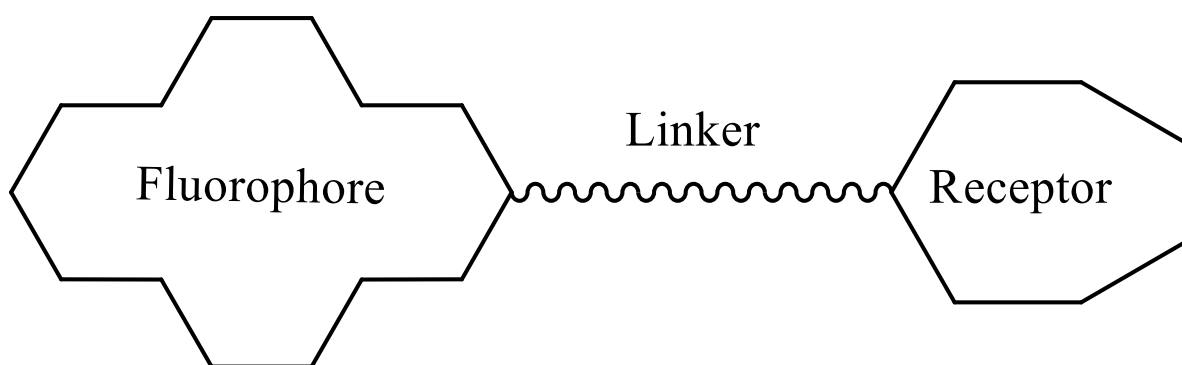
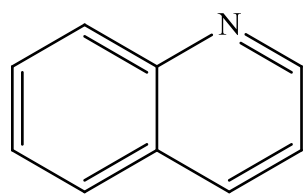


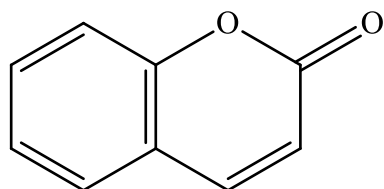
Figure 1.1: General structure of a chemosensor.

1.2.1.1 Fluorophore bases

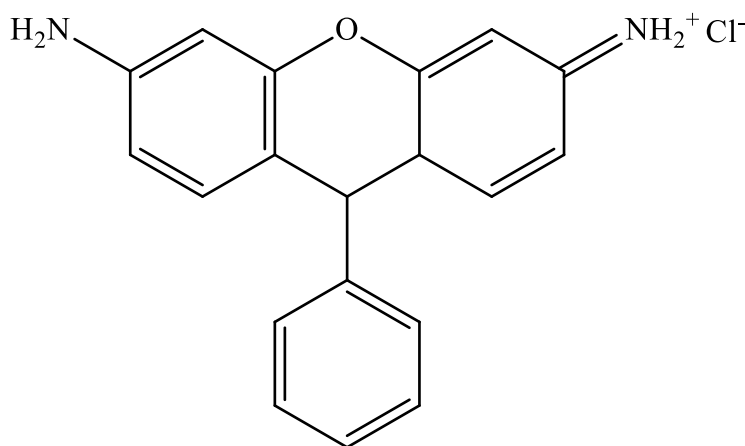
The fluorophore is part of the chemosensor molecule that mainly provides photophysical changes associated with the interaction with an analyte. The fluorophore functions as the backbone to attach substituents easily. Various fluorophores (**Figure 1.2**) that have been used include coumarin,¹⁷ rhodamines,¹⁸ and quinoline¹⁹; these are three of the most widely used fluorophores.



Quinoline



Coumarin



Rhodamine

Figure 1.2: Structures of common chemosensor fluorophores.

The major downfall of these fluorophores is low solubilities in some solvents, which limits their application in aqueous systems. However, this can be improved by adding various substituents on the backbone.

1.2.1.2 Presence of substituents on a chemosensor

It has been proven that the photophysical properties of the chemosensors can depend on the types and positions of substituents. The chemosensor's electronic properties are influenced by the substituents connected to the fluorophore, which can result in a push-pull system. In a push-pull system, the metal cation (electron withdrawing groups - EWG) “pulls” electrons from the binding site, which is counteracted by the “pushing” of electrons, into the system, from the substituents (electron donating group - EDG).^{21–23} A combination of EDG and EWG (push-pull system) has been proven to lead to maximum photophysical properties of the chemosensor.²⁰ Coumarins are classic examples of a fluorophore which can be modified into a push-pull system, as positions three and seven, **Figure 1.3**, can easily be modified.²¹ EDG (e.g., -NR₂, -OR etc.) at positions six, seven or eight, and EWG (NO₂, CN, SO₃⁻, COR, etc.) at position three can enhance the push-pull effect. In addition, it has been shown that photophysical properties, such as fluorescence, can be enhanced or quenched depending on the type and location of substituents.^{21,24,25}

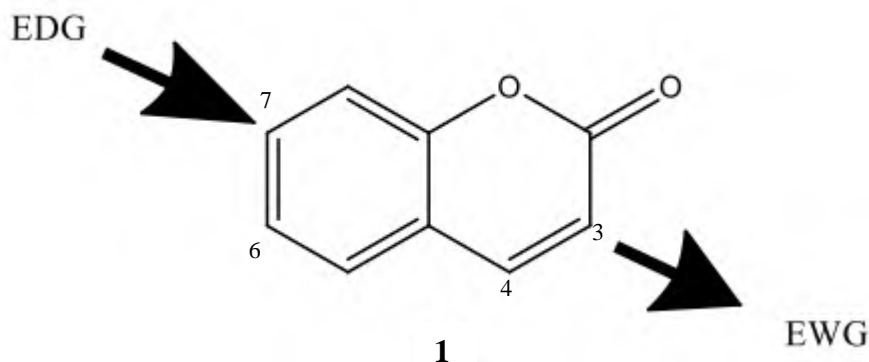


Figure 1.3: Illustration of an electron “push-pull” system on the coumarin backbone.¹⁷

1.2.1.3 Bindings sites

The binding site contains atoms which specifically interact with an analyte. Cations such as metal ions coordinate with oxygen, nitrogen, and sulphur, whereas anions such as halide ions interact with hydrogens (using hydrogen bonds, covalent bonds or abstraction of the hydrogen).^{11,12} In addition, pi-bonds as binding sites can contribute to the cationic species' binding process.

Binding sites such as triazole rings can interact with both anions and cations. A triazole ring, shown in **Figure 1.4**, is a five-membered ring containing three nitrogen atoms at positions one, two and three with a double bond between positions two and three. The ring also includes a carbon-carbon double bond between positions four and five.

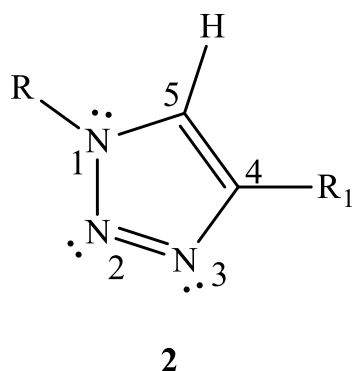


Figure 1.4: The structure of a triazole ring.

The hydrogen at position five of the triazole ring (**Figure 1.4**) can interact with an anion due to the partial positivity resulting from the ring's resonance. The nitrogens at positions two and three carry lone pairs of electrons capable of coordinating with metal cations.^{26,27} Hence the triazole binding unit can be used for the detection of both cationic and anionic species

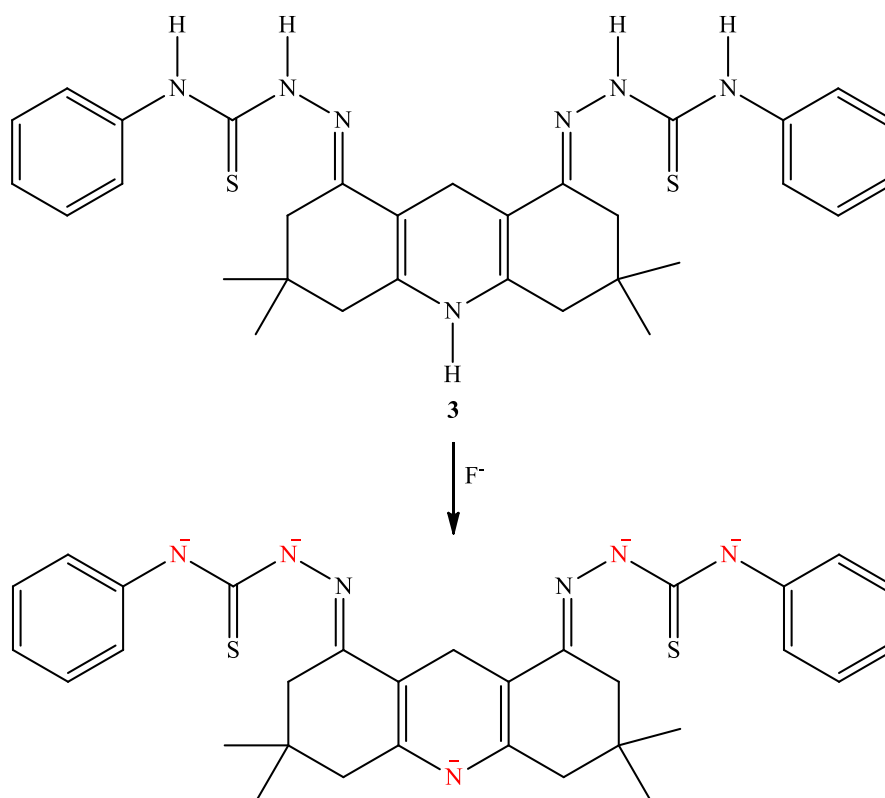
1.3 Uses of chemosensors

Chemosensors have seen relevance in several scientific fields over the years, and the list is growing. In this project, the application of chemosensors in the environment will be the main focus. This includes detecting and quantifying toxic ionic analytes (anions and cations).

1.3.1 Detection of anions

A wide variety of anions can be studied due to their environmental effects or biological importance. Most anions that are found in the environment include halides (e.g. F^- , Cl^- , and Br^-) and halide-containing ions (e.g. CF_3CO_2^- and ClO_4^-), cyanides (e.g. CN^- and SCN^-), sulphur-containing anions (e.g. HSO_4^- and SO_4^{2-}), phosphorus-containing anions (e.g. H_2PO_4^- and PO_4^{3-}), and nitrogen-containing oxoanions (e.g. NO_3^-).^{28–30} Some of these anions are also important in biosensing, such as halides, phosphates, nitrates, acetates, ascorbates, and citrates.³¹ Although some of these anions are important in living organisms and humans, an excess can be detrimental. Hence reliable methods that can detect and measure these ions are vital.

In a study by Ibanga Okon Isaac and his research team, chemosensor **3** was found to be able to detect fluoride ions (F^-) in acetonitrile. The interaction between F^- and sensor **3** could be observed by naked eye detection, UV-vis absorption, and fluorescence. ^1H NMR spectroscopic experiments showed the F^- ions abstracted hydrogens from the nitrogens to form a negatively charged nitrogen, indicated by red, as shown in **Figure 1.5**. The study concluded that the small size and high basicity of fluoride lead to the abstraction of the proton from **3** to induce the change in colour and observations in UV-vis, fluorescence and ^1H NMR spectra.³¹



*Figure 1.5: Interaction of chemosensor **3** with F^- via proton abstraction.*

1.3.2 Detection of cations

Some metal cations play a vital role in living organisms, and probably the most known example is iron in haemoglobin and myoglobin. However, iron can be toxic if in excess in the body, causing damage to the liver and heart and can cause neuroinflammation and Alzheimer's disease.³² Furthermore, metals such as lead inhibits the synthesis of the heme protein, causing a decrease in haemoglobin and affecting multiple body processes.⁵

Thus, the detection and quantification of these metal cations is important. The metal cations tested in this project includes: Zn^{2+} , Cd^{2+} , Hg^{2+} , Sn^{2+} , Pb^{2+} , Ag^+ , Fe^{2+} , Fe^{3+} , Bi^{2+} , Co^{2+} , Ni^{2+} , Cu^{2+} , Ca^{2+} , Al^{3+} , Na^+ , K^+ , Ba^{2+} , Cr^{2+} , Cr^{3+} , and Mg^{2+} .^{10,29,33–35}

In a study by Lei Wang and his team, a quinoline-based fluorescent chemosensor, **4**, was synthesised and confirmed to be able to selectively detect palladium ions in an aqueous solution even in the presence of competing ions. The interaction was found to be a 1:1 stoichiometry ratio between the sensor and Pd^{2+} , which was confirmed by mass spectroscopy. Up to 92.7% average sensor recovery was obtained during the real-world samples, showing the practical real-world application. Furthermore, the complex was completely reversible using EDTA as

the chelating agent.³⁶ The predicted complexation between **4** and Pd²⁺ is shown in **Figure 1.6**. Complexation occurred between the quinoline nitrogen and imidazole, forming a stable six-membered ring.

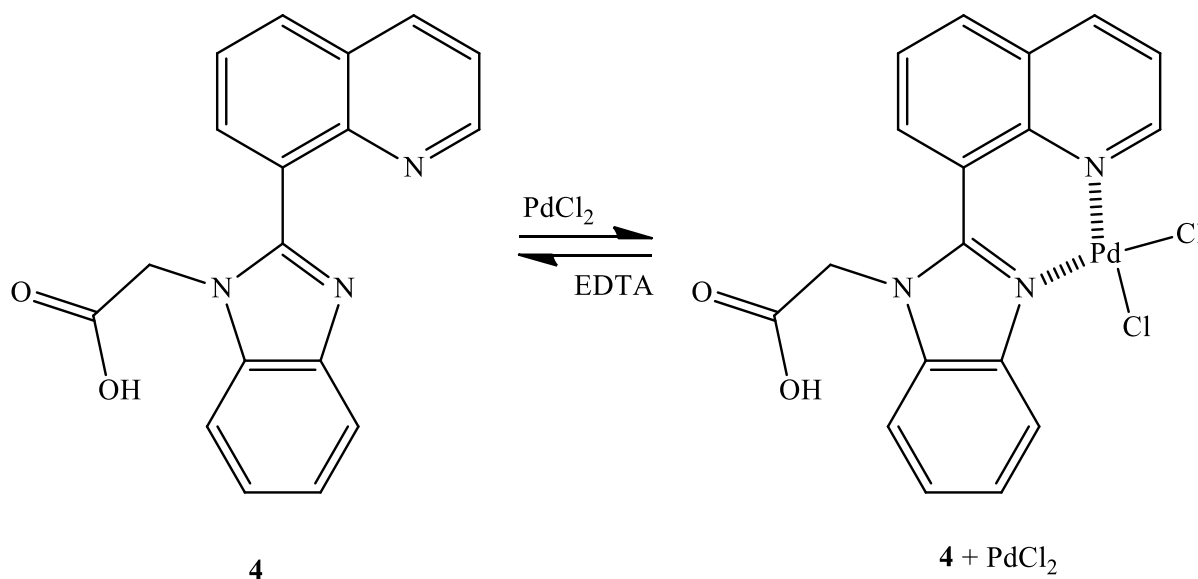


Figure 1.6: Quinoline-based fluorescent chemosensor **4** and the complex formed in the presence of PdCl₂.

1.4 Advantages of chemosensors

Chemosensors have the benefits of convenience, meaning the sample can be analysed on-site, giving a real-time response capable of being analysed, understood, and explained by the public. In addition, chemosensors also contain production advantages such as being safe to handle, low costs, and easy to synthesise at large scale. Chemosensors can be used in various solvents and can also be used on one-off-use paper probes. Chemosensors are highly selective, with high sensitivity and very low detection limits.^{28,36,38}

1.5 Importance of chemosensors

Metals play a vital role in our everyday lives. There is no escape from metals as they sustain life to aid in our daily lives. The problem comes in when the balance is disrupted. The effects of too much or too little can cause severe and irreversible damage.

Biological metals such as; Na, K, Mg, Ca, Fe, Zn, Mn, Cu, Co, Cr, Mo, Rb, Al, Ni, Ti, and Ba are present in the human body ranging from a few grams to a few micrograms.^{39–41} These metals are essential for normal cellular function, with each ion performing a specific function.

The concentrations of these cations are vital for normal function, as too much or too little can lead to health risks. Magnesium represents as much as 25 g in an average 80 kg person. However, abnormal concentrations of Mg^{2+} have been linked to health risks such as diabetes, hypertension, epilepsy, and Alzheimer's.^{38,41}

Non-biological metals such as mercury and cadmium can bioaccumulate in seafood and plants, which are part of the foods we eat, resulting in these metals accumulating in humans.⁸ Mercury poisoning can cause neurological, kidney, and heart damage and immunological, motor, reproductive and genetic disorders.^{42,43}

Thus, chemosensors can detect and quantify these metals to keep them below the recommended levels at locations close to labs and in remote locations where clean water is limited.

1.6 Types of chemosensors

Over the years, many types of sensors have been designed, synthesised, and used to detect different analytes. The detection mechanism can be used to classify different types of sensors:

- Piezoelectric sensors: a solid matrix (such as a supported polymer or a molecularly imprinted polymer) selectively interacts with a target analyte resulting in a mass increase that can be detected by a mass-sensitive device (such as quartz crystal microbalance).²⁵
- Chemomechanical sensors: In this type of sensing, effector molecules (such as hydrogels and peptides) can be triggered into changing their size upon exposure to specific analytes (such as cations).⁴⁴
- Electrochemical sensors: compounds that yield a change in the electrical conductivity in response to the presence of an analyte. The interactions can be detected by cyclic voltammetry.²⁵
- Photophysical sensors: These are colourimetric and fluorescence sensors that use UV-visible or fluorescent light changes to measure the interactions caused by a specific analyte.

This project's primary focus will be on using photophysical sensors to detect ionic species.

1.6.1 Colourimetric sensors

These chemosensors are based on changes in the compound's absorption properties in the UV and visible range of the electromagnetic spectrum. Changes in the absorption properties could

be both in the absorption band intensity, at a fixed wavelength, or in wavelength shifts measured by UV-vis spectroscopy.²⁵

Compound **5** is an example of a colourimetric chemosensor used to detect mercury with a detection limit of 4.65 μM and a limit of quantification of 14.08 μM . As seen in **Figure 1.7**, the sensor displayed a visible colour change from yellow to purple upon interaction with mercury. This colour change was accompanied by a gradual decrease of the band at 340 nm, while a new band was formed at 570 nm in the absorbance spectra. Due to these colour changes, this chemosensor could be used for “naked-eye” detection of mercury.⁴⁵

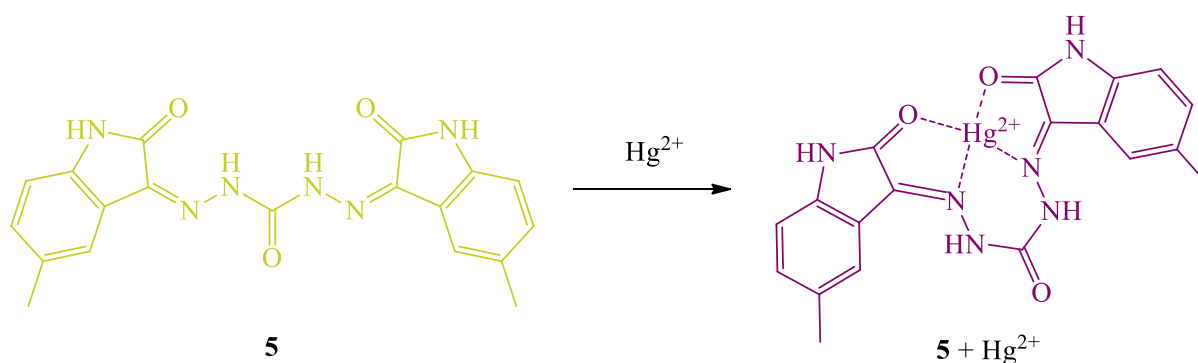


Figure 1.7: A colourimetric chemosensor, **5**, for detecting mercury.⁴⁵

1.6.2 Fluorescent sensors

These types of sensors are based on changes in a compound's intensity and wavelength upon interaction with the analyte. These changes can be observed using a fluorescent spectrometer.²⁵

H. Li and their team synthesised a fluorescent chemosensor, **6** (**Figure 1.8**), which had a weak fluorescence band at 550 nm. The fluorescence band shifted to 475 nm with increased intensity upon interaction with mercury ions. This interaction resulted in an increased quantum yield of chemosensor **6** from 0.0195 to 0.1895 with the addition of mercury.⁴⁶

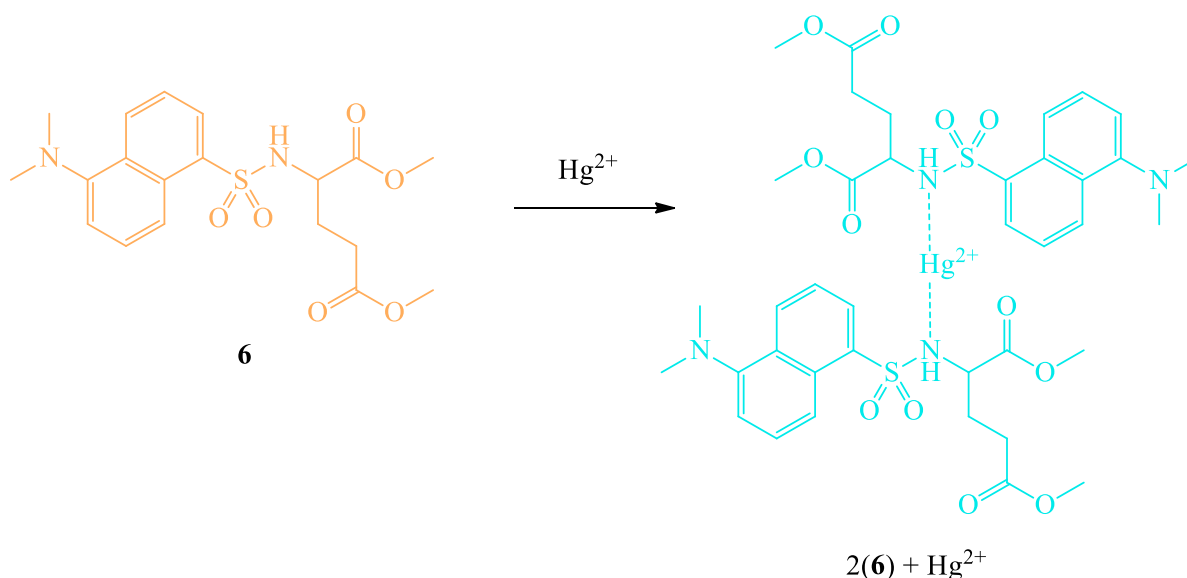


Figure 1.8: A fluorescent chemosensor, **6**, used to detect mercury. The sensor has a weak orange fluorescence which changes to a bright light blue upon adding mercury.⁴⁶

The benefit of this method is the inherent sensitivity of the fluorescence technique. Trace amounts of the sensor and analyte can be applied using this method.

1.6.3 Dual sensors

Dual sensors apply both colourimetric and fluorescent techniques, each with separate analytes without interfering with each other.

Yongjie Ding and his team synthesised a quinoline-based chemosensor, **7**, capable of selectively detecting aluminium using fluorescent techniques and iron(II) using colourimetric methods (**Figure 1.9**). Aluminium enhanced the emissions of the quinoline-based sensor, which could be related to the amount of aluminium present. When the quinoline-based chemosensor was excited at 350 nm, the sensor showed a weak emissions band at 520 nm (attributed to the C=N isomerisation). In the presence of aluminium, the band shifted to 545 nm, and the emission was enhanced. The enhancement of their sensor was confirmed to be caused by the chelation-enhanced fluorescence (CHEF) effect, which inhibited the C=N isomerisation effect, according to the paper.⁴⁷

The chemosensor, **7**, exhibited a strong absorption band at 344 nm. In the presence of Fe^{2+} , the primary absorption band was red-shifted to 363 nm with a new band at 670 nm, coinciding with the visual colour change from pale yellow to dark green. The absorption bands were

attributed to the $n-\pi^*$ transitions from the nitrogen and oxygen atoms to ligand π^* orbitals of the ligand.⁴⁷

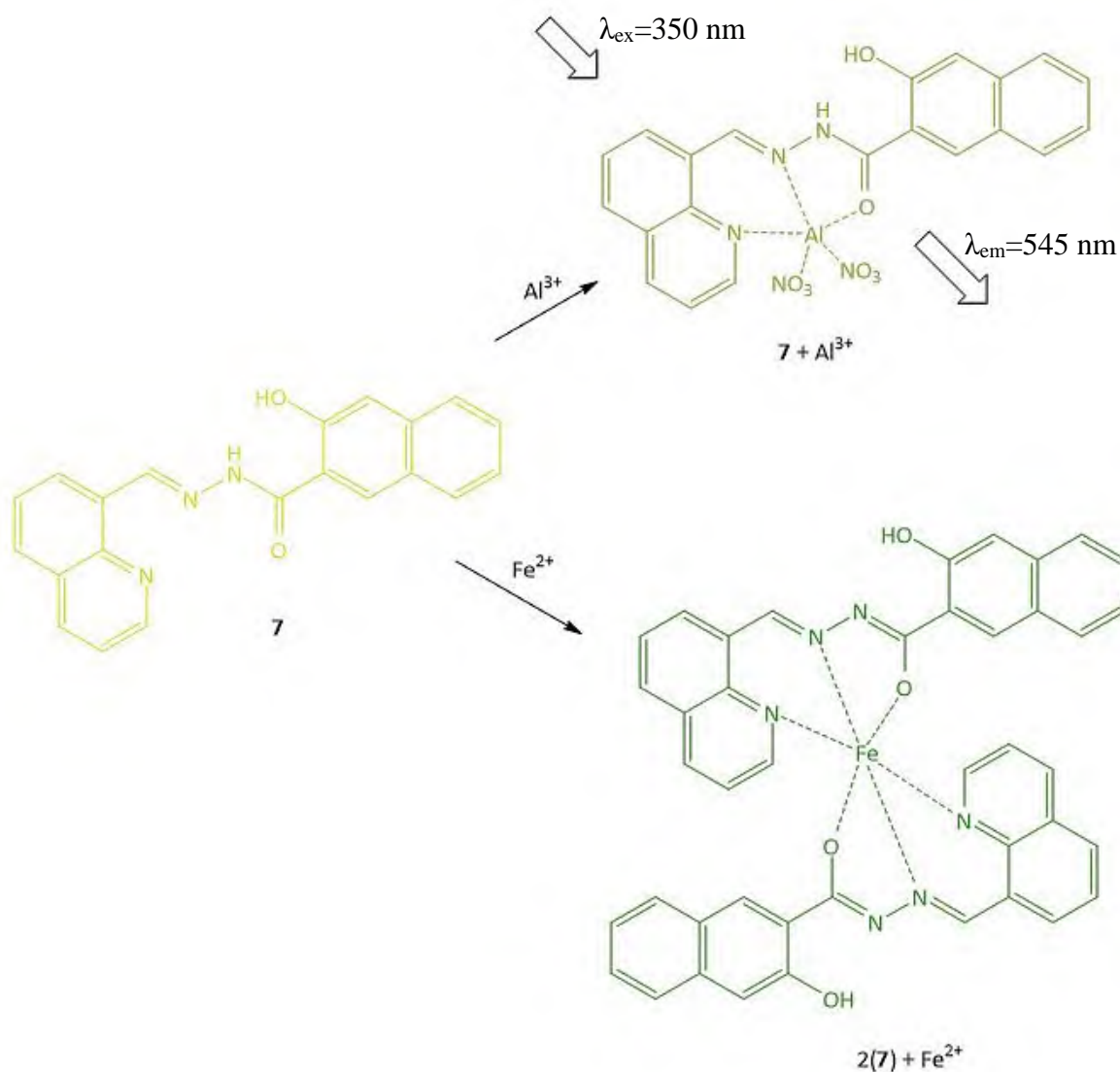


Figure 1.9: A chemosensor, **7**, with a colourimetric and fluorescent component.⁴⁷

This type of dual sensor provides the benefit of detecting two analytes at the same time.

1.6.4 Ratiometric sensors

Ratiometric sensors are types of sensors that use a band on the electromagnetic spectrum of a non-complexed compound and compare it to a new band developed due to the formation of the complex. The ratio between the newly formed band and the initial band is used to determine the presence and concentration of an analyte. Furthermore, if the original band stays constant and the newly formed band change in intensity, it is called a “single-signal pattern”, However,

if both bands change in the presence of the analyte, it is then called a “two-signal pattern” as shown in **Figure 1.10**.⁴⁸

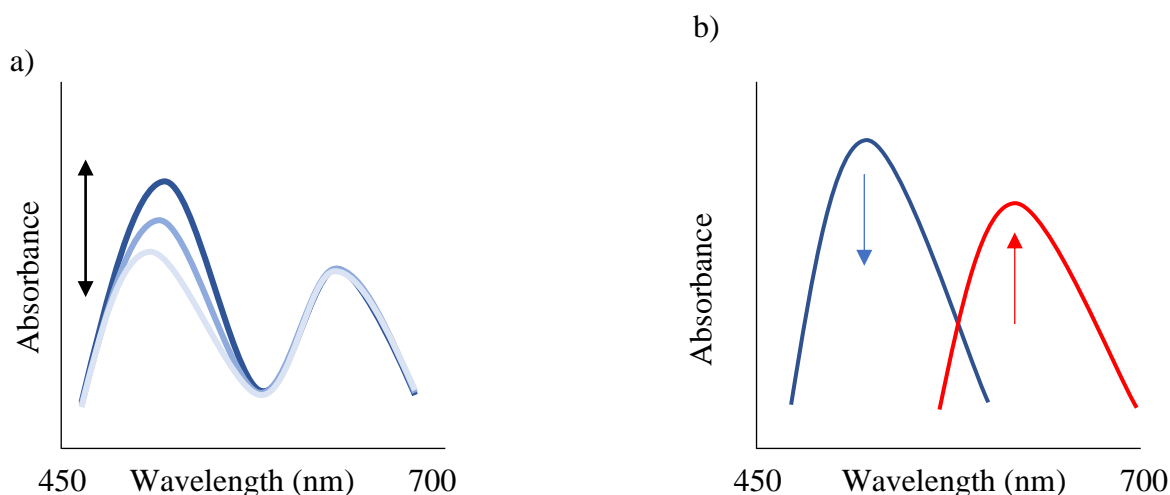


Figure 1.10: A graph depicting the absorbance spectrum of a) “single-signal pattern” and b) “two-signal pattern” ratiometric sensor.

1.6.5 “On-off” and “off-on” sensors

“On-off” sensors initially have strong photophysical properties; however, when interacting with an analyte, the sensor can completely lose its photophysical properties. On the other hand, an “off-on” sensor shows low photophysical properties. However, the sensor gains these properties in the presence of a specific analyte, resulting in a detectable spectrum capable of being analysed.

K. Muthu Vengaiyan et al. proposed an “on-off-on” type chemosensor that was selective for Hg^{2+} . The chemosensor **8**, shown in **Figure 1.11**, completely loses its fluorescence in the presence of Hg^{2+} and regains its fluorescence by adding S^{2-} . The observed reversibility was attributed to the higher affinity Hg^{2+} has for S^{2-} to form HgS .⁴⁹

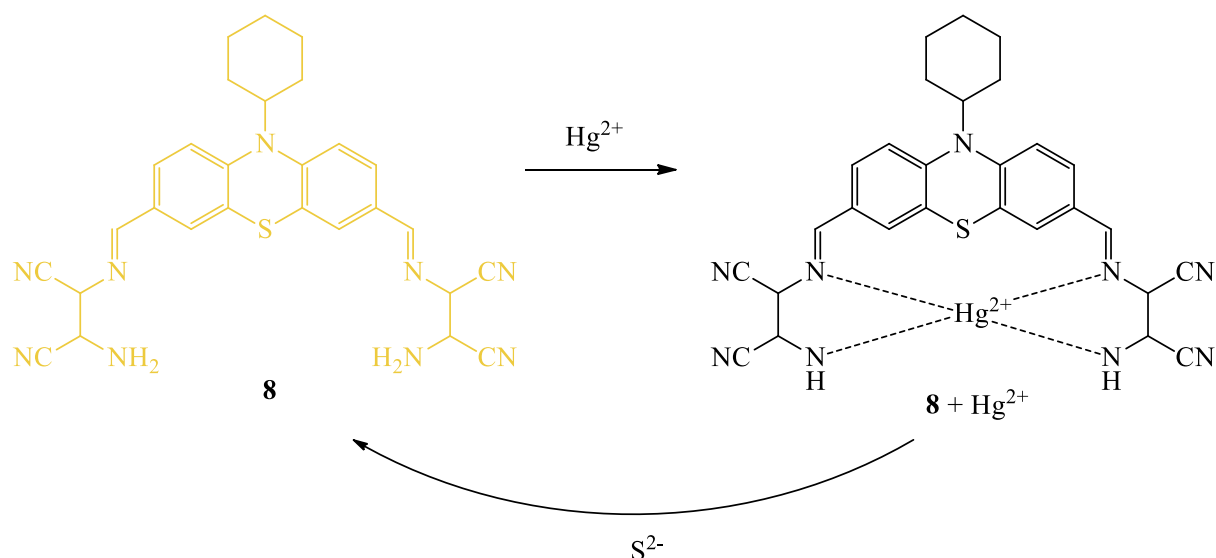


Figure 1.11: “On-Off-On” chemosensor, **8** used for detecting Hg^{2+} , quenched, the complex is reversed adding S^{2-} , fluorescence regained.

These on-off/off-on types of sensors benefit from the signal being present or not. The sensors that exhibit a “turn-on” response upon binding with metal ions are less sensitive than the “turn-off” sensors due to the lack of a background signal.⁴⁹

1.7 Photophysical properties

Photophysical properties of chemosensors can be used to determine the presence or absence of an analyte. These properties include measurable techniques such as the absorption and emissions spectra, the fluorescence quantum yields, the fluorescence decay times, molecular brightness, photostability, and photo-switching.^{50,51} These measurable variables can be used to determine the amount of an analyte present in a sample.

1.7.1 Absorption properties

The ability of a compound to absorb electromagnetic radiation is measured as absorptivity. In UV-visible spectroscopy, absorptivity is measured in both the UV range (190 nm – 350 nm) and the visible range (300 nm – 1100 nm).⁵² The absorption of UV or visible light is governed by Lambert-Beer’s Law: “When a beam of monochromatic radiation passes through homogeneous absorbing media, the rate of decrease of radiation intensity with the thickness of absorbing medium is proportional to the intensity of the incident radiation.”⁵³ In mathematical terms

$$A = \frac{I_0}{I}$$

Where A is the absorbance and I_0 is the incident radiation, and I is the transmitted radiation.

A shift in the chemosensor's band wavelength (λ_{\max}) is observed during complexation between an analyte and a chemosensor. Possible shifts of the λ_{\max} are shown in **Figure 1.12**. The hypsochromic shift is also known as a blueshift due to the shifting of λ_{\max} to shorter wavelengths. In contrast, bathochromic shifts are also known as red-shifts due to the shift of λ_{\max} to longer wavelengths. Hyperchromic and hypochromic is a shift in the intensity of λ_{\max} .⁵³

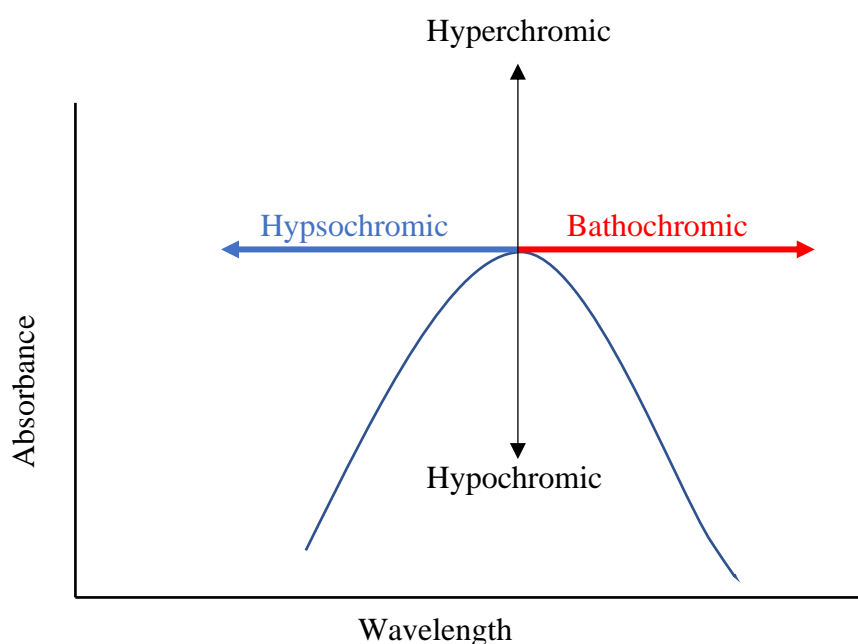


Figure 1.12: Shifts observed in absorption spectra.

Hafiz Muhammad Junaid and co-workers reported various chemosensors that can detect a range of different anions. One of these sensors could detect acetate and bicarbonate in dimethyl sulfoxide (DMSO). The 2-((E)-((4-chloro-3-(trifluoromethyl) phenyl)imino)methyl)-4-((E)-naphthalene-1-yl diazenyl)phenol, **9**, chemosensor has a pale-yellow colour which has a λ_{\max} at 380 nm. However, in the presence of acetate, the complexation induces a bathochromic shift of 100 nm, resulting in the λ_{\max} at 480 nm leading to the formation of a red complex.^{54,55}

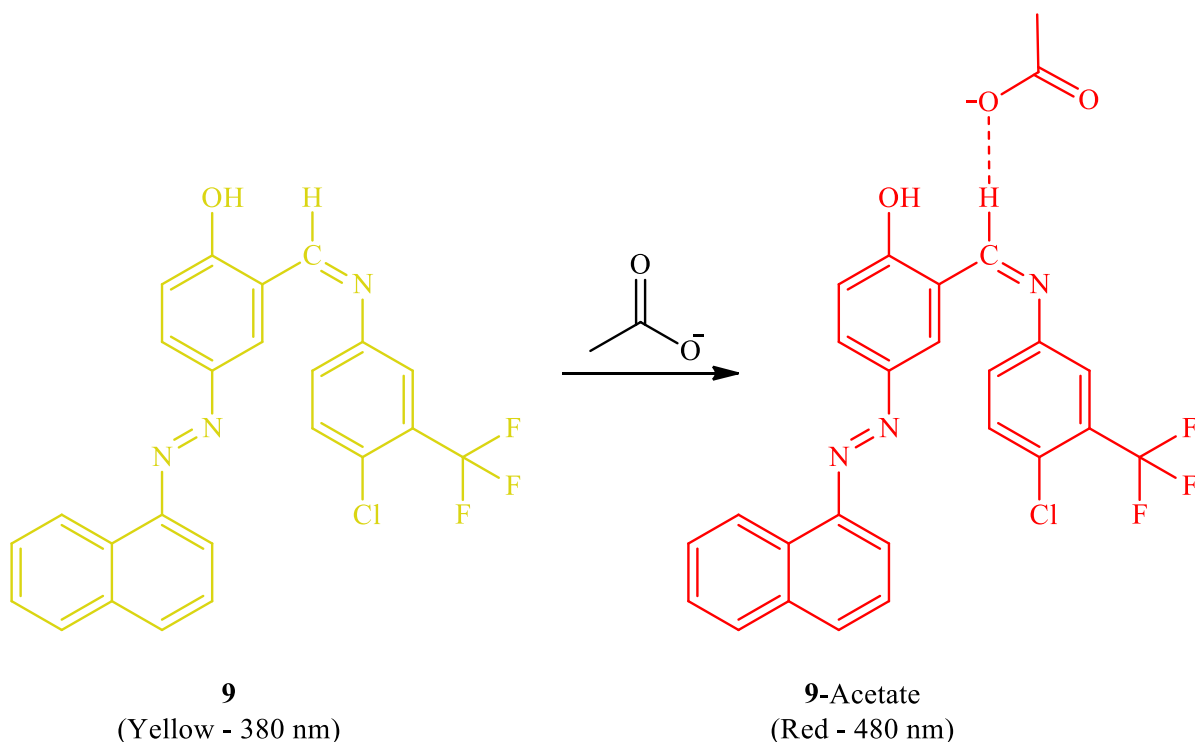


Figure 1.13: Chemosensor, **9**, used for naked-eye chemosensing of acetate in DMSO.⁵⁴

1.7.2 Emissions properties

Emission properties are determined by the ability of a compound to absorb radiation which is then emitted at a different wavelength. The absorbed radiation can excite a compound from the ground state (S_0) to a subsequent excited state (e.g., first excited state S_1). During excitation, an electron from the ground state is excited from the highest occupied molecular orbital (HOMO) to the lowest unoccupied molecular orbital (LUMO).^{53,56}

The absorbed energy can be released either via non-radiative means, shown in **Figure 1.14**, or radiative means, shown in **Figure 1.15**. Non-radiative relaxation releases the absorbed energy through vibrations, heat, or transference. In **Figure 1.14**, an excited electron returns to the ground state through internal conversion (IC).^{53,56}

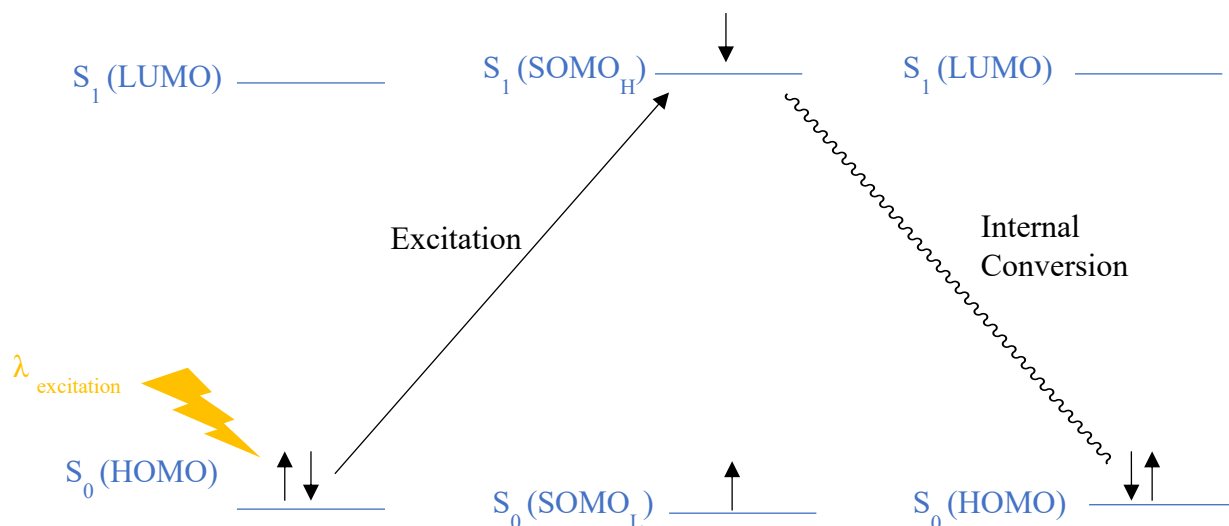


Figure 1.14: A energy diagram depicting the non-radiative relaxation of an excited electron.

Radiative relaxation entails releasing the absorbed energy as a photon, known as fluorescence and phosphorescence. In fluorescence, the electron returns directly to the ground state by emitting light at a specific wavelength ($\lambda_{\text{emission}}$), as seen in **Figure 1.15** below.^{53,56}

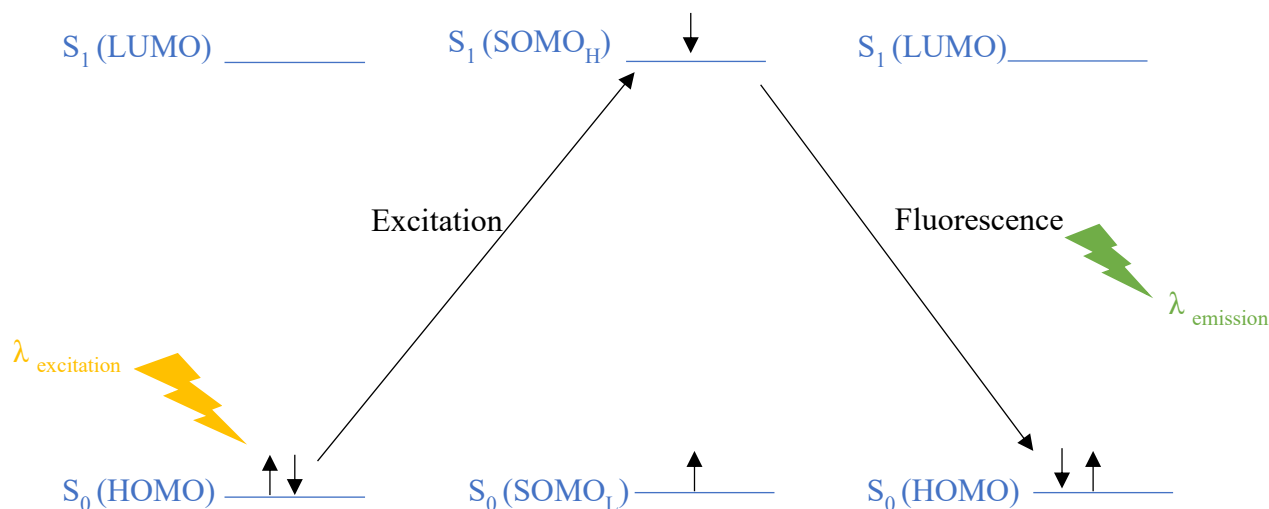


Figure 1.15: A energy diagram depicting the radiative relaxation of fluorescence.

Phosphorescence (**Figure 1.16**) is a radiative process in which the excited electron first undergoes intersystem crossing by which the electron exists in the triplet state. The electron in the triplet state has to change back to its normal state, which is not as immediate as fluorescence, hence the energy is released as a photon ($\lambda_{\text{emission}}$) over time.^{53,56}

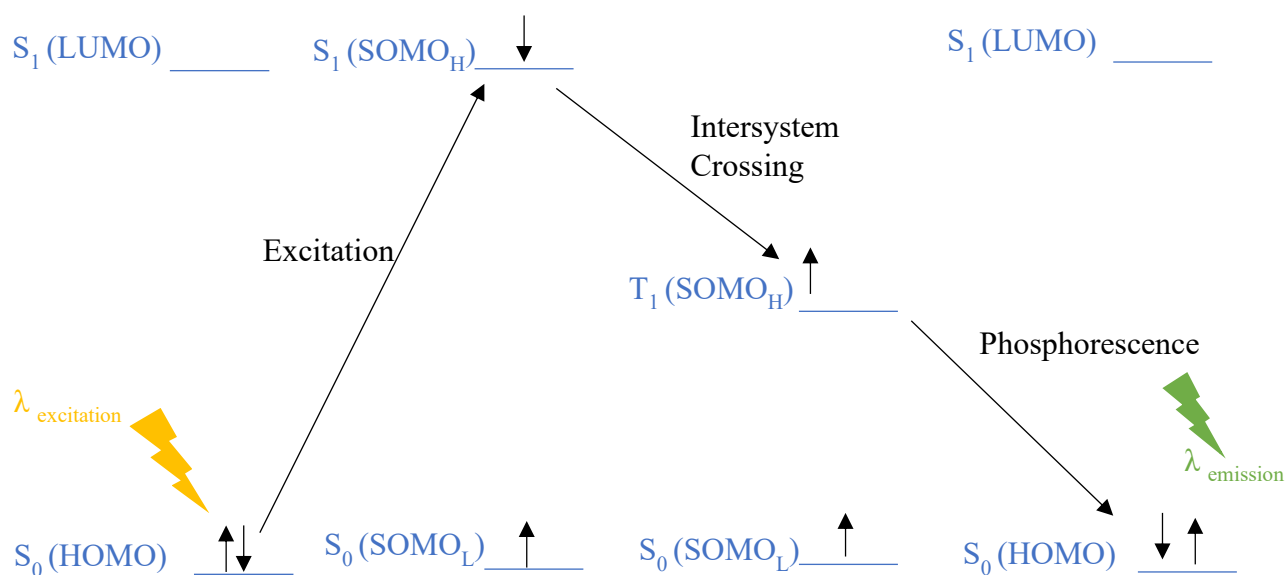


Figure 1.16: A energy diagram depicting radial relaxation of phosphorescence.

Fluorescence spectroscopy or fluorimetry is a technique which measures the emissivity, how much radiation energy is emitted by the compound.⁵²

Fluorescence can be induced or quenched through several photochemical processes, namely, photo-induced electron transfer (PET), energy transfer (ET), proton transfer (PT), Hydrogen atom transfer (H-a), photodissociation (DIS), valence photoisomerisation (VI) and photo-substitution (sub) to name a few.⁵⁶

1.7.2.1 Photo-induced Electron Transfer (PET)

Photoexcitation gets electrons moving from the ground state to an excited state. PET systems donate the electron from the excited state to an acceptor in the ground state, as shown in **Figure 1.17**.⁵⁷ The electron, from a donor site, is excited by absorbing light, thus moving from the HOMO to the LUMO. In close proximity, an acceptor site donates a ground state electron while taking the excited electron. In an intermediate complex (*Donor⁻Acceptor⁺), shown in **Figure 1.17**, the donor site is excited with a negative charge, and the acceptor site is positively charged. Thus, a PET active system is non-fluorescent.^{58,59}

However, when an analyte binds or disrupts the acceptor site, it can disrupt the PET active system, and therefore fluorescence is induced, hence PET is inactive, known as an on-off system.

The reverse is also possible. In an off-on PET system, the complexation of an analyte can induce a PET-active system by which the analyte provides the electron.

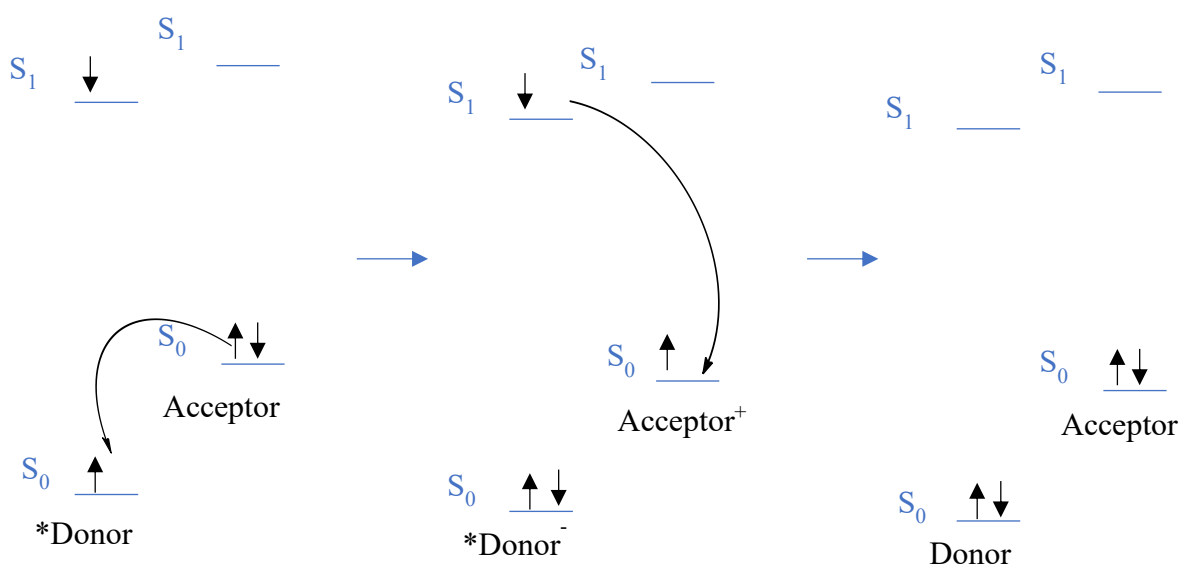


Figure 1.17: PET system showing the transference of the electron between the donor site and the acceptor site.⁵⁷

Xiang and co-workers have synthesised a novel Schiff base fluorescent chemosensor, **10**, which could bind selectively to zinc (II) in a DMSO/H₂O mixture. The free sensor has weak fluorescence due to the active PET system between the amine and imine, as shown in **Figure 1.18**. Furthermore, when the chemosensor complexes with zinc, the PET system is disrupted and cannot occur. Hence fluorescence occurs by releasing a photon with a wavelength of 506 nm. The limit of detection (LOD) for this chemosensor was 39 mM with an association constant of $1.18 \times 10^5 \text{ M}^{-1}$.⁶⁰

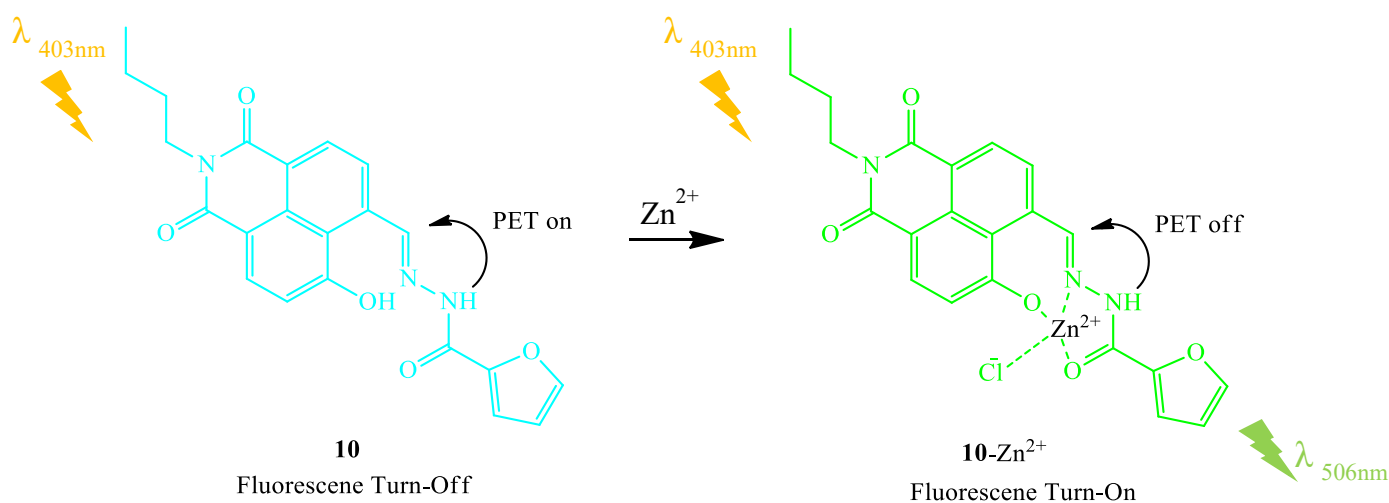


Figure 1.18: Fluorescent Schiff base chemosensor, **10**, showing on-off PET system.⁶⁰

1.7.2.2 Energy Transfer (ET)

Two mechanisms can be considered in ET, namely, the Dexter exchange and the Coulomb-based Förster resonance energy transfer (FRET) mechanisms.

1.7.2.2.1 Dexter exchange

The Dexter exchange mechanism involves the transfer of electrons between an excited donor and an acceptor in the ground state. The transference of electrons occurs through a collision between the donor and the acceptor; therefore, the distance between the two species plays a significant role, less than 10 Å. In **Figure 1.19**, a Dexter exchange mechanism is shown. The donor absorbs light which excites an electron, and the excited molecule collides with an acceptor in the ground state. During the collision, the excited electron is transferred to the LUMO of the acceptor, by which a ground-state electron is transferred back to the ground state of the donor.^{56,59,61} The Dexter interaction is usually associated with quenching of the fluorescence.⁵⁹

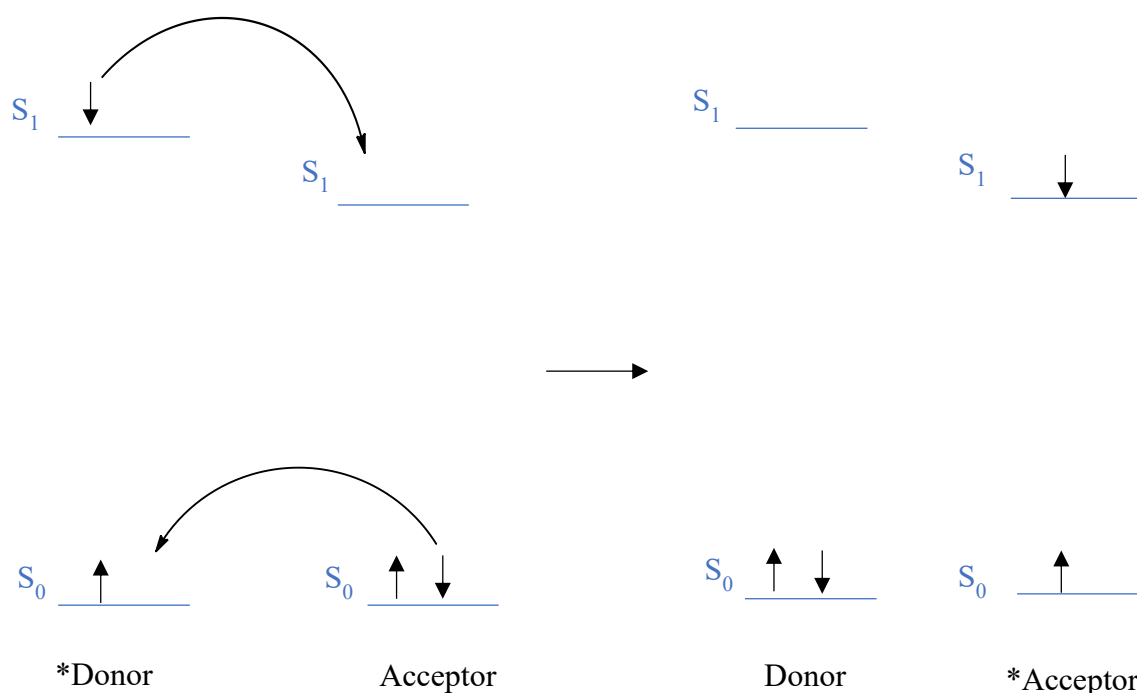


Figure 1.19: Dexter exchange diagram showing the double electron transfer between the excited donor and an acceptor in the ground state.

Electron transfer intermediates form during collisions and is seen as complexes, excimers and exciplexes. These intermediates only exist in the excited state and decompose when returning

to the ground state. Excimers are complexes that contain two of the same unit, whereas exciplexes consist of two different units (**Figure 1.20**).⁵⁶

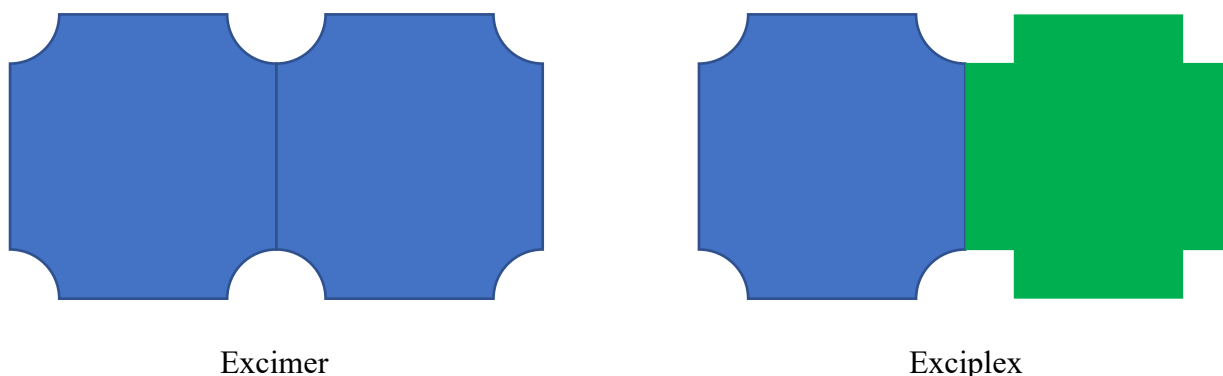


Figure 1.20: Illustration of the excimer and exciplex intermediates.

1.7.2.2.2 Förster Resonance Energy Transfer (FRET)

FRET transfers energy from an excited donor site to a ground-state acceptor.⁶² FRET is named after Theodor Förster. He proposed the equation to quantify the electronic excitation transfer efficiency from an energy donor to an acceptor back in 1948. FRET is a non-radiative process in which energy is transferred through long-range dipole-dipole interactions between an excited donor site and an acceptor site linked together by a non-conjugated spacer. **Figure 1.21** shows the FRET system in which an excited donor site relaxes back to the ground state. In turn, without releasing a photon, the energy is transferred to an acceptor in the ground state through long-range dipole-dipole interactions and Coulombic force. Resulting in a ground state donor and an excited state acceptor site.^{62–64}

FRET systems have three main characteristics:^{62–64}

1. Distance plays a significant role in FRET systems, in which a donor and acceptor site has a distance between 10 – 100 Å.
2. A significant overlap between the acceptor site's absorption spectrum and the donor site's emission spectrum is required.
3. Lastly, the donor and acceptor site must have an appropriate orientation for dipole-dipole interaction.

FRET is a distance-dependent energy transfer process. FRET-based fluorescent chemosensors display a significant sensitivity to the environment on and around the chemosensors.⁶⁴

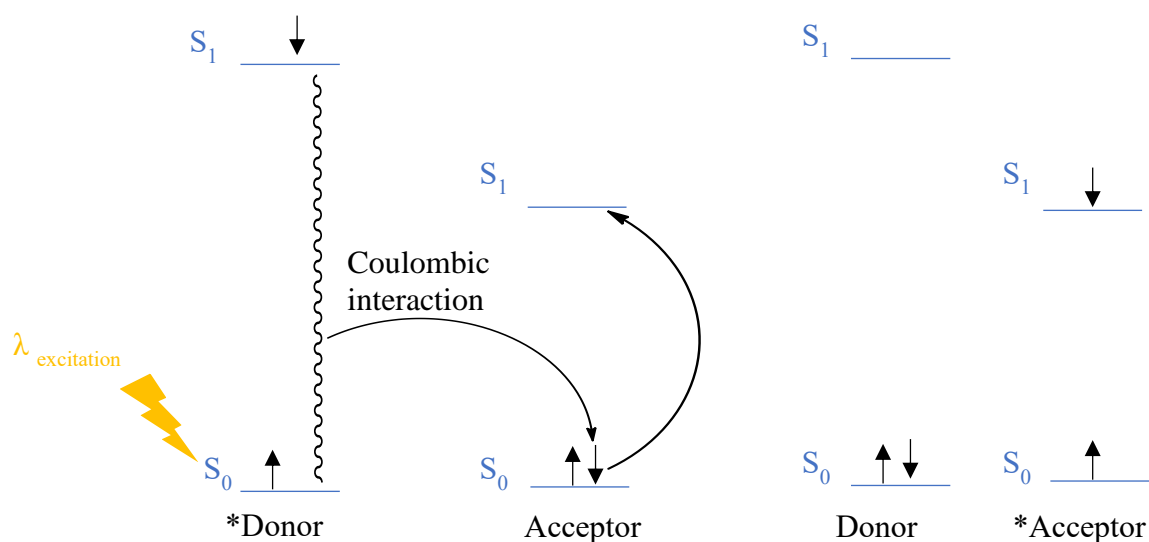


Figure 1.21: FRET system showing an excited donor site transferring energy through Coulombic interaction to an acceptor site in the ground state, resulting in a donor site and an excited acceptor site.

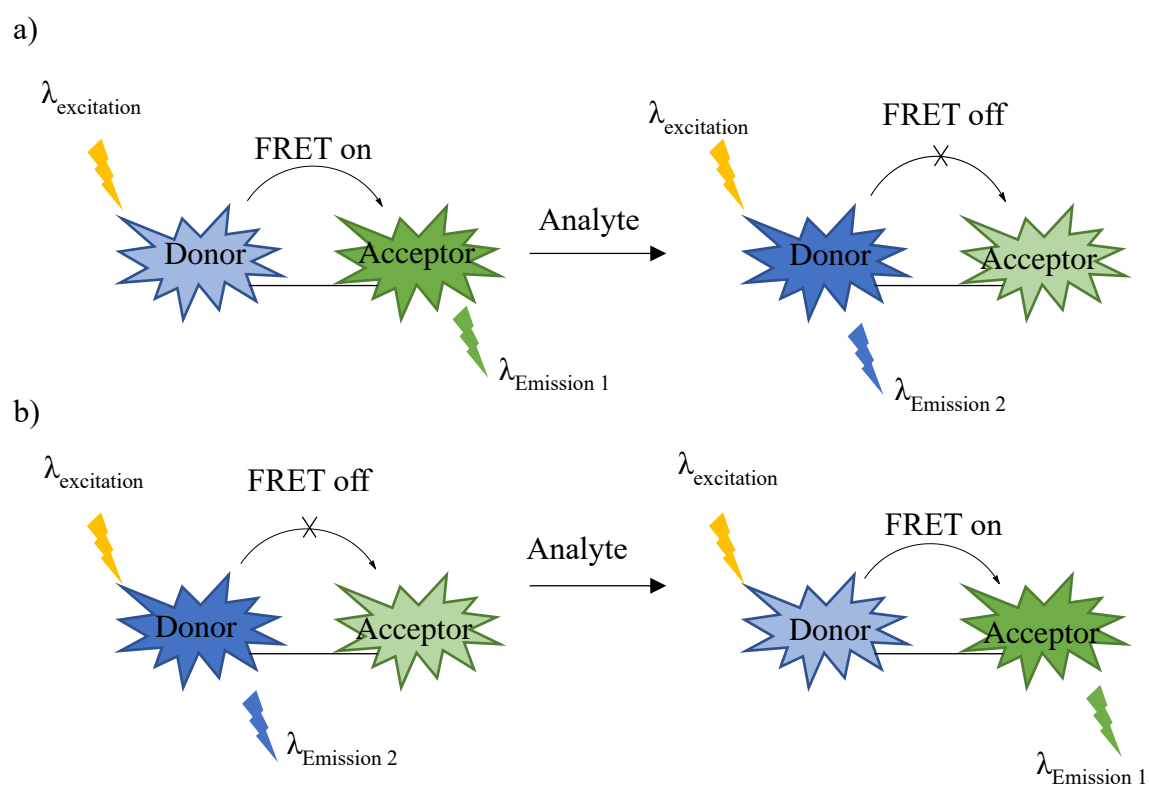


Figure 1.22: FRET a) on-off and b) off-on systems.⁶⁴

The on-off FRET system is illustrated in **Figure 1.22 a**); in this system, the donor site is excited, which in turn transfers the energy to the acceptor site, releasing a photon to return to the ground state. When an analyte complexes with a compound, the FRET system is broken, which stops the transference and allows the donor site to emit a photon at a different wavelength.

Off-on FRET system is illustrated in **Figure 1.22 b**); in this type of system, the complexation of an analyte allows the transference, which switches the FRET system on.

Luling et al. reported on a chemosensor, **11**, which contains a quinoline– benzothiazole-based donor and rhodamine-based acceptor (**Figure 1.23**). This compound complexed selectively with Cd^{2+} . The chemosensor had an excitation wavelength of 360 nm, resulting in a strong emission at 470 nm from the donor, quinoline–benzothiazole. In this state, the FRET system is off. It was predicted that the rhodamine acceptor site exists in a spirolactam form which prevents the emission of the acceptor at 585 nm.⁶⁴

In the presence of Cd^{2+} , a new complex is formed, as shown in **Figure 1.23**. The complex resulted in a new emission band at 585 nm. The complexation of Cd^{2+} opened the spirolactam of the rhodamine moiety, which allowed for the FRET system to occur between the quinoline–benzothiazole, donor, and rhodamine acceptor. The **11**- Cd^{2+} complex was confirmed with single-crystal X-ray analysis, which showed the six-coordinate Cd^{2+} binding centre. The ratio of $\frac{I_{585}}{I_{470}}$ in emission intensity displayed a linear relationship with the increase of Cd^{2+} concentration (between 0 - 9.5 mM).⁶⁴

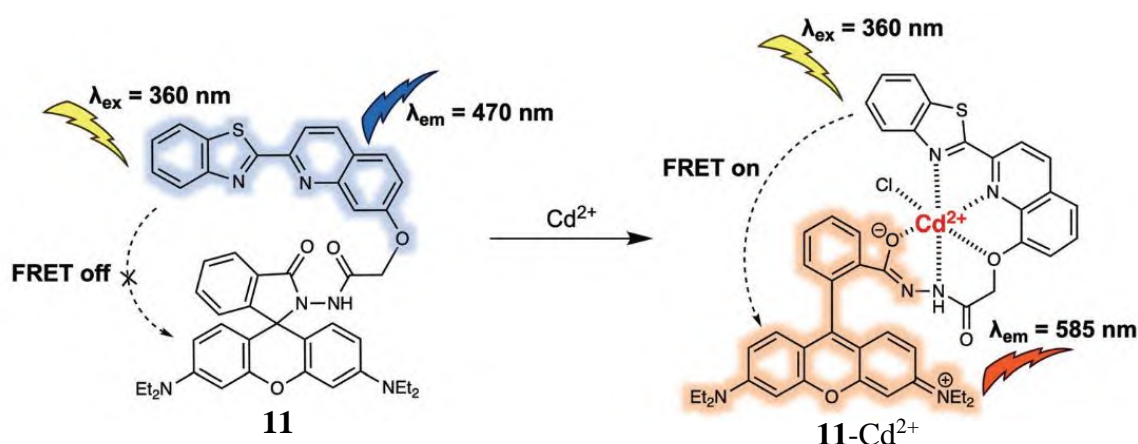
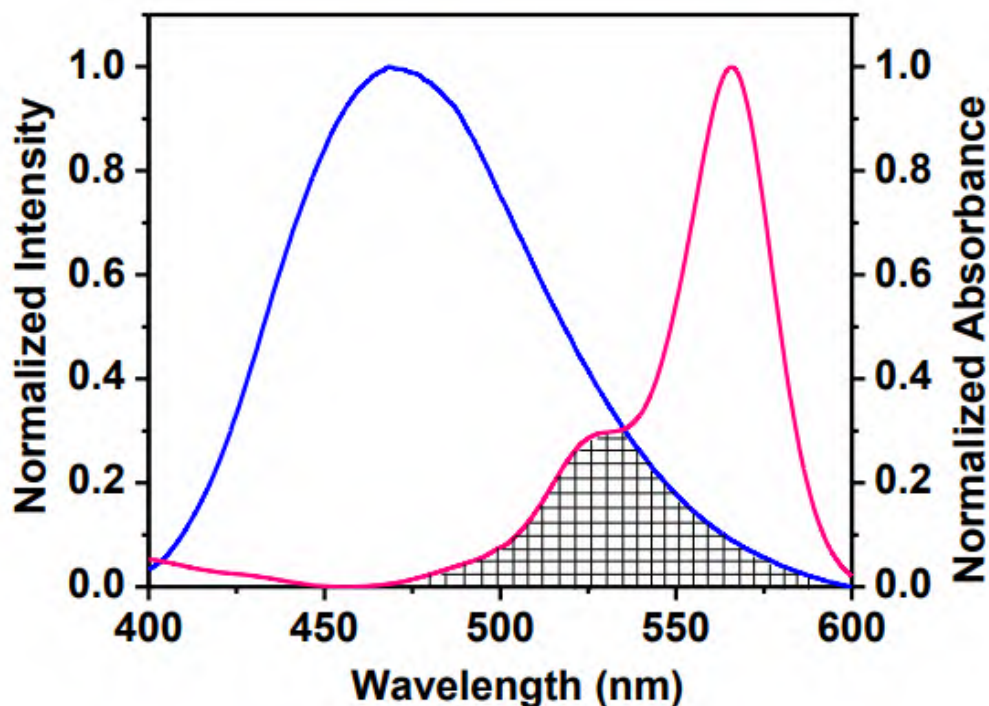


Figure 1.23: The off-on FRET system in chemosensor **11**, which contains a quinoline–benzothiazole, donor site, and the rhodamine as acceptor site.⁶⁴

The FRET system requires a spectral overlap between the donor and acceptor, which was observed in chemosensor **11**. The quinoline-benzothiazole donor site emissions spectra overlapped with the rhodamine acceptor's absorbance spectra, as seen in **Figure 1.24**.



*Figure 1.24: The spectral overlap of quinoline-benzothiazole donor emission (blue line) and rhodamine acceptor absorbance (pink line) of **11**.⁶⁴*

1.7.2.3 Proton transfer

Photochemical proton transfer is observed in response to a considerable change in the acidity or basicity of organic compounds during photoexcitation. During excitation, redistribution of electronic density in the molecule is observed, transition into a singlet excited state; this promotes the redistribution of protons.⁵⁶

Proton transfer reactions can be divided into two main classes: intramolecular and intermolecular proton transfer.

In intramolecular proton transfer, the proton donor site and the proton acceptor site are in the same compound and often directly connected through a hydrogen bond, as shown in **Figure 1.25**. In this method, the proton transfer does not necessarily result in the formation of charged species. It is sometimes considered hydrogen atom transfer due to similarities to keto-

enol tautomerisation. In addition, the process does not depend on the involvement of the solvent.⁶⁵

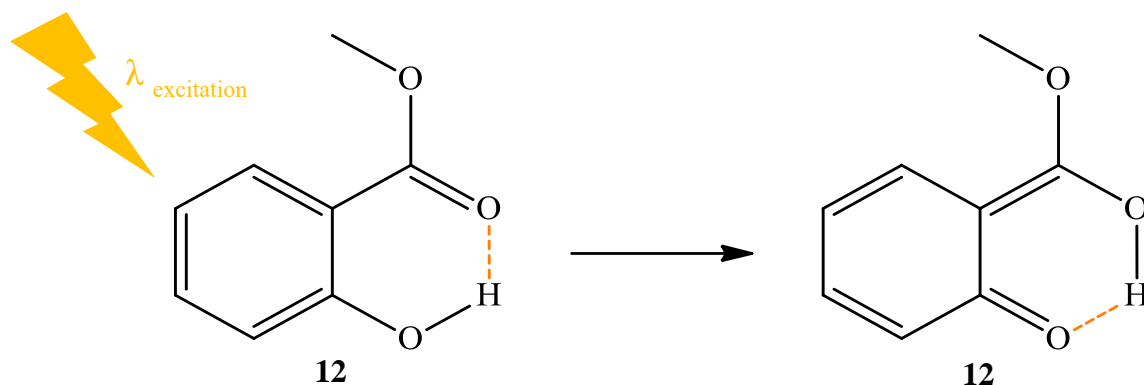


Figure 1.25: Intramolecular proton transfer through hydrogen bonding in compound **12**.⁶⁵

In the intermolecular proton transfer, the proton is transferred either to an external acceptor, acting as an organic base, or to the solvent. This proton transfer can result in the formation of ion pairs. Therefore, the transfer is strongly encouraged by the solvent.⁶⁵

Jin et al. worked on chemosensor **13**, which demonstrated intermolecular proton transfer properties in acetonitrile in the presence of fluoride anions (**Figure 1.26**).³⁰ The colourimetric signalling chemosensor was extensively collaborated with computational chemistry to confirm the deprotonation.

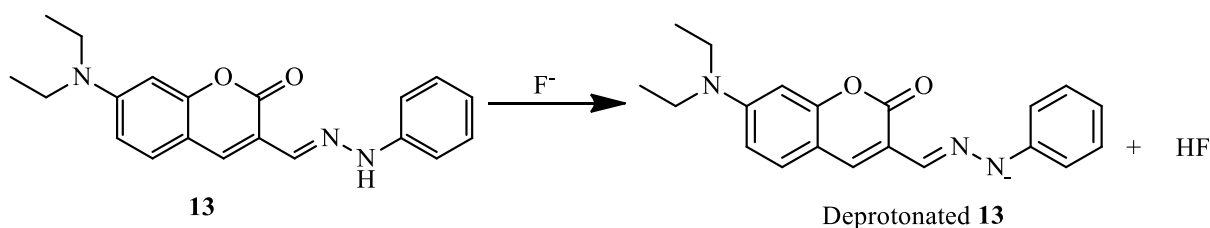


Figure 1.26: Intermolecular proton transfer in the presence of F^- in acetonitrile as solvent.³⁰

1.7.2.3.1 Excited state intramolecular proton transfer (ESIPT)

ESIPT is a relatively new area of research⁶⁶, and it is used to describe the transference of a proton in an excited compound. ESIPT is an ultrafast process in which the transformation from normal form (ground state form) to tautomer form (excited state form) will undergo a four-level photocycle process shown in **Figure 1.27**.⁶⁷

Excitation of a compound induces an electron density shift away from a proton donor group (functional groups such as -NH, -OH). In the presence of a basic proton acceptor (functional groups such as $>\text{C}=\text{N}-$, $>\text{C}=\text{O}$), ESIPT can occur, and the photon is transferred. After ESIPT, the excited state relaxes through radiative or non-radiative relaxation as the tautomer reverts to its normal form in the ground state through reverse proton transfer. The proton donor and proton acceptor can either be independent or covalently linked moieties for inter- and intramolecular excited state proton transfer.⁶⁶

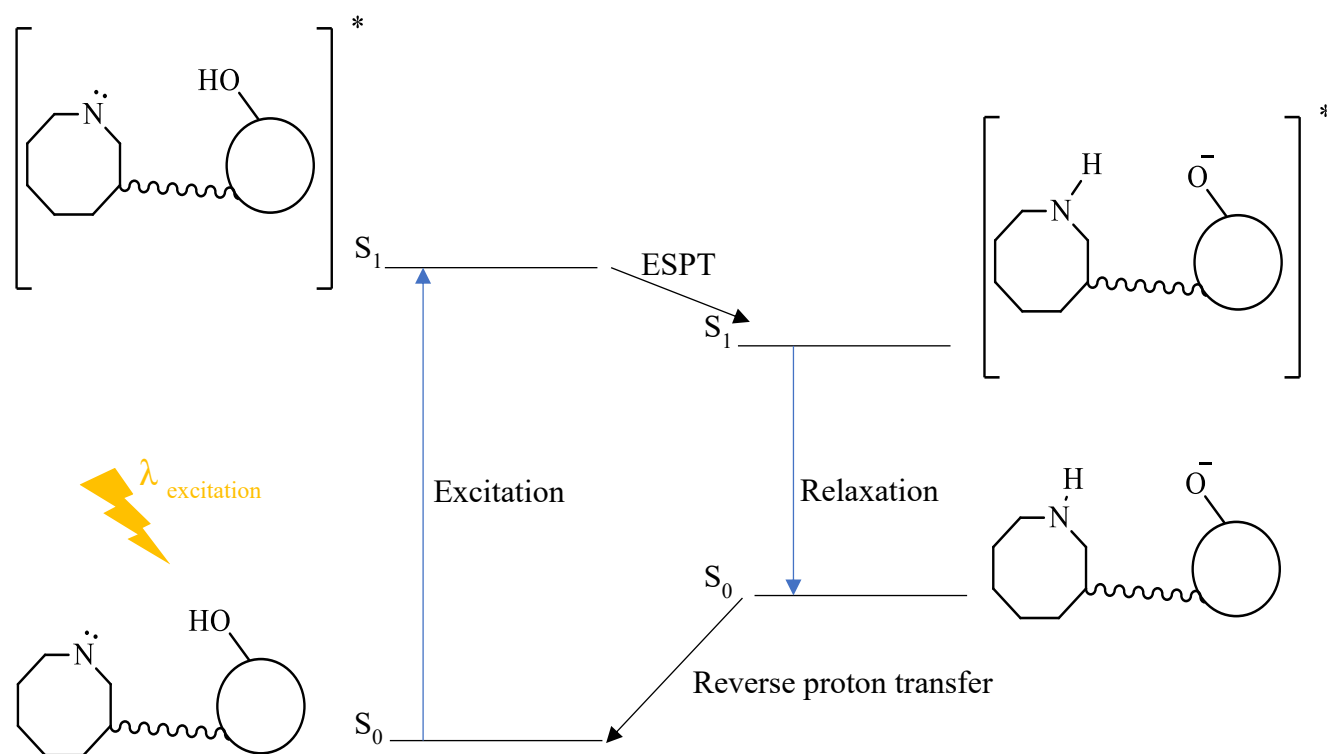


Figure 1.27: Four-level ESIPT cycle showing the transference of a proton in the excited state and deprotonation to return to the ground state.⁶⁶

In 2022, Riya Bag and co-workers published a benzimidazole-based ESIPT chemosensor, **14**, capable of detecting Cu^{2+} in the nanomolar range (28.5 nM) in a 90% aqueous solution. The quantum yields drastically decreased from 0.237 for the free chemosensor to 0.028 for the Cu^{2+} complex. The free chemosensor absorbed at 327 nm and emitted at 474 nm, which contributed to the four-level ESIPT cycle. Cu^{2+} interrupts the cycle due to the location of the binding site (**Figure 1.28**); thus, no emissions were observed for the complex. Real-world studies were also conducted, which produced promising results indicating that **14** can be used efficiently for groundwater samples and biological cell lines.⁶⁸

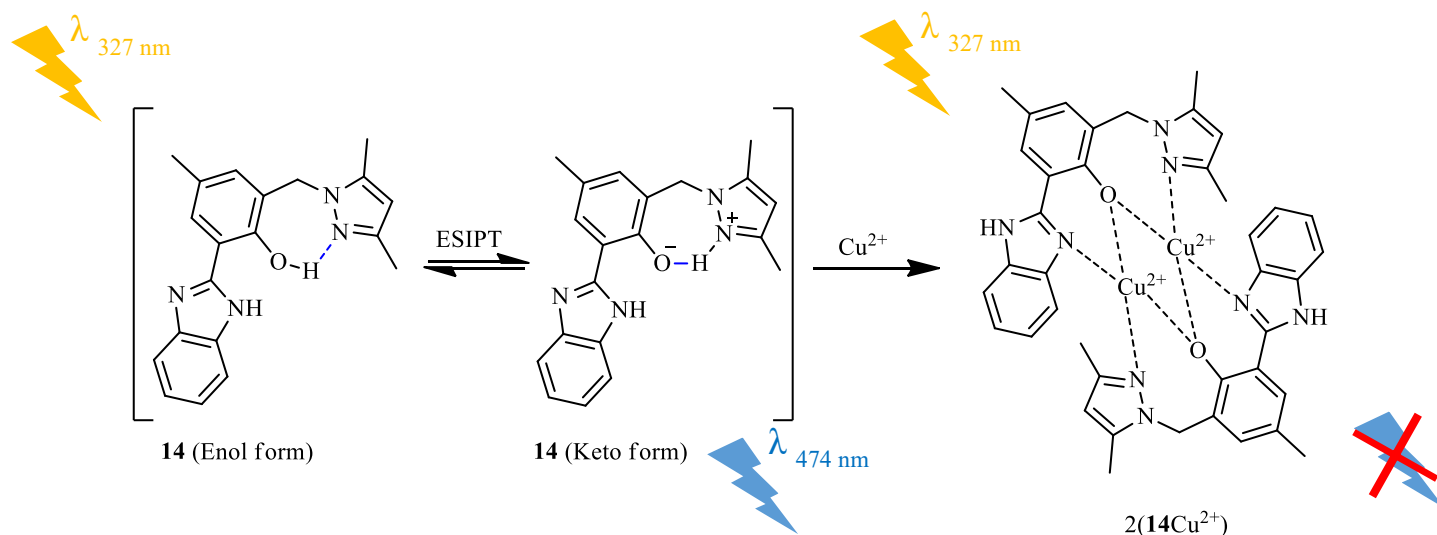


Figure 1.28: Benzimidazole-based ESIPT chemosensor, **14**, capable of detecting Cu^{2+} . The enol and keto forms, with the hydrogen bond for each, are shown.

Herein various chemosensors will be synthesised and tested for their chemosensing abilities towards ionic analytes. These novel compounds will be comprised of a coumarin backbone functionalised with reactive sites such as Schiff bases, enone linkers and hydrazides. These functional groups will form part of the binding sites that various metal cations can interact with during complexation. Furthermore, chemical manipulation of the coumarin backbone via thionation processes will be attempted in order to produce a chemosensor that can interact exclusively with mercury (II) in the presence of other metal ions. Lastly, real-world application of these compounds will be evaluated using water samples from various sources in the Nelson Mandela Metropolitan area.

Reference

- (1) Jean-Pierre Candelone, Sungmin Hong, Christian Pellone, C. F. B. Post-Industrial Revolution Changes in Large-Scale Atmospheric Pollution of the Northern Hemisphere by Heavy Metals in a Pioneering Paper Twenty Five Years Ago Evidenced for the First Time That the Arctic Atmosphere Was [Murozumi Using Revolutionary Ultra. *J. Geophys. Res.* **1995**, *100* (8), 16605–16616.
- (2) Harrison, R. M.; Laxen, D. P. H. *Lead Pollution, Causes and Control*, 1 St.; Chapman and Hall: London, **1981**; Vol. 28. [https://doi.org/10.1016/0143-1471\(82\)90149-0](https://doi.org/10.1016/0143-1471(82)90149-0).
- (3) Yang, Y.; Huang, B.; Xu, J.; Li, Z.; Tang, Z.; Wu, X. Heavy Metal Domestication Enhances Beneficial Effects of Arbuscular Mycorrhizal Fungi on Lead (Pb) Phytoremediation Efficiency of *Bidens Parviflora* through Improving Plant Growth and Root Pb Accumulation. *Environ. Sci. Pollut. Res.* **2022**, No. 0123456789. <https://doi.org/10.1007/s11356-022-18588-2>.
- (4) Cheng, H.; Hu, Y. Lead (Pb) Isotopic Fingerprinting and Its Applications in Lead Pollution Studies in China: A Review. *Environ. Pollut.* **2010**, *158* (5), 1134–1146. <https://doi.org/10.1016/j.envpol.2009.12.028>.
- (5) Sukhadeorao Dongre, R. Lead: Toxicological Profile, Pollution Aspects and Remedial Solutions. *Intechopen* **2020**, 1–22. <https://doi.org/10.5772/intechopen.93095>.
- (6) Yamada, D.; Hiwatari, M.; Hangoma, P.; Narita, D.; Mphuka, C.; Chitah, B.; Yabe, J.; Nakayama, S. M. M.; Nakata, H.; Choongo, K.; Ishizuka, M. Assessing the Population-Wide Exposure to Lead Pollution in Kabwe, Zambia: An Econometric Estimation Based on Survey Data. *Sci. Rep.* **2020**, *10* (1), 1–11. <https://doi.org/10.1038/s41598-020-71998-5>.
- (7) Hua, C. jun; Zheng, H.; Zhang, K.; Xin, M.; Gao, J. rong; Li, Y. jin. A Novel Turn off Fluorescent Sensor for Fe(III) and PH Environment Based on Coumarin Derivatives: The Fluorescence Characteristics and Theoretical Study. *Tetrahedron* **2016**, *72* (51), 8365–8372. <https://doi.org/10.1016/j.tet.2016.08.023>.
- (8) Johnson, A. D.; Curtis, R. M.; Wallace, K. J. Low Molecular Weight Fluorescent Probes (LMFPs) to Detect the Group 12 Metal Triad. *Chemosensors* **2019**, *7* (2), 22. <https://doi.org/10.3390/chemosensors7020022>.

- (9) Bayindir, S. A Simple Rhodanine-Based Fluorescent Sensor for Mercury and Copper: The Recognition of Hg^{2+} in Aqueous Solution, and $\text{Hg}^{2+}/\text{Cu}^{2+}$ in Organic Solvent. *J. Photochem. Photobiol. A Chem.* **2019**, 372 (December 2018), 235–244. <https://doi.org/10.1016/j.jphotochem.2018.12.021>.
- (10) Ghezelsefloo, S.; Keyvan Rad, J.; Hajiali, M.; Mahdavian, A. R. Rhodamine-Based Fluorescent Polyacrylic Nanoparticles: A Highly Selective and Sensitive Chemosensor for Fe (II) and Fe (III) Cations in Water. *J. Environ. Chem. Eng.* **2021**, 9 (2). <https://doi.org/10.1016/j.jece.2021.105082>.
- (11) Warriar, S.; Kharkar, P. S. Highly Selective On-off Fluorescence Recognition of Fe^{3+} Based on a Coumarin Derivative and Its Application in Live-Cell Imaging. *Spectrochim. Acta - Part A Mol. Biomol. Spectrosc.* **2018**, 188, 659–665. <https://doi.org/10.1016/j.saa.2017.07.068>.
- (12) Puthiyedath, T.; Bahulayan, D. A Click Derived Triazole-Coumarin Derivative as Fluorescence on-off PET Based Sensor for Ca^{2+} and Fe^{3+} Ions. *Sensors Actuators, B Chem.* **2018**, 272, 110–117. <https://doi.org/10.1016/j.snb.2018.05.126>.
- (13) Yue, X. li; Wang, Z. qing; Li, C. Rui; Yang, Z. yin. A Highly Selective and Sensitive Fluorescent Chemosensor and Its Application for Rapid On-Site Detection of Al^{3+} . *Spectrochim. Acta - Part A Mol. Biomol. Spectrosc.* **2018**, 193, 415–421. <https://doi.org/10.1016/j.saa.2017.12.053>.
- (14) Cui, J.; Wang, S.; Huang, K.; Li, Y.; Zhao, W.; Shi, J.; Gu, J. Conjugation-Induced Fluorescence Labelling of Mesoporous Silica Nanoparticles for the Sensitive and Selective Detection of Copper Ions in Aqueous Solution. *New J. Chem.* **2014**, 38 (12), 6017–6024. <https://doi.org/10.1039/c4nj01428f>.
- (15) Skowronski, L.; Krupka, O.; Smokal, V.; Grabowski, A.; Naparty, M.; Derkowska-Zielinska, B. Optical Properties of Coumarins Containing Copolymers. *Opt. Mater. (Amst)*. **2015**, 47, 18–23. <https://doi.org/10.1016/j.optmat.2015.06.047>.
- (16) Maity, D.; Govindaraju, T. Conformationally Constrained (Coumarin-Triazolyl-Bipyridyl) Click Fluoroionophore as a Selective Al^{3+} Sensor. *Inorg. Chem.* **2010**, 49 (16), 7229–7231. <https://doi.org/10.1021/ic1009994>.
- (17) Mama, N.; Battison, A. Synthesis and Application of a Fluorescent \leftrightarrow turn-Off \leftrightarrow

- Triazolyl-Coumarin-Based Fluorescent Chemosensor for the Sensing of Fe³⁺ Ions in Aqueous Solutions. *Arkivoc* **2020**, 2020, 1–27. <https://doi.org/10.24820/ARK.5550190.P011.283>.
- (18) Kim, M. S.; Jo, T. G.; Yang, M.; Han, J.; Lim, M. H.; Kim, C. A Fluorescent and Colorimetric Schiff Base Chemosensor for the Detection of Zn²⁺ and Cu²⁺: Application in Live Cell Imaging and Colorimetric Test Kit. *Spectrochim. Acta - Part A Mol. Biomol. Spectrosc.* **2019**, 211, 34–43. <https://doi.org/10.1016/j.saa.2018.11.058>.
- (19) Mohanasundaram, D.; Bhaskar, R.; Gangatharan Vinoth Kumar, G.; Rajesh, J.; Rajagopal, G. A Quinoline Based Schiff Base as a Turn-On Fluorescence Chemosensor for Selective and Robust Detection of Cd²⁺ Ion in Semi-Aqueous Medium. *Microchem. J.* **2021**, 106030. <https://doi.org/10.1016/j.microc.2021.106030>.
- (20) Raju B., B.; Varadarajan, T. S. Substituent and Solvent Effects on the Twisted Intramolecular Charge Transfer of Three New 7-(Diethylamino)Coumarin-3-Aldehyde Derivatives. *J. Phys. Chem.* **1994**, 98 (36), 8903–8905. <https://doi.org/10.1021/j100087a014>.
- (21) Yang, L.; Wang, C.; Chang, G.; Ren, X. Facile Synthesis of New Coumarin-Based Colorimetric and Fluorescent Chemosensors: Highly Efficient and Selective Detection of Pd²⁺ in Aqueous Solutions. *Sensors Actuators, B Chem.* **2017**, 240, 212–219. <https://doi.org/10.1016/j.snb.2016.08.132>.
- (22) Arcos-Ramos, R.; Maldonado-Domínguez, M.; Ordóñez-Hernández, J.; Romero-Ávila, M.; Farfán, N.; Carreón-Castro, M. del P. 3-Substituted-7-(Diethylamino)Coumarins as Molecular Scaffolds for the Bottom-up Self-Assembly of Solids with Extensive π -Stacking. *J. Mol. Struct.* **2017**, 1130, 914–921. <https://doi.org/10.1016/j.molstruc.2016.10.080>.
- (23) Yee, D. J.; Balsanek, V.; Sames, D. New Tools for Molecular Imaging of Redox Metabolism: Development of a Fluorogenic Probe for 3 α -Hydroxysteroid Dehydrogenases. *J. Am. Chem. Soc.* **2004**, 126 (8), 2282–2283. <https://doi.org/10.1021/ja039799f>.
- (24) Donovalová, J.; Cigán, M.; Stankovičová, H.; Gašpar, J.; Danko, M.; Gáplovský, A.; Hrdlovič, P. Spectral Properties of Substituted Coumarins in Solution and Polymer Matrices. *Molecules* **2012**, 17 (3), 3259–3276.

<https://doi.org/10.3390/molecules17033259>.

- (25) García, J. M.; García, F. C.; Serna, F.; De La Peña, J. L. Fluorogenic and Chromogenic Polymer Chemosensors. *Polym. Rev.* **2011**, *51* (4), 341–390. <https://doi.org/10.1080/15583724.2011.616084>.
- (26) Kushwaha, D.; Singh, R. S.; Tiwari, V. K. Fluorogenic Dual Click Derived Bis-Glycoconjugated Triazolocoumarins for Selective Recognition of Cu(II) Ion. *Tetrahedron Lett.* **2014**, *55* (33), 4532–4536. <https://doi.org/10.1016/j.tetlet.2014.06.052>.
- (27) Bryant, J. J.; Bunz, U. H. F. Click to Bind: Metal Sensors. *Chemistry - An Asian Journal*. John Wiley & Sons, Ltd July 1, **2013**, pp 1354–1367. <https://doi.org/10.1002/asia.201300260>.
- (28) Chua, M. H.; Shah, K. W.; Zhou, H.; Xu, J. Recent Advances in Aggregation-Induced Emission Chemosensors for Anion Sensing. *Molecules*. **2019**. <https://doi.org/10.3390/molecules24152711>.
- (29) Guo, Z. hao; Li, Y. yi; Ding, C. ping; Hu, X. jun; Wen, Y.; Wang, B. A Novel Pb 2+ - Selective Micellar Self-Assembled Fluorescent Chemosensor Based on Amino Thiadiazole Calix[4]Arene Derivative. *Inorg. Chem. Commun.* **2019**, *103*, 43–46. <https://doi.org/10.1016/j.inoche.2019.03.009>.
- (30) Jin, R.; Irfan, A. Theoretical Study of Coumarin Derivatives as Chemosensors for Fluoride Anion. *Comput. Theor. Chem.* **2012**, *986*, 93–98. <https://doi.org/10.1016/j.comptc.2012.02.018>.
- (31) Isaac, I. O.; Munir, I.; Al-Rashida, M.; Ali, S. A.; Shafiq, Z.; Islam, M.; Ludwig, R.; Ayub, K.; Khan, K. M.; Hameed, A. Novel Acridine-Based Thiosemicarbazones as “turn-on” Chemosensors for Selective Recognition of Fluoride Anion: A Spectroscopic and Theoretical Study. *R. Soc. Open Sci.* **2018**, *5* (7). <https://doi.org/10.1098/rsos.180646>.
- (32) Tamil Selvan, G.; Varadaraju, C.; Tamil Selvan, R.; Enoch, I. V. M. V.; Mosae Selvakumar, P. On/Off Fluorescent Chemosensor for Selective Detection of Divalent Iron and Copper Ions: Molecular Logic Operation and Protein Binding. *ACS Omega* **2018**, *3* (7), 7985–7992. <https://doi.org/10.1021/acsomega.8b00748>.

- (33) Wu, G.; Gao, Q.; Li, M.; Tang, X.; Lai, K. W. C.; Tong, Q. A Ratiometric Probe Based on Coumarin-Quinoline for Highly Selective and Sensitive Detection of Zn²⁺ Ions in Living Cells. *J. Photochem. Photobiol. A Chem.* **2018**, 355, 487–495. <https://doi.org/10.1016/j.jphotochem.2017.05.006>.
- (34) Rull-Barrull, J.; d'Halluin, M.; Le Grogne, E.; Felpin, F. X. A Highly Selective Colorimetric and Fluorescent Chemosensor for Cr²⁺ in Aqueous Solutions. *Tetrahedron Lett.* **2017**, 58 (6), 505–508. <https://doi.org/10.1016/j.tetlet.2016.12.038>.
- (35) Chalmardi, G. B.; Tajbakhsh, M.; Hasani, N.; Bekhradnia, A. A New Schiff-Base as Fluorescent Chemosensor for Selective Detection of Cr³⁺: An Experimental and Theoretical Study. *Tetrahedron* **2018**, 74 (18), 2251–2260. <https://doi.org/10.1016/j.tet.2018.03.046>.
- (36) Wang, L.; Zheng, X. Y.; Zhang, X.; Zhu, Z. J. A Quinoline-Based Fluorescent Chemosensor for Palladium Ion (Pd²⁺)-Selective Detection in Aqueous Solution. *Spectrochim. Acta - Part A Mol. Biomol. Spectrosc.* **2021**, 249, 119283. <https://doi.org/10.1016/j.saa.2020.119283>.
- (37) Tawfik, H. A.; Ewies, E. F.; El-Hamouly, W. S. ChemInform Abstract: Synthesis of Chromones and Their Applications During the Last Ten Years. *ChemInform* **2015**, 46 (13). <https://doi.org/10.1002/chin.201513331>.
- (38) Orrego-Hernández, J.; Nuñez-Dallos, N.; Portilla, J. Recognition of Mg²⁺ by a New Fluorescent “Turn-on” Chemosensor Based on Pyridyl-Hydrazono-Coumarin. *Talanta* **2016**, 152, 432–437. <https://doi.org/10.1016/j.talanta.2016.02.020>.
- (39) Maret, W. The Metals in the Biological Periodic System of the Elements: Concepts and Conjectures. *Int. J. Mol. Sci.* **2016**, 17 (1), 66. <https://doi.org/10.3390/ijms17010066>.
- (40) Buccella, D.; Lim, M. H.; Morrow, J. R. Metals in Biology: From Metallomics to Trafficking. *Inorg. Chem.* **2019**, 58 (20), 13505–13508. <https://doi.org/10.1021/acs.inorgchem.9b02965>.
- (41) Crichton, R. R. An Overview of the Role of Metals in Biology. In *Practical Approaches to Biological Inorganic Chemistry*; Elsevier, **2020**; pp 1–16. <https://doi.org/10.1016/B978-0-444-64225-7.00001-8>.
- (42) Hande, P. E.; Samui, A. B.; Kulkarni, P. S. Selective Nanomolar Detection of Mercury

- Using Coumarin Based Fluorescent Hg(II)—Ion Imprinted Polymer. *Sensors Actuators, B Chem.* **2017**, *246*, 597–605. <https://doi.org/10.1016/j.snb.2017.02.125>.
- (43) Bazzicalupi, C.; Caltagirone, C.; Cao, Z.; Chen, Q.; Dinatale, C.; Garau, A.; Lippolis, V.; Lvova, L.; Liu, H.; Lundström, I.; Mostallino, M. C.; Nieddu, M.; Paolesse, R.; Prodi, L.; Sgarzi, M.; Zaccheroni, N. Multimodal Use of New Coumarin-Based Fluorescent Chemosensors: Towards Highly Selective Optical Sensors for Hg²⁺ Probing. *Chem. - A Eur. J.* **2013**, *19* (43), 14639–14653. <https://doi.org/10.1002/chem.201302090>.
- (44) Schneider, H.-J.; Kato, K.; Strongin, R. Chemomechanical Polymers as Sensors and Actuators for Biological and Medicinal Applications. *Sensors* **2007**, *7* (8), 1578–1611. <https://doi.org/10.3390/s7081578>.
- (45) Krishna, A.; Tekuri, V.; Mohan, M.; Trivedi, D. R. Selective Colorimetric Chemosensor for the Detection of Hg²⁺ and Arsenite Ions Using Isatin Based Schiff's Bases; DFT Studies and Applications in Test Strips. *Sensors Actuators, B Chem.* **2019**, *284* (July 2018), 271–280. <https://doi.org/10.1016/j.snb.2018.12.003>.
- (46) Li, H. W.; Wang, B.; Dang, Y. Q.; Li, L.; Wu, Y. A Highly Selective Fluorescent Sensor for Mercury Ions in Aqueous Solution: Detection Based on Target-Induced Aggregation. *Sensors Actuators, B Chem.* **2010**, *148* (1), 49–53. <https://doi.org/10.1016/j.snb.2010.03.060>.
- (47) Ding, Y.; Zhao, C.; Zhang, P.; Chen, Y.; Song, W.; Liu, G.; Liu, Z.; Yun, L.; Han, R. A Novel Quinoline Derivative as Dual Chemosensor for Selective Sensing of Al³⁺ by Fluorescent and Fe²⁺ by Colorimetric Methods. *J. Mol. Struct.* **2021**, *1231*, 129965. <https://doi.org/10.1016/j.molstruc.2021.129965>.
- (48) Shen, Y.; Wei, Y.; Zhu, C.; Cao, J.; Han, D.-M. Ratiometric Fluorescent Signals-Driven Smartphone-Based Portable Sensors for On-site Visual Detection of Food Contaminants. *Coord. Chem. Rev.* **2022**, *458*, 214442. <https://doi.org/10.1016/j.ccr.2022.214442>.
- (49) Vengaiyan, K. M.; Britto, C. D.; Sekar, K.; Sivaraman, G.; Singaravadivel, S. Fluorescence "On-off-on" Chemosensor for Selective Detection of Hg²⁺ and S²⁻: Application to Bioimaging in Living Cells. *RSC Adv.* **2016**, *6* (9), 7668–7673. <https://doi.org/10.1039/c5ra26281j>.

- (50) Güsten, H.; Rinke, M.; Wirth, H. O. Photophysical Properties and Laser Performance of Photostable UV Laser Dyes - III. Sterically Hindered p-Quaterphenyls. *Appl. Phys. B Photophysics Laser Chem.* **1988**, 45 (4), 279–284. <https://doi.org/10.1007/BF00687157>.
- (51) Adhikari, D. P.; Biener, G.; Stoneman, M. R.; Badu, D. N.; Paprocki, J. D.; Eis, A.; Park, P. S. H.; Popa, I.; Raicu, V. Comparative Photophysical Properties of Some Widely Used Fluorescent Proteins under Two-Photon Excitation Conditions. *Spectrochim. Acta - Part A Mol. Biomol. Spectrosc.* **2021**, 262. <https://doi.org/10.1016/j.saa.2021.120133>.
- (52) Soffiantini, V. *Analytical Chemistry*; De Gruyter: Boston, **2021**. <https://doi.org/10.1515/9783110721201-202>.
- (53) Dash, D. C. *ANALYTICAL CHEMISTRY*, 2nd ed.; PHI Learning Private Limited: Delhi, **2017**.
- (54) Junaid, H. M.; Batool, M.; Harun, F. W.; Akhter, M. S.; Shabbir, N. Naked Eye Chemosensing of Anions by Schiff Bases. *Crit. Rev. Anal. Chem.* **2022**, 52 (3), 463–480. <https://doi.org/10.1080/10408347.2020.1806703>.
- (55) Parchegani, F.; Orojloo, M.; Zendehdel, M.; Amani, S. Spectrochimica Acta Part A : Molecular and Biomolecular Spectroscopy Simultaneous Measurement of Hydrogen Carbonate and Acetate Anions Using Biologically Active Receptor Based on Azo Derivatives of Naphthalene. *Spectrochim. Acta Part A Mol. Biomol. Spectrosc.* **2020**, 229, 117925. <https://doi.org/10.1016/j.saa.2019.117925>.
- (56) Malkin, J. *Photophysical and Photochemical Properties of Aromatic Compounds*; CRC Press, Inc., **1992**.
- (57) Marie, J.; Ngororabanga. Synthesis and Investigation of the Chemosensing Properties of Novel Fluorescent Triazolyl Coumarin-Based Polymers, Nelson Mandela Metropolitan, **2017**.
- (58) Ooyama, Y.; Sumomogi, M.; Nagano, T.; Kushimoto, K.; Komaguchi, K.; Imae, I.; Harima, Y. Detection of Water in Organic Solvents by Photo-Induced Electron Transfer Method. *Org. Biomol. Chem.* **2011**, 9 (5), 1314–1316. <https://doi.org/10.1039/C0OB00933D>.
- (59) Lakowicz, J. R. Mechanisms and Dynamics of Fluorescence Quenching. In *Principles of Fluorescence Spectroscopy*; Springer US: Boston, MA, **2006**; pp 331–351.

https://doi.org/10.1007/978-0-387-46312-4_9.

- (60) Xiang, D.; Zhang, S.; Wang, Y.; Sun, K.; Xu, H. A Novel Naphthalimide-Based “Turn-on” Fluorescent Chemosensor for Highly Selective Detection of Zn²⁺. *Tetrahedron* **2022**, *106–107*, 132648. <https://doi.org/10.1016/j.tet.2022.132648>.
- (61) Hsu, C. P. The Electronic Couplings in Electron Transfer and Excitation Energy Transfer. *Acc. Chem. Res.* **2009**, *42* (4), 509–518. <https://doi.org/10.1021/ar800153f>.
- (62) Raicu, V. Ab Initio Derivation of the FRET Equations Resolves Old Puzzles and Suggests Measurement Strategies. *Biophysj* **2019**, *116* (7), 1313–1327. <https://doi.org/10.1016/j.bpj.2019.02.016>.
- (63) Xu, D.; Jia, H.; Niu, Y.; Yin, S. Fluorine-Boron Compound-Based Fluorescent Chemosensors for Heavy Metal Ion Detection. *Dye. Pigment.* **2022**, *200* (February), 110185. <https://doi.org/10.1016/j.dyepig.2022.110185>.
- (64) Wu, L.; Huang, C.; Emery, B. P.; Sedgwick, A. C.; Bull, S. D.; He, X.-P. P.; Tian, H.; Yoon, J.; Sessler, J. L.; James, T. D. Förster Resonance Energy Transfer (FRET)-Based Small-Molecule Sensors and Imaging Agents. *Chem. Soc. Rev.* **2020**, *49* (15), 5110–5139. <https://doi.org/10.1039/C9CS00318E>.
- (65) Kumpulainen, T.; Lang, B.; Rosspeintner, A.; Vauthey, E. Ultrafast Elementary Photochemical Processes of Organic Molecules in Liquid Solution. *Chem. Rev.* **2017**, *117* (16), 10826–10939. <https://doi.org/10.1021/acs.chemrev.6b00491>.
- (66) Posey, V.; Hanson, K. Chirality and Excited State Proton Transfer: From Sensing to Asymmetric Synthesis. *ChemPhotoChem* **2019**. <https://doi.org/10.1002/cptc.201900097>.
- (67) Su, S.; Sun, G.; Liang, X.; Fang, H. Effectively Controlling the ESIPT Behavior and Fluorescence Feature of 2-(2'-Hydroxyphenyl)-4-Chloromethylthiazole by Changing Its π -Conjugation: A Theoretical Exploration. *J. Photochem. Photobiol. A Chem.* **2022**, *422* (May 2021), 113548. <https://doi.org/10.1016/j.jphotochem.2021.113548>.
- (68) Bag, R.; Sikdar, Y.; Sahu, S.; Das Mukhopadhyay, C.; Drew, M. G. B.; Goswami, S. Benzimidazole Based ESIPT Active Chemosensors Enable Nano–Molar Detection of Cu²⁺ in 90% Aqueous Solution, MCF–7 Cells, and Plants. *J. Photochem. Photobiol. A Chem.* **2022**, *431* (February), 114006. <https://doi.org/10.1016/j.jphotochem.2022.114006>.

Chapter 2

Schiff-based Chemosensors

Summary

Herein, five Schiff-based chemosensors were successfully synthesised and characterised using NMR, FT-IR and molecular modelling studies using Spartan computational program. Of these five compounds, two (**S2** and **S6**) displayed colourimetric properties in the presence of selected cations, while **S1** and **S9** responded to the test anions. **S2** changed from a clear to a blue solution when Cu^{2+} was added only after 25 min. Therefore, **S2** can not be used in real-time. **S6** (colourless) showed to be a colourimetric chemosensor towards three different metal cations Ni^{2+} (change to yellow), Fe^{2+} (change to red), and Cu^{2+} (change to blue). **S6** prefers the cations in the order of $\text{Cu}^{2+} > \text{Ni}^{2+} > \text{Fe}^{2+}$. However, with no observable selectivity for any of these cations. In addition, **S1** and **S9** showed strong interactions with iodide ions, with **S1** showing a higher preference over **S9**. The observed complex showed a LOD of 0.027 mM and a LOQ of 0.083 mM, which showed a linear relationship up to 0.30 mM. The selected solvents were noted to play a significant role in the complexation as it was observed that the selectivity towards cations and anions changes depending on the solvent.

Table of Contents

Summary	41
List of Figures	43
List of Schemes	45
List of Tables	45
List of selected Abbreviations	46
2 Schiff-based chemosensors	47
2.1 Introduction	47
2.2 Aim and objectives	50
2.3 Synthesis of Schiff bases	50
2.4 Absorption studies of Schiff base derivatives	58
2.5 Application of Schiff bases as chemosensors	60
2.5.1 Screening of metal ions	60
2.5.2 Screening of anions	66
2.5.3 The proposed binding site and computational studies	69
2.6 Conclusion	80
2.7 Experimental	82
2.7.1 General information	82
2.7.2 General procedure for the synthesis of Schiff base derivatives S1-S9	83
References	87
Supplementary information	89
List of supplementary figures	89

List of Figures

Figure 2.1: Binding mechanism of **2** and acetate via hydrogen bonding to the Schiff base.³ 49

Figure 2.2: Cationic sensing of the Schiff base chemosensor **3** for Hg^{2+} and Cu^{2+} .⁵49

Figure 2.3: ^1H NMR spectra of a) **S1**, b) **S2**, c) **S3** and d) **S6** in CDCl_3 (red indicates the hydroxyl protons, green indicates the Schiff base proton, blue indicates the aromatic protons, and purple indicates the alkane protons where present).....52

Figure 2.4: ^1H NMR spectrum of **S9** in CDCl_3 (green indicates the Schiff base proton, blue and turquoise indicate the aromatic protons, and purple indicates the alkane protons).....53

Figure 2.5: ^{13}C NMR spectrum of **S3** in CDCl_353

Figure 2.6: FT-IR spectrum of **S3**.....54

Figure 2.7: UV-vis spectra of **S1** (red), **S2** (yellow), **S3** (green), **S6** (light blue) and **S9** (purple) in acetonitrile (solid lines) and methanol (dash lines) with a concentration of 0.1 mM.....59

Figure 2.8: Computational electrostatic potential map of a) **S6** and b) **S9**.59

Figure 2.9: The screening of metal cations (0.167 mM) using **S2** (0.167 mM). a) **S2** (blue) in acetonitrile has two bands at 271 nm and 335 nm, and a newly formed band appears at 575 nm in the presence of Cu^{2+} (green). b) **S2** (blue) in methanol showed no change in the spectra with the addition of the metal cations.61

Figure 2.10: The screening of metal cations (0.167 mM) using **S6** (0.167 mM). a) **S6** (blue) in acetonitrile has two absorbance bands, 253 nm and 314 nm, with the addition of Ni^{2+} (yellow), a new band formed at 402 nm. In Fe^{2+} (red) presence, a new band has formed at 515 nm. Cu^{2+} (green) induced a new band at 655 nm. b) **S6** (blue) in methanol. In Fe^{2+} (red) and Fe^{3+} (yellow) presence, **S6** had a new band at 510 nm for both cations. Inset: Photographic image of colour change induced by the addition of the metal ions.....61

Figure 2.11: A photographic image of **S6** (colourless) in the presence of various metal ions showing the colour change induced by Fe^{2+} (red), Ni^{2+} (yellow) and Cu^{2+} (blue).62

Figure 2.12: Absorbance of **S2**- Cu^{2+} complex at 575 nm in acetonitrile over time.63

Figure 2.13: Competition studies of S6 (0.167 mM) in acetonitrile. a) Ni^{2+} (0.167 mM), b) Fe^{2+} (0.167 mM), and c) Cu^{2+} (0.167 mM). Each experiment was conducted in the presence of 0.167 mM competing metal cation.	65
Figure 2.14: Screening of various anions (grey, 0.05 mM and 0.167 mM) using S1 (blue, 0.167 mM) in a) acetonitrile and b) methanol. Iodide (red) induced a hyperchromic shift in acetonitrile.....	66
Figure 2.15: Screening of various anions (grey, 0.1 mM) using S9 (blue, 0.1 mM) in a) acetonitrile and b) methanol. Iodide (red) induced a hyperchromic shift in acetonitrile, whereas cyanate (green) induced a hyperchromic shift in methanol.	67
Figure 2.16: Competition studies of I^- (0.05 mM) with competing anions (0.05 mM) in acetonitrile towards S1 (0.1 mM).	68
Figure 2.17: Titration studies of S1 (0.033 mM) with the addition of I^-	68
Figure 2.18: a) Absorbance of the S1 - I^- complex at 245 nm as a function of the I^- concentration. b) Exponential relationship of the absorption of S1 - I^- complex at 245 nm and 315 nm as a function of I^- concentration.	69
Figure 2.19: Benesi-Hildebrand plot of S1 (0.033 mM) with I^- in acetonitrile.	71
Figure 2.20: ^1H NMR spectra of S1 with and without varying quantities of I^- . Solvent: Acetonitrile- d_3	71
Figure 2.21: Four stable S1 - I^- complex conformers.	72
Figure 2.22: Computational illustration of the S1 - I^- complex in a) acetonitrile and b) methanol.	73
Figure 2.23: Computational illustration of the most preferred conformer of a) S2 and b) S2 - Cu^{2+} complex. The complexes are shown in their density map.....	74
Figure 2.24: S2 - Cu^{2+} complex in acetonitrile.	74
Figure 2.25: Most stable conformer for S6	75

Figure 2.26: Benesi-Hildebrand plot of S6 (0.167 mM) with Cu^{2+} in acetonitrile.	75
Figure 2.27: Job's plot of S6 with Cu^{2+} in acetonitrile with an overall concentration of 0.167 mM.	76
Figure 2.28: Initial molecular modelling of S6-2Cu²⁺ complex at MMFF level.	76
Figure 2.29: Mode of binding of S6-2Cu²⁺ complex at PM3 level. a) Side-view and b) front view.	77
Figure 2.30: ^1H NMR titrations of S6 with subsequent additions of Cu^{2+} in acetonitrile- d_3	78
Figure 2.31: Complexation of S9 with a) I^- and b) NCO^- computed with Spartan Student software.	79
Figure 2.32: ^1H NMR spectra of S9 with the subsequent additions of I^- in acetonitrile- d_3	79
Figure 2.33: Structure of S9 labelled to identify ^1H NMR peaks in Figure 2.28	80

List of Schemes

Scheme 2.1: Generalised condensation reaction yielding a Schiff base, 1.	47
Scheme 2.2: Mechanism of Schiff base formation. ⁴	48
Scheme 2.3: Condensation reaction to synthesise Schiff-based chemosensors. a) Ethanol.	50
Scheme 2.4: Synthesis of Schiff bases S1 – S9 . a) salicylaldehyde-derived chemosensors. b) benzaldehyde-derived chemosensor.	51

List of Tables

Table 2.1: All nine attempted Schiff-based chemosensors.	55
--	----

List of selected Abbreviations

DMSO – Dimethyl sulfoxide

FT-IR – Fourier Transform Infrared

LOD – Limit of Detection

LOQ – Limit of Quantification

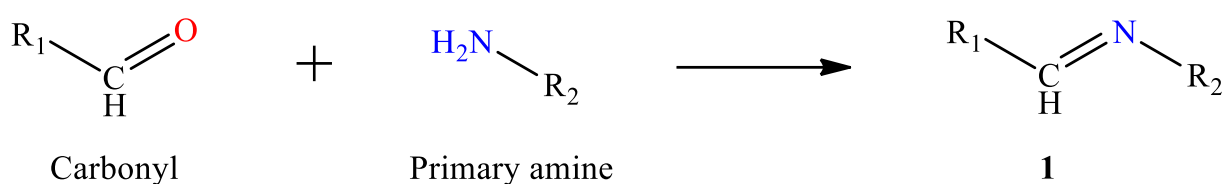
NMR – Nuclear Magnetic Resonance

UV-vis – Ultraviolet-visible

2 Schiff-based chemosensors

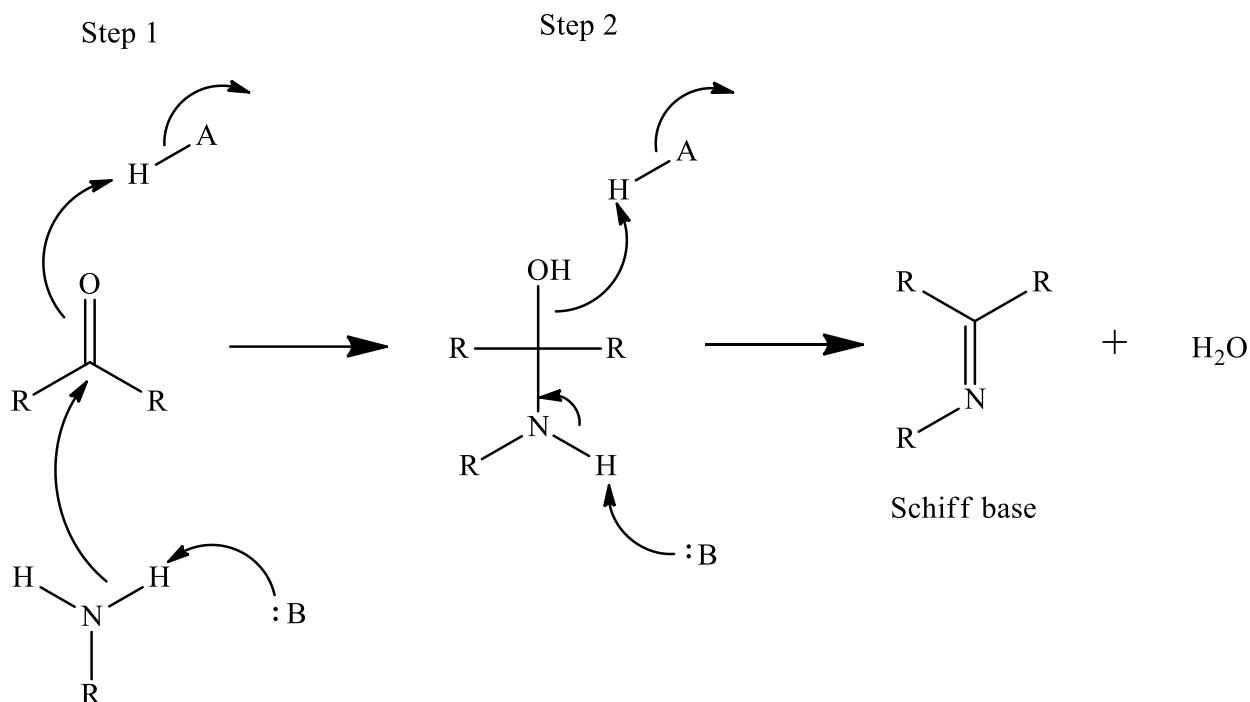
2.1 Introduction

Schiff bases, first synthesised by Hugo Schiff in 1864, also known as imine or azomethine, are the nitrogen analogue of carbonyl groups such as aldehydes or ketones. These compounds can be obtained through a condensation reaction between a primary amine and a carbonyl compound, yielding a Schiff base, as shown in **Scheme 2.1**. Compared to alkyl-substituted Schiff bases, Schiff bases with an aryl group substitution are typically easier to synthesise and more stable because of their superior conjugation.¹⁻³



Scheme 2.1: Generalised condensation reaction yielding a Schiff base, **1**.

Mechanistically, a Schiff base is formed in a two steps process shown in **Scheme 2.2**. In the first step, the amine nitrogen acts as a nucleophile, attacking the electrophilic carbonyl carbon (ketone or aldehyde). In the second step, the nitrogen is deprotonated, and electrons from the N-H bond form a C=N double bond, which in turn pushes the oxygen off the carbon, eliminating water and yielding the complete Schiff base.⁴



Scheme 2.2: Mechanism of Schiff base formation.⁴

Schiff bases are extensively known for their uses in chemosensors due to their ability to form complexes with metal cations and the detection of anion analytes. Different mechanisms have been proposed for the interaction between an analyte and the Schiff base moiety, these mechanisms include:^{1,3}

- Via the carbon atoms (electron deficient site)
 - Hydrogen bonding
 - Deprotonation of the Schiff base moiety
 - Electrostatic interactions
- Via the nitrogen atom (electron-rich site)
 - Intramolecular charge transfer in the Schiff base moiety

The electron-deficient site is of great interest to anion sensing, whereas the electron-rich site prefers cationic analytes.^{1,3}

Junaid and co-workers reported on the colourimetric Schiff-based chemosensors, **2**, used for anion sensing. The anion sensor was sensitive toward acetate and carbonate in a water and DMSO mixture. The sensor showed a LOD of 2.33 μM towards carbonate and was much more sensitive toward acetate with a LOD of 0.554 μM . The sensor displayed a significant colour

change from pale yellow to red in the presence of acetate and carbonate. The interaction was attributed to hydrogen bonding between the anion and the Schiff base proton, as shown in **Figure 2.1**.³

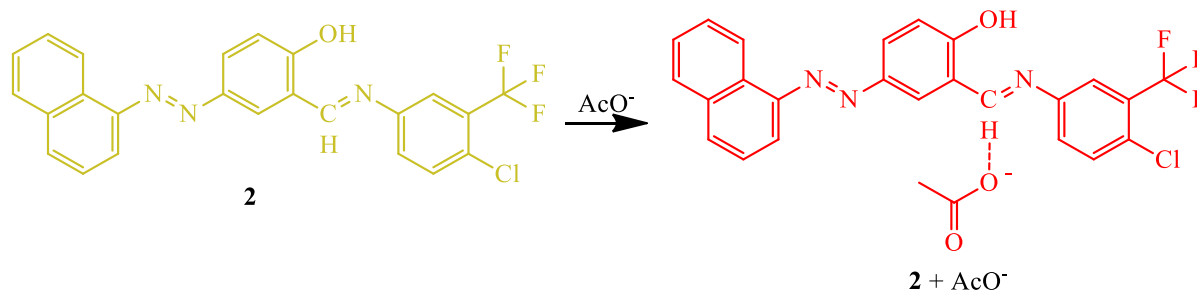


Figure 2.1: Binding mechanism of **2** and acetate via hydrogen bonding to the Schiff base.³

The colourimetric cationic Schiff-based chemosensor **3** was designed and synthesised by Nancy Sidana and her team. Chemosensor **3** showed high selectivities towards Hg^{2+} and Cu^{2+} in an alcoholic medium. The sensor displayed a significant colour change, from clear to pale yellow in the presence of Cu^{2+} and pale orange when complexed with Hg^{2+} . The binding ratio was determined using a Job's plot and found to have a binding ratio of 2:1 (sensor: metal). The binding was determined to involve the Schiff base moiety and was assisted by the neighbouring sulphur group, as shown in **Figure 2.2**.⁵

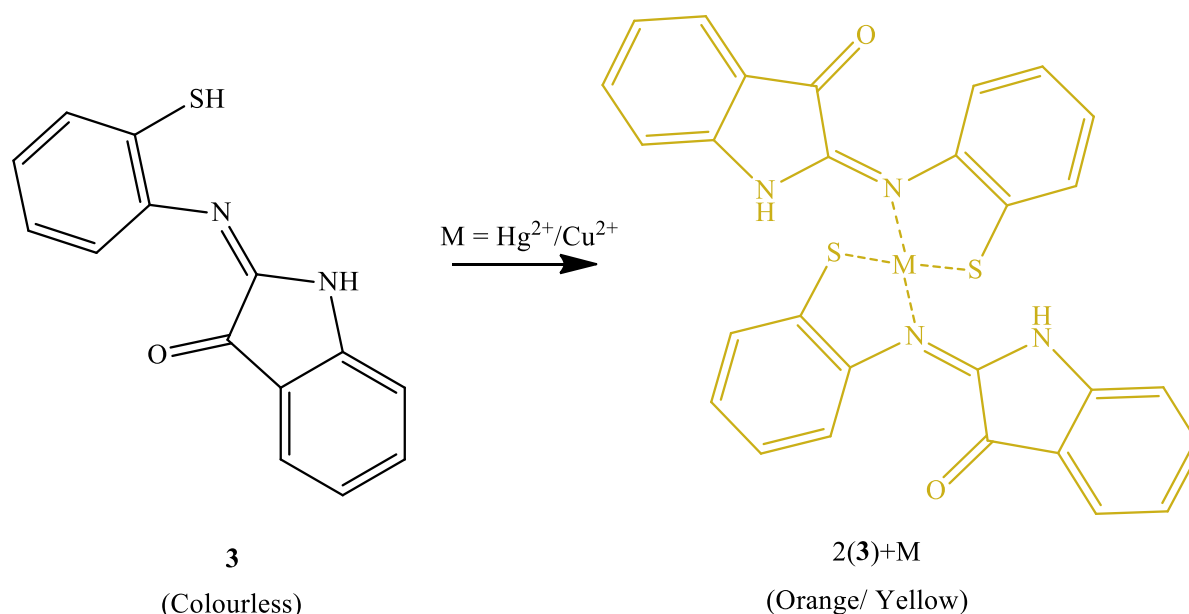


Figure 2.2: Cationic sensing of the Schiff base chemosensor **3** for Hg^{2+} and Cu^{2+} .⁵

2.2 Aim and objectives

Developing a chemosensor, which is useful in detecting metal ions, is important for application in biological industry and environmental processes. Due to their capacity to form coordination complexes with various ions, Schiff base moieties are important in chemosensing applications. Schiff bases have been reported in the literature for the use of colourimetric chemosensors detection of analytes.^{2,3}

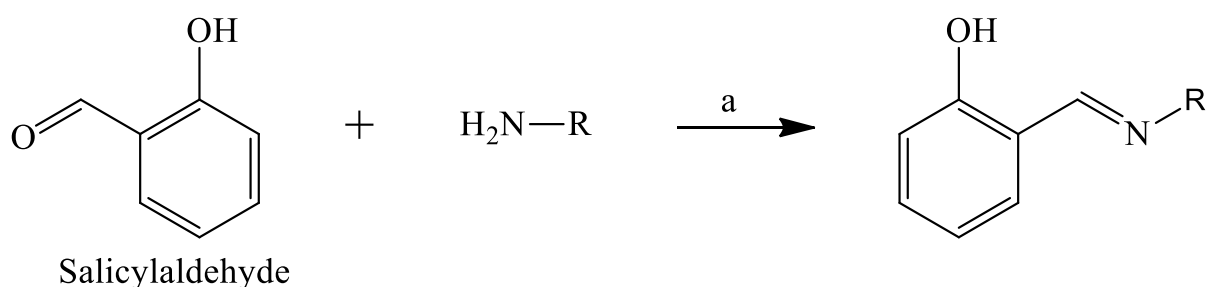
Therefore, chemosensors were designed and synthesised in this chapter to obtain various compounds containing Schiff base moieties.

Salicylaldehyde will be used as the main precursor in this chapter to react in a condensation reaction with various primary amines.

These compounds will be confirmed using ^1H NMR, ^{13}C NMR and FT-IR. The application of the novel Schiff bases as chemosensors towards various analytes will be investigated using their photophysical properties in acetonitrile (polar aprotic) and methanol (polar protic) solutions.

2.3 Synthesis of Schiff bases

This section contains a simple synthesis (one-step reaction) for preparing Schiff base compounds using salicylaldehyde as starting material. Following a well-established literature method, the condensation reaction (**Scheme 2.3**) between salicylaldehyde and an appropriate primary amine was carried out at room temperature in an alcoholic medium.⁶

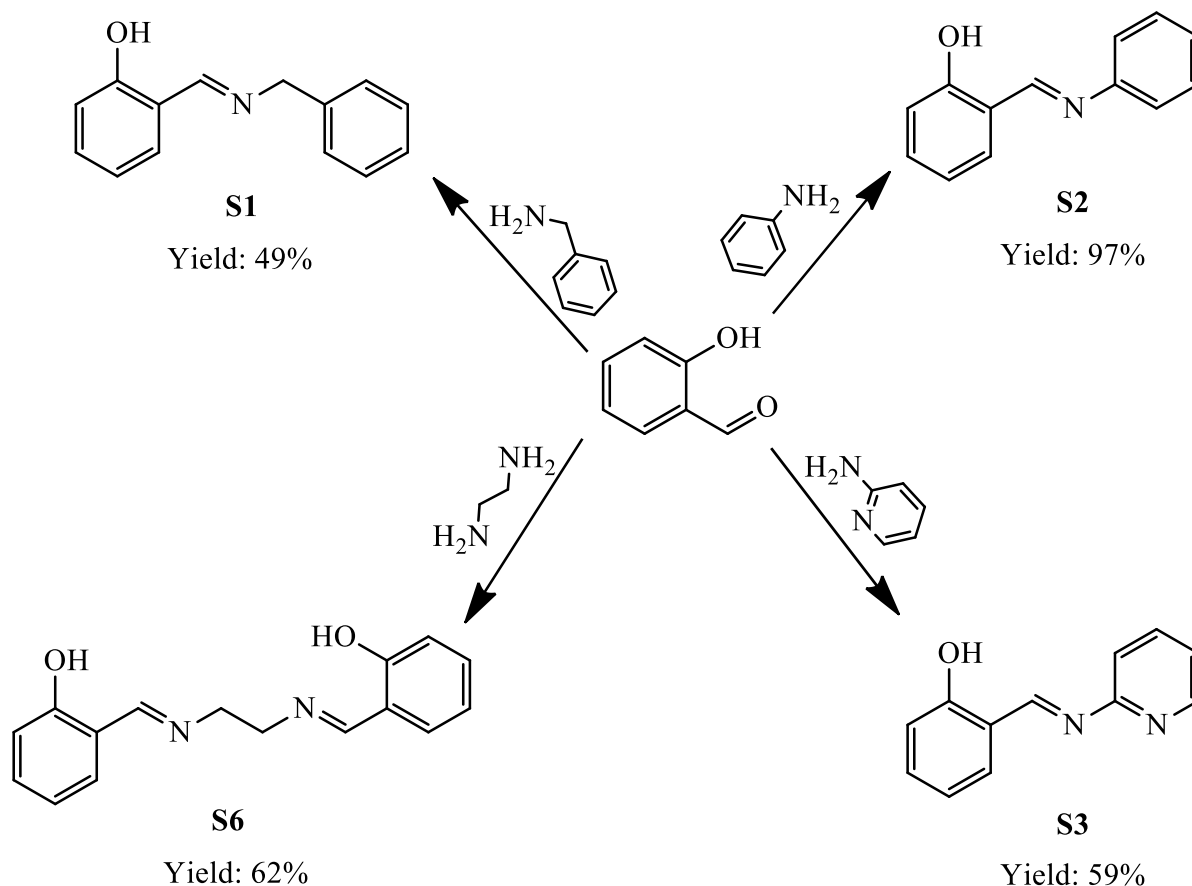


Scheme 2.3: Condensation reaction to synthesise Schiff-based chemosensors. a) Ethanol.

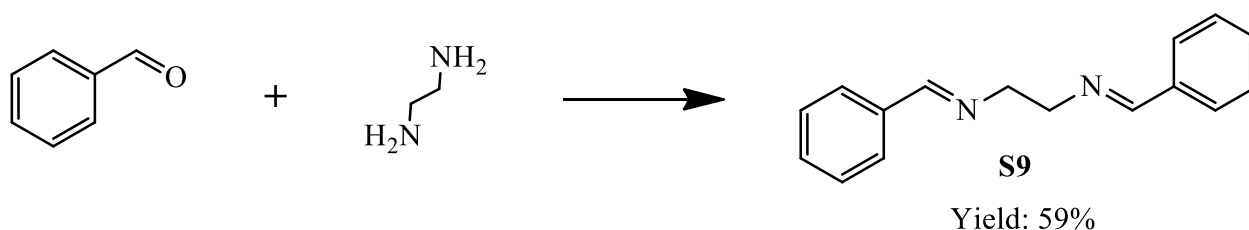
Scheme 2.4 shows the five compounds that were successfully synthesised with reasonable yields. The respective amines were dissolved in ethanol, followed by adding the aldehyde.

After stirring the mixture overnight, these novel Schiff bases were isolated as solids and recrystallised in ethanol to obtain pure products.

a)



b)



Scheme 2.4: Synthesis of Schiff bases **S1** – **S9**. a) salicylaldehyde-derived chemosensors. b) benzaldehyde-derived chemosensor.

These compounds were characterised using ^1H NMR, ^{13}C NMR and FT-IR spectroscopy.

The ^1H NMR analysis of the hydroxyl-Schiff-based derivatives (**S1**, **S2**, **S3** and **S6**) are shown in **Figure 2.3**. Important to note in these ^1H NMR spectra is the disappearance of the two

primary amine protons and the aldehyde proton and the appearance of the newly formed Schiff base proton (green) at 8.38 - 8.66 ppm with **S3**, containing a pyridine group, resulting in a significant downfield shift to 9.46 ppm. The aromatic protons were observed between 6.86 and 7.81 ppm. For **S1** and **S6**, the methylene protons were observed at 4.85 and 3.96 ppm, respectively.

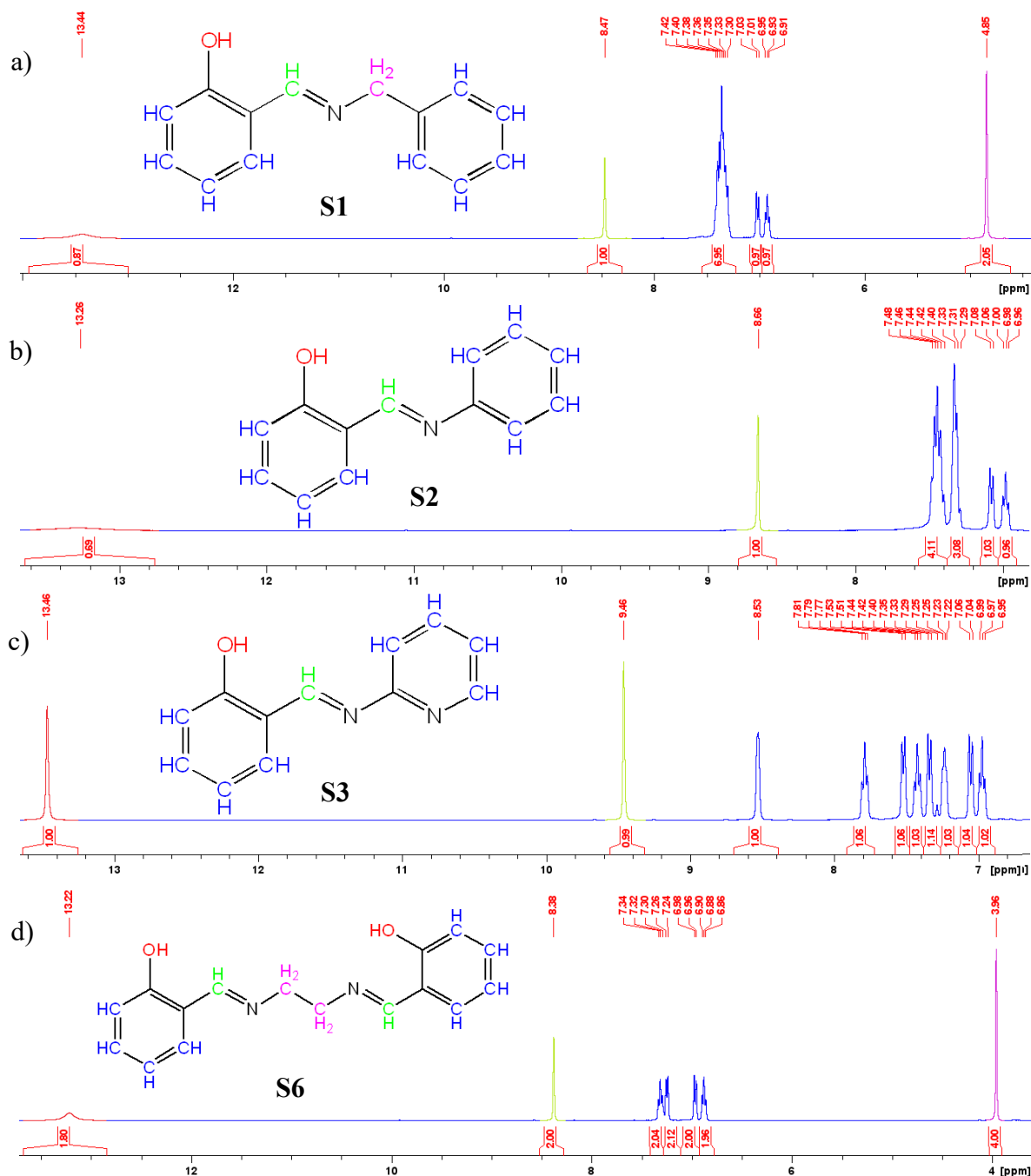


Figure 2.3: ¹H NMR spectra of a) **S1**, b) **S2**, c) **S3** and d) **S6** in CDCl₃ (red indicates the hydroxyl protons, green indicates the Schiff base proton, blue indicates the aromatic protons, and purple indicates the alkane protons where present).

The ^1H NMR spectrum for **S9** is shown in **Figure 2.4**. The newly Schiff base proton can be seen at 8.32 ppm as a singlet (green), with the aromatic protons at 7.42 and 7.72 ppm and the ethylene protons at 4.00 ppm, thus, indicating that the synthesis was successful.

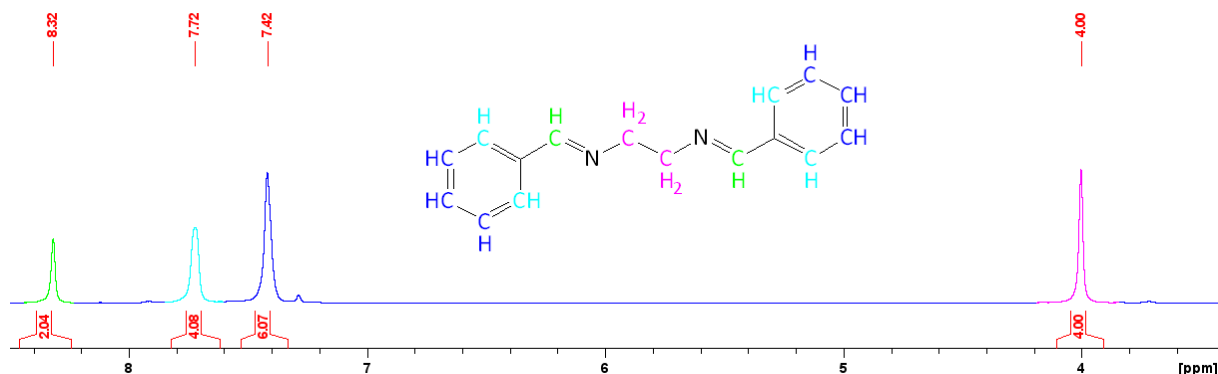


Figure 2.4: ^1H NMR spectrum of **S9** in CDCl_3 (green indicates the Schiff base proton, blue and turquoise indicate the aromatic protons, and purple indicates the alkane protons).

The newly prepared Schiff bases were further characterised using ^{13}C NMR spectra. **S1** (**Figure S 2.1**), **S2** (**Figure S 2.5**), **S6** (**Figure S 2.11**) and **S9** (**Figure S 2.15**) can be seen in the supplementary information. The ^{13}C NMR of **S3** is shown in **Figure 2.5**, the carbon in the Schiff base moiety is seen at 164.78 ppm and the carbon connected to the hydroxyl group is observed at 161.91 ppm. From the ^{13}C NMR spectra, the carbon in the imine functional group shifted upfield from the carbonyl range, and the imine peaked at 165.65, 162.69, 166.51 and 162.71 ppm for **S1**, **S2**, **S6** and **S9** respectively. Furthermore, the hydroxyl functional groups on **S1**, **S2**, and **S6** were observed at 161.16, 161.20, and 161.01 ppm, respectively.

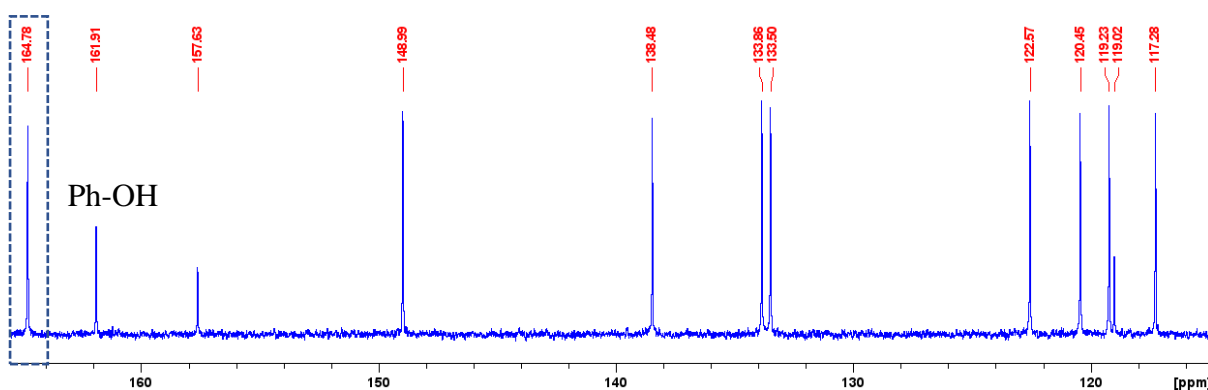


Figure 2.5: ^{13}C NMR spectrum of **S3** in CDCl_3 .

The FT-IR of the Schiff-based compounds **S1** (**Figure S 2.2**), **S2** (**Figure S 2.6**), **S6** (**Figure S 2.12**) and **S9** (**Figure S 2.16**) are shown in the supplementary information.

The IR spectra show the presence of hydroxyl functional groups above 3000 cm^{-1} , as expected. A paper by G. Erten and co-workers proposed that the imine Schiff base can be identified by a peak at 1610 cm^{-1} .⁷ The Schiff base functional group was observed between 1608 cm^{-1} and 1627 cm^{-1} for **S1**, **S2**, **S3** and **S6**. **S9** displayed a more shifted peak at 1638 cm^{-1} . **S3** is shown in **Figure 2.6**, the peak from the pyridine moiety is observed at 3651 cm^{-1} with the hydroxyl peak at 3054 cm^{-1} . The Schiff base displayed a strong peak at 1613 cm^{-1} .

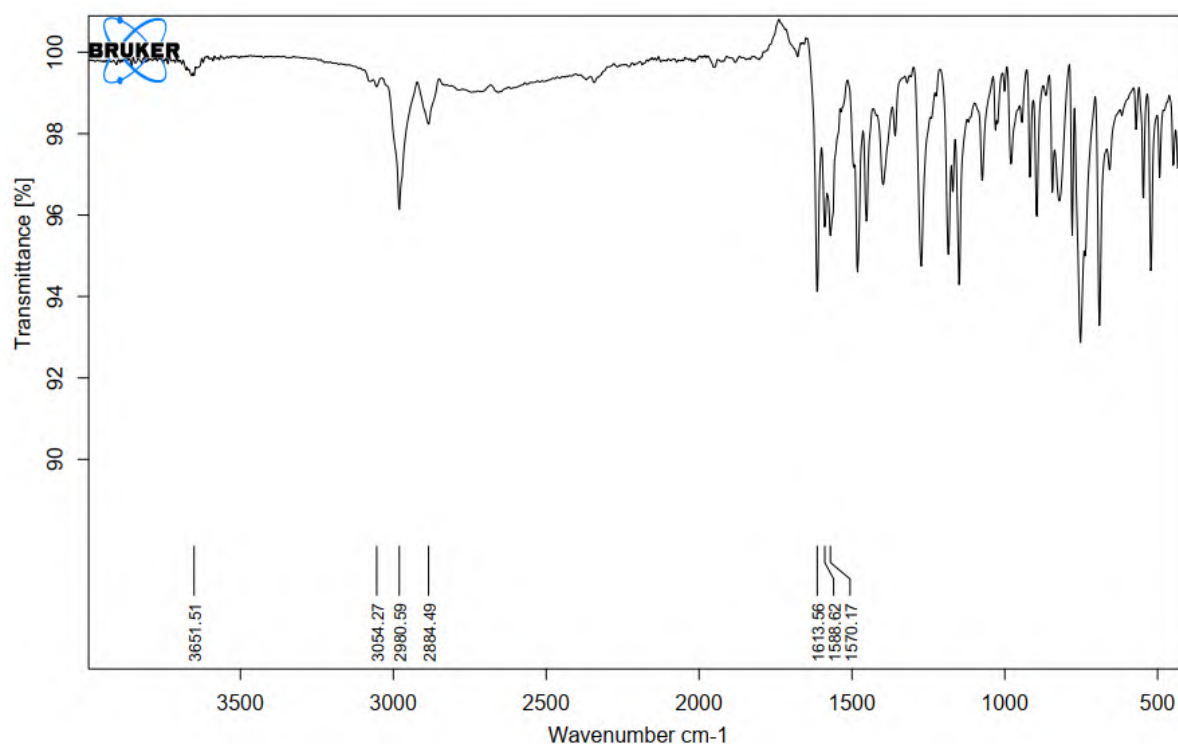
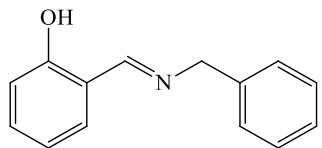
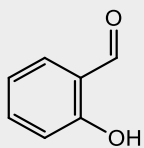
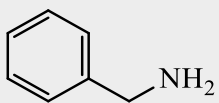
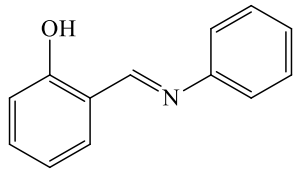
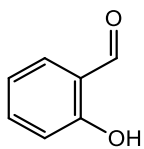
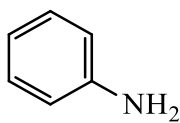
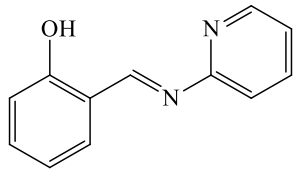
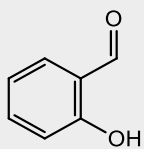
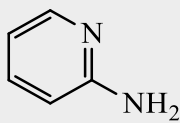
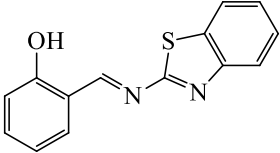
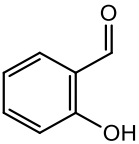
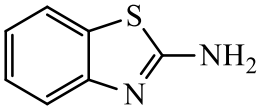
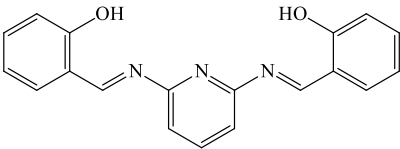
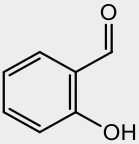
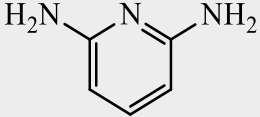
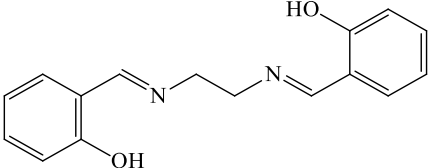
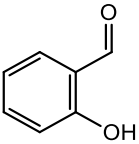
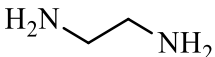
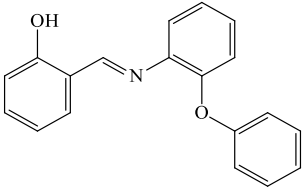
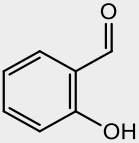
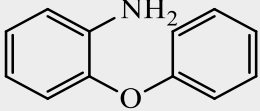


Figure 2.6: FT-IR spectrum of **S3**.

Table 2.1: All nine attempted Schiff-based chemosensors.

Compound	Aldehyde	Amine	Resulting product	Precipitate colour
 <p>S1</p>	 <p>Salicylaldehyde</p>	 <p>Benzylamine</p>	Pure S1	Yellow
 <p>S2</p>	 <p>Salicylaldehyde</p>	 <p>Aniline</p>	Pure S2	Yellow
 <p>S3</p>	 <p>Salicylaldehyde</p>	 <p>Pyridin-2-amine</p>	Pure S3	Yellow-Orange

 <p>S4</p>	 <p>Salicylaldehyde</p>	 <p>2-Aminobenzothiazole</p>	2-Aminobenzothiazole	n/a
 <p>S5</p>	 <p>Salicylaldehyde</p>	 <p>Pyridine-2,6-diamine</p>	Pyridine-2,6-diamine & Salicylaldehyde	Dark brown
 <p>S6</p>	 <p>Salicylaldehyde</p>	 <p>Ethane-1,2-diamine</p>	Pure S6	Yellow
 <p>S7</p>	 <p>Salicylaldehyde</p>	 <p>2-Phenoxyaniline</p>	2-Phenoxyaniline & Salicylaldehyde	Black

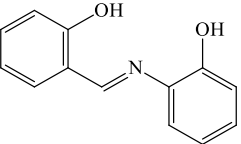
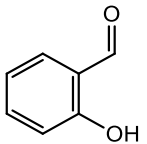
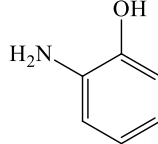
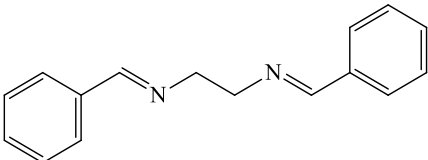
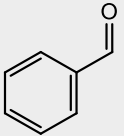
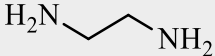
 <p>S8</p>	 <p>Salicylaldehyde</p>	 <p>2-Aminophenol</p>	Salicylaldehyde & 2-Aminophenol	n/a
 <p>S9</p>	 <p>Benzaldehyde</p>	 <p>Ethane-1,2-diamine</p>	Pure S9	Yellow

Table 2.1 shows the results of these reactions. Not all the intended compounds were successfully synthesised as in some cases, the amides and salicylaldehyde were identified as the final products (**S4**, **S5**, **S7** and **S8**) as the primary amide and aldehyde protons were observed in the ^1H NMR. However, only five Schiff bases were successfully prepared (**S1**, **S2**, **S3**, **S6** and **S9**). The four salicylaldehyde-based compounds (**S1**, **S2**, **S3** and **S6**) and the benzaldehyde-derived compound, **S9**, are shown in **Scheme 2.4**. **S9** was synthesised to compare and determine the hydroxyl group's function during complexation.

2.4 Absorption studies of Schiff base derivatives

The absorbance spectra of the Schiff base derivatives **S1**, **S2**, **S3**, **S6** and **S9** were obtained and investigated in a polar aprotic and protic solvent. Due to their environmentally favourable properties, it was decided to use acetonitrile as the aprotic solvent and methanol as the protic solvent.

The absorbance spectra of all the synthesised Schiff bases are shown in **Figure 2.7** using both the polar solvents, acetonitrile, shown with a solid line and methanol, indicated with a dashed line. **S1** (shown in red) displayed two bands, 254 nm and 315 nm, in both acetonitrile and methanol. Notable is the hyperchromic shift of 14% observed at 254 nm in the presence of the polar protic solvent, methanol, which was not observed in the aprotic solvent. This could be attributed to the solvent effect. However, **S2** (shown in orange) showed no change between the two polar solvents. **S2** displayed two absorbance bands at 270 nm and 335 nm. In contrast, the Schiff base containing a pyridine substituent, **S3** (green in **Figure 2.7**), displayed a hypochromic shift in the presence of methanol as compared to acetonitrile. **S3** shows a band at 302 nm with two shoulder bands on either side, 270 nm and 344 nm, respectively. **S6** (blue in **Figure 2.7**), which closely resembles **S1**, displayed the same bands, 254 nm and 315 nm, in both acetonitrile and methanol, with a hyperchromic shift of 10%. In addition, **S6** has a hyperchromic shift (22% in acetonitrile and 18% methanol) compared to **S1**, which can be attributed to the second Schiff base in **S6**. **S9**, which does not contain any hydroxyl groups, had the strongest absorbance among all the chemosensors. **S9** (shown in purple) has an absorbance band at 245 nm in acetonitrile and 247 nm in methanol, a slight bathochromic shift.

When **S9** is compared to **S6**, **S9** has a hyperchromic shift of 56% in acetonitrile and 48% in methanol. This difference between these absorbances can be attributed to the hydroxyl groups' effects on the Schiff bases, as seen in **Figure 2.8 a**). The hydroxyl groups can lead to hydrogen bonding (yellow dashed line) with the nitrogen in the Schiff base moiety, resulting in a more rigid conformer. In addition, the electron-rich (red region) oxygen from the hydroxyl group can result in an inductive withdrawing effect from the Schiff base, causing a partial positive region on the hydrogen – indicated by the blue region. The resonance caused by the phenol group could also potentially contribute to the difference in intensities. The molecular modelling studies confirmed this effect and were recently published by our group.⁸

In the literature, it is reported that the phenol group can display two absorption bands between 200 and 360 nm. The same behaviour was observed for compounds **S1**, **S2**, **S3**, and **S6**.⁹ Furthermore, it has been observed in the literature that solvents can also contribute to the spectral changes of phenol groups.^{9,10} The same effect was observed with our Schiff bases containing the hydroxy group.

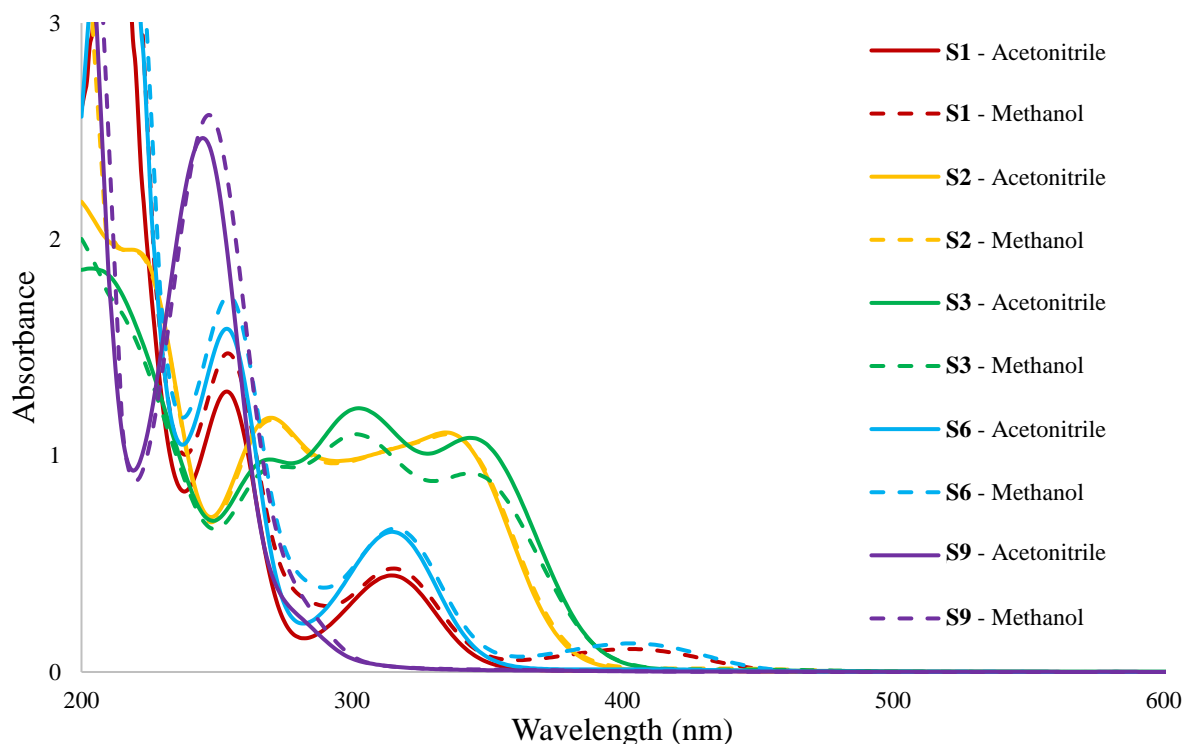


Figure 2.7: UV-vis spectra of **S1** (red), **S2** (yellow), **S3** (green), **S6** (light blue) and **S9** (purple) in acetonitrile (solid lines) and methanol (dash lines) with a concentration of 0.1 mM.

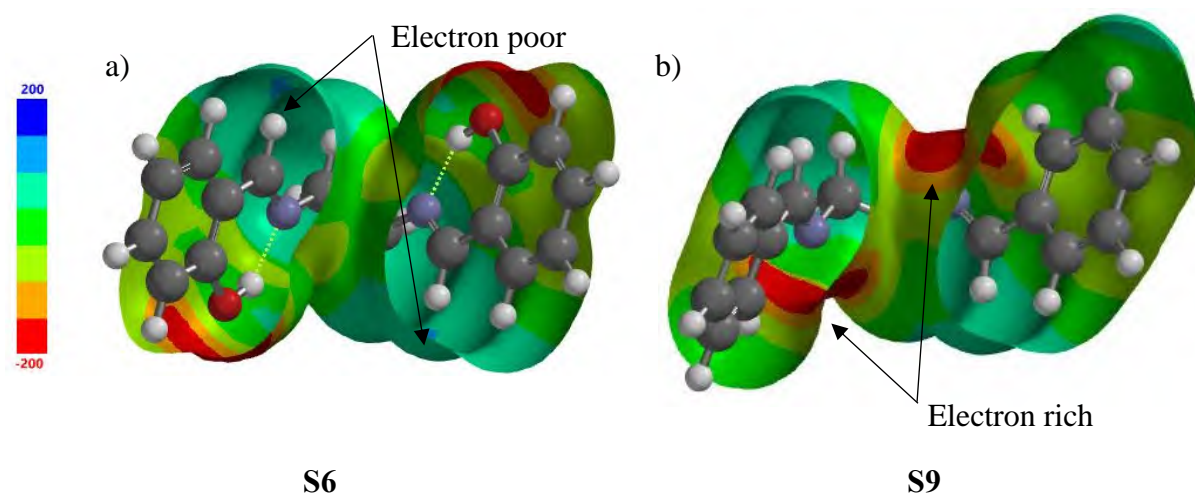


Figure 2.8: Computational electrostatic potential map of a) **S6** and b) **S9**.

2.5 Application of Schiff bases as chemosensors

2.5.1 Screening of metal ions

The application of Schiff bases as chemosensors for cation detection was investigated using their absorption characteristics in the presence of various metal cations. These metal cations include Na^+ , Mg^{2+} , Al^{3+} , K^+ , Ca^{2+} , Cr^{3+} , Mn^{2+} , Fe^{2+} , Fe^{3+} , Co^{3+} , Ni^{2+} , Cu^{2+} , Zn^{2+} , Pb^{2+} , Ag^+ , Cd^{2+} , Ba^{2+} , and Hg^{2+} . The screening was conducted in both acetonitrile and methanol.

Compounds **S1**, **S3** and **S9** showed no significant changes in the absorbance spectra. Thus, no complexation occurred with the metal cations tested in either solvent and can be found in the supplementary information, **Figure S 2.3**, **Figure S 2.9** and **Figure S 2.17**, respectively.

However, **S2** displayed a unique interaction with Cu^{2+} with a new band forming at 575 nm, which yields a colour change from clear to blue, as shown in green in **Figure 2.9 a**). Furthermore, Cu^{2+} also induced a blue shift (hypsochromic shift) towards 251 nm (from 271 nm) and 320 nm (from 335 nm) in addition to the hypochromic shift. It was also observed that the interaction was not immediate, leading to a time study being conducted in **section 2.5.1.1** below. A colourimetric change was also observed from a clear solution to a blue solution (please see **Figure S 2.7** in the supplementary information).

The testing of **S2** was also conducted in methanol. However, no interaction of interest was observed. Therefore, it can be concluded that the solvent assisted in the complexation of Cu^{2+} .

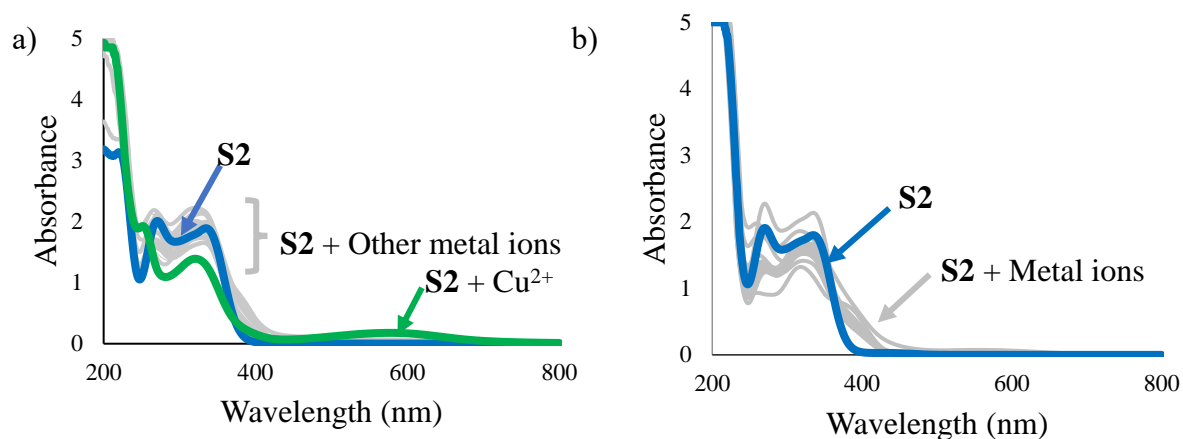


Figure 2.9: The screening of metal cations (0.167 mM) using S2 (0.167 mM). a) S2 (blue) in acetonitrile has two bands at 271 nm and 335 nm, and a newly formed band appears at 575 nm in the presence of Cu²⁺ (green). b) S2 (blue) in methanol showed no change in the spectra with the addition of the metal cations.

S6 also displayed interesting and unique interactions upon the addition of Ni²⁺, Fe²⁺ and Cu²⁺ in acetonitrile, **Figure 2.10 a)** and Fe²⁺ and Fe³⁺ in methanol, **Figure 2.10 b)**.

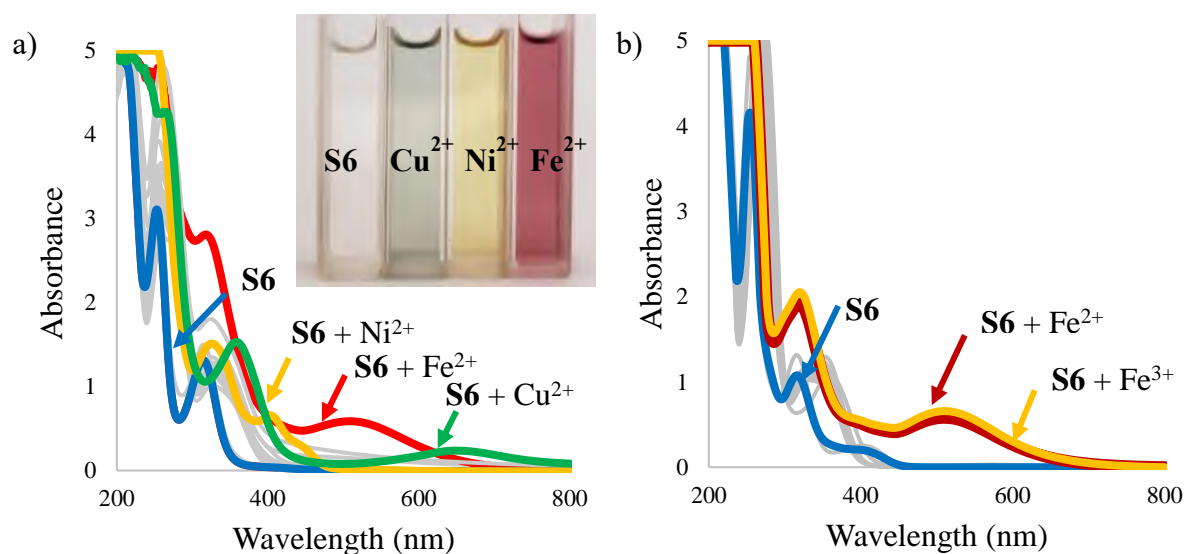


Figure 2.10: The screening of metal cations (0.167 mM) using S6 (0.167 mM). a) S6 (blue) in acetonitrile has two absorbance bands, 253 nm and 314 nm, with the addition of Ni²⁺ (yellow), a new band formed at 402 nm. In Fe²⁺ (red) presence, a new band has formed at 515 nm. Cu²⁺ (green) induced a new band at 655 nm. b) S6 (blue) in methanol. In Fe²⁺ (red) and Fe³⁺ (yellow) presence, S6 had a new band at 510 nm for both cations. Inset: Photographic image of colour change induced by the addition of the metal ions.

With the addition of Ni^{2+} in acetonitrile, a new band formed at 402 nm resulting in a colourimetric change to yellow, as seen in **Figure 2.11**. Fe^{2+} induced a red colourimetric change in **S6** and formed a new band at 515 nm (**Figure 2.10 a**). Cu^{2+} formed a new band at 655 nm resulting in a blue-green colour change. The bands arising from the hydroxyl substituent also showed spectral changes, indicating that the hydroxyl group contributes towards complexation. This is also supported by the fact that **S9**, having no hydroxyl groups, shows no selectivity towards these ions (**Figure S 2.17**).

Chemosensor **S6** can uniquely identify three different cations, namely Ni^{2+} , Fe^{2+} and Cu^{2+} , with each having its characteristic colour, yellow, red, and blue, respectively, as seen in **Figure 2.11**. As seen from **Figure 2.11**, except for Fe^{3+} , which has a slight pink tone, no other metal induces a colour change.



Figure 2.11: A photographic image of **S6** (colourless) in the presence of various metal ions showing the colour change induced by Fe^{2+} (red), Ni^{2+} (yellow) and Cu^{2+} (blue).

It was also observed from the literature that a similar Schiff-based chemosensor capped onto gold nanoparticles could display selectivity towards Ni^{2+} , Fe^{3+} , and Cu^{2+} . However, the colourimetric change was the same for all three metal cations, from red to purple.¹¹

2.5.1.1 Time study of **S2**- Cu^{2+} complex formation

It was observed that the complexation between **S2** and Cu^{2+} was not immediate as seen for **S6** and Cu^{2+} . A time study was then conducted to determine the effectiveness of **S2** as a fast and real-time chemosensor. Cu^{2+} (0.167 mM) was introduced to **S2** (0.167 mM) in acetonitrile, and the absorbance was measured at 575 nm. A new band emerged as the complex was forming.

Figure 2.12 shows the resulting formation of the **S2**- Cu^{2+} complex over time (0 – 30 minutes). The complex does not form rapidly as suspected, and the linear correlation ends after 5 minutes,

after which the complexation takes longer to form, with a saturation point observed after 25 minutes.

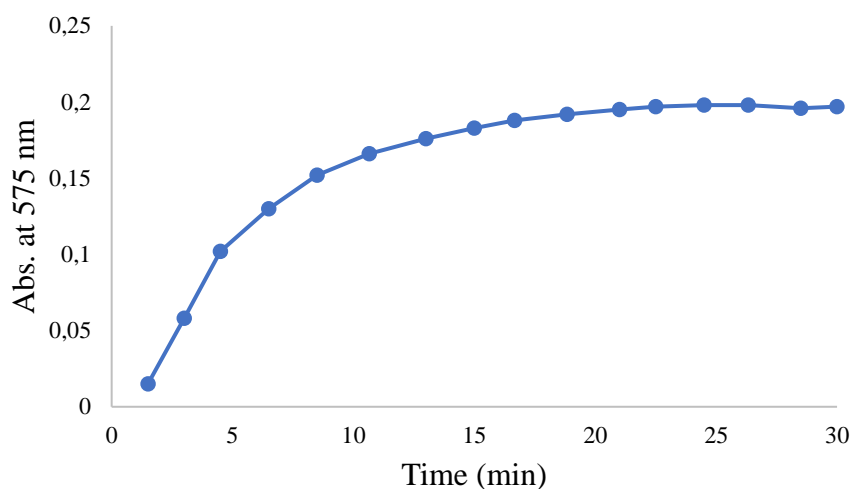


Figure 2.12: Absorbance of **S2**-Cu²⁺ complex at 575 nm in acetonitrile over time.

Due to the slow formation of the **S2**-Cu²⁺ complex, **S2** has proven not to be a reliable chemosensor for real-life applications. Hence further investigation was halted.

2.5.1.2 Metal ion competition studies of **S6**-Ni²⁺, **S6**-Fe²⁺, and **S6**-Cu²⁺ complexes

Our primary focus of this investigation was to design a chemosensor capable of identifying a specific metal ion in the presence of other ions with conclusive results. Hence, competition studies were conducted to determine the selectivity of **S6** towards a preferred metal ion in the presence of competing ions.

The observed selectivity of **S6** towards Ni²⁺, Fe²⁺ and Cu²⁺ were tested in the presence of other metal ions. This was achieved by adding the two competing cations (equal amounts, 0.167 mM) in the cuvette. **S6** (0.167 mM) is added to the mixture, and the absorbance is measured, as shown in **Figure 2.13**. The competition studies for each metal were performed at each respective absorbance band; 402 nm, 515 nm, and 655 nm, respectively.

Surprisingly, **S6** did not show any selectivity for the preferred cations (Ni²⁺, Fe²⁺ and Cu²⁺) in the presence of competing cations. Although **S6** slightly preferred Cu²⁺ (Cu²⁺ > Ni²⁺ > Fe²⁺), it

would not accurately determine the presence or concentration, as the colour is not as intense as observed in the screening.

This led us to conclude that as much as **S6** shows unique interactions with Ni^{2+} , Fe^{2+} and Cu^{2+} during complexation, other ions strongly affect this interaction. Hence, **S6** was found not to be a reliable chemosensor in the presence of competing cations. Therefore, further studies were halted for **S6**.

Note: Titration studies can be found in the supplementary information **Figure S 2.13**.

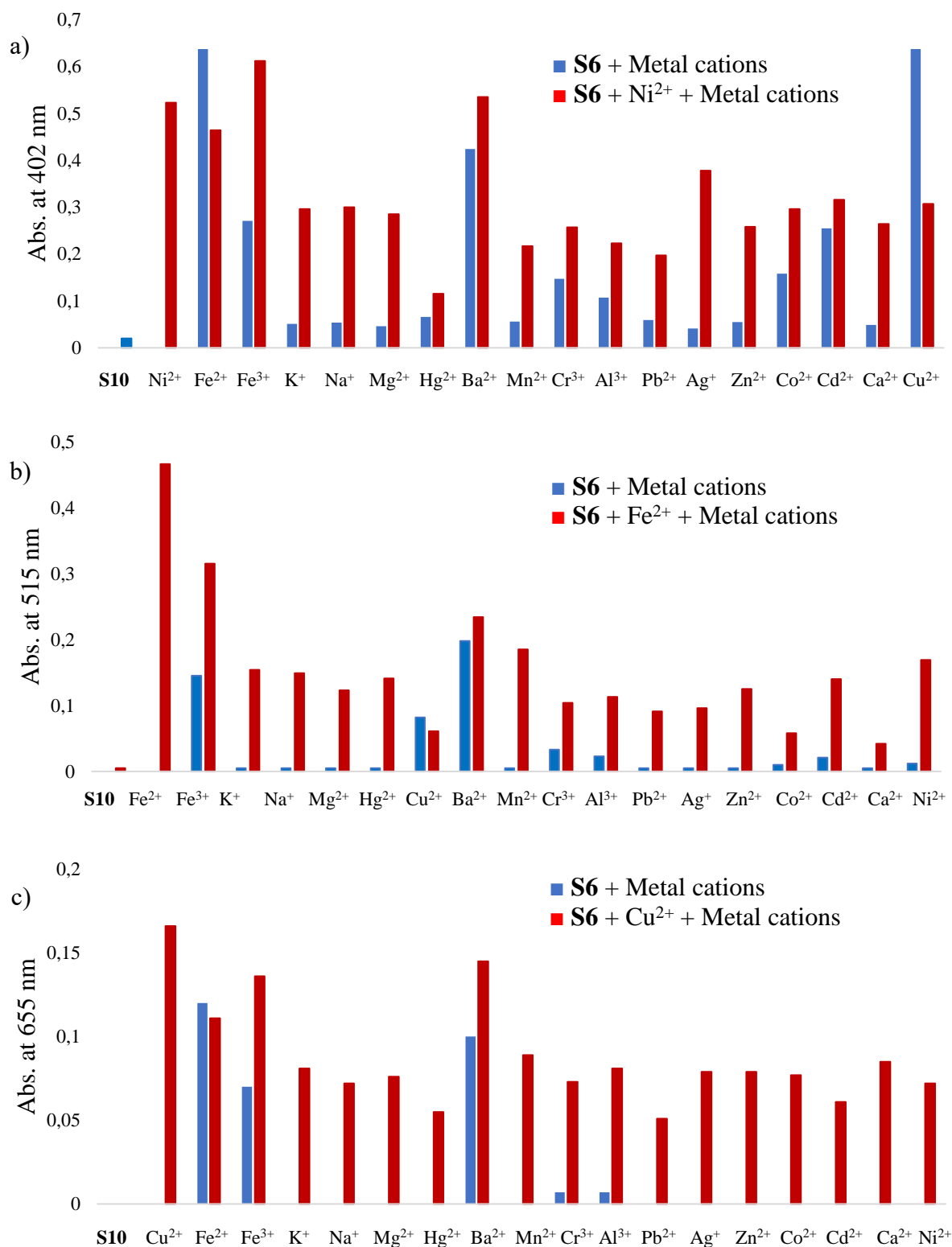


Figure 2.13: Competition studies of *S6* (0.167 mM) in acetonitrile. a) Ni²⁺ (0.167 mM), b) Fe²⁺ (0.167 mM), and c) Cu²⁺ (0.167 mM). Each experiment was conducted in the presence of 0.167 mM competing metal cation.

2.5.2 Screening of anions

Investigation into the potential application of the newly developed Schiff base as anionic chemosensors were explored by screening for; F^- , Cl^- , Br^- , I^- , AcO^- , NC^- , NCS^- , NCO^- , $H_2PO_4^-$ and HSO_4^- tetrabutylammonium salts in acetonitrile and methanol. NO_3^- was not considered as it was the counter ion in **Section 2.5**.

Compounds **S2**, **S3** and **S6** showed no observable interactions towards any anionic analyte tested, as can be seen in the supplementary information, **Figure S 2.8**, **Figure S 2.10**, and **Figure S 2.14**, respectively.

However, **S1** showed interesting results as an anionic chemosensor as it displayed a significant hyperchromic shift (88%), **Figure 2.14 a**) in the presence of iodide with acetonitrile as solvent. Interestingly, the same interaction between **S1** and I^- was not observed in methanol, **Figure 2.14 b**). This could be attributed to the possible interactions of I^- with the hydroxy group via hydrogen bonding. Hence, **S1** could be a better chemosensor for I^- in an aprotic solvent than in a protic solvent.

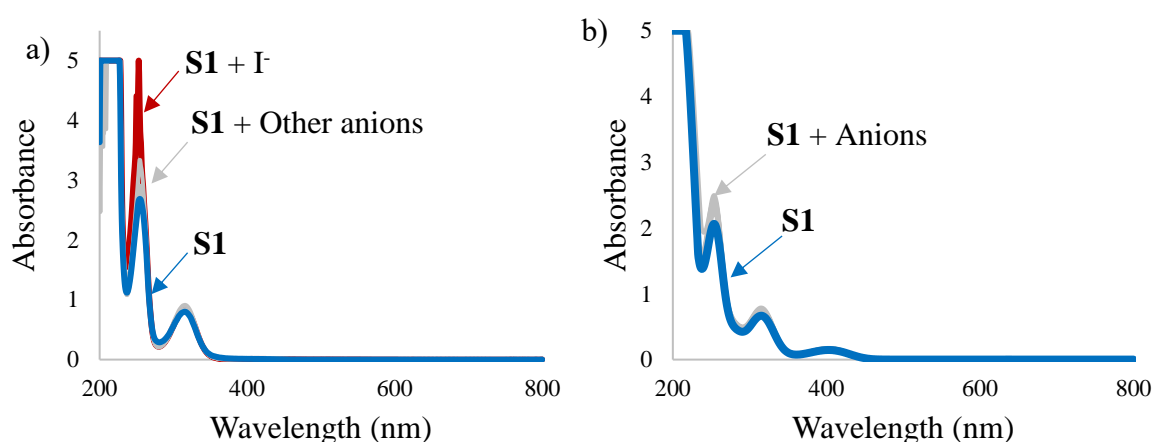


Figure 2.14: Screening of various anions (grey, 0.05 mM and 0.167 mM) using **S1** (blue, 0.167 mM) in a) acetonitrile and b) methanol. Iodide (red) induced a hyperchromic shift in acetonitrile.

However, **S9**, which does not contain a hydroxyl functional group, also had an interesting interaction with I^- in acetonitrile (**Figure 2.15 a**).

S9 showed remarkable dual sensing capabilities, I^- in acetonitrile (**Figure 2.15 a**) and NCO^- in methanol (**Figure 2.15 b**). However, no colour changes were observed for the interaction of **S9** with the screening of anions. Both I^- and NCO^- resulted in a hyperchromic shift of 74% at 245 nm in acetonitrile and 247 nm in methanol.

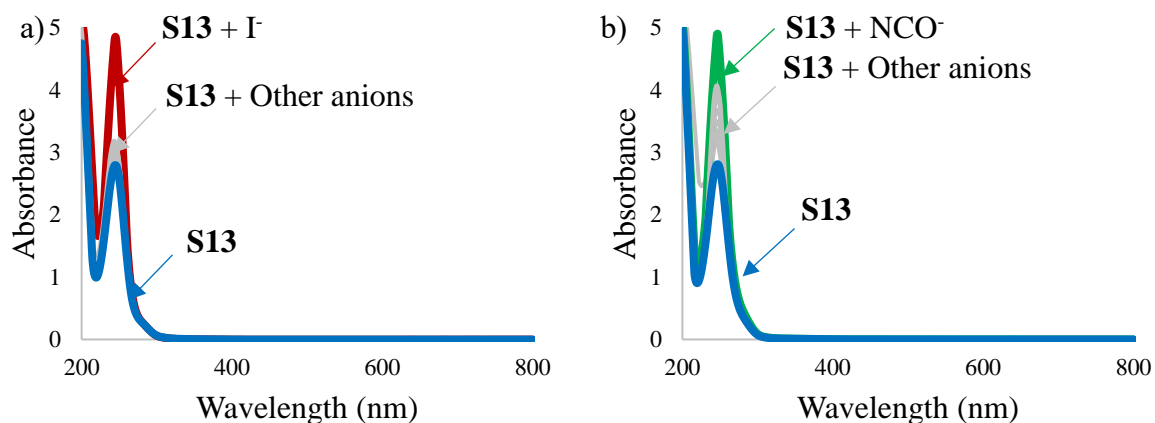


Figure 2.15: Screening of various anions (grey, 0.1 mM) using **S9** (blue, 0.1 mM) in a) acetonitrile and b) methanol. Iodide (red) induced a hyperchromic shift in acetonitrile, whereas cyanate (green) induced a hyperchromic shift in methanol.

2.5.2.1 Anion competition studies

Iodide has eluded chemosensors as the analyte of choice due to its larger size and weaker basicity than other halogen ions (F^- , Cl^- and Br^-).¹² Furthermore, the binding capacities of iodide with the chemosensor are the weakest of the halogen ions, which tend to have a binding order of $\text{F}^- > \text{Cl}^- > \text{Br}^- > \text{I}^-$.¹² Therefore, further investigation into **S1** and **S9** anionic sensing capabilities was performed.

Competition studies were conducted on **S1** to determine the selectivity towards I^- in the presence of other anions in acetonitrile. **Figure 2.16** revealed that **S1** has a higher affinity towards I^- than other anions. Fluoride ions posed some interference, however, **S1** still showed a higher affinity towards I^- .

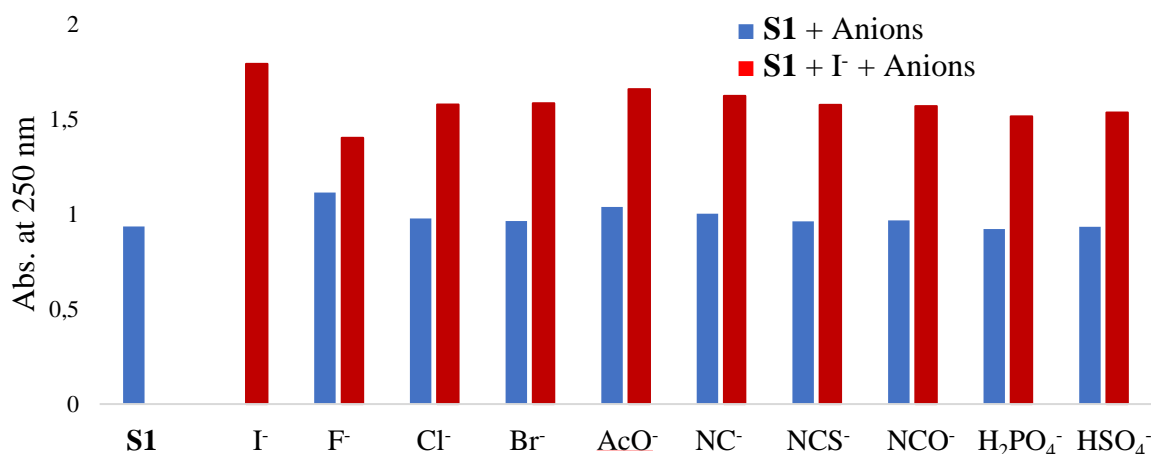


Figure 2.16: Competition studies of I^- (0.05 mM) with competing anions (0.05 mM) in acetonitrile towards **S1** (0.1 mM).

However, **S9** showed no selectivity for I^- , in acetonitrile, and NCO^- , in methanol, above other competing anions. Results for these experiments are illustrated in **Figure S 2.18** for I^- and **Figure S 2.19** for NCO^- in the supplementary information section.

2.5.2.2 Titrations studies

To gain further insights into the chemosensor properties of **S1** towards I^- sensing, titration studies (**Figure 2.17**) were performed in acetonitrile. The titration studies revealed that the band at 315 nm remained relatively constant even with the increased amounts of I^- . However, the band at 254 nm displayed a gradual hypsochromic shift to 245 nm with the increased amounts of I^- ; however, no colour change was observed.

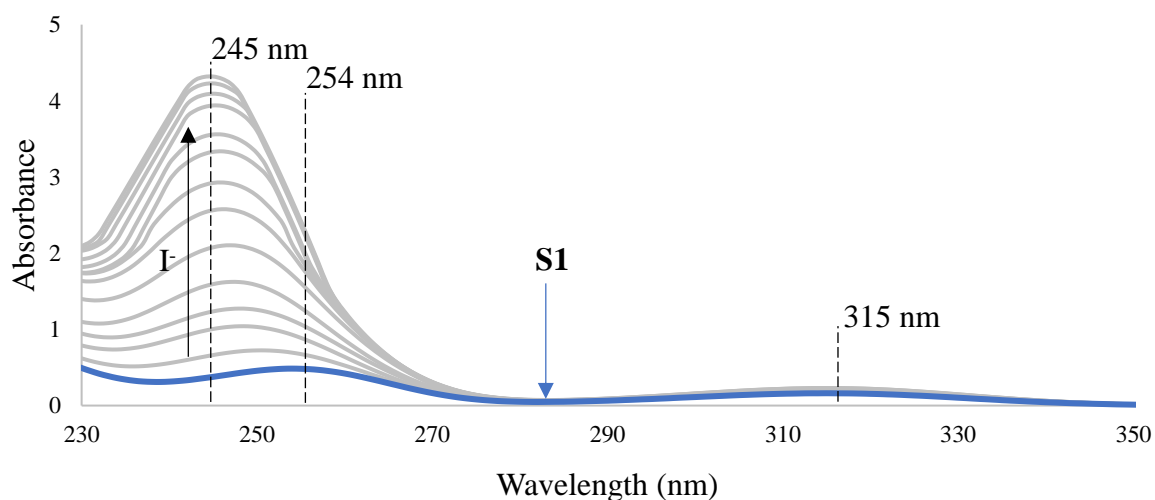


Figure 2.17: Titration studies of **S1** (0.033 mM) with the addition of I^- .

For these results, a limit of detection (LOD) could be determined and was calculated to be 0.027 mM, and the limit of quantification (LOQ) was determined to be 0.083 mM.

To obtain the concentration range at which the chemosensor **S1** can be used, further data processing was performed in which the absorbance at 245 nm was plotted against the concentration of I⁻. A linear relationship was obtained in **Figure 2.18 a)**. Two outliers were observed, as shown in **Figure S 2.4**. As inconsistencies (outliers) can occur, a ratiometric-like approach was considered in which the band at 315 nm is used as internal calibration. An exponential relationship was observed due to the band at 315 nm remaining relatively constant. Interestingly, the two outliers from **a)** fall on the exponential trendline in **b)** (shown in orange), which shows the importance of calibration and standardisation of the 315 nm band. Thus, using **S1** as a single pattern ratiometric chemosensor fits the data more accurately than using a single wavelength band.

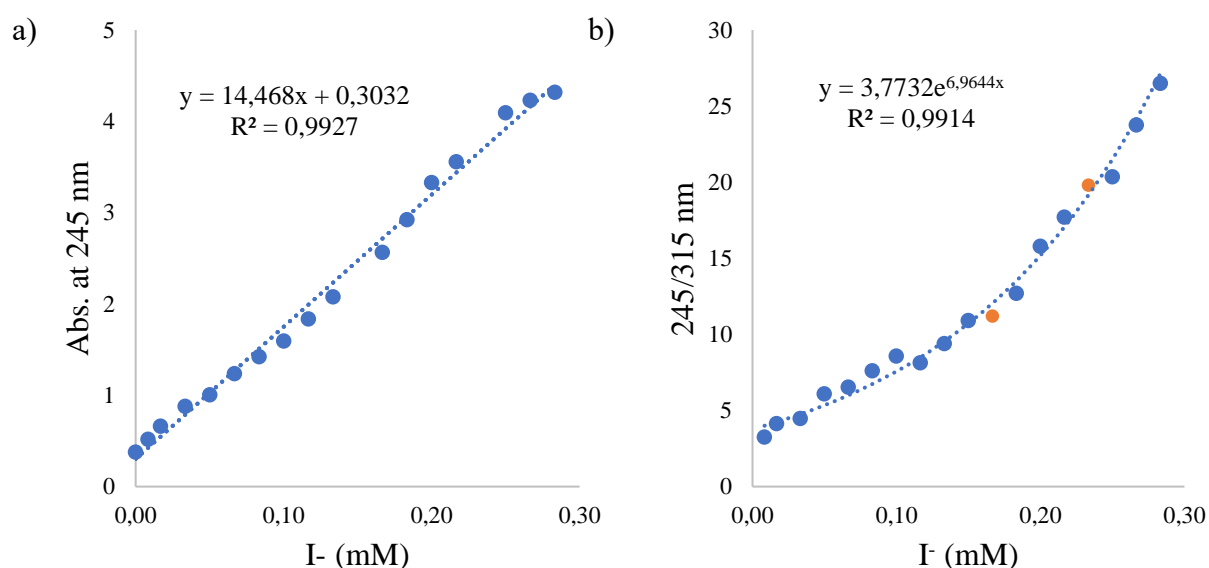


Figure 2.18: a) Absorbance of the **S1**-I⁻ complex at 245 nm as a function of the I⁻ concentration. b) Exponential relationship of the absorption of **S1**-I⁻ complex at $\frac{245 \text{ nm}}{315 \text{ nm}}$ as a function of I⁻ concentration.

2.5.3 The proposed binding site and computational studies

Further understanding of the formation and interaction of the complexation between chemosensors **S1**, **S2**, **S6** and **S9** with their respective analytes were investigated using ¹H NMR spectrometry and computational studies. Computational studies were performed using

Spartan Student v8 at PM3 equilibrium geometry, after performing conformer distribution at the MMFF level.

2.5.3.1 **S1** binding studies

S1 showed selective affinity towards I⁻. Therefore, further investigation into the binding mode between **S1** and I⁻ was done. The Benesi-Hildebrand plot was constructed from the titration data to determine the binding ratio, ¹H NMR titrations indicated the protons involved in complexation, and with the aid of computational chemistry, the possible binding sites were determined and visually illustrated. The computational studies, combined with ¹H NMR, provide valuable insights into the complexation mechanism. ¹H NMR studies were performed in deuterated acetonitrile to maintain the complex as the complex did not form in the polar protic solvent, methanol.

The Benesi-Hildebrand plot was derived using the Benesi-Hildebrand equation (1) given below.

$$\frac{1}{(A - A_0)} = \left(\frac{1}{K(A_{max} - A_0)[M]_n} \right) + \left(\frac{1}{(A_{max} - A_0)} \right) \quad (1)$$

In the above equation (1), A is the absorbance of the sensor-analyte complex at a particular wavelength, and A₀ is the absorbance of the sensor in the absence of the analyte, K is the binding constant for the sensor-analyte complex, and [M]_n represents the concentration of the analyte.¹³ Therefore a linear plot of 1/A-A₀ vs 1/[I⁻] could be constructed for the **S1**-I⁻ complex, as shown in **Figure 2.19**. The linearity of the trend line (R² = 0.9951) suggests a 1:1 binding ratio between **S1** and I⁻. The binding constant was determined to be 2,63 x 10³ M⁻¹, indicating the bond's strength between the two components in the complex.^{13,14}

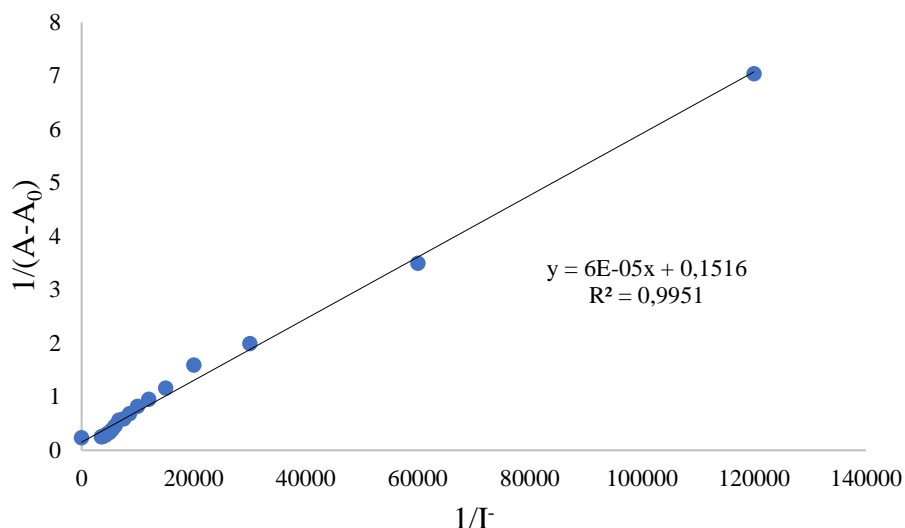


Figure 2.19: Benesi-Hildebrand plot of **S1**(0.033 mM) with I^- in acetonitrile.

Figure 2.20 shows the ^1H NMR spectra of **S1** with subsequent additions of I^- . The most significant change in the spectra was observed at 13.45 ppm, which was assigned to the hydroxyl proton in the phenyl ring (shown in the dotted box). This suggests that the hydroxyl proton contributes the most towards the complexation with I^- . Furthermore, the peak does not entirely disappear, which could indicate that the proton is not abstracted, and no bonds are broken. Moreover, it is also important to note that the Schiff base proton peak at 8.61 ppm displayed no change in position or intensity, suggesting that the Schiff base moiety is not likely to be involved with the formation of the complex with I^- .

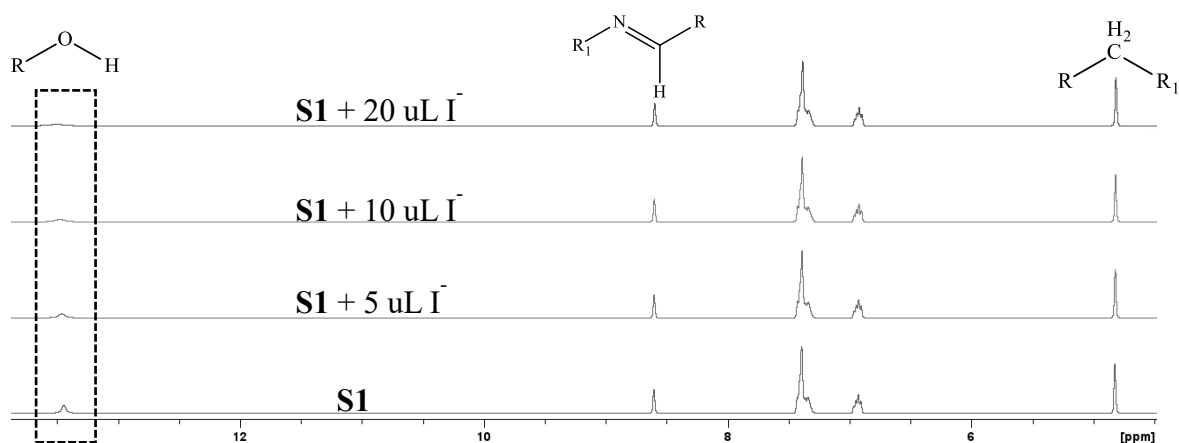


Figure 2.20: ^1H NMR spectra of **S1** with and without varying quantities of I^- . Solvent: Acetonitrile- d_3 .

Computational chemistry was advised to gain more insights into the binding mechanism. Six stable complex conformers were identified, from which four conformers showed unique binding locations, as shown in **Figure 2.21**. The conformers a) and b) illustrate similar binding interactions at either side of the Schiff base, and the hydroxy proton is hydrogen bonded to the nitrogen Schiff base. On the other hand, in conformer c), three sites are involved, the Schiff base proton, benzene, and hydroxyl proton, to stabilise the big I⁻ atom. However, the ¹H NMR spectra showed that the Schiff base proton does not contribute towards complexation between the iodide ion and **S1**, therefore, ruling out conformers a), b), and c). The last conformer, d), shows the possible involvement of the hydroxyl proton and the phenyl ring. The phenyl proton had only slight changes in the NMR spectra, but this can be explained by the stabilisation of electrons through resonance in the highly conjugated system of the benzene ring. The involvement of the hydroxyl group could be supported by the NMR studies (**Figure 2.20**), together with the fact that the complex could only be formed in an aprotic solvent (**Figure 2.14**).

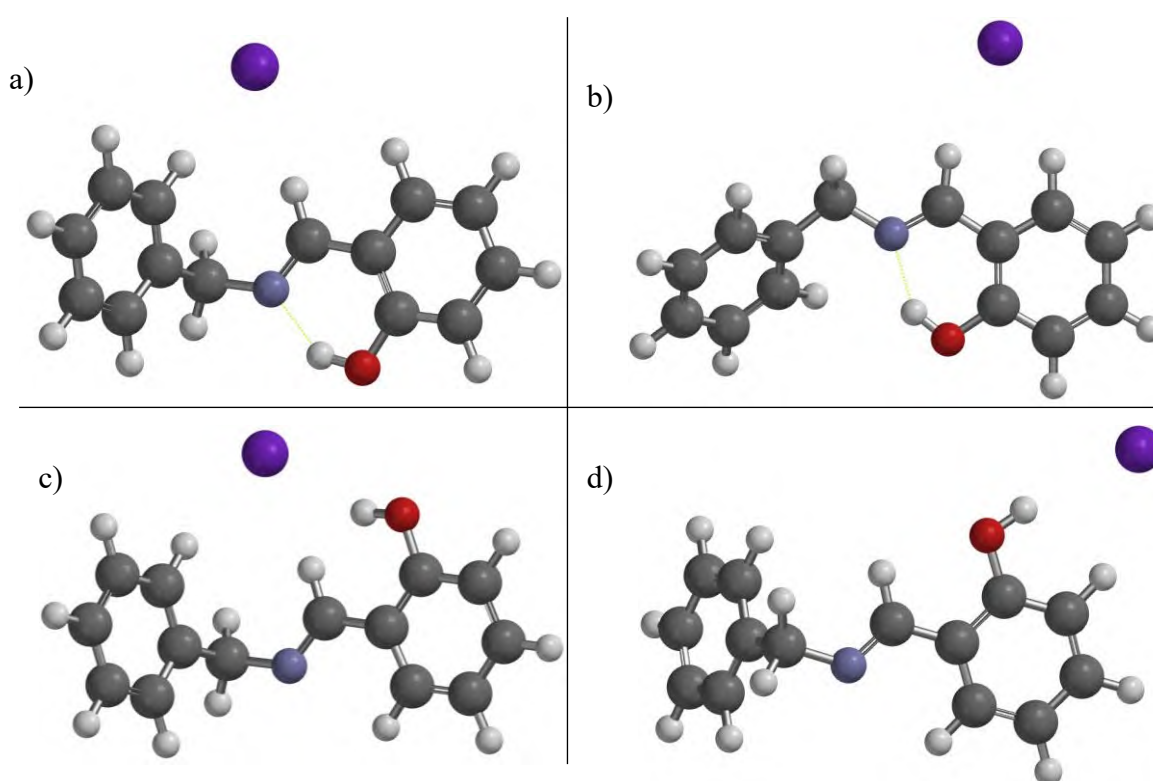


Figure 2.21: Four stable **S1-I⁻** complex conformers.

Further investigation into the effects of the solvent was conducted at the PM3 level. As seen in **Figure 2.22**, the solvent plays a significant role in the complexation of **S1** and I⁻.

Figure 2.22 a) shows the complex with three acetonitrile molecules. Two acetonitrile molecules stabilise the complex showing the same binding site as predicted in **Figure 2.21 b)**. In contrast, in methanol, **Figure 2.22 b)**, the binding site is completely displaced, and the primary form of stabilisation of I⁻ has shifted to methanol, which matched the experimental data.

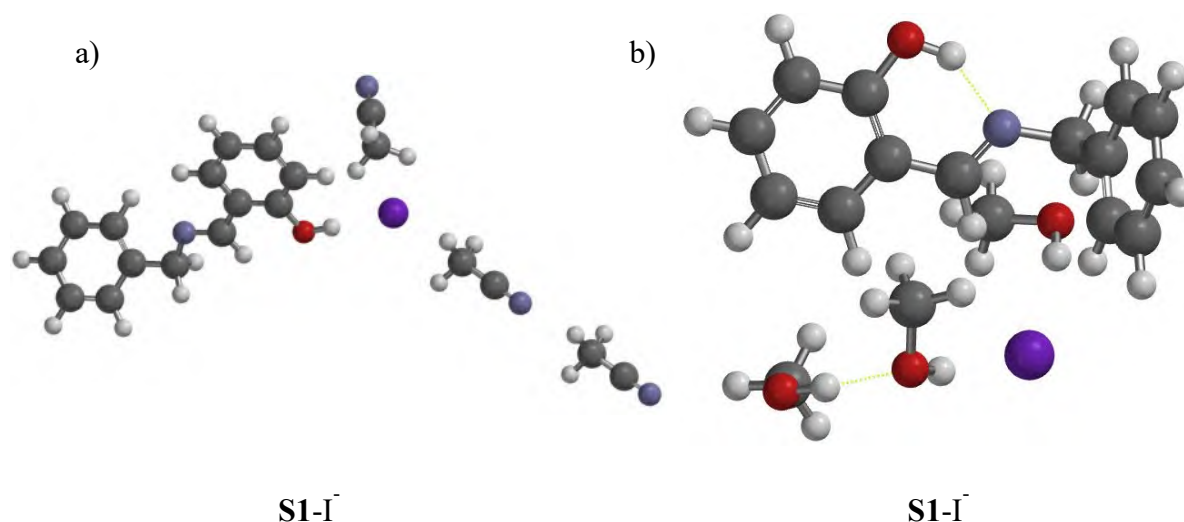


Figure 2.22: Computational illustration of the **S1-I** complex in a) acetonitrile and b) methanol.

2.5.3.2 **S2** binding studies

The complexation of **S2** with Cu²⁺ induced a colour change from clear to blue over time. It is known from the literature that the nitrogen from the Schiff base aid in the complexation of metal cations. Computational chemistry was employed to visualise the **S2-Cu²⁺** complex.

The free **S2** chemosensor is stabilised through hydrogen bonding, as seen in **Figure 2.23 a)**. with the addition of Cu²⁺, the conformer changes by which the hydrogen bond is broken, and the phenyl ring rotates towards the copper ion. The two electronegative atoms (oxygen and nitrogen in the Schiff base) on **S2** stabilise the Cu²⁺ dication, forming a stable six-membered ring (**Figure 2.23 b)**.

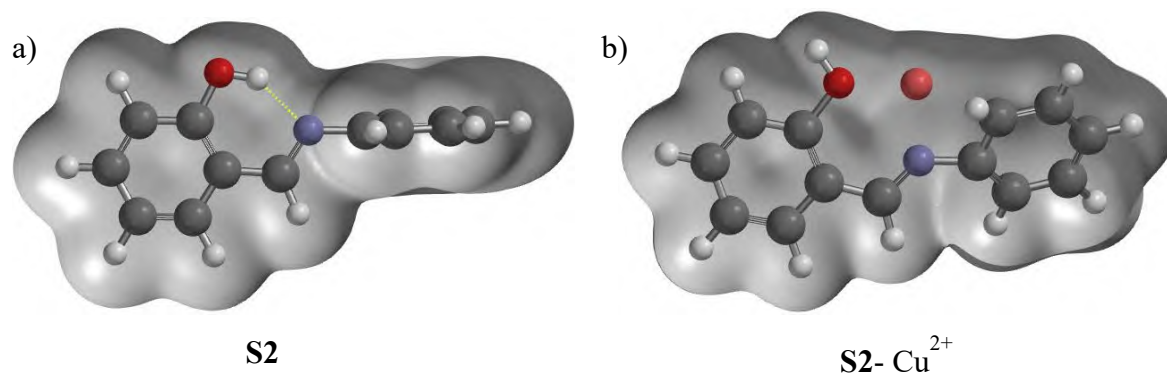


Figure 2.23: Computational illustration of the most preferred conformer of a) **S2** and b) **S2-Cu²⁺** complex. The complexes are shown in their density map.

Further analysis of the complex in the presence of acetonitrile was investigated. The acetonitrile molecules are shown to be involved in the Cu²⁺ complex through the nitrogens (**Figure 2.24**), and the phenyl moiety of **S2** bends away to reduce the steric hindrance seen in **Figure 2.23 b**), leading to the formation of a stable six-membered ring.

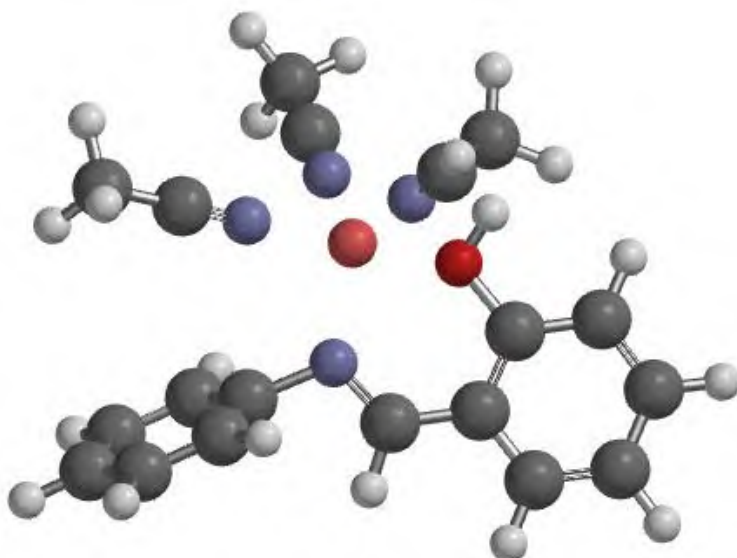


Figure 2.24: **S2-Cu²⁺** complex in acetonitrile.

2.5.3.3 **S6** binding studies

S6 displayed a range of colourimetric changes in the presence of Cu²⁺, Fe²⁺, and Ni²⁺, resulting in colour changes from clear to blue, red, and yellow, respectively. **S6** is a symmetrical compound with two phenol rings and two Schiff bases moieties connected by an ethyl group. The ethyl group allows the molecule to fold on top of each other, as shown in **Figure 2.25 a**).

The Schiff base moiety is stabilised via hydrogen bonding from the phenol ring, as seen for **S1** and **S2**.

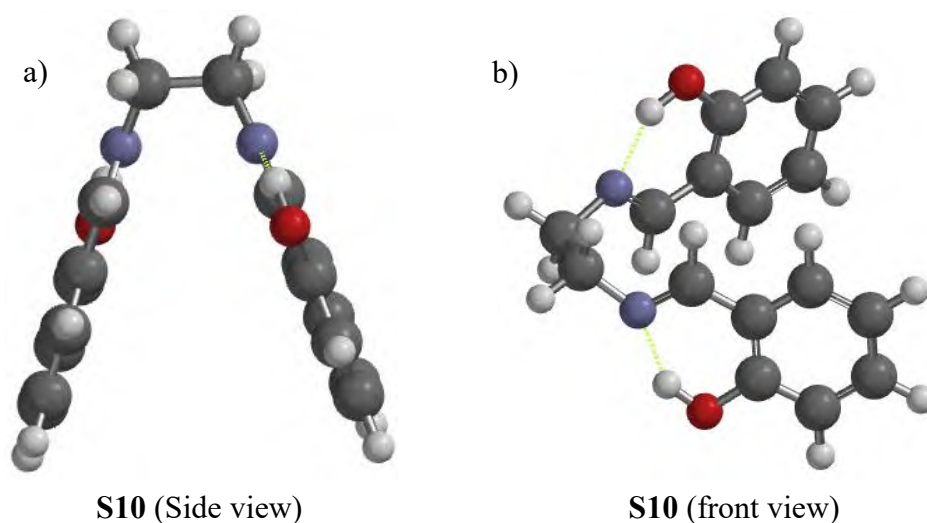


Figure 2.25: Most stable conformer for **S6**.

As **S6** has multiple binding modes, the Schiff base moiety and the hydroxy group, the binding ratio between **S6** and Cu^{2+} was determined using the Benesi-Hildebrand plot, **Figure 2.26**. As seen in **Figure 2.26** below, the trend line does not fit the linear Benesi-Hildebrand equation (1), thus indicating that the binding ratio is not a 1:1 complex and, therefore, the binding constant could not be determined.

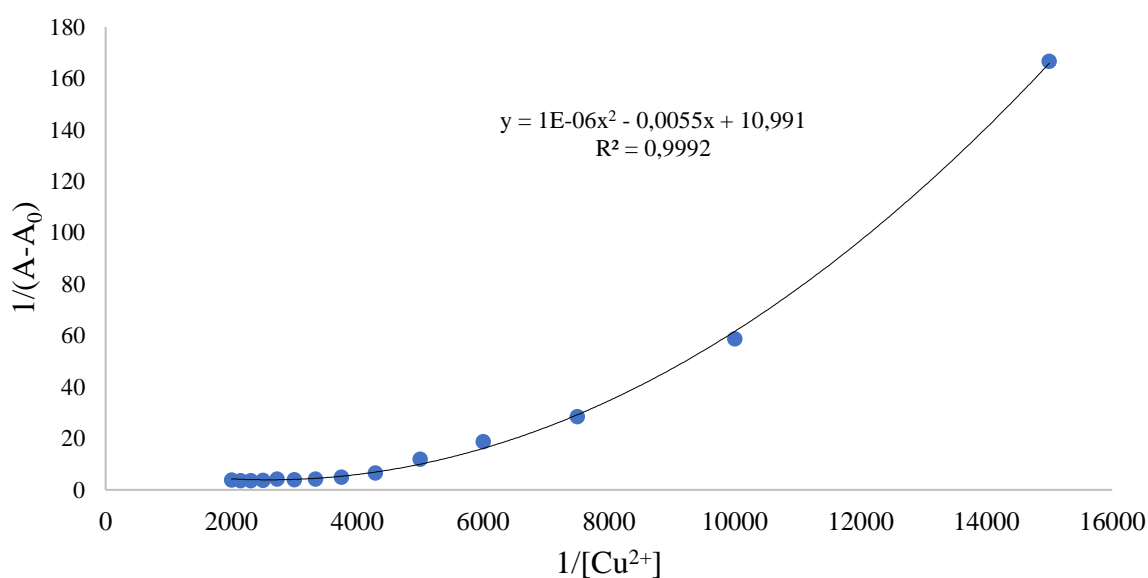


Figure 2.26: Benesi-Hildebrand plot of **S6** (0.167 mM) with Cu^{2+} in acetonitrile.

Hence, a Job's plot was constructed using the continuous method, and the overall concentration was kept constant. The Job's plot in **Figure 2.27** indicated that the binding ratio between **S6** and Cu^{2+} is 1:2 (**S6**: 2Cu^{2+}).¹⁵

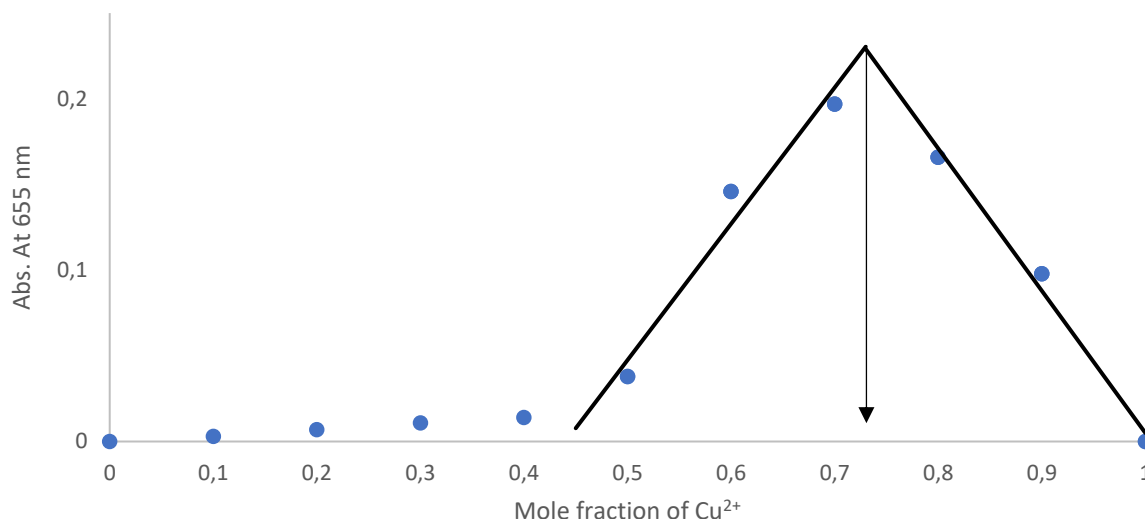


Figure 2.27: Job's plot of **S6** with Cu^{2+} in acetonitrile with an overall concentration of 0.167 mM.

Molecular modelling was employed to illustrate the binding mode for the **S6**- 2Cu^{2+} complex using results from the Job's plot. The modelling studies in **Figure 2.28** concluded that the two Cu^{2+} ions mainly use the two phenyl rings of **S6**. Surprisingly, the hydroxy groups and the Schiff moieties are not involved in the complexation process.

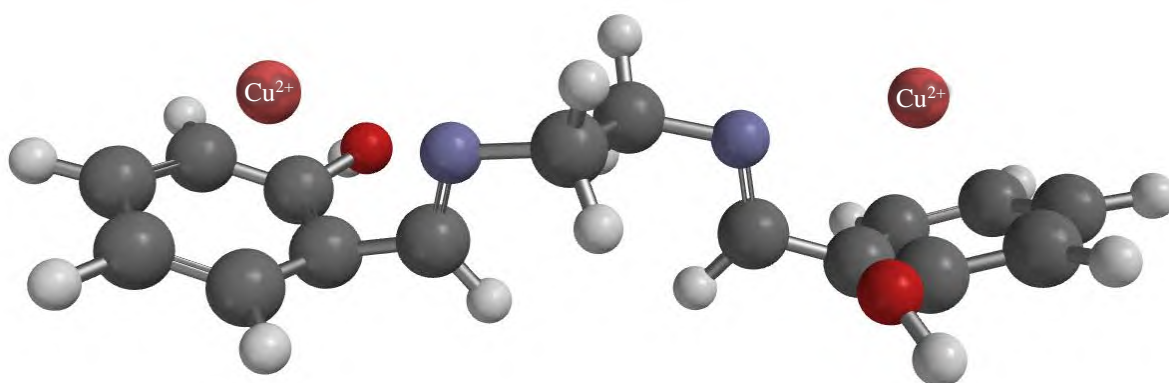


Figure 2.28: Initial molecular modelling of **S6**- 2Cu^{2+} complex at MMFF level.

Higher-level calculations were performed using PM3 calculations, which follows the Hartree-Fock method, used for organometallic molecules.¹⁶ The complex obtained in **Figure 2.29**

revealed an interesting conformer for the complex. The conformer for the complex display a close resemblance to the free **S6**, as seen in **Figure 2.25**. However, the two benzene rings stack much closer to each other due to the presence of the Cu^{2+} atom, the second Cu^{2+} atom complex between the Schiff base nitrogen and the hydroxyl oxygen.

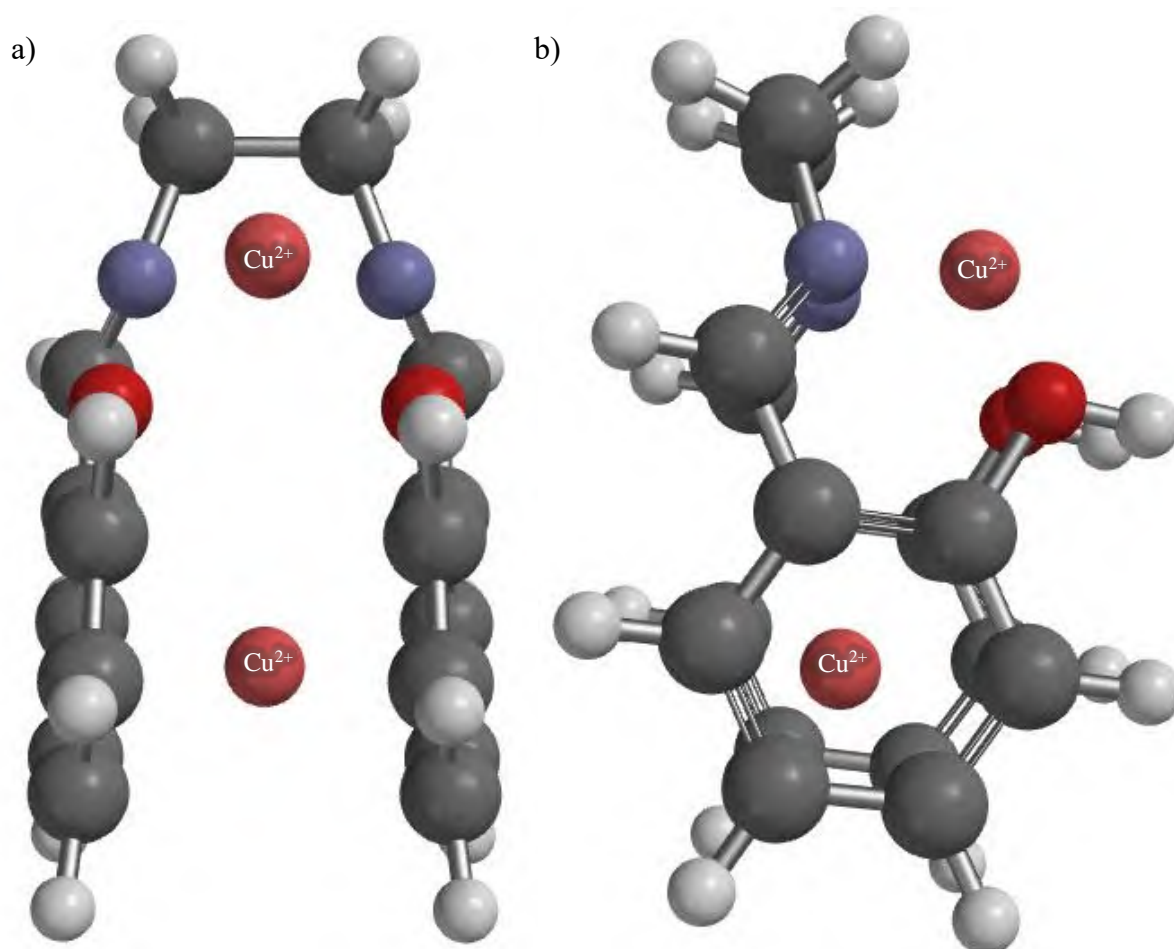


Figure 2.29: Mode of binding of **S6-2Cu²⁺** complex at PM3 level. a) Side-view and b) front view.

¹H NMR titration studies were performed in acetonitrile-d₃ to determine which protons are associated with the complexation process. **Figure 2.30** shows the ¹H NMR spectra of **S6** and **S6-Cu²⁺** complex. As illustrated by the dotted box, the intensity of the hydroxyl proton decreases with subsequent additions of Cu^{2+} . Modelling of the complex, **Figure 2.29**, revealed that one of the Cu^{2+} ions complexes through the hydroxy oxygen, and this hydroxy proton is observed to disappear in the NMR spectra below. The proton from the Schiff base moiety does not seem to be affected by the presence of Cu^{2+} . This could mean the C=N electrons are not involved in the complexation. In addition, the Cu^{2+} ion between the two benzene rings also

does not induce any shift in the protons from the phenyl rings. Two simple reasons could account for these observations: firstly, the effect of the Cu^{2+} atom is shared between 12 carbon atoms, which minimises the effect through resonance stability. Secondly, the interaction between the sensor **S6** and the metal is very weak, as seen by the poor selectivity in **Figure 2.13**, leading to minimal changes in protons of the complex compared to **S6**.

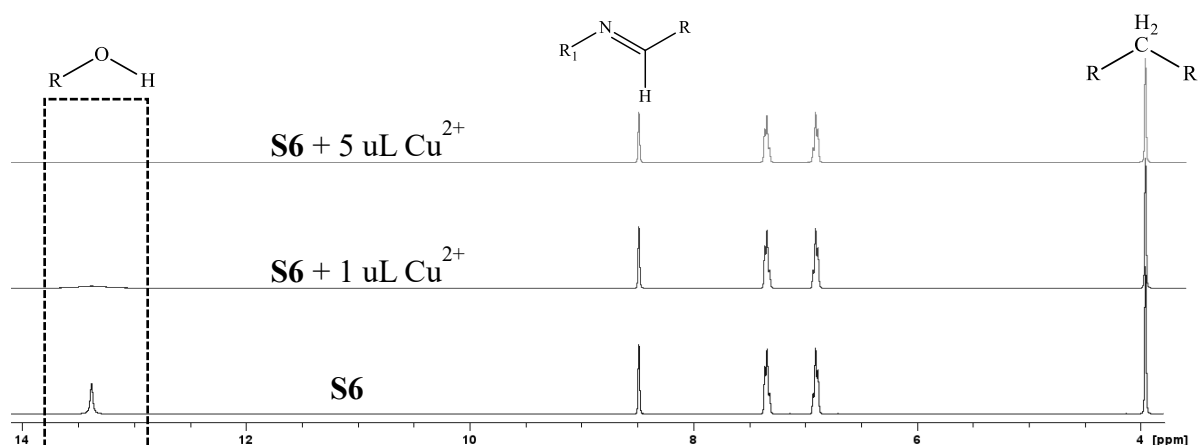


Figure 2.30: ^1H NMR titrations of **S6** with subsequent additions of Cu^{2+} in acetonitrile- d_3 .

In addition, the titration study in **Figure S 2.13** in the supplementary information suggests that the binding mode is related to the amount of Cu^{2+} present. At lower amounts of Cu^{2+} , a new band at 550 nm forms, but at equimolar amounts of Cu^{2+} and the sensor, the spectra have a band at 550 nm and a band at 650 nm. At higher concentrations of Cu^{2+} , only the band at 650 nm persists. This indicates that at lower concentrations, **S6** and Cu^{2+} form a 1:1 complex; at higher concentrations, the **S6** and Cu^{2+} form a 1:2 complex. This confirms that the formation of the complex involves two different binding sites that are not equally accessible to the analyte.

2.5.3.4 **S9** binding studies

S9 unexpectedly formed a complex with iodide, in acetonitrile, and cyanate, in methanol. As explained, **S1**- I^- complexation is mainly complexed through the hydroxyl proton. However, **S9** does not contain a hydroxyl functional group; therefore, the **S9** complexation must interact through a different binding site.

Computational studies were conducted to visualise the complexation. **Figure 2.31** shows the complexation of (a) **S9**- I^- and (b) **S9**- NCO^- . In the **S9**- I^- complex, the binding site involves the two Schiff base protons and benzene ring protons. Similarly, in the **S9**- NCO^- complex, the

same binding site is used with the cavity for NCO^- slightly bigger to accommodate the bigger anion. Shown in **Figure 2.31** is the conformer of the complexes in the gas phase to show the binding site. Please see **Figure S 2.20** in the supplementary information for the complexes in appropriate solvents.

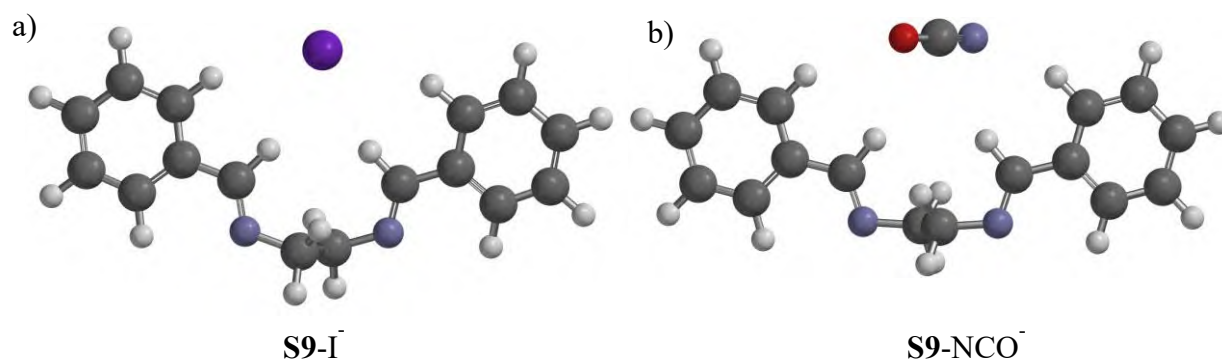


Figure 2.31: Complexation of **S9** with a) I^- and b) NCO^- computed with Spartan Student software.

To confirm the binding sites determined by computational means, ^1H NMR titration studies were performed on the **S9-I⁻** complex, using acetonitrile- d_3 as the solvent, as shown in **Figure 2.32**. It was observed that peak a) shifted upfield with the increase of I^- concentration. The same trend was observed for peak b). Peaks c) and d) displayed no change in the spectra.

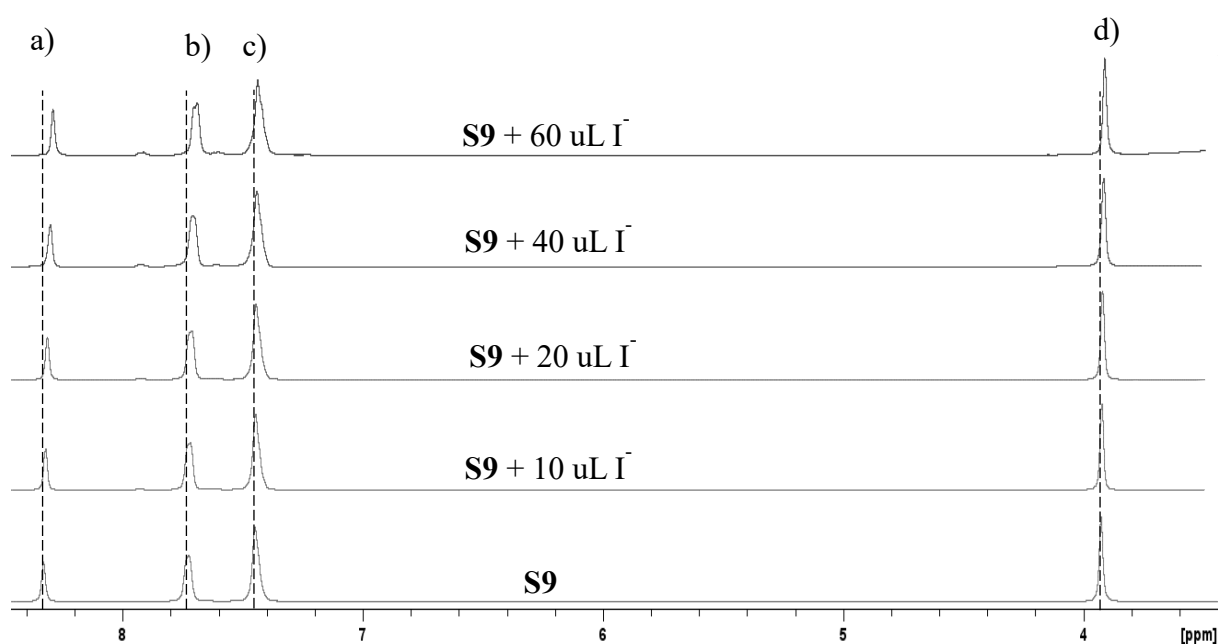


Figure 2.32: ^1H NMR spectra of **S9** with the subsequent additions of I^- in acetonitrile- d_3 .

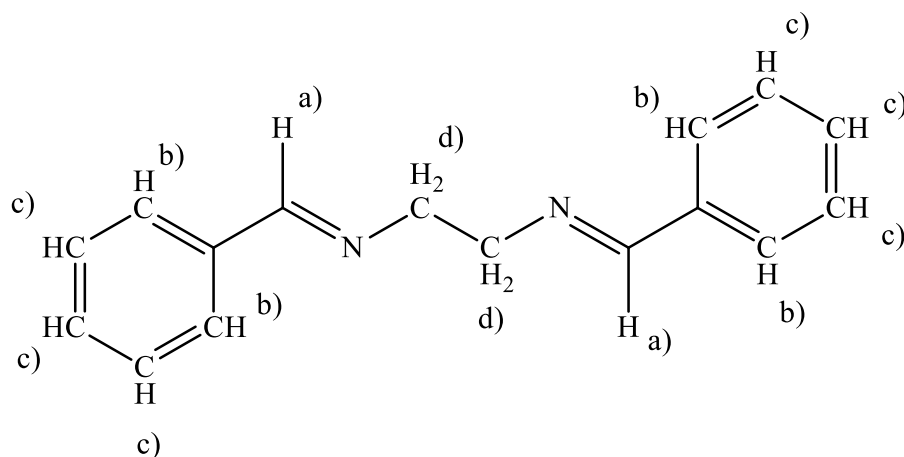


Figure 2.33: Structure of **S9** labelled to identify ^1H NMR peaks in **Figure 2.32**.

These observations in **Figure 2.31 a)** (and **Figure 2.32**) strongly supported the observed binding sites from the modelling studies of the **S9-I⁻** complex. Both benzene rings (peak b) are involved in the complexation assisted by protons (peak a) from Schiff base moieties.

2.6 Conclusion

Five compounds (**S1**, **S2**, **S3**, **S6**, and **S9**) were synthesised successfully using literature procedures. These compounds were characterised using ^1H NMR, ^{13}C NMR and FT-IR. Of these five compounds, two were confirmed to display colourimetric properties towards cations, and two were determined to be anionic chemosensors.

S3 showed no chemosensing properties for both cations and anions. Meanwhile **S2** and **S6** displayed some colourimetric chemosensing abilities for cations in acetonitrile solvent. **S2** (clear) turned blue in the presence of Cu^{2+} . However, it was observed that the formation of the complex does take time, approximately 25 min. This eliminated **S2** as a suitable real-time chemosensor. **S6**, on the other hand, showed a colourimetric chemosensor towards three different metal cations Ni^{2+} , Fe^{2+} , and Cu^{2+} . Nickel induced a colour change from clear to yellow, and iron induced a red colour change, whereas copper resulted in a blue-coloured solution. Further selectivity studies showed that **S6** prefers the cations in the order of $\text{Cu}^{2+} > \text{Ni}^{2+} > \text{Fe}^{2+}$. However, other competing metals have been shown to interfere with the complexation. Thus, **S6** cannot be used as a selective colourimetric chemosensor.

S1 and **S9** were tested for their chemosensing properties towards anions. Both compounds showed strong interactions with iodide ions. However, competition studies showed that **S1**

shows some preference towards I^- whereas **S9** does not. In addition, **S9** also showed some interaction towards cyanate in methanol. However, selectivity studies also showed no preference for any of the tested anions.

^1H NMR titration studies and computational chemistry using Spartan software were employed to determine the binding mechanism. In cationic complexation, the hydroxyl proton played the primary role in **S2**- Cu^{2+} . Moreover, in **S6**- M^{2+} ($\text{M} = \text{Ni}, \text{Fe}$ or Cu), the two hydroxyl oxygens and the two Schiff base nitrogens complex with the metal cation. In anionic complexation, the hydroxyl hydrogen in **S1** and the Schiff base hydrogens in **S9** resulted in the formation of the complex.

Moreover, the solvent played a significant role in the complexation as it was observed that the selectivity towards cations and anions changes depending on the solvent.

2.7 Experimental

2.7.1 General information

All starting materials and solvents were purchased from Sigma Aldrich or Merck and used as received without further purification unless otherwise stated.

^1H NMR and ^{13}C NMR spectra were recorded on a Bruker Advance DPX 400 (400 MHz) spectrometer. The NMR samples were prepared in deuterated solvents (CDCl_3 , DMSO-d_6 , and Acetonitrile- d_3), and the samples were analysed at room temperature unless otherwise stated. Chemical shifts are expressed in parts per million (ppm) using tetramethylsilane (TMS) as the internal reference.

Infrared FT-IR spectra were recorded on a Bruker TENSOR 27 FT-IR spectrometer.

Thin layer chromatography (TLC) analyses were performed on pre-coated silica gel 60 F254 aluminium sheets (0.063-0.2 mm/70 - 230 mesh) using a 50:50% solution of ethyl acetate: hexane; compounds were detected by observation under UV light and exposed to iodine vapour.

UV-vis absorbance studies were recorded on a Shimadzu UV-3100 spectrophotometer with a 1 cm quartz cuvette (3 mL). Spectroscopic measurements were performed after each aliquot of selected cationic and anionic solutions.

Stock solutions of the sensors (0.1 M) were prepared by dissolving the samples in acetonitrile and diluting them to the desired concentrations. Metal cations (0.05 M) solutions were prepared using the nitrate salts (except for Fe^{2+} , which used the sulphate salt) and dissolved in Millipore water. The anion (0.05 M) solutions were prepared using the tetrabutylammonium salts and dissolved in Millipore water.

Molecular modelling was done as published by [A. Battison, S. Schoeman and N. Mama, 2022](#)⁸ using Spartan Student Version 8.0.6, Oct 8 2020. Computational chemistry was utilised to compare and visually illustrate different chemosensors and complex conformers. The conformers were obtained by conformer distribution at the MMFF level. Calculations of the most energetically preferred conformation were determined by equilibrium geometry at the PM3 level.

The detection limit (LOD) and quantification (LOQ) were calculated according to the equation:

$$LOD = 3.3 \times \frac{\sigma}{m}$$

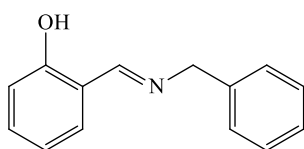
$$LOQ = 10 \times \frac{\sigma}{m}$$

Where σ is the standard deviation and m is the slope of the trend line.

2.7.2 General procedure for the synthesis of Schiff base derivatives S1-S9

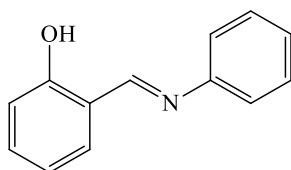
A mixture of an appropriate aldehyde, amine and alcoholic solvent was stirred overnight at room temperature. The resulting precipitate was filtered and washed with ice-cold solvent, followed by recrystallisation to obtain a pure product.⁶

2.7.2.1 2-((benzylimino)methyl)phenol – S1



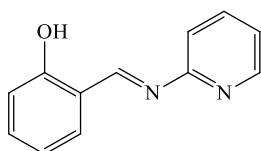
Salicylaldehyde (1 g, 8.19 mmol) and benzylamine (0.99 g, 9.24 mmol) were stirred overnight in a small amount of ethanol (5 mL). The resulting precipitate was filtered and washed with ice-cold ethanol. After recrystallisation in ethanol, the product was obtained as a yellow solid. **Yield: 49%.** IR ν_{\max} (cm⁻¹): 3058-3028 (-OH stretching), 1952-1818 (C-H bending, Aromatic), 1628 (C=N stretching, Schiff base). ¹H NMR (CDCl₃): δ_{H} /ppm = 13.44 (1H, broad s, -OH), 8.47 (1H, s, =CH), 7.42-7.30 (7H, m, Aromatic H), 7.03-7.01 (1H, d, Aromatic H), 6.95-6.91 (1H, t, Aromatic H), 4.85 (2H, s, -CH₂). ¹³C NMR (CDCl₃) δ_{C} /ppm = 165.65, 161.16, 138.20, 132.39, 131.45, 128.70, 127.79, 127.38, 118.87, 118.65, 117.08, 63.22.

2.7.2.2 2-((phenylimino)methyl)phenol – S2



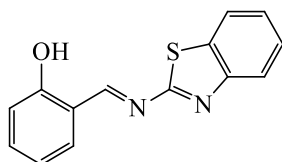
Salicylaldehyde (1 g, 8.19 mmol) and aniline (1.02 g, 10.95 mmol) were stirred overnight in a small amount of ethanol (5 mL). The resulting precipitate was filtered and washed with ice-cold ethanol. A pure product was obtained. **Yield: 97%**. IR ν_{\max} (cm⁻¹): 3076-3054 (-OH stretching, intramolecular bonded), 2981-2884 (C-H stretching, Alkene), 1948 (C-H bending, Aromatic), 1614 (C=N stretching, Schiff base). ¹H NMR (CDCl₃): δ_{H} /ppm = 13.26 (1H, broad s, -OH), 8.66 (1H, s, =CH), 7.48-7.40 (4H, m, Aromatic H), 7.33-7.29 (3H, m, Aromatic H), 7.03-7.01 (1H, d, Aromatic H), 6.95-6.91 (1H, t, Aromatic H). ¹³C NMR (CDCl₃) δ_{C} /ppm = 162.69, 161.20, 148.54, 133.15, 132.29, 129.42, 126.91, 121.18, 119.27, 119.08, 117.30.

2.7.2.3 2-((pyridin-2-ylimino)methyl)phenol – S3



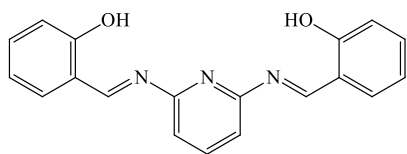
Salicylaldehyde (1.13 g, 9.25 mmol) and pyridin-2-amine (1 g, 10.63 mmol) were stirred overnight in a small amount of ethanol (5 mL). The resulting precipitate was filtered and washed with ice-cold ethanol. A pure product was obtained. **Yield: 59%**. IR ν_{\max} (cm⁻¹): 3652 (C-N stretching, pyridine), 3054 (-OH stretching, intramolecular bonded), 2981-2884 (C-H stretching, Alkene), 1614 (C=N stretching, Schiff base). ¹H NMR (CDCl₃): δ_{H} /ppm = 13.46 (1H, s, -OH), 9.46 (1H, s, =CH), 8.50 (1H, m, Aromatic H), 7.81-6.95 (7H, m, Aromatic H). ¹³C NMR (CDCl₃) δ_{C} /ppm = 164.78, 161.91, 157.63, 148.99, 138.48, 133.86, 133.50, 122.57, 120.45, 119.23, 119.02, 117.28.

2.7.2.4 2-((benzothiazol-2-ylimino)methyl)phenol – S4



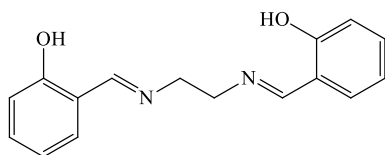
Salicylaldehyde (1 g, 8.19 mmol) and 2-aminobenzothiazole (1 g, 6.66 mmol) were stirred overnight in a small amount of ethanol (5 mL). 2-Aminobenzothiazole was recovered according to NMR.

2.7.2.5 2,2'-((1,1')-(pyridine-2,6-diylbis(azanylylidene))bis(methanylylidene)) diphenol – S5



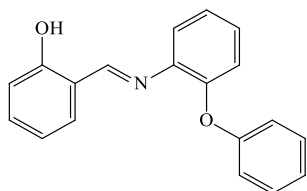
Salicylaldehyde (1.24 g, 10.15 mmol) and pyridine-2,6-diamine (0.64 g, 5.86 mmol) were stirred overnight in a small amount of ethanol (5 mL). Pyridine-2,6-diamine and salicylaldehyde were observed according to TLC.

2.7.2.6 2,2'-((1,1')-(ethane-1,2-diylbis(azanylylidene))bis(methanylylidene)) diphenol – S6



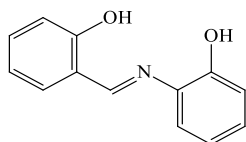
Salicylaldehyde (1.30 g, 10.65 mmol) and ethylenediamine (0.61 g, 10.15 mmol) were stirred overnight in a small amount of ethanol (5 mL). The resulting precipitate was filtered and washed with ice-cold ethanol. A pure product was obtained. **Yield: 62%**. IR ν_{max} (cm^{-1}): 3051 (-OH stretching, intramolecular bonded), 3009-2900 (C-H stretching, Alkene), 1942 (C-H bending, Aromatic), 1677-1627 (C=N stretching, Schiff base). ^1H NMR (CDCl_3): $\delta_{\text{H}}/\text{ppm}$ = 13.22 (1H, s, -OH), 8.38 (1H, s, =CH), 7.34-6.86 (8H, m, Aromatic H), 3.96 (4H, s, -CH₂). ^{13}C NMR (CDCl_3) $\delta_{\text{C}}/\text{ppm}$ = 166.51, 161.01, 132.40, 131.49, 118.68, 118.65, 116.96, 59.76.

2.7.2.7 2-(((2-phenoxyphenyl)imino)methyl)phenol – S7



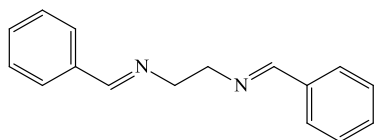
Salicylaldehyde (1.01 g, 8.27 mmol) and 2-phenoxyaniline (1.14 g, 6.15 mmol) were stirred overnight in a small amount of ethanol (5 mL). Salicylaldehyde and 2-phenoxyaniline were observed according to TLC.

2.7.2.8 2-((2-hydroxybenzylidene)amino)phenol – S8



Salicylaldehyde (1 g, 8.19 mmol) and 2-aminophenol (0.64 g, 10.83 mmol) were stirred overnight in a small amount of ethanol (5 mL). Salicylaldehyde and 2-aminophenol were observed according to TLC.

2.7.2.9 (N1,N2)-N1,N2-dibenzylideneethane-1,2-diamine– S9



Benzaldehyde (2.5 g, 23.6 mmol) and ethylenediamine (0.61 g, 10.15 mmol) were stirred overnight in a small amount of ethanol (5 mL). The resulting precipitate was filtered and washed with ice-cold ethanol. A pure product was obtained. **Yield: 59%**. IR ν_{max} (cm⁻¹): 2930-2846 (C-H stretching, Alkene), 1961-1820 (C-H bending, Aromatic), 1677-1639 (C=N stretching, Schiff base). ¹H NMR (CDCl₃): δ_{H} /ppm = 8.32 (1H, s, N=CH), 7.72 (4H, s, Aromatic H), 7.42 (6H, s, Aromatic H), 4.00 (4H, s, -CH₂). ¹³C NMR (CDCl₃) δ_{C} /ppm = 162.71, 136.15, 130.61, 129.75, 129.01, 128.55, 128.09, 61.63.

References

- (1) Battison, A. L. Synthesis and Applications of Novel Fluorescent and Colorimetric Coumarin-Based Sensors towards Analyte Sensing in Aqueous Systems By Supervisor : Dr . N . Mama Declaration, Nelson Mandela University, **2022**.
- (2) Kolhe, S.; Patil, D. Application of Schiff Base as a Fluorescence Sensor. *J. Emerg. Technol. Innov. Res.* **2019**, 6 (3), 175–181.
- (3) Junaid, H. M.; Batool, M.; Harun, F. W.; Akhter, M. S.; Shabbir, N. Naked Eye Chemosensing of Anions by Schiff Bases. *Crit. Rev. Anal. Chem.* **2022**, 52 (3), 463–480. <https://doi.org/10.1080/10408347.2020.1806703>.
- (4) Sani, U.; Na'ibi, H. U.; Dailami, S. A. In Vitro Antimicrobial and Antioxidant Studies on N-(2- Hydroxylbenzylidene) Pyridine -2-Amine and Its M(II) Complexes. *Niger. J. Basic Appl. Sci.* **2018**, 25 (1), 81. <https://doi.org/10.4314/njbas.v25i1.11>.
- (5) Sidana, N.; Devi, P.; Kaur, H. Thiophenol Amine-Based Schiff Base for Colorimetric Detection of Cu²⁺ and Hg²⁺ Ions. *Opt. Mater. (Amst).* **2022**, 124 (January), 111985. <https://doi.org/10.1016/j.optmat.2022.111985>.
- (6) Battison, A.; Schoeman, S. A Coumarin-Azo Derived Colorimetric Chemosensor for Hg²⁺ Detection in Organic and Aqueous Media and Its Extended Real-World Applications. **2022**. <https://doi.org/10.21203/RS.3.RS-1621696/V1>.
- (7) Erten, G.; Karcı, F.; Demirçalı, A.; Söyleyici, S. 1H-Pyrazole- Azomethine Based Novel Diazo Derivative Chemosensor for the Detection of Ni²⁺. *J. Mol. Struct.* **2020**, 1206. <https://doi.org/10.1016/j.molstruc.2020.127713>.
- (8) Battison, A.; Schoeman, S.; Mama, N. A Coumarin-Azo Derived Colorimetric Chemosensor for Hg²⁺ Detection in Organic and Aqueous Media and Its Extended Real-World Applications. *J. Fluoresc.* **2022**. <https://doi.org/10.1007/s10895-022-03065-3>.
- (9) Dearden, J. C.; Forbes, W. F. Light Absorption Studies. *Can. J. Chem.* **1959**, 37 (6).
- (10) Coggeshall, N. D.; Lang, E. M. No Title. *J. Am. Chem. Soc.* **1948**, 70 (3283).
- (11) Čonková, M.; Montes-García, V.; Konopka, M.; Ciesielski, A.; Samori, P.; Stefankiewicz, A. R. Schiff Base Capped Gold Nanoparticles for Transition Metal Cation Sensing in Organic Media. *Chem. Commun.* **2022**, 5773–5776. <https://doi.org/10.1039/d2cc00497f>.
- (12) Wang, X.; Zhang, C.; Feng, L.; Zhang, L. Screening Iodide Anion with Selective Fluorescent Chemosensor. *Sensors Actuators, B Chem.* **2011**, 156 (1), 463–466. <https://doi.org/10.1016/j.snb.2011.04.023>.
- (13) Fateh, F.; Yildirim, A.; Bhatti, A. A.; Yilmaz, M. A New Benzothiazin-Functionalized Calix[4]Arene-Based Fluorescent Chemosensor for the Selective Detection of Co²⁺ Ion. *J. Fluoresc.* **2021**, 31 (4), 1075–1083. <https://doi.org/10.1007/s10895-021-02745-w>.

- (14) Roy, D.; Chakraborty, A.; Ghosh, R. Perimidine Based Selective Colorimetric and Fluorescent Turn-off Chemosensor of Aqueous Cu^{2+} : Studies on Its Antioxidant Property along with Its Interaction with Calf Thymus-DNA. *RSC Adv.* **2017**, 7 (64), 40563–40570. <https://doi.org/10.1039/c7ra06687b>.
- (15) Prabhu, S.; Saravanamoorthy, S.; Ashok, M.; Velmathi, S. Colorimetric and Fluorescent Sensing of Multi Metal Ions and Anions by Salicylaldimine Based Receptors. *J. Lumin.* **2012**, 132 (4), 979–986. <https://doi.org/10.1016/j.jlumin.2011.09.051>.
- (16) Wavefunction. Spartan '10 Tutorial and User's Guide. Wavefunction. **2011**.

Supplementary information

List of supplementary figures

Figure S 2.1: ^{13}C NMR spectrum of S1 in CDCl_3	90
Figure S 2.2: IR spectrum of S1	91
Figure S 2.3: The screening of metal cations (0.167 mM) using S1 (0.167 mM). S1 has two bands at 254 nm and 315 nm. a) Acetonitrile. b) Methanol.	91
Figure S 2.4: Regression statistics to identify the two outliers (red) in the titration studies of S1 and I^-	91
Figure S 2.5: ^{13}C NMR spectrum of S2 in CDCl_3	92
Figure S 2.6: IR spectrum of S2	92
Figure S 2.7: Photographic image of S2 in the absence and presence of Cu^{2+} in acetonitrile after 30 min.	92
Figure S 2.8: Anion (0.167 mM) screening of S2 (0.167 mM) in a) acetonitrile (bands at 269 nm and 336 nm) and b) methanol (bands at 270 nm and 335 nm).	93
Figure S 2.9: Screening of metal cations (0.167 mM) using S3 . S3 has three bands at 272 nm, 303 nm and 344 nm. a) Acetonitrile. b) Methanol.....	93
Figure S 2.10: Anion (0.167 mM) screening of S3 (0.167 mM) in a) acetonitrile (bands at 270 nm, 303 nm, and 344 nm) and b) methanol (bands at 272 nm, 301 nm, and 343 nm).	93
Figure S 2.11: ^{13}C NMR spectrum of S6 in CDCl_3	94
Figure S 2.12: IR spectrum of S6	94
Figure S 2.13: a) Titration studies of S6 (0.167 mM) with the addition of Cu^{2+} . b) Absorbance of the S6 - Cu^{2+} complex at 655 nm as a function of the Cu^{2+} concentration.....	95
Figure S 2.14: Anion (0.167 mM and 0.1 mM, respectively) screening in a) acetonitrile containing 0.167 mM S6 and b) methanol containing 0.1 mM S6	95

Figure S 2.15: ^{13}C NMR spectrum of S9 in CDCl_3 .	96
Figure S 2.16: IR spectrum of S9 .	96
Figure S 2.17: Metal cation (0.1 mM) screening of S9 (0.1 mM) in a) acetonitrile (band at 246 nm) and b) methanol (band at 247 nm).	96
Figure S 2.18: Competition studies of S9 (0.1 mM) with I^- (0.1 mM) in acetonitrile in the presence of other metals(0.1 mM).	97
Figure S 2.19: Competition studies of S9 (0.1 mM) with NCO^- (0.1 mM) in methanol in the presence of other metals (0.1 mM).	97
Figure S 2.20: Complexation of S9 with a) I^- in acetonitrile and b) NCO^- with methanol using Spartan Student software.	97

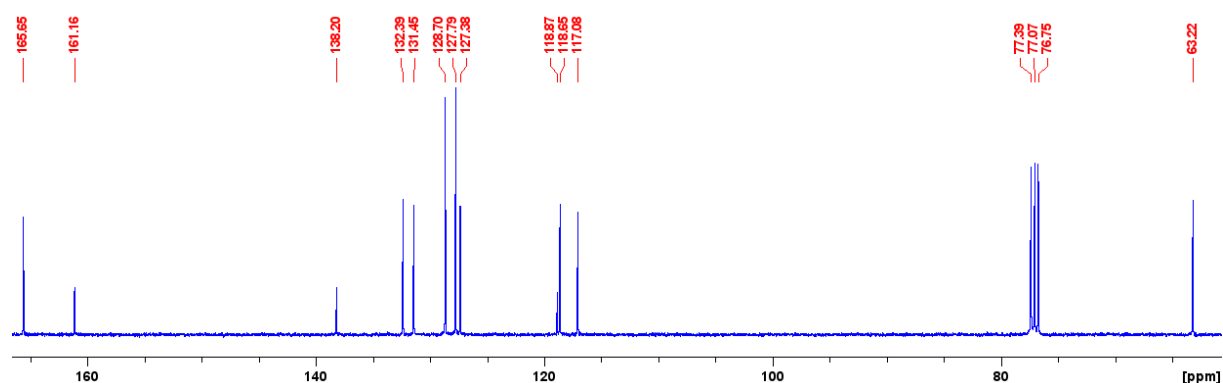


Figure S 2.1: ^{13}C NMR spectrum of **S1** in CDCl_3 .

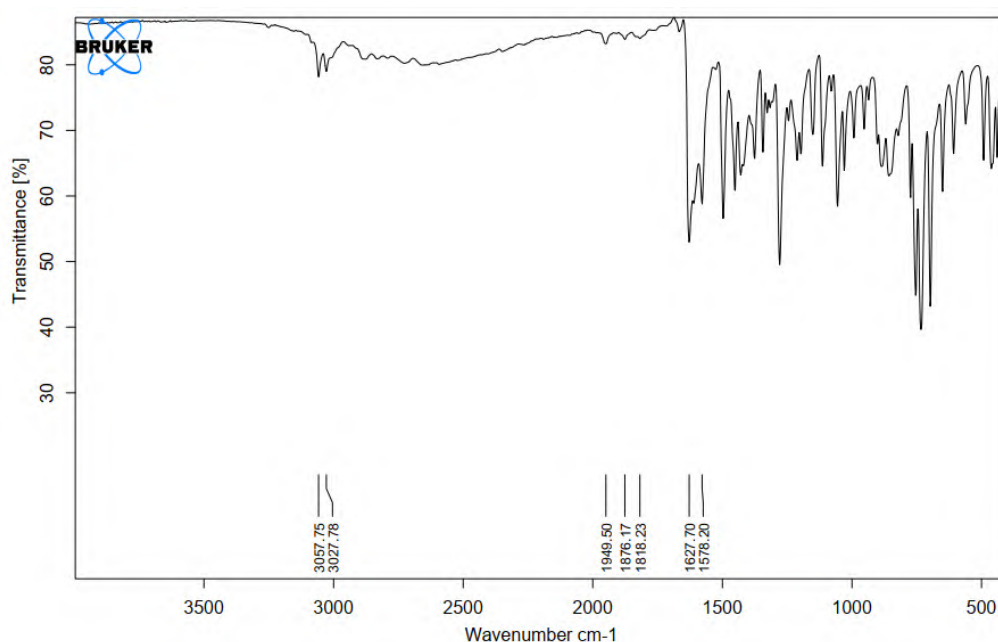


Figure S 2.2: IR spectrum of *S1*.

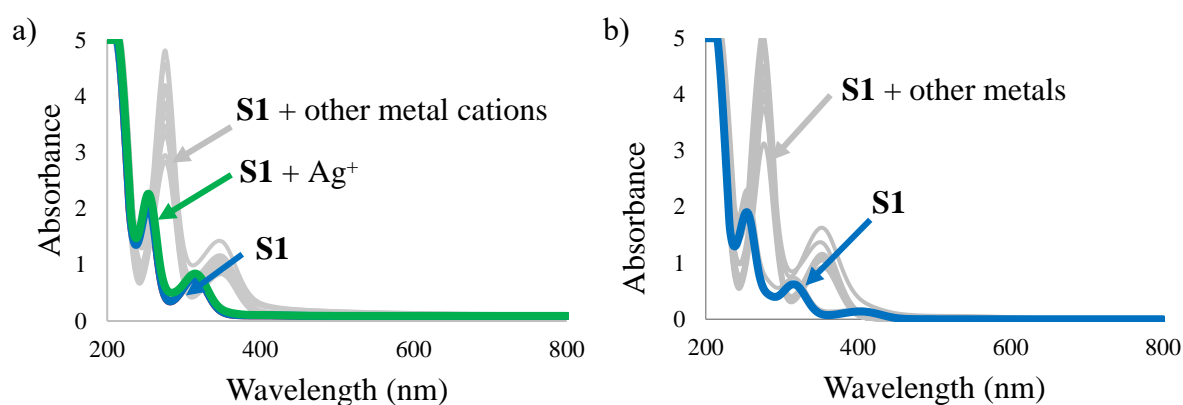


Figure S 2.3: The screening of metal cations (0.167 mM) using *S1* (0.167 mM). *S1* has two bands at 254 nm and 315 nm. a) Acetonitrile. b) Methanol.

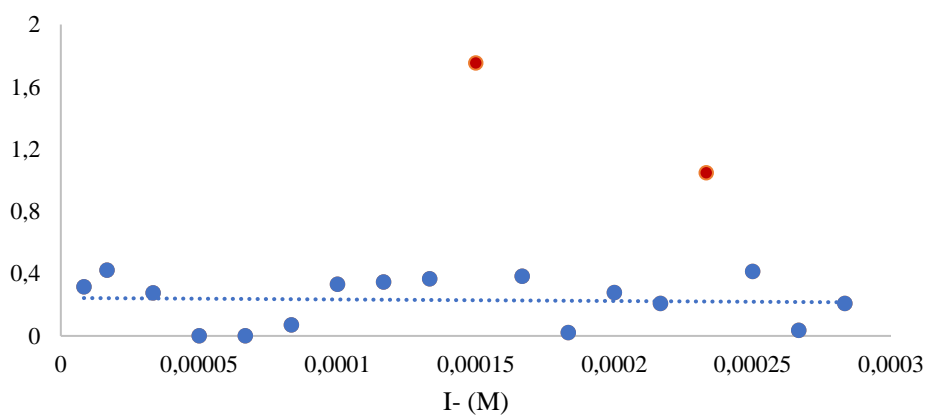


Figure S 2.4: Regression statistics to identify the two outliers (red) in the titration studies of *S1* and *I*.

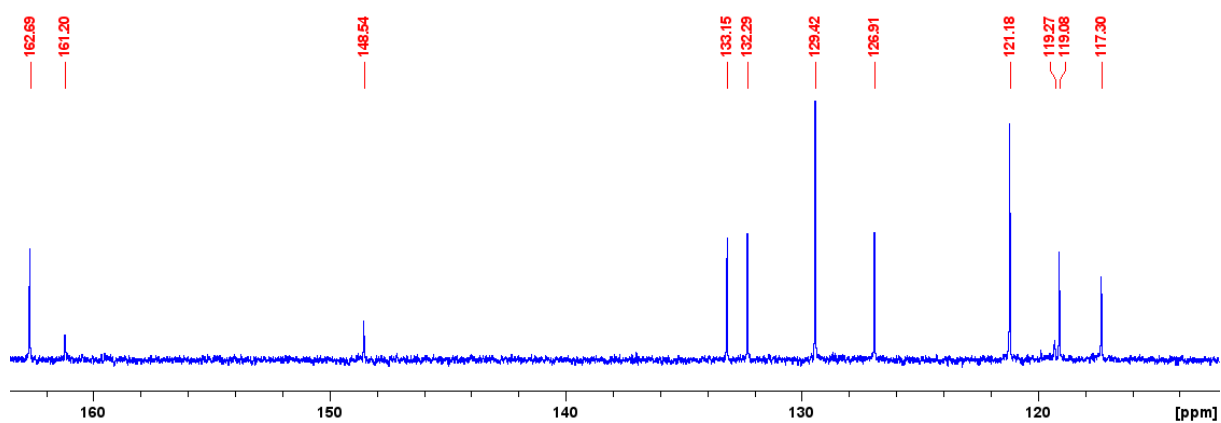


Figure S 2.5: ^{13}C NMR spectrum of S2 in CDCl_3 .

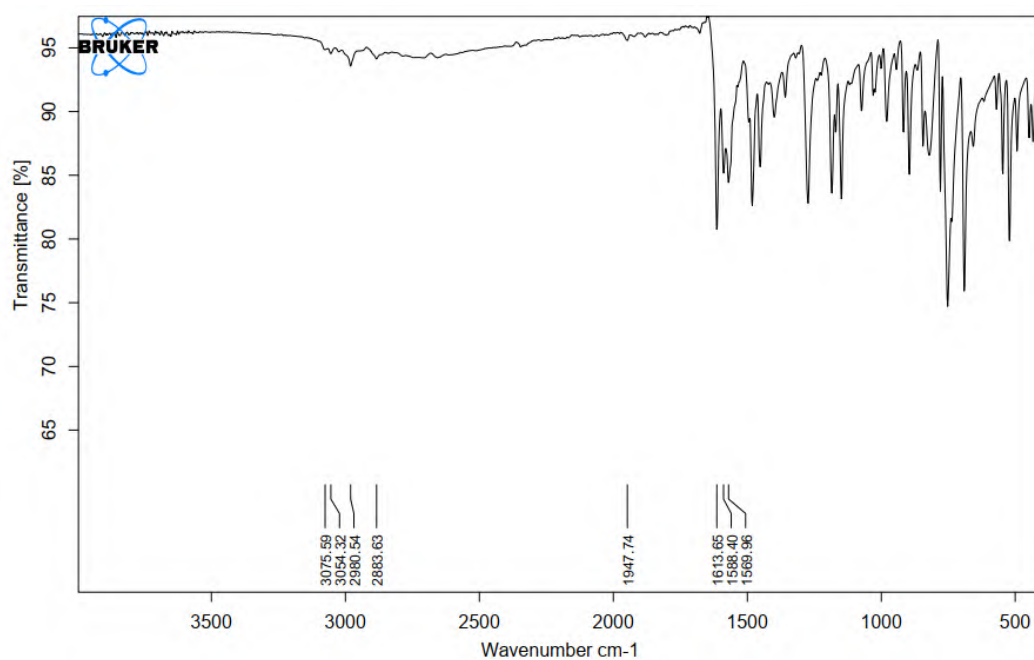


Figure S 2.6: IR spectrum of S2.

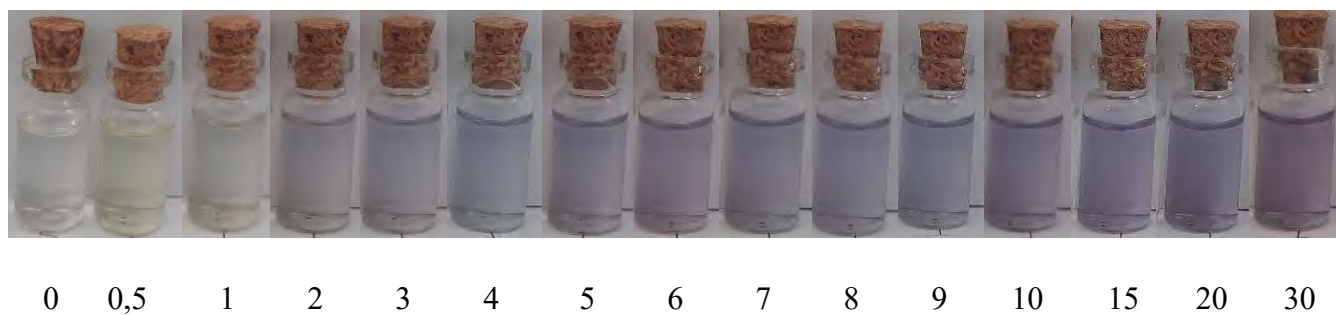


Figure S 2.7: Photographic image of S2 in the absence and presence of Cu^{2+} in acetonitrile after 30 min.

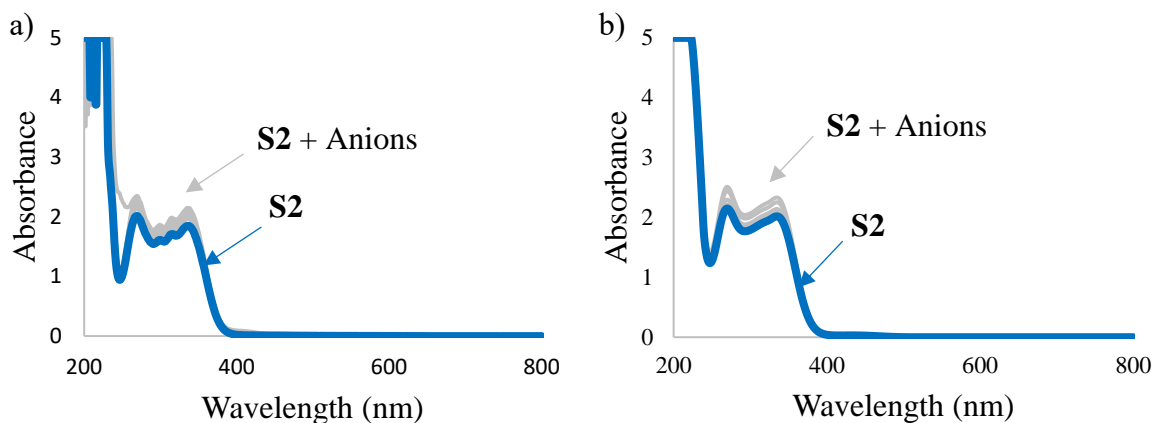


Figure S 2.8: Anion (0.167 mM) screening of S2 (0.167 mM) in a) acetonitrile (bands at 269 nm and 336 nm) and b) methanol (bands at 270 nm and 335 nm).

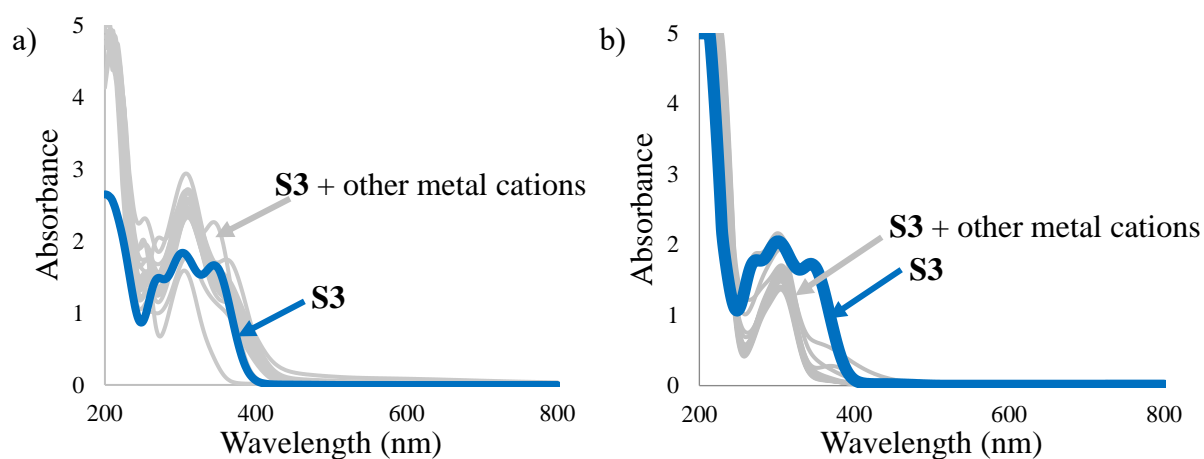


Figure S 2.9: Screening of metal cations (0.167 mM) using S3. S3 has three bands at 272 nm, 303 nm and 344 nm. a) Acetonitrile. b) Methanol.

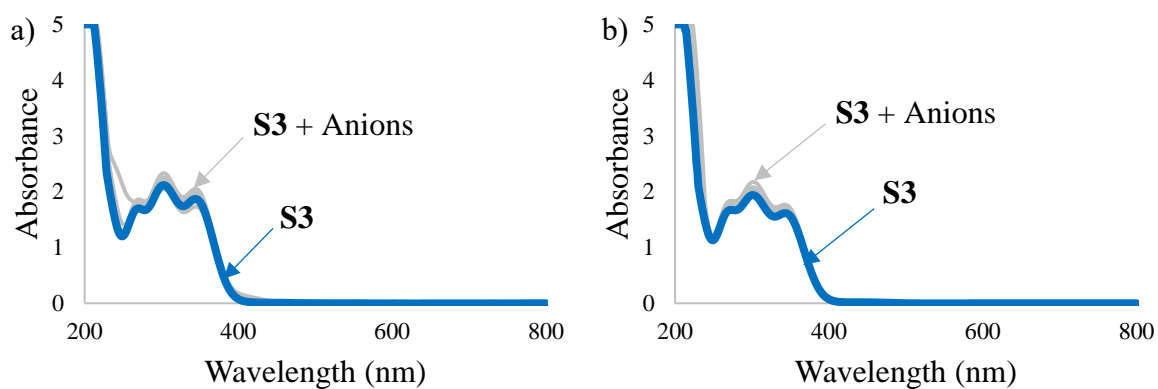


Figure S 2.10: Anion (0.167 mM) screening of S3 (0.167 mM) in a) acetonitrile (bands at 270 nm, 303 nm, and 344 nm) and b) methanol (bands at 272 nm, 301 nm, and 343 nm).

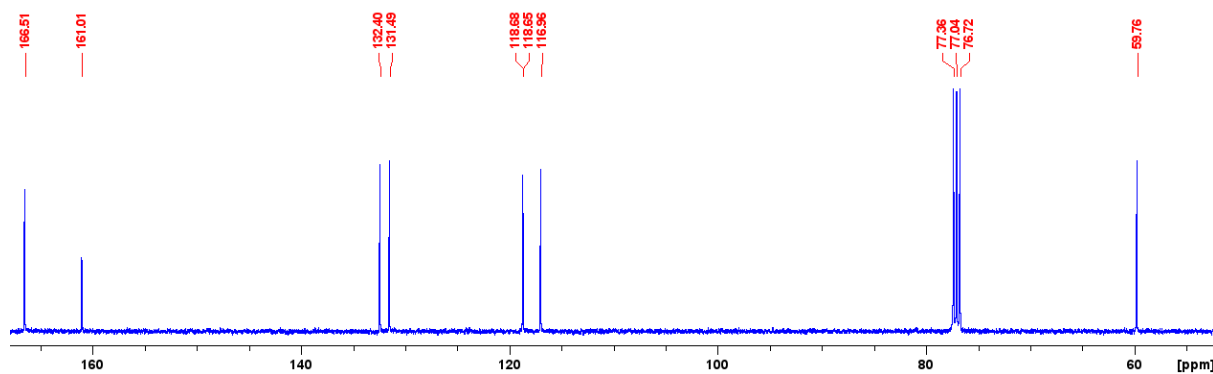


Figure S 2.11: ¹³C NMR spectrum of S6 in CDCl₃.

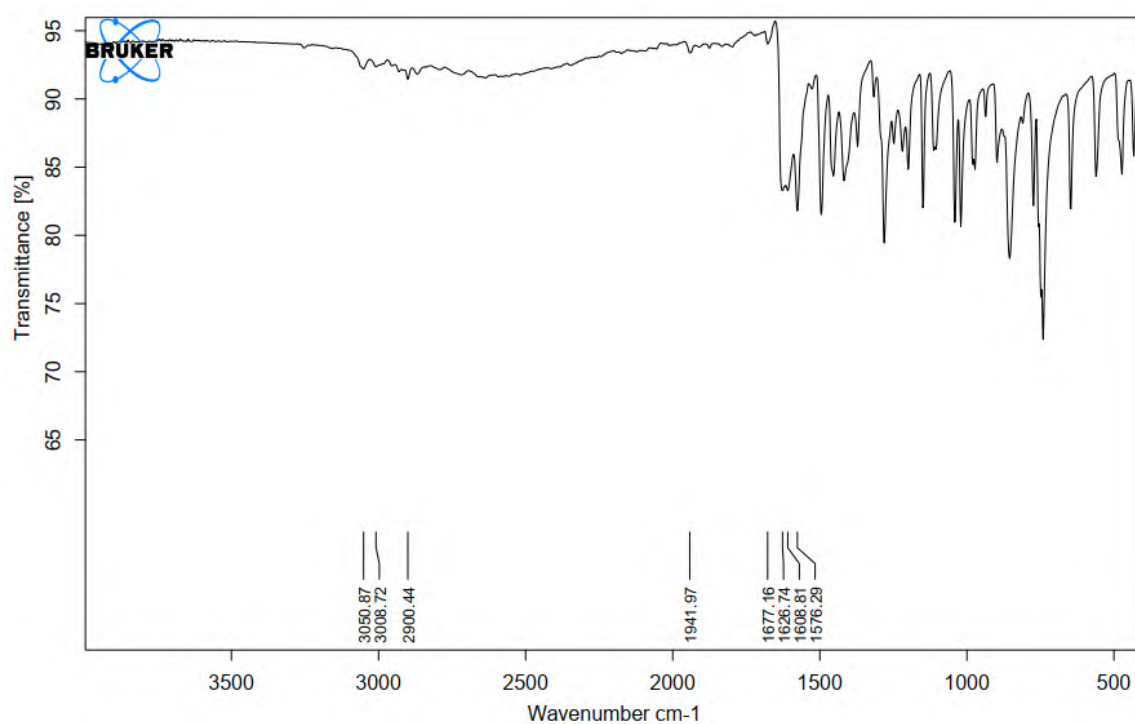


Figure S 2.12: IR spectrum of S6.

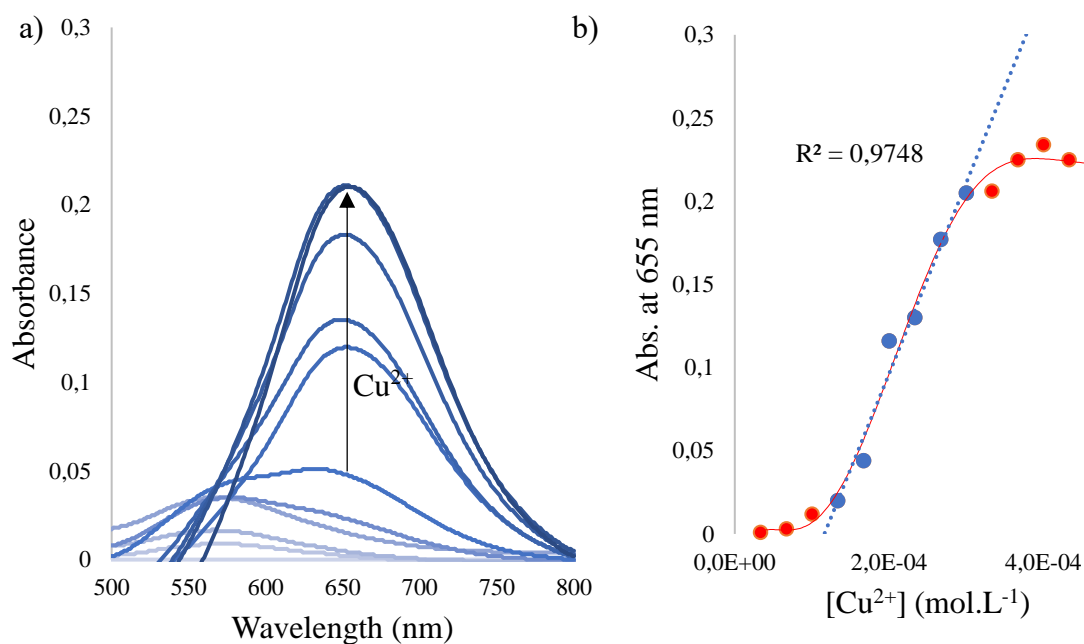


Figure S 2.13: a) Titration studies of **S6** (0.167 mM) with the addition of Cu^{2+} . b) Absorbance of the **S6**- Cu^{2+} complex at 655 nm as a function of the Cu^{2+} concentration.

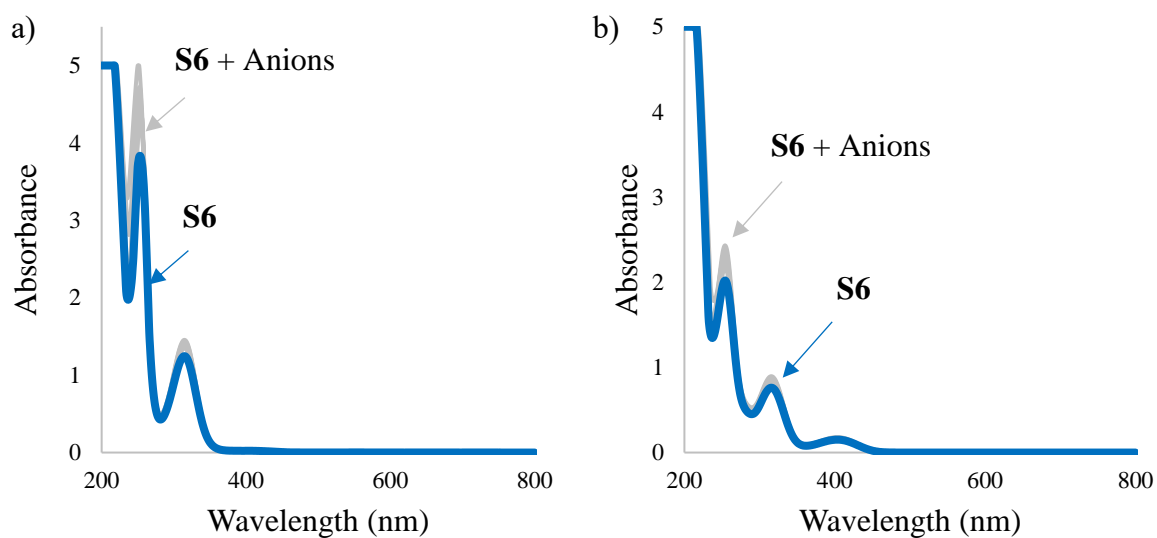


Figure S 2.14: Anion (0.167 mM and 0.1 mM, respectively) screening in a) acetonitrile containing 0.167 mM **S6** and b) methanol containing 0.1 mM **S6**.

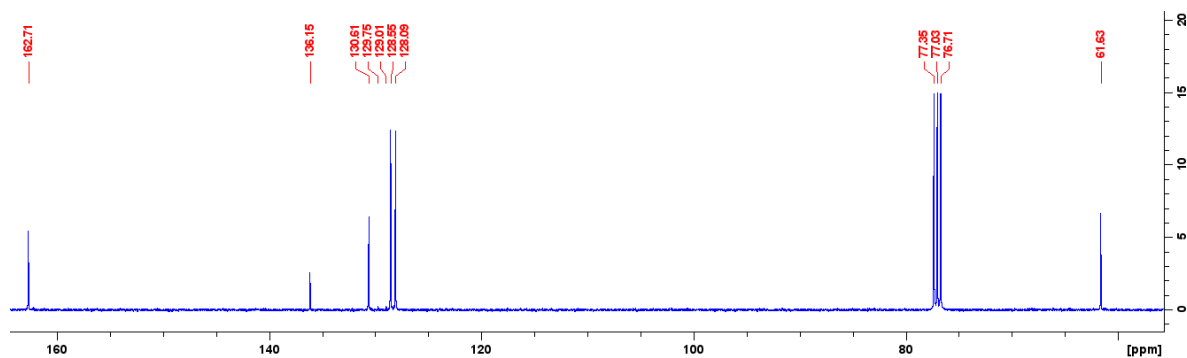


Figure S 2.15: ^{13}C NMR spectrum of **S9** in CDCl_3 .

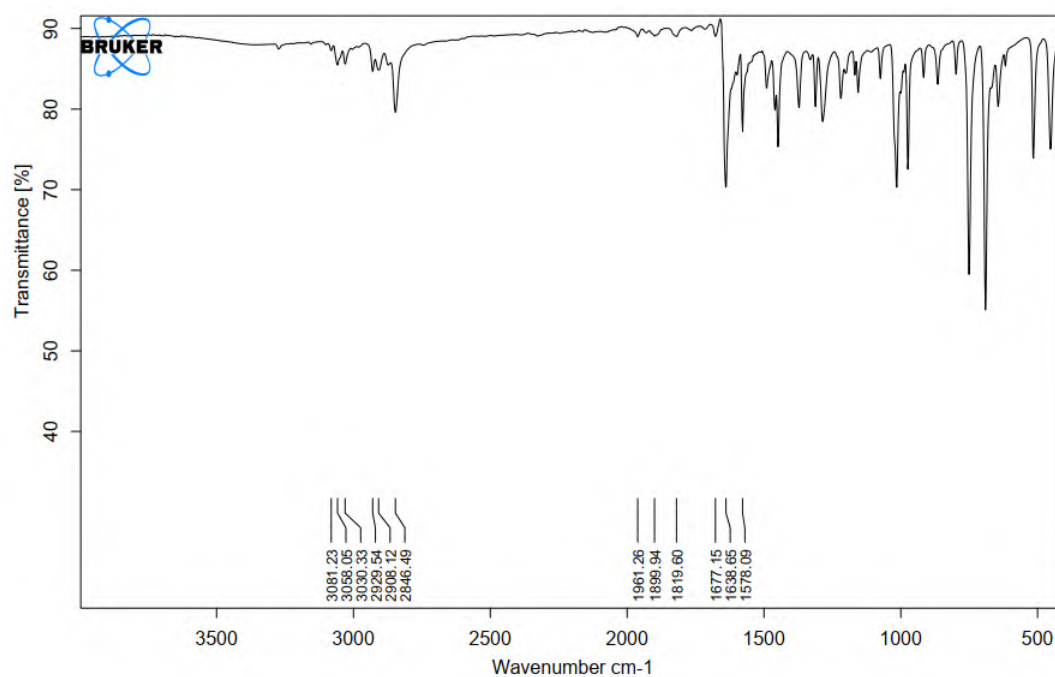


Figure S 2.16: IR spectrum of **S9**.

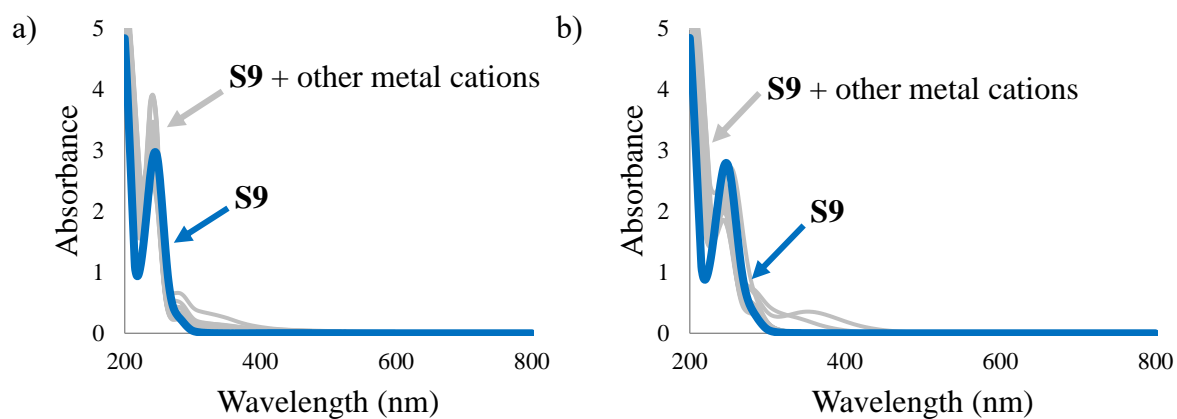


Figure S 2.17: Metal cation (0.1 mM) screening of **S9** (0.1 mM) in a) acetonitrile (band at 246 nm) and b) methanol (band at 247 nm).

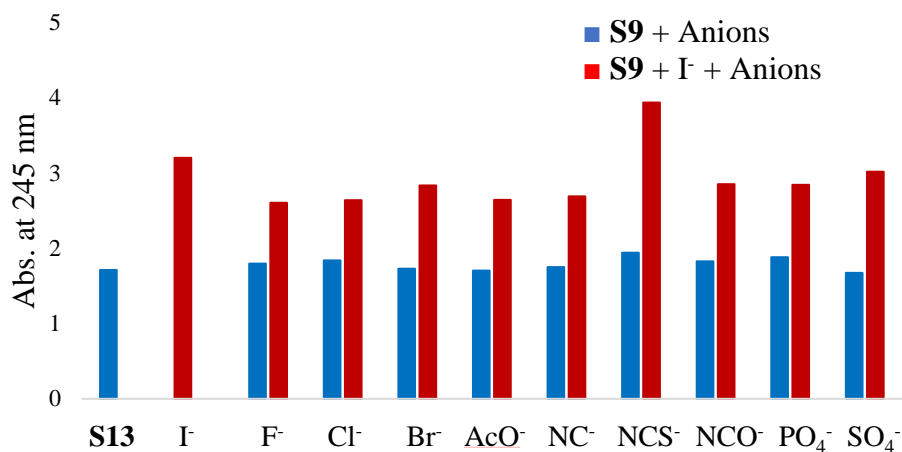


Figure S 2.18: Competition studies of S9 (0.1 mM) with I⁻ (0.1 mM) in acetonitrile in the presence of other metals(0.1 mM).

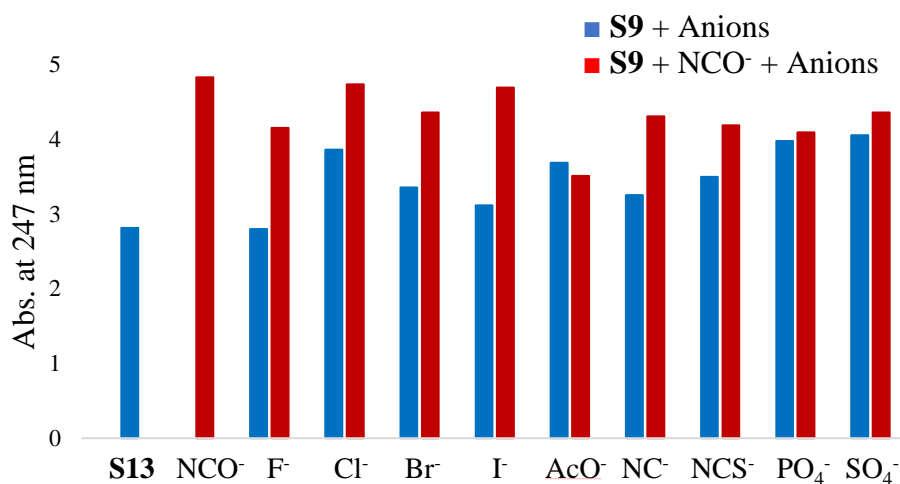


Figure S 2.19: Competition studies of S9 (0.1 mM) with NCO⁻ (0.1 mM) in methanol in the presence of other metals (0.1 mM).

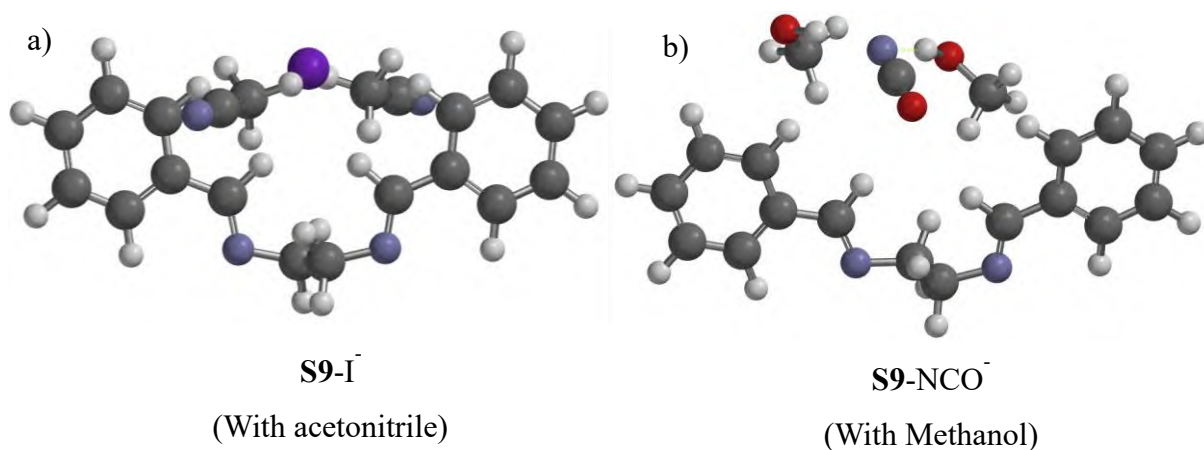


Figure S 2.20: Complexation of S9 with a) I⁻ in acetonitrile and b) NCO⁻ with methanol using Spartan Student software.

Chapter 3

Mix ligand Chemosensors

Summary

Chemosensor 7-(diethylamino)-3-(3-(2-methoxyphenyl)acryloyl)-2H-chromen-2-one, **E2**, was compared to the mixed ligand **E6** which contained the **E2** chemosensor and o-anisaldehyde, **o-A**, as a supporting ligand. **E2** was synthesised and characterised using NMR, FT-IR and single X-ray crystallography. Absorption studies of **E2** and **E6** showed that **o-A** does not interact or change the absorbance of **E2**, but during screening, **E6** performed slightly better than **E2**, showing less interaction with other metal cations. The emission studies of **E2** and **E6** showed that the **o-A** in **E6** quenched the fluorescence of **E2**. Hence, **o-A** is not a suitable cooperative ligand; ^{13}C NMR also showed that **o-A** does not participate in complexation.

Further emission studies into **E2** were conducted. It was suggested that **E2** is a PET “on-off” type mechanism to detect Fe^{2+} in methanol selectively. Competition studies showed that **E2** was highly selective for Fe^{2+} , even in the presence of other competing metal cations. LOD and LOQ were determined to be 0.024 mM and 0.074 mM, respectively, with a saturation point of 0.183 mM. Static quenching with non-cooperativity was observed for the 1:1 **E2**- Fe^{2+} complex. Reversibility studies concluded that the **E2**- Fe^{2+} complex was partially reversible using EDTA and H_2O_2 . Molecular modelling was utilised to visualise the binding between the carbonyl oxygens of **E2** and the $\text{Fe}(\text{II})$ cation. Lastly, **E2** was tested as an anion chemosensor. Both absorbance and emissions studies indicated that **E2** could not be used as an anion chemosensor.

Table of Contents

Summary	98
List of Figures	101
List of Schemes	103
List of Tables	103
List of selected Abbreviations	104
3 Mix ligand chemosensors	105
3.1 Introduction	105
3.2 Aim of chapter.....	109
3.3 Synthesis of chemosensor E2	112
3.3.1 X-ray studies for compounds E1 and E2	114
3.4 UV-vis absorption studies of E2 and E6	115
3.4.1 Screening of cations using E2 and E6	116
3.4.2 E2 screening towards anions	120
3.5 Fluorescence studies of E2 and E6	121
3.5.1 Mode of fluorescence of E2	121
3.5.2 Fluorescent screening of E2 for the detection of cations.....	123
3.5.3 Competition studies of E2 -Fe ²⁺ complex	124
3.5.4 Titration studies and binding site studies of E2	124
3.5.5 Reversibility studies.....	130
3.5.6 Job's plot of E2 and Fe ²⁺	133
3.5.7 Emission study of the mixed ligand chemosensor E6	137
3.5.8 E2 screening of anions.....	138
3.6 Conclusion.....	140
3.7 Experimental	142
3.7.1 General information	142
3.7.2 Synthesis of compounds	143

References	145
Supplementary information	150
List of supplementary figures	150
List of supplementary tables	151

List of Figures

Figure 3.1: Mixed-ligand Cu(II) complex 2	109
Figure 3.2: Binding ratios between a chemosensor (s) and a metal cation (M^{n+}).....	110
Figure 3.3: Example of the a) classical chemosensor versus b) a mixed-ligand type chemosensor.....	111
Figure 3.4: ^1H NMR spectrum of E1 in CDCl_3	112
Figure 3.5: ^1H NMR spectrum of E2 in CDCl_3	113
Figure 3.6: Structures of attempted chemosensors E3 and E4	113
Figure 3.7: Single crystal XRD analysis of E1 at two angles.....	114
Figure 3.8: Single crystal XRD analysis of E2 showing two molecules in the asymmetric unit cell from two different perspectives.	114
Figure 3.9: Absorbance spectra of E2 (blue), o-A (green) and E6 (red) in a) acetonitrile and b) methanol with a concentration of 0.0833 mM.	115
Figure 3.10: Screening of metal cations (0.167 mM) in acetonitrile using chemosensors a) E2 and b) E6 . Both sensors had a final concentration of 0.0833 mM.....	116
Figure 3.11: Screening of various cations (0.167 mM) in methanol using chemosensors a) E2 and b) E6 . Both chemosensors had a final concentration of 0.0833 mM.	117
Figure 3.12: Photographic image of E2-Fe ²⁺ and E2-Fe ³⁺ complexes and E2 in a) acetonitrile, b) the same sample left overnight, c) in methanol and d) the same sample left overnight....	118
Figure 3.13: Photographic image of E6-Fe ²⁺ and E6-Fe ³⁺ complexes and E6 in a) acetonitrile, b) the same sample left overnight, c) in methanol and d) the same sample left overnight....	119
Figure 3.14: Screening of various anions (0.167 mM) using chemosensor E2 (0.0833 mM) in a) acetonitrile and b) methanol.	120
Figure 3.15: Absorbance spectra of I^- (green), E2 (blue) and the complex, E2-I ⁻ (red).....	121

Figure 3.16: Normalised absorbance (red) and emissions (blue) of E2 in MetOH indicate spectral overlap. $\lambda_{\text{excitation}} = 440 \text{ nm}$.	122
Figure 3.17: HOMO and LUMO of E2 obtained using molecular modelling.	122
Figure 3.18: Metal cation (0.167 mM) screening of E2 (0.409 μM) in a) acetonitrile and b) methanol. $\lambda_{\text{excitation}} = 440 \text{ nm}$.	123
Figure 3.19: Competition study of a) E2-Fe²⁺ in the presence of various competing metal cations in MetOH. b) Comparison between E2 in the presence of various competing metal cations (blue bars) and E2-Fe²⁺ in the presence of various competing metal cations (red bars) in equal amounts at 485 nm. $\lambda_{\text{excitation}} = 440 \text{ nm}$.	124
Figure 3.20: Titration of E2 with increasing aliquots of Fe²⁺ in MetOH. $\lambda_{\text{excitation}} = 440 \text{ nm}$.	125
Figure 3.21: Calibration curve of E2-Fe²⁺ complex at 485 nm. $\lambda_{\text{excitation}} = 440 \text{ nm}$.	126
Figure 3.22: Benesi-Hildebrand plot of E2-Fe²⁺ complex.	126
Figure 3.23: Stern-Volmer plot of E2-Fe²⁺ in methanol.	128
Figure 3.24: Hill plot of the fluorescence quenching response of E2 towards Fe²⁺ in methanol.	129
Figure 3.25: Reversibility study of the E2-Fe²⁺ complex using EDTA.	131
Figure 3.26: Recycling of E2 fluorescence intensity using EDTA.	131
Figure 3.27: Reversibility study of E2 using H₂O₂ .	132
Figure 3.28: Comparison of intensity between E2-Fe²⁺ and E2-Fe³⁺ .	133
Figure 3.29: Job's plot of E2 and Fe²⁺ in Methanol. The absorbance was measured at 440 nm.	133
Figure 3.30: HSQC NMR of E2 in deuterated acetonitrile.	134

Figure 3.31: ^{13}C NMR of E2 (blue) and the E2-Fe²⁺ complex (red) identifying complexing carbons in deuterated acetonitrile.	135
Figure 3.32: ^{13}C NMR of E6 (blue), o-A (red) and E6-Fe²⁺ complex (green) in deuterated acetonitrile.....	135
Figure 3.33: Octahedral E2-Fe²⁺ complex with H_2O	136
Figure 3.34: Trigonal prismatic E2-Fe²⁺ complex with CH_3CN	137
Figure 3.35: Emissions spectra of E2 (blue) and E6 (red) in acetonitrile (solid line) and methanol (dotted line) with a concentration of $0.409\ \mu\text{M}$. $\lambda_{\text{excitation}} = 440\ \text{nm}$	138
Figure 3.36: Screening of various anions ($0.167\ \text{mM}$) for E2 ($0.409\ \mu\text{M}$) in a) acetonitrile and b) methanol. $\lambda_{\text{excitation}} = 440\ \text{nm}$	139

List of Schemes

Scheme 3.1: Generalised reaction to form the enone functional group, 1	105
Scheme 3.2: Base catalysed aldol condensation mechanism to form the enone functional group. ^{3,4}	106
Scheme 3.3: Dehydration mechanism via enolate ion step to form the enone functional group. ^{3,4}	107
Scheme 3.4: The four groups of applications of mixed-ligand MNP. ¹	108
Scheme 3.5: Synthesis route to form chemosensors E1 and E2 . a) Ethyl acetoacetate, ethanol, piperidine, glacial acetic acid, reflux, 4 hours. b) o-Anisaldehyde, ethanol, piperidine, reflux, 24 hours.....	112
Scheme 3.6: Complexation of EDTA with a metal cation.	130

List of Tables

Table 3.1: Absorbance bands, in nm, for all compounds in acetonitrile and methanol. Maximum absorbance bands are bolded.....	115
---	-----

Table 3.2: Energy profiles of E2-Fe²⁺ complex in various coordination complexes obtained using Spartan.....	136
--	-----

List of selected Abbreviations

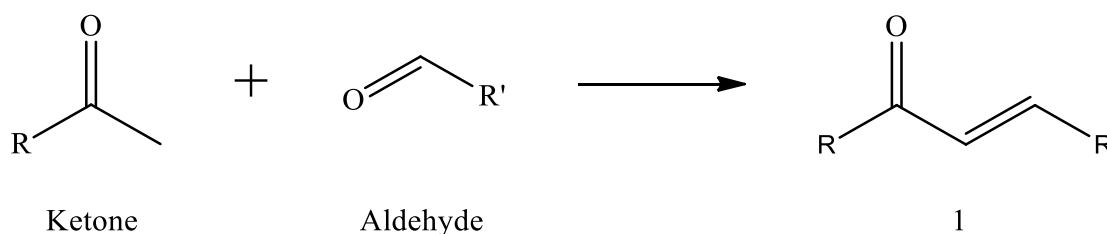
CH₃CN – Acetonitrile
DMSO – Dimethyl sulfoxide
EDG – Electron Donating Group
FRET – Förster Resonance Energy Transfer
FT-IR – Fourier Transform Infrared
HSQC – Heteronuclear Single Quantum Coherence
MetOH – Methanol
MNP – Magnetic Nanoparticle
NMR – Nuclear Magnetic Resonance
o-A – o-Anisaldehyde
PET – Photoinduced Electron Transfer
UV-vis – Ultraviolet-visible
WHO – World Health Organisation
XRD – X-ray Diffraction

3 Mix ligand chemosensors

3.1 Introduction

The two essential components of a chemosensor are the recognition and signalling units, with each of these components having qualities that, when combined, determine the chemosensor's quality. The recognition site of an ideal chemosensor should be sensitive, selective, and rapidly interacting with trace amounts of the analyte. At the same time, a good signalling unit needs to demonstrate a quick response time, be affordable with a high signal-to-noise ratio.¹ Coumarin is an example of such a signalling unit which can also easily be modified to further improve these properties. A wide variety of recognition sites have been used, in which the focus was on different functional groups. The electron donating group (EDG), enone,² is one of the functional groups which can be used as a recognition site. Besides the functional group, another approach to alter the recognition site affinity towards certain analytes is introduction of mixed ligand chemosensors that can assist each other.

Enone functional group is an EDG which consists of a carbonyl group situated next to an unsaturated C-C double bond, as shown in **Scheme 3.1**.



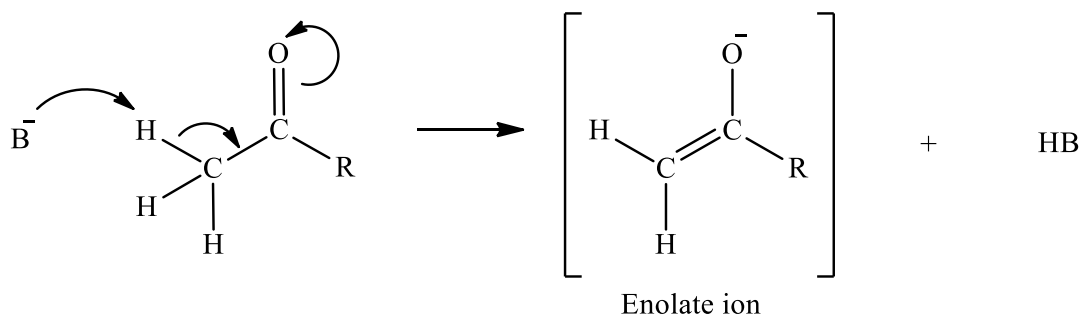
Scheme 3.1: Generalised reaction to form the enone functional group, **1**.

This functional groups can be synthesised in an aldol-condensation reaction catalysed by an acid or base (**Scheme 3.1**).^{3,4} The formation mechanism can be divided into two steps: the aldol condensation step, **Scheme 3.2**, and the dehydration step via enolate the formation, **Scheme 3.3**.

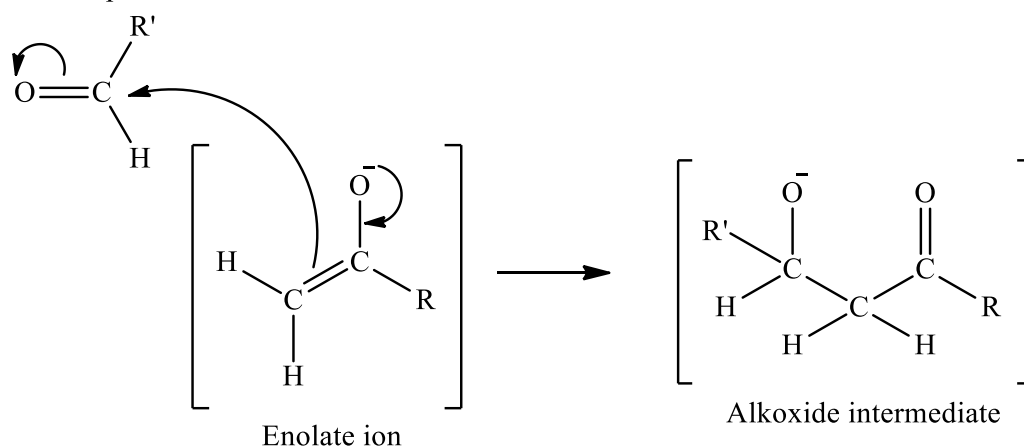
In **Scheme 3.2**, the first step is the formation of the enolate ion. A base, such as piperidine, abstracts the acidic α -hydrogen of the ketone compound in an acid-base reaction. In the next step, the resulting nucleophilic enolate ion attacks the electrophilic carbonyl carbon of the aldehyde which results in the formation of an alkoxide ion intermediate. In the last step, the

alkoxide ion intermediate takes a hydrogen from the conjugate acid, creating a hydroxide in the neutral aldol condensation product and the regenerated base catalyst.^{3,4}

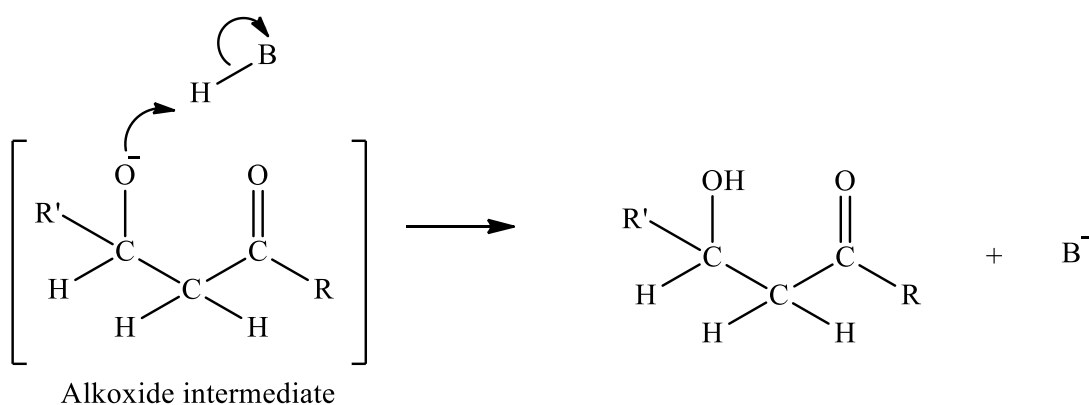
1. Enolate formation



2. Nucleophilic attack



3. Protonation

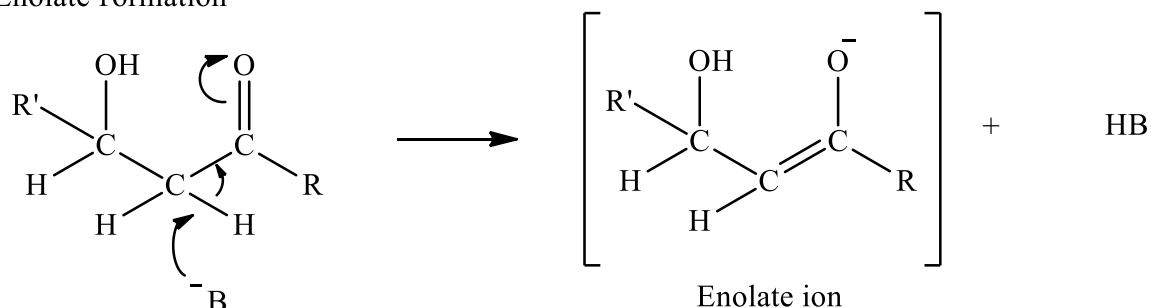


Scheme 3.2: Base catalysed aldol condensation mechanism to form the enone functional group.^{3,4}

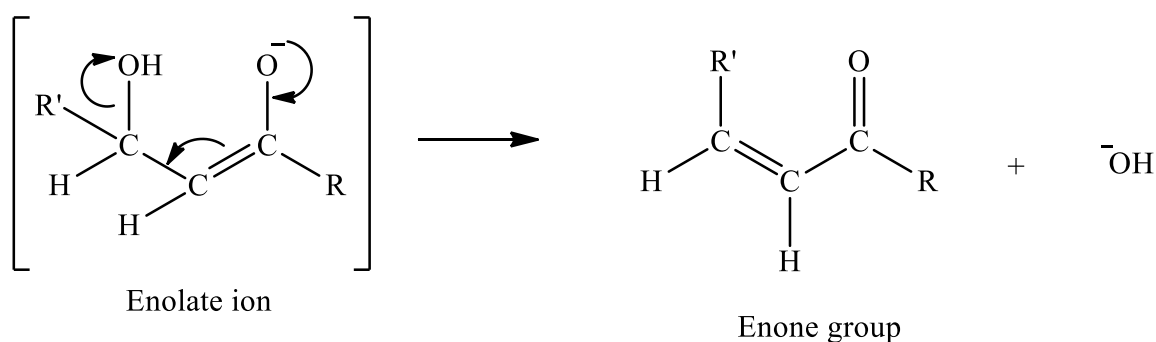
Generally, hydroxide moieties do not undergo dehydration easily as the hydroxide group is a poor leaving group. However, the aldol condensation product dehydrates easily due to the β -

carbonyl group. In **Scheme 3.3**, the acid-base reaction between the acidic α -hydrogen and the base results in the enolate ion intermediate. The enolate ion expels the hydroxide under basic conditions in an E1cB reaction, resulting in the conjugated enone functional group.^{3,4}

1. Enolate formation



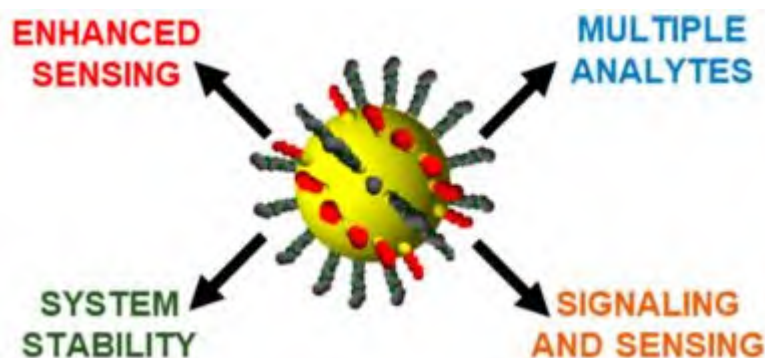
2. Enone formation



Scheme 3.3: Dehydration mechanism via enolate ion step to form the enone functional group.^{3,4}

In comparison, during acidic conditions, the hydroxide group is first protonated and is then expelled as water through an E1 or E2 reaction, depending on the reaction conditions.⁴

Alternatively, the mixed-ligands monolayer is widely used in magnetic nanoparticles (MNP) due to the properties it provides. These mixed-ligand MNP sensing applications can be divided into four groups, as shown in **Scheme 3.4**. Each group uses the mixed-ligand monolayer's multiple functionalities and ligand conformation to achieve a specific function.¹



Scheme 3.4: The four groups of applications of mixed-ligand MNP.¹

- The first group (**red** in **Scheme 3.4**) combines two ligands to improve and enable highly selective and sensitive sensing.
- The second group (**blue**) uses multiple functional ligands to detect multiple analytes.
- The third group (**orange**) combines the recognition ligand with another ligand that aids in the complexation process to form a more multifaceted sensing system.
- The final group (**green**) employs mixed ligands to improve sensor stability.¹

Ketan S. Patel and coworkers have worked on a newly synthesised octahedral copper complex consisting of a coumarin and clioquinol ligand. The mixed-ligand complex was obtained by refluxing the two ligands in the presence of $\text{Cu}(\text{NO}_3)_2$ for five hours in an ethanolic solution, the solution was concentrated, and a fine product precipitated out overnight. The precipitate, complex **2**, shown in **Figure 3.1**, was washed with ether and dried. X-ray diffraction studies confirmed the structure of complex **2**.⁵

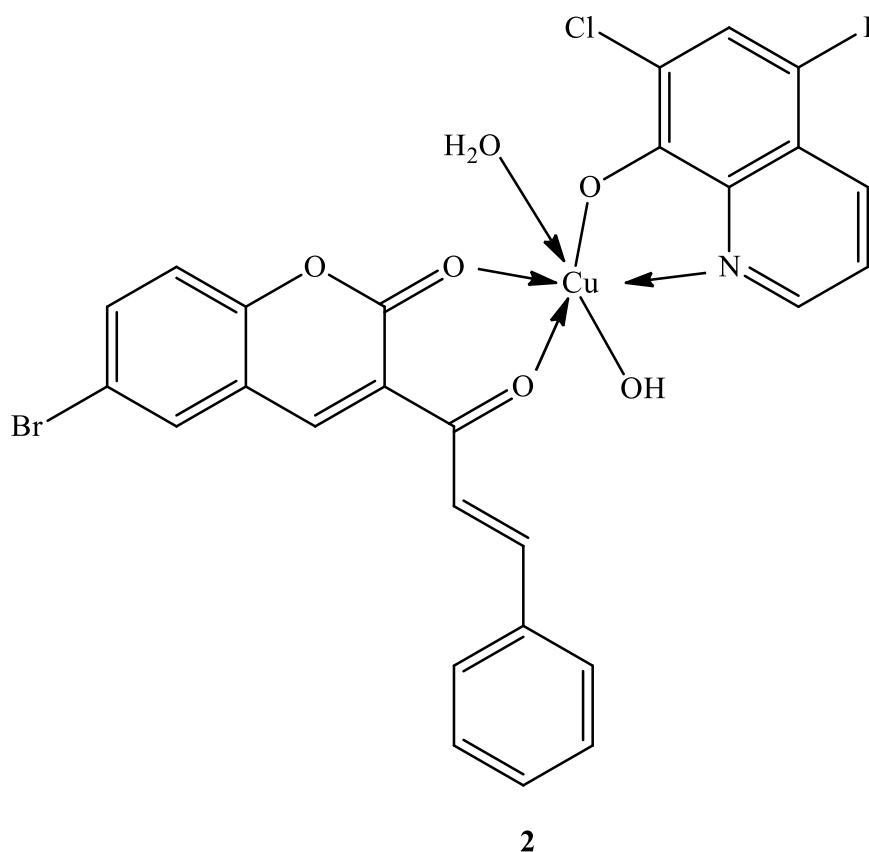


Figure 3.1: Mixed-ligand Cu(II) complex 2.

The study focused on the heating rate kinetic parameters, thermal, and X-ray diffraction studies of the mixed-ligand Cu(II) complex.

A similar mixed ligand study was done by Şahin et al. for the formation of Co(II), Ni(II), Cu(II), and Zn(II) complexes. The two ligands used were acesulfame and 1,10-phenanthroline. The X-ray diffraction studies indicated that many different configurations were observed for these complexes.⁶

Neither of these studies uses the mixed ligands as a chemosensor. In this study, mixed ligand complexed will be investigated for their sensing abilities of metal cations.

3.2 Aim of chapter

It is known that metal cations form complexes with ligands such as water and various solvents. In the presence of chemosensors, some of the ligands are replaced and a metal-chemosensor complex forms. These complexes can exist in many binding ratios between the chemosensor (S) and metal cations (M^{n+}), as shown in **Figure 3.2**.

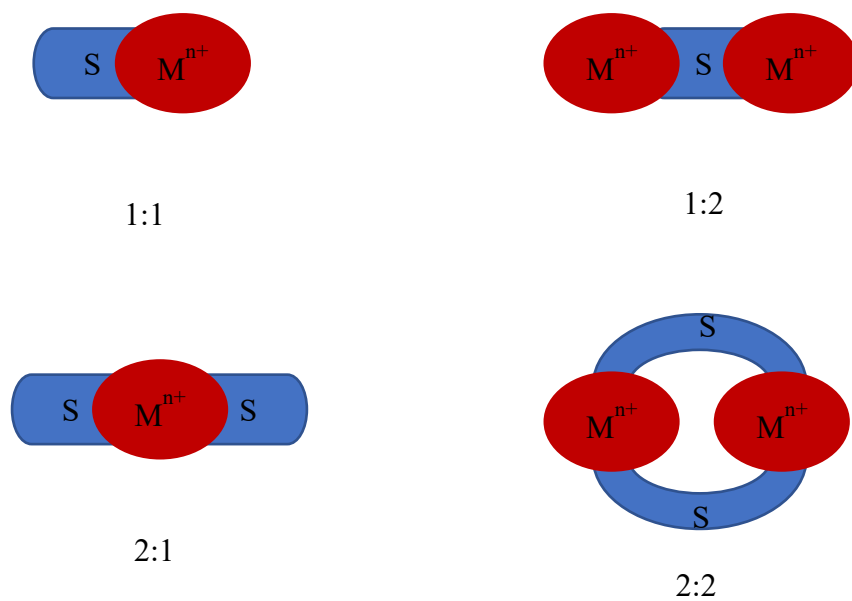


Figure 3.2: Binding ratios between a chemosensor (s) and a metal cation (M^{n+}).

This chapter compares a classical chemosensor (**E2**) to a mixed ligand chemosensor (**E6**); as shown in **Figure 3.3** to illustrate the theoretical complexation.

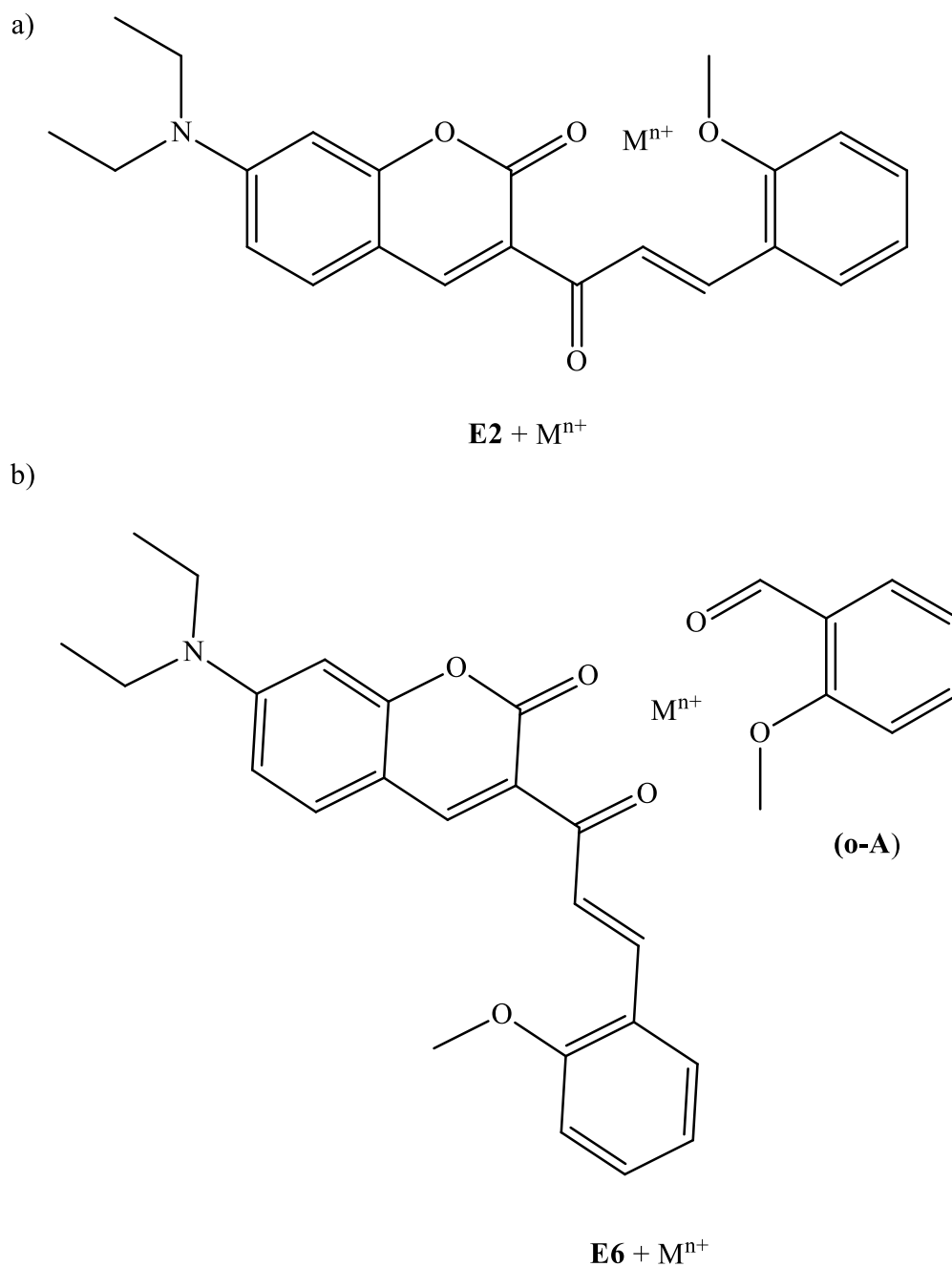


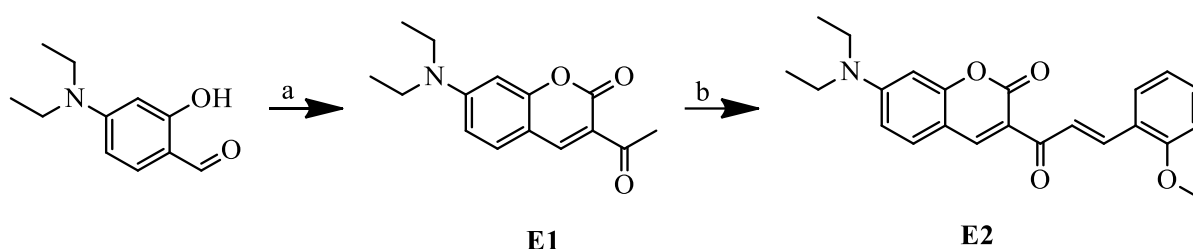
Figure 3.3: Example of the a) classical chemosensor versus b) a mixed-ligand type chemosensor.

Three key questions in this chapter are:

- Does the ligand o-anisaldehyde (**o-A**) affect the chemosensor abilities of **E2**?
- Does the mixed ligand chemosensor (consisting of **E2** and **o-A**), **E6**, performs better than **E2** as a metal cation detector?
- Which chemosensor, **E2** or **E6**, performs better in acetonitrile and methanol?
- Can chemosensor **E2** be used as an anion chemosensor in acetonitrile or methanol?

3.3 Synthesis of chemosensor **E2**

The synthesis of the target chemosensor **E2** was done via the ketone precursor **E1** as shown in **Scheme 3.5**. **E1** was prepared using 4-(diethylamino)salicylaldehyde as starting compound together with ethyl acetoacetate. This condensation reaction was done in ethanol using piperidine as a catalyst. The chemosensor **E2** was then synthesised through an aldol condensation reaction which involved **E1** and o-anisaldehyde, **o-A**, in piperidine as a base as shown in **Scheme 3.5**.^{7,8}



Scheme 3.5: Synthesis route to form chemosensors **E1** and **E2**. a) Ethyl acetoacetate, ethanol, piperidine, glacial acetic acid, reflux, 4 hours. b) o-Anisaldehyde, ethanol, piperidine, reflux, 24 hours.

All synthesised compounds were characterised using ¹H NMR, ¹³C NMR and FT-IR spectroscopies. **Figure 3.4** shows the proton NMR for the precursor **E1**. The reaction was confirmed to be successful due to the presence of the additional aromatic proton at 8.45 ppm (purple) and the newly formed acetyl group at 2.70 ppm (orange) compared to the starting 4-(Diethylamino)salicylaldehyde.

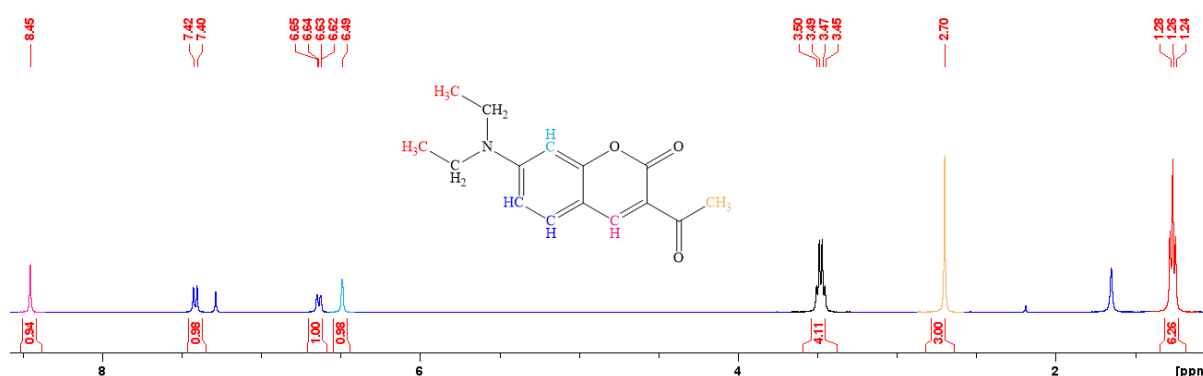


Figure 3.4: ¹H NMR spectrum of **E1** in CDCl₃.

Compound **E2** was subsequently synthesised and characterised with proton NMR as shown in **Figure 3.5**. The success of the reaction was verified by the presence of the double bond protons (shown in grey) at 6.94 ppm and 7.76 ppm with a coupling constant of 7.69 Hz. In addition, the disappearance of the acetyl protons of **E1** (2.70 ppm) further confirms the formation of **E2**.

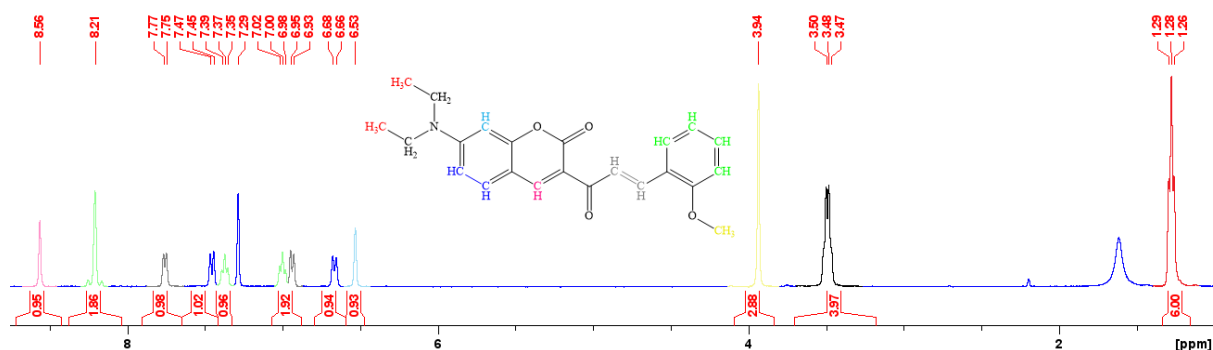


Figure 3.5: ^1H NMR spectrum of **E2** in CDCl_3 .

The ^{13}C NMR spectra of **E1** and **E2** are shown in the supplementary information as **Figure S 3.1** and **Figure S 3.3**, respectively.

FT-IR spectra of compounds **E1** and **E2** can be found in the supplementary information, **Figure S 3.2** and **Figure S 3.4**, respectively. Interesting to note is the shift observed from 1678.94 cm^{-1} , the ketone in **E1**, to 1647 cm^{-1} for the enone linker in **E2**.

In addition to compound **E2**, two enone derivatives, **E3** and **E4**, were also considered (**Figure 3.6**). **E3** contained hydrogen in the place of an ether group, and **E4** had a hydroxyl group in the same position. However, the synthesis of these two compounds was unsuccessful.

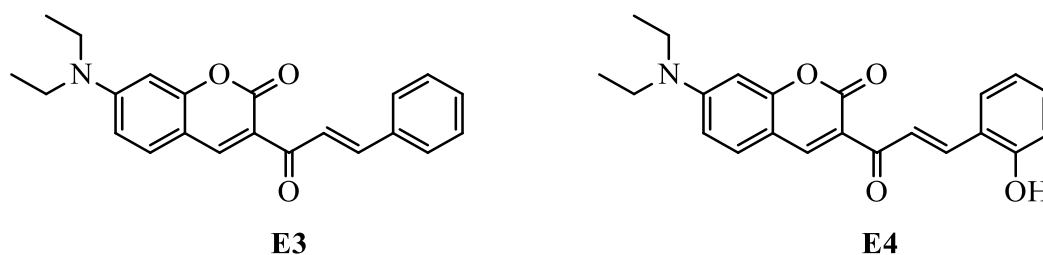
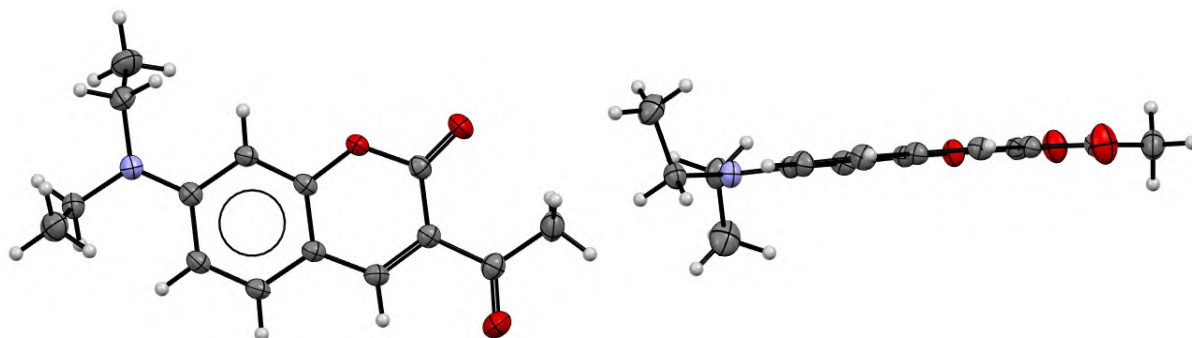


Figure 3.6: Structures of attempted chemosensors **E3** and **E4**.

As seen by **Figure S 3.5** and **Figure S 3.6** in the supplementary information, the reaction was unsuccessful as the acetyl CH_3 remained present after refluxing the reaction overnight as at 2.68 and 2.71 ppm, respectively.

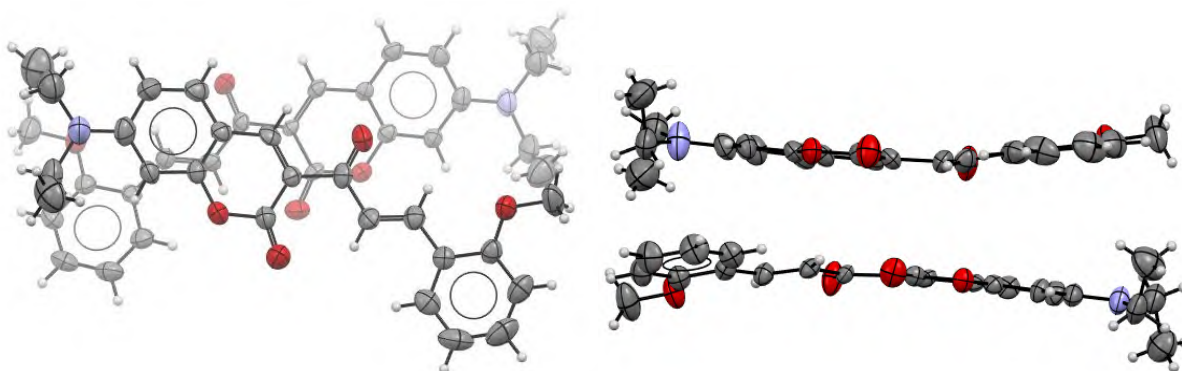
3.3.1 X-ray studies for compounds **E1** and **E2**

Crystals of **E1** and **E2** were obtained by dissolving the pure compound in ethanol. The crystals were then formed by slow evaporation. The single crystal X-ray diffraction (XRD) of both **E1** and **E2** confirms the structures of the expected compounds. **E1** is shown in **Figure 3.7**. The coumarin ring, amine, and acetyl functionality, are shown to be on the same plane with the ethyl groups perpendicular to the coumarin system.



*Figure 3.7: Single crystal XRD analysis of **E1** at two angles.*

E2 is shown below in **Figure 3.8**. The amine, coumarin ring, and carbonyl moiety resemble the structure of **E1**. Furthermore, the crystal structure reveals the presence of the enone functional group and that chemosensor **E2** exist as the E-conformer. The methoxyphenyl moiety was also observed to be on the same plane as the coumarin ring.



*Figure 3.8: Single crystal XRD analysis of **E2** showing two molecules in the asymmetric unit cell from two different perspectives.*

In addition, **E1** was crystallised in a monoclinic crystal system which contained a C2/c space group and **E2** also crystallised in a monoclinic crystal system but with a P21 space group with

two molecules in the asymmetric unit cell. For more information on the crystal structure, please see **Table S 3.1** in the supported information.

3.4 UV-vis absorption studies of **E2** and **E6**

The absorption spectra of all these compounds were obtained on an Evolution 201 UV-Visible Spectrophotometer, using a concentration of 0.0833 mM in acetonitrile and methanol as polar aprotic and protic solvents, respectively.

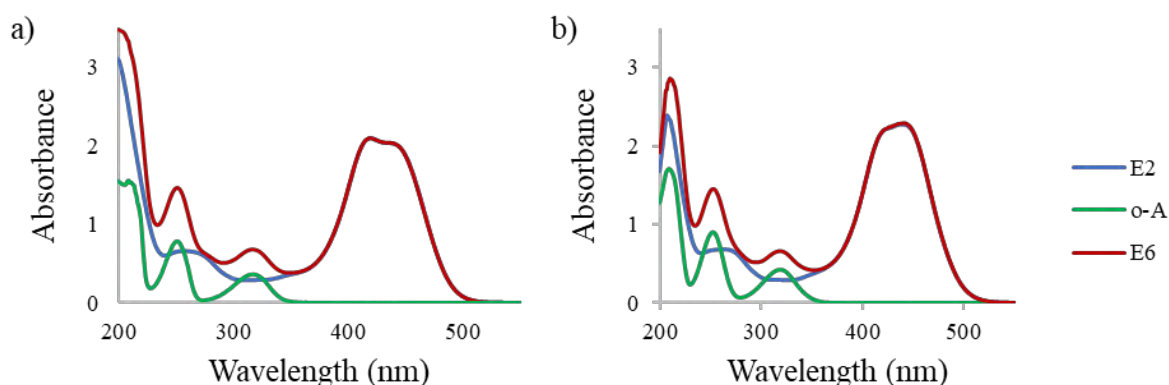


Figure 3.9: Absorbance spectra of **E2** (blue), **o-A** (green) and **E6** (red) in a) acetonitrile and b) methanol with a concentration of 0.0833 mM.

As seen in **Figure 3.9** and **Table 3.1**, the solvent did not induce significant changes in the absorption spectra of these compounds. In addition, it was observed that the presence of **o-A** does not interfere with or induce a significant shift in the absorption band of **E2**; however, a combined spectra (**E2** and **o-A**) are observed for **E6**, as expected.

Table 3.1: Absorbance bands, in nm, for all compounds in acetonitrile and methanol. Maximum absorbance bands are bolded.

	E2	o-A	E6
Acetonitrile	441 , 421, 255	318, 251	441 , 419, 317, 251
Methanol	442 , 254	319, 253	440 , 319, 253

3.4.1 Screening of cations using **E2** and **E6**

The chemosensing properties of **E2** and **E6** were investigated using metal cations in acetonitrile (polar aprotic) and methanol (polar protic). These metal cations include Na^+ , Mg^{2+} , Al^{3+} , K^+ , Ca^{2+} , Cr^{3+} , Mn^{2+} , Fe^{2+} , Fe^{3+} , Co^{3+} , Ni^{2+} , Cu^{2+} , Zn^{2+} , Pb^{2+} , Ag^+ , Cd^{2+} , Ba^{2+} , and Hg^{2+} .

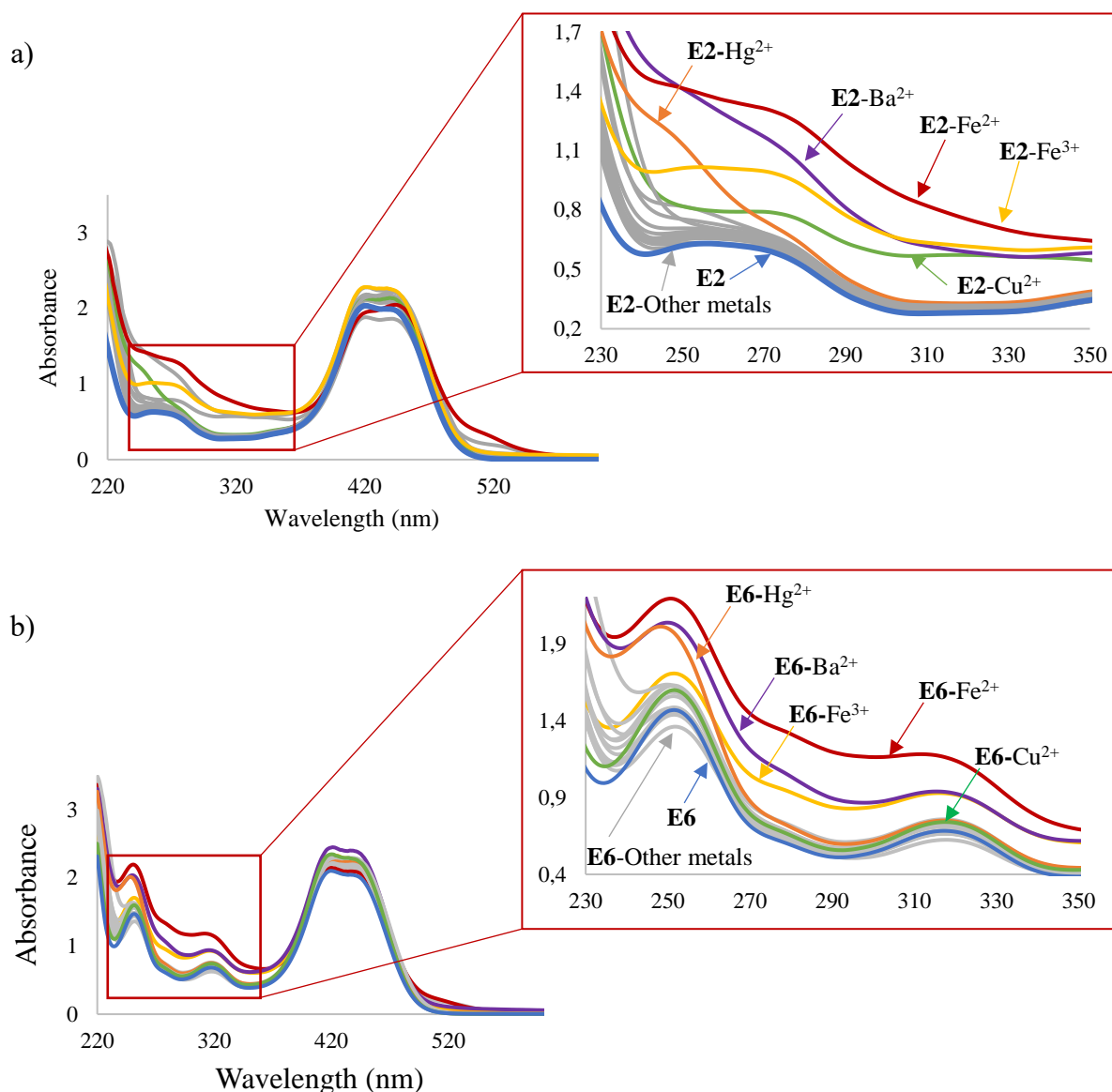


Figure 3.10: Screening of metal cations (0.167 mM) in acetonitrile using chemosensors a) **E2** and b) **E6**. Both sensors had a final concentration of 0.0833 mM.

As illustrated in **Figure 3.10 a)**, **E2** showed observable interactions with Fe^{2+} (red), Fe^{3+} (yellow), Cu^{2+} (green), Ba^{2+} (purple) and Hg^{2+} (orange) in acetonitrile, and **E6**, **Figure 3.10 b)**, showed slightly less interactions with cations such as Cu^{2+} and Hg^{2+} . This might indicate that

E6 is more selective than **E2**. However, this absorbance change is not observed at the λ_{max} but in the shorter wavelengths.

Similar observations were made when methanol was used as the solvent in **Figure 3.11**. In methanol, **E2** showed fewer interactions as only two metals ions (Fe^{2+} (red) and Fe^{3+} (yellow)) induced significant interactions in the absorbance spectra of **E2**. It was also observed that in acetonitrile, the mixed ligand chemosensor **E6** showed “more selective” interactions with Fe^{2+} (red) and Fe^{3+} (yellow). It is worth noting that the presence of metal ions diminishes the absorption band of **o-A**, at 253 and 319 nm in **Figure 3.11 b**).

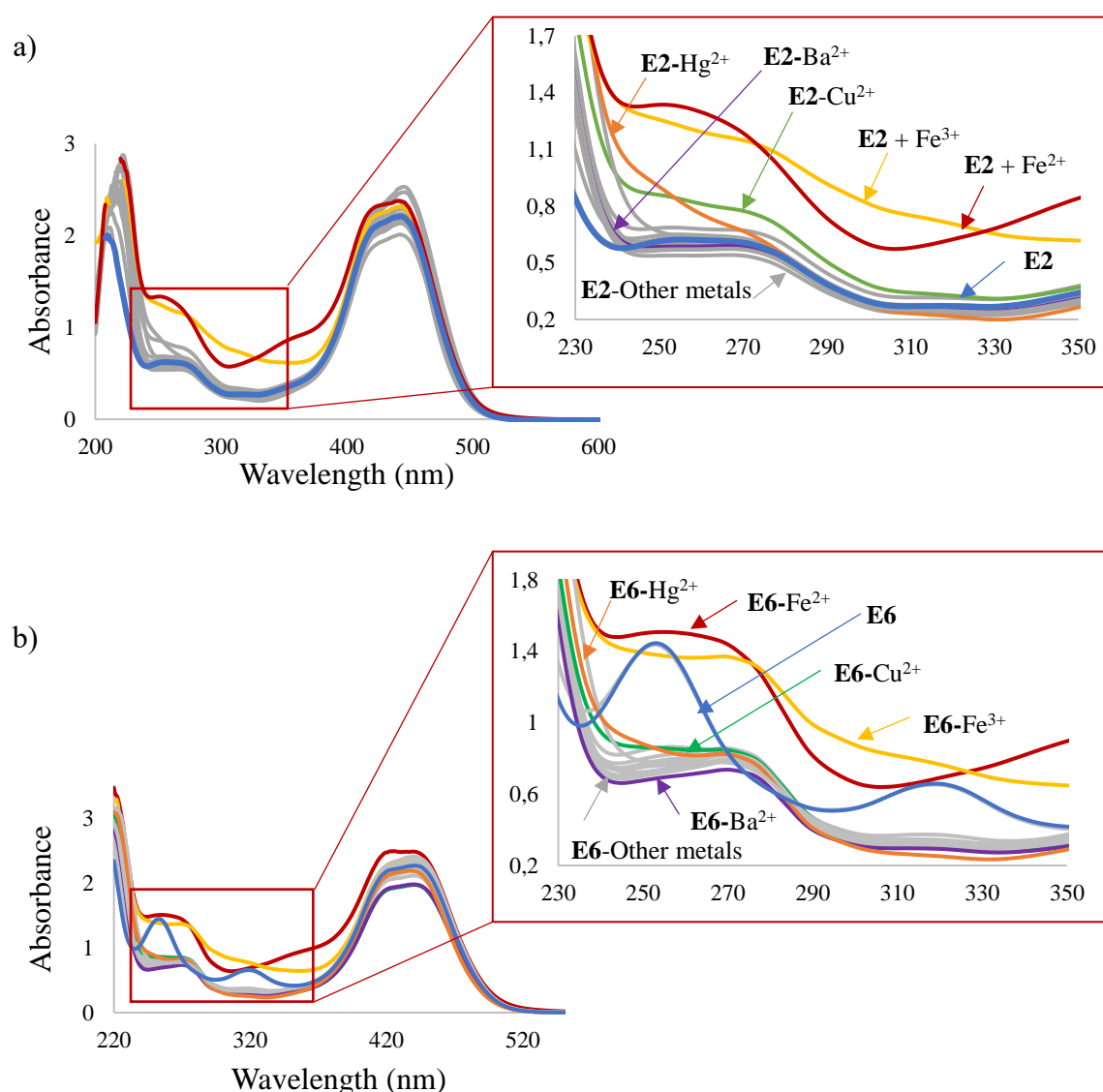


Figure 3.11: Screening of various cations (0.167 mM) in methanol using chemosensors a) **E2** and b) **E6**. Both chemosensors had a final concentration of 0.0833 mM.

The absorbance of **o-A** with Fe^{2+} and Fe^{3+} in methanol was also obtained. The results are illustrated in the supplementary information, **Figure S 3.8**. It was observed that the **o-A** absorbance spectrum does not change in the presence of iron.

In acetonitrile, the **E2**- Fe^{2+} complex induces a slight colour change from yellow to orange, and the **E2**- Fe^{3+} complex caused the same effect with less intensity. No other colour changes were observed for the **E2**-metal complexes. Moreover, in methanol, the **E2**- Fe^{2+} complex induced the same colour change from a yellow to an orange and the **E2**- Fe^{3+} complex only induced a slight colour change, from a yellow to a transparent orange, as seen in **Figure 3.12**.

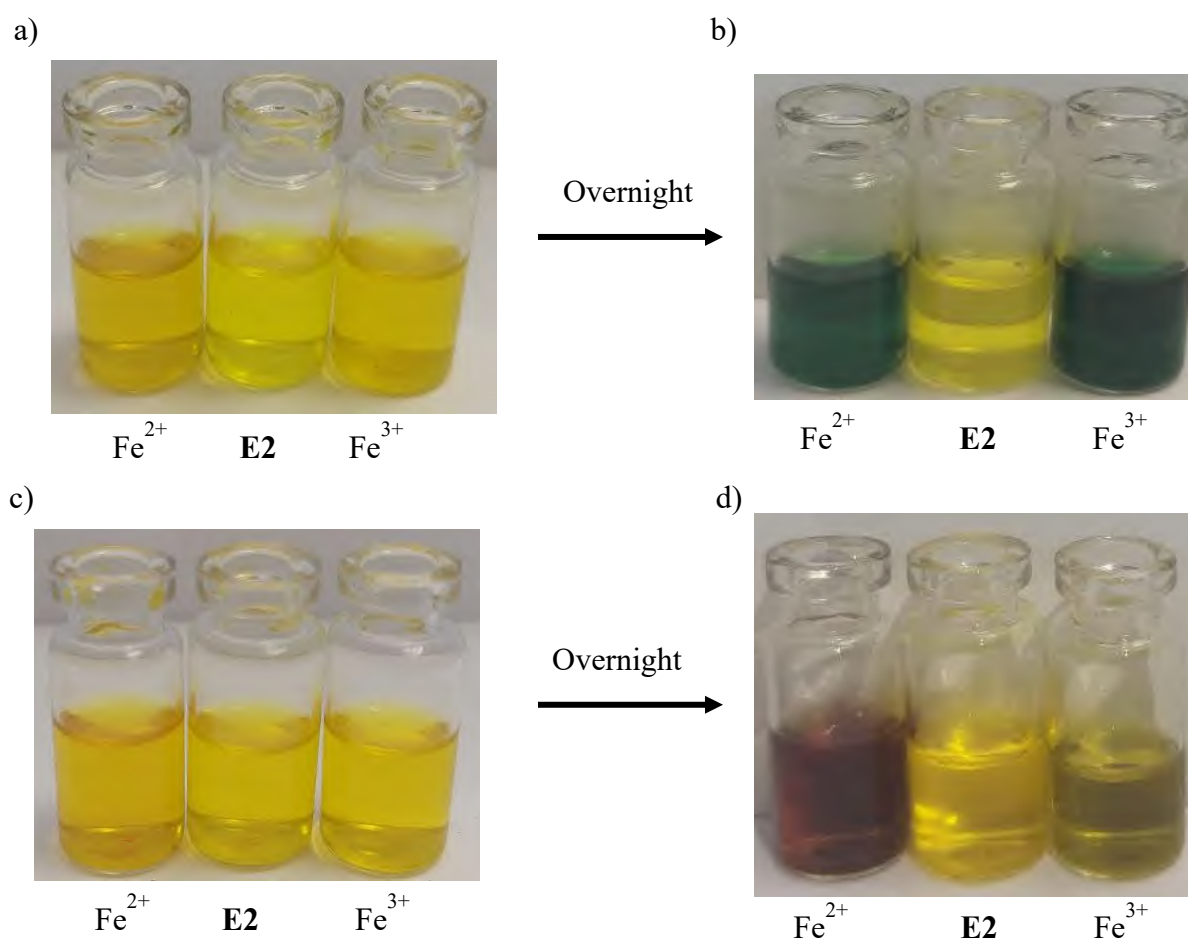


Figure 3.12: Photographic image of **E2**- Fe^{2+} and **E2**- Fe^{3+} complexes and **E2** in a) acetonitrile, b) the same sample left overnight, c) in methanol and d) the same sample left overnight.

Figure 3.12 shows the visual image of the screening of **E2** in the presence of iron in acetonitrile and methanol. The **E2**- Fe^{2+} complex in both solvents induced a darker orange colour compared to the **E2**- Fe^{3+} complex. However, when the samples were left overnight, a more significant

colourimetric change was observed, as shown in **Figure 3.12** and the absorbance spectra in **Figure S 3.7** of the supplementary information.

After the samples were left overnight [**Figure 3.12 b**) and **c**) and **Figure S 3.7**], the two samples containing just **E2** remain yellow. In contrast, both iron complexes in acetonitrile changed to a green solution, with **E2-Fe²⁺** having a new absorbance band at 603 nm and **E2-Fe³⁺** having a new absorbance band at 605 nm. In methanol, the **E2-Fe²⁺** complex turned into a red solution with a new absorbance band at 565 nm while **E2-Fe³⁺** complex displayed no significant changes in the absorbance spectra after the period mentioned earlier.

The same experiment was performed for **E6** complexes under similar conditions as shown in **Figure 3.13**. It was observed that similar results were obtained as in **E2** complexes, which indicates that the **o-A** ligand played no significant part during the complexation process or the ligand did not change the complex properties.

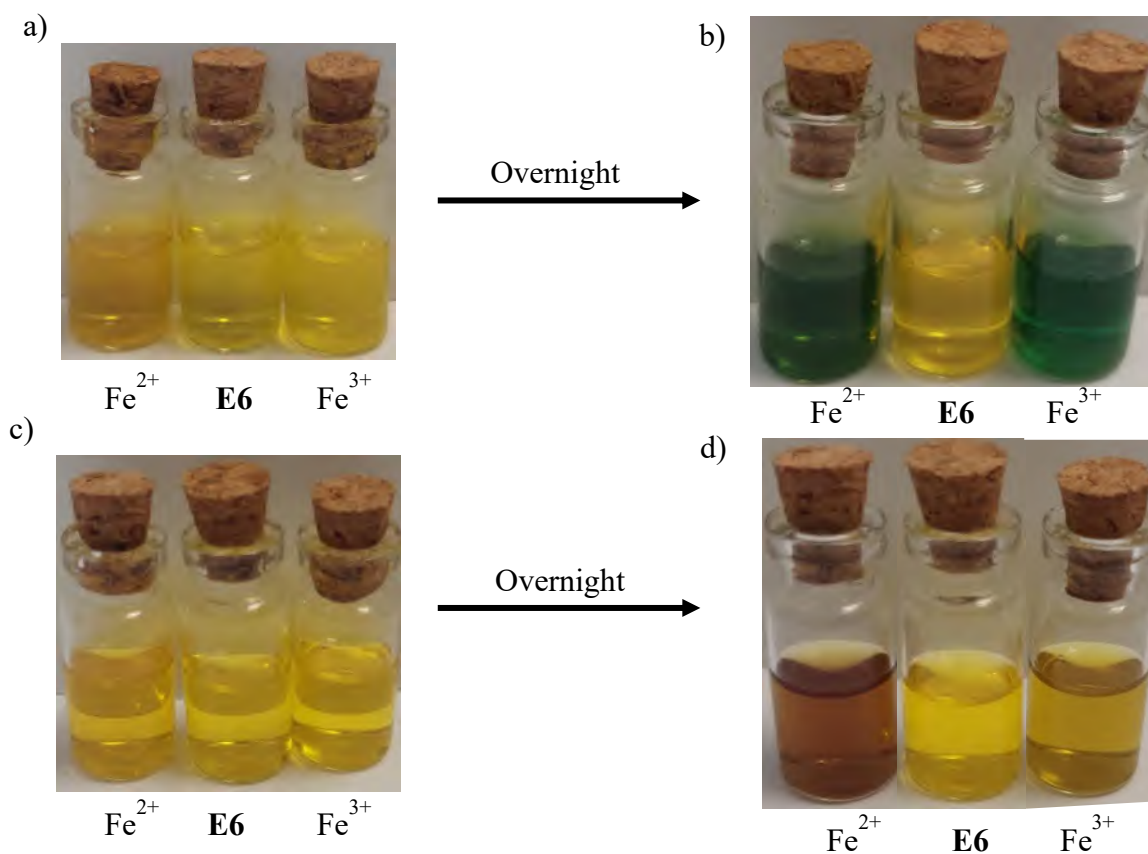


Figure 3.13: Photographic image of **E6-Fe²⁺** and **E6-Fe³⁺** complexes and **E6** in a) acetonitrile, b) the same sample left overnight, c) in methanol and d) the same sample left overnight.

3.4.2 E2 screening towards anions

Investigation of the anionic chemosensing abilities of **E2** was explored by screening using; F^- , Cl^- , Br^- , I^- , AcO^- , NC^- , NCS^- , NCO^- , PO_4^- , and SO_4^- in acetonitrile and methanol.

E2 displayed similar interactions with all anions tested except for I^- , which induced a substantial change in the absorbance band around 245 nm for acetonitrile and 220 nm for methanol, **Figure 3.14**, and from 254 nm to 245 nm for **E2** in acetonitrile. The absorbance band around 250 nm in methanol solution showed no significant change as in acetonitrile. However, the band at 220 nm showed a hyperchromic shift induced by the presence of I^- anion.

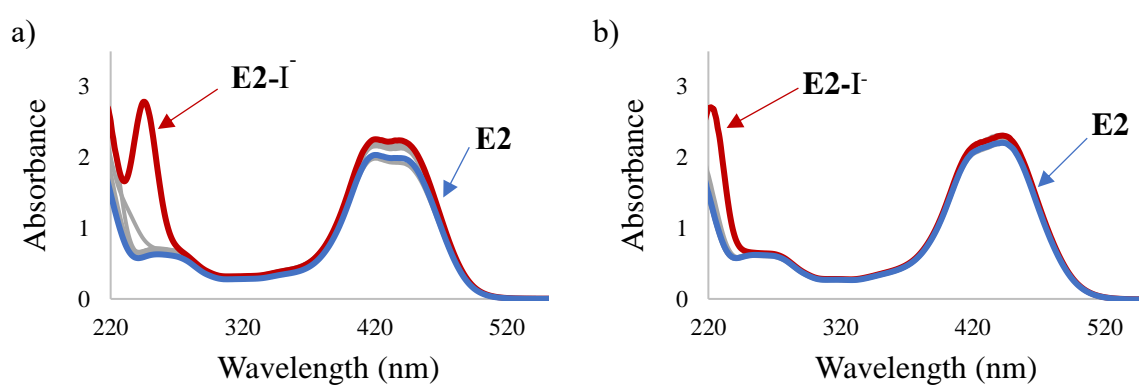


Figure 3.14: Screening of various anions (0.167 mM) using chemosensor **E2** (0.0833 mM) in a) acetonitrile and b) methanol.

With further investigation, it was found that free I^- have a strong absorbance band at 226 nm in an aqueous solution, according to a study published by S. V. Kireev and S. L. Shnyrev, 2015.⁹ Therefore, a UV-Vis spectrum of I^- was obtained to compare to the peak observed for **E2-I⁻** complex. As seen in **Figure 3.15**, the absorbance band observed at 246 nm, in red, is from I^- and not from the **E2-I⁻** complex, as I^- alone have the same absorbance band at 246 nm, and the shift in the peak from the published 226 nm is due to the solvent used.

Based on these results, it was concluded that, the changes observed in the bands around 245 nm were not due to the complexation between **E2** and I^- .

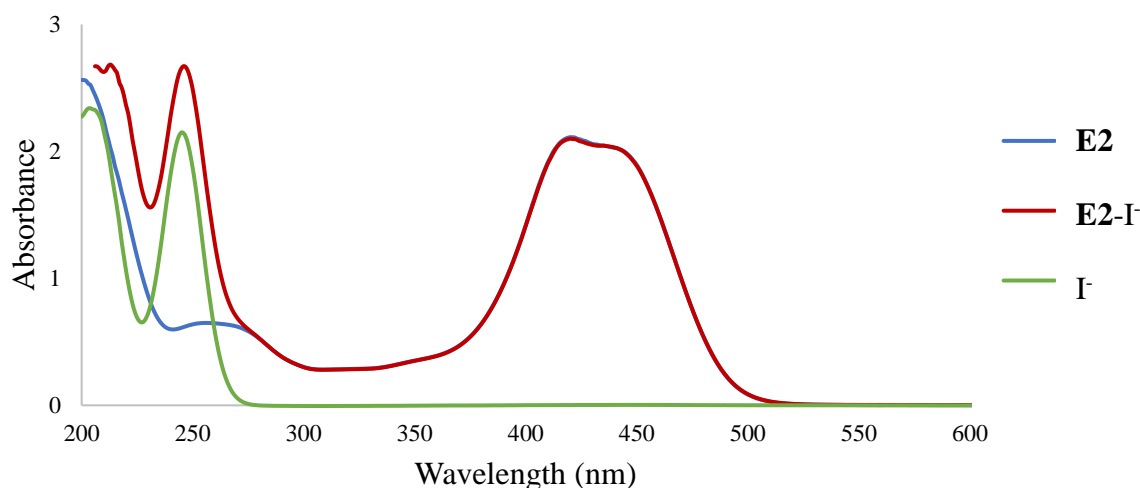


Figure 3.15: Absorbance spectra of I^- (green), E2 (blue) and the complex, E2- I^- (red).

3.5 Fluorescence studies of E2 and E6

3.5.1 Mode of fluorescence of E2

Fluorescence can occur in various ways, as described in **Chapter 1, Section 1.7.2**. These mechanisms include the Förster resonance energy transfer (FRET) and Photoinduced electron transfer (PET). In a FRET system, the energy is transferred from an excited donor site to a ground-state acceptor and have three main characteristics:¹⁰⁻¹²

1. Distance plays a significant role in FRET systems, in which a donor and acceptor site is located within a distance of 10 – 100 Å.
2. A significant overlap between the acceptor site's absorption spectrum and the donor site's emission spectrum is required.
3. Lastly, the donor and acceptor site must have an appropriate orientation for dipole-dipole interaction.

FRET is a distance-dependent energy transfer process. In addition, a FRET-based fluorescent chemosensors displays significant sensitivity to the environment on and around the chemosensors.¹²

Thus, for a FRET system, the three main characteristics need to be met. **Figure 3.16** shows the spectral overlap of E2 between the absorbance (red) and the emissions spectra (blue) required

for a FRET system between 450 and 500 nm. This considerable overlap suggests a long-range dipole-dipole interactions between an excited donor site and an acceptor site.¹¹

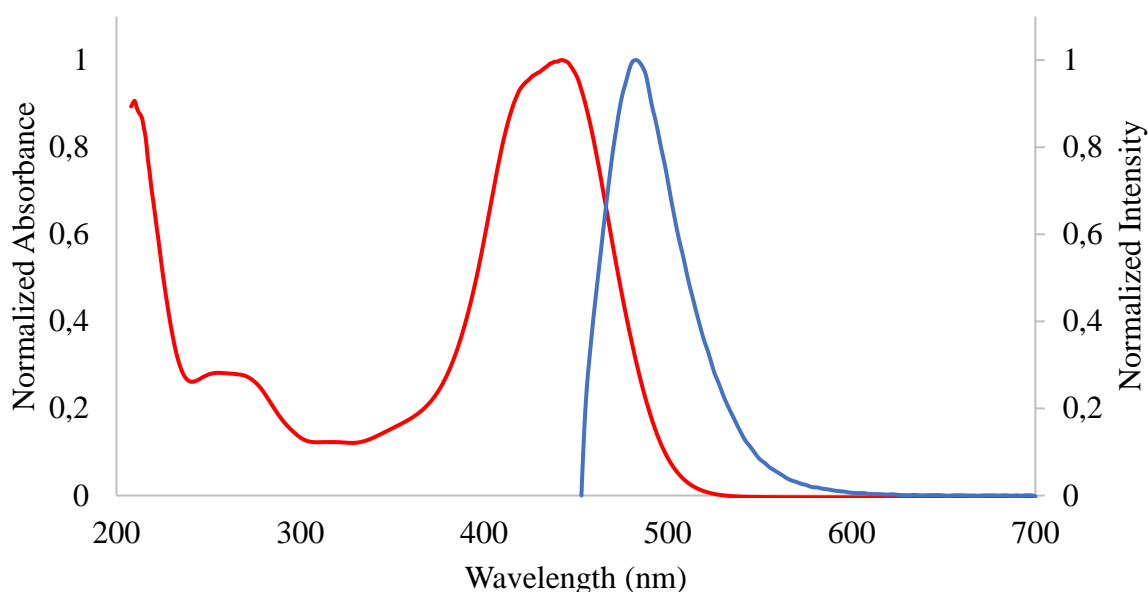


Figure 3.16: Normalised absorbance (red) and emissions (blue) of **E2** in MetOH indicate spectral overlap. $\lambda_{\text{excitation}} = 440 \text{ nm}$.

Furthermore, FRET systems are distance-dependent energy transfer processes which require a distance greater than 10\AA between the donor and acceptor site. **Figure 3.17** shows that both the donor (HOMO) and acceptor (LUMO) sites in **E2** are on the coumarin backbone. Therefore, **E2** does not align with the three main characteristics of a FRET system.

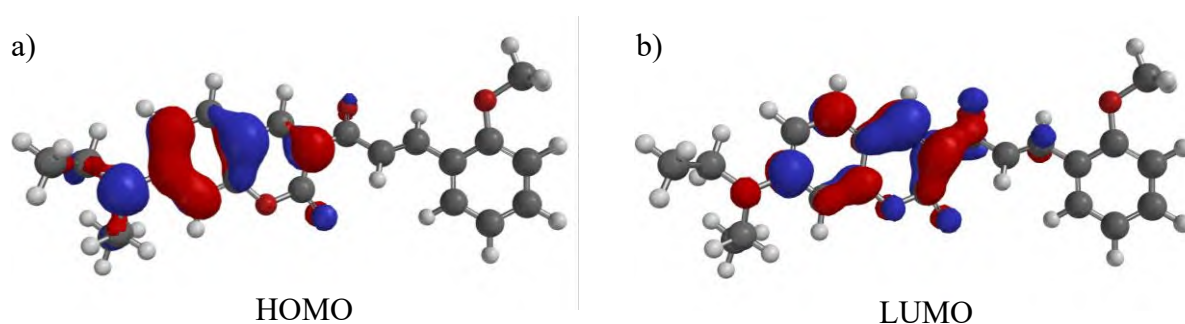


Figure 3.17: HOMO and LUMO of **E2** obtained using molecular modelling.

On the other hand, photoinduced electron transfer (PET) is the process in which a photoexcitation gets electrons moving from the ground state to an excited state. PET systems donate the electron from the excited state to an acceptor in the ground state.¹³ The electron,

from a donor site, is excited by absorbing light, thus moving from the HOMO to the LUMO. In close proximity, an acceptor site donates a ground state electron while taking the excited electron. In an intermediate complex ($\text{*Donor}^-\text{Acceptor}^+$), the donor site is excited with a negative charge, and the acceptor site is positively charged. Thus, a PET active system is non-fluorescent.^{14,15}

The HOMO and LUMO in **Figure 3.17** suggest the potential of a PET “on-off” system. Additionally, no hypsochromic nor a bathochromic shift in absorption wavelength (440 nm) was observed with the addition of Fe^{2+} (in **Figure 3.11**). Supporting the suggestion that **E2** displays PET-type “on-off” fluorescence quenching.

3.5.2 Fluorescent screening of **E2** for the detection of cations

The interaction between **E2** and the metal cations was studied in acetonitrile and methanol. As shown in **Figure 3.18 a)**, Ba^{2+} ions had the most significant enhancement, followed by Fe^{2+} , Fe^{3+} and Al^{3+} . The remainder of the cations demonstrated a quenching effect on **E2** in acetonitrile. In contrast, **Figure 3.18 b)** showed that Fe^{2+} uniquely quenched the fluorescence of **E2**. At the same time, the other cations, such as Ba^{2+} and Al^{3+} , displayed an enhancement effect. These observations confirmed a well-documented effect of the solvents in the complexation process.

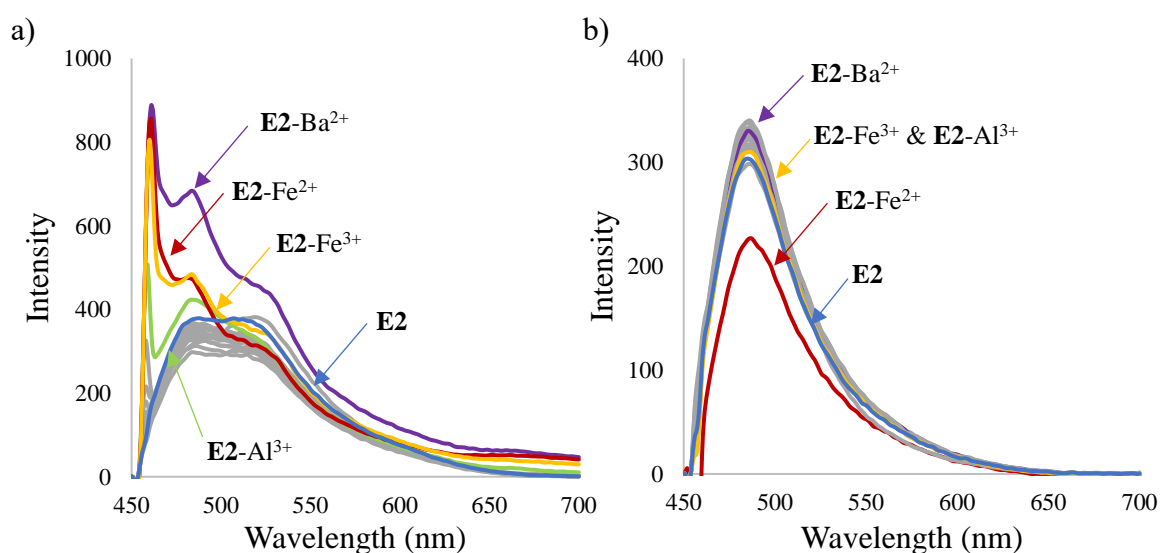


Figure 3.18: Metal cation (0.167 mM) screening of **E2** (0.409 μM) in a) acetonitrile and b) methanol. $\lambda_{\text{excitation}} = 440 \text{ nm}$.

3.5.3 Competition studies of $\mathbf{E2-Fe^{2+}}$ complex

Due to unique interactions between **E2** and Fe^{2+} , competition studies were done to investigate the effect of other competing metal ions has on the formation of the $\mathbf{E2-Fe^{2+}}$ complex. In **Figure 3.19**, the blue bars indicate the emissions intensity of **E2** alone and in the presence of the various metal cations. The red bars indicate **E2** in the presence of both competing metal cations. Chemosensor **E2** was added a mixture of the two metal cations, ensuring that **E2** could equally interact with both cations. Thus, if the red bar is in line with the $\mathbf{E2-Fe^{2+}}$ complex (first red bar), then the $\mathbf{E2-Fe^{2+}}$ complex is preferred above the other metal cation. **Figure 3.19 b)** shows that **E2** demonstrate a reasonable selectivity for Fe^{2+} even in the presence of other competing metal cations.

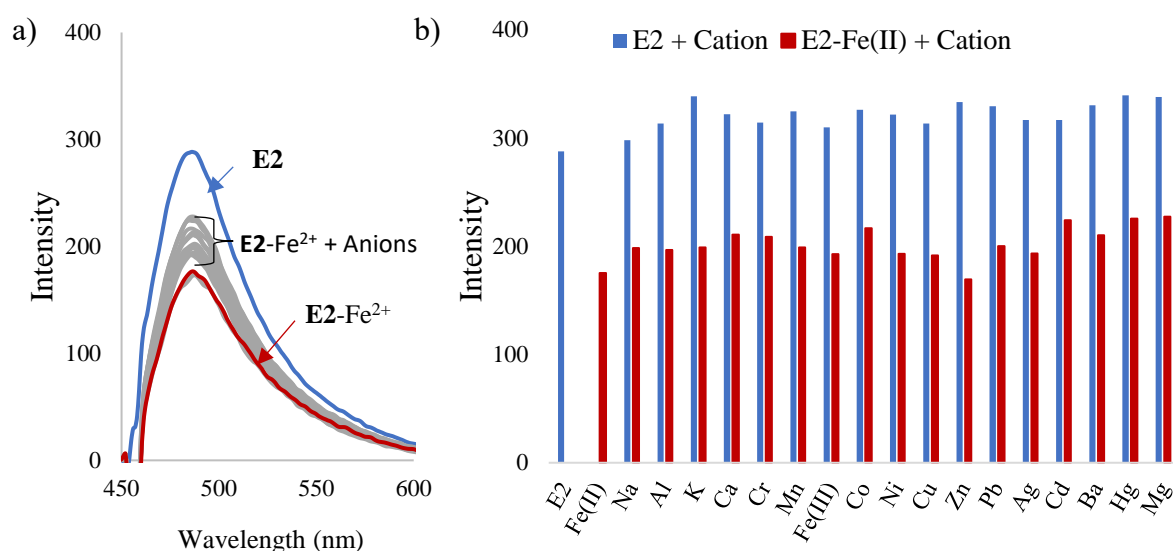


Figure 3.19: Competition study of a) $\mathbf{E2-Fe^{2+}}$ in the presence of various competing metal cations in MetOH. b) Comparison between **E2** in the presence of various competing metal cations (blue bars) and $\mathbf{E2-Fe^{2+}}$ in the presence of various competing metal cations (red bars) in equal amounts at 485 nm. $\lambda_{\text{excitation}} = 440 \text{ nm}$.

3.5.4 Titration and binding site studies of **E2**

In order to determine the concentration range at which **E2** can be used for the detection of Fe^{2+} and obtain the calibration curve for the complexation between **E2** and Fe^{2+} . Titration studies were performed in which increasing amounts of Fe^{2+} were added to **E2** in methanol. The increasing amounts of Fe^{2+} resulted in a quenching effect on the emission intensity, as seen in

Figure 3.20. Up to 72,5% decrease in the emission intensity of **E2** was observed with the addition of 0.833 mM Fe^{2+} .

A calibration curve, **Figure 3.21**, was constructed from these results. The addition of Fe^{2+} was observed to be non-linear between 0 mM and 0.833 mM, as seen in **Figure 3.21 a)**. However, a linear relationship was observed between 0 mM and 0.183 mM with an R^2 value of 0.9865 (**Figure 3.21 b)**. The LOD and LOQ were determined to be 0.024 mM and 0.074 mM, respectively, at this range.

The World Health Organisation (WHO) states that elevated iron levels influence water's taste, turbidity and colour. In addition, when iron is $5.37\ \mu\text{M}$ and above, iron can cause stains on laundry and plumbing fixtures. Elevated iron concentrations can also promote the growth of “iron bacteria”, which leads to further health concerns.¹⁶ However, higher concentrations of iron in the human body can cause “iron overload”, which can lead to haemochromatosis, retinitis, choroiditis, conjunctivitis, cancer and heart diseases¹⁷

The WHO also states that iron(II) is essential to human nutrition. The estimated minimum daily requirement of iron is 0.179 mM – 0.895 mM depending on age, sex, physiological status and iron bioavailability.¹⁶

Thus, chemosensor **E2** can determine the presence and concentration of Fe^{2+} at recommended daily consumption.

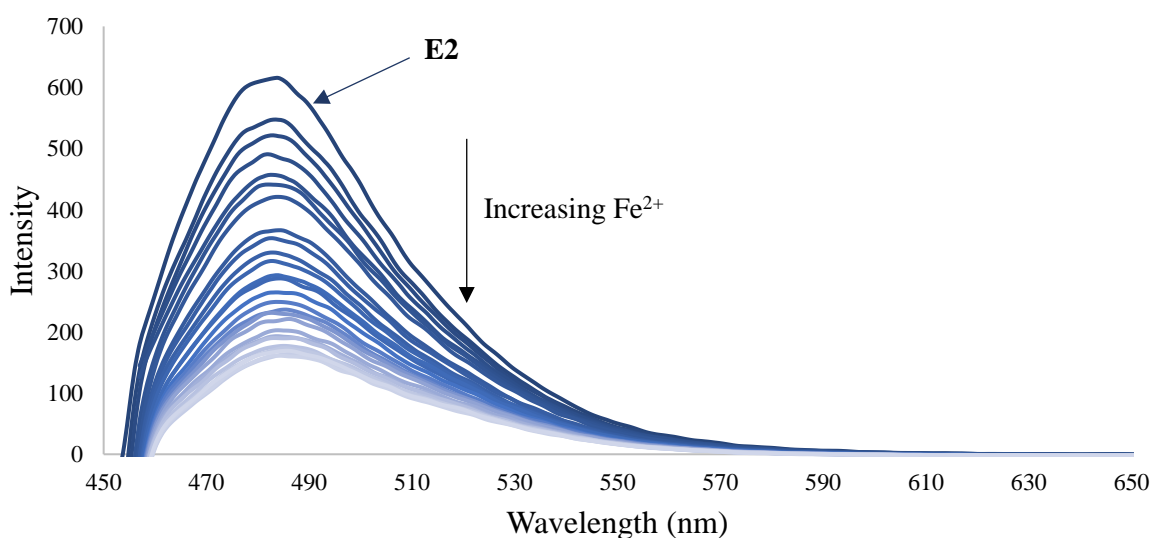


Figure 3.20: Titration of **E2** with increasing aliquots of Fe^{2+} in MetOH. $\lambda_{\text{excitation}} = 440\ \text{nm}$.

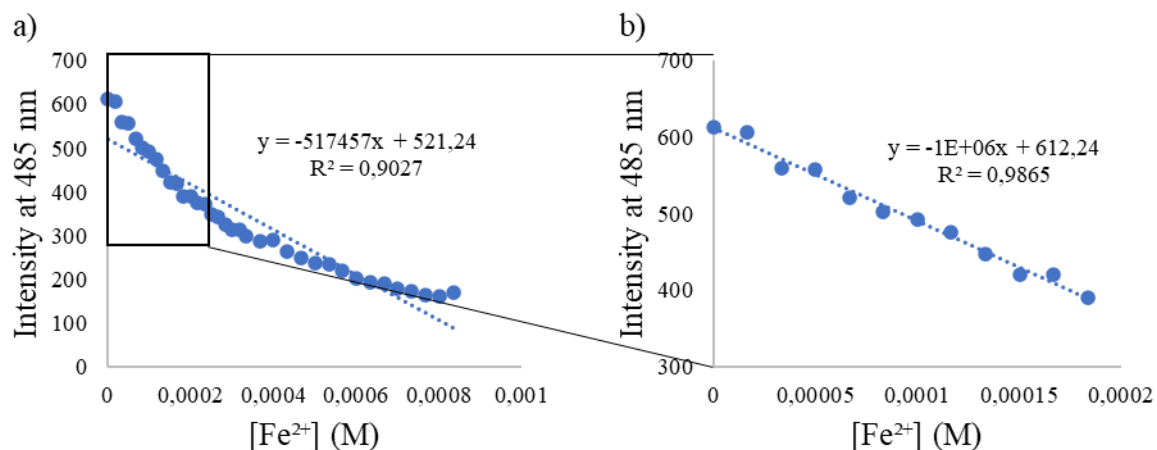


Figure 3.21: Calibration curve of **E2-Fe²⁺** complex at 485 nm. $\lambda_{excitation} = 440$ nm.

3.5.4.1 Benesi-Hildebrand plot of **E2-Fe²⁺** complex

The Benesi-Hildebrand (BH) plot was constructed to determine the binding coefficient, and the binding ratio following a procedure described in **Chapter 2, Section 2.4.3.1**. The BH plot was done in methanol with an increase of Fe²⁺ from 0 to 0.833 mM. The BH plot, **Figure 3.22** displayed a positive slope with a good linear regression coefficient, R^2 , of 0.9872. The binding coefficient, K , from **Equation 1** (**Chapter 2, Section 2.4.3.1**) was calculated from the ratio of the intercept to the slope of **Figure 3.22**.^{18,19} The binding coefficient was determined to be $3.873 \times 10^3 \text{ M}^{-1}$.

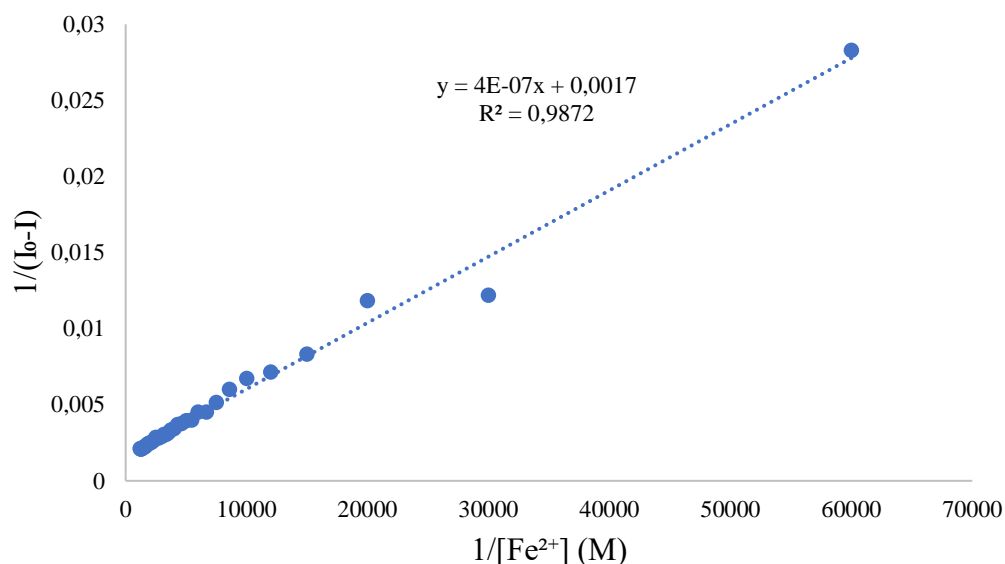


Figure 3.22: Benesi-Hildebrand plot of **E2-Fe²⁺** complex.

As seen in **Figure 3.22**, the linearity of the slope ($R^2 = 0.9872$) indicates that a 1:1 binding ratio is most likely to occur between **E2** and Fe^{2+} .²⁰ This binding ratio was later verified and supported by the Hill plot (**Figure 3.24**) and the Jobs plot analysis (**Figure 3.29**).

*3.5.4.2 Construction of the Stern-Volmer plot for the **E2**- Fe^{2+} complex*

A Stern-Volmer plot can provide insight into the mechanism of the quenching of **E2**. The plot can indicate the presence of dynamic or static quenching by the linearity of the slope.^{21,22}

Dynamic quenching results from energy transfer during collisions of the quencher (analytes) and the chemosensor²³ and is indicated by a deviation from linearity in the Stern-Volmer plot.²²

Whereas, static quenching results from complexation between the quencher and the chemosensor²³ and is indicated by a linear slope in the Stern-Volmer plot.²² The Stern-Volmer plot is constructed by using the Stern-Volmer equation (1):

$$\frac{I_0}{I} = 1 + K_{sv}[Q] \quad (1)$$

Where I_0 is the fluorescence intensity of the chemosensor in the absence of the metal ion, I is the fluorescence intensity of the chemosensor in presence of the metal ion. K_{sv} is the static quenching constant, and $[Q]$ is the quencher concentration.¹⁸

A Stern-Volmer plot was constructed for **E2** in the presence of Fe^{2+} between 0 and 0.833 mM in methanol, as shown in **Figure 3.23**. The slope of the graph indicated that the mechanism of quenching is static quenching ($R^2 = 0.9926$) with a Stern-Volmer constant of 3695 M^{-1} .

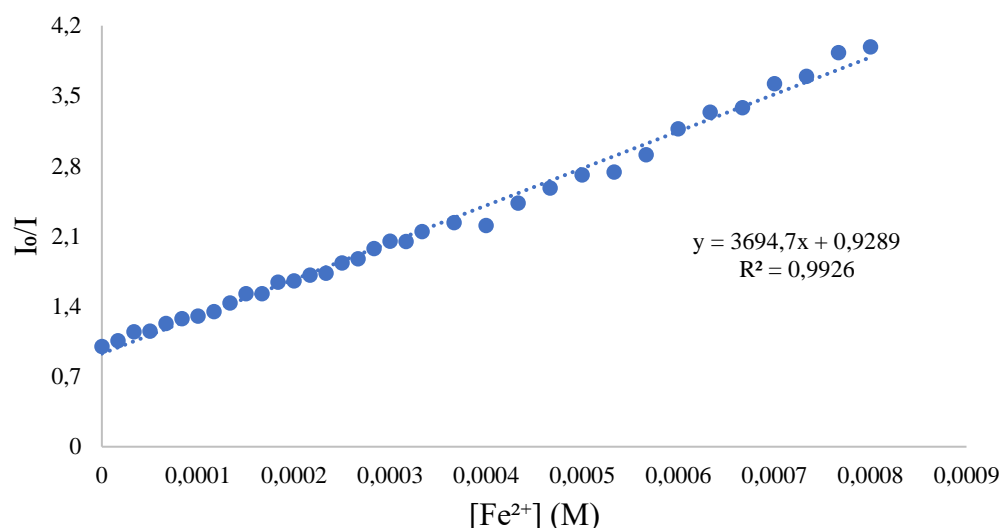


Figure 3.23: Stern-Volmer plot of $E2-Fe^{2+}$ in methanol.

Furthermore, the Stern-Volmer plot can also be used to determine the limit of detection (LOD) using equation 2:

$$LOD = \frac{3\sigma}{K_{sv}} \quad (2)$$

Where σ is the standard error and K_{sv} is the Stern-Volmer constant.^{21,24,25}

The LOD was calculated to be 0.0674 mM which falls between the LOD (0.024 mM) and LOQ (0.074 mM) calculated from the calibration curve.

3.5.4.3 Hill plot analysis of the $E2-Fe^{2+}$ complex

A Hill plot was constructed to gain further insight into the quenching mode. Additionally, it provides more information on the binding ratio, association constant and the cooperativity during the complexation.²⁶ The Stern-Volmer plot (**Figure 3.23**) indicated that a complex does form, resulting in static quenching. The Hill plot can further classify the cooperativity of binding. The Hill plot, which is also known as the double logarithmic plot, can be constructed by using the Hill equation (3):

$$\log\left(\frac{I}{I_0 - I}\right) = n \log[Q] - \log K_d \quad (3)$$

Where I is the fluorescence intensity of the chemosensor in the presence of the quencher, and I_0 is the fluorescence intensity of the chemosensor in the absence of the quencher. n is the Hill coefficient, Q is the concentration of the quencher, and K is the association constant.^{27,28}

The Hill coefficient, n , indicates the type of cooperativity between the chemosensor and the quencher. If $n > 1$, positive cooperativity is observed, in which the binding of the first metal increases the affinity for a second metal. The opposite is also true; if $n < 1$, negative cooperativity is observed, in which the binding of the first metal impedes the binding of a second metal. If $n = 1$, non-cooperativity is observed, meaning that the binding is entirely independent, and whether or not a metal is bonded does not influence the binding.^{29–31}

The Hill plot indicated that non-cooperation is most likely to occur during the complexation of **E2** with Fe^{2+} , as seen by $n = 1.01$ in **Figure 3.24**. In addition, n suggested that the binding ratio between **E2** and Fe^{2+} is 1:1, which supports the prediction made by the BH plot (**Figure 3.22**).^{28,32}

The association constant was calculated from the log of the intercept to be $4,47 \times 10^{-3} \text{ M}^{-2}$.

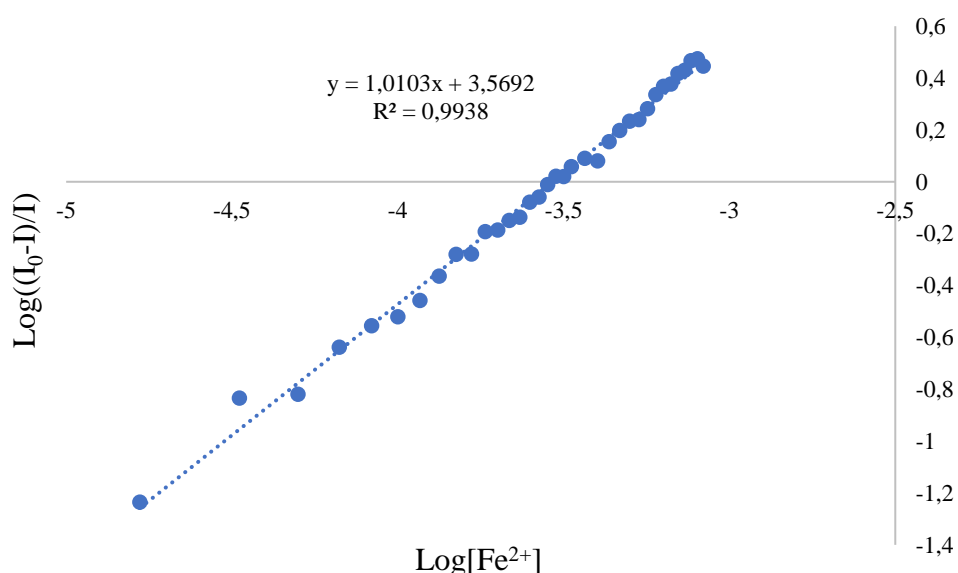


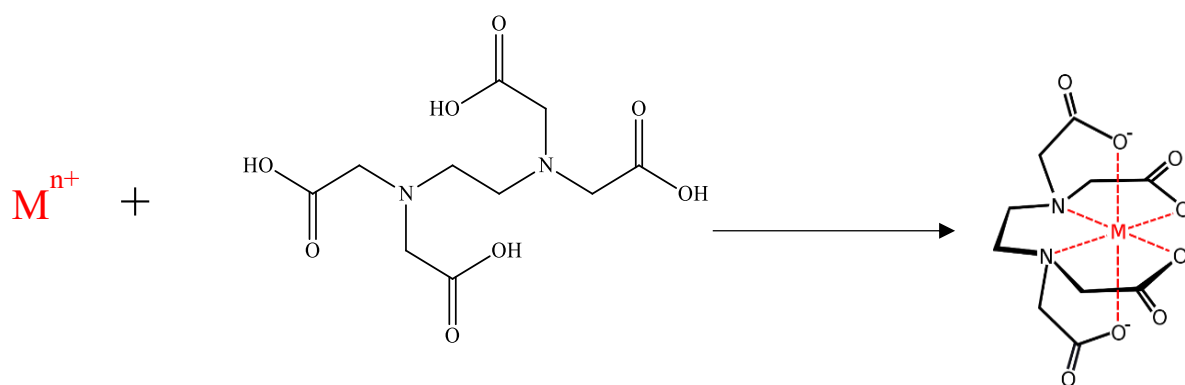
Figure 3.24: Hill plot of the fluorescence quenching response of **E2** towards Fe^{2+} in methanol.

3.5.5 Reversibility studies

It is well known that the reversibility of a chemosensor is an important and valuable property that improves the chemosensor's practicality, applicability and desirability.^{33,34} Reversible chemosensors can be recovered after use and reused, hence known as reusable chemosensors.³⁵ Reusable chemosensors are particularly useful in applications where frequent or continuous detection of analytes is necessary, such as environmental monitoring, food safety, and biomedical diagnostics. They are more cost-effective and environmentally friendly than single-use sensors, as they can be used multiple times before needing to be replaced. Hence reusable chemosensors can potentially reduce the cost and environmental impact of these compounds.

3.5.5.1 Using EDTA as a chelating agent

Ethylenediaminetetraacetic acid (EDTA) is a chelating agent that forms six coordinating bonds with metal cations as shown in **Scheme 3.6**, four from the oxygens and two from the nitrogens.³⁶ The chelated metal complex tends to be thermodynamically more stable and thus displaces monodentate ligands. The chelation is an entropy-favoured reaction and, thus, is spontaneous.³⁷ Other chelating agents such as diethylenetriamine pentaacetate (DTPA)³⁶ and nitrilotriacetic acid (NTA)³⁸ can also be used but were not available for this project.



Scheme 3.6: Complexation of EDTA with a metal cation.

The reversibility studies of the **E2**-Fe²⁺ were performed in methanol and shown in **Figure 3.25**. It was observed that the fluorescent intensity of **E2** (blue) was not fully regained after one equivalent EDTA (green) was added.

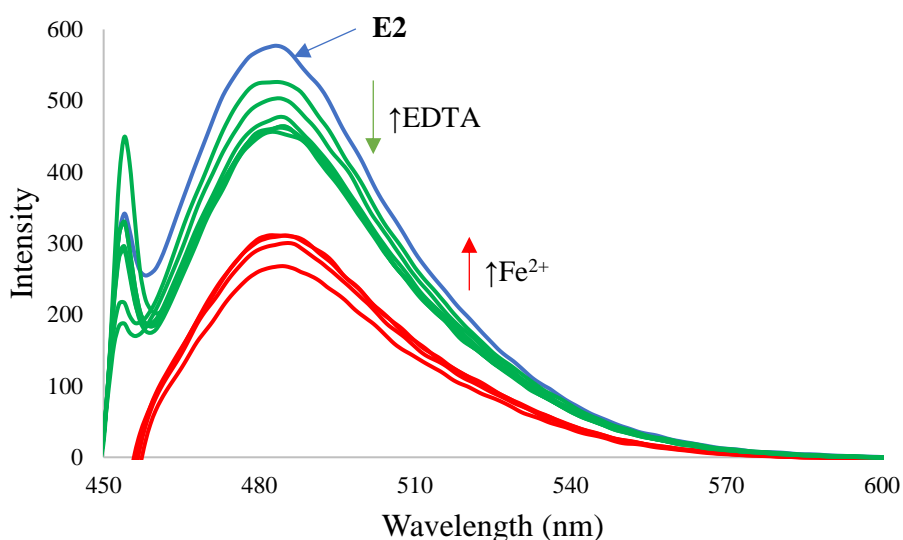


Figure 3.25: Reversibility study of the $E2-Fe^{2+}$ complex using EDTA.

Further investigation was done in which Fe^{2+} (red) was added again, followed by one equivalent EDTA (green). This resulted in various cycles of Fe^{2+} detection and EDTA reversibility. **Figure 3.26** shows that the sensitivity of **E2** towards Fe^{2+} and the reversibility effect of EDTA decrease after each cycle. Furthermore, EDTA was added in excess (1.75 equivalent), but the fluorescence was still not fully regained.

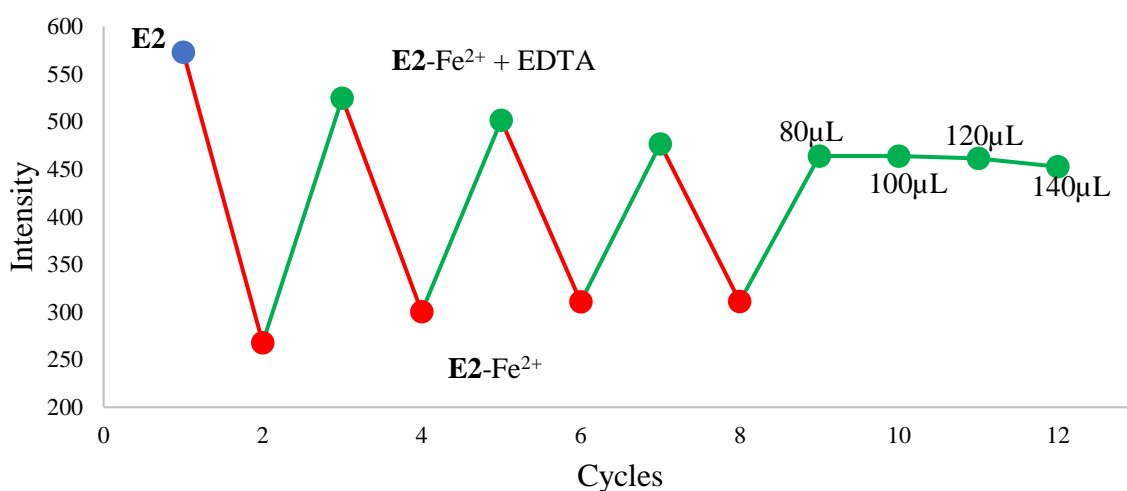


Figure 3.26: Recycling of **E2** fluorescence intensity using EDTA.

3.5.5.2 Using H_2O_2 as the oxidising agent

Iron's two most important oxidation states are +II and +III. Iron(II) exists in a d^6 low-spin electronic configuration, whereas iron(III) exists in a d^5 high-spin configuration. In the

presence of oxygen, iron(II) species can easily be oxidised to iron(III).^{3,39,40} Hydrogen peroxide (H_2O_2) was used by W. Zeng et al., 2014 to oxidise Cu(I) to Cu(II) in order to regain the fluorescence intensity of their chemosensor. H_2O_2 was able to restore the fluorescence intensity of their chemosensor successfully.⁴¹

Following their idea, H_2O_2 was used as an oxidising agent to determine if it could be used to regain the fluorescent intensity of **E2** from the quenched complex. **Figure 3.27** shows the titration of H_2O_2 in methanol. After the first equivalence of H_2O_2 was added, the fluorescence intensity increased until the intensity plateaued at five equivalencies.

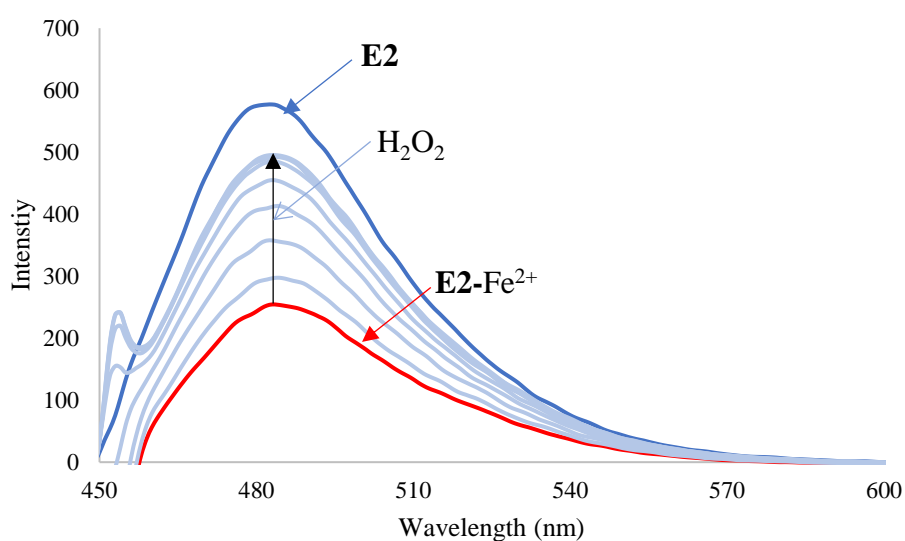


Figure 3.27: Reversibility study of **E2** using H_2O_2 .

As mentioned earlier, the H_2O_2 is used to oxidise the Fe^{2+} to Fe^{3+} , which in turn changes the **E2-Fe²⁺** complex to the **E2-Fe³⁺** complex. To confirm this hypothesis, the **E2-Fe³⁺** complex was compared to that of the oxidised complex. **Figure 3.28** illustrate that the fluorescence spectrum of the oxidised **E2-Fe²⁺** (light blue) is equivalent to that of the **E2-Fe³⁺** fluorescence spectrum. Thus, indicating that all of the Fe^{2+} ions in the solution were oxidised to Fe^{3+} , which the **E2** chemosensor could accurately detect to form a new complex **E2-Fe³⁺** resulting to enhancement of fluorescence.

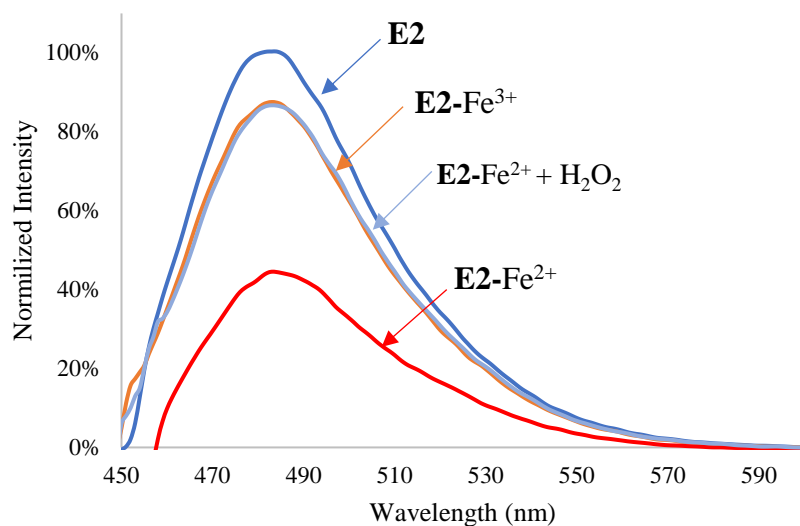


Figure 3.28: Comparison of intensity between $E2-Fe^{2+}$ and $E2-Fe^{3+}$.

3.5.6 Job's plot of $E2$ and Fe^{2+}

As stated in **Chapter 2, Section 2.4.3.3**, the Job's plot plays a significant role in determining the binding ratio between the analyte and chemosensor. The Jobs plot for $E2$ and Fe^{2+} was constructed in methanol using the UV-vis Spectrometer.

The binding ratio was determined to be 1:1 ($E2:Fe^{2+}$) according to the Job's plot in **Figure 3.29**. The binding mode was also supported by the Benesi-Hildebrand plot (**Figure 3.22**) and the Hill plot (**Figure 3.24**).

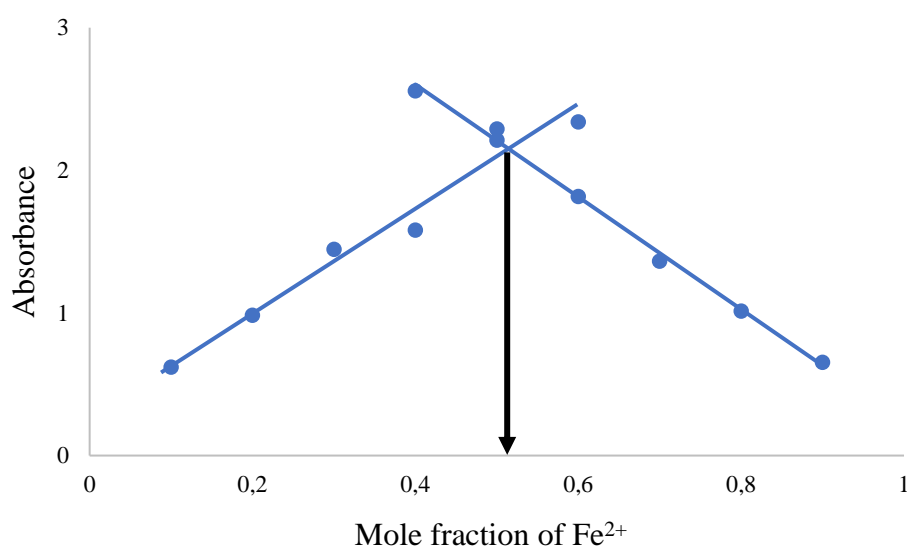


Figure 3.29: Job's plot of $E2$ and Fe^{2+} in Methanol. The absorbance was measured at 440 nm.

3.5.6.1 The proposed binding site and computational studies $\mathbf{E2-Fe^{2+}}$ complex

As observed and known from the literature, transition metals such as Fe^{2+} can form stable complexes with organic compounds.^{17,42–44} Further investigation into the $\mathbf{E2-Fe^{2+}}$ complex was conducted using NMR and Molecular Modelling.

The 2D HSQC (Heteronuclear Single Quantum Coherence) NMR experiment was conducted on chemosensor **E2**, shown in **Figure 3.30**. HSQC experiments are used to determine the proton-carbon bond connections, however, tertiary carbons, such as carbonyls, are not shown. Moreover, other carbons such as the double bond in the enone linker, were identified as shown in grey (120.9 ppm and 128 ppm) in **Figure 3.30**. The identity of the carbons, shown in **Figure 3.30**, was used to postulate the binding site between **E2** and Fe^{2+} .

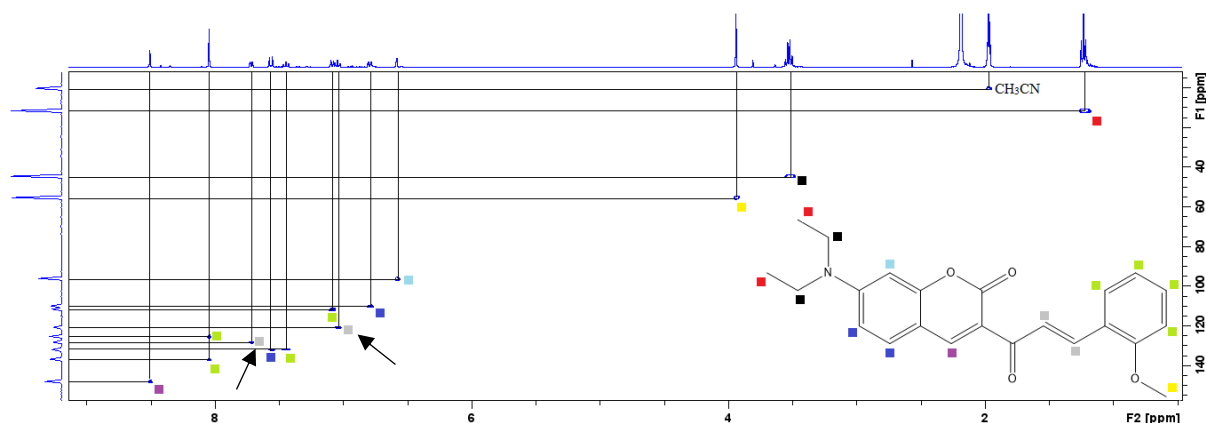


Figure 3.30: HSQC NMR of **E2** in deuterated acetonitrile.

The ^{13}C NMR spectrum of **E2** (blue spectrum in **Figure 3.31**) was compared to the ^{13}C NMR spectrum of the $\mathbf{E2-Fe^{2+}}$ complex (red spectrum in **Figure 3.31**). It was observed that peaks disappeared in the presence of the Fe dication. These carbon peaks were assigned to the enone carbonyl carbon (pink, 187.20 ppm), the carbonyl in the lactone ring (pink, 161.12 ppm) the -CH carbon in the lactone ring (purple, 148.71 ppm) and two -CH carbons in the anisole moiety (green, 137.58 ppm and 126.09 ppm). The missing peaks confirmed the involvement of these peaks during the complexation between Fe^{2+} and the chemosensor **E2**. The literature shows that the lactone ring carbonyl oxygen is known to complex with iron.^{44,45} As mentioned previously, the enone carbonyl oxygen is also a possible site with which a metal cation can interact. This binding site between the two carbonyl oxygens, which forms a stable six-membered ring, can draw from the lactone -CH carbon which can explain the reduction in the peak intensity at 148.71 ppm for the $\mathbf{E2-Fe^{2+}}$ complex. Furthermore, the anisole moiety also

interacts with the complex, which can be explained by molecular modelling in **Figure 3.33**, by which the solvent ligands hydrogen bonds with the ether oxygen.

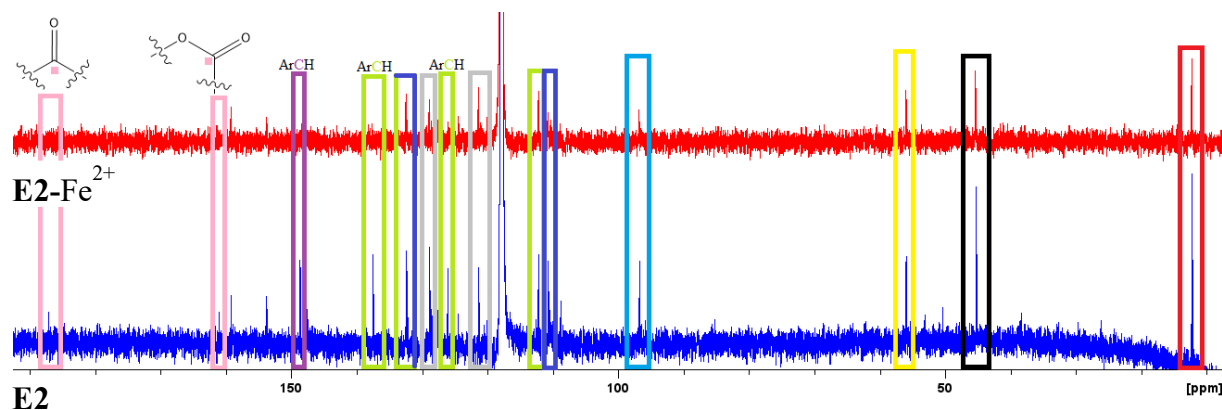


Figure 3.31: ^{13}C NMR of **E2** (blue) and the **E2-Fe²⁺** complex (red) identifying complexing carbons in deuterated acetonitrile.

The fluorescent studies indicated that the *o*-anisaldehyde in **E6** does not interact with the iron complex. This was tested using the ^{13}C NMR spectra of the **E6** (blue spectrum), **o-A** (red spectrum) and **E6-Fe²⁺** complex (green spectrum), shown in **Figure 3.32**. As indicated by the box insertions, the **o-A** carbon peaks are not affected during the formation of the complex. Hence **o-A** is not involved in the complexation process.

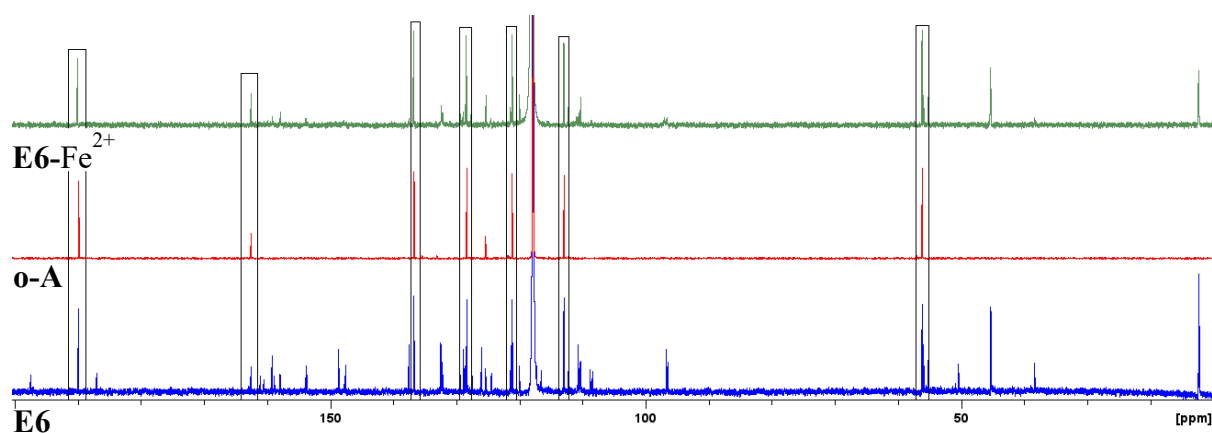


Figure 3.32: ^{13}C NMR of **E6** (blue), **o-A** (red) and **E6-Fe²⁺** complex (green) in deuterated acetonitrile.

According to literature, iron(II) can form four-, five-, six- and eight-coordination complexes, with the octahedral geometry (coordination number of six) being the most common.^{39,46} These coordination numbers were used to determine the most stable complex. Calculations were done in the presence of water and acetonitrile. These results are stipulated in **Table 3.2**.

Table 3.2: Energy profiles of $E2-Fe^{2+}$ complex in various coordination complexes obtained using Spartan.

Coordination number	H ₂ O (kJ/mol)	Geometry in H ₂ O	CH ₃ CN (kJ/mol)	Geometry in CH ₃ CN
Four	1153.90	Tetrahedral	438.96	Tetrahedral
Five	806.52	Square pyramid	128.23	Square pyramid
Six	-1028.50	Octahedral	-845.00	Trigonal prismatic
Eight	n/a	n/a	n/a	n/a

The two four-coordinated complexes were observed with a tetrahedral geometry, with acetonitrile (**Figure S 3.10**) being more stable than water (**Figure S 3.9**). The five-coordinated complexes resemble a square pyramidal geometry (**Figure S 3.11** and **Figure S 3.12**), and the six-coordinated complexes showed a significant drop in the complex energy. The complex containing water was the most stable, with an energy of -1028.50 kJ/mol. In addition, the two complexes (**Figure 3.33** and **Figure 3.34**) displayed different geometries, with the water complex having the preferred octahedral geometry, **Figure 3.33**. Lastly, during computational studies, the eight-coordination complexes (**Figure S 3.13** and **Figure S 3.14**) did not form for both water and acetonitrile. Hence it is unlikely that they readily formed.

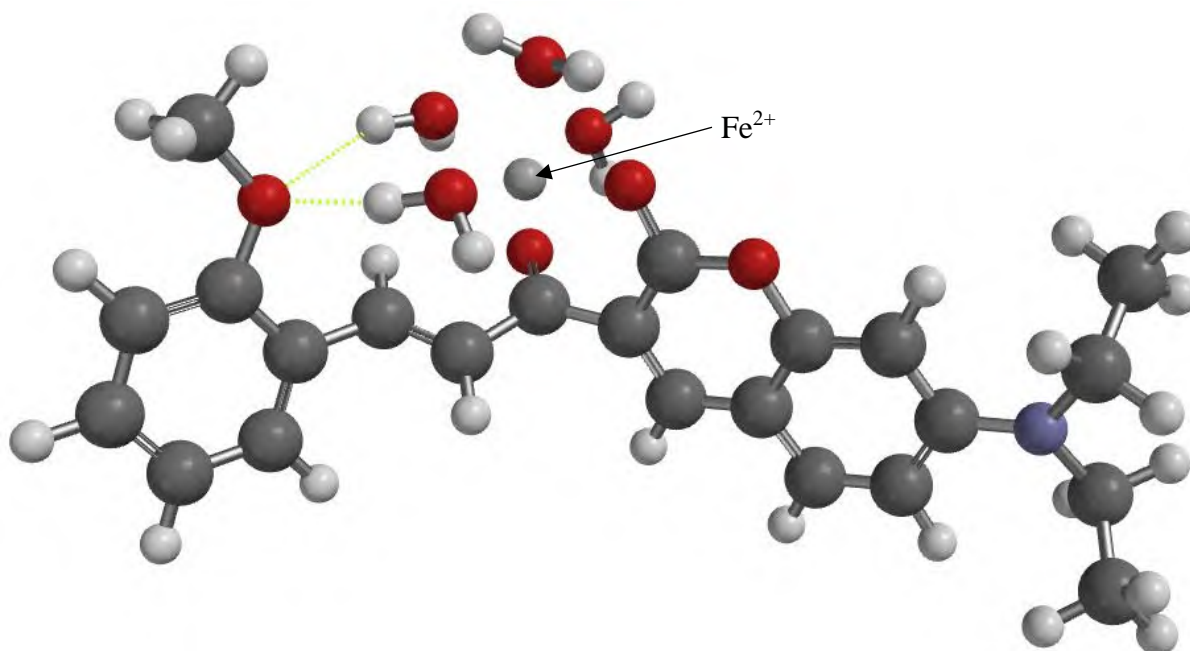


Figure 3.33: Octahedral $E2-Fe^{2+}$ complex with H₂O.

Figure 3.33 illustrates the binding between the Fe^{2+} ion and the chemosensor **E2** in water. As supported by the ^{13}C NMR (**Figure 3.31**), the two carbonyl oxygens are the primary binding site for the Fe^{2+} ion, and the ether oxygen stabilises the complex through hydrogen bonding (yellow dotted lines in **Figure 3.33**) with the solvent ligands.

In contrast, **Figure 3.34** illustrates the trigonal prismatic binding between the Fe^{2+} and the chemosensor **E2** in the presence of acetonitrile. As with the previous complex, the two carbonyl oxygens are the binding site between the iron cation and **E2**.

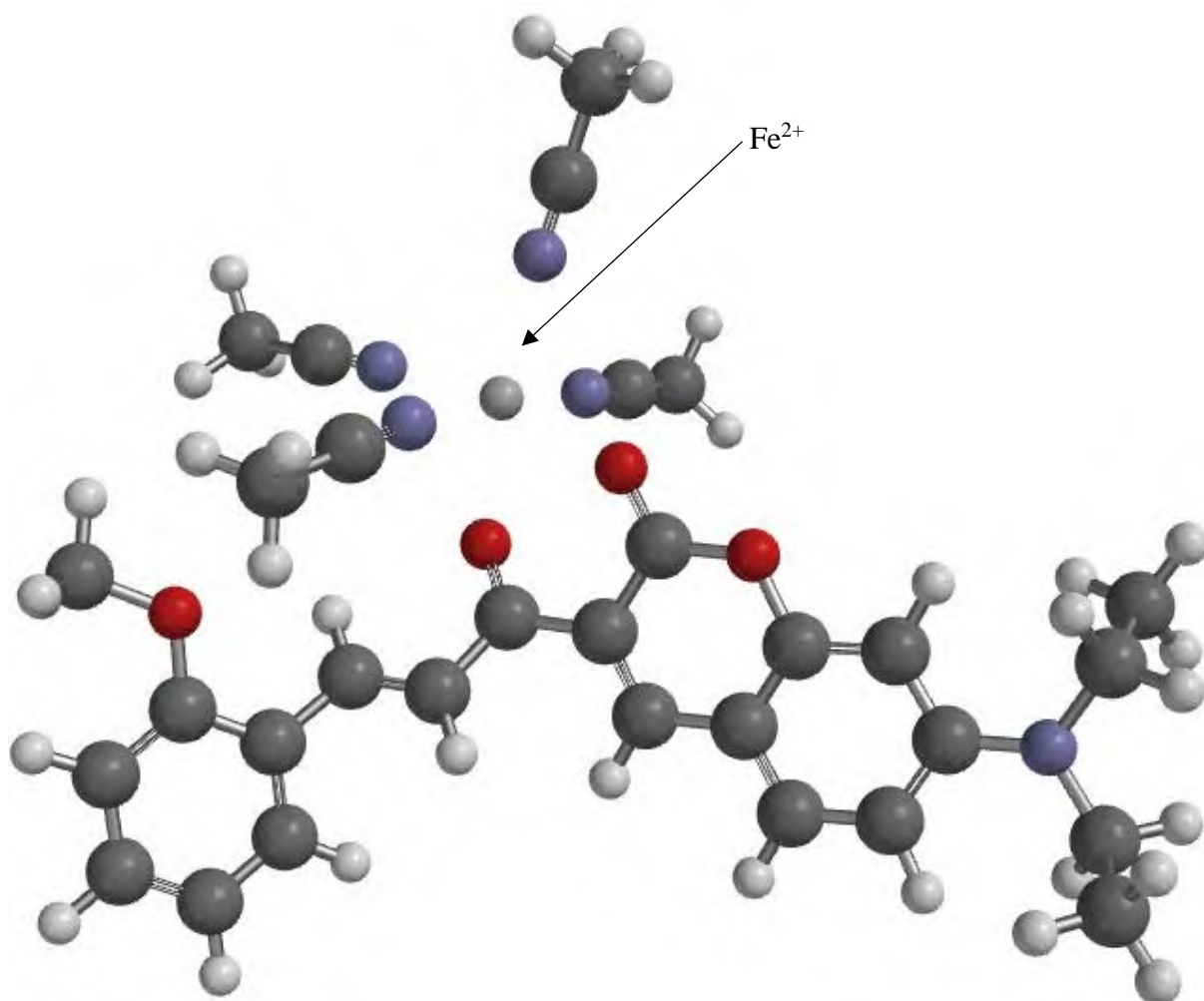


Figure 3.34: Trigonal prismatic E2-Fe^{2+} complex with CH_3CN .

3.5.7 Emission study of the mixed ligand chemosensor **E6**

Although, chemosensor, **E6** showed no selectivity towards metal cations, it is of interest to investigate the effect of **o-A** (non-fluorescent) in the emission properties of **E6**. This was done by comparing the emission spectra of **E2** and **E6** in acetonitrile and methanol, as shown in

Figure 3.35. In acetonitrile (blue), the emission spectra of **E2** (solid blue line) were significantly quenched in the presence of **o-A**. Whereas in methanol (red), the opposite was observed; the **o-A** enhanced the emissions of **E2**. Furthermore, the emissions band of **E6** has broadened compared to **E2** in the same solvent (methanol). From these observations, it was concluded that the **o-A** ligand does indeed affect emission properties of **E2** in both solvent systems. Thus, the **o-A** ligand interferes with the emissions of **E2** and would not be suitable for further investigation.

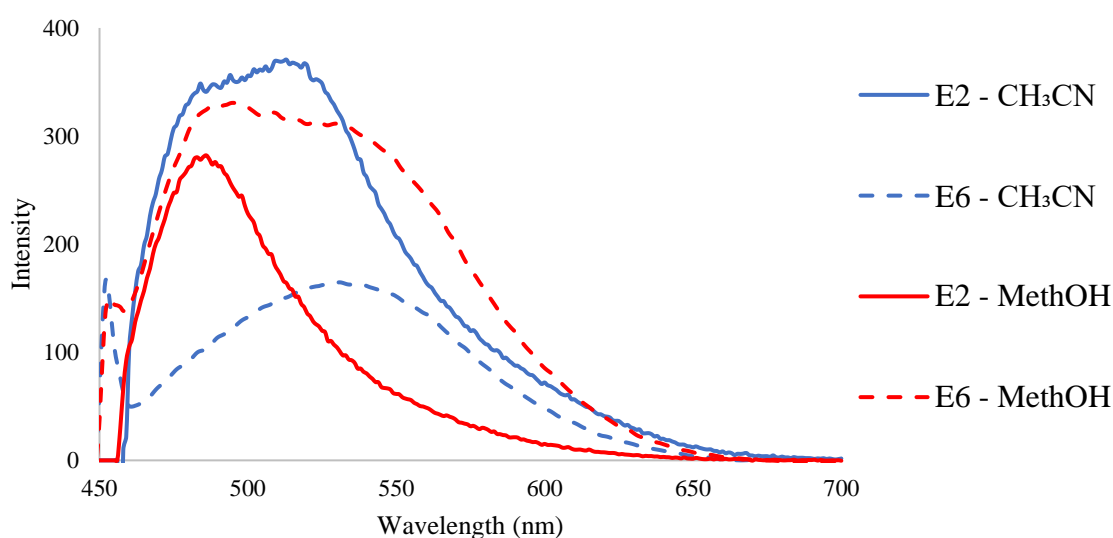


Figure 3.35: Emissions spectra of **E2** (blue) and **E6** (red) in acetonitrile (solid line) and methanol (dotted line) with a concentration of $0.409 \mu\text{M}$. $\lambda_{\text{excitation}} = 440 \text{ nm}$.

3.5.8 **E2** screening of anions

Anion selectivity studies were done only on **E2**. The analysis was performed in acetonitrile and methanol, as shown in **Figure 3.36**. In acetonitrile (**Figure 3.36 a**), the fluorescence of **E2** in combination with each anion resulted in a reduced intensity. In contrast, in methanol (**Figure 3.36 b**), the fluorescence of **E2** in the presence of the anions resulted in enhanced fluorescence. This fluorescence change can result from the solvent's polarity and availability of a labile proton.⁴⁷ The solvent polarity can influence the conformation and the rigidity of the local environment. Photophysical properties such as changes in radiative and non-radiative decay rates, presence or absence of internal charge transfer and proton transfer and excited state reactions can also be affected by the solvent.⁴⁸ In a study done by Hishimone et al., 2021, it was concluded that “the solvent effect does play a major role in the recognition of ionic

species” and that the solvent effect inhibited their chemosensors’ ability to sense the various anions they tested.

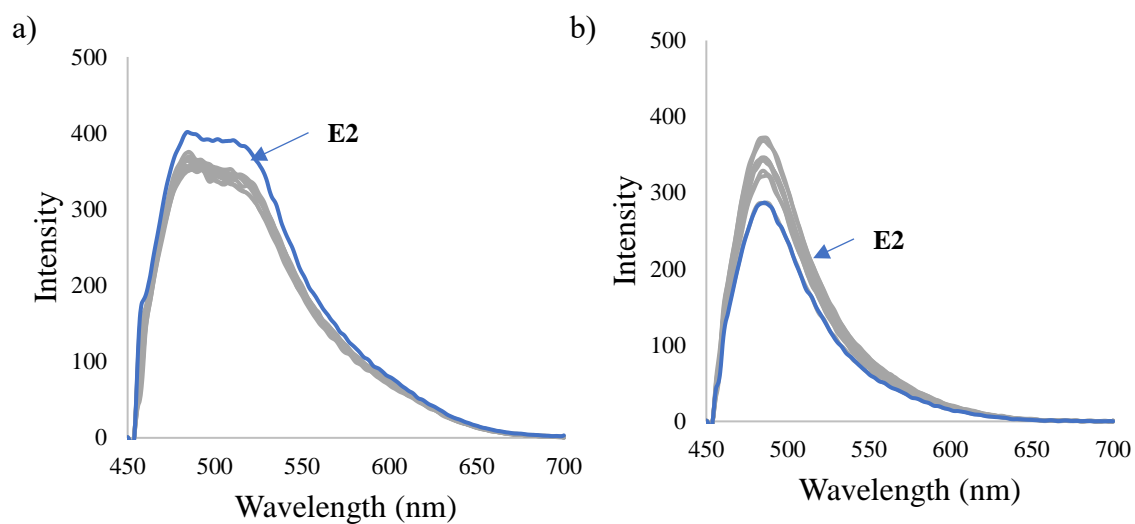


Figure 3.36: Screening of various anions (0.167 mM) for E2 (0.409 μM) in a) acetonitrile and b) methanol. $\lambda_{\text{excitation}} = 440 \text{ nm}$.

3.6 Conclusion

In this chapter, one chemosensor containing an anisole moiety connected via an enone linker to the coumarin backbone was synthesised. This chemosensor 7-(diethylamino)-3-(3-(2-methoxyphenyl)acryloyl)-2H-chromen-2-one, **E2**, was compared to the mixed ligand **E6** chemosensor, which contained the **E2** chemosensor with o-anisaldehyde, **o-A**, as a supporting ligand. **E2** was successfully synthesised and characterised using NMR, FT-IR and single X-ray crystallography. XRD analysis confirmed that **E2** exist as the E-conformer.

Absorption studies of **E2** and **E6** showed that **o-A** does not interact or change the absorbance of **E2**, but during screening, **E6** performed slightly better than **E2**, showing less interaction with other metal cations. However, neither **E2** nor **E6** presented immediate identifiable changes in the presence of the cations tested. A timed study was performed in which it was observed that both **E2** and **E6** had a delayed colourimetric response to iron. In acetonitrile, **E2** and **E6** changed from a yellow to a green solution with Fe^{2+} and Fe^{3+} . In methanol, **E2** and **E6** turned into a red/orange solution in the presence of Fe^{2+} and an orange/yellow solution with Fe^{3+} .

The emission studies of **E2** and **E6** showed that the **o-A** in **E6** quenched the fluorescence of **E2**. Hence, **o-A** is not a suitable cooperative ligand, with the ^{13}C NMR also showing that **o-A** does not participate in the complexation. Further emission studies into **E2** were conducted. It is suggested that **E2** is a PET “on-off” type mechanism to detect Fe^{2+} in methanol selectively. Competition studies showed that **E2** was highly selective for Fe^{2+} , even in the presence of other competing metal cations. LOD and LOQ were determined to be 0.024 mM and 0.074 mM, respectively, with a saturation point of 0.183 mM. This range barely overlaps with the estimated minimum daily requirement of iron is 0.179 mM – 0.895 mM.¹⁶ The binding coefficient was determined, using the Benesi-Hildebrand plot, to be $3.873 \times 10^3 \text{ M}^{-1}$. The Stern-Volmer plot indicated that static quenching was observed, supporting the formation of a complex. Stern-Volmer constant was calculated to be 3695 M^{-1} . The Hill plot showed that non-cooperation was observed with a 1:1 binding ratio, supported by the Job’s plot. Reversibility studies concluded that the **E2**- Fe^{2+} complex was partially reversible using EDTA with a decreased sensitivity towards iron(II) after each cycle. H_2O_2 was used to oxidise Fe^{2+} to Fe^{3+} , which was successfully tracked by **E2** regaining its fluorescent properties, to which **E2** detected the resulting Fe^{3+} present.

Lastly, **E2** was tested as an anion chemosensor. Both absorbance and emissions studies indicated that **E2** could not be used as an anion chemosensor.

3.7 Experimental

3.7.1 General information

All starting materials and solvents were purchased from Sigma Aldrich or Merck and used as received without further purification unless otherwise stated.

^1H NMR and ^{13}C NMR spectra were recorded on a Bruker Advance DPX 400 (400 MHz) spectrometer. The NMR samples were prepared in deuterated solvents (CDCl_3 , DMSO-d_6 , and Acetonitrile- d_3). The samples were run at room temperature. Chemical shifts are expressed in parts per million (ppm) using trimethyl silane (TMS) as the internal reference.

Infrared FT-IR spectra were recorded on a Bruker TENSOR 27 FT-IR spectrometer.

Thin layer chromatography (TLC) analyses were performed on pre-coated silica gel 60 F254 aluminium sheets (0.063-0.2 mm/70 - 230 mesh) using a 50:50% solution of ethyl acetate: hexane; compounds were detected by observation under UV light or exposure to iodine vapour.

Stock solutions of the chemosensors (0.05 M) were prepared by dissolving the samples in acetonitrile and diluting them to the desired concentrations, 10% CHCl_3 was added to **E1**, and 10% DMSO was added to **E2** due to the solubility constraints. Metal cations (0.05 M) solutions were prepared using the nitrate salts (except for Fe^{2+} , which used the sulphate salt) and dissolved in Millipore water. The anion (0.05 M) solutions were prepared using the tetrabutylammonium salts and dissolved in Millipore water.

UV-Vis absorbance studies were recorded on a Thermo Scientific™ Evolution 201 UV-Vis spectrophotometers and the fluorescent emissions studies were conducted on a PerkinElmer LS 45 Fluorescence Spectrometer using a 1 cm quartz cuvette (3 mL). Spectroscopic measurements were performed after each aliquot of selected cationic and anionic solutions.

Spartan Student Version 8.0.6, Oct 8 2020, Computational chemistry was utilised to compare and visually illustrate different free chemosensors and complexes conformers. The conformers were obtained by conformer distribution at the MMFF level. Calculations of the most energetically preferred conformation were determined by equilibrium geometry at the PM3 level.

The detection limit (LOD) and quantification (LOQ) were calculated according to the equation:

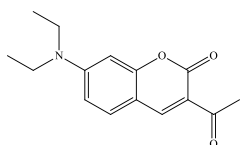
$$LOD = 3.3 \times \frac{\sigma}{m}$$

$$LOQ = 10 \times \frac{\sigma}{m}$$

Where σ is the standard deviation and m is the slope of the trend line.

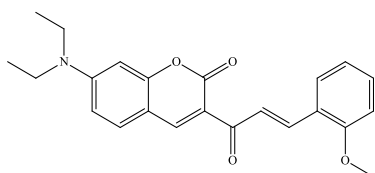
3.7.2 Synthesis of compounds

3.7.2.1 3-acetyl-7-(diethylamino)-2H-chromen-2-one – E1



It was synthesised according to known literature procedure.⁸ IR ν_{\max} (cm^{-1}): 3114-2972 (C-H stretching, Alkene), 1704 (C=O stretching, Lactone ring), 1679 (C=O, Ketone). ^1H NMR (CDCl_3): δ_{H} /ppm = 8.45 (1H, s, Aromatic H), 7.42-7.40 (1H, d, Aromatic H), 6.65-6.62 (1H, m, Aromatic H), 6.49 (1H, s, Aromatic H), 3.50-3.45 (4H, q, $-\text{CH}_2$), 2.70 (3H, s, $-\text{CH}_3$), 1.28-1.24 (6H, t, $-\text{CH}_3$). ^{13}C NMR (CDCl_3) δ_{C} /ppm = 195.74, 160.88, 158.77, 153.03, 147.86, 131.90, 116.13, 109.85, 108.18, 96.60, 45.15, 30.58, 12.44.

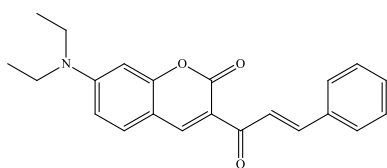
3.7.2.2 E-7-(diethylamino)-3-(3-(2-methoxyphenyl)acryloyl)-2H-chromen-2-one – E2



3-acetyl-7-(diethylamino)-2H-chromen-2-one, **E1**, (1.01 g, 3.90 mmol) and o-anisaldehyde (0.84 g, 6.17 mmol) was reflux with a few drops of piperidine for 24 hours in absolute ethanol. After the time had elapsed, the mixture was poured into the ice-cold water resulting in a fine precipitate forming. The product was filtered and recrystallised from ethanol.⁷ **Yield: 27.2%**. IR ν_{\max} (cm^{-1}): 3090-2973 (C-H stretching, Alkene), 1704 (C=O stretching, Lactone ring),

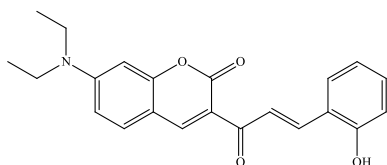
1647 (C=O, Enone). ^1H NMR (CDCl_3): $\delta_{\text{H}}/\text{ppm}$ = 8.58 (1H, s, Aromatic H), 8.21 (2H, s, Aromatic H), 7.77-7.75 (1H, d, CH=CH, J = 7.69 Hz), 7.47-7.45 (1H, s, Aromatic H), 7.39-7.35 (1H, t, Aromatic H), 7.02-6.98 (1H, t, Aromatic H), 6.95-6.93 (1H, d, CH=CH, J = 7.69 Hz), 6.68-6.66 (1H, d, Aromatic H), 6.53 (1H, s, Aromatic H), 3.94 (3H, s, -CH₃), 3.50-3.47 (4H, q, -CH₂), 1.29-1.26 (6H, t, -CH₃). ^{13}C NMR (CDCl_3) $\delta_{\text{C}}/\text{ppm}$ = 186.92, 158.83, 158.61, 152.73, 148.51, 138.61, 131.70, 131.48, 129.10, 125.28, 124.49, 120.68, 117.37, 111.10, 109.87, 108.79, 96.84, 55.53, 45.24, 12.46.

3.7.2.3 3-cinnamoyl-7-(diethylamino)-2H-chromen-2-one – **E3**



3-acetyl-7-(diethylamino)-2H-chromen-2-one, **E1**, (1.01 g, 3.90 mmol) and benzaldehyde (0.92 g, 8.67 mmol) was reflux with a few drops of piperidine for 24 hours in absolute ethanol.⁷ As seen in **Figure S 3.5**, the ketone peak is present at 2.68 ppm, and no characteristic double bond peaks for the enone functional group are seen; hence the reaction was unsuccessful.

3.7.2.4 7-(diethylamino)-3-(3-(2-hydroxyphenyl)acryloyl)-2H-chromen-2-one – **E4**



3-acetyl-7-(diethylamino)-2H-chromen-2-one, **E1**, (1.02 g, 3.93 mmol) and salicylaldehyde (0.92 g, 7.53 mmol) was reflux with a few drops of piperidine for 24 hours in absolute ethanol.⁷ As seen in **Figure S 3.6**, the ketone peak is present at 2.71 ppm, which should have disappeared if the reaction was successful; hence the reaction was unsuccessful.

References

- (1) Zeiri, O. Metallic-Nanoparticle-Based Sensing: Utilisation of Mixed-Ligand Monolayers. *ACS Sensors* **2020**, *5* (12), 3806–3820. <https://doi.org/10.1021/acssensors.0c02124>.
- (2) Alsaee, S. K.; Abu Bakar, M. A.; Zainuri, D. A.; Anizaim, A. H.; Zaini, M. F.; Rosli, M. M.; Abdullah, M.; Arshad, S.; Abdul Razak, I. Nonlinear Optical Properties of Pyrene-Based Chalcone: (E)-1-(4'-Bromo-[1,1'-Biphenyl]-4-Yl)-3-(Pyren-1-Yl)Prop-2-En-1-One, a Structure-Activity Study. *Opt. Mater. (Amst)*. **2022**, *128*, 112314. <https://doi.org/10.1016/j.optmat.2022.112314>.
- (3) Rawn, J. D.; Ouellette, R. J. *Organic Chemistry : Structure, Mechanism, Synthesis*, 2nd ed.; Elsevier Inc.: London, 2018.
- (4) McMurry, J. E. *Organic Chemistry*., 9th ed.; Cengage Learning: Boston, 2015.
- (5) Patel, K. S.; Patel, J. C.; Dholariya, H. R.; Patel, K. D. Multiple Heating Rate Kinetic Parameters, Thermal, X-Ray Diffraction Studies of Newly Synthesised Octahedral Copper Complexes Based on Bromo-Coumarins along with Their Antioxidant, Anti-Tubercular and Antimicrobial Activity Evaluation. *Spectrochim. Acta - Part A Mol. Biomol. Spectrosc.* **2012**, *96*, 468–479. <https://doi.org/10.1016/j.saa.2012.05.057>.
- (6) Şahin, Z. S.; Demir, M.; Yıldırım, T.; Yurdakul, Ö.; Köse, D. A. Novel Mixed Ligand Complexes of Co(II), Ni(II), Cu(II), and Zn(II) with 1,10-Phenanthroline and Acesulfame. Synthesis, Structural Analysis and Hydrogen Adsorption Study. *Int. J. Hydrogen Energy* **2021**, *46* (54), 27631–27642. <https://doi.org/10.1016/j.ijhydene.2021.06.026>.
- (7) Yeap, G. Y.; Hrishikesan, E.; Chan, Y. H.; Mahmood, W. A. K. A New Emissive Chalcone-Based Chemosensor Armed by Coumarin and Naphthol with Fluorescence “Turn-on” Properties for Selective Detection of F[−] Ions. *J. Fluoresc.* **2017**, *27* (1), 105–110. <https://doi.org/10.1007/s10895-016-1938-5>.
- (8) Evans, Vikki, Duncanson, Philip, Motevalli, Majid, Watkinson, M.; Evans, V.; Duncanson, P.; Motevalli, M.; Watkinson, M. An Investigation into the Synthesis of Azido-Functionalised Coumarins for Application in 1,3-Dipolar “Click” Cycloaddition Reactions. *Dye. Pigment.* **2016**, *135* (5), 36–40. <https://doi.org/10.1016/j.dyepig.2016.06.028>.
- (9) Kireev, S. V.; Shnyrev, S. L. Study of Molecular Iodine, Iodate Ions, Iodide Ions, and Triiodide Ions Solutions Absorption in the UV and Visible Light Spectral Bands. *Laser Phys.* **2015**, *25* (7), 75602. <https://doi.org/10.1088/1054-660X/25/7/075602>.
- (10) Raicu, V. Ab Initio Derivation of the FRET Equations Resolves Old Puzzles and Suggests Measurement Strategies. *Biophys. J.* **2019**, *116* (7), 1313–1327. <https://doi.org/10.1016/j.bpj.2019.02.016>.
- (11) Xu, D.; Jia, H.; Niu, Y.; Yin, S. Fluorine-Boron Compound-Based Fluorescent Chemosensors for Heavy Metal Ion Detection. *Dye. Pigment.* **2022**, *200* (February),

110185. <https://doi.org/10.1016/j.dyepig.2022.110185>.
- (12) Wu, L.; Huang, C.; Emery, B. P.; Sedgwick, A. C.; Bull, S. D.; He, X.-P. P.; Tian, H.; Yoon, J.; Sessler, J. L.; James, T. D. Förster Resonance Energy Transfer (FRET)-Based Small-Molecule Sensors and Imaging Agents. *Chem. Soc. Rev.* **2020**, *49* (15), 5110–5139. <https://doi.org/10.1039/C9CS00318E>.
 - (13) Marie, J.; Ngororabanga. Synthesis and Investigation of the Chemosensing Properties of Novel Fluorescent Triazolyl Coumarin-Based Polymers, Nelson Mandela Metropolitan, 2017.
 - (14) Ooyama, Y.; Sumomogi, M.; Nagano, T.; Kushimoto, K.; Komaguchi, K.; Imae, I.; Harima, Y. Detection of Water in Organic Solvents by Photo-Induced Electron Transfer Method. *Org. Biomol. Chem.* **2011**, *9* (5), 1314–1316. <https://doi.org/10.1039/C0OB00933D>.
 - (15) Lakowicz, J. R. Mechanisms and Dynamics of Fluorescence Quenching. In *Principles of Fluorescence Spectroscopy*; Springer US: Boston, MA, 2006; pp 331–351. https://doi.org/10.1007/978-0-387-46312-4_9.
 - (16) World Health Organization. Guidelines for Drinking-Water Quality, 4th Edition, Incorporating the 1st Addendum. **2017**.
 - (17) Pandey, G.; Tharmavaram, M.; Phadke, G.; Rawtani, D.; Ranjan, M.; Sooraj, K. P. Silanized Halloysite Nanotubes as ‘Nano-Platform’ for the Complexation and Removal of Fe (II) and Fe (III) Ions from Aqueous Environment. *Sep. Purif. Technol.* **2022**, *293*, 121141. <https://doi.org/10.1016/j.seppur.2022.121141>.
 - (18) Fateh, F.; Yildirim, A.; Bhatti, A. A.; Yilmaz, M. A New Benzothiazin-Functionalized Calix[4]Arene-Based Fluorescent Chemosensor for the Selective Detection of Co²⁺ Ion. *J. Fluoresc.* **2021**, *31* (4), 1075–1083. <https://doi.org/10.1007/s10895-021-02745-w>.
 - (19) Roy, D.; Chakraborty, A.; Ghosh, R. Perimidine Based Selective Colorimetric and Fluorescent Turn-off Chemosensor of Aqueous Cu²⁺: Studies on Its Antioxidant Property along with Its Interaction with Calf Thymus-DNA. *RSC Adv.* **2017**, *7* (64), 40563–40570. <https://doi.org/10.1039/c7ra06687b>.
 - (20) Goswami, S.; Aich, K.; Das, A. K.; Manna, A.; Das, S.; Manuscript, A. A Naphthalimide–Quinoline Based Probe for Selective, Fluorescence Ratiometric Sensing of Trivalent Ions. *RSC Adv.* **2013**, *3* (7), 2412. <https://doi.org/10.1039/c2ra22624c>.
 - (21) Singh, M.; Kumar, G.; Neogi, S. Devising Mixed-Ligand Based Robust Cd(II)-Framework From Bi-Functional Ligand for Fast Responsive Luminescent Detection of Fe³⁺ and Cr(VI) Oxo-Anions in Water With High Selectivity and Recyclability. *Front. Chem.* **2021**, *9* (May), 1–12. <https://doi.org/10.3389/fchem.2021.651866>.
 - (22) Arulraj, A. D.; Devasenathipathy, R.; Chen, S. M.; Vasantha, V. S.; Wang, S. F. Highly Selective and Sensitive Fluorescent Chemosensor for Femtomolar Detection of Silver Ion in Aqueous Medium. *Sens. Bio-Sensing Res.* **2015**, *6*, 19–24. <https://doi.org/10.1016/j.sbsr.2015.10.004>.

- (23) Lakowicz, J. R. *Principles of Fluorescence Spectroscopy*; Springer US: Boston, MA, 1983. <https://doi.org/10.1007/978-1-4615-7658-7>.
- (24) Wang, Y. N.; Wang, S. D.; Fan, Y.; Yu, L.; Zha, R. H.; Liu, L. J.; Wen, L. M.; Chang, X. P.; Liu, H. Q.; Zou, G. D. A Dual-Chemosensor Based on Ni-CP: Fluorescence Turn-on Sensing toward Ascorbic Acid and Turn-off Sensing toward Acetylacetone. *J. Lumin.* **2022**, *243* (October 2021). <https://doi.org/10.1016/j.jlumin.2021.118680>.
- (25) Hall, R. D.; Chignell, C. F. Steady-State Near-Infrared Detection of Singlet Molecular Oxygen: A Stern-Volmer Quenching Experiment With Sodium Azide. *Photochem. Photobiol.* **1987**, *45* (4), 459–464. <https://doi.org/10.1111/J.1751-1097.1987.TB05403.X>.
- (26) Ngororabanga, J. M. V.; Tshentu, Z. R.; Mama, N. A New Highly Selective Colorimetric and Fluorometric Coumarin-Based Chemosensor for Hg²⁺. *J. Fluoresc.* **2020**, *30* (5), 985–997. <https://doi.org/10.1007/S10895-020-02542-X/TABLES/3>.
- (27) Lissi, E.; Calderón, C.; Campos, A. Evaluation of the Number of Binding Sites in Proteins from Their Intrinsic Fluorescence: Limitations and Pitfalls. *Photochem. Photobiol.* **2013**, *89* (6), 1413–1416. <https://doi.org/10.1111/php.12112>.
- (28) Ho, I. T.; Lai, T. L.; Wu, R. T.; Tsai, M. T.; Wu, C. M.; Lee, G. H.; Chung, W. S. Design and Synthesis of Triazolyl Coumarins as Hg²⁺ Selective Fluorescent Chemosensors. *Analyst* **2012**, *137* (24), 5770–5776. <https://doi.org/10.1039/c2an36076d>.
- (29) Cattoni, D. I.; Chara, O.; Kaufman, S. B.; González Flecha, F. L. Cooperativity in Binding Processes: New Insights from Phenomenological Modeling. *PLoS One* **2015**, *10* (12), e0146043. <https://doi.org/10.1371/journal.pone.0146043>.
- (30) Alon, U. *An Introduction to Systems Biology. Design Principles of Biological Circuits*, 2nd ed.; CRC Press, Inc., 2020; Vol. 62.
- (31) Hunter, C. A.; Anderson, H. L. What Is Cooperativity? *Angew. Chemie Int. Ed.* **2009**, *48* (41), 7488–7499. <https://doi.org/10.1002/anie.200902490>.
- (32) Rout, K.; Manna, A. K.; Sahu, M.; Patra, G. K. A Guanidine Based Bis Schiff Base Chemosensor for Colorimetric Detection of Hg(II) and Fluorescent Detection of Zn(II) Ions. *Inorganica Chim. Acta* **2019**, *486* (November 2018), 733–741. <https://doi.org/10.1016/j.ica.2018.11.021>.
- (33) Ozmen, P.; Demir, Z.; Karagoz, B. An Easy Way to Prepare Reusable Rhodamine-Based Chemosensor for Selective Detection of Cu²⁺ and Hg²⁺ Ions. *Eur. Polym. J.* **2022**, *162* (November 2021), 110922. <https://doi.org/10.1016/j.eurpolymj.2021.110922>.
- (34) Ma, Q. J.; Zhang, X. B.; Zhao, X. H.; Jin, Z.; Mao, G. J.; Shen, G. L.; Yu, R. Q. A Highly Selective Fluorescent Probe for Hg²⁺ Based on a Rhodamine-Coumarin Conjugate. *Anal. Chim. Acta* **2010**, *663* (1), 85–90. <https://doi.org/10.1016/j.aca.2010.01.029>.
- (35) Singh, H.; Rajeshwari, M.; Khurana, J. M. Synthesis, Photophysical Studies, and Application of Novel 2,7-Bis((1-Butyl-1H-1,2,3-Triazol-4-Yl)Methoxy)Naphthalene as a Highly Selective, Reversible Fluorescence Chemosensor for Detection Fe³⁺ Ions. *J.*

Photochem. Photobiol. A Chem. **2018**, *353*, 424–432.
<https://doi.org/10.1016/j.jphotochem.2017.12.003>.

- (36) Jit Kaur, P.; Pant, K. K.; Chauhan, G.; Nigam, K. D. P. *Sustainable Metal Extraction from Waste Streams*; Wiley-VCH, 2020.
- (37) Harvey, D. Complexation Titration
https://chem.libretexts.org/Ancillary_Materials/Demos_Techniques_and_Experiments/General_Lab_Techniques/Titration/Complexation_Titration (accessed Dec 10, 2022).
- (38) Chussain, haudhery Mustansar Mishra, A. K. *Handbook of Smart Photocatalytic Materials: Fundamentals, Fabrications and Water Resources Applications*; Elsevier, 2020.
- (39) Burgess, J.; Twigg, M. V. *Iron: Inorganic & Coordination Chemistry*; John Wiley & Sons, Ltd, 2006. <https://doi.org/10.1002/0470862106.ia108>.
- (40) Ding, W.; Xu, J.; Chen, T.; Liu, C.; Li, J.; Wu, F. Co-Oxidation of As(III) and Fe(II) by Oxygen through Complexation between As(III) and Fe(II)/Fe(III) Species. *Water Res.* **2018**, *143*, 599–607. <https://doi.org/10.1016/j.watres.2018.06.072>.
- (41) Zeng, W.; Yang, X.; Chen, X.; Yan, Y.; Lu, X.; Qu, J.; Liu, R. Conjugated Polymers Containing 2-Thiohydantoin: Detection of Cuprous Ion, Hydrogen Peroxide and Glucose. *Eur. Polym. J.* **2014**, *61*, 309–315.
<https://doi.org/10.1016/j.eurpolymj.2014.10.015>.
- (42) Ohno, T.; Kubicki, J. D.; Amirbahman, A. Molecular Orbital Study of Fe(II) and Fe(III) Complexation with Salicylate and Citrate Ligands: Implications for Soil Biogeochemistry. *Soil Sci. Soc. Am. J.* **2022**, *86* (2), 181–194.
<https://doi.org/10.1002/saj2.20339>.
- (43) Sahoo, C. R.; Sahoo, J.; Mahapatra, M.; Lenka, D.; Kumar Sahu, P.; Dehury, B.; Nath Padhy, R.; Kumar Paidesetty, S. Coumarin Derivatives as Promising Antibacterial Agent(S). *Arab. J. Chem.* **2021**, *14* (2), 102922.
<https://doi.org/10.1016/j.arabjc.2020.102922>.
- (44) Mama, N.; Battison, A. Synthesis and Application of a Fluorescent turn-Off Triazolyl-Coumarin-Based Fluorescent Chemosensor for the Sensing of Fe^{3+} Ions in Aqueous Solutions. *Arkivoc* **2020**, *2020*, 1–27.
<https://doi.org/10.24820/ARK.5550190.P011.283>.
- (45) Ngororabanga, J. M. V.; Plessis, J. Du; Mama, N. Fluorescent Polymer Incorporating Triazolyl Coumarin Units for Cu^{2+} Detection via Planarization of Ict-Based Fluorophore. *Sensors (Switzerland)* **2017**, *17* (9). <https://doi.org/10.3390/s17091980>.
- (46) Bauer, I.; Knölker, H. J. *Iron Catalysis in Organic Chemistry: Reactions and Applications*; Wiley-VCH, 2008. <https://doi.org/10.1002/9783527623273.ch1>.
- (47) Sharma, R.; Joshi, S.; Bhattacharjee, R.; Pant, D. D. Solvent Effect on Absorption and Fluorescence Spectra of Cinchonine and Cinchonidine Dications: Estimation of Ground and Excited State Dipole Moments by Experimental and Numerical Studies. *J. Mol. Liq.*

2015, 206, 159–164. <https://doi.org/10.1016/j.molliq.2015.02.002>.

- (48) Lakowicz, J. R. Solvent and Environmental Effects. In *Principles of Fluorescence Spectroscopy*; Springer US: Boston, MA, 2006; pp 205–235. https://doi.org/10.1007/978-0-387-46312-4_6.

Supplementary information

List of supplementary figures

Figure S 3.1: ^{13}C NMR spectrum of E1 in CDCl_3	151
Figure S 3.2: FT-IR spectrum of E1	151
Figure S 3.3: ^{13}C NMR spectrum of E2 in CDCl_3	152
Figure S 3.4: FT-IR spectrum of E2	152
Figure S 3.5: ^1H NMR spectrum of the attempted E3 compound in CDCl_3	152
Figure S 3.6: ^1H NMR spectrum of the attempted E4 compound in CDCl_3	153
Figure S 3.7: Absorbance spectra of E2 (blue), E2-Fe²⁺ (red) and E2-Fe³⁺ (yellow) complexes after standing overnight in a) acetonitrile and b) methanol. Inset: Photographic image of the complexes of respective spectra. a) E2 - yellow solution, E2-Fe²⁺ - green solution and E2-Fe³⁺ - darker green solution. b) E2 - yellow solution, E2-Fe²⁺ - red solution and E2-Fe³⁺ - darker yellow solution.....	153
Figure S 3.8: Absorbance spectra of o-A with Fe^{2+} and Fe^{3+} in methanol.	154
Figure S 3.9: Coordination number 4 for E2-Fe²⁺ in water obtained using Spartan.	154
Figure S 3.10: Coordination number 4 for E2-Fe²⁺ in acetonitrile obtained using Spartan.	155
Figure S 3.11: Coordination number 5 for E2-Fe²⁺ in water showing the square pyramidal geometry obtained using Spartan.....	155
Figure S 3.12: Coordination number 5 for E2-Fe²⁺ in acetonitrile showing the square pyramidal geometry obtained using Spartan.....	156
Figure S 3.13: E2-Fe²⁺ displaying a coordination number of 6 instead of 8 in water obtained using Spartan.....	157
Figure S 3.14: E2-Fe²⁺ displaying a coordination number of 7 instead of 8 in acetonitrile obtained using Spartan.	157

List of supplementary tables

Table S 3.1: Crystallographic data for E1 and E2 .	158
---	-----

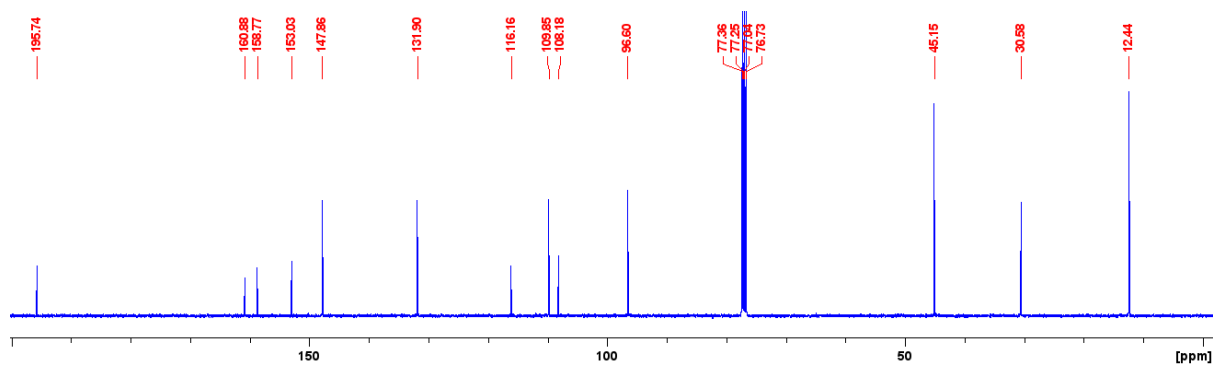


Figure S 3.1: ^{13}C NMR spectrum of **E1** in CDCl_3 .

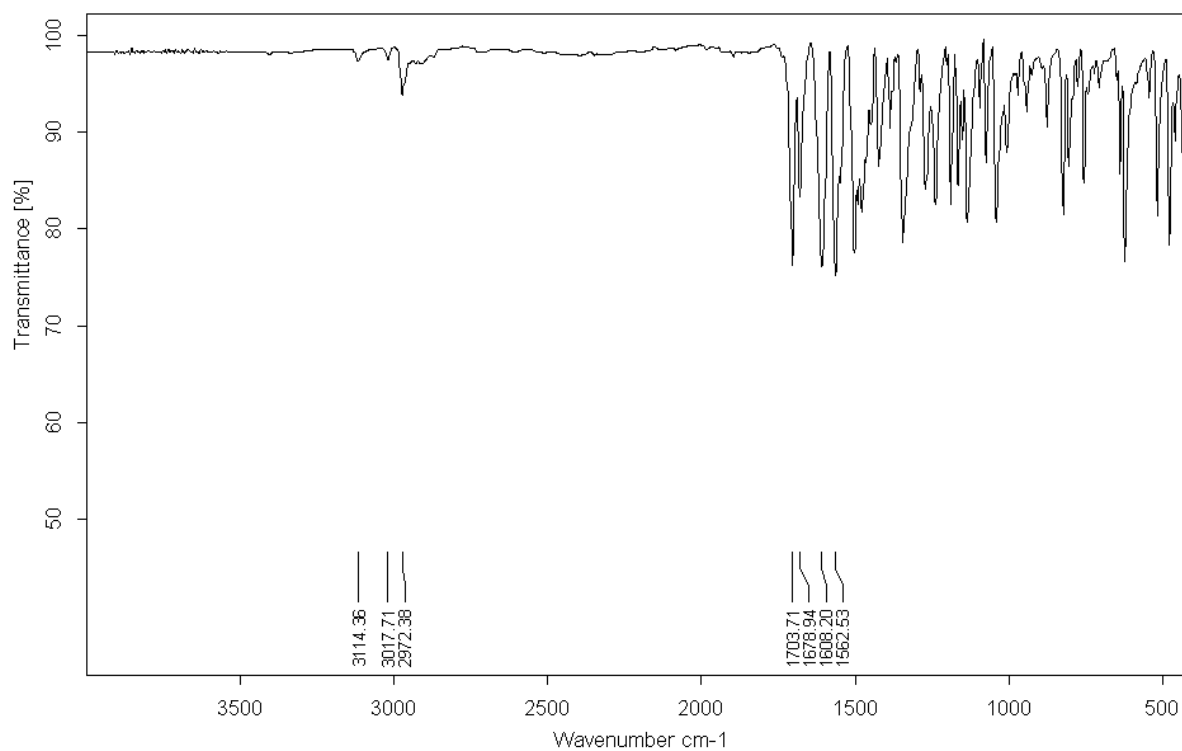


Figure S 3.2: FT-IR spectrum of **E1**.

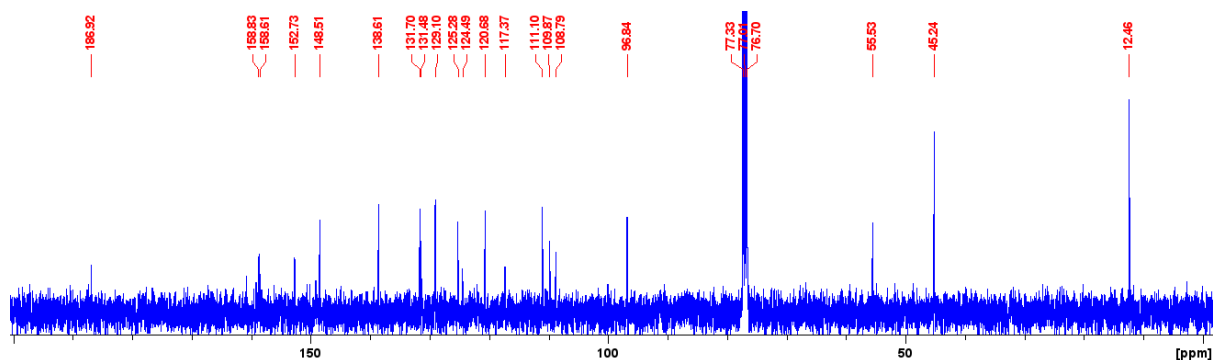


Figure S 3.3: ^{13}C NMR spectrum of **E2** in CDCl_3 .

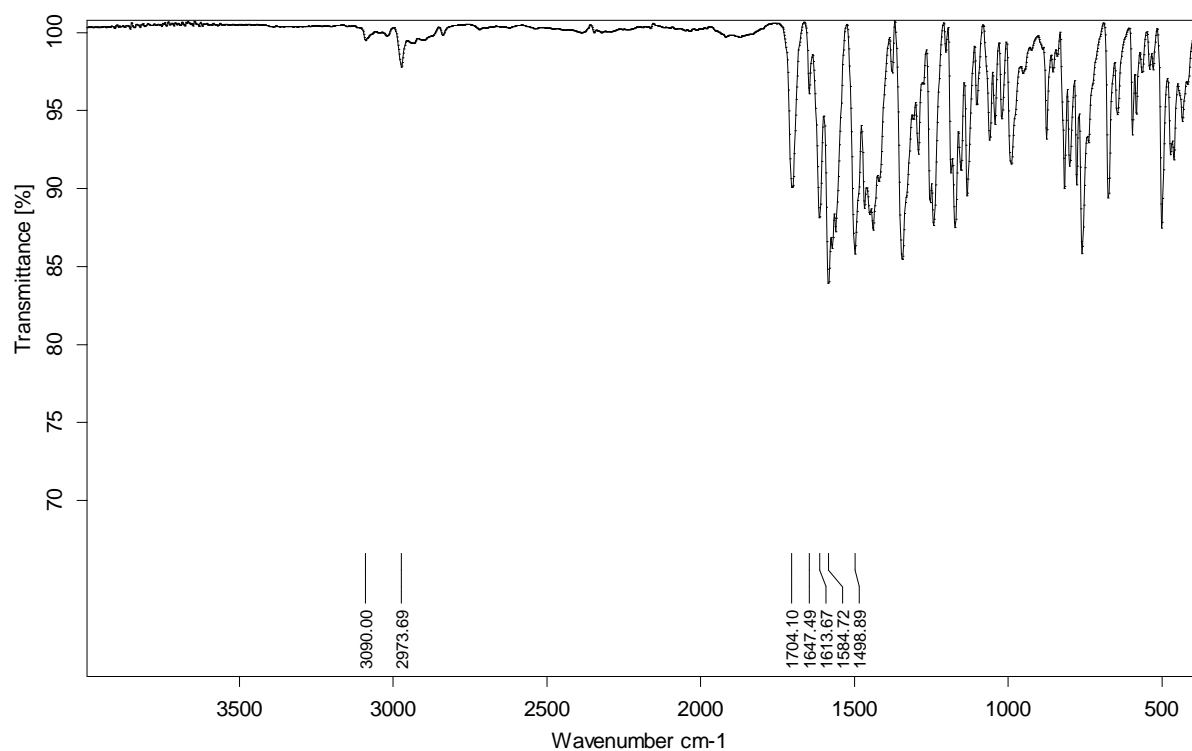


Figure S 3.4: FT-IR spectrum of **E2**.

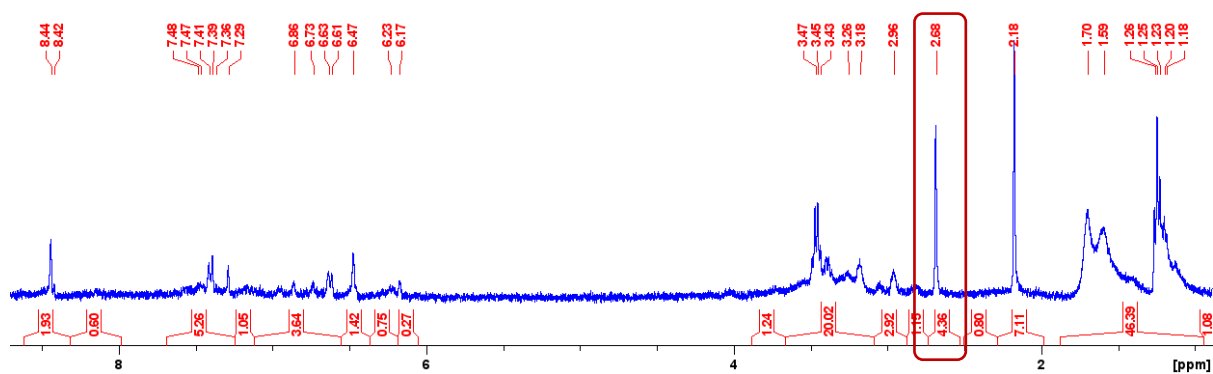


Figure S 3.5: ^1H NMR spectrum of the attempted **E3** compound in CDCl_3 .

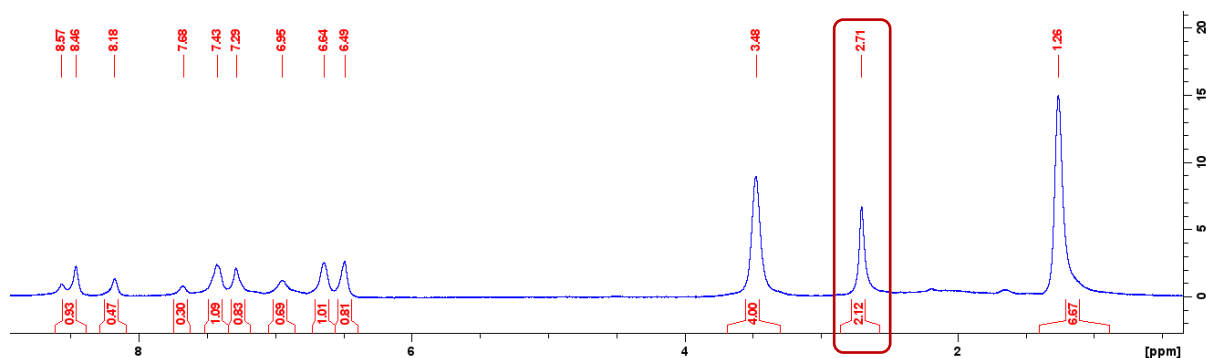


Figure S 3.6: ^1H NMR spectrum of the attempted **E4** compound in CDCl_3 .

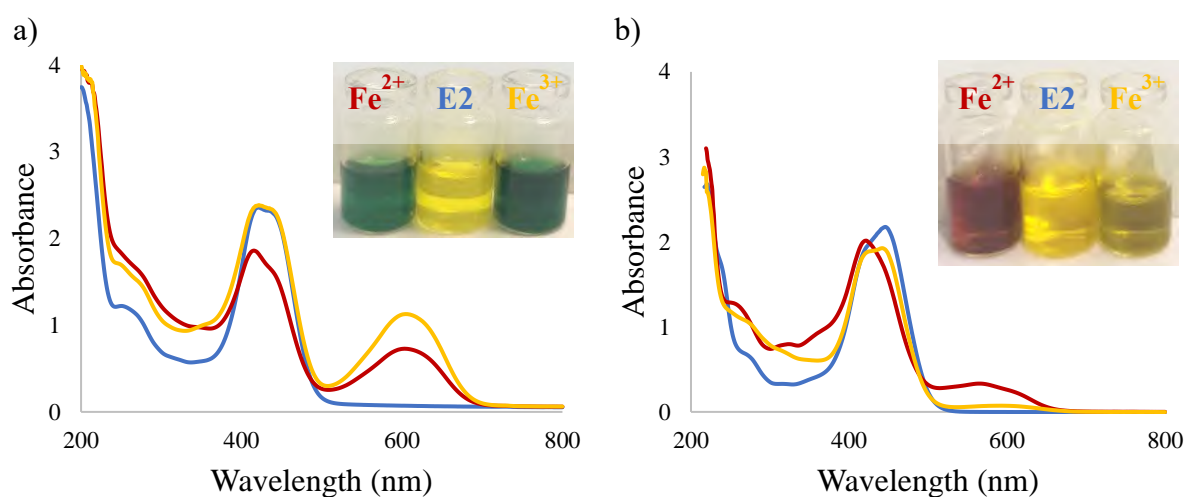


Figure S 3.7: Absorbance spectra of **E2** (blue), **E2-Fe²⁺** (red) and **E2-Fe³⁺** (yellow) complexes after standing overnight in a) acetonitrile and b) methanol. Inset: Photographic image of the complexes of respective spectra. a) **E2** - yellow solution, **E2-Fe²⁺** - green solution and **E2-Fe³⁺** - darker green solution. b) **E2** - yellow solution, **E2-Fe²⁺** - red solution and **E2-Fe³⁺** - darker yellow solution.

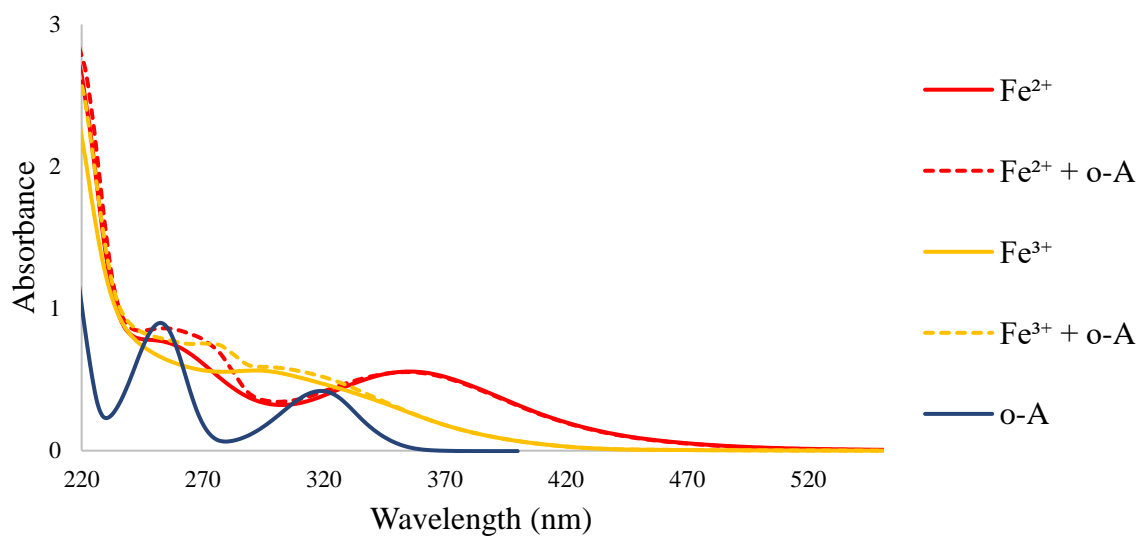


Figure S 3.8: Absorbance spectra of o-A with Fe^{2+} and Fe^{3+} in methanol.

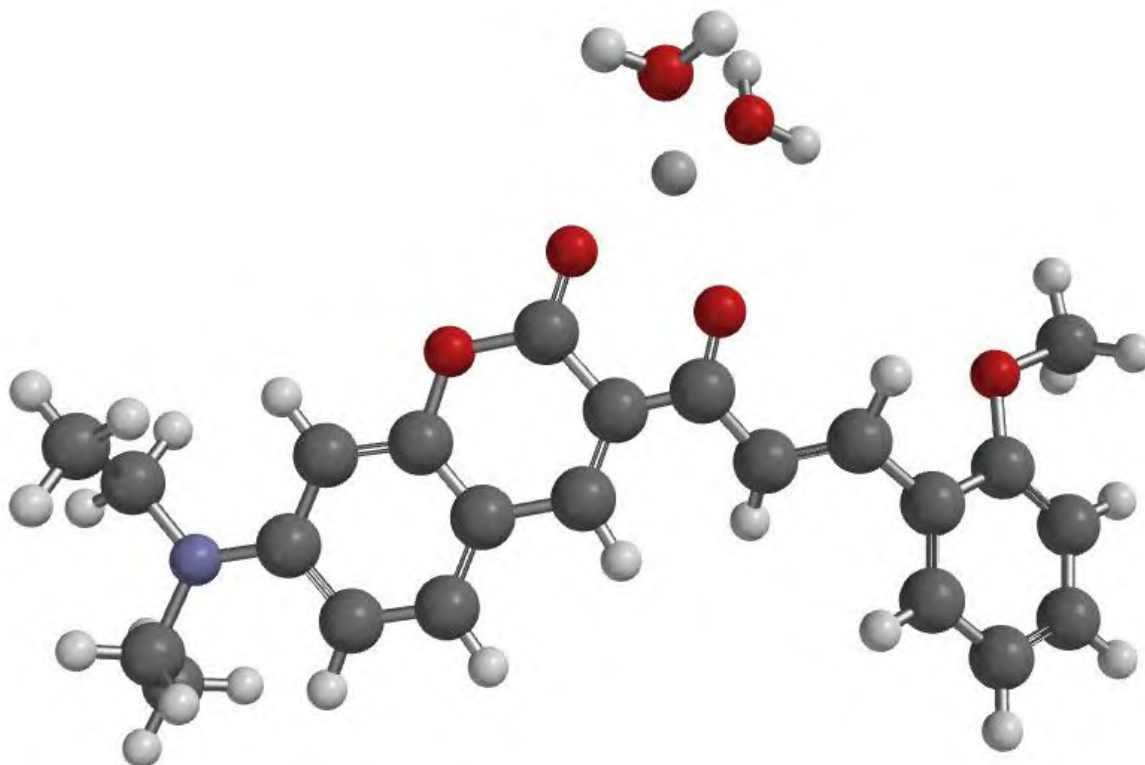


Figure S 3.9: Coordination number 4 for E2-Fe^{2+} in water obtained using Spartan.

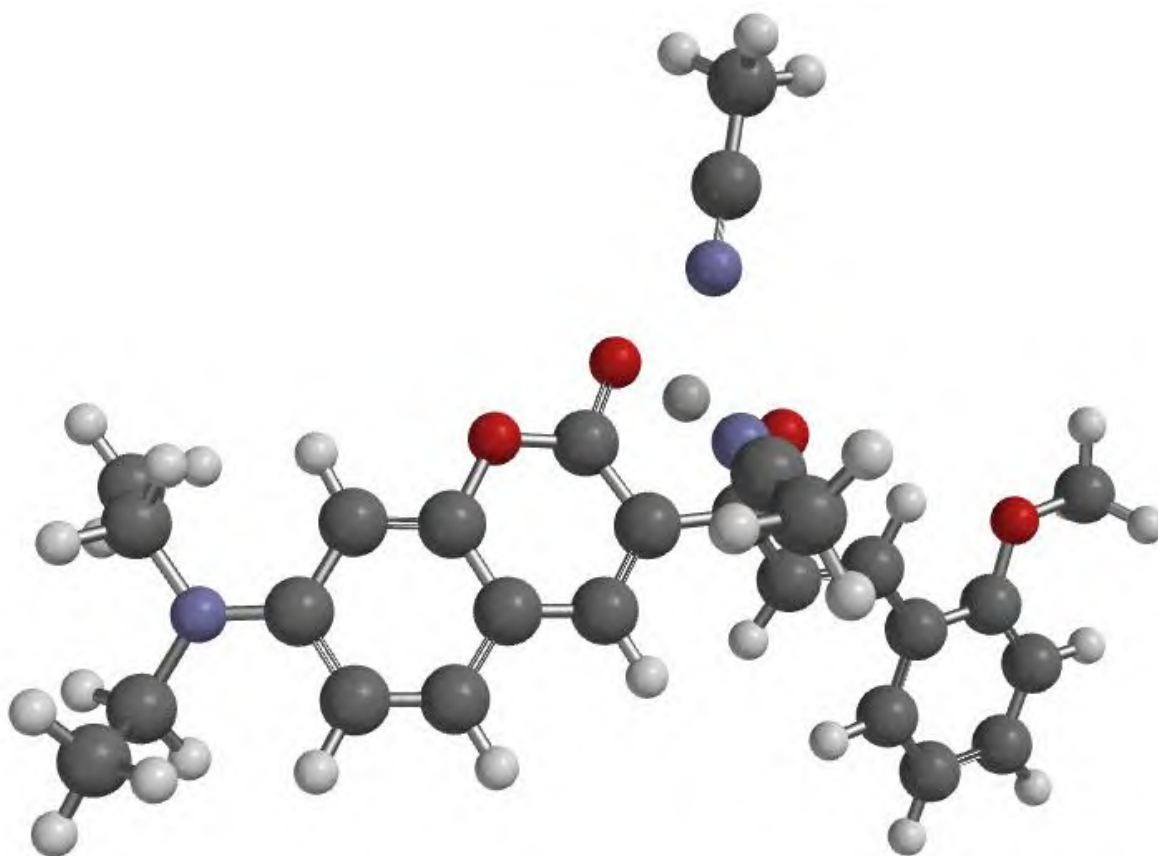


Figure S 3.10: Coordination number 4 for E2-Fe²⁺ in acetonitrile obtained using Spartan.

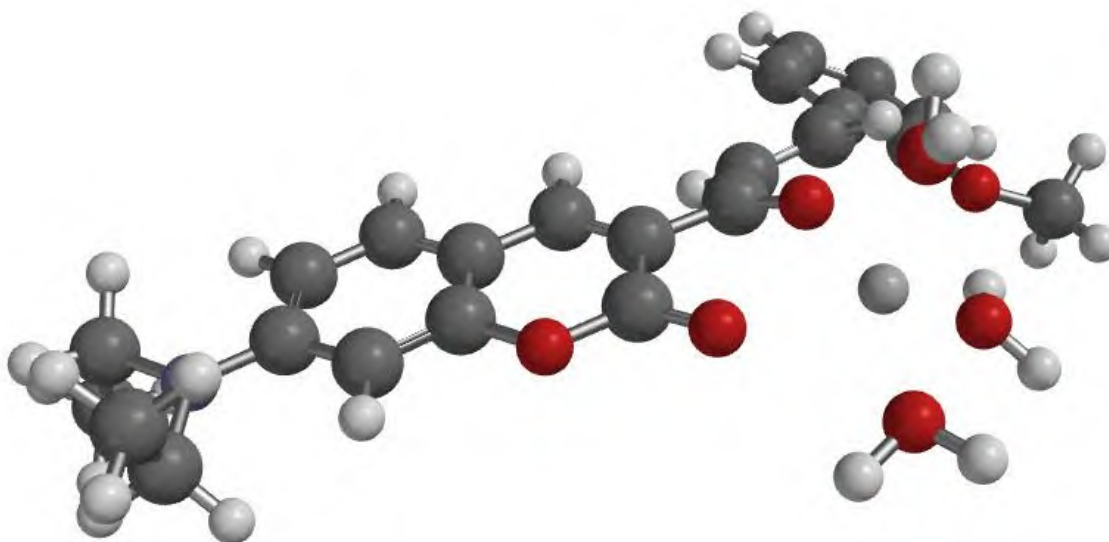


Figure S 3.11: Coordination number 5 for E2-Fe²⁺ in water showing the square pyramidal geometry obtained using Spartan.

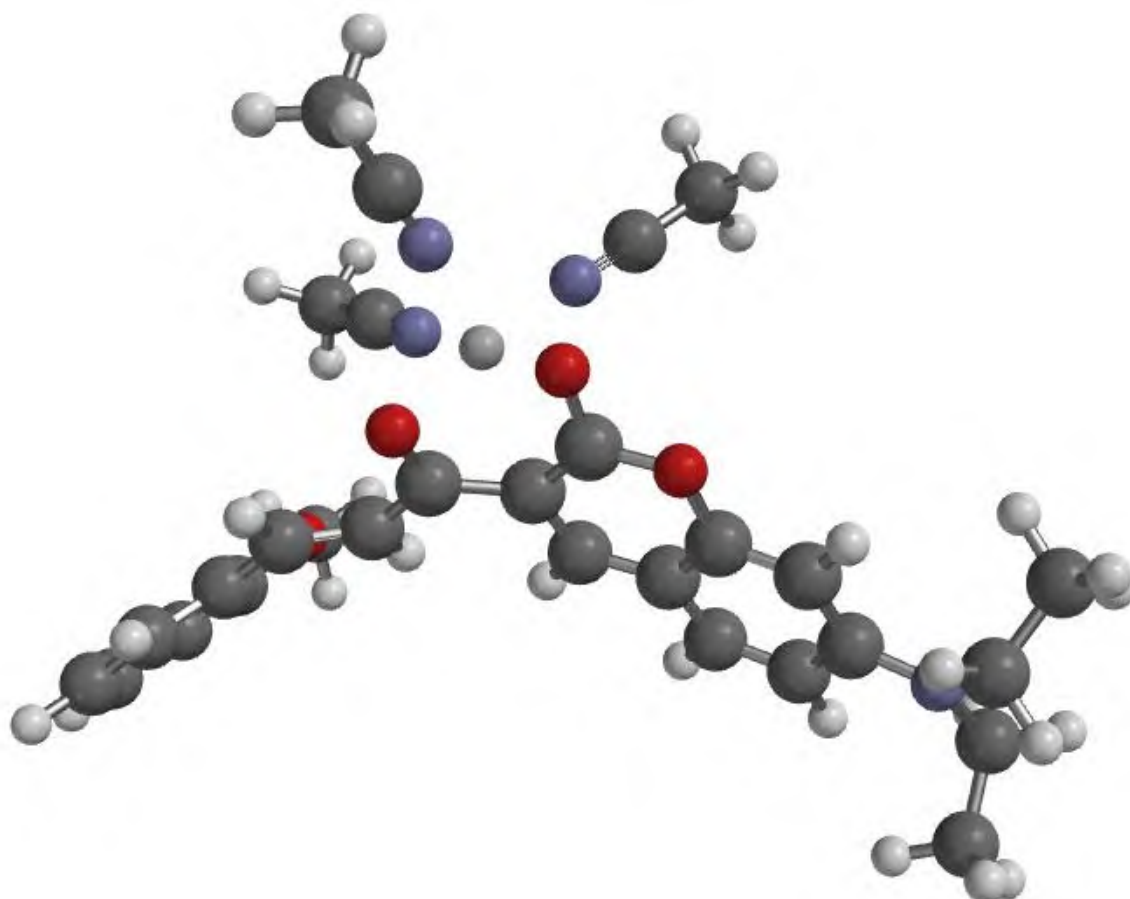


Figure S 3.12: Coordination number 5 for E2-Fe²⁺ in acetonitrile showing the square pyramidal geometry obtained using Spartan.

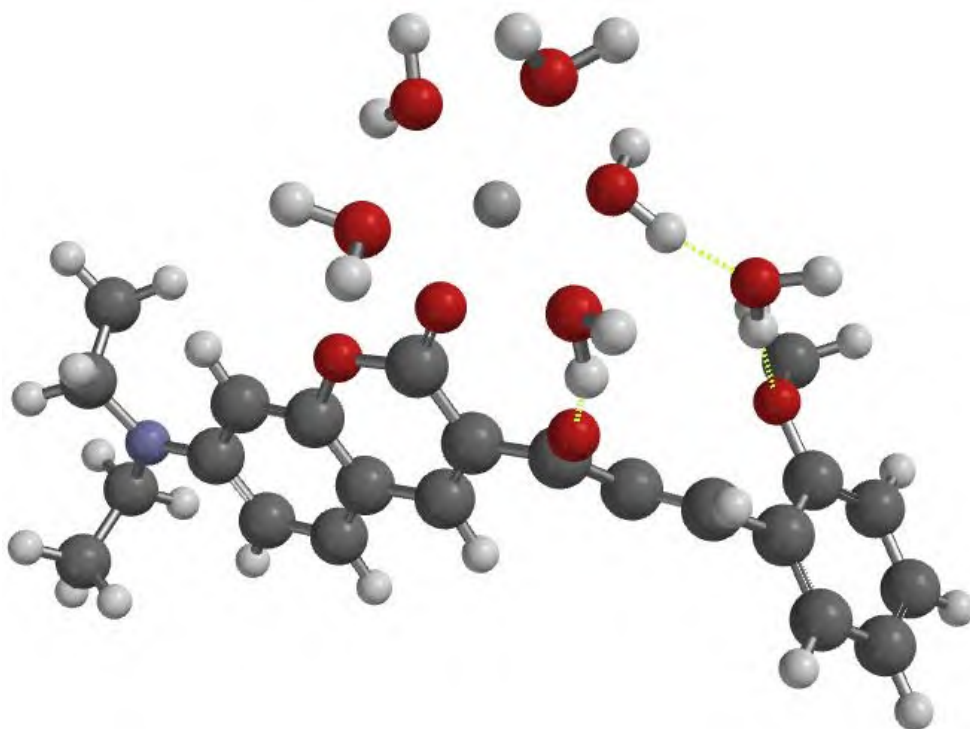


Figure S 3.13: E2-Fe²⁺ displaying a coordination number of 6 instead of 8 in water obtained using Spartan.

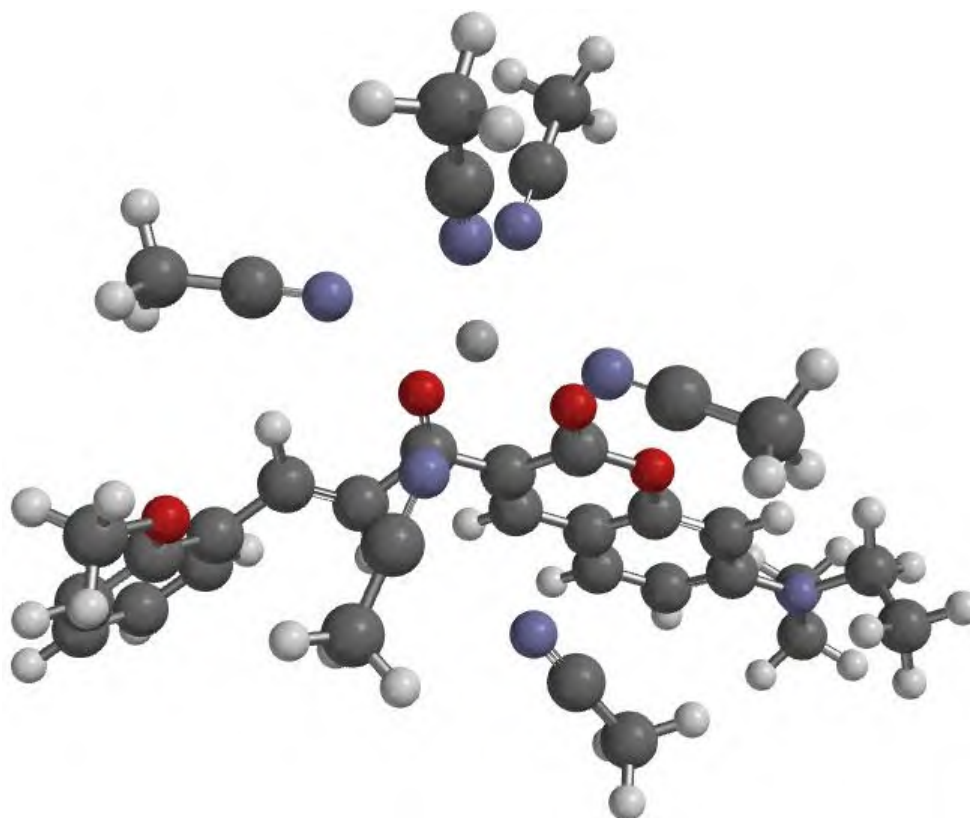

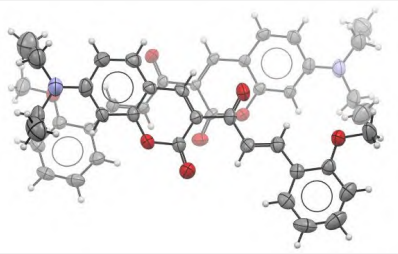


Figure S 3.14: E2-Fe²⁺ displaying a coordination number of 7 instead of 8 in acetonitrile obtained using Spartan.

Table S 3.1: Crystallographic data for **E1** and **E2**.

	E1	E2
Structure		
Formula	C ₁₅ H ₁₇ NO ₃	C ₂₃ H ₂₃ NO ₄
Molecular Weight	259.30	377.42
Temperature (K)	200	296
Crystal system	monoclinic	monoclinic
Space group	C2/c	P21
a (Å)	17.2617(10)	7.3807(7)
b (Å)	7.4372(4)	12.4445(13)
c (Å)	21.8565(13)	21.481(2)
α (°)	90	90
β (°)	108.542(2)	98.791(6)
γ (°)	90	90
V (Å³)	2660.3(3)	1949.8(3)
Z	8	4
D_c (g/ cm⁻³)	1.295	1.286
μ (mm⁻¹)	0.090	0.088
Reflections collected	24170	43702
Unique reflections	3307	9373
R_{int}	0.023	0.050
wR₂	0.1109	0.2548

Chapter 4

Dimer compounds as Chemosensors

Summary

In this chapter, two dimer compounds (**D1** and **D2**) were successfully synthesised and tested for their chemosensor abilities in acetonitrile. **D2** had no florescent properties, and no responses were observed in the presence of various metal cations and anions. **D1**, on the other hand, was completely quenched in the presence of Cu^{2+} . Competition studies showed that additional metal cations interfere with the complexation between **D1** and Cu^{2+} . Titration studies revealed that the complexation is linear and quantifiable between 0.249 μM to 0.795 μM with a LOD of 0.082 μM , which is well below the health limit of 31 μM , set by the WHO. Molecular modelling studies in combination with NMR experiments illustrated that the 1:1 binding between **D1** and Cu^{2+} occurs between the two carbonyl oxygens of the coumarin and the adjacent enone linker. Lastly, it was observed that no identifiable change in emission spectra of **D1** and **D2** was detected in the presence of various anion analytes.

Table of Contents

Summary	159
List of Figures	161
List of Schemes	163
List of Tables	163
List of selected Abbreviations	164
4 Dimer compounds as chemosensors	165
4.1 Introduction	165
4.2 Aim of chapter.....	166
4.3 Synthesis of dimer compounds D1 and D2	167
4.3.1 X-ray structure of E1 and compound 2	170
4.4 Absorbance and emission studies of dimer chemosensors D1 and D2	171
4.5 Application of D1 and D2 dimer compounds as chemosensors for metal cations..	174
4.5.1 Screening of metal cations using D1 and D2	174
4.5.2 Metal ion competition studies using D1 as a chemosensor	176
4.5.3 D1 Titrations studies with Cu ²⁺	177
4.5.4 Reversibility studies of D1	180
4.5.5 pH studies of D1 and D2	183
4.6 Application of D1 and D2 dimer compounds as chemosensors for anions	184
4.6.1 Screening of anions.....	184
4.7 The proposed binding site and computational studies	187
4.7.1 NMR titrations of D1 with Cu ²⁺	187
4.7.2 Molecular modelling of complexation between D1 and Cu ²⁺	189
4.8 Conclusion.....	193
4.9 Experimental	195
4.9.1 General information	195
4.9.2 Synthesis of compounds	196
References.....	201

Supplementary information	204
List of Supplementary Figures.....	204

List of Figures

Figure 4.1: Structures of chemosensors D1 and D2	166
Figure 4.2: ^1H NMR spectrum of D1 in DMSO.....	168
Figure 4.3: ^1H NMR spectrum of D2 in DMSO.....	169
Figure 4.4: X-ray structure of aldehyde compound 2	171
Figure 4.5: Absorbance spectra of D1 (blue) and D2 (red). A concentration of 16.7 μM was used.	171
Figure 4.6: Emission spectra of D1 (solid lines) and D2 (dash lines) in various solvents. A concentration of 0.1 μM was used. $\lambda_{\text{excitation}}$: 487 nm	172
Figure 4.7: 3D emission spectra of a) D1 and b) D2 in acetonitrile.	173
Figure 4.8: Normalised spectra of D1 showing the absorbance and emission overlap. $\lambda_{\text{excitation}}$: 487 nm.....	173
Figure 4.9: Screening various metal cations (0.167 μM) in acetonitrile using chemosensor D1 (0.0334 μM). $\lambda_{\text{excitation}}$: 487 nm	175
Figure 4.10: Photographic illustration of D1 compared to D1 -metal complexes under a) normal light (top) and b) UV-light (bottom, $\lambda_{\text{excitation}}$: 365 nm)	175
Figure 4.11: Photographic illustration of D2 compared to D2 -metal complexes under a) normal light (top) and b) UV-light (bottom, $\lambda_{\text{excitation}}$: 365 nm).....	176
Figure 4.12: Competition studies between D1 - Cu^{2+} complexes and various competing metal cations measuring the intensity at 573 nm. $\lambda_{\text{excitation}}$: 487 nm	177

Figure 4.13: a) D1 (0.1 μM) titration with Cu^{2+} in acetonitrile. b) Calibration curve of D1 - Cu^{2+} complex (at 573 nm) showing a linear region between 0 and 0.795 μM with R^2 of 0.993. $\lambda_{\text{excitation}}$: 487 nm.....	178
Figure 4.14: Benesi-Hildebrand plot of D1 - Cu^{2+} complex.....	179
Figure 4.15: Stern-Volmer plot of D1 with Cu^{2+}	179
Figure 4.16: Jobs plot of D1 with Cu^{2+}	180
Figure 4.17: Reversibility study of chemosensor D1 (0.1 μM) and Cu^{2+} (1.25 μM) with EDTA (1.25 μM). $\lambda_{\text{excitation}}$: 487 nm.	181
Figure 4.18: Reversibility study of chemosensor D1 (0.1 μM) and Cu^{2+} (1.25 μM) using NC^- (1.25 μM). $\lambda_{\text{excitation}}$: 487 nm.	182
Figure 4.19: Reversibility study of chemosensor D1 (0.1 μM) and Cu^{2+} (1.25 μM) using sodium ascorbate (NaAsc, 1.25 μM). $\lambda_{\text{excitation}}$: 487 nm.....	183
Figure 4.20: pH study of D1 (blue, 0.1 μM) and D2 (red, 0.1 μM) in aqueous buffer solutions. $\lambda_{\text{excitation}}$: 487 nm.....	183
Figure 4.21: pH study of D1 (blue, 0.1 μM) and D1 - Cu^{2+} (green) in aqueous buffer solutions. $\lambda_{\text{excitation}}$: 487 nm.....	184
Figure 4.22: Screening of D1 (0.0334 μM) with various anions (0.167 μM) in acetonitrile. $\lambda_{\text{excitation}}$: 487 nm.....	185
Figure 4.23: Photographic illustration of D1 in the presence of various anions in a) normal light and b) UV light ($\lambda_{\text{excitation}}$: 365 nm).....	186
Figure 4.24: Screening of D2 (0.0334 μM) with various anions (0.167 μM) in acetonitrile. $\lambda_{\text{excitation}}$: 487 nm.....	186
Figure 4.25: Photographic illustration of D2 in the presence of various anions in a) normal light and b) UV light ($\lambda_{\text{excitation}}$: 365 nm).....	187
Figure 4.26: ^1H NMR of a) D1 - Cu^{2+} complex and b) D1 in acetonitrile showing the effect of the complex formation on the enone moiety.....	188

Figure 4.27: ^{13}C NMR of a) D1 - Cu^{2+} complex and b) D1 in acetonitrile.....	189
Figure 4.28: Complex 1, a four-coordination D1 - Cu^{2+} complex with one acetonitrile molecule.	190
Figure 4.29: Complex 2, a five-coordination D1 - Cu^{2+} complex with two acetonitrile molecules.	190
Figure 4.30: Complex 3, a five-coordination D1 - Cu^{2+} complex with three acetonitrile molecules as co-ligands.	191
Figure 4.31: Six-coordination D1 - Cu^{2+} complex with four acetonitrile molecules as co-ligand.	192

List of Schemes

Scheme 4.1: Synthesis route to make D1 . a) diethyl acetoacetate, ethanol, piperidine, AcOH, reflux, 4h. b) HCl, AcOH, RT, Stir for 24h. c) DMF, POCl_3 , N_2 Atmosphere, 60°C , 24h. d) ethyl acetoacetate, ethanol, piperidine, AcOH, reflux, 4h. e) ethanol, piperidine, reflux, 24h.	167
Scheme 4.2: Synthesis route to make D2 . a) ethyl acetoacetate, ethanol, piperidine, AcOH, reflux, 4h. b) diethyl acetoacetate, ethanol, piperidine, AcOH, reflux, 4h. c) HCl, AcOH, RT, Stir for 24h. d) DMF, POCl_3 , N_2 Atmosphere, 60°C , 24h. e) ethanol, piperidine, reflux, 48h.	168
Scheme 4.3: Synthesis route to make D3 . a) ethyl acetoacetate, ethanol, piperidine, AcOH, reflux, 4h. b) DMF, POCl_3 , N_2 Atmosphere, 60°C , 24h. c) ethanol, piperidine, reflux, 24h.	169
Scheme 4.4: Attempted synthesis of D4 and D5	170

List of Tables

Table 4.1: Concentrations of interest for Cu^{2+}	178
Table 4.2: Coordination complexes of D1 - Cu^{2+}	193

List of selected Abbreviations

AcOH – Acetic acid

CH₃CN – Acetonitrile

CHQF – Chelation Quenched Fluorescent

DMF – Dimethylformamide

DMSO – Dimethyl sulfoxide

EDG – Electron Donating Group

EDTA – Ethylenediaminetetraacetic Acid

EtOH – Ethanol

EWG – Electron Withdrawing Group

FRET – Förster resonance energy transfer

H₂O – Water

MetOH – Methanol

NaAsc – Sodium Ascorbate

NC⁻ – Cyanide

NMR – Nuclear Magnetic Resonance

POCl₃ – Phosphoryl chloride

WHO – World Health Organisation

4 Dimer compounds as chemosensors

4.1 Introduction

Fluorescence-based chemosensors offer significant advantages over colourimetric chemosensors, such as high sensitivity, high selectivity, ease of operation and instantaneous detection.¹ The coumarin moiety is an excellent fluorophore for fluorescence-based chemosensors, not only for its high molar absorptivity, high quantum yield and high photostability but also for its ease of modification. Photophysical and spectral properties of coumarin derivatives can be easily modified by introducing an electron-donating group (EDG) at position seven and an electron-withdrawing group (EWG) at position three.² This combination can lead to a stronger push-pull electronic system which improves the properties of the compound.³

A dimer is a compound classified as an oligomer consisting of two monomers or similar parts joined by a linker or spacer moiety.⁴ In a study by Kaeswurm et al., they synthesised dimer compounds that had roughly double the absorption coefficient compared to the monomers.⁵

Copper is one of the essential metal cations found in trace amounts in the human body and is the third most abundant element in the earth's crust.⁶⁻⁸ Even in trace amounts, copper(II) performs and participate in many physiological processes.^{7,8} If the concentration of copper(II) exceeds the health limit of 31 μM set by the World Health Organisation (WHO)⁹, then copper(II) toxicity can occur. Copper(II) toxicity can affect organs (such as the liver and kidneys), inhibit various enzymatic pathways, and lead to severe neurodegenerative disease.^{7,8} Elevated levels of copper(II) have been linked to neurodegenerative illnesses such as Alzheimer's, Wilson's, and Menke's diseases.^{6-8,10} Copper pollution can arise mainly from coal mining, metal manufacturing industries, electroplating processes and corrosion of copper pipes.⁷

4.2 Aim of chapter

Coumarin-based dimer chemosensors were synthesised with an EDG at positions seven and eight and an EWG at position three. The diethyl amino ($-N(CH_3)_2$) group, which is known to be an excellent EDG¹¹, was added at position seven of the coumarin moiety of **D1**, whereas a weaker EDG, ethoxy¹² ($-OCH_2CH_3$), was added at position eight of the coumarin moiety of **D2**. In both dimers, the coumarin units are connected via an enone moiety at position three.

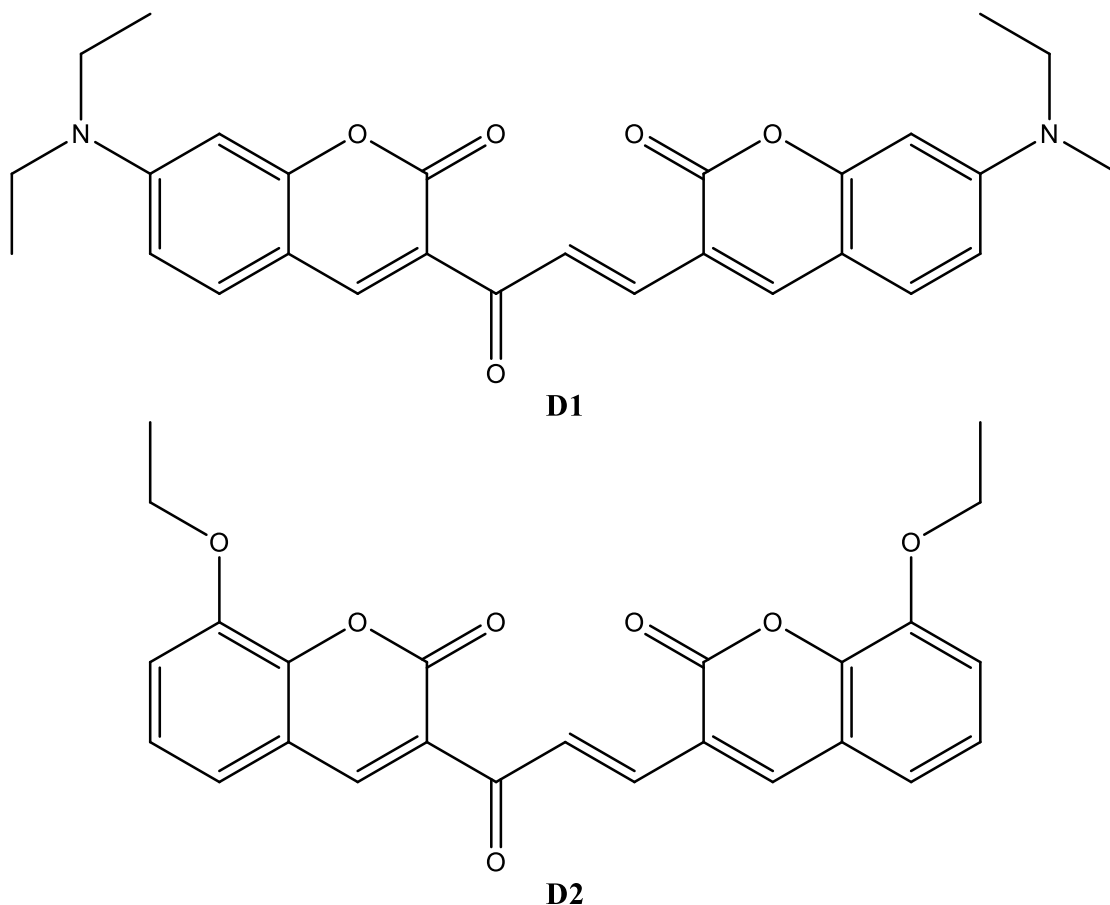


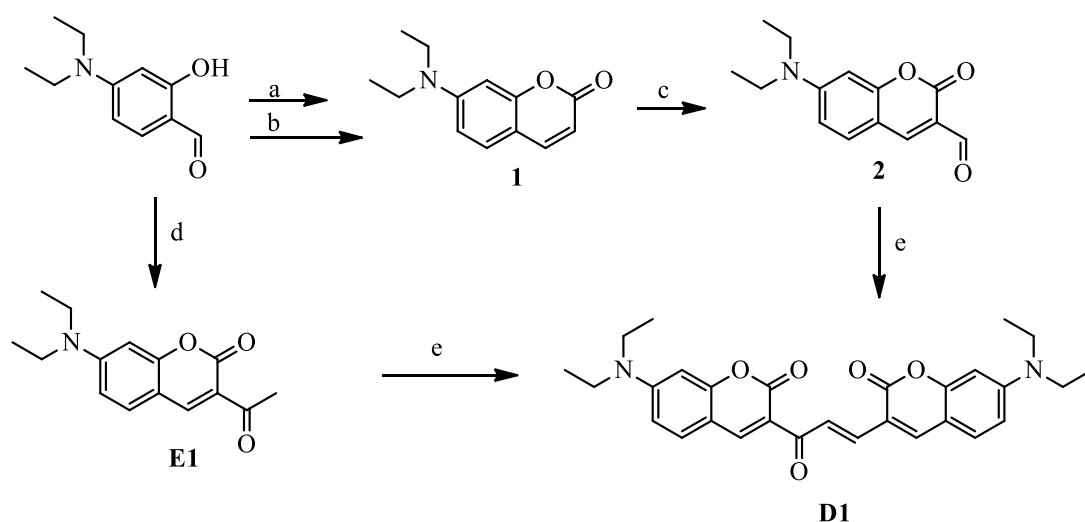
Figure 4.1: Structures of chemosensors **D1** and **D2**.

Key research questions:

- Can these novel chemosensors, **D1** and **D2** (**Figure 4.1**), be used as fluorescent chemosensors for detecting cations or anions?
- How does the presence of the EDG at position seven (**D1**) and the EDG at position eight of **D2** affect the selectivity of these compounds?

4.3 Synthesis of dimer compounds **D1** and **D2**

The dimer coumarin base chemosensors **D1** and **D2** were synthesised according to the reactions outlined in **Scheme 4.1** and **Scheme 4.2**, respectively. Dimer **D1** contains two diethyl amino groups originating from the 4-diethylsalicylaldehyde starting compound. 4-Diethylsalicylaldehyde was reacted with ethyl acetoacetate (route d in **Scheme 4.1**) in order to form the intermediate **E1**. The aldehyde derivative **2** (**Figure S 4.7**) was successfully prepared from compound **1**, as shown in **Scheme 4.1**.



Scheme 4.1: Synthesis route to make **D1**. a) diethyl acetoacetate, ethanol, piperidine, AcOH, reflux, 4h. b) HCl, AcOH, RT, Stir for 24h. c) DMF, POCl₃, N₂ Atmosphere, 60°C, 24h. d) ethyl acetoacetate, ethanol, piperidine, AcOH, reflux, 4h. e) ethanol, piperidine, reflux, 24h.

The structure of **D1** was confirmed using NMR spectroscopy, as seen by the ¹H NMR in **Figure 4.2**. The ¹H NMR shows the presence of the double bond protons from the enone linker with a coupling constant of 15.2865 Hz. The NMR also indicates that the E conformer was the only formed product. Furthermore, the aldehyde peak from the starting compound, **2** (**Figure S 4.7**), is not present in the ¹H NMR of compound **D1**; instead, the newly formed double-bond protons are observed at 7.61-7.57 ppm in **Figure 4.2**. The ¹³C NMR is shown in **Figure S 4.9** in the supplementary information. In addition, the absence of the methyl group in the ¹H NMR spectrum (**Figure 4.2**) indicates a successful conversion of the keto group into enone functionality.

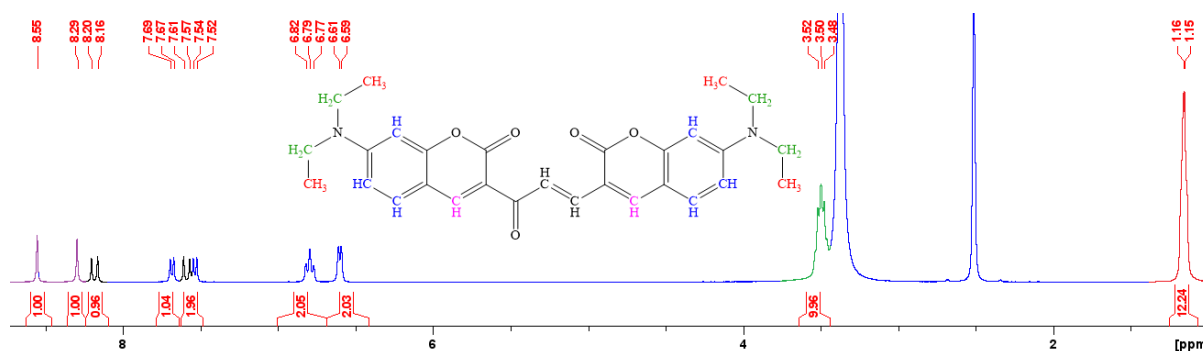
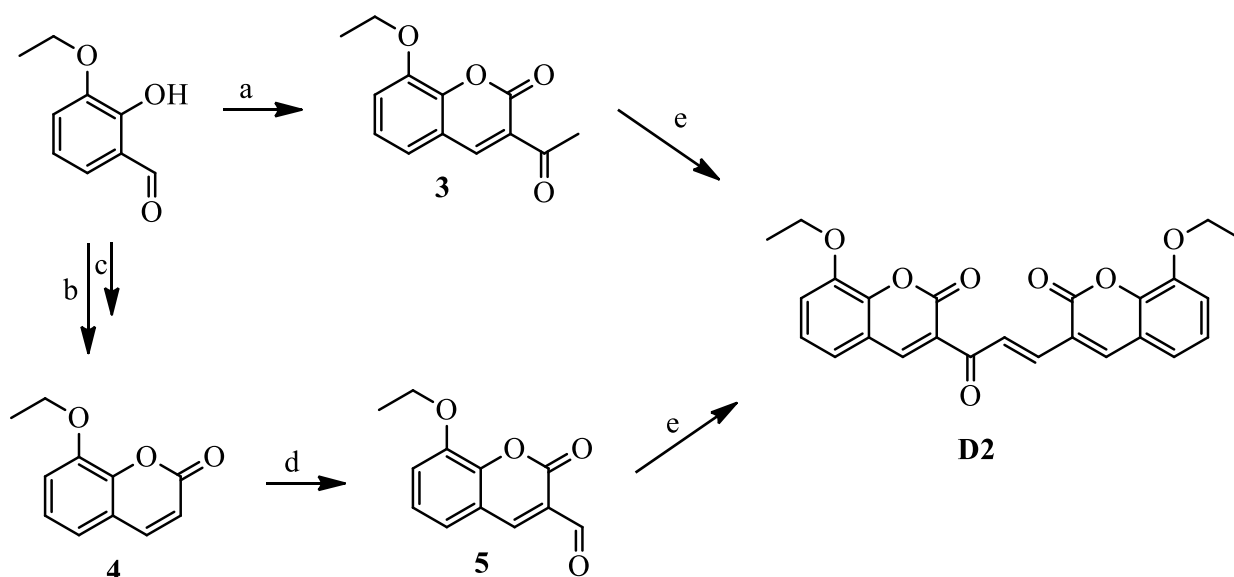


Figure 4.2: ^1H NMR spectrum of **D1** in DMSO.

The dimer **D2** followed a similar synthetic route as **D1**. However, in the place of 4-diethylaminosalicylaldehyde, 3-ethoxysalicylaldehyde was used, which carries an ethoxy group. Compounds **3-5** were successfully synthesised in which their ^1H and ^{13}C NMR spectra are shown in the supplementary information, **Figure S 4.14 - Figure S 4.21**. The HSQC spectrum of compound **5** (**Figure S 4.22**) was obtained to verify the positions of the coumarin hydrogens linked to the carbons.



Scheme 4.2: Synthesis route to make **D2**. a) ethyl acetoacetate, ethanol, piperidine, AcOH, reflux, 4h. b) diethyl acetoacetate, ethanol, piperidine, AcOH, reflux, 4h. c) HCl, AcOH, RT, Stir for 24h. d) DMF, POCl_3 , N_2 Atmosphere, 60°C , 24h. e) ethanol, piperidine, reflux, 48h.

D2 was obtained in better yields than **D1** but at a slower rate. This slower rate is attributed to the strength of the electron-donating group present in the starting compound.¹⁴

Dimer **D2** was successfully synthesised from the condensation reaction between compounds **3** and **5**, as shown in **Figure 4.3**. The presence of the double bond in the enone linker, **D2**, and the disappearance of the aldehyde peak (~10 ppm in compound **5**) confirmed the success of the reaction.

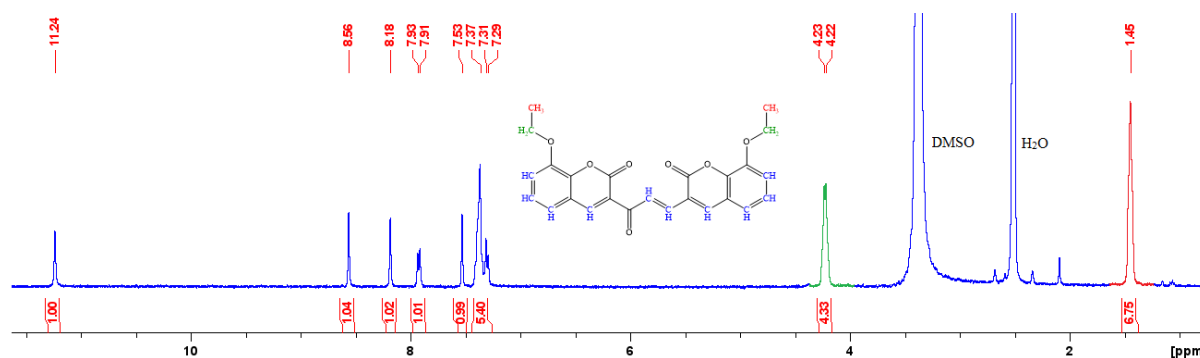
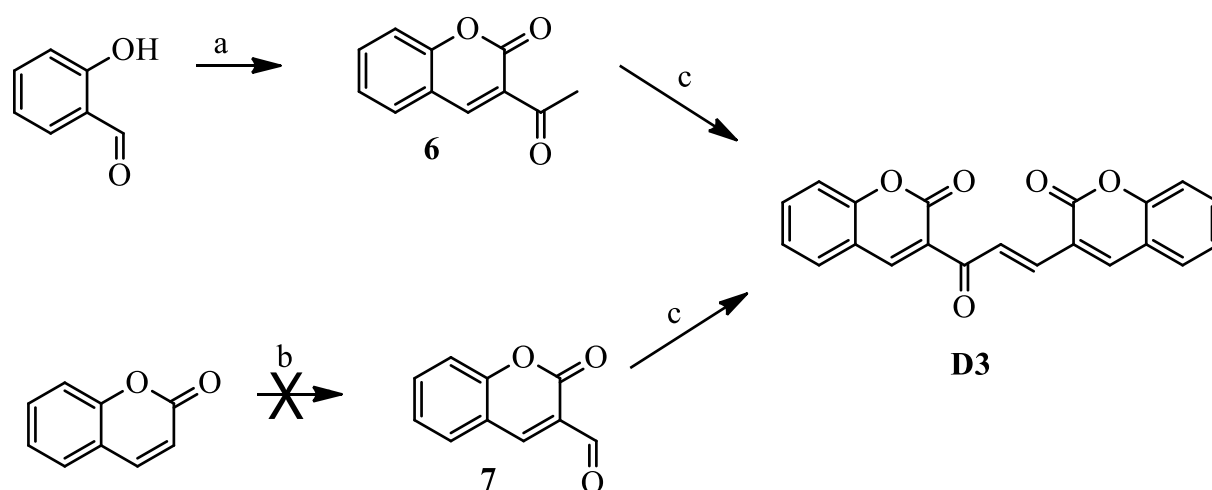


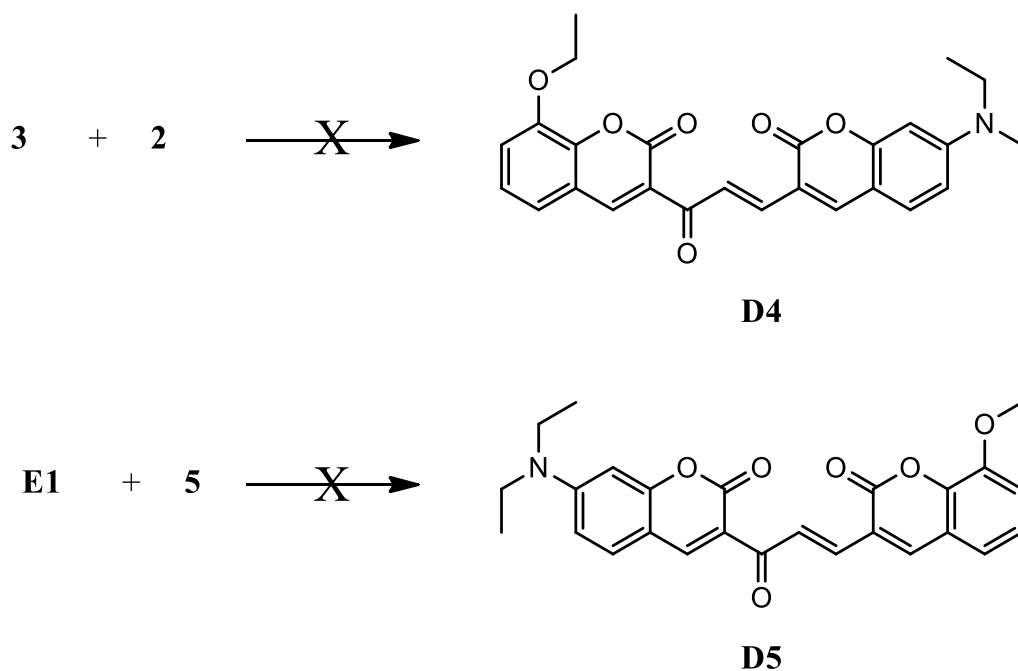
Figure 4.3: ^1H NMR spectrum of **D2** in DMSO.

Other coumarin-based dimer compounds, **D3**, **D4**, and **D5**, were also attempted for this section. The respective coumarins containing an aldehyde and ketone functional group were obtained to synthesise **D3**, a dimer compound without substituents, as shown in **Scheme 4.3**. However, an attempt at synthesising compound **7**, a precursor for dimer **D3** (containing hydrogen at position seven), was unsuccessful, as shown in **Scheme 4.3**. Confirmation from the ^1H NMR of compound **7** showed the presence of only the starting material shown in **Figure S 4.27**.



Scheme 4.3: Synthesis route to make **D3**. a) ethyl acetoacetate, ethanol, piperidine, AcOH, reflux, 4h. b) DMF, POCl_3 , N_2 Atmosphere, 60°C , 24h. c) ethanol, piperidine, reflux, 24h.

Using the compounds already synthesised, **E1**, **2**, **3** and **5**, **D4** and **D5** were also attempted. These dimers would have resulted in novel dimer-like compounds with different substituents at positions seven and eight, as shown in **Scheme 4.4**. However, in the synthesis of compound **D4**, only the starting compounds **2** and **3** were isolated in the end, as confirmed by ^1H NMR analysis (**Figure S 4.28**). Compound **D5** was also attempted without success, as only **E1** was isolated, as shown in **Figure S 4.29** in the supplementary information.



Scheme 4.4: Attempted synthesis of **D4** and **D5**.

4.3.1 X-ray structure of **E1** and compound **2**

The crystal structure of compound **E1** was provided in **Section 3.3.1** in **Chapter 3** and in the supplementary information **Table S 4.1**. Compound **2** was obtained by dissolving the pure compound in ethanol, and the crystals were then formed by slow evaporation. The single crystal X-ray diffraction (XRD) of both **E1** and **2** confirms the structures of these compounds. In compound **2**, shown in **Figure 4.4**, the coumarin backbone, amine, and the ketone functionality, at position three are shown to be in the same plane with the ethyl groups perpendicular to the coumarin moiety. Compound **2** crystallised in a monoclinic crystal system containing a C2/c space group similar to the literature's reported structure. Further information can be found in the supplementary information **Table S 4.1**.³

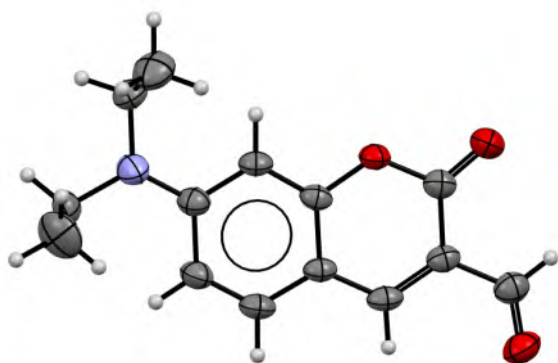
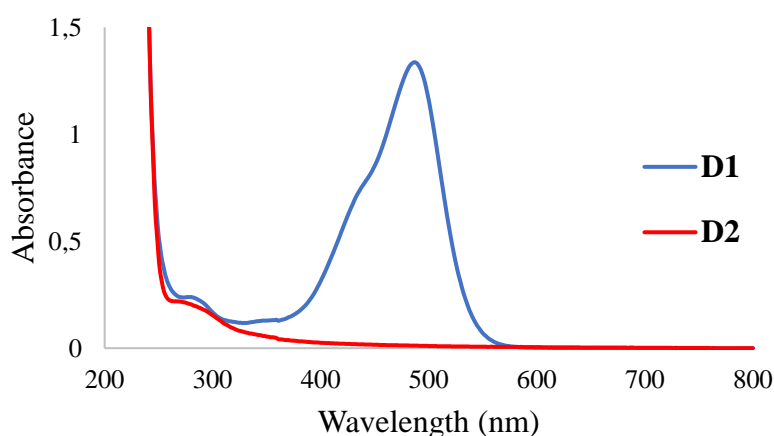


Figure 4.4: X-ray structure of aldehyde compound 2.

4.4 Absorbance and emission studies of dimer chemosensors **D1** and **D2**

The absorbance studies for dimers **D1** and **D2** were conducted in acetonitrile with a concentration of 16.7 μM using a Shimadzu UV-3100 spectrophotometer. As shown in **Figure 4.5**, **D1** (blue spectrum) has a relatively strong absorbance band at 487 nm, which was not observed in the **D2** (red spectrum) absorbance spectrum. Surprisingly, compound **D2** showed no absorption properties even at elevated concentrations, as shown in **Figure S 4.30** in the supplementary information. These observations further illustrate the improvements in the photophysical properties of **D1** due to the “push-pull” system between the strong electron-donating diethylamino group at position seven and the enone linker at position three. In **D2**, the photophysical properties were essentially lost due to the deviation from a “push-pull” system between positions seven and three, as the electron-donating group of **D2** resides at position eight. Furthermore, resonance effect from the ethoxy group at position eight could have disrupted the resonance of the coumarin moiety to such an extent that the photophysical properties further decreased to the point observed in **Figure 4.5**.



*Figure 4.5: Absorbance spectra of **D1** (blue) and **D2** (red).*

Investigation into the emission properties of **D1** and **D2** was done whereby various solvents were used to determine the solvent that provides better emission properties. **Figure 4.6** shows the emission spectra of all solvents tested; acetonitrile (CH_3CN), ethanol (EtOH), methanol (MeOH), water (H_2O), dimethyl-formamide (DMF), and dimethyl sulfoxide (DMSO). As seen in **Figure 4.6**, acetonitrile yielded the highest emission intensities for the dimer **D1**, followed by DMF with water resulting in no emission response. Once again, **D2** showed no emission properties in all the tested solvents in alignment with the absorption response.

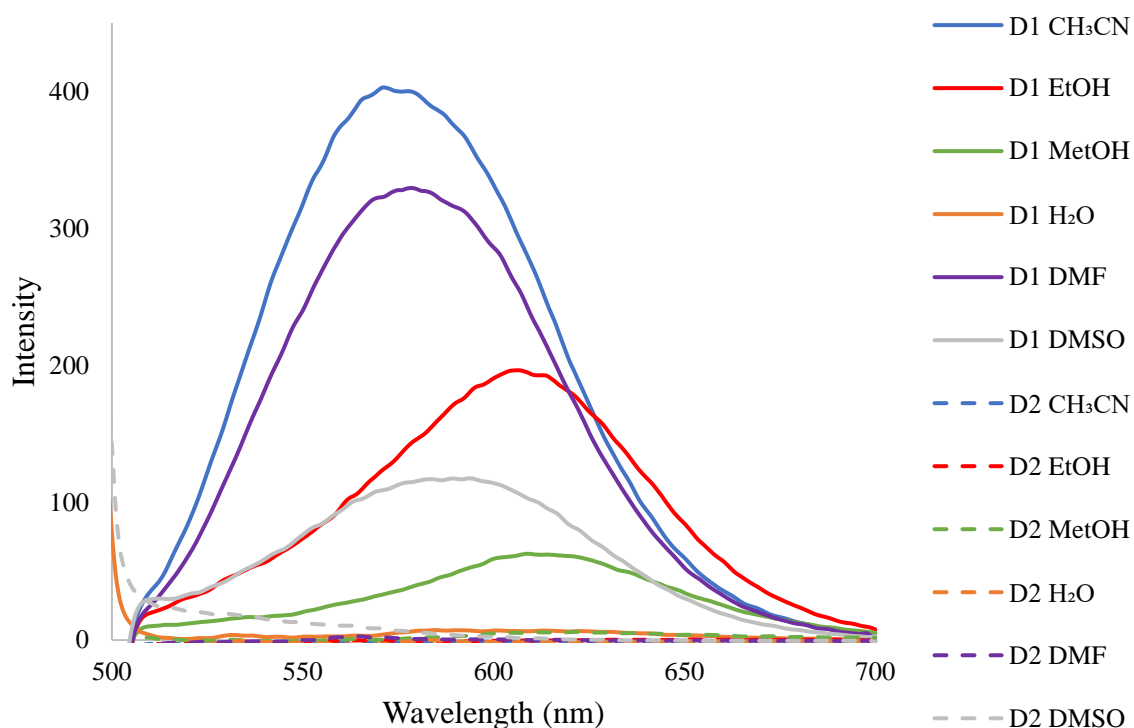


Figure 4.6: Emission spectra of **D1** (solid lines) and **D2** (dash lines) in various solvents. A concentration of $0.1 \mu\text{M}$ was used. $\lambda_{\text{excitation}}$: 487 nm

Further investigation was done to determine if **D2** have a different excitation wavelength than **D1**. Hence, **D1** and **D2** were subjected to a 3D emission scan. In the 3D emission scan, the excitation wavelength was varied from 300 nm to 600 nm in 10 nm increments. As seen in **Figure 4.7 a**), the excitation band at 490 nm is noted, confirming the excitation wavelength of 487 nm for **D1**. Furthermore, **Figure 4.7 b**) shows no significant emission peaks for **D2**, thus indicating no emission properties as a free compound. It was also observed in **Figure 4.7** is the first and second-order Rayleigh scattering from light passing through the emission monochromator.¹⁵

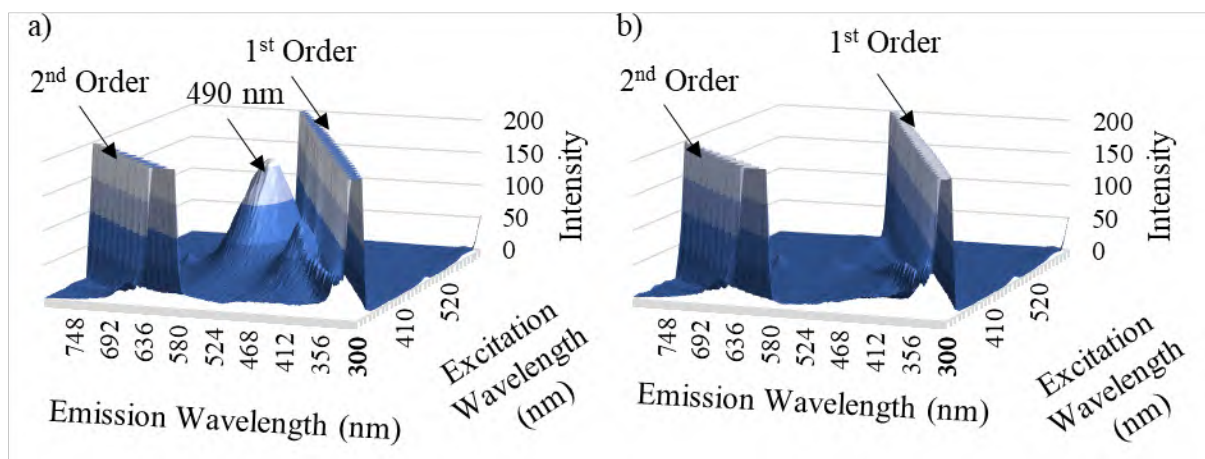


Figure 4.7: 3D emission spectra of a) **D1** and b) **D2** in acetonitrile.

The spectral overlap of the absorbance of **D1** and emissions of **D1** are shown in **Figure 4.8**. It is important to note that only a small portion of spectral overlap is observed, signifying that Förster resonance energy transfer (FRET) is unlikely to occur.

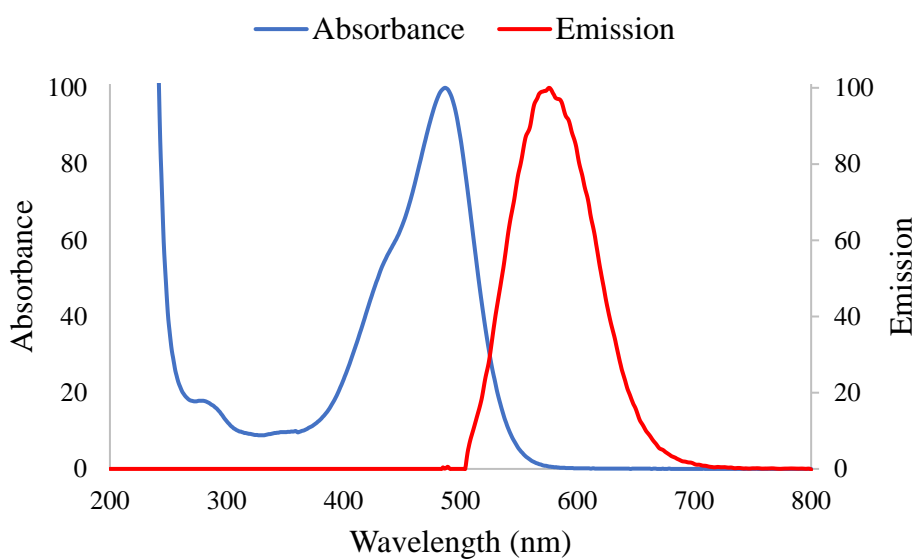


Figure 4.8: Normalised spectra of **D1** showing the absorbance and emission overlap.

$\lambda_{excitation}$: 487 nm

4.5 Application of **D1** and **D2** dimer compounds as chemosensors for metal cations

4.5.1 Screening of metal cations using **D1** and **D2**

The chemosensing abilities of **D1** and **D2** were investigated using emission properties. Even though **D2** did show no photophysical properties, a **D2**-metal complex can still result in an “off-on” type fluorescence mechanism. The screening of metal cations was performed in acetonitrile due to the improved emissions of **D1** in this solvent, as observed in **Figure 4.6**. The metal cations studied include Na^+ , Mg^{2+} , Al^{3+} , K^+ , Ca^{2+} , Cr^{3+} , Mn^{2+} , Fe^{2+} , Fe^{3+} , Co^{3+} , Ni^{2+} , Cu^{2+} , Zn^{2+} , Pb^{2+} , Ag^+ , Cd^{2+} , Ba^{2+} , and Hg^{2+} .

Figure 4.9 displays the emission spectra of **D1** (blue) and various **D1**-metal complexes. In the presence of Ba^{2+} , the fluorescence is enhanced compared to all the other metal cations, which quenched the fluorescence. However, the most noteworthy observation is the Cu^{2+} complex. The copper ions entirely quench the fluorescence of **D1**, whereas Fe^{2+} and other cations only partially quench the fluorescence.

It is known in the literature that metal cations can quench the fluorescence of chemosensors mainly through the heavy atom effect or via spin-orbit coupling.¹⁶ Further research has shown that copper commonly acts as a quencher through the energy/electron transfer processes, resulting in non-fluorescent complexes.⁸

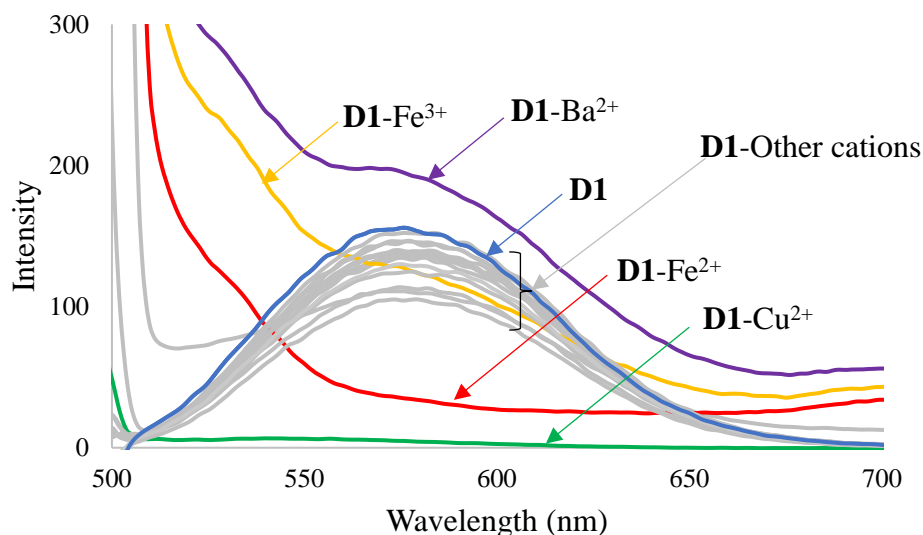


Figure 4.9: Screening various metal cations ($0.167 \mu\text{M}$) in acetonitrile using chemosensor **D1** ($0.0334 \mu\text{M}$). $\lambda_{\text{excitation}}$: 487 nm

Figure 4.10 visually shows the effect of metal cation on **D1**. As seen in **Figure 4.10 a)**, chemosensor **D1** does not display colourimetric sensing properties. When Fe^{2+} , Fe^{3+} and Ba^{2+} were added to a solution of **D1**, a decrease in opaqueness with no colour change was observed in all three samples. In **Figure 4.10 b)**, Fe^{2+} , Fe^{3+} , and Ba^{2+} showed no noticeable effect on the fluorescence. However, a significant quenching effect in the fluorescence of **D1** was observed upon the addition of Cu^{2+} .

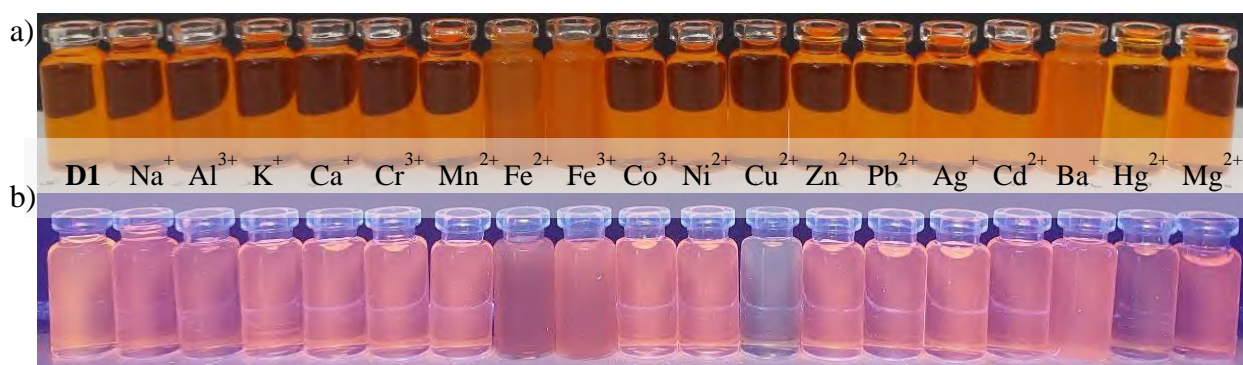


Figure 4.10: Photographic illustration of **D1** compared to **D1-metal** complexes under a)normal light (top) and b) UV-light (bottom, $\lambda_{\text{excitation}}$: 365 nm)

The screening of **D2** was also done to determine if **D2** is an “off-on” type chemosensor for metal cations. The screening was done in acetonitrile at the excitation wavelength of 487 nm . **Figure S 4.31** in the supplementary information show that no emission band was observed, with Fe^{2+} , Fe^{3+} and Ba^{2+} slightly increasing the intensities, although it could just be lagging

scattering from the first-order Rayleigh scattering. Nonetheless, a 3D emissions scan (**Figure S 4.32**) was performed on the **D2**-Ba²⁺ complex to verify that the correct excitation wavelength was used. It was determined that no emission band relating to the **D2**-Ba²⁺ complex could be established. As seen in **Figure 4.11** below, neither colourimetric nor fluorometric responses were observed for the **D2**-metal complexes. Therefore, **D2** could not be used as a chemosensor for detecting metal cations.

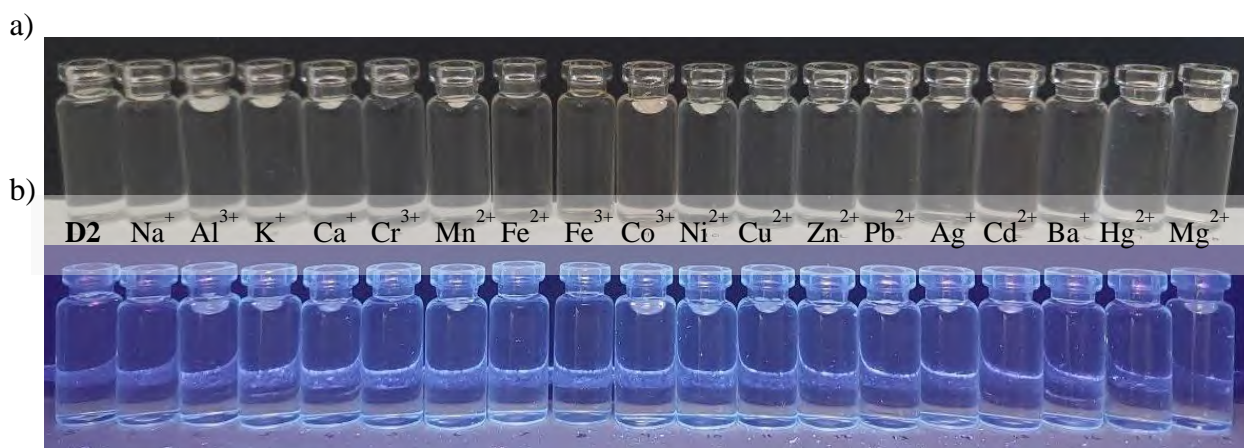


Figure 4.11: Photographic illustration of **D2** compared to **D2**-metal complexes under

a) normal light (top) and b) UV-light (bottom, $\lambda_{excitation}$: 365 nm)

4.5.2 Metal ion competition studies using **D1** as a chemosensor

The competition studies were performed to determine the preference **D1** has towards copper in the presence of competing metal cations. The experiment was done in acetonitrile containing copper (0.167 μ M) and 0.167 μ M of the competing metal cation, and 0.167 μ M of **D1**. The emission spectra were obtained, and the intensity at 573 nm was used to construct **Figure 4.12**. The selectivity of **D1** towards Cu²⁺ was affected by the presence of other metal cations, as seen by the fluctuation in the red bars in **Figure 4.12**. Therefore, the presence of other cations in the solution can significantly affect the detection and quantification of copper.

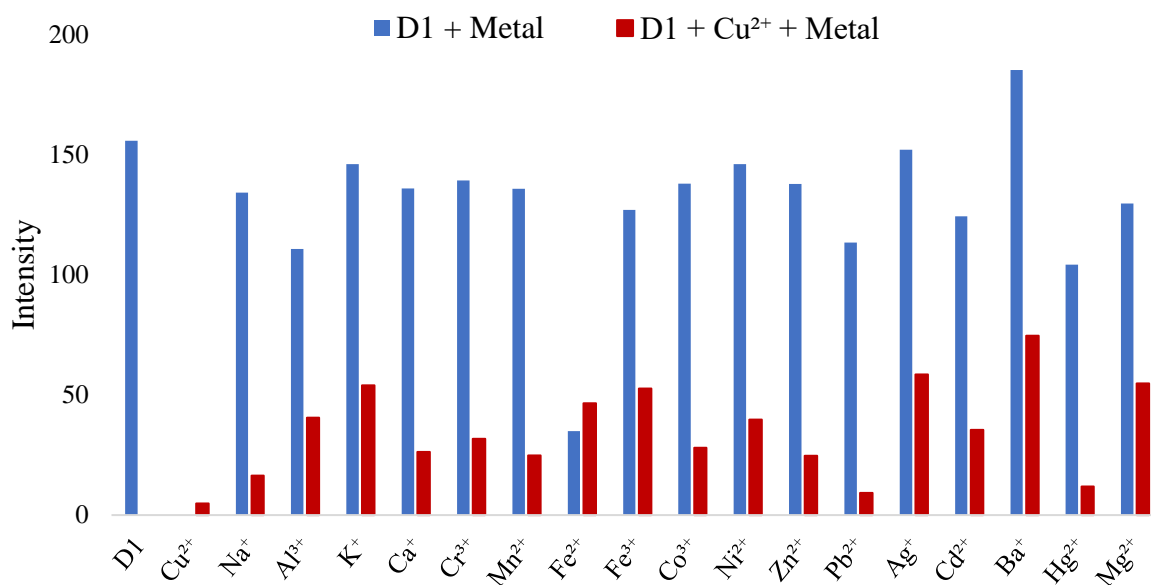


Figure 4.12: Competition studies between **D1**-Cu²⁺ complexes and various competing metal cations measuring the intensity at 573 nm. $\lambda_{excitation}$: 487 nm

4.5.3 **D1** Titrations studies with Cu²⁺

The emission titration of **D1** with Cu²⁺ was conducted in acetonitrile and is shown in **Figure 4.13 a)**. Evidently, as Cu²⁺ was added, the fluorescent intensity of **D1** was gradually quenched until the fluorescence was quenched entirely at a concentration of 1.48 μ M. A calibration curve (emission wavelength of 573 nm) was constructed and shown in **Figure 4.13 b)**. The increase of Cu²⁺ initially resulted in a linear decrease in the emissions, as indicated by the orange portion of the calibration curve. The second part (blue region) showed an exponential decrease in the quenching rate as the amount of Cu²⁺ steadily increased, followed by the saturation point at a concentration of 1.48 μ M. The LOD, LOQ, and endpoint were determined and shown in **Table 4.1** below. The health limit of 31 μ M, set by the WHO⁹, is well above this limit which means that at the tested concentration of **D1**, **D1** was much more sensitive than required. The endpoint refers to the concentration at which the concentration can no longer be accurately measured (shown in **Figure S 4.33** in the supplementary information), while the saturation point refers to the concentration at which the fluorescence is completely quenched.

Table 4.1: Concentrations of interest for Cu^{2+}

	LOD	LOQ	End point	Saturation point	WHO
Cu^{2+}	0.082 μM	0.249 μM	0.795 μM	1.48 μM	31 μM

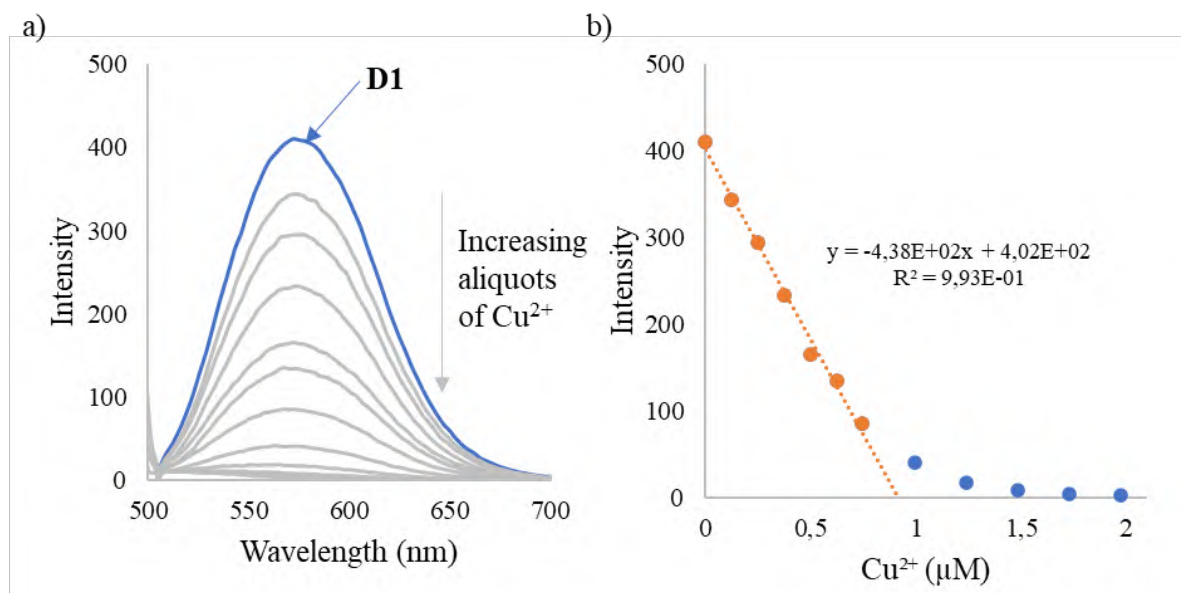


Figure 4.13: a) **D1** (0.1 μM) titration with Cu^{2+} in acetonitrile. b) Calibration curve of **D1**- Cu^{2+} complex (at 573 nm) showing a linear region between 0 and 0.795 μM with R^2 of 0.993. $\lambda_{\text{excitation}}$: 487 nm

4.5.3.1 Benesi-Hildebrand plot of **D1**- Cu^{2+} complex

The Benesi-Hildebrand plot (**Figure 4.14**) was constructed for the **D1**- Cu^{2+} complex using the titration values in the linear region of **Figure 4.13 b**). The association constant was determined to be $41,79 \times 10^4 \text{ M}^{-1}$ using the intercept and the slope ratio. The association constant K_a indicates the strength of the bond between **D1** and Cu^{2+} .¹⁷ This high K_a could explain the formation of chelation quenched fluorescent (CHQF) effect¹⁸ at higher concentrations (blue region of **Figure 4.13**), resulting in a complete quenching process. The linearity of the trend line ($R^2 = 0.994$) further indicates the formation of a 1:1 complex.

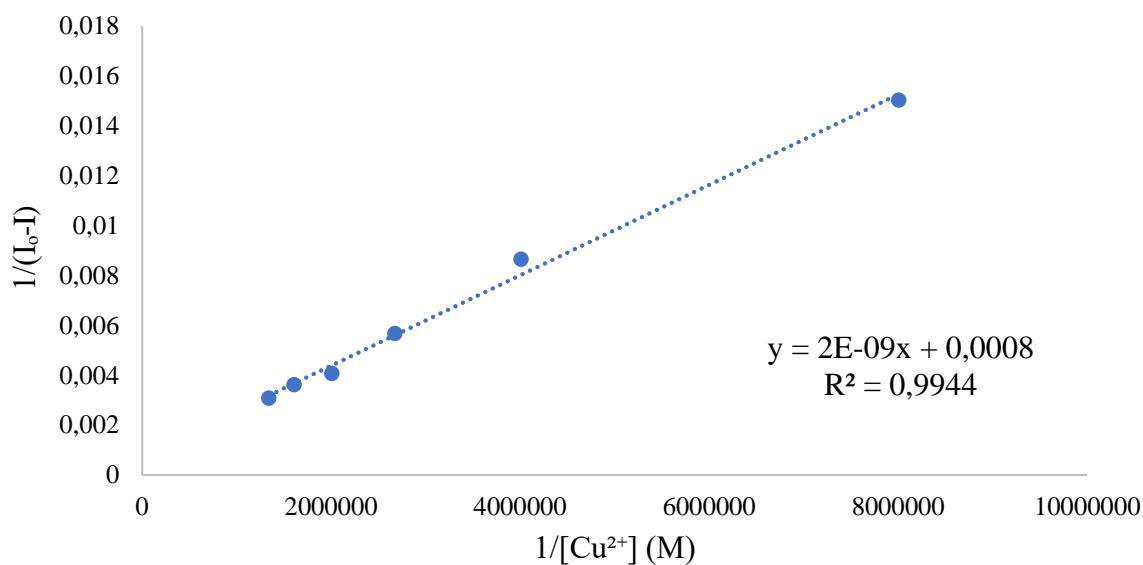


Figure 4.14: Benesi-Hildebrand plot of **D1**- Cu^{2+} complex.

4.5.3.2 Stern-Volmer plot of **D1**- Cu^{2+} complex

The Stern-Volmer plot was then constructed, shown in **Figure 4.15**, to investigate the quenching mode. As seen in **Figure 4.15**, the data deviates slightly from linearity. This indicates that both static and dynamic quenching are likely involved in the quenching process.

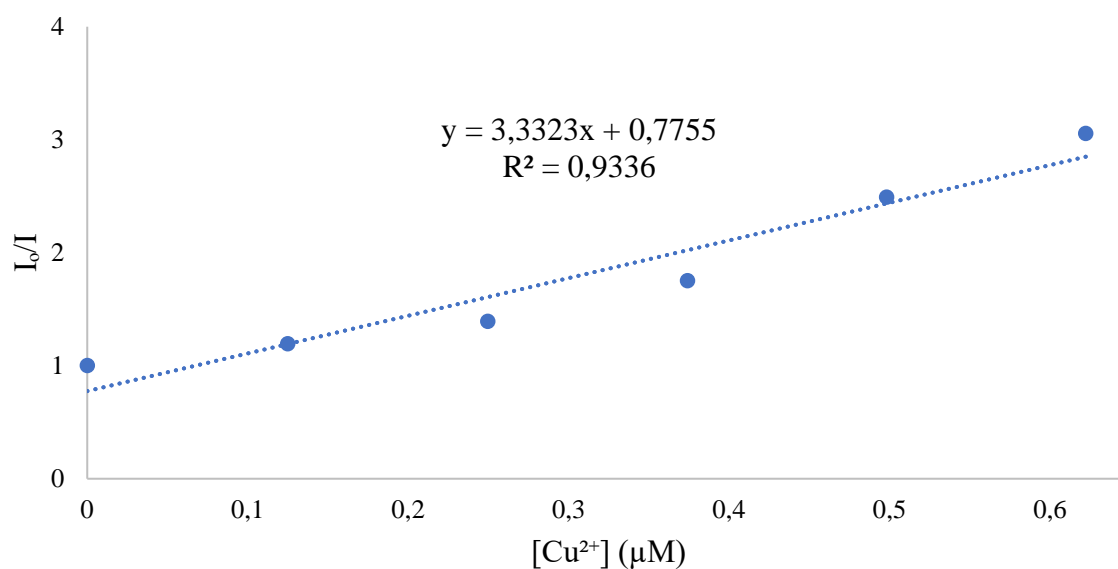
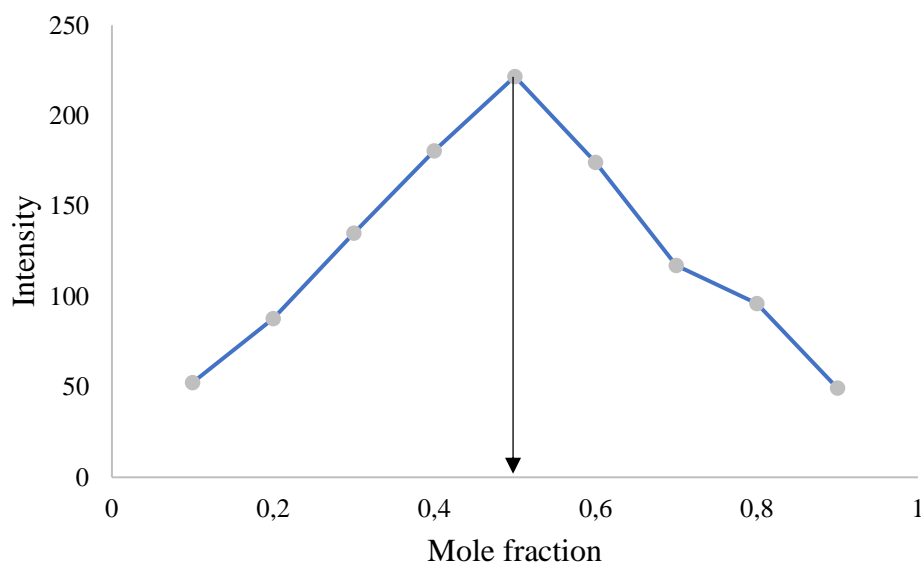


Figure 4.15: Stern-Volmer plot of **D1** with Cu^{2+} .

4.5.3.3 Jobs plot of **D1** with Cu^{2+}

The Jobs experiment was performed in order to determine the binding ratio between **D1** and Cu^{2+} . The Jobs plot in **Figure 4.16** indicated that the binding ratio between **D1** and Cu^{2+} is 1:1.



*Figure 4.16: Jobs plot of **D1** with Cu^{2+} .*

4.5.4 Reversibility studies of **D1**

4.5.4.1 EDTA as chelating agent

Ethylenediaminetetraacetic acid (EDTA) is one of the most common methods to test the reversibility of a chemosensor due to the excellent chelation effects of EDTA.²⁰

Figure S 4.34, in the supplementary information, showed that there is no interaction between **D1** and EDTA. In **Figure 4.17** below, it is evident that the **D1**- Cu^{2+} complex was not reversible, as the emissions of **D1** were slightly regained. However, no increased regenerative emission properties were observed in excess EDTA.

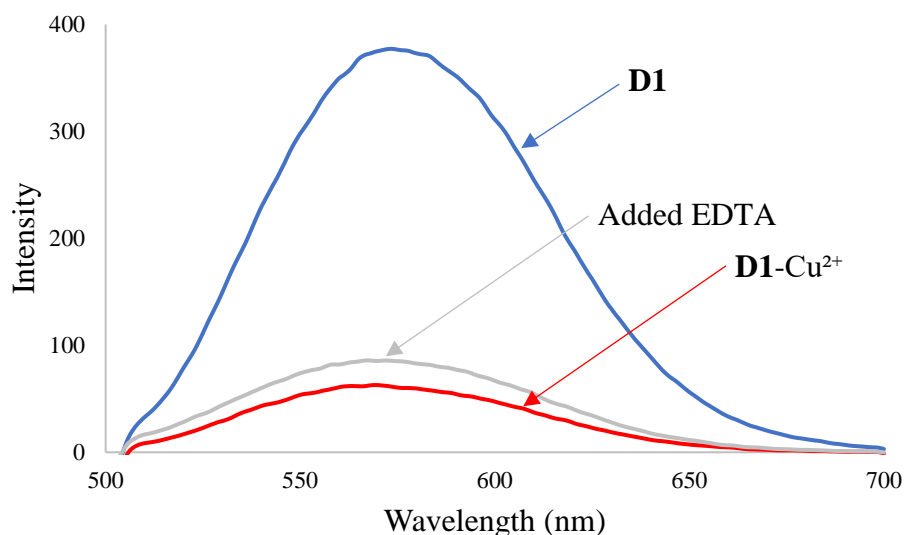


Figure 4.17: Reversibility study of chemosensor **D1** ($0.1 \mu\text{M}$) and Cu^{2+} ($1.25 \mu\text{M}$) with EDTA ($1.25 \mu\text{M}$). $\lambda_{\text{excitation}}$: 487 nm .

4.5.4.2 Ligand displacement detection system for the detection of NC^-

Cao et al. investigated the applicability of a complex-based fluorescence chemosensor for detecting cyanide (NC^-) ions.⁸ The hypothesis was that their chemosensor was selective for Cu^{2+} , which showed an on-off fluorescent effect. However, when NC^- was added, the cyanide and copper could complex, forming the stable $[\text{Cu}(\text{CN})_x]^{n-}$ complex by releasing the chemosensor and resulting in an on-off-on type fluorescent chemosensor or a ligand displacement detection system.⁸

Following Cao et al. method,⁸ the ligand (Cu^{2+}) displacement for detecting NC^- was investigated using a quenched **D1**- Cu^{2+} complex, as shown in **Figure 4.18**. Unfortunately, the fluorescent properties of chemosensor **D1** were not regained in the presence of NC^- . Therefore, the **D1**- Cu^{2+} complex could not be used to detect cyanide, nor was it reversible in the presence of cyanide.

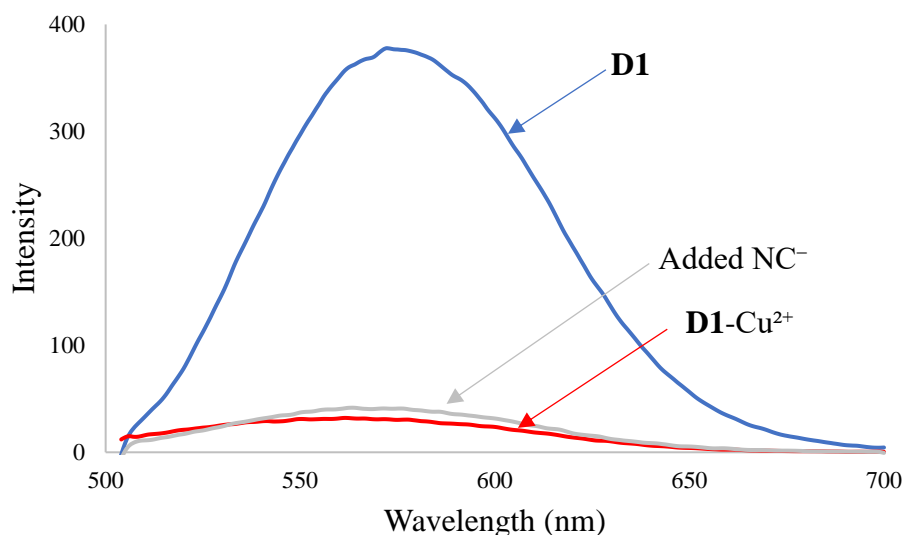


Figure 4.18: Reversibility study of chemosensor **D1** ($0.1 \mu\text{M}$) and Cu^{2+} ($1.25 \mu\text{M}$) using NC^- ($1.25 \mu\text{M}$). $\lambda_{\text{excitation}}$: 487 nm .

4.5.4.3 Sodium ascorbate as a reducing agent

Ascorbic acid, also known as vitamin C, is a widely anti-oxidant that can also be used as a reducing agent.²¹ In reactions such as the Copper-Catalysed Azide-Alkyne Cycloaddition (CuAAC or “Click”) reaction, sodium ascorbate (NaAsc) is used to reduce copper(II) to copper(I), *in situ*, which is needed as a catalyst.^{22–24}

The possibility of using NaAsc to reduce Cu^{2+} to Cu^+ from a quenched **D1**- Cu^{2+} complex was investigated, whereby the results are shown in **Figure 4.19**. Once again, the fluorescence of the complex (**D1**- Cu^{2+}) was not restored. These observations lead to the conclusion that NaAsc could not reduce Cu^{2+} to Cu^+ in solution. This could be attributed to the strength of the interaction between **D1** and Cu^{2+} ions, which does not allow the release of the metal.

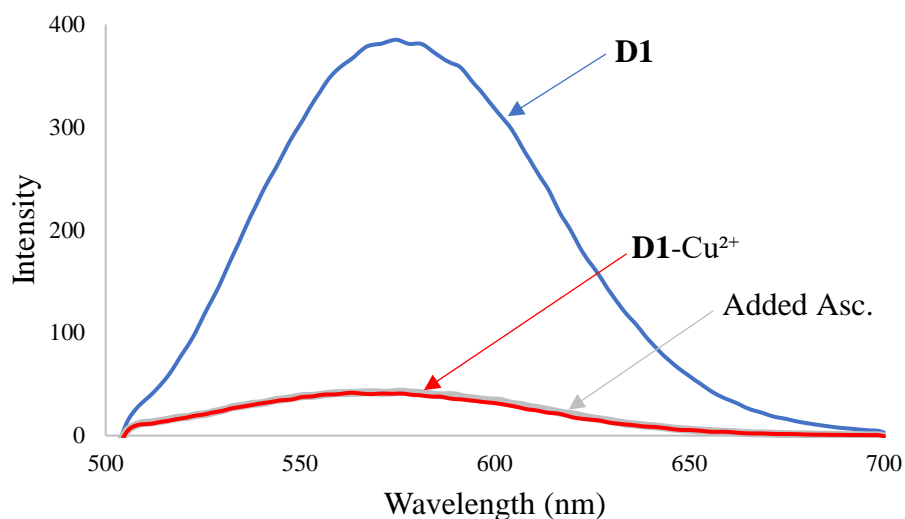


Figure 4.19: Reversibility study of chemosensor **D1** ($0.1 \mu\text{M}$) and Cu^{2+} ($1.25 \mu\text{M}$) using sodium ascorbate (NaAsc , $1.25 \mu\text{M}$). $\lambda_{\text{excitation}}$: 487 nm .

4.5.5 pH studies of **D1** and **D2**

The emission spectra of **D1** and **D2** in different pH buffer solutions (4.8, 6.2, 7.5 and 10.9) were obtained in water to investigate the effects of pH on these compounds' fluorescent properties. As expected, the emission intensity was very low for both **D1** and **D2**, as observed from solvent screening in **Figure 4.6**. However, it was observed in **Figure 4.20** that **D1** displayed better fluorescent properties at a neutral pH (7.5), whereas **D2** emissions (at 573 nm) were enhanced at higher basic solutions (10.9).

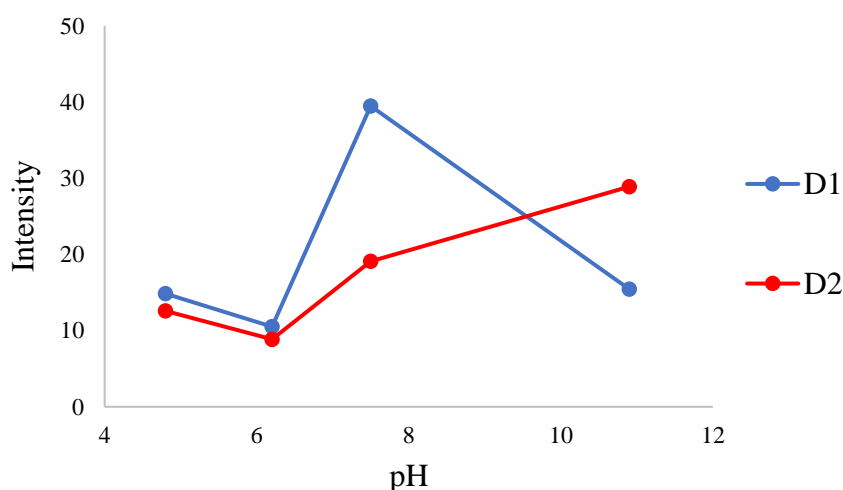


Figure 4.20: pH study of **D1** (blue, $0.1 \mu\text{M}$) and **D2** (red, $0.1 \mu\text{M}$) in aqueous buffer solutions. $\lambda_{\text{excitation}}$: 487 nm .

Further investigation into the detection ability of **D1** in various pH solutions was conducted in which the emissions of the **D1**-Cu²⁺ complex were measured at these different pH ranges. **Figure 4.21** indicates that the copper ions quench the fluorescence of **D1** (emission wavelength of 573 nm) over the entire pH range tested. It has been observed in the literature that it is easier to detect heavy metal ions in organic solvents than directly using aqueous solutions due to the strong hydration of water.¹

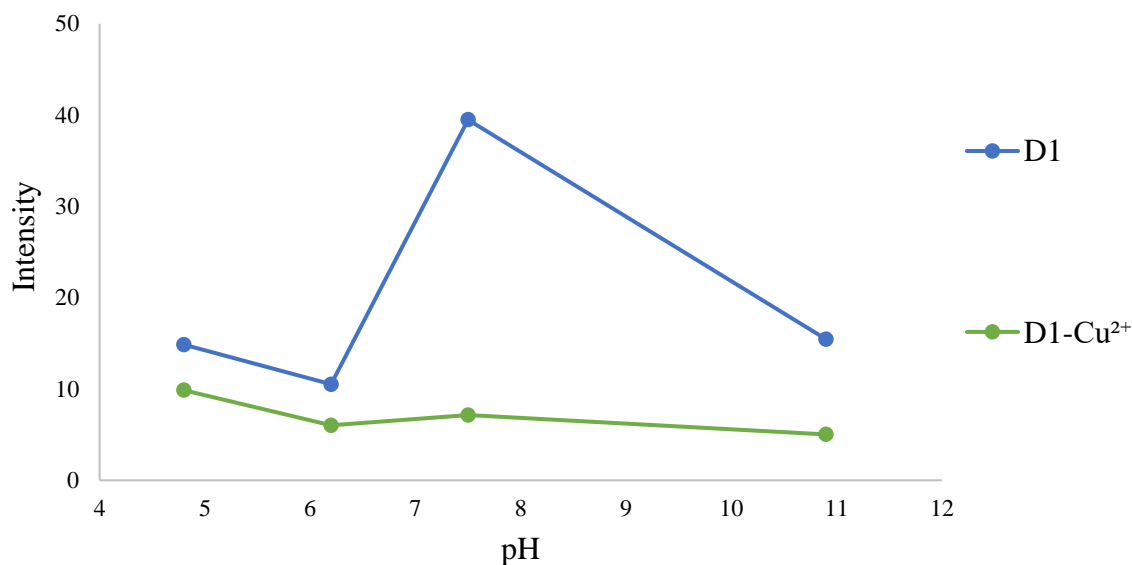


Figure 4.21: pH study of **D1** (blue, 0.1 μ M) and **D1**-Cu²⁺ (green) in aqueous buffer solutions. $\lambda_{excitation}$: 487 nm.

4.6 Application of **D1** and **D2** dimer compounds as chemosensors for anions

4.6.1 Screening of anions

The development of anion chemosensors has gained much attention as a field of study due to their numerous applications in pharmacy, biology, analytics, forensics, catalysis, green chemistry, environment and separating mixtures of anions in industrial systems and biochemical processes.^{25,26} Halide ions are commonly found in nature and have a variety of important biological functionalities. However, halide ions in excess may also be toxic to biological organisms. Due to the toxic effects of these anions, there is a need for a fast and inexpensive method to detect anions.²⁷

The anionic chemosensor properties of **D1** and **D2** were determined in acetonitrile and using anions such as F^- , Cl^- , Br^- , I^- , AcO^- , NC^- , NCS^- , NCO^- , $H_2PO_4^-$, and HSO_4^- . The screening of these anions with **D1** is shown in **Figure 4.22**. It can be seen in **Figure 4.22** that all the tested anions slightly quenched the fluorescence of **D1** with no selectivity observed. Hence **D1** was concluded not to be a good chemosensor for anions.

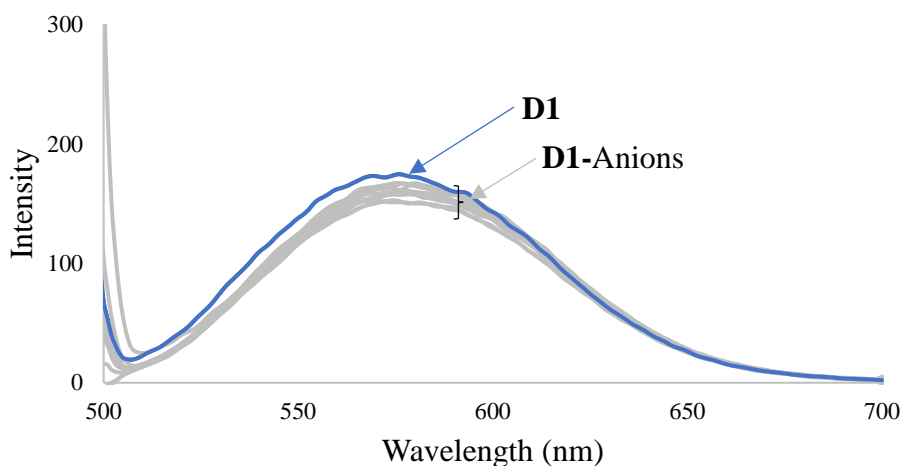


Figure 4.22: Screening of **D1** ($0.0334 \mu M$) with various anions ($0.167 \mu M$) in acetonitrile. $\lambda_{excitation}$: 487 nm.

In **Figure 4.23 a)**, no colourimetric effect can be observed for the samples containing anions. Furthermore, in **Figure 4.23 b)**, it is observed that the fluorescence was quenched due to the presence of the anions; however, no distinguishing features were observed between the various samples.

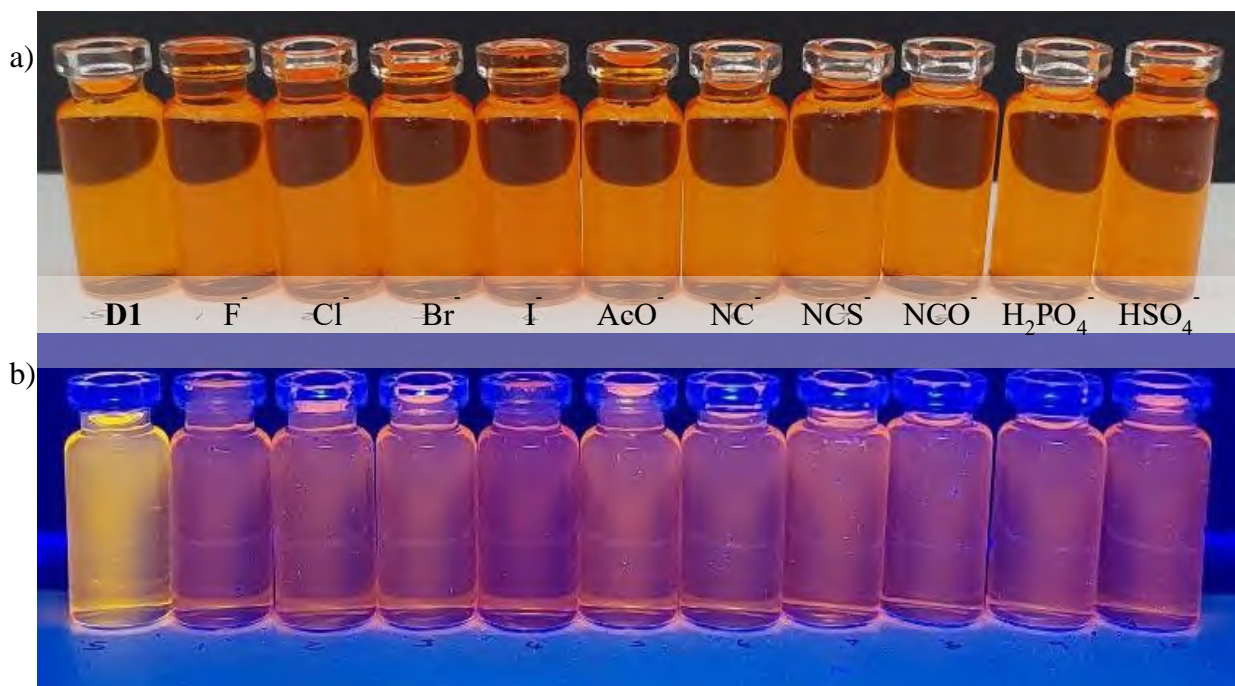


Figure 4.23: Photographic illustration of **D1** in the presence of various anions in a) normal light and b) UV light ($\lambda_{\text{excitation}}$: 365 nm).

The anionic screening was also done for **D2**. However, no colourimetric nor fluorometric chemosensor responses were observed, as seen in **Figure 4.24** and **Figure 4.25**.

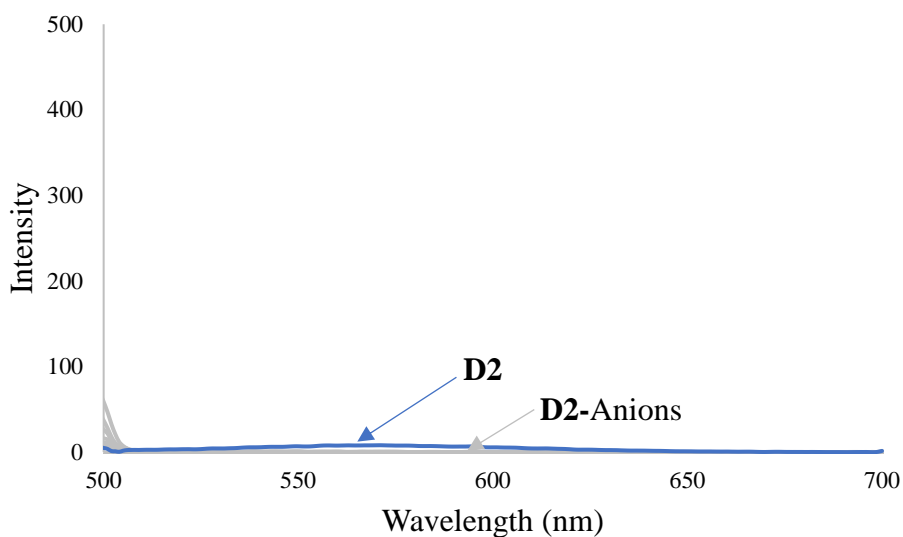


Figure 4.24: Screening of **D2** ($0.0334 \mu\text{M}$) with various anions ($0.167 \mu\text{M}$) in acetonitrile. $\lambda_{\text{excitation}}$: 487 nm.

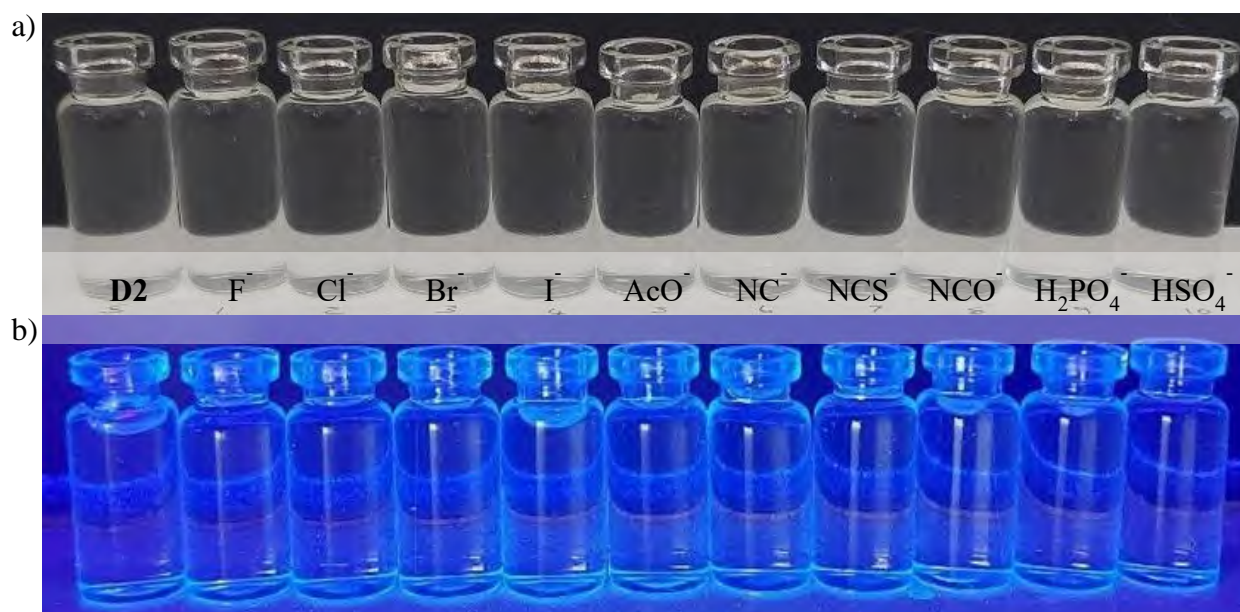


Figure 4.25: Photographic illustration of **D2** in the presence of various anions in a) normal light and b) UV light ($\lambda_{\text{excitation}}$: 365 nm).

4.7 The proposed binding site and computational studies

Copper(II) has a $3d^9$ electron configuration with a coordination number around the copper centre, ranging between four and six.^{28,29} Therefore, copper complexes can be tetrahedral, square planar, trigonal bipyramidal, square pyramidal, octahedral or trigonal prismatic. The possible binding site was investigated using NMR titrations and molecular modelling studies.

4.7.1 NMR titrations of **D1** with Cu^{2+}

In deuterated acetonitrile, NMR titration studies were performed on **D1** and the **D1**- Cu^{2+} complex and were used to determine the interaction sites. Proton (**Figure S 4.8**), carbon (**Figure S 4.10**), DEPT-135 (**Figure S 4.11**) and HSQC (**Figure S 4.12**) NMR experiments are shown in the supplementary information and were used to identify and assign the peaks to the corresponding atom in **D1**.

The proton NMR of chemosensor **D1** (**Figure 4.26 b**) was compared to that of the **D1**- Cu^{2+} complex (**Figure 4.26 a**) and is shown in **Figure 4.26**. The presence of Cu^{2+} impacts the chemical environment of the enone moiety, as seen by the complete disappearance of the α -hydrogen peak and the reduced intensity of the β -hydrogen peak. This can either indicate that

the α -hydrogen directly interacts with the metal cation or that the carbonyl group from the enone moiety is the main site of binding.

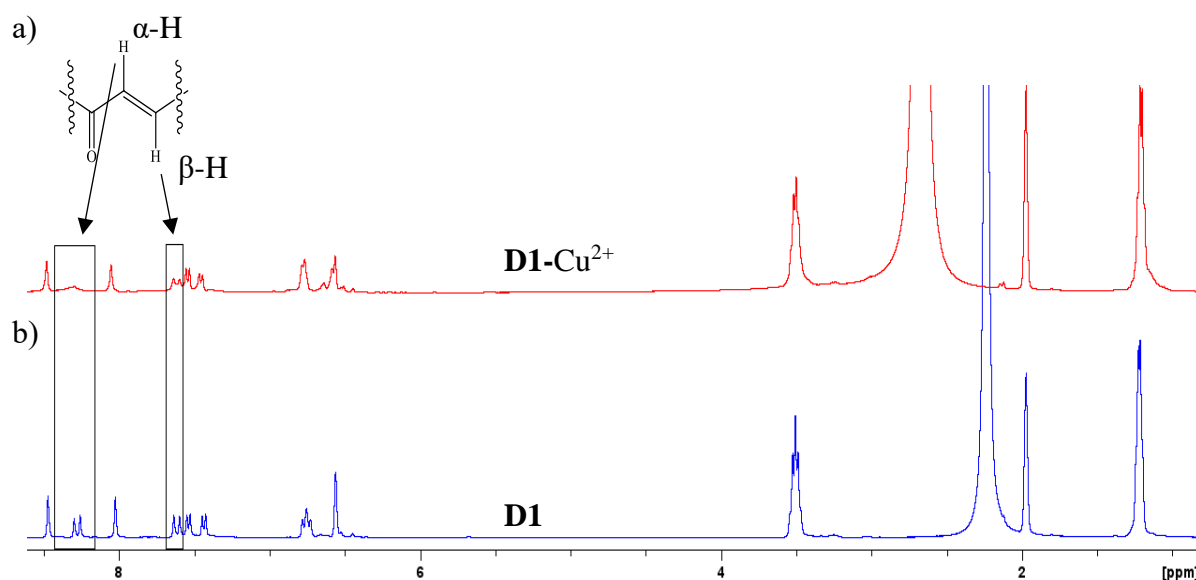


Figure 4.26: ^1H NMR of a) D1-Cu^{2+} complex and b) D1 in acetonitrile showing the effect of the complex formation on the enone moiety.

^{13}C NMR spectra of **D1** (**Figure 4.27 b**) and copper complex (**Figure 4.27 a**) were obtained to investigate the involvement of the carbonyl carbons in the enone moiety and from the coumarin chromophores. The carbonyl carbon from the enone moiety is shown in the blue oval in **Figure 4.27**; the intensity of this peak was significantly reduced in the presence of Cu^{2+} . This reduction in the intensity was also observed for the coumarin moiety carbonyl peaks (indicated by the triangle), but to a lesser extent. This can suggest that either one of the carbonyls interacts with copper. Alternately, both carbonyls could be involved in the complexation; however, the effect is shared by both carbons. Furthermore, the $\beta\text{-CH}$ (indicated with the star) was barely affected, as was seen by the ^1H NMR (**Figure 4.26**), whereas the $\alpha\text{-CH}$ peak (highlighted by the black box) has completely disappeared. Lastly, a new peak was observed at 40 ppm (indicated by the diamond).

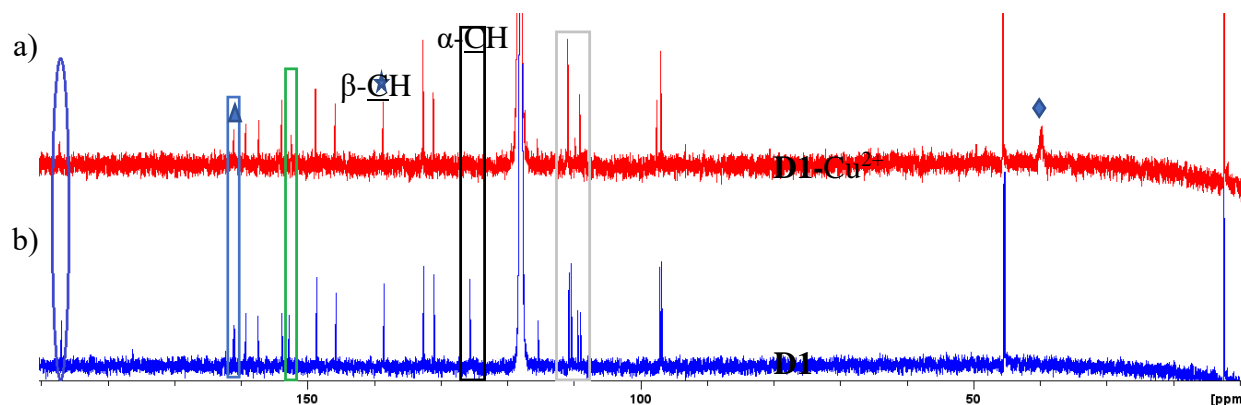
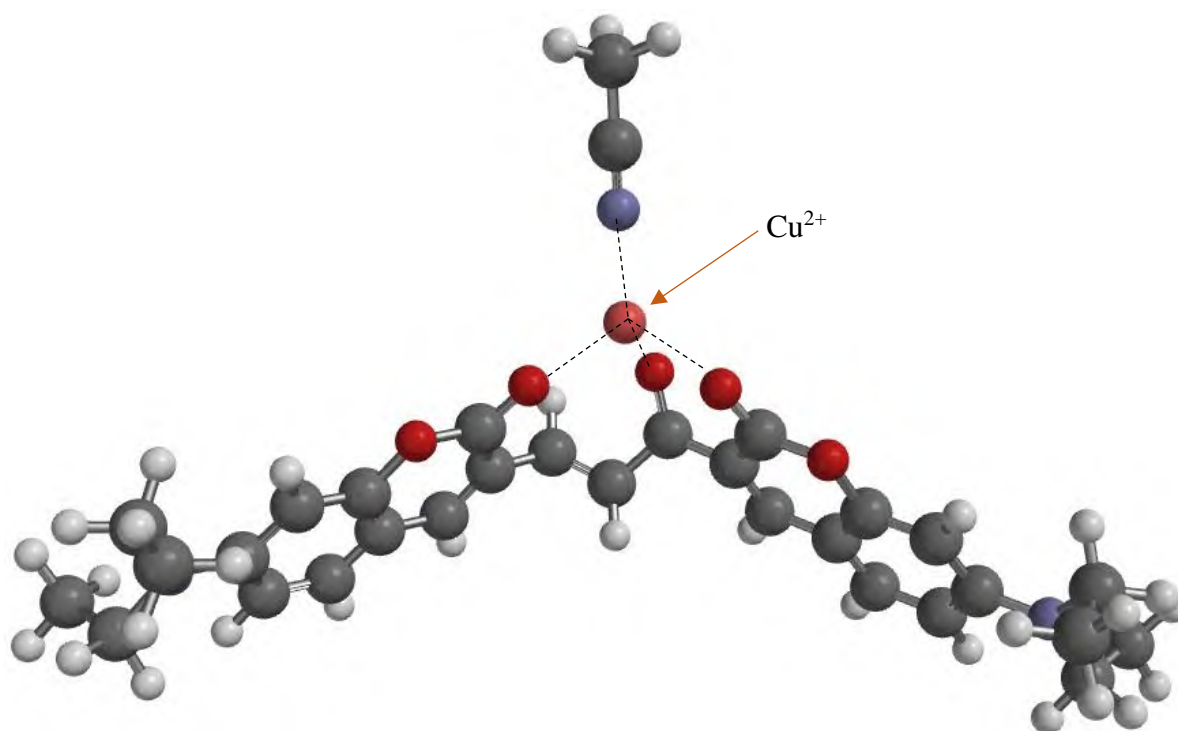


Figure 4.27: ^{13}C NMR of a) **D1**- Cu^{2+} complex and b) **D1** in acetonitrile.

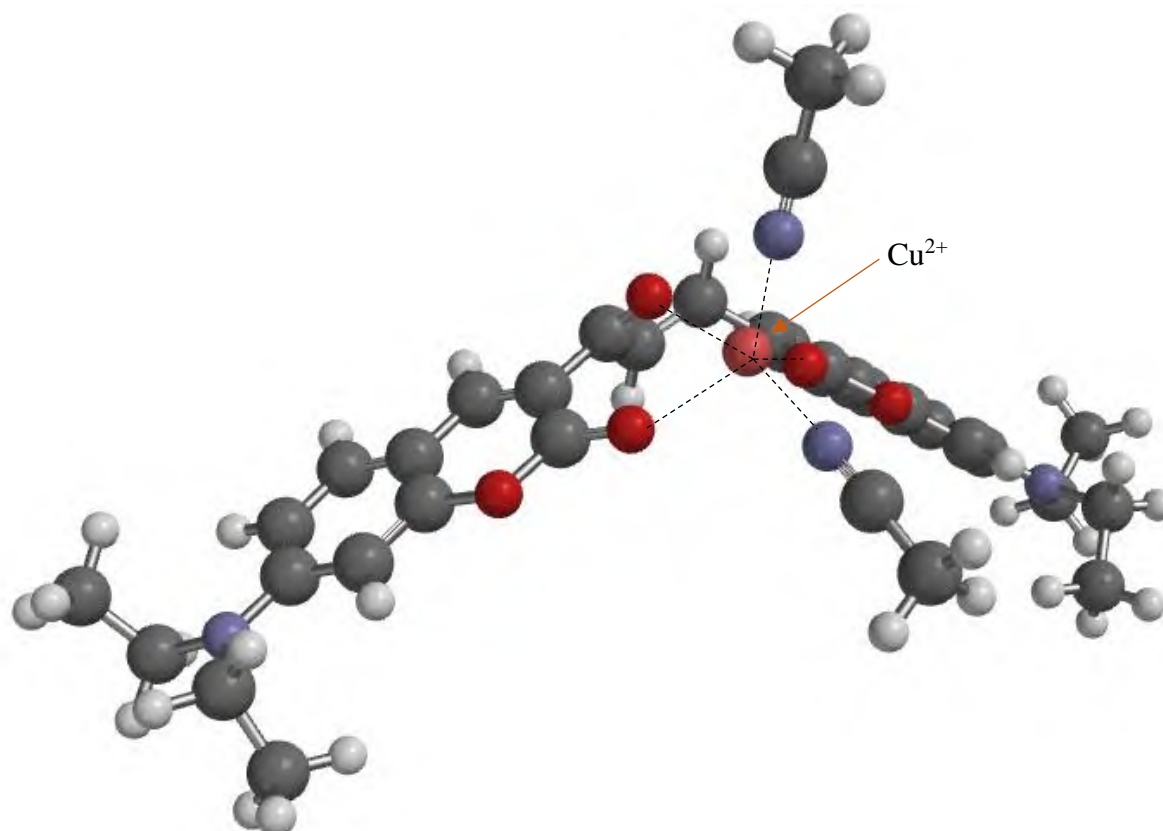
4.7.2 Molecular modelling of complexation between **D1** and Cu^{2+}

Copper(II) is versatile regarding the coordination number. As mentioned earlier, copper can form coordination with four and six ligands.^{28,29} However, seven-coordinated complexes rarely forms due to their destabilising nature.³⁰

As seen in **Figure 4.28** (complex 1), Cu^{2+} forms a complex with **D1** by interacting with both lactone carbonyl and the enone carbonyl and one acetonitrile ligand to form a tetrahedral geometry with the copper atom at the centre. In this scenario, the copper has a coordination number of four. This complexation geometry can be disregarded as the NMR experiments indicated that not all the lactone carbonyls interact with the copper. **Table 4.2** also shows the highest energy levels for complex 1 compared to the other possible complexes. With the addition of another acetonitrile molecule, **Figure 4.29** (complex 2), the geometry changes to a five-coordinated square pyramidal complex with Cu^{2+} at the centre. As with complex 1, complex 2 also interact with all three carbonyl oxygens, and although more stable, still relatively high energy thus can also be disregarded.



*Figure 4.28: Complex 1, a four-coordinate **DI**-Cu²⁺ complex with one acetonitrile molecule.*



*Figure 4.29: Complex 2, a five-coordinate **DI**-Cu²⁺ complex with two acetonitrile molecules.*

With three acetonitrile molecules in the copper coordination complex, complex 3 in **Figure 4.30** shows that the coordination geometry remained square pyramidal as with complex 2. In complex 3, the one lactone carbonyl was replaced with an acetonitrile molecule, resulting in a relatively significant change in the energy level of the complex. The remaining carbonyls form a stable six-membered ring with copper. This complexation scenario corresponds with the NMR experiments, which indicated that the enone carbonyl and one of the lactone carbonyls interact with copper cation to form complex 3.

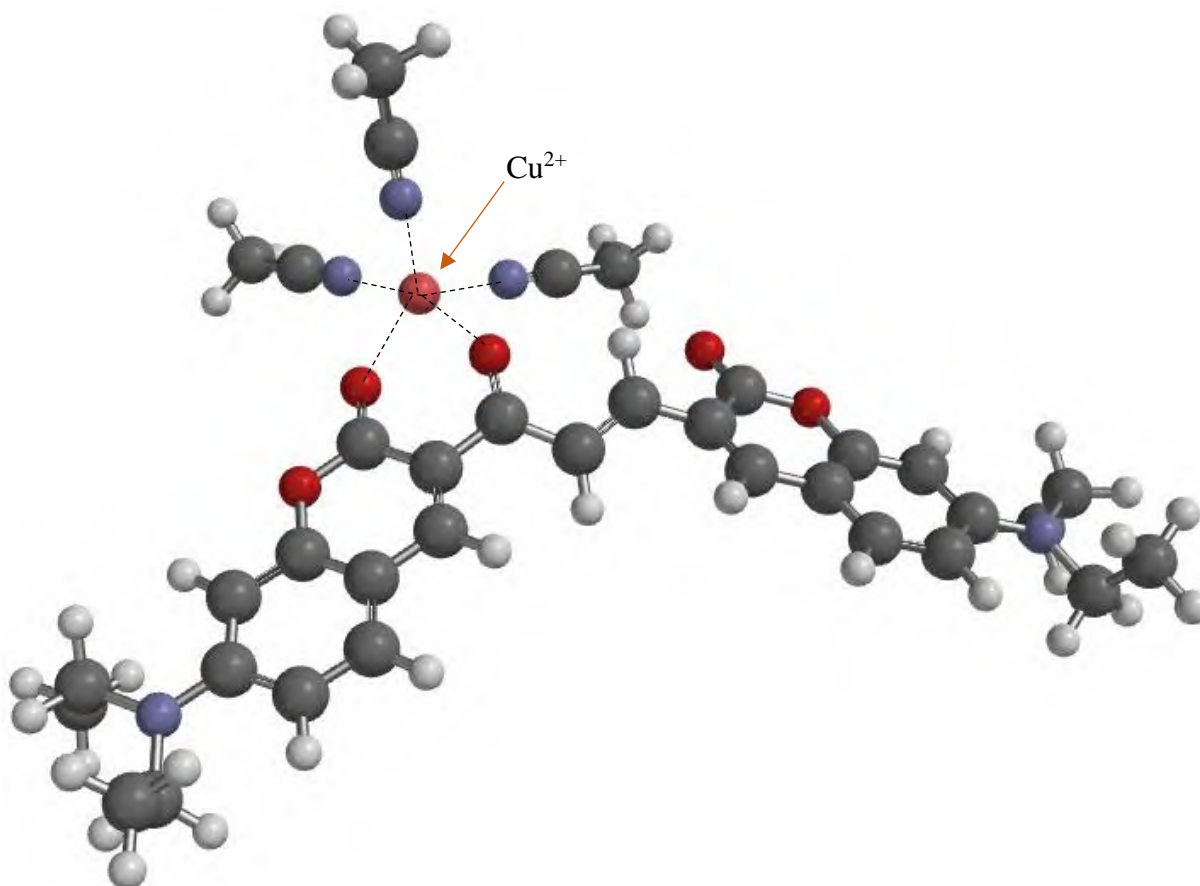


Figure 4.30: Complex 3, a five-coordination $D1\text{-Cu}^{2+}$ complex with three acetonitrile molecules as co-ligands.

Complex 4 (**Figure 4.31**) is a six-coordinated octahedral copper complex containing four acetonitrile ligands and two carbonyl oxygens, as in complex 3. At close inspection, distortion in the octahedral geometry is observed, in which the two perpendicular groups, one acetonitrile and the enone carbonyl, are further away than the plainer groups. In addition, three acetonitrile molecules and the lactone carbonyl formed part of the octahedral complex. This distortion could be explained by the Jahn-Teller effect, which reduces the symmetry and energy of the

complex.^{28,30} This accounts for the lower energy observed in **Table 4.2**. However, this contradicts the NMR experiments, which showed strong interaction with the enone moiety and the disappearance of the α -hydrogen peak. Thus, even though complex 4 was lower in energy compared to complex 3, the experimental measurements indicate that complex 3 is most likely to be the main form of complex formed between **D1** and Cu^{2+} .

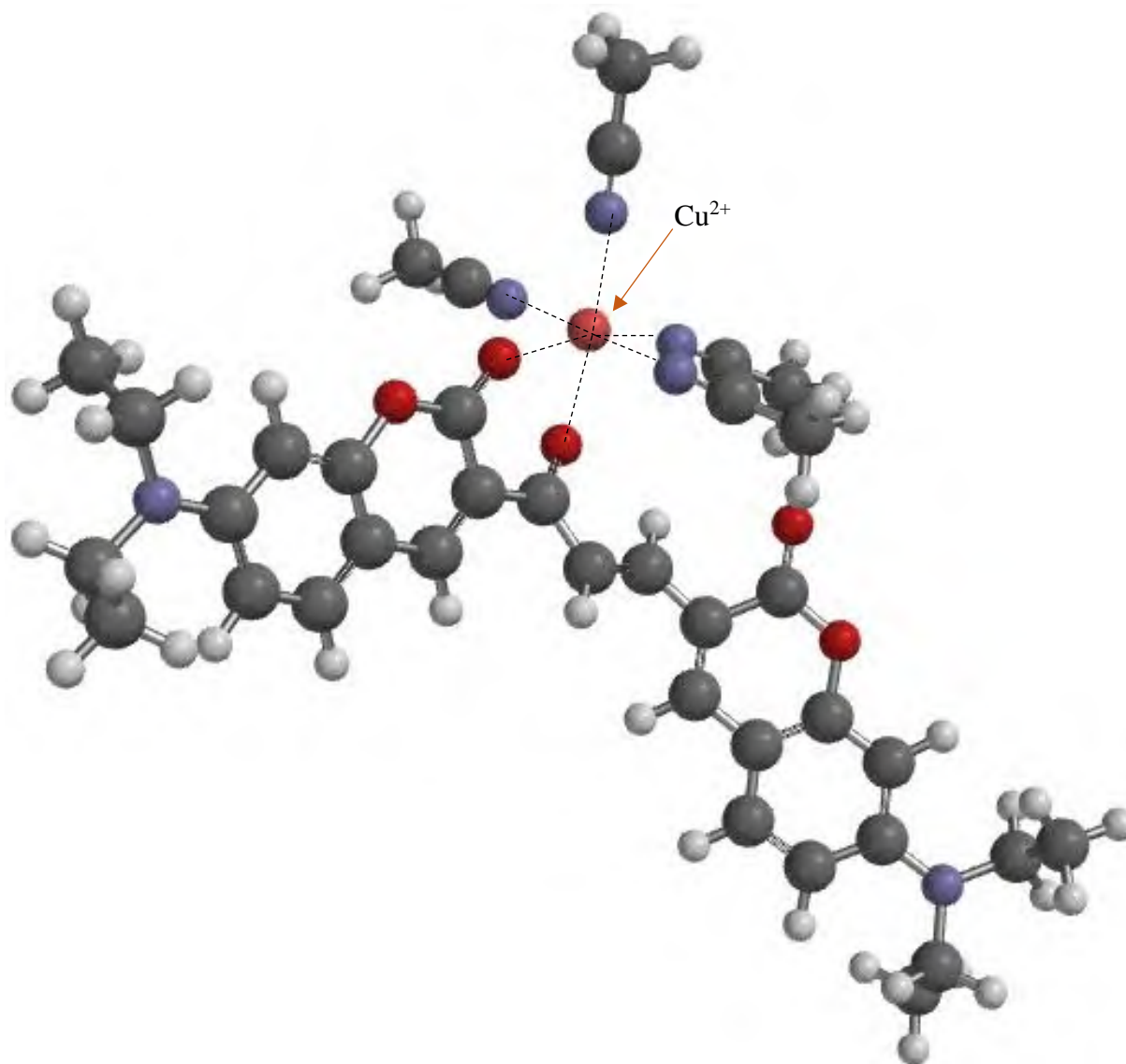


Figure 4.31: Six-coordination **D1**- Cu^{2+} complex with four acetonitrile molecules as co-ligand.

With the addition of another acetonitrile molecule, a seven-coordinated complex was formed; according to the literature, seven-coordination complexes are highly unstable and, therefore, were not considered to be possible in this experiment.

Table 4.2: Coordination complexes of **D1**-Cu²⁺

Figure Number	Coordination Number	Geometry	Energy (kJ/mol)	Number of CH ₃ CN
Figure 4.28	4	Tetrahedral	-299.35	1
Figure 4.29	5	Square pyramidal	-479.93	2
Figure 4.30	5	Square pyramidal	-639.32	3
Figure 4.31	6	Octahedral	-781.24	4

4.8 Conclusion

In this study, two dimeric coumarin chemosensors containing an enone linker were successfully synthesised. One chemosensor has a diethylamino EDG at position seven, **D1**, and the other has an ethoxy EDG at position eight, **D2**. The diethylamino EDG compound **D1** reacted faster than the weaker ethoxy EDG compound **D2**, which reacted for 48 hours, and this slower reactivity was supported by the literature.

The fluorescent properties of **D1** and **D2** were investigated in acetonitrile. It was observed that **D2** was inert in both UV-vis and fluorescence spectra even in the presence of various analytes (and in six different solvents); thus, **D2** can not be used as an “off-on” chemosensor. **D1** had a maximum absorbance band at 487 nm resulting in a maximum emission band at 573 nm. **D1** interacted with all metal cations tested, but Cu²⁺ resulted in complete fluorescence quenching. Competition studies were also done, which revealed that **D1** does not selectively bind to copper as other metals interfere in its complexation.

Further titration studies revealed that the complexation is linear and quantifiable between 0.249 µM to 0.795 µM with a LOD of 0.082 µM. After 0.795 µM, the quenching is exponential, with complete quenching occurring at 1.48 µM of Cu²⁺. The Stern-Volmer plot indicated that static quenching is the main form of quenching with some dynamic quenching present. The Benesi-Hildebrand plot and Job’s plot showed a 1:1 binding ratio between **D1** and Cu²⁺. Reversibility studies using EDTA, cyanide and sodium ascorbate were unsuccessful; therefore, **D1** can only be used as a once-off Cu²⁺ chemosensor. The lack of reversibility and the low

selectivity in the presence of competing cations suggest that chemosensor **D1** easily forms complexes with any cation. However, when chemosensor **D1** complex with Cu^{2+} , a very stable complex is formed, which evidently can not be separated.

D1 and **D2** were also tested for their anionic chemosensor abilities, to which no identifiable changes were observed in the emission spectra.

Molecular modelling studies illustrated and confirmed the binding site between **D1** and Cu^{2+} . The binding site was concluded to be between the lactone ring's carbonyl and the enone linker's adjacent carbonyl, forming a six-coordinated square pyramidal complex containing three acetonitrile molecules as co-ligands. This complex configuration corresponded with the experimental NMR data obtained.

4.9 Experimental

4.9.1 General information

All starting materials and solvents were purchased from Sigma Aldrich or Merck and used as received without further purification unless otherwise stated.

^1H NMR and ^{13}C NMR spectra were recorded on a Bruker Advance DPX 400 (400 MHz) spectrometer. The NMR samples were prepared in deuterated solvents (CDCl_3 , DMSO-d_6 , and Acetonitrile- d_3). The samples were run at room temperature. Chemical shifts are expressed in parts per million (ppm) using trimethyl silane (TMS) as the internal reference.

Infrared FT-IR spectra were recorded on a Bruker TENSOR 27 FT-IR spectrometer.

Thin layer chromatography (TLC) analyses were performed on pre-coated silica gel 60 F254 aluminium sheets (0.063-0.2 mm/70 - 230 mesh) using a 50:50% solution of ethyl acetate: hexane; compounds were detected by observation under UV light or exposure to iodine vapour.

UV-Vis absorbance studies were recorded on a Shimadzu UV-3100 spectrophotometer with a 1 cm quartz cuvette (3 mL). Spectroscopic measurements were performed after each aliquot of selected cationic and anionic solutions.

Stock solutions of the sensors (0.01 M) were prepared by dissolving the samples in acetonitrile and diluting them to the desired concentrations. Metal cations (0.05 M) solutions were prepared using the nitrate salts (except for Fe^{2+} , which used the sulphate salt) and dissolved in Millipore water. The anion (0.05 M) solutions were prepared using the tetrabutylammonium salts and dissolved in Millipore water.

Computational chemistry, Spartan Student Version 8.0.6, Oct 8 2020, was utilised to compare and visually illustrate different conformers of free chemosensors and complexes. The conformers were obtained by conformer distribution at the MMFF level. Calculations of the most energetically preferred conformation were determined by equilibrium geometry at the PM3 level.

The detection limit (LOD) and quantification (LOQ) were calculated according to the equation:

$$LOD = 3.3 \times \frac{\sigma}{m}$$

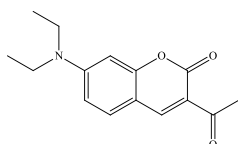
$$LOQ = 10 \times \frac{\sigma}{m}$$

Where σ is the standard deviation and m is the slope of the trend line.

pH studies were conducted in a 1:2 ratio water to buffer solution to which the chemosensor was added. Buffer solutions were bought from Merck.

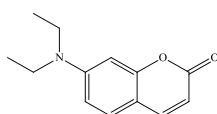
4.9.2 Synthesis of compounds

4.9.2.1 3-acetyl-7-(diethylamino)-2H-chromen-2-one – **E1**



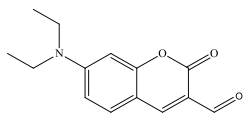
E1 was synthesised according to known literature procedure.³¹ IR ν_{\max} (cm^{-1}): 3114-2972 (C-H stretching, Alkene), 1704 (C=O stretching, Lactone ring), 1679 (C=O, Ketone). ^1H NMR (CDCl_3): $\delta_{\text{H}}/\text{ppm}$ = 8.45 (1H, s, Aromatic H), 7.42-7.40 (1H, d, Aromatic H), 6.65-6.62 (1H, m, Aromatic H), 6.49 (1H, s, Aromatic H), 3.50-3.45 (4H, q, $-\text{CH}_2-\text{CH}_3$), 2.70 (3H, s, $-\text{CH}_3$), 1.28-1.24 (6H, t, $-\text{CH}_2-\text{CH}_3$). ^{13}C NMR (CDCl_3) $\delta_{\text{C}}/\text{ppm}$ = 195.74, 160.88, 158.77, 153.03, 147.86, 131.90, 116.13, 109.85, 108.18, 96.60, 45.15, 30.58, 12.44.

4.9.2.2 7-(diethylamino)-2H-chromen-2-one – **1**



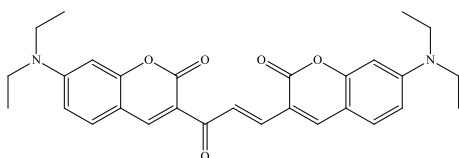
1 Was synthesised according to known literature procedure.³² IR ν_{\max} (cm^{-1}): 3069-2981 (C-H stretching, Alkene), 1702 (C=O stretching, Lactone ring). ^1H NMR (DMSO): $\delta_{\text{H}}/\text{ppm}$ = 7.83-7.80 (1H, d, Aromatic H), 7.43-7.41 (1H, d, Aromatic H), 6.69-6.67 (1H, d, Aromatic H), 6.51 (1H, s, Aromatic H), 6.00-5.97 (1H, d, Aromatic H), 3.43-3.40 (4H, q, $-\text{CH}_2-\text{CH}_3$), 1.13-1.10 (6H, t, $-\text{CH}_2-\text{CH}_3$). ^{13}C NMR (DMSO) $\delta_{\text{C}}/\text{ppm}$ = 161.47, 156.81, 150.95, 144.94, 129.76, 109.25, 108.64, 108.13, 97.08, 44.49, 12.76.

4.9.2.3 7-(diethylamino)-2-oxo-2H-chromene-3-carbaldehyde – 2



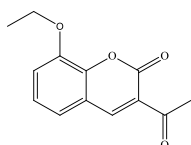
2 Was synthesised according to known literature procedure.³² ^1H NMR (DMSO): $\delta_{\text{H}}/\text{ppm}$ = 9.90 (1H, s, $-\text{HC}=\text{O}$), 8.45 (1H, s, Aromatic H), 7.70-7.68 (1H, d, Aromatic H), 6.85-6.82 (1H, d, Aromatic H), 6.62 (1H, s, Aromatic H), 3.55-3.49 (4H, q, $-\text{CH}_2-\text{CH}_3$), 1.18-1.14 (6H, t, $-\text{CH}_2-\text{CH}_3$).

4.9.2.4 (E)-3,3'-acryloylbis(7-(diethylamino)-2H-chromen-2-one) – D1



7-(diethylamino)-2H-chromen-2-one, **1**, (1.01 g, 3.90 mmol) and 7-(diethylamino)-2-oxo-2H-chromene-3-carbaldehyde, **2**, (0.84 g, 6.17 mmol) was reflux with a few drops of piperidine for 24 hours in absolute ethanol. After the time had elapsed, the mixture was poured into the ice-cold water resulting in a fine precipitate forming. The product was filtered and recrystallised from ethanol.¹³ IR ν_{max} (cm^{-1}): 2971-2927 (C-H stretching, Alkene), 1703 (C=O stretching, Lactone ring), 1638 (C=O, Enone). ^1H NMR (DMSO): $\delta_{\text{H}}/\text{ppm}$ = 8.55 (1H, s, Aromatic H), 8.29 (1H, s, Aromatic H), 8.20-8.16 (1H, d, $\text{CH}=\text{CH}$, $J = 15.29$ Hz), 7.69-7.67 (1H, d, Aromatic H), 7.61-7.57 (1H, d, $\text{CH}=\text{CH}$, $J = 15.29$ Hz), 7.54-7.52 (1H, d, Aromatic H), 6.82-6.77 (2H, q, Aromatic H), 6.61-6.59 (2H, d, Aromatic H), 3.52-3.48 (8H, q, $-\text{CH}_2-\text{CH}_3$), 1.16-1.15 (12H, t, $-\text{CH}_2-\text{CH}_3$). ^{13}C NMR (DMSO) $\delta_{\text{C}}/\text{ppm}$ = 153.37, 147.66, 145.84, 138.40, 131.33, 124.98, 116.27, 114.46, 111.19, 110.29, 108.85, 96.69, 96.39, 44.92, 44.79, 12.84.

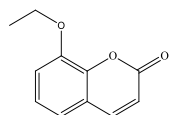
4.9.2.5 3-acetyl-8-ethoxy-2H-chromen-2-one – 3



3 Was synthesised according to known literature procedure, 3-ethoxysalicylaldehyde was used instead of 4-(diethylamino)salicylaldehyde.³¹ IR ν_{max} (cm^{-1}): 2979-2876 (C-H stretching,

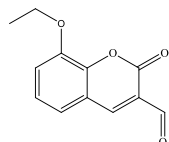
Alkene), 1703 (C=O stretching, Lactone ring), 1635 (C=O, Ketone). ^1H NMR (DMSO): $\delta_{\text{H}}/\text{ppm}$ = 8.60 (1H, s, Aromatic H), 7.47-7.31 (3H, m, Aromatic H), 4.22-4.16 (2H, q, -CH₂-CH₃), 2.28 (3H, s, -CH₃), 1.43-1.39 (3H, t, -CH₂-CH₃). ^{13}C NMR (DMSO) $\delta_{\text{C}}/\text{ppm}$ = 195.64, 158.68, 147.75, 145.93, 144.47, 125.32, 124.94, 122.07, 119.23, 117.76, 65.00, 30.46, 15.01.

4.9.2.6 8-ethoxy-2H-chromen-2-one – 4



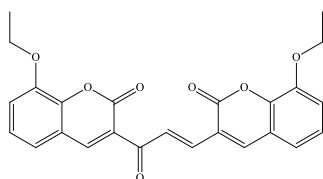
4 Was synthesised according to known literature procedure, 3-ethoxysalicylaldehyde was used instead of 4-(diethylamino)salicylaldehyde.³² IR ν_{max} (cm⁻¹): 3095-2889 (C-H stretching, Alkene), 1745 (C=O stretching, Lactone ring). ^1H NMR (CDCl₃): $\delta_{\text{H}}/\text{ppm}$ = 8.94 (1H, s, Aromatic H), 7.42-7.30 (3H, d, Aromatic H), 4.28-4.23 (2H, q, -CH₂-CH₃), 1.61-1.54 (3H, t, -CH₂-CH₃). ^{13}C NMR (CDCl₃) $\delta_{\text{C}}/\text{ppm}$ = 163.89, 162.51, 151.76, 146.82, 144.35, 126.13, 121.23, 119.20, 118.18, 114.94, 65.33, 14.64.

4.9.2.7 8-ethoxy-2-oxo-2H-chromene-3-carbaldehyde – 5



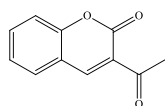
5 Was synthesised according to known literature procedure, compound **3** was used instead of compound **1**.³² ^1H NMR (DMSO): $\delta_{\text{H}}/\text{ppm}$ = 10.25 (1H, s, -HC=O), 10.16 (1H, s, Aromatic H), 7.26-7.24 (2H, d, Aromatic H), 6.93-6.89 (1H, m, Aromatic H), 4.12-4.07 (2H, q, -CH₂-CH₃), 1.38-1.35 (3H, t, -CH₂-CH₃). ^{13}C NMR (DMSO) $\delta_{\text{C}}/\text{ppm}$ = 192.97, 151.35, 147.89, 122.91, 121.01, 119.76, 119.32, 64.87, 15.00.

4.9.2.8 3,3'-acryloylbis(8-ethoxy-2H-chromen-2-one) – D2



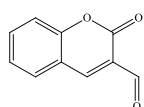
3-acetyl-8-ethoxy-2H-chromen-2-one, **3**, (1.01 g, 3.90 mmol) and 8-ethoxy-2-oxo-2H-chromene-3-carbaldehyde, **5**, (0.84 g, 6.17 mmol) was reflux with a few drops of piperidine for 48 hours in absolute ethanol. After the time had elapsed, the mixture was poured into the ice-cold water resulting in a fine precipitate forming. The product was filtered and recrystallised from ethanol.¹³ IR ν_{\max} (cm⁻¹): 2979-2934 (C-H stretching, Alkene), 1702 (C=O stretching, Lactone ring), 1636 (C=O, Enone). ¹H NMR (DMSO): $\delta_{\text{H/ppm}}$ = 11.24 (1H, s, Aromatic H), 8.56 (1H, s, Aromatic H), 8.18 (1H, s, Aromatic H), 7.93-7.91 (1H, d, Aromatic H), 7.53 (1H, s, Aromatic H), 7.37-7.29 (5H, m, Aromatic H) 4.23-4.22 (4H, q, -CH₂-CH₃), 1.45 (6H, t, -CH₂-CH₃). ¹³C NMR (DMSO) $\delta_{\text{C/ppm}}$ = 161.27, 159.48, 147.13, 146.01, 143.95, 143.66, 143.22, 125.68, 125.59, 125.25, 120.71, 120.30, 119.09, 116.54, 116.15, 115.55, 114.56, 113.79, 106.05, 64.97, 64.91, 15.08.

4.9.2.9 3-acetyl-2H-chromen-2-one – **6**



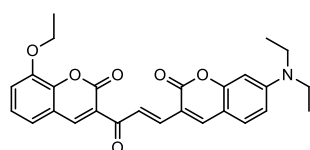
Synthesised according to known literature procedure.³¹ ¹H NMR (CDCl₃): $\delta_{\text{H/ppm}}$ = 8.52 (1H, s, Aromatic H), 7.69-7.65 (2H, m, Aromatic H), 7.40-7.34 (2H, m, Aromatic H), 2.74 (3H, t, -CH₃).

4.9.2.10 2-oxo-2H-chromene-3-carbaldehyde – **7**



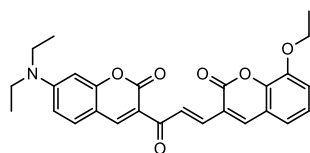
7 Was synthesised according to known literature procedure.³¹ Product was not formed as coumarin was isolated.

4.9.2.11 7-(diethylamino)-3-(3-(8-ethoxy-2-oxo-2H-chromen-3-yl)-3-oxoprop-1-en-1-yl)-2H-chromen-2-one – **D4**



Synthesised using the method for **D2**.¹³ **D4** was not isolated. Compounds **2** and **3** were isolated, with compound **3** being double the concentration of **2**, and the peak for the enone linker was also not observed

4.9.2.12 7-(diethylamino)-3-(3-(8-ethoxy-2-oxo-2H-chromen-3-yl)acryloyl)-
2H-chromen-2-one – **D5**



Synthesised using the method for **D2**.¹³ **D5** was not isolated. **E1** was isolated.

References

- (1) Arulraj, A. D.; Devasenathipathy, R.; Chen, S. M.; Vasantha, V. S.; Wang, S. F. Highly Selective and Sensitive Fluorescent Chemosensor for Femtomolar Detection of Silver Ion in Aqueous Medium. *Sens. Bio-Sensing Res.* **2015**, *6*, 19–24. <https://doi.org/10.1016/j.sbsr.2015.10.004>.
- (2) Tan, D.; Akdag, A. Synthesis of New Flexible Coumarin Dimers for Sodium and Potassium Differentiation. *J. Fluoresc.* **2020**, *30* (1), 27–34. <https://doi.org/10.1007/s10895-020-02492-4>.
- (3) Arcos-Ramos, R.; Maldonado-Domínguez, M.; Ordóñez-Hernández, J.; Romero-Ávila, M.; Farfán, N.; Carreón-Castro, M. del P. 3-Substituted-7-(Diethylamino)Coumarins as Molecular Scaffolds for the Bottom-up Self-Assembly of Solids with Extensive π -Stacking. *J. Mol. Struct.* **2017**, *1130*, 914–921. <https://doi.org/10.1016/j.molstruc.2016.10.080>.
- (4) Muller, P. Glossary of Terms Used in Physical Organic Chemistry. *Pure Appl. Chem* **1994**, *66* (5), 1077–1184.
- (5) Kaeswurm, J. A. H.; Scharinger, A.; Teipel, J.; Buchweitz, M. Absorption Coefficients of Phenolic Structures in Different Solvents Routinely Used for Experiments. *Molecules* **2021**, *26* (15), 1–15. <https://doi.org/10.3390/molecules26154656>.
- (6) Shan, Y.; Liu, Z.; Cao, D.; Liu, G.; Guan, R.; Sun, N.; Wang, C.; Wang, K. Coumarinic Chalcone Derivatives as Chemosensors for Cyanide Anions and Copper Ions. *Sensors Actuators, B Chem.* **2015**, *221*, 463–469. <https://doi.org/10.1016/j.snb.2015.06.118>.
- (7) Ramesh, M.; You, Y. R.; Shellaiah, M.; Wu, M. C.; Lin, H. C.; Chu, C. W. Star-Shaped Self-Assembly of an Organic Thin Film Transistor Sensor in the Presence of Cu²⁺ and CN⁻ Ions. *Org. Electron.* **2014**, *15* (2), 582–589. <https://doi.org/10.1016/j.orgel.2013.12.007>.
- (8) Cao, W.; Zheng, X. J.; Fang, D. C.; Jin, L. P. A Highly Selective and Sensitive Zn(II) Complex-Based Chemosensor for Sequential Recognition of Cu(II) and Cyanide. *Dalt. Trans.* **2014**, *43* (19), 7298–7303. <https://doi.org/10.1039/c3dt53647e>.
- (9) World Health Organization. Guidelines for Drinking-Water Quality, 4th Edition, Incorporating the 1st Addendum. **2017**.
- (10) Anbu, S.; Ravishankaran, R.; Guedes Da Silva, M. F. C.; Karande, A. A.; Pombeiro, A. J. L. Differentially Selective Chemosensor with Fluorescence Off-on Responses on Cu²⁺ and Zn²⁺ Ions in Aqueous Media and Applications in Pyrophosphate Sensing, Live Cell Imaging, and Cytotoxicity. *Inorg. Chem.* **2014**, *53* (13), 6655–6664. <https://doi.org/10.1021/ic500313m>.
- (11) Jia, L.; Liu, Y. The Effects of Electron-Withdrawing and Electron-Donating Groups on the Photophysical Properties and ESIPT of Salicylideneaniline. *Spectrochim. Acta - Part A Mol. Biomol. Spectrosc.* **2020**, *242*, 118719. <https://doi.org/10.1016/j.saa.2020.118719>.

- (12) Sivakumar, S.; Reddy, M. L. P.; Cowley, A. H.; Vasudevan, K. V. Synthesis and Crystal Structures of Lanthanide 4-Benzyloxy Benzoates: Influence of Electron-Withdrawing and Electron-Donating Groups on Luminescent Properties. *Dalt. Trans.* **2010**, 39 (3), 776–786. <https://doi.org/10.1039/b917256d>.
- (13) Yeap, G. Y.; Hrishikesan, E.; Chan, Y. H.; Mahmood, W. A. K. A New Emissive Chalcone-Based Chemosensor Armed by Coumarin and Naphthol with Fluorescence “Turn-on” Properties for Selective Detection of F[−] Ions. *J. Fluoresc.* **2017**, 27 (1), 105–110. <https://doi.org/10.1007/s10895-016-1938-5>.
- (14) Hanley, P. S.; Marković, D.; Hartwig, J. F. Intermolecular Insertion of Ethylene and Octene into a Palladium-Amide Bond. Spectroscopic Evidence for an Ethylene Amido Intermediate. *J. Am. Chem. Soc.* **2010**, 132 (18), 6302–6303. <https://doi.org/10.1021/JA102172M>.
- (15) Lakowicz, J. R. *Principles of Fluorescence Spectroscopy*, Third.; Springer Science & Business Media, 2007.
- (16) Prabakaran, G.; Vickram, R.; Velmurugan, K.; Immanuel David, C.; Prince Makarios Paul, S.; Suresh Kumar, R.; Almansour, A. I.; Perumal, K.; Abiram, A.; Prabhu, J.; Nandhakumar, R. A Lead Selective Dimeric Quinoline Based Fluorescent Chemosensor and Its Applications in Milk and Honey Samples, Smartphone and Bio-Imaging. *Food Chem.* **2022**, 395 (September 2021), 133617. <https://doi.org/10.1016/j.foodchem.2022.133617>.
- (17) Battison, A. Synthesis and Applications of Novel Fluorescent and Colorimetric Coumarin-Based Sensors towards Analyte Sensing in Aqueous Systems By Supervisor : Dr . N . Mama Declaration, Nelson Mandela University, 2022.
- (18) Afaneh, A. T.; Schreckenbach, G. Fluorescence Enhancement/Quenching Based on Metal Orbital Control: Computational Studies of a 6-Thienyllumazine-Based Mercury Sensor. *J. Phys. Chem. A*, **2015**, 119 (29), 8106–8116. <https://doi.org/10.1021/acs.jpca.5b04691>.
- (19) Ngororabanga, J. M. V.; Tshentu, Z. R.; Mama, N. A New Highly Selective Colorimetric and Fluorometric Coumarin-Based Chemosensor for Hg²⁺. *J. Fluoresc.* **2020**, 30 (5), 985–997. <https://doi.org/10.1007/S10895-020-02542-X/TABLES/3>.
- (20) Sidana, N.; Devi, P.; Kaur, H. Thiophenol Amine-Based Schiff Base for Colorimetric Detection of Cu²⁺ and Hg²⁺ Ions. *Opt. Mater. (Amst)*. **2022**, 124 (January), 111985. <https://doi.org/10.1016/j.optmat.2022.111985>.
- (21) Wang, Y. N.; Wang, S. D.; Fan, Y.; Yu, L.; Zha, R. H.; Liu, L. J.; Wen, L. M.; Chang, X. P.; Liu, H. Q.; Zou, G. D. A Dual-Chemosensor Based on Ni-CP: Fluorescence Turn-on Sensing toward Ascorbic Acid and Turn-off Sensing toward Acetylacetone. *J. Lumin.* **2022**, 243 (October 2021). <https://doi.org/10.1016/j.jlumin.2021.118680>.
- (22) Kolb, H. C.; Finn, M. G.; Sharpless, K. B. Click Chemistry: Diverse Chemical Function from a Few Good Reactions. *Angew. Chemie - Int. Ed.* **2001**, 40 (11), 2004–2021. [https://doi.org/10.1002/1521-3773\(20010601\)40:11<2004::AID-ANIE2004>3.0.CO;2-](https://doi.org/10.1002/1521-3773(20010601)40:11<2004::AID-ANIE2004>3.0.CO;2-)

- (23) Hu, Y.; Shen, H.; Zhang, X.; Liu, Y.; Sun, X. Synthesis and Spectroscopic Investigation of a Novel Sensitive and Selective Fluorescent Chemosensor for Ag⁺ Based on a BINOL-Glucose Derivative. *RSC Adv.* **2018**, 8 (41), 23252–23256. <https://doi.org/10.1039/c8ra04429e>.
- (24) Mama, N.; Battison, A. Synthesis and Application of a Fluorescent \leftarrow turn-Off \rightarrow Triazolyl-Coumarin-Based Fluorescent Chemosensor for the Sensing of Fe³⁺ Ions in Aqueous Solutions. *Arkivoc* **2020**, 2020, 1–27. <https://doi.org/10.24820/ARK.5550190.P011.283>.
- (25) Parchegani, F.; Orojloo, M.; Zendehdel, M.; Amani, S. Spectrochimica Acta Part A : Molecular and Biomolecular Spectroscopy Simultaneous Measurement of Hydrogen Carbonate and Acetate Anions Using Biologically Active Receptor Based on Azo Derivatives of Naphthalene. *Spectrochim. Acta Part A Mol. Biomol. Spectrosc.* **2020**, 229, 117925. <https://doi.org/10.1016/j.saa.2019.117925>.
- (26) Junaid, H. M.; Batool, M.; Harun, F. W.; Akhter, M. S.; Shabbir, N. Naked Eye Chemosensing of Anions by Schiff Bases. *Crit. Rev. Anal. Chem.* **2022**, 52 (3), 463–480. <https://doi.org/10.1080/10408347.2020.1806703>.
- (27) Šídlo, M.; Lubal, P.; Anzenbacher, P. Colorimetric Chemosensor Array for Determination of Halides. *Chemosensors* **2021**, 9 (2), 1–16. <https://doi.org/10.3390/chemosensors9020039>.
- (28) González-García, C.; Mendiola, M. A.; Perles, J.; López-Torres, E. Structural Diversity and Supramolecular Architectures of Zn(II), Cu(II) and Ni(II) Complexes by Selective Control of the Degree of Deprotonation of Diacetyl Bis(4-Isopropyl-3-Thiosemicarbazone). *CrystEngComm* **2017**, 19 (7), 1035–1044. <https://doi.org/10.1039/c6ce02488b>.
- (29) Sagdinc, S.; Pir, H. Spectroscopic and DFT Studies of Flurbiprofen as Dimer and Its Cu(II) and Hg(II) Complexes. *Spectrochim. Acta - Part A Mol. Biomol. Spectrosc.* **2009**, 73 (1), 181–194. <https://doi.org/10.1016/j.saa.2009.02.022>.
- (30) Vaughn, B. A.; Brown, A. M.; Ahn, S. H.; Robinson, J. R.; Boros, E. Is Less More? Influence of the Coordination Geometry of Copper(II) Picolinate Chelate Complexes on Metabolic Stability. *Inorg. Chem.* **2020**, 59 (22), 16095–16108. <https://doi.org/10.1021/acs.inorgchem.0c02314>.
- (31) Evans, Vikki, Duncanson, Phulip, Motevalli, Majid, Watkinson, M.; Evans, V.; Duncanson, P.; Motevalli, M.; Watkinson, M. An Investigation into the Synthesis of Azido-Functionalised Coumarins for Application in 1,3-Dipolar “Click” Cycloaddition Reactions. *Dye. Pigment.* **2016**, 135 (5), 36–40. <https://doi.org/10.1016/j.dyepig.2016.06.028>.
- (32) García-Beltrán, O.; Cassels, B. K.; Mena, N.; Nuñez, M. T.; Yañez, O.; Caballero, J. A Coumarinyldoxime as a Specific Sensor for Cu²⁺ and Its Biological Application. *Tetrahedron Lett.* **2014**, 55 (4), 873–876. <https://doi.org/10.1016/j.tetlet.2013.12.033>.

Supplementary information

List of Supplementary Figures

Figure S 4.1: ^1H NMR spectrum of compound E1 in CDCl_3	206
Figure S 4.2: ^{13}C NMR spectrum of compound E1 in CDCl_3	206
Figure S 4.3: FT-IR spectrum of E1	207
Figure S 4.4: ^1H NMR spectrum of compound 1 in DMSO.....	207
Figure S 4.5: ^{13}C NMR spectrum of compound 1 in DMSO.....	208
Figure S 4.6: FT-IR spectrum of compound 1	208
Figure S 4.7: ^1H NMR spectrum of compound 2 in DMSO.....	208
Figure S 4.8: ^1H NMR spectrum of compound D1 in CD_3CN	209
Figure S 4.9: ^{13}C NMR spectrum of D1 in DMSO.....	209
Figure S 4.10: ^{13}C NMR spectrum of D1 in CD_3CN	209
Figure S 4.11: ^{13}C NMR with DEPT-135 overlay of D1 in CD_3CN . The black boxes indicate the tertiary carbons, the red oval indicates the $-\text{CH}_2$ carbons, and the blue diamond shows the $-\text{CH}_3$ carbon. The carboxyl carbon is seen at 186.89 ppm, and the other peaks represent the $-\text{CH}$ carbons.	210
Figure S 4.12: HSQC spectrum of D1 in CD_3CN	210
Figure S 4.13: FT-IR spectrum of D1	211
Figure S 4.14: ^1H NMR spectrum of compound 3 in DMSO.....	211
Figure S 4.15: ^{13}C NMR spectrum of compound 3 in DMSO.....	212
Figure S 4.16: FT-IR spectrum of compound 3	212
Figure S 4.17: ^1H NMR spectrum of compound 4 in CDCl_3	212

Figure S 4.18: ^{13}C NMR spectrum of compound 4 in CDCl_3 .	213
Figure S 4.19: FT-IR spectrum of compound 4 .	213
Figure S 4.20: ^1H NMR spectrum of compound 5 in DMSO.	213
Figure S 4.21: ^{13}C NMR spectrum of compound 5 in DMSO.	214
Figure S 4.22: HSQC spectrum of compound 5 in DMSO.	214
Figure S 4.23: Overlay of compound 3 (red), 5 (green) and D2 (blue) ^1H NMR spectra in DMSO.	214
Figure S 4.24: ^{13}C NMR spectrum of D2 in DMSO.	215
Figure S 4.25: FT-IR spectrum of D2 .	215
Figure S 4.26: ^1H NMR spectrum of compound 6 in CDCl_3 .	215
Figure S 4.27: Attempted synthesis of compound 7 resulted in the isolation of coumarin.	216
Figure S 4.28: Attempted synthesis of D4 resulted in the isolation of 2 and 3 with a ratio of 2:1, respectively.	216
Figure S 4.29: Attempted synthesis of D5 , which resulted in the isolation of E1 .	216
Figure S 4.30: Absorbance spectra of D2 at various concentrations, 16.7 μM (red), 66.6 μM (orange), and 333 μM (yellow).	217
Figure S 4.31: Screening various metal cations in acetonitrile using compound D2 (blue, 0.0333 μM or 33.3 nM). $\lambda_{\text{excitation}}$: 487 nm.	217
Figure S 4.32: 3D emission scan of D2 - Ba^{2+} complex.	218
Figure S 4.33: Calibration curve of D1 - Cu^{2+} in acetonitrile.	218
Figure S 4.34: Emission spectra of D1 in the absence (blue) and presence of EDTA (red).	219

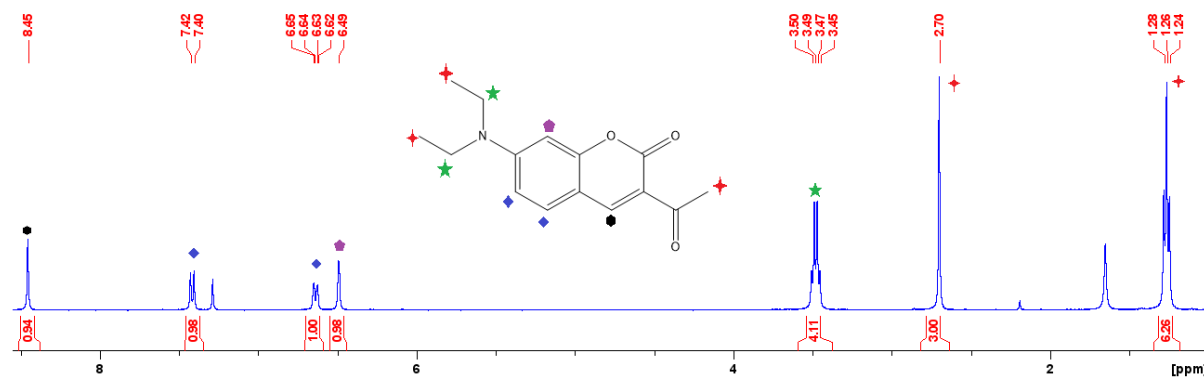


Figure S 4.1: ¹H NMR spectrum of compound **E1** in CDCl₃.

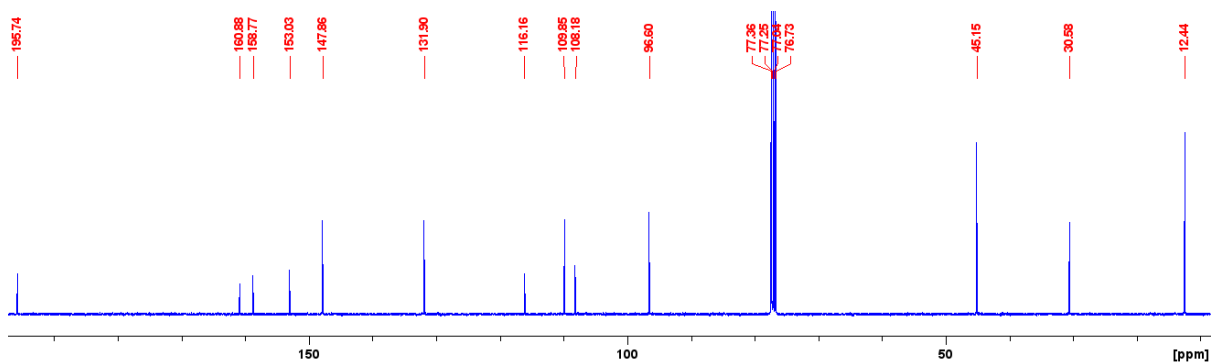


Figure S 4.2: ¹³C NMR spectrum of compound **E1** in CDCl₃.

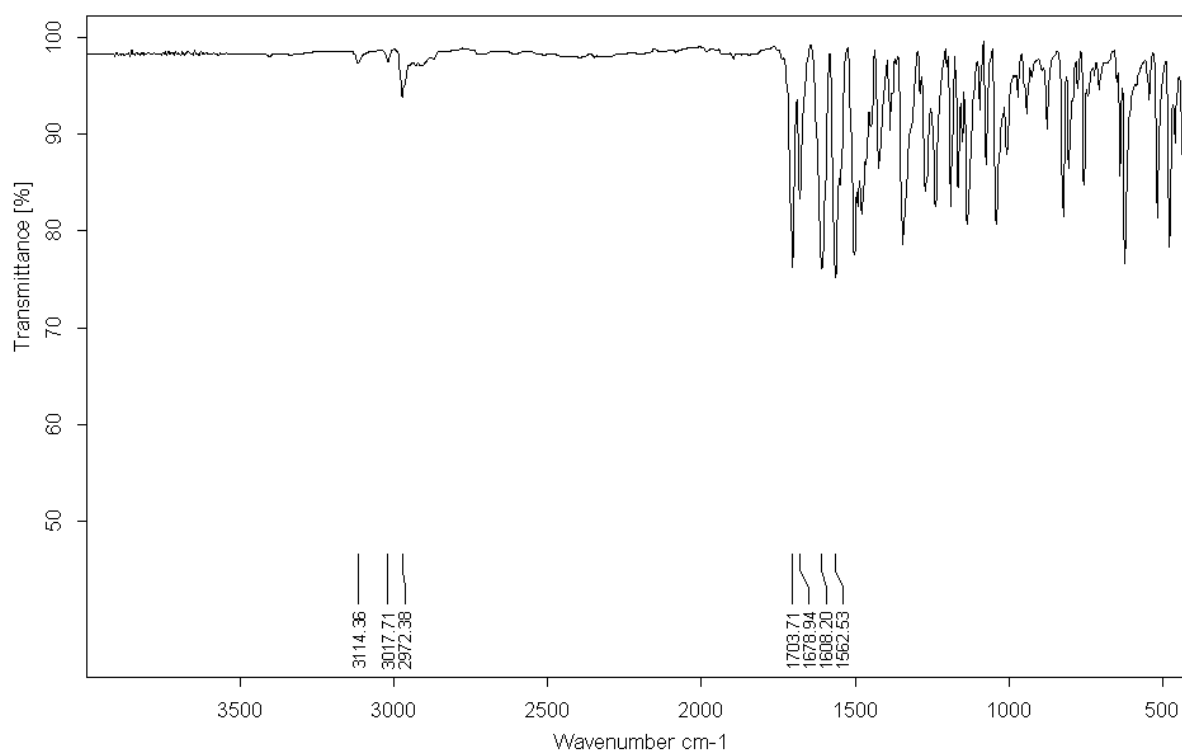


Figure S 4.3: FT-IR spectrum of E1.

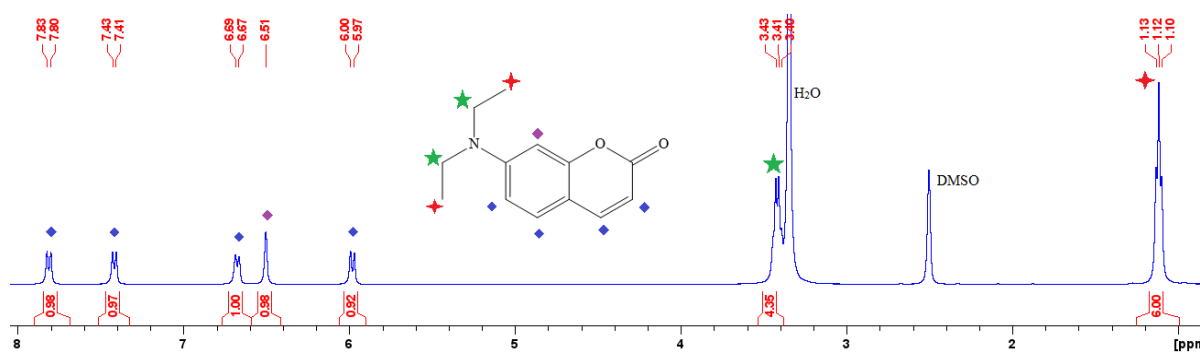


Figure S 4.4: ¹H NMR spectrum of compound 1 in DMSO.

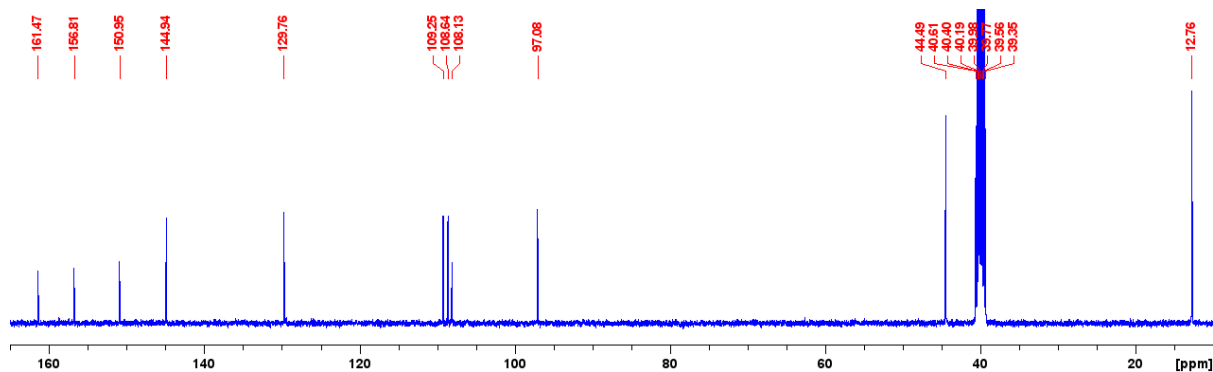


Figure S 4.5: ^{13}C NMR spectrum of compound **1** in DMSO.

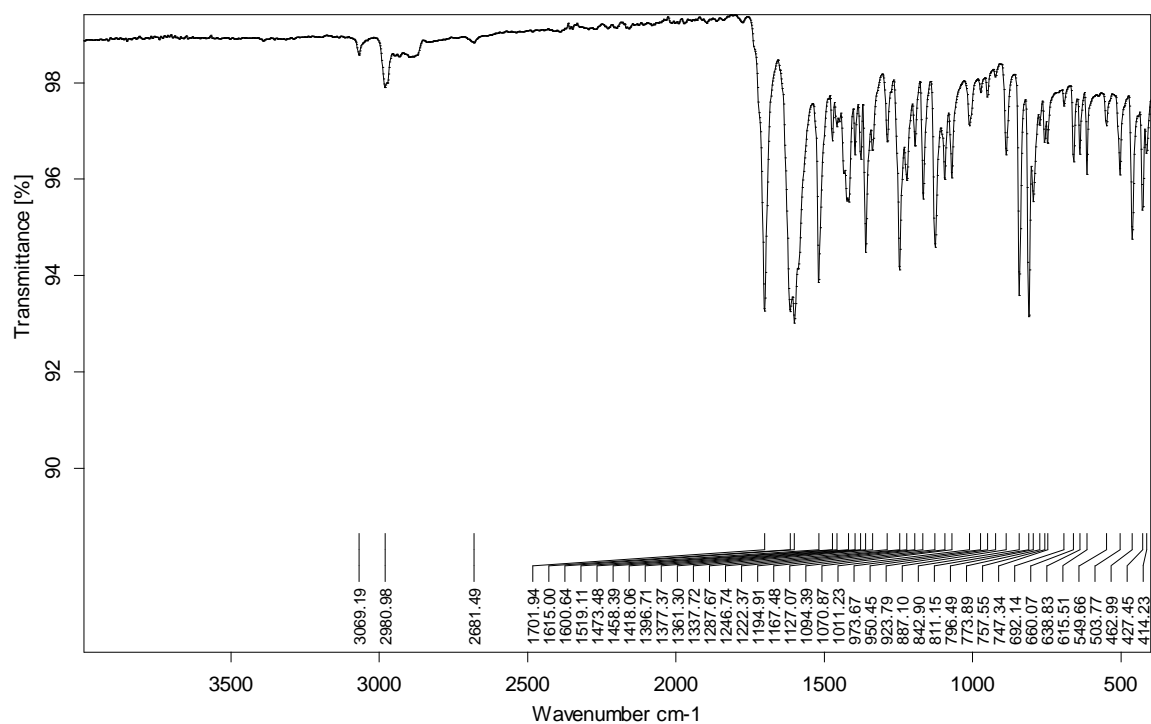


Figure S 4.6: FT-IR spectrum of compound **1**.

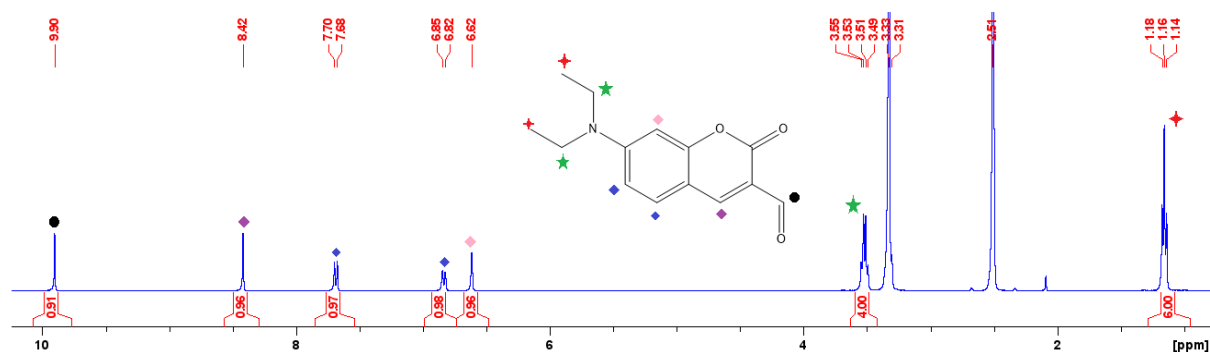


Figure S 4.7: ^1H NMR spectrum of compound **2** in DMSO.

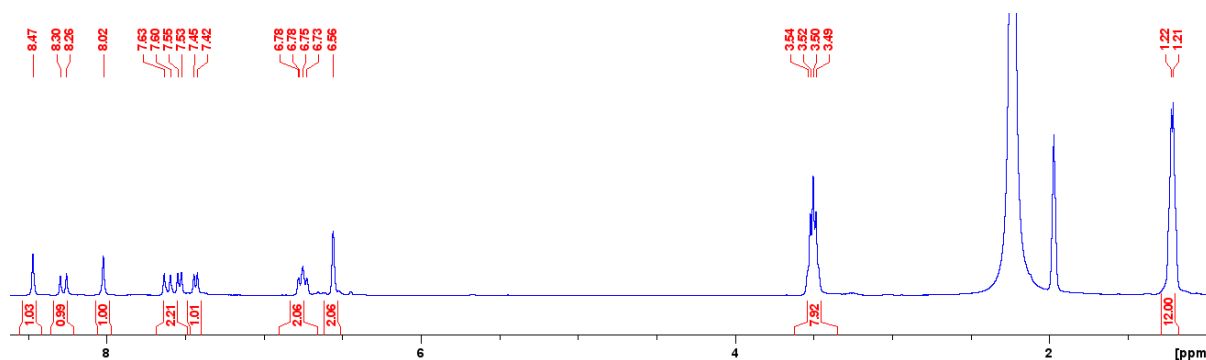


Figure S 4.8: ¹H NMR spectrum of compound **D1** in CD₃CN.

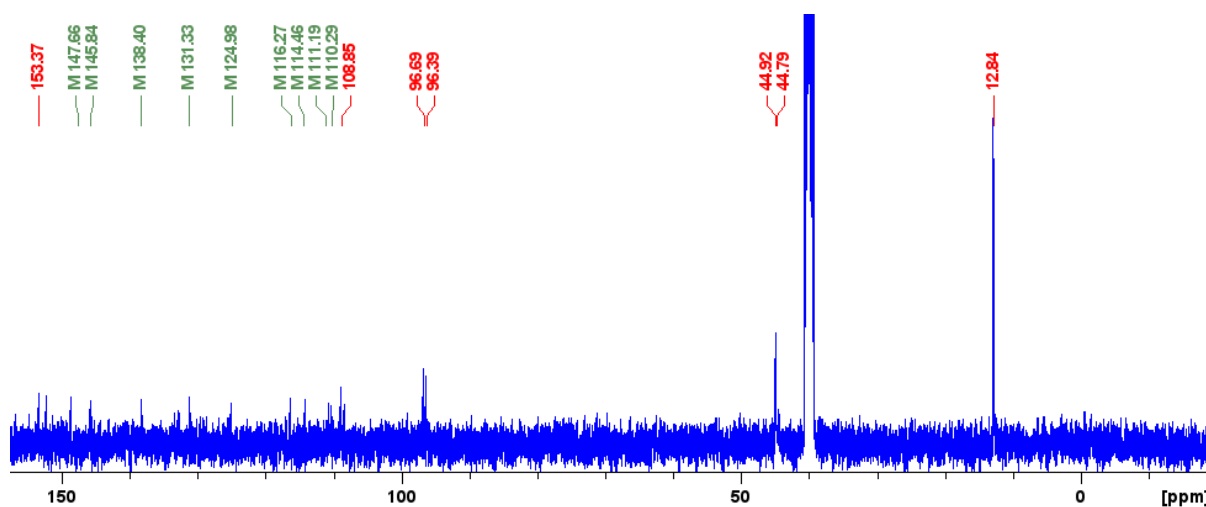


Figure S 4.9: ¹³C NMR spectrum of **D1** in DMSO.

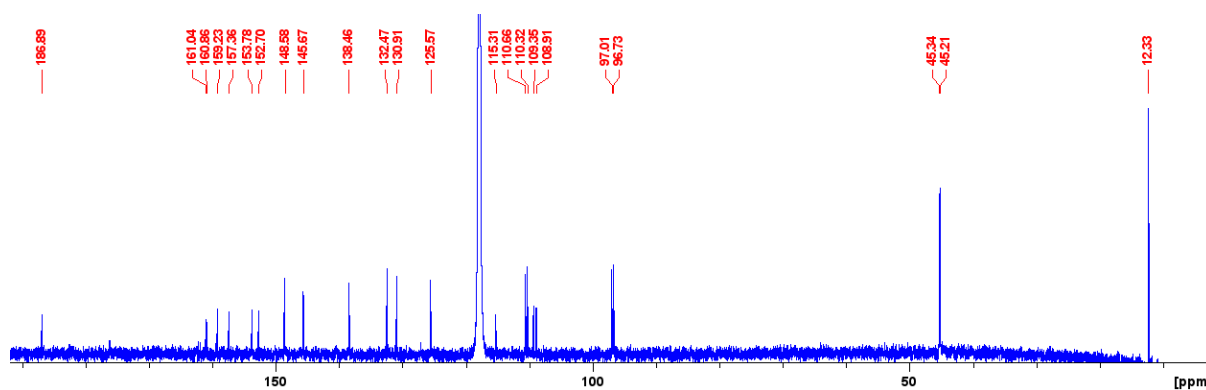


Figure S 4.10: ¹³C NMR spectrum of **D1** in CD₃CN.

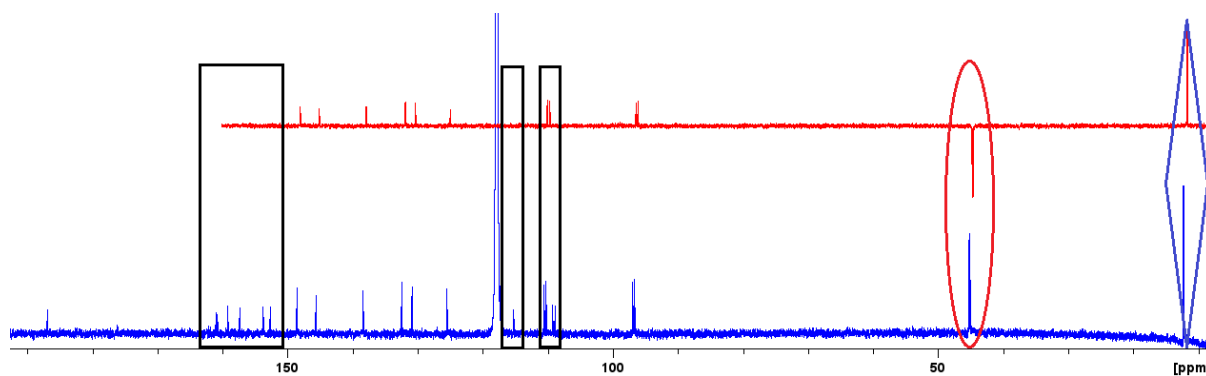


Figure S 4.11: ^{13}C NMR with DEPT-135 overlay of **D1** in CD_3CN . The black boxes indicate the tertiary carbons, the red oval indicates the $-\text{CH}_2$ carbons, and the blue diamond shows the $-\text{CH}_3$ carbon. The carboxyl carbon is seen at 186.89 ppm, and the other peaks represent the $-\text{CH}$ carbons.

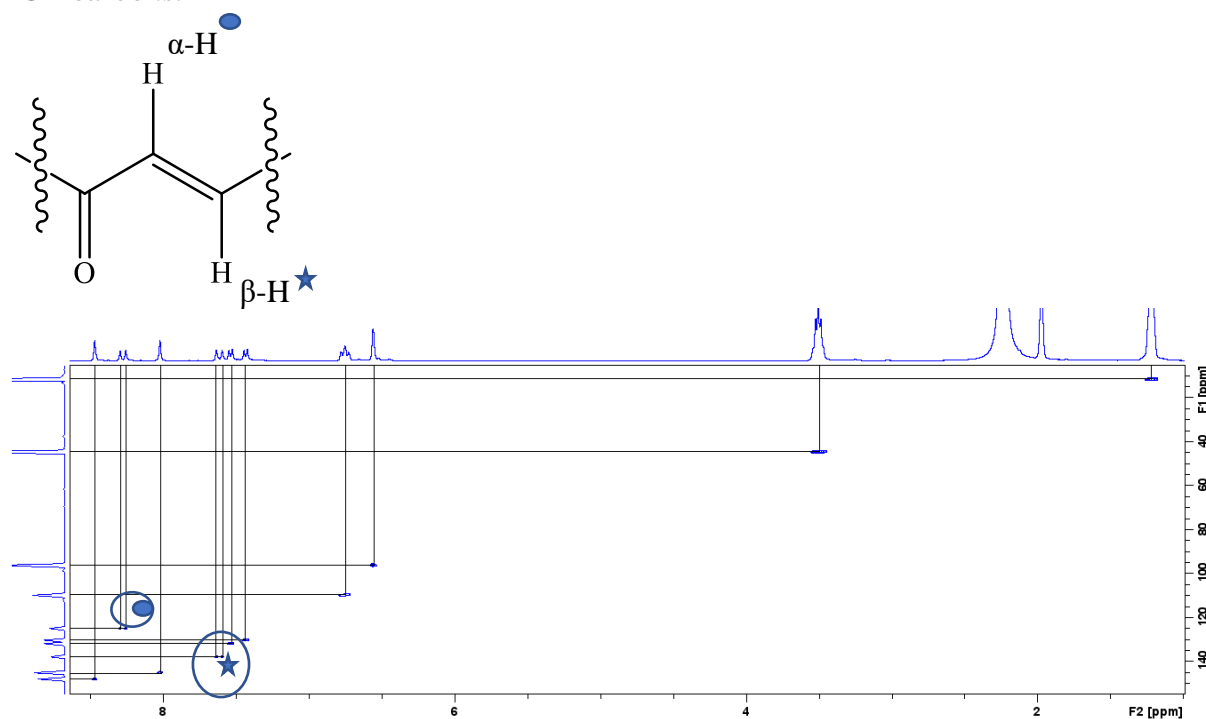


Figure S 4.12: HSQC spectrum of **D1** in CD_3CN .

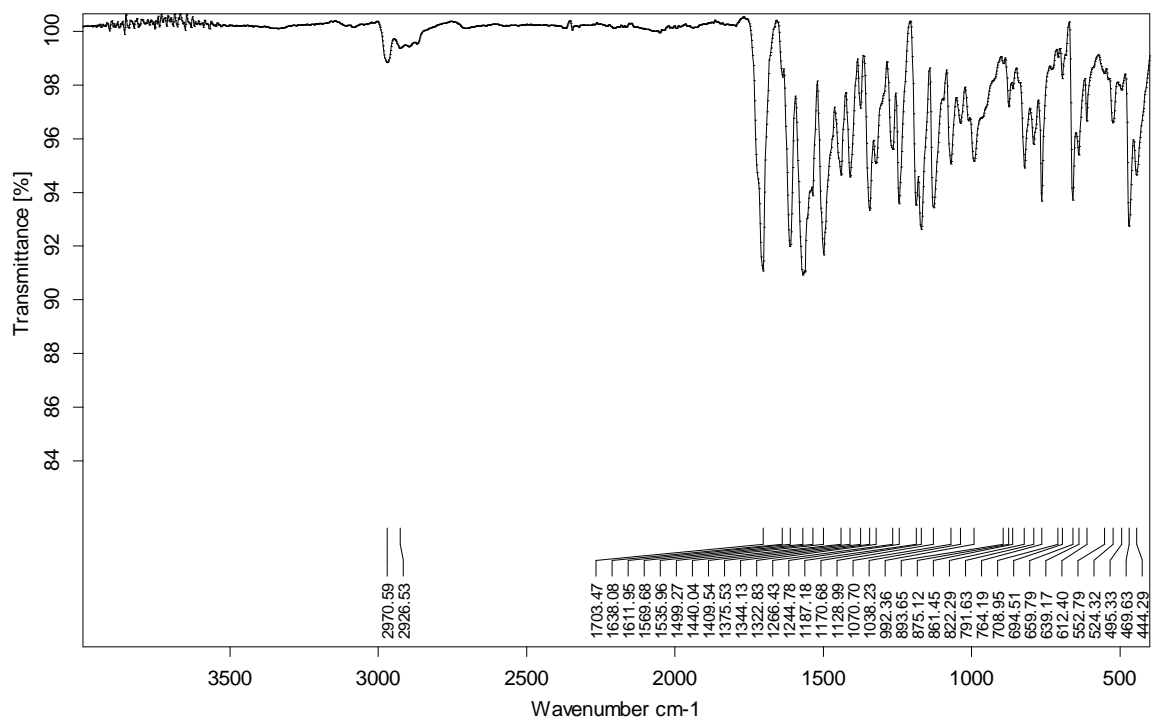


Figure S 4.13: FT-IR spectrum of **DL**.

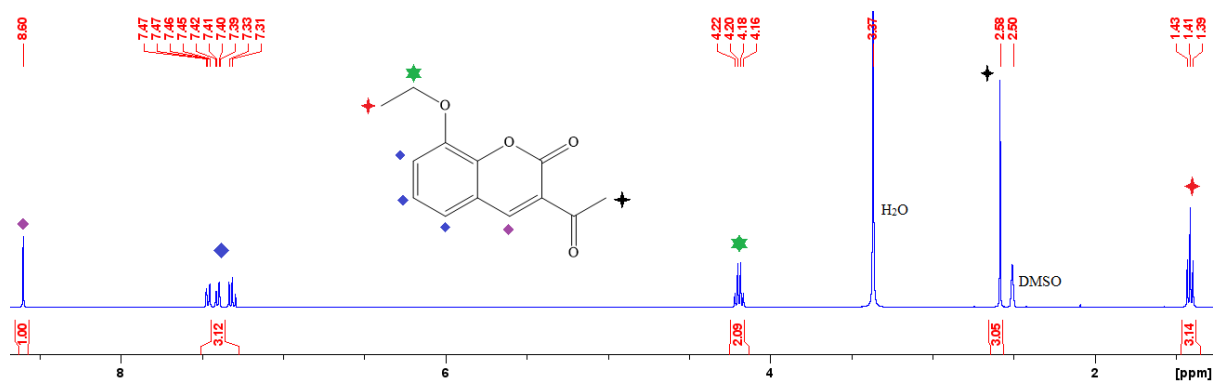


Figure S 4.14: ^1H NMR spectrum of compound **3** in DMSO.

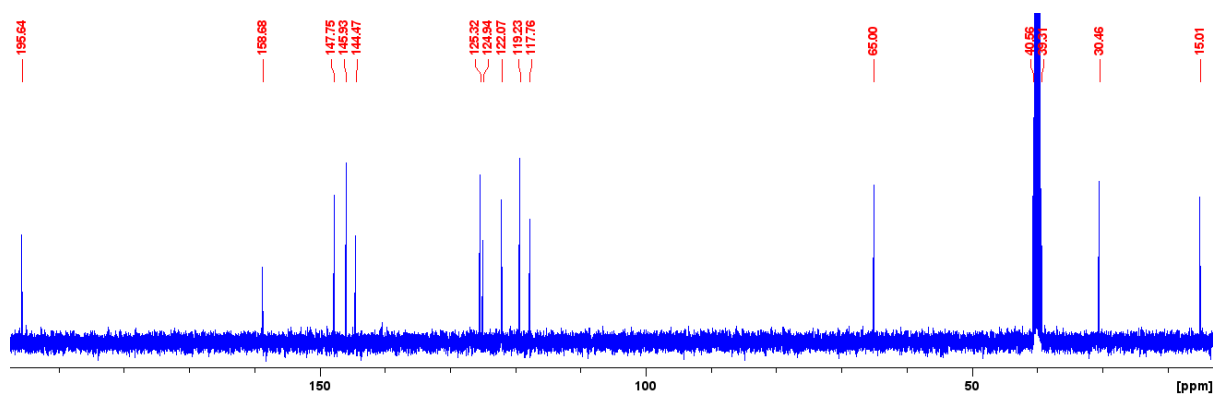


Figure S 4.15: ^{13}C NMR spectrum of compound **3** in DMSO.

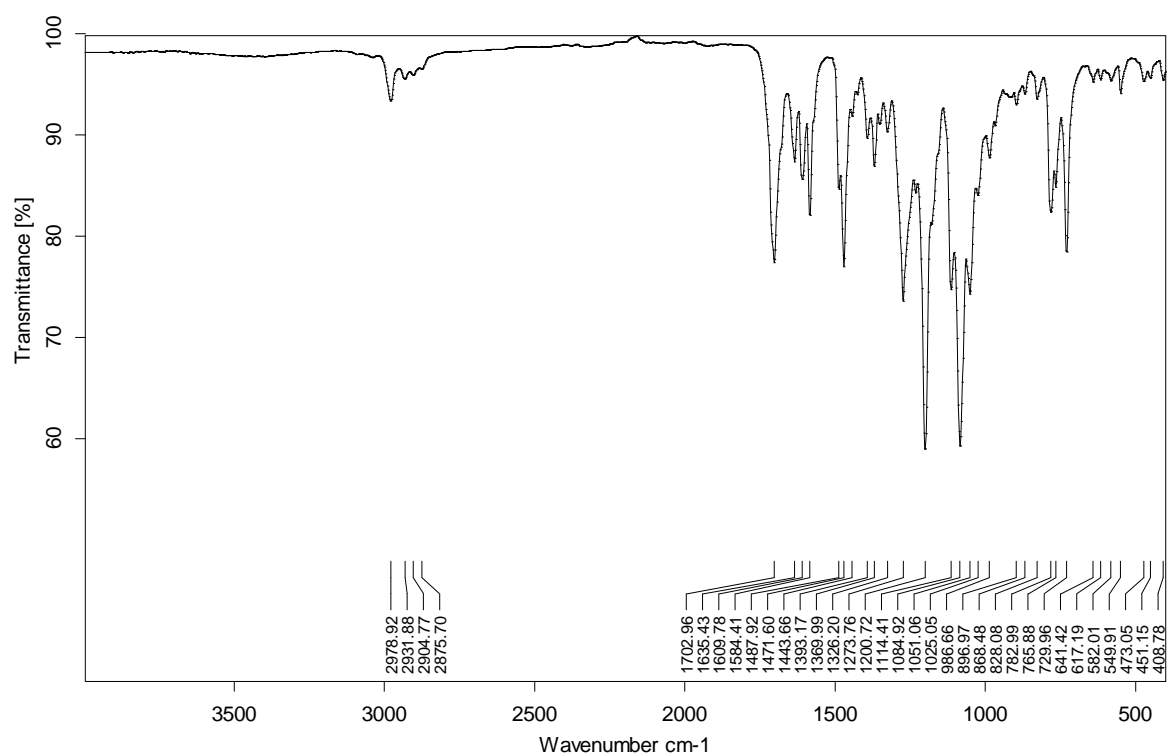


Figure S 4.16: FT-IR spectrum of compound **3**.

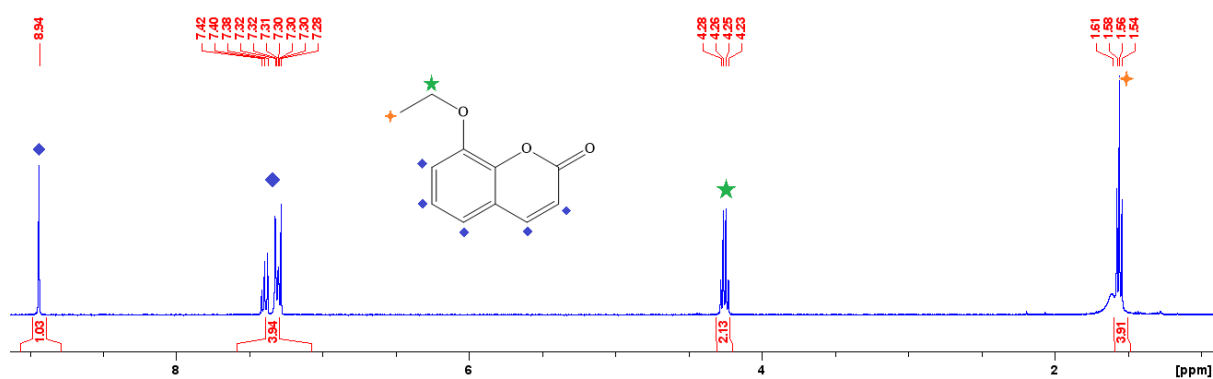


Figure S 4.17: ^1H NMR spectrum of compound **4** in CDCl_3 .

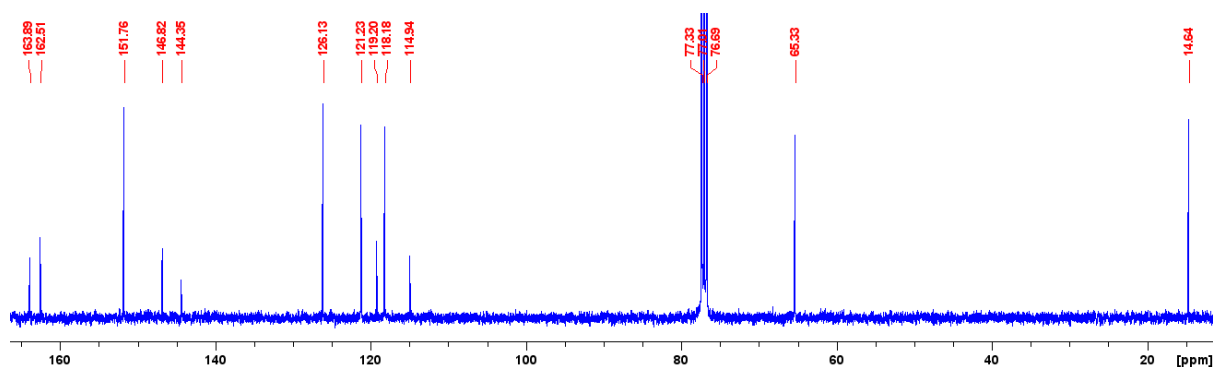


Figure S 4.18: ^{13}C NMR spectrum of compound 4 in CDCl_3 .

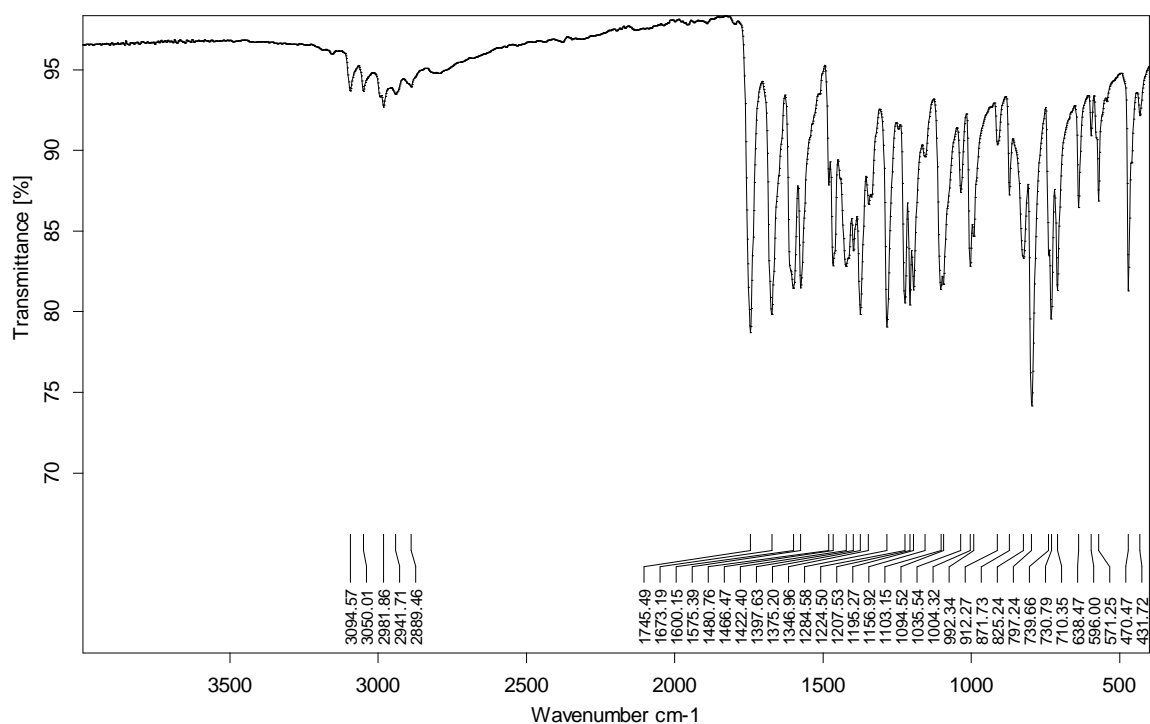


Figure S 4.19: FT-IR spectrum of compound 4.

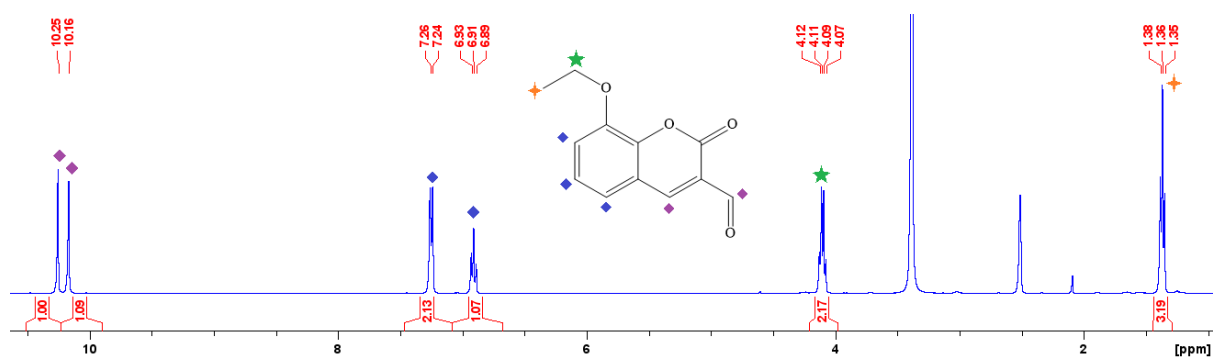


Figure S 4.20: ^1H NMR spectrum of compound 5 in DMSO .

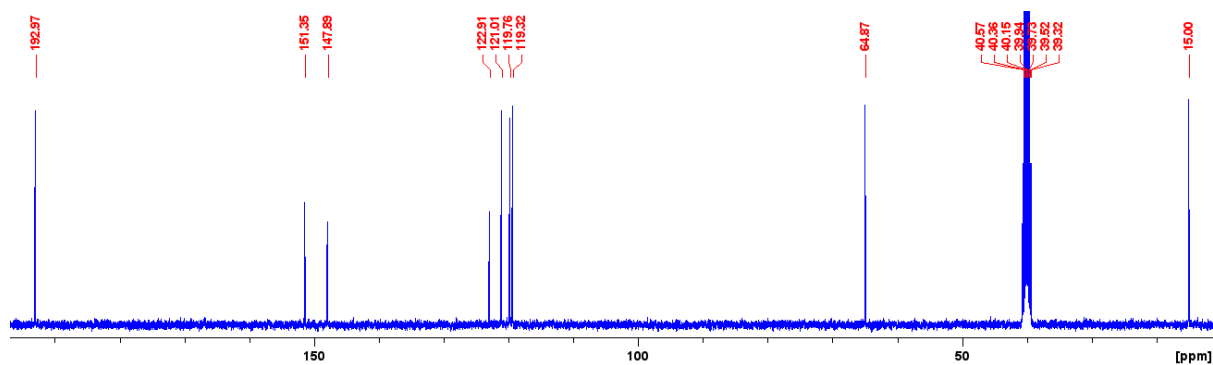


Figure S 4.21: ^{13}C NMR spectrum of compound 5 in DMSO.

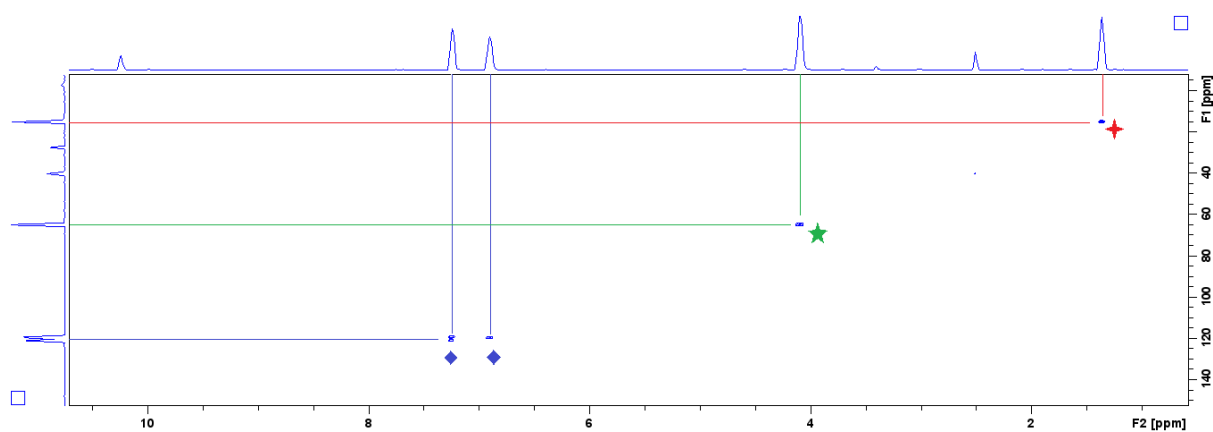


Figure S 4.22: HSQC spectrum of compound 5 in DMSO.

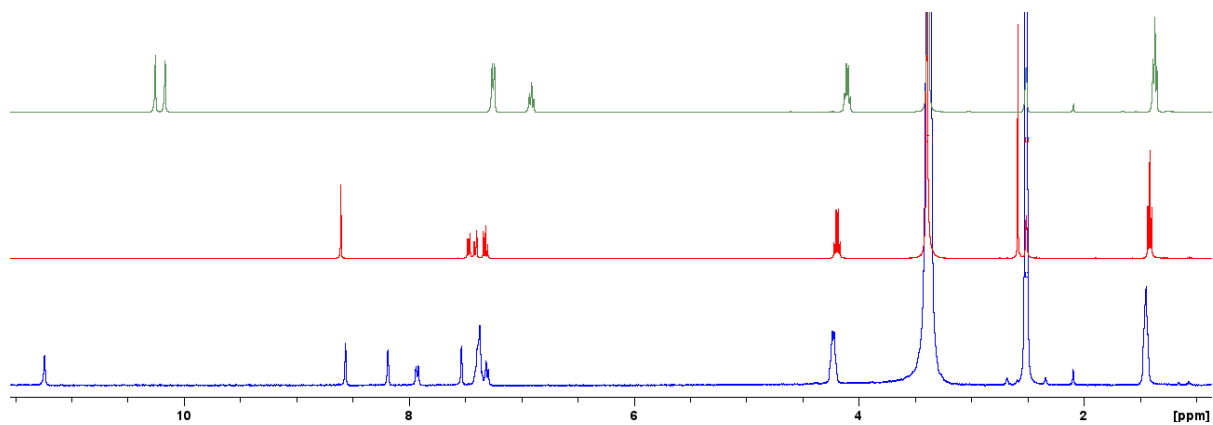


Figure S 4.23: Overlay of compound 3 (red), 5 (green) and D2 (blue) ^1H NMR spectra in DMSO.

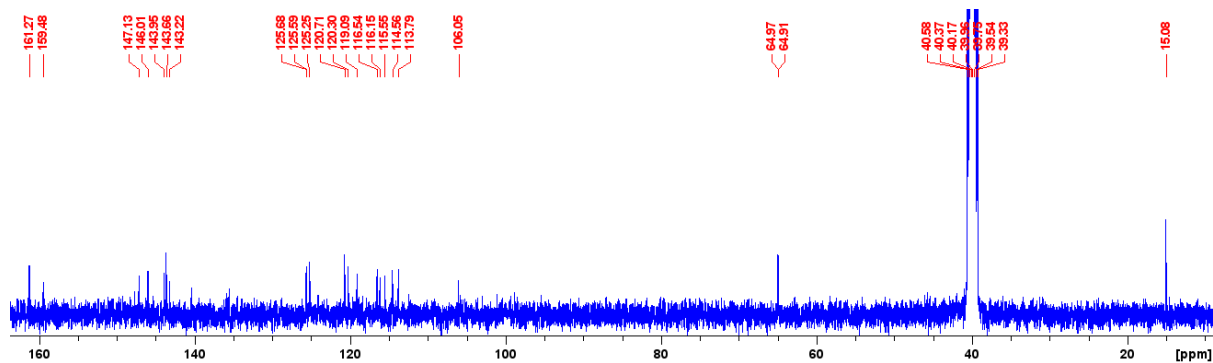


Figure S 4.24: ^{13}C NMR spectrum of **D2** in DMSO.

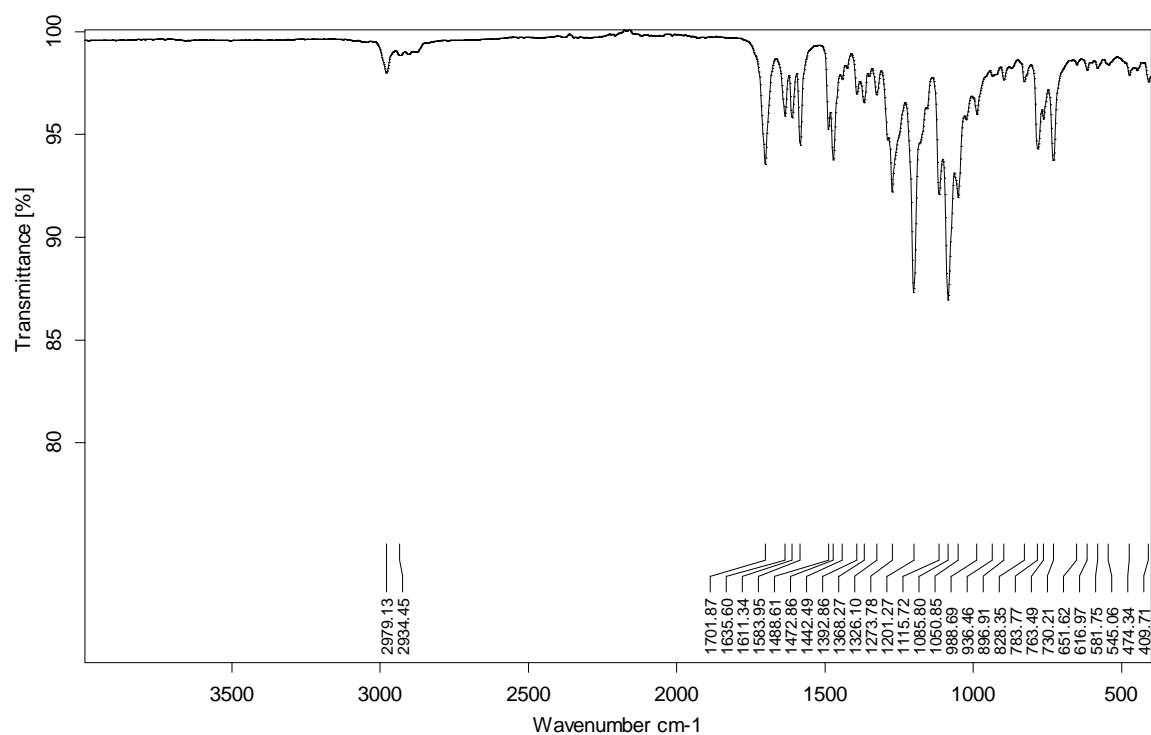


Figure S 4.25: FT-IR spectrum of **D2**.

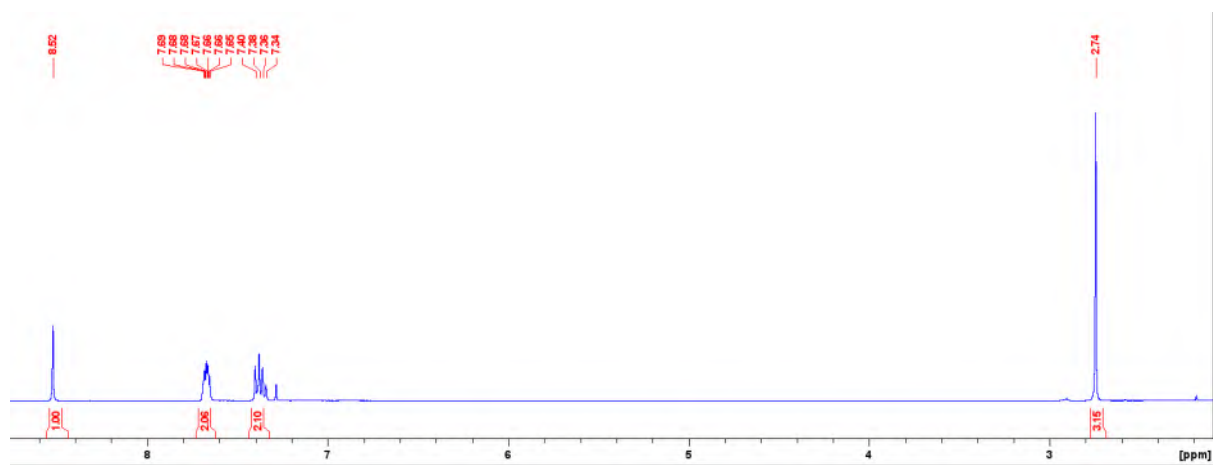


Figure S 4.26: ^1H NMR spectrum of compound **6** in CDCl_3 .

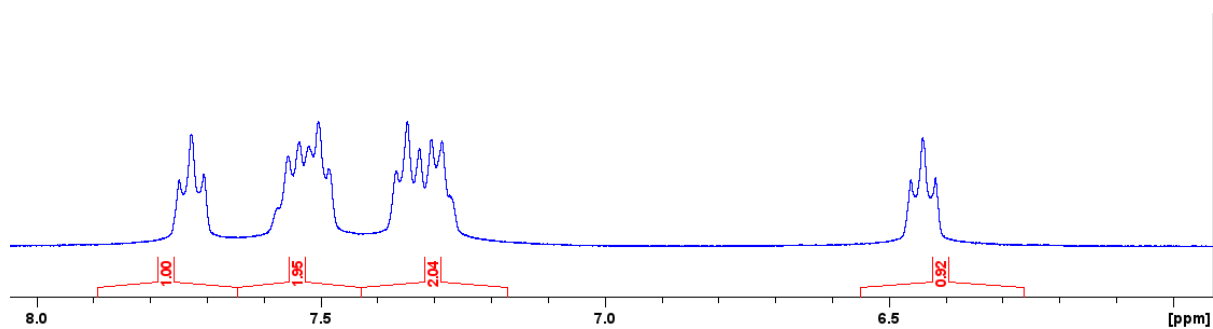


Figure S 4.27: Attempted synthesis of compound 7 resulted in the isolation of coumarin.

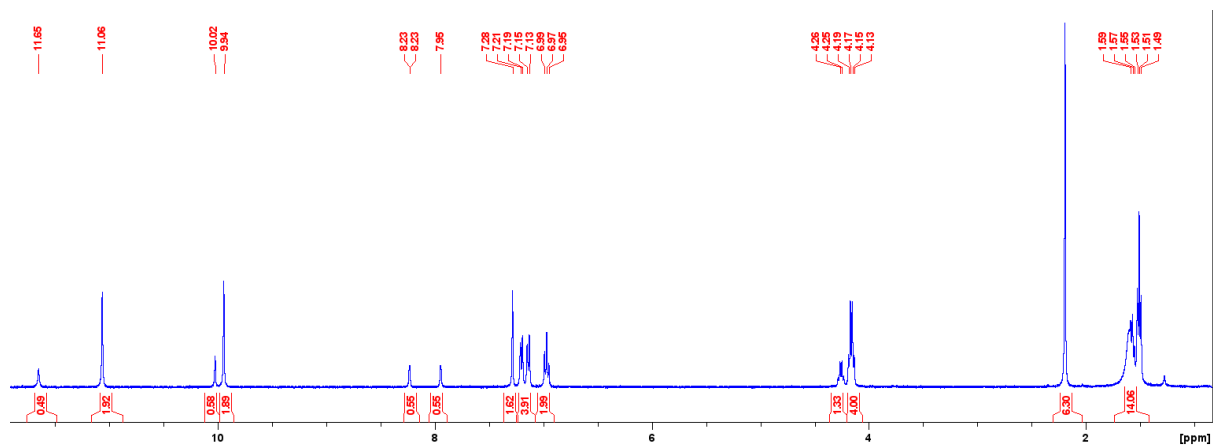


Figure S 4.28: Attempted synthesis of D4 resulted in the isolation of 2 and 3 with a ratio of 2:1, respectively.

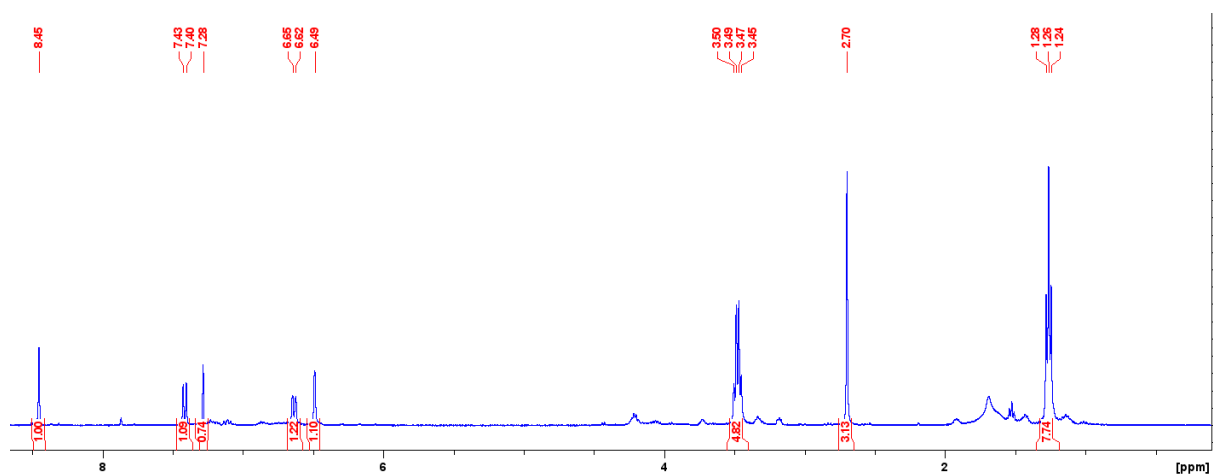


Figure S 4.29: Attempted synthesis of D5, which resulted in the isolation of E1.

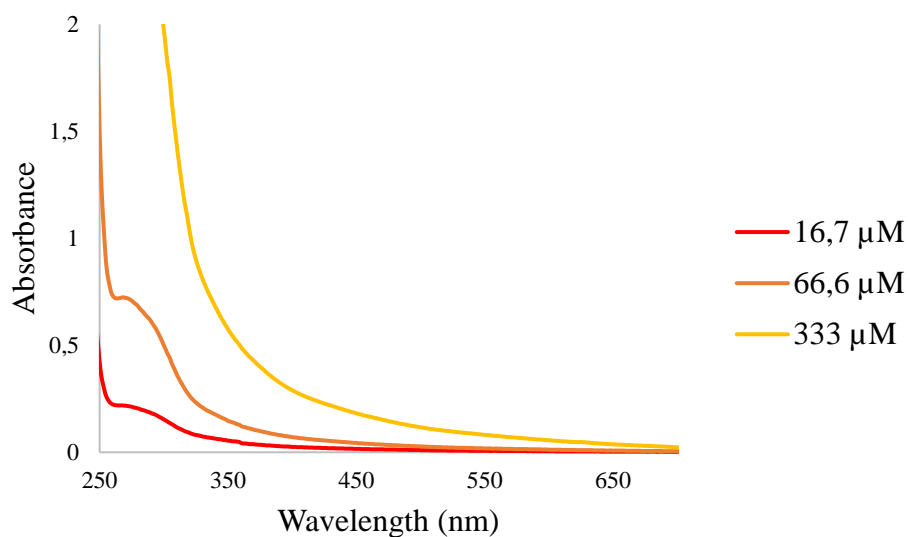


Figure S 4.30: Absorbance spectra of **D2** at various concentrations, 16.7 μM (red), 66.6 μM (orange), and 333 μM (yellow).

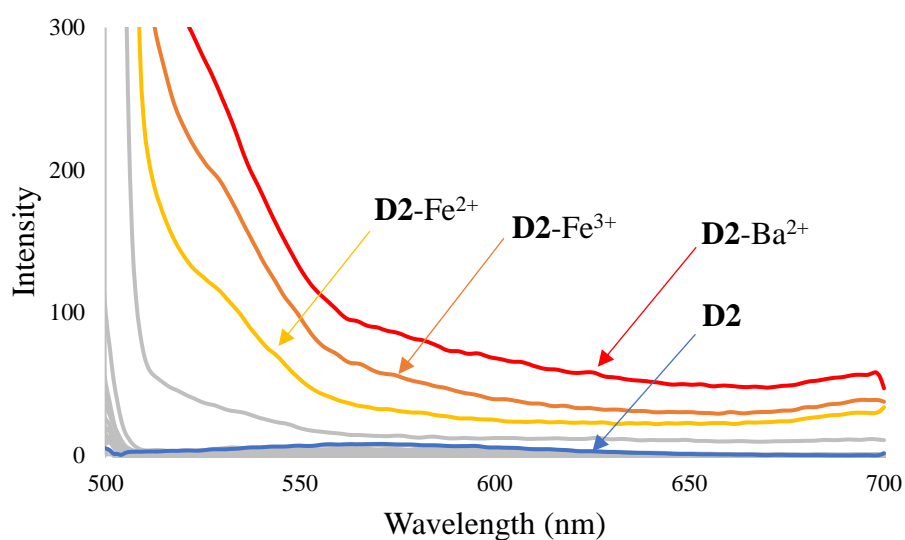


Figure S 4.31: Screening various metal cations in acetonitrile using compound **D2** (blue, 0.0333 μM or 33.3 nM). $\lambda_{\text{excitation}}$: 487 nm

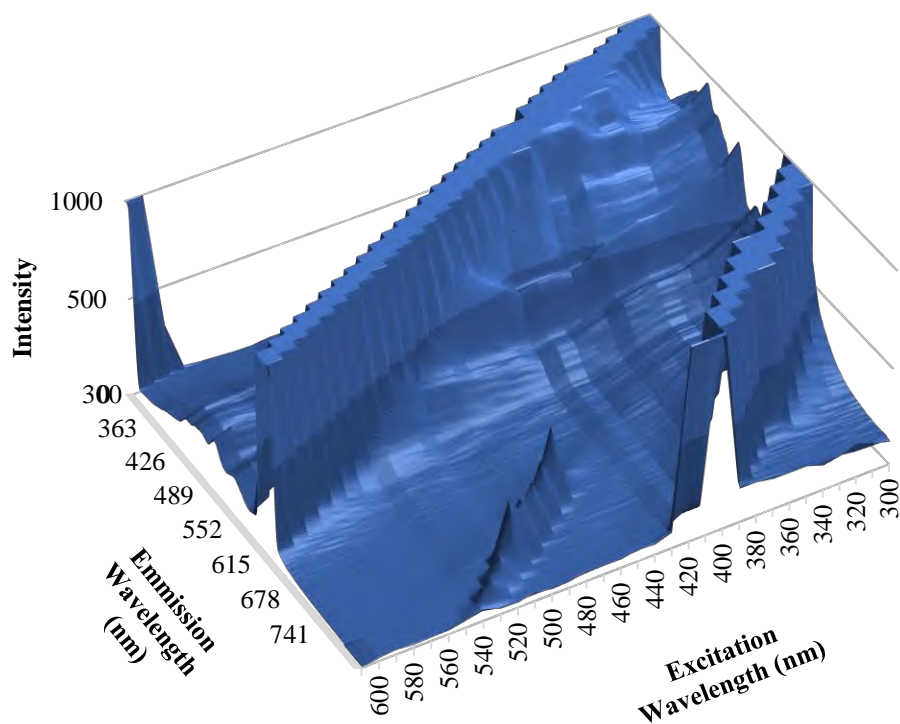


Figure S 4.32: 3D emission scan of **D2-Ba²⁺** complex.

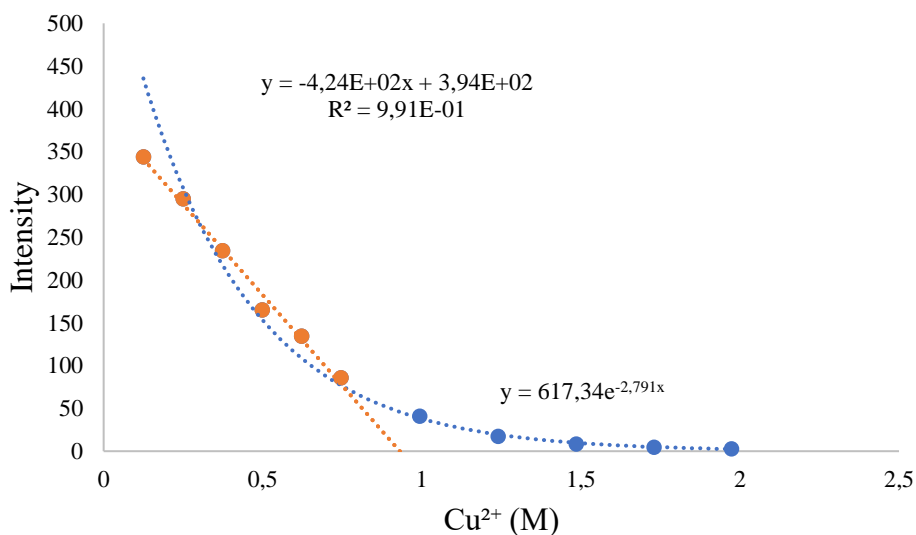
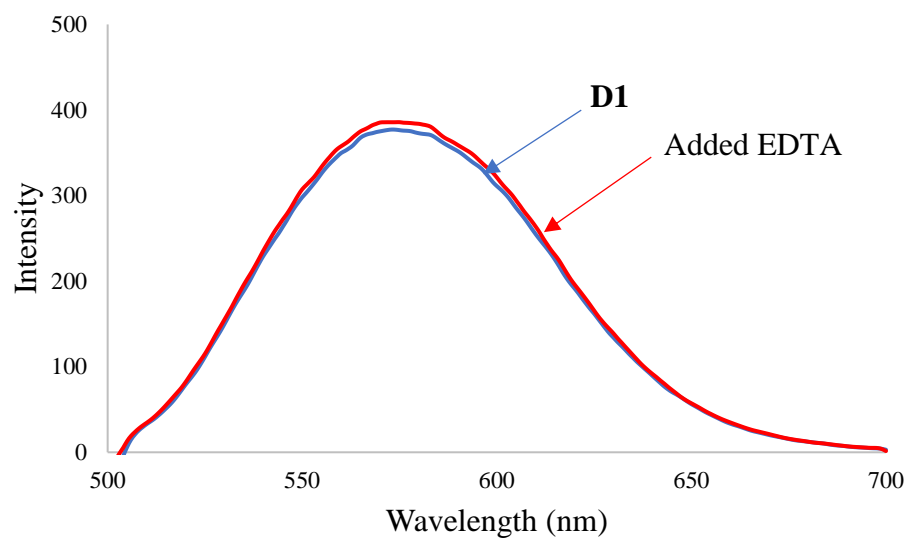


Figure S 4.33: Calibration curve of **D1-Cu²⁺** in acetonitrile.

Shown in **Figure S 4.33** are the two trend lines for the linear region and the entire concentration range. The second intercept indicates the point of deviating from linearity, hence the endpoint at which the concentration can accurately be measured, which is calculated to be 0.795 μ M.



*Figure S 4.34: Emission spectra of **D1** in the absence (blue) and presence of EDTA (red).*

Table S 4.1: X-ray data of E1 and compound 2.

	E1	2
Formula	C ₁₅ H ₁₇ NO ₃	C ₁₄ H ₁₅ NO ₃
Molecular Weight	259.30	245.27
Temperature (K)	200	200
Crystal system	monoclinic	monoclinic
Space group	C2/c	C2/c
a (Å)	17.2617(10)	25.372(3)
b (Å)	7.4372(4)	7.7357(9)
c (Å)	21.8565(13)	12.5335(13)
α (°)	90	90
β (°)	108.542(2)	93.394(5)
γ (°)	90	90
V (Å³)	2660.3(3)	2455.6(5)
Z	8	8
D_c (g/ cm⁻³)	1.295	1.327
μ (mm⁻¹)	0.090	0.094
Reflections collected	24170	26377
Unique reflections	3307	3068
R_{int}	0.023	0.046
wR₂	0.1109	0.1250

Chapter 5

Thio-analogue Chemosensors

Summary

In this chapter, an ester-functionalised coumarin compound was successfully monosubstituted into the sulphur analogue. In the ^{13}C NMR of **T1**, the lactone carbonyl ($-\text{O}-\text{C}=\text{O}$) was observed at 156.24 ppm, which after the successful thionation, shifted to 192.13 ppm as the thiocarbonyl ($-\text{O}-\text{C}=\text{S}$) **T2**. The ester carbonyl peak stayed relatively constant, 163.04 ppm in **T1** and 164.97 ppm in **T2**. Molecular modelling was employed to illustrate the change in the electronic environment due to the presence of the sulphur atom. The thionation of **T1** resulted in the shift of the electron density, the HOMO and the LUMO. Lastly, cationic chemosensor screening tests were performed in which **T1** interacted strongly with Fe^{2+} , whereas **T2** resulted in a shift in selectivity towards Hg^{2+} and Fe^{2+} .

.

Table of Contents

Summary	221
List of Figures	223
List of Schemes	224
List of Tables	224
List of selected Abbreviations	224
5 Thio-analogue chemosensors.....	225
5.1 Introduction	225
5.2 Aim of chapter.....	228
5.3 Synthesis of T1 and thio analogue compounds.....	229
5.4 Predicted complexation site for compounds T1 and T2	233
5.5 UV-vis spectrum of T1 and T2	236
5.5.1 Cationic screening using T1 and T2	236
5.6 Conclusion.....	239
5.7 Experimental	240
5.7.1 General information	240
5.7.2 Synthesis of compounds	241
References.....	243
Supplementary information	245
List of Supplementary Figures.....	245

List of Figures

Figure 5.1: Structure of Lawesson's reagent.	225
Figure 5.2: Other commercially available thionating reagents.	227
Figure 5.3: General structure of the Woollins reagent.	227
Figure 5.4: Ester-functionalised coumarin, T1 , and various sulphur analogue compounds T2 – T3	228
Figure 5.5: ^1H NMR spectrum of compound T1 , in CDCl_3	229
Figure 5.6: ^1H NMR spectra of a) First isolated fraction from reaction a overlayed with T1 in DMSO.	232
Figure 5.7: ^1H NMR spectra of a) Second fraction isolated from reaction a overlayed with T1 in DMSO.	232
Figure 5.8: ^{13}C NMR spectra of a) Second fraction isolated from reaction a overlayed with T1 , in DMSO.	233
Figure 5.9: ^{13}C NMR spectra of a) the fraction isolated from reaction b overlayed with T1 in DMSO.	233
Figure 5.10: Electrostatic potential map of compound T1 and the thio analogue T2	234
Figure 5.11: HOMO of T1 and T2	235
Figure 5.12: LUMO of T1 and T2	235
Figure 5.13: Absorbance spectra of T1 and T2 in acetonitrile.	236
Figure 5.14: T1 screening against various metal cations in acetonitrile.	237
Figure 5.15: T2 screening of various metal cations in acetonitrile.	238

List of Schemes

Scheme 5.1: Equilibrium reaction of Lawesson's reagent (LR) and reactive species dithiophosphine ylide, 1	226
Scheme 5.2: Thionation mechanism using Lawesson's reagent.	226
Scheme 5.3: Synthesis of T1 . a) Diethyl malonate, ethanol, piperidine, GAA, reflux, 4h. ...	229
Scheme 5.4: Synthesis of sulphur analogue T2 , T3 and T4 . Reaction conditions: toluene. N ₂ atmosphere. 12h.	230

List of Tables

Table 5.1: Predicted ¹³ C NMR shifts for the respective carbonyl and thio analogue groups.	231
---	-----

List of selected Abbreviations

GAA – Glacial Acetic Acid

HOMO – Highest Occupied Molecular Orbital

LR – Lawesson's Reagent

LUMO – Lowest Unoccupied Molecular Orbital

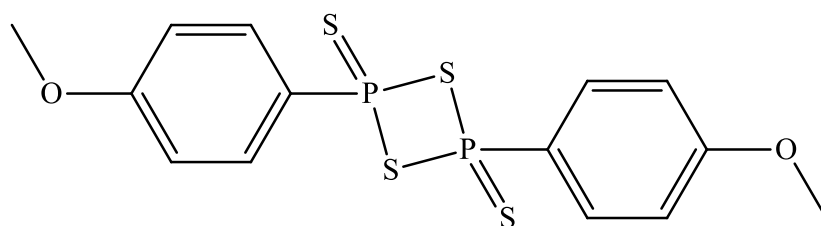
TLC – Thin Layer Chromatography

5 Thio-analogue chemosensors

5.1 Introduction

Most chemosensors in literature to date use oxygen and nitrogen atoms as the main binding sites for cations.¹⁻⁴ However, as seen in previous chapters and from literature, oxygen and nitrogens have a stronger affinity for iron and copper cations.⁴⁻⁶ Other cations have also been seen to form complexes with these two atoms. Schiff bases ($>\text{C}=\text{N}$) are the nitrogen analogue of carbonyl groups ($>\text{C}=\text{O}$), as mentioned in previous chapters.⁷ However, other analogues can also be synthesised, namely the thiocarbonyls ($>\text{C}=\text{S}$) and selenium ($>\text{C}=\text{Se}$) analogues. Oxygens, nitrogens and sulphur are electron donors, with sulphur being well suited for selective recognition of mercury (Hg^{2+}) due to the strong S-Hg interactions.^{8,9}

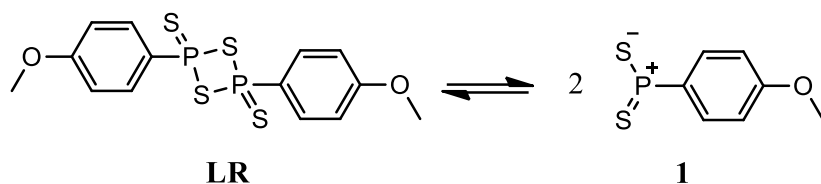
Thio analogues of amides, hydroxyls, ether, esters and carbonyl functional groups¹⁰ have started to track interest in the field of chemosensors due to their ease of thionation using Lawesson's reagent (LR) (**Figure 5.1**).¹¹



Lawesson's reagent

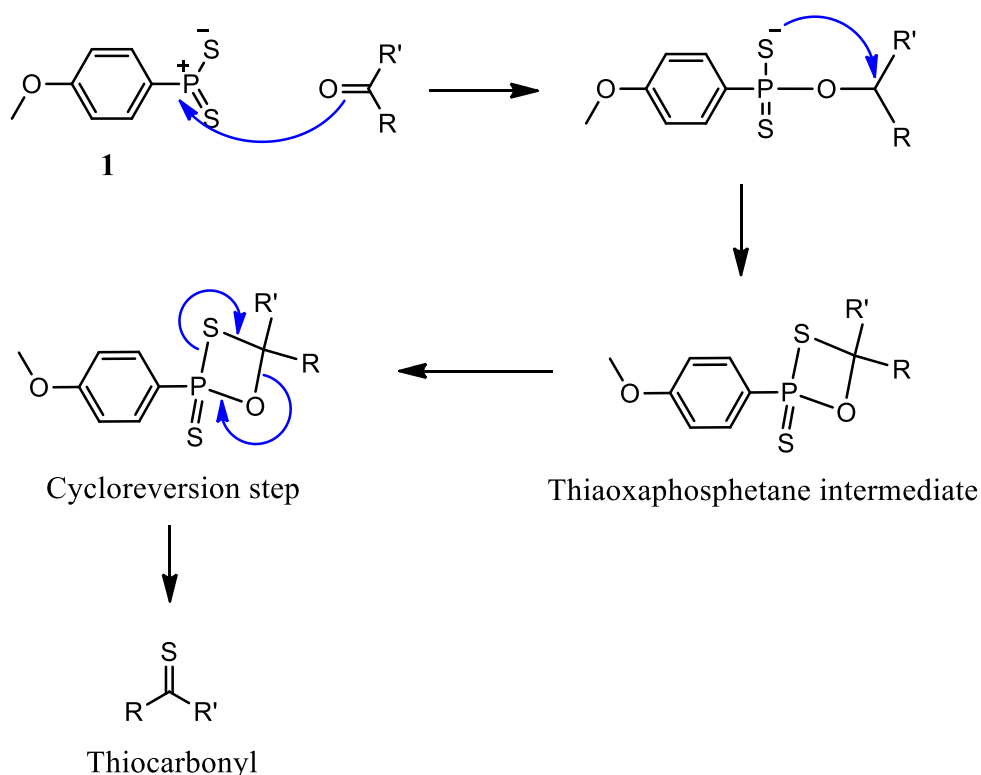
Figure 5.1: Structure of Lawesson's reagent.

Lawesson's reagent was first mentioned in publications by Lawesson and co-workers in 1978 for converting carbonyl groups to thiocarbonyls.¹⁰ However, Hoffman and Schuhmacher published the use of this reagent in 1967 for the synthesis of thiobenzophenone.¹² **Scheme 5.1** and **Scheme 5.2** illustrate a detailed mechanism for converting a carbonyl group to the thiocarbonyl analogue.



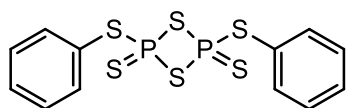
Scheme 5.1: Equilibrium reaction of Lawesson's reagent (**LR**) and reactive species dithiophosphine ylide, **1**.

In solution, the LR dissociates (**Scheme 5.1**) into the more reactive species dithiophosphine ylide, **1**. This reactive species, **1**, can then be attracted by the carbonyl oxygen, as shown in **Scheme 5.2**, which results in cyclisation forming the thioxaphosphetane intermediate. During cycloreversion, the thermodynamically stable P=O bond is formed, releasing the thiocarbonyl compound in a similar mechanism to a Wittig reaction.^{10,12}

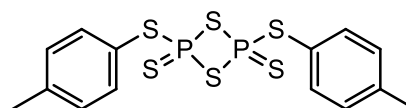


Scheme 5.2: Thionation mechanism using Lawesson's reagent.

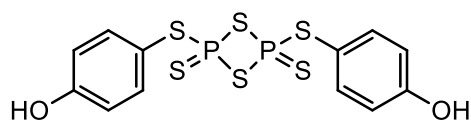
Other thionating reagents (**Figure 5.2**) that are commercially available include P₄S₁₀, the Japanese reagent, the Davy reagent, the Yokoyama reagent and the Belleau reagent.^{12–14}



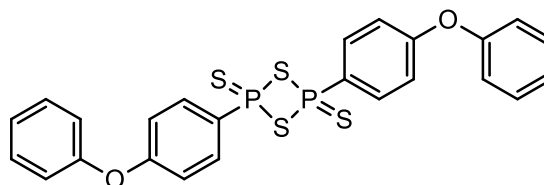
Japanese reagent



Davy reagent



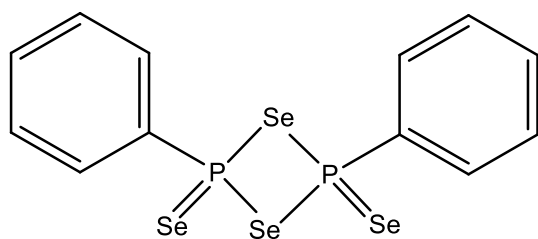
Yokoyama reagent



Belleau's reagent

Figure 5.2: Other commercially available thionating reagents.

The selenium analogue of the thionating reagent is known as the Woollins reagent.¹⁵ As with Lawesson's reagent, Woollins reagent converts the oxygen carbonyl into the selenium carbonyl analogue. This change in chemical environment can cause a chemosensor to change its selectivity from one cation to another, as it was observed for sulfur which prefers to bind with mercury complexes; selenium also has a similar affinity for mercury.¹⁶



Woollins reagent

Figure 5.3: General structure of the Woollins reagent.

5.2 Aim of chapter

Oxygens, nitrogens, and sulphur are electron donors that can interact and coordinate with metal cations.^{8,9} Herein, the synthesis of the sulphur analogue of compound **T1** will be investigated. Ethyl 8-ethoxy-2-oxo-2H-chromene-3-carboxylate, **T1**, will be synthesised and characterised using ^1H and ^{13}C NMR. **T1** will then be used with the Lawesson's reagent (LR) in order to synthesise **T2**, **T3** and **T4** (Figure 5.4).

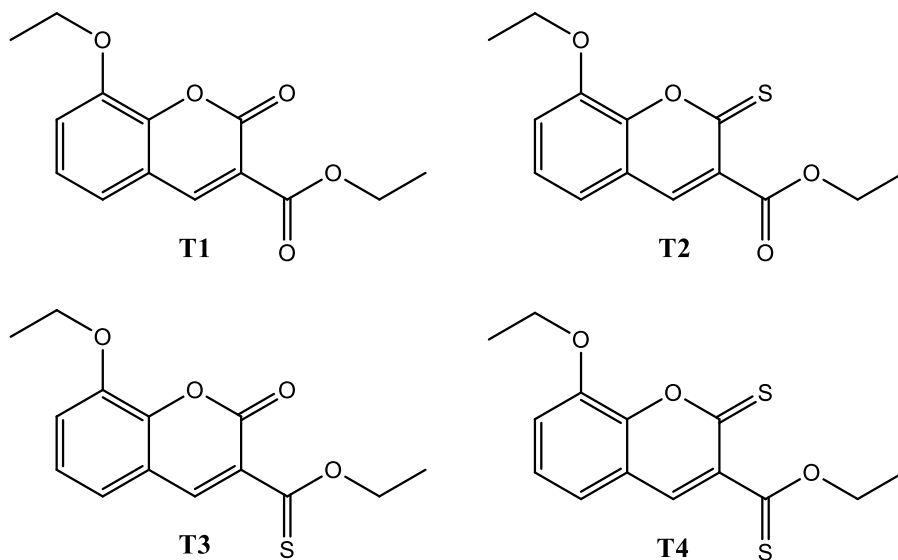
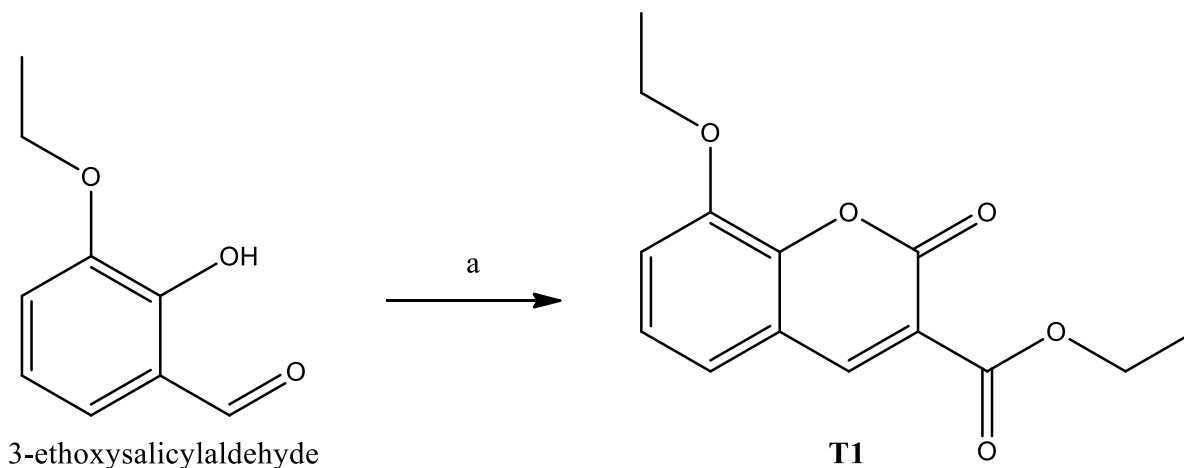


Figure 5.4: Ester-functionalised coumarin, **T1**, and various sulphur analogue compounds **T2 – T3**.

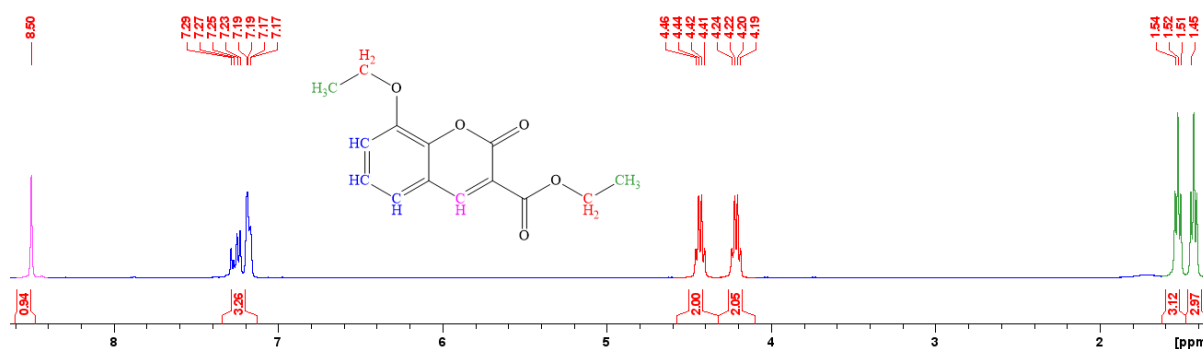
5.3 Synthesis of **T1** and thio analogue compounds

The ester derivative, **T1**, with a coumarin backbone, was synthesised using 3-ethoxysalicylaldehyde in a condensation reaction, as described in **Chapter 3**, with diethyl malonate.¹⁷ After recrystallisation of the crude product using ethanol, **T1** was isolated in good yields as a white solid.



*Scheme 5.3: Synthesis of **T1**. a) Diethyl malonate, ethanol, piperidine, GAA, reflux, 4h.*

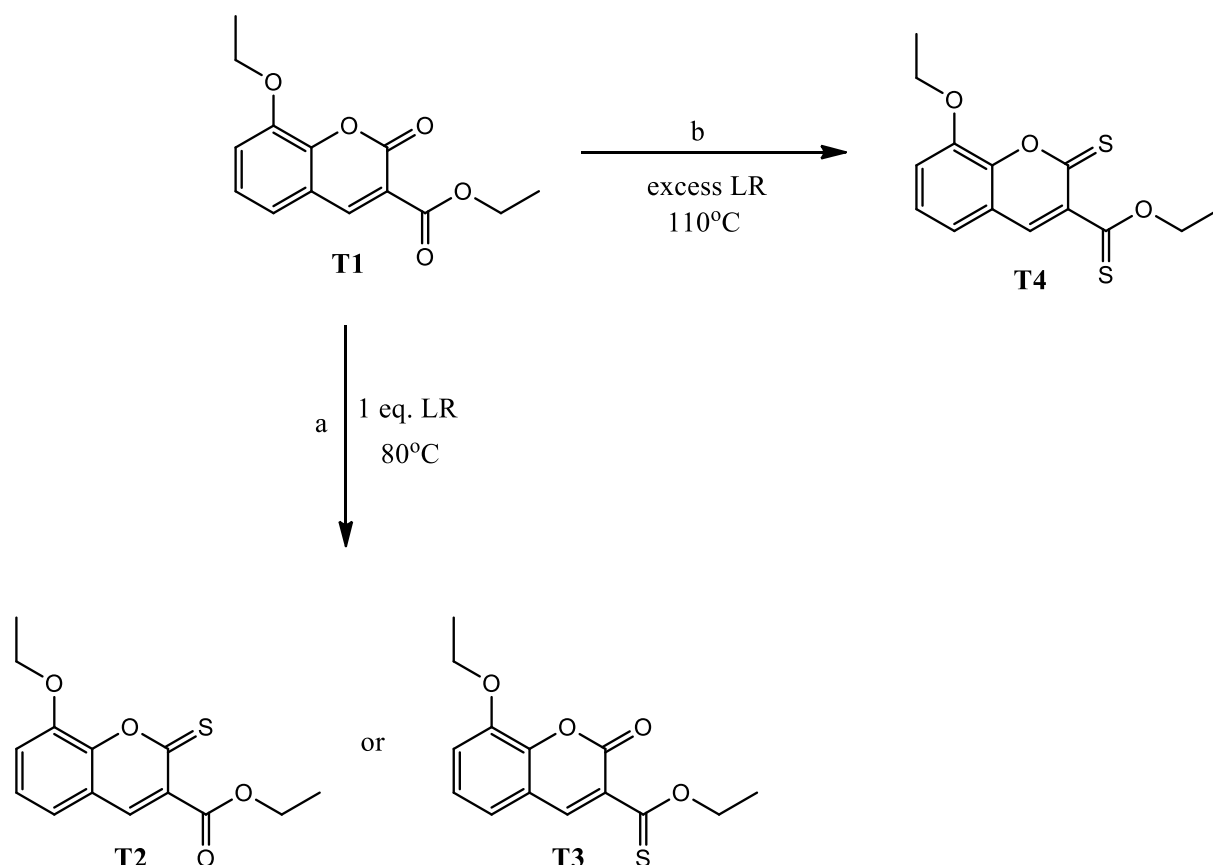
The resulting product was confirmed by ^1H (**Figure 5.5**) and ^{13}C NMR (**Figure S 5.1**). **Figure 5.5** shows a new peak formed at 8.50 ppm, confirming the presence of the lactone moiety protons with coumarin ring protons observed at 7.17 – 7.29 ppm. The two ethylene protons were observed as two quartets between 4.19 – 4.24 ppm and 4.41 – 4.46 ppm.



*Figure 5.5: ^1H NMR spectrum of compound **T1**, in CDCl_3 .*

Compound **T1** was then used to synthesise the sulphur analogue derivatives, as shown in **Scheme 5.4**. The LR was used in the thionation reaction for 12 hours under an N_2 atmosphere in toluene, using **T1** under two conditions. In reaction (a), one equivalence of LR was used, and the temperature was maintained at 80°C . In the second reaction, excess thionating reagent

(LR) was used, and the temperature was maintained at 110°C. From the literature, most of the compounds undergoing thionation utilise microwave radiation, which forms products under five minutes with good yields, in their synthesis methods.^{10,12,18–20} The synthesis of coumarin-based thio analogue has been scarcely reported. In our case, two methods were attempted using lab bench reaction conditions.



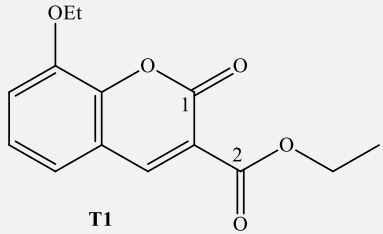
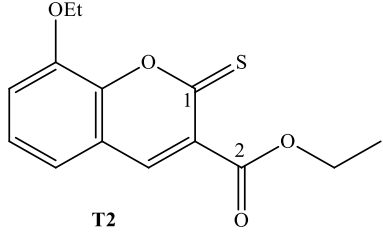
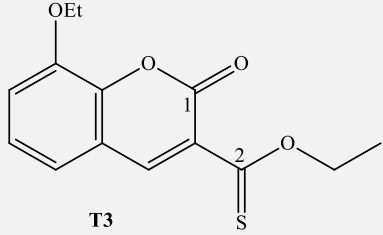
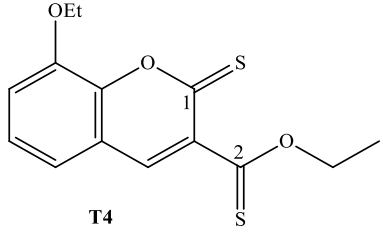
Scheme 5.4: Synthesis of sulphur analogue **T2**, **T3** and **T4**. Reaction conditions: toluene. N_2 atmosphere. 12h.

Reaction (a), in **Scheme 5.4**, uses a lower temperature (80°C) and one molar equivalence LR in toluene. In these conditions, **T2** or **T3** is expected to form. In reaction (b), higher temperatures (110°C) were applied to excess LR to achieve the dithionated product **T4**.

Molecular modelling studies were employed to determine these compounds' expected ^{13}C NMR chemical shifts. Specifically, the carbonyl carbon in the lactone ring (C-1) and the carbonyl carbon in the enone moiety (C-2), as shown in **Table 5.1**. These theoretical chemical

shifts can then be compared to the products' experimental chemical shifts to confirm the product's formation.

Table 5.1: Predicted ^{13}C NMR shifts for the respective carbonyl and thio analogue groups.

	C-1 (ppm)	C-2 (ppm)
 <p>T1</p>	156.2	163.0
 <p>T2</p>	190.6	167.4
 <p>T3</p>	156.5	210.8
 <p>T4</p>	190.3	213.5

Reaction (a) yielded a mixture of products, which were separated using prep thin layer chromatography (TLC) using a 50:50 Hexane: Ethyl acetate mixture. The first fraction from reaction (a) was identified as the unreacted starting compound, **T1**, as shown by the ^1H NMR spectra in **Figure 5.6** and ^{13}C NMR in **Figure S 5.7**.

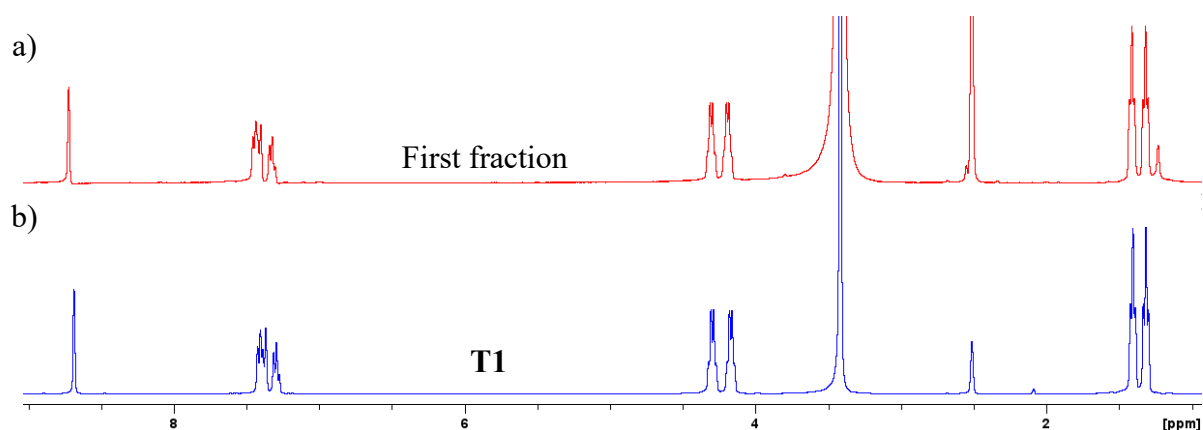


Figure 5.6: ^1H NMR spectra of a) First isolated fraction from reaction a overlaid with **T1** in DMSO.

The second fraction of reaction (a) was collected, and the ^1H NMR (**Figure S 5.8**) and ^{13}C NMR (**Figure S 5.9**) were obtained. As shown in **Figure 5.7**, shifts were noted in the ^1H NMR of this fraction compared to the peaks of **T1** (**Figure 5.7 b**). These observations provided us with the hope that the reaction was successful. Hence ^{13}C NMR characterisation was done and compared to **T1**.

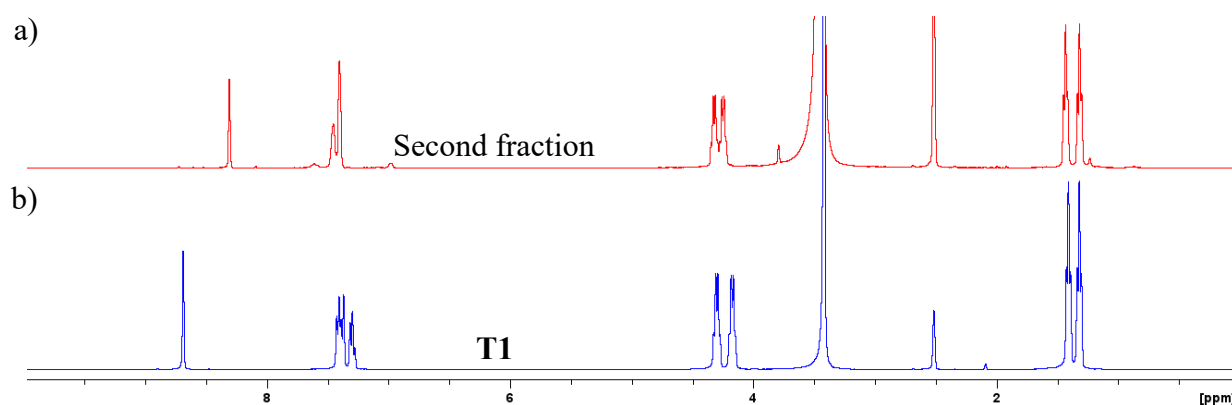


Figure 5.7: ^1H NMR spectra of a) Second fraction isolated from reaction a overlaid with **T1** in DMSO.

An overly ^{13}C NMR spectra of the second fraction and **T1** are shown in **Figure 5.8** to determine the location of the thionated carbonyl. The carbonyl carbon peak at 156.24 ppm and 163.04 ppm of **T1** moved to 192.13 ppm and 164.97 ppm in the fraction.

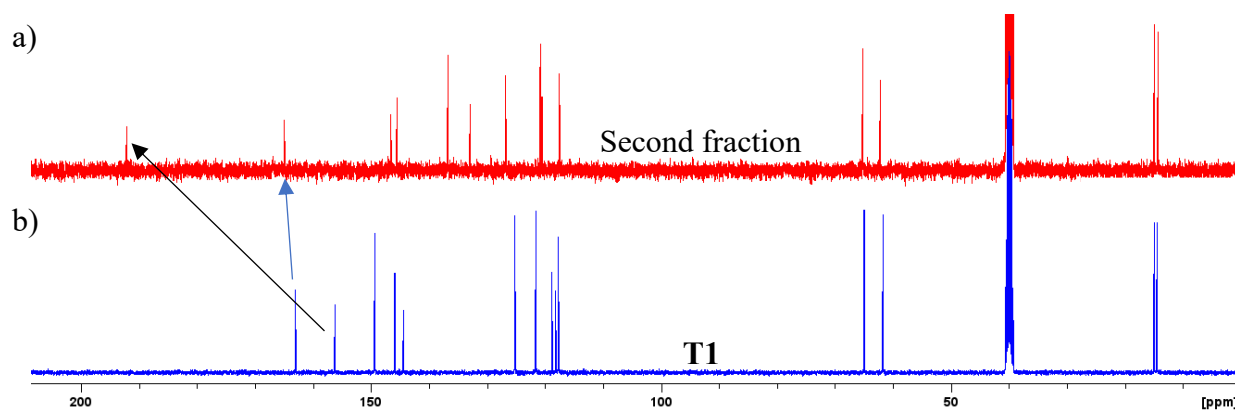


Figure 5.8: ^{13}C NMR spectra of a) Second fraction isolated from reaction a overlaid with **T1**, in DMSO.

It was then concluded that the second fraction of reaction (a) was the desired product **T2** by using the experimental shifts compared to the theoretical shifts in **Table 5.1**.

Reaction (b) yielded one fraction on the prep TLC plate. This fraction was characterised by ^1H NMR (**Figure S 5.10**) and ^{13}C NMR (**Figure S 5.11**). As seen in **Figure 5.9** (and **Figure S 5.12 - Figure S 5.13**), the two carbonyl chemical shifts resemble the shifts observed in the **T2** analogue spectrum, which leads to the conclusion that reaction (b) also produced one thio analogue (**T2**).

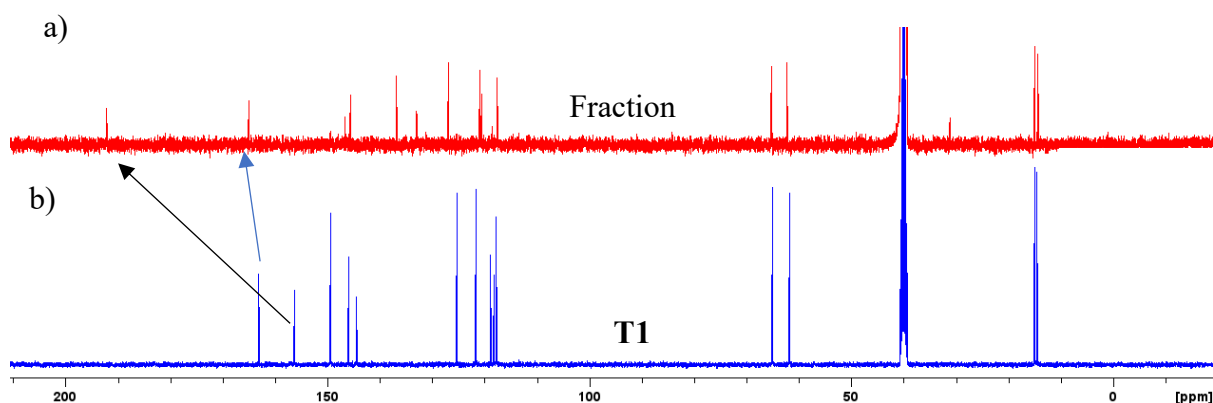


Figure 5.9: ^{13}C NMR spectra of a) the fraction isolated from reaction b overlaid with **T1** in DMSO.

5.4 Predicted complexation site for compounds **T1** and **T2**

Molecular modelling was employed to visualise the sulphur group's effect on the coumarin moiety's chemical environment. As illustrated in **Figure 5.10**, the sulphur group (indicated by

the blue moon) in **T2** has a more prominent area surrounding the thiocarbonyl than the carbonyl in **T1**, indicated by the red star. Furthermore, the carbonyl (indicated by the star) in **T1** has a much higher electron density (indicated by the red map) compared to the relatively neutral (indicated by the green map) thiocarbonyl (indicated by the blue moon) in **T2**.

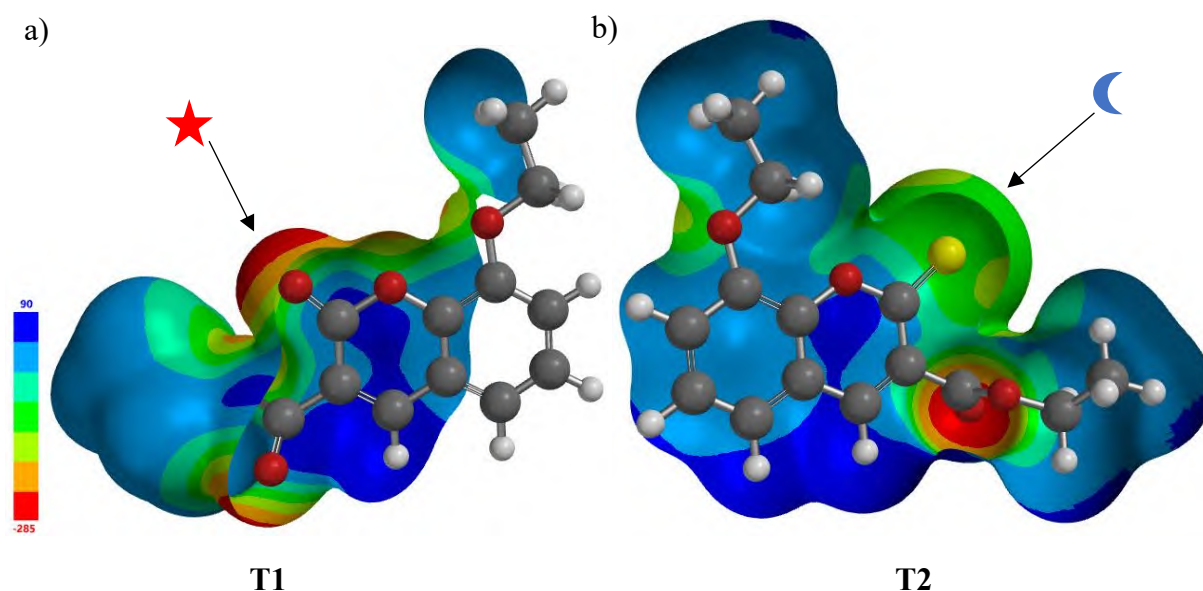


Figure 5.10: Electrostatic potential map of compound **T1** and the thio analogue **T2**.

In addition, the thionation of the lactone carbonyl group changes the highest occupied molecular orbital (HOMO) and lowest unoccupied molecular orbital (LUMO). **Figure 5.11** illustrate the MOMO orbitals of **T1** and **T2** in which a significant change is observed between the carbonyl (indicated by the red star in **Figure 5.11 a**) and the thiocarbonyl (indicated by the blue moon in **Figure 5.11 b**).

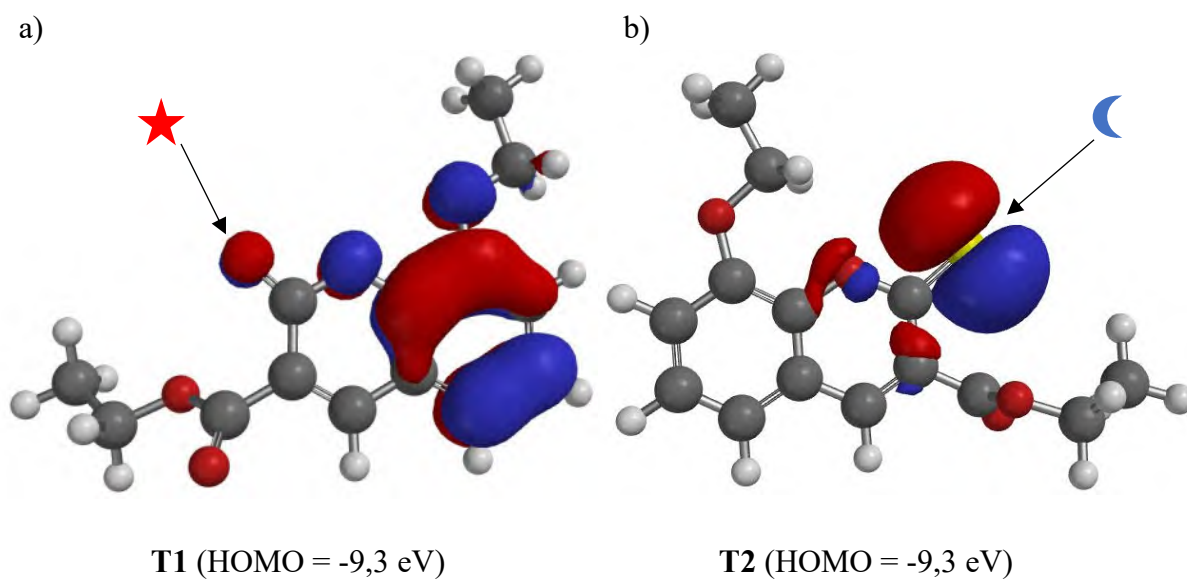


Figure 5.11: HOMO of T1 and T2.

Furthermore, the LUMO orbitals of **T1** and **T2** illustrated the effect of thionation on the electronic environment. The sulphur atom (indicated by the blue moon in **Figure 5.12 b**) is significantly involved in the HOMO and LUMO.

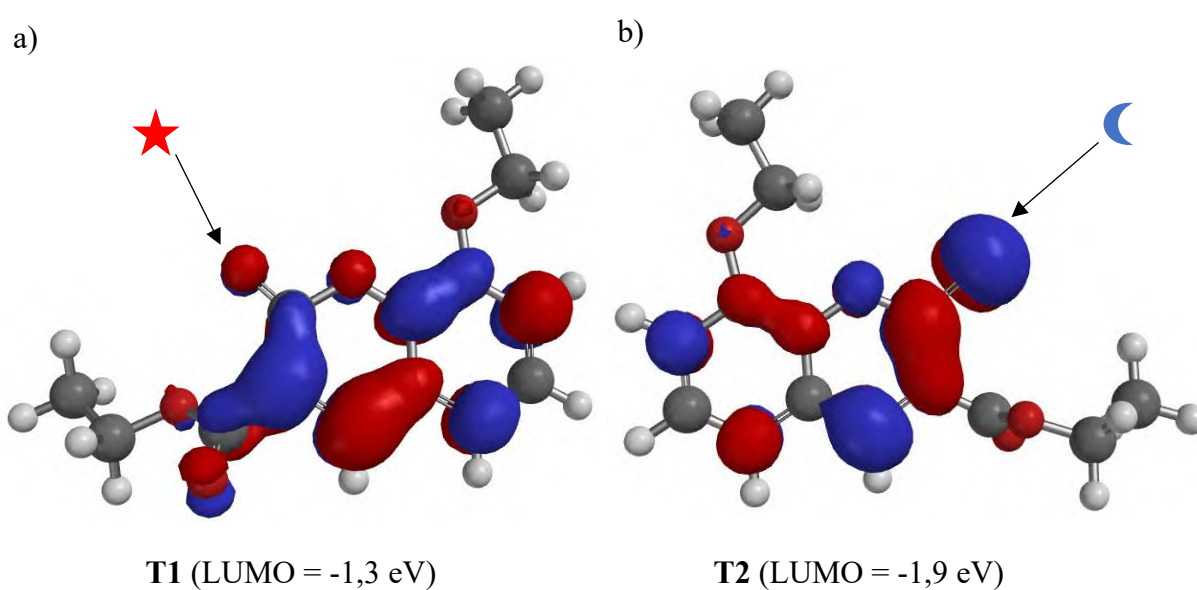


Figure 5.12: LUMO of T1 and T2.

5.5 UV-vis spectrum of **T1** and **T2**

UV-vis spectra of **T1** and **T2** were obtained in acetonitrile and shown in **Figure 5.13**. As shown in **Figure 5.10**, the change in the electronic environment between **T1** and **T2** resulted in the significant differences observed in these compounds' absorbance spectra (**Figure 5.13**). **T1** has a maximum absorption band at 309 nm with a smaller band at 251 nm. The thionated **T2** compound had significantly different absorption spectra, with a broad band from 410 nm to 357 nm and a maximum absorption band at 285 nm. This change in the absorption bands from **T1** to **T2** could be due to the thionation of the lactone carbonyl group in the coumarin ring.

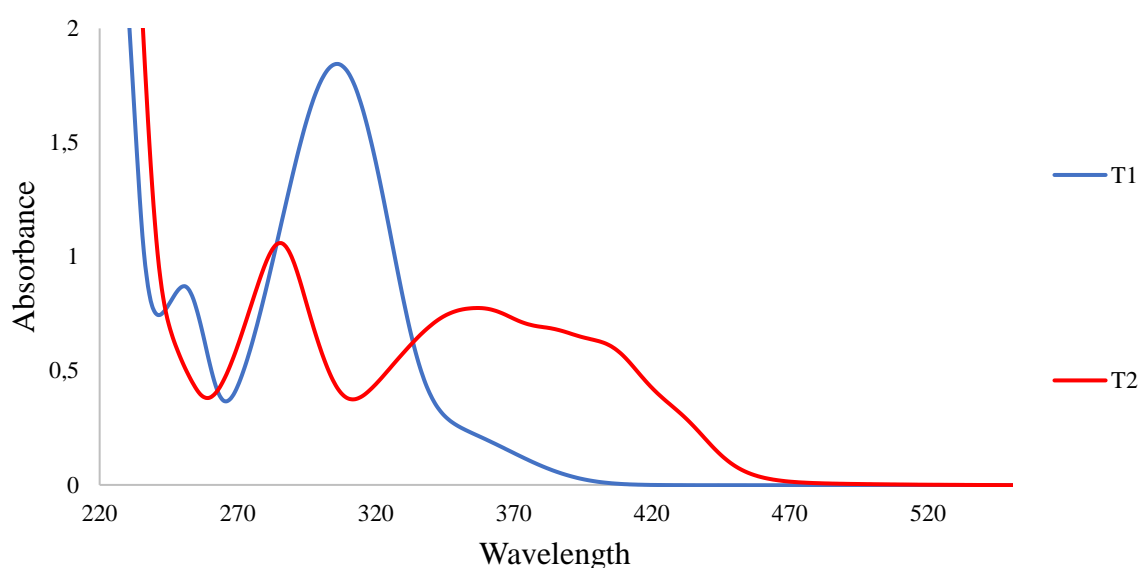


Figure 5.13: Absorbance spectra of **T1** and **T2** in acetonitrile.

5.5.1 Cationic screening using **T1** and **T2**

Compounds **T1** and **T2** were tested for their abilities as a chemosensor for cations using UV-vis analysis in acetonitrile. The metal cations screened include Na^+ , Mg^{2+} , Al^{3+} , K^+ , Ca^{2+} , Cr^{3+} , Mn^{2+} , Fe^{2+} , Fe^{3+} , Co^{3+} , Ni^{2+} , Cu^{2+} , Zn^{2+} , Pb^{2+} , Ag^+ , Cd^{2+} , Ba^{2+} , and Hg^{2+} . As seen for **T1** in **Figure 5.14**, all the metals increase the absorbance of **T1**. However, this increase in the absorbance was significantly higher with Fe^{2+} for both bands observed at 309 nm and 251 nm.

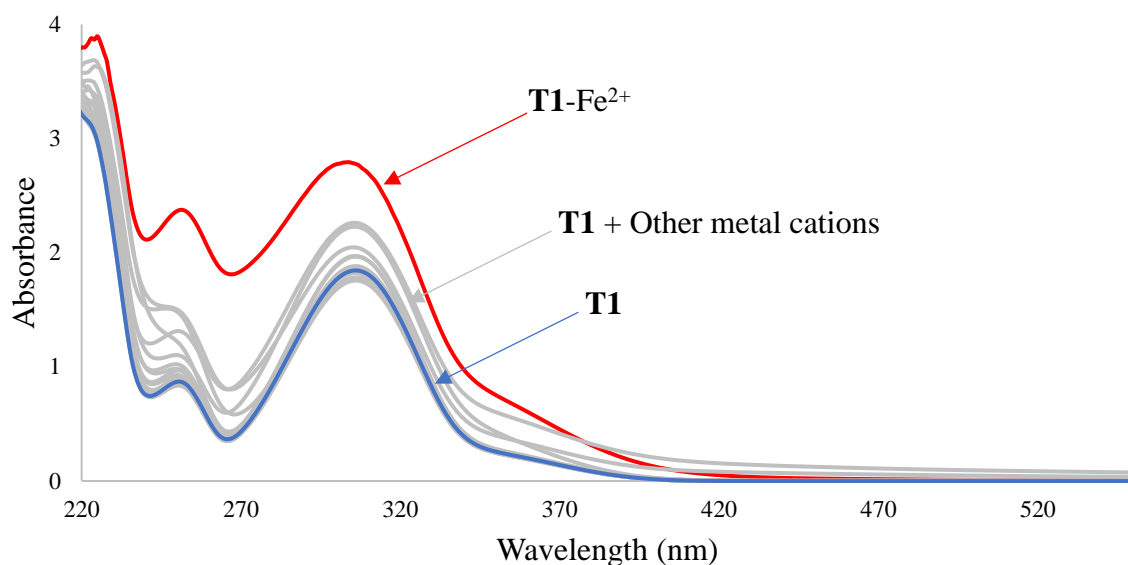


Figure 5.14: *T1 screening against various metal cations in acetonitrile.*

The thio analogue **T2** was also tested for its chemosensors' ability. **Figure 5.15** illustrate the absorption spectra of **T2** (blue spectrum) and **T2** in the presence of the various metal cations (grey spectra). As with **T1**, all the cations increased the absorbance, with Fe^{2+} inducing the most significant increase. However, as predicted, the sulphur atom present in **T2**, this analogue, interacted differently with the Hg^{2+} ions due to the high-affinity sulphur has towards Hg^{2+} .^{8,9} The affinity of **T2** towards Hg^{2+} is observed in the absorbance spectra of **T2-Hg**²⁺ (green spectra in **Figure 5.15**). In the complexation, mercury cation resulted in the bathochromic (red) shift from 285 nm to 302 nm.

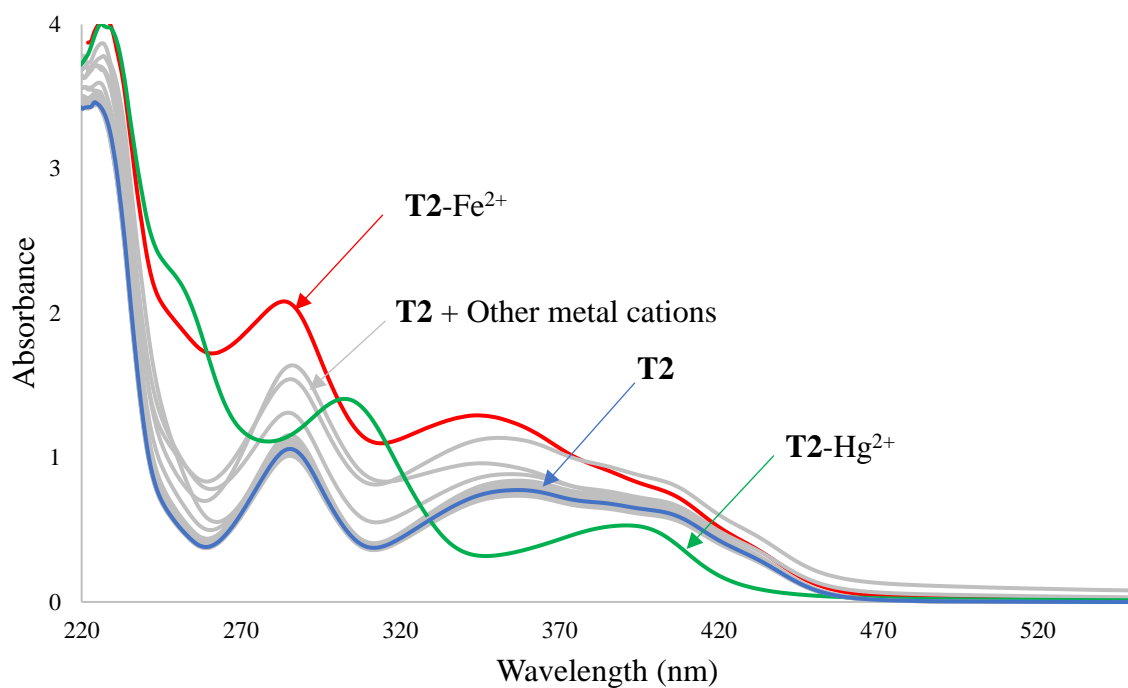


Figure 5.15: T2 screening of various metal cations in acetonitrile.

These observations provided the possibility that the **T2** analogue can be used as a chemosensor for detecting Hg^{2+} in the presence of other cations. However, due to very low yields in preparing these compounds, further investigation could not proceed.

5.6 Conclusion

In this chapter, the ester-functionalised compound **T1** was successfully synthesised. **T1** was reacted with Lawesson's reagent (LR) to convert the oxygen in the carbonyl groups into the sulphur analogue, thiocarbonyl. Two reaction conditions were employed, as no reaction conditions were found in the literature. Reaction (a), using one equivalence LR at 80°C, yielded two products identified as the starting compound, **T1**, and the monosubstituted sulphur analogue, **T2**. In reaction (b), using excess LR at 110°C, only one compound was isolated, containing the monosubstituted **T2**. Thus, the higher temperature and higher equivalence of the LR resulted in the full conversion from **T1** to **T2**.

The changes observed in the electrostatic potential map, HOMO and the LUMO are good indicators that the compound's selectivity or sensitivity towards analytes could change with an easy thionation reaction.

Lastly, as predicted, substituting one oxygen group into the thio analogue resulted in a shift in selectivity from Fe^{2+} in **T1** to Hg^{2+} in **T2**. However, **T2** still interacted strongly with Fe^{2+} . Thus, further test into the selectivity needs to be performed. In addition, the selectivity of **T4** (thionation occurring in both carbonyl groups) also needs to be investigated.

This chapter opens up a relatively new path of changing not only functional groups but individual atoms in the quest to find more selective and sensitive chemosensors for detecting toxic analytes.

5.7 Experimental

5.7.1 General information

All starting materials and solvents were purchased from Sigma Aldrich or Merck and used as received without further purification unless otherwise stated.

^1H NMR and ^{13}C NMR spectra were recorded on a Bruker Advance DPX 400 (400 MHz) spectrometer. The NMR samples were prepared in deuterated solvents (CDCl_3 , DMSO-d_6 , and Acetonitrile- d_3). The samples were run at room temperature. Chemical shifts are expressed in parts per million (ppm) using trimethyl silane (TMS) as the internal reference.

Infrared FT-IR spectra were recorded on a Bruker TENSOR 27 FT-IR spectrometer.

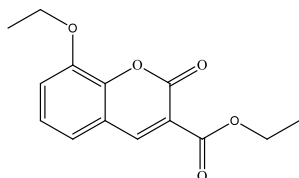
Thin layer chromatography (TLC) analyses were performed on pre-coated silica gel 60 F254 aluminium sheets (0.063-0.2 mm/70 - 230 mesh) using a 50:50% solution of ethyl acetate: hexane; compounds were detected by observation under UV light.

Computational chemistry, Spartan Student Version 8.0.6, Oct 8 2020, was utilised to compare and visually illustrate different conformers of free chemosensors and complexes. The conformers were obtained by conformer distribution at the MMFF level. Calculations of the most energetically preferred conformation were determined by equilibrium geometry at the PM3 level.

Stock solutions of the sensors (0.01 M) were prepared by dissolving the samples in acetonitrile and diluting them to the desired concentrations. Metal cations (0.05 M) solutions were prepared using the nitrate salts (except for Fe^{2+} , which used the sulphate salt) and dissolved in Millipore water.

5.7.2 Synthesis of compounds

5.7.2.1 ethyl 8-ethoxy-2-oxo-2H-chromene-3-carboxylate – **T1**



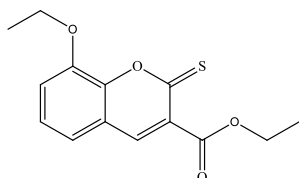
3-Ethoxysalicylaldehyde (5.4 g, 32.49 mmol) and diethyl malonate (6.30 g, 39.33 mmol) were dissolved in ethanol (20 ml) with catalytic amounts of piperidine. This mixture was refluxed for 4 hours, and the mixture was concentrated under reduced pressure. After cooling the mixture on ice, the resulting precipitate was filtered to obtain a fine white powder.¹⁷ **Yield: 95%.** IR ν_{max} (cm^{-1}): 3088-2887 (C-H stretching, Alkene), 1754 (C=O, Ester), 1702 (C=O stretching, Lactone ring). ^1H NMR (DMSO): $\delta_{\text{H}}/\text{ppm}$ = 8.69 (1H, s, Aromatic H), 7.43-7.30 (3H, d, Aromatic H), 4.31-4.29 (2H, q, $-\text{CH}_2$), 4.18-4.17 (2H, q, $-\text{CH}_2$), 1.43-1.39 (3H, s, $-\text{CH}_3$), 1.34-1.30 (3H, t, $-\text{CH}_3$). ^{13}C NMR (DMSO) $\delta_{\text{C}}/\text{ppm}$ = 163.04, 156.24, 149.36, 145.92, 144.40, 125.23, 121.56, 118.83, 118.19, 117.73, 64.98, 61.73, 14.99, 14.50.

5.7.2.2 Thionation reactions

5.7.2.2.1 Reaction (a)

Ethyl 8-ethoxy-2-oxo-2H-chromene-3-carboxylate, **T1**, (1.5 g, 5.70 mmol) and LR (2.3 g, 5.69 mmol) were dissolved in 20 mL of toluene. The solution was stirred at 80°C for 12 hours under a nitrogen atmosphere. The solvent was removed under reduced pressure, followed by prep TLC to obtain two fractions.¹⁰

The first fraction was identified as unreacted **T1**.



The second fraction was confirmed, using NMR, to be ethyl 8-ethoxy-2-thioxo-2H-chromene-3-carboxylate, **T2**. ^1H NMR (DMSO): $\delta_{\text{H}}/\text{ppm}$ = 8.31 (1H, s, Aromatic H), 7.46-7.40 (3H, d,

Aromatic H), 4.35-4.30 (2H, q, -CH₂), 4.28-4.22 (2H, q, -CH₂), 1.45-1.42 (3H, s, -CH₃), 1.34-1.30 (3H, t, -CH₃). ¹³C NMR (DMSO) δ_C/ppm = 192.13, 164.97, 146.59, 145.58, 136.74, 132.91, 126.82, 120.85, 120.54, 117.52, 65.23, 62.22, 14.96, 14.32.

5.7.2.2.2 Reaction (b)

Ethyl 8-ethoxy-2-oxo-2H-chromene-3-carboxylate, **T1**, (5.72 mmol) and LR (4.6 g, 11.38 mmol) were dissolved in 20 mL of toluene. The solution was refluxed at 110°C for 12 hours under a nitrogen atmosphere. The solvent was removed under reduced pressure, followed by prep TLC to yield **T2** as the only fraction present.¹⁰ A yellow powder, which was identified as ethyl 8-ethoxy-2-thioxo-2H-chromene-3-carboxylate, **T2**.

References

- (1) Sahoo, C. R.; Sahoo, J.; Mahapatra, M.; Lenka, D.; Kumar Sahu, P.; Dehury, B.; Nath Padhy, R.; Kumar Paidesetty, S. Coumarin Derivatives as Promising Antibacterial Agent(S). *Arab. J. Chem.* **2021**, *14* (2), 102922. <https://doi.org/10.1016/j.arabjc.2020.102922>.
- (2) Carneiro, A.; Matos, M. J.; Uriarte, E.; Santana, L. Trending Topics on Coumarin and Its Derivatives in 2020. *Molecules* **2021**, *26* (2), 1–15. <https://doi.org/10.3390/molecules26020501>.
- (3) Di Stasi, L. C. Coumarin Derivatives in Inflammatory Bowel Disease. *Molecules* **2021**, *26* (2). <https://doi.org/10.3390/molecules26020422>.
- (4) Yan, T.; Feringa, B. L.; Barta, K. Iron Catalysed Direct Alkylation of Amines with Alcohols. *Nat. Commun.* **2014**, *5*, 1–7. <https://doi.org/10.1038/ncomms6602>.
- (5) Mama, N.; Battison, A. Synthesis and Application of a Fluorescent “turn-Off” Triazolyl-Coumarin-Based Fluorescent Chemosensor for the Sensing of Fe³⁺ Ions in Aqueous Solutions. *Arkivoc* **2020**, 2020, 1–27. <https://doi.org/10.24820/ARK.5550190.P011.283>.
- (6) Ngororabanga, J. M. V.; Plessis, J. Du; Mama, N. Fluorescent Polymer Incorporating Triazolyl Coumarin Units for Cu²⁺ Detection via Planarization of Ict-Based Fluorophore. *Sensors (Switzerland)* **2017**, *17* (9). <https://doi.org/10.3390/s17091980>.
- (7) Junaid, H. M.; Batool, M.; Harun, F. W.; Akhter, M. S.; Shabbir, N. Naked Eye Chemosensing of Anions by Schiff Bases. *Crit. Rev. Anal. Chem.* **2022**, *52* (3), 463–480. <https://doi.org/10.1080/10408347.2020.1806703>.
- (8) Xu, D.; Jia, H.; Niu, Y.; Yin, S. Fluorine-Boron Compound-Based Fluorescent Chemosensors for Heavy Metal Ion Detection. *Dye. Pigment.* **2022**, *200* (February), 110185. <https://doi.org/10.1016/j.dyepig.2022.110185>.
- (9) Bebout, D. C. Mercury: Inorganic & Coordination Chemistry. *Encycl. Inorg. Bioinorg. Chem.* **2011**.
- (10) Khatoon, H.; Abdulmalek, E. A Focused Review of Synthetic Applications of Lawesson’s Reagent in Organic Synthesis. *Molecules* **2021**, *26* (22), 6937. <https://doi.org/10.3390/molecules26226937>.
- (11) Kaleta, Z.; Makowski, B. T.; Soós, T.; Dembinski, R. Thionation Using Fluorous Lawesson’s Reagent. *Org. Lett.* **2006**, *8* (8), 1625–1628. <https://doi.org/10.1021/ol060208a>.
- (12) Jesberger, M.; Davis, T. P.; Barner, L. Applications of Lawesson’s Reagent in Organic and Organometallic Syntheses. *Synthesis (Stuttg.)* **2003**, No. 13, 1929–1958. <https://doi.org/10.1055/s-2003-41447>.
- (13) Ozturk, T.; Ertas, E.; Mert, O. Use of Lawesson’s Reagent in Organic Syntheses. *Chem.*

Rev. **2007**, *107* (11), 5210–5278. <https://doi.org/10.1021/cr040650b>.

- (14) Sağlam, E. G.; Bulat, E.; Zeyrek, C. T.; Akkoç, S.; Zorlu, Y.; Yılmaz, H. 2,4-Bis(2,4-Dimethoxyphenyl)-1,3-Dithia-2,4-Diphosphetane 2,4-Disulfide and Its Derivatives: Syntheses, Structural Characterisations, Anticancer Activities, and Theoretical Studies on Some Dithiophosphonato Ni(II) Complex. *J. Mol. Struct.* **2023**, *1272*, 134197. <https://doi.org/10.1016/j.molstruc.2022.134197>.
- (15) Bethke, J.; Karaghiosoff, K.; Wessjohann, L. A. Synthesis of N,N-Disubstituted Selenoamides by O/Se-Exchange with Selenium–Lawesson’s Reagent. *Tetrahedron Lett.* **2003**, *44* (36), 6911–6913. [https://doi.org/10.1016/S0040-4039\(03\)01690-3](https://doi.org/10.1016/S0040-4039(03)01690-3).
- (16) Farina, M.; Rocha, J. B. T.; Aschner, M. Mechanisms of Methylmercury-Induced Neurotoxicity: Evidence from Experimental Studies. *Life Sci.* **2011**, *89* (15–16), 555–563. <https://doi.org/10.1016/j.lfs.2011.05.019>.
- (17) Patil, S. A.; Unki, S. N.; Kulkarni, A. D.; Naik, V. H.; Badami, P. S. Synthesis, Characterization, in Vitro Antimicrobial and DNA Cleavage Studies of Co(II), Ni(II) and Cu(II) Complexes with ONOO Donor Coumarin Schiff Bases. *J. Mol. Struct.* **2011**, *985* (2–3), 330–338. <https://doi.org/10.1016/j.molstruc.2010.11.016>.
- (18) Gayen, K. S.; Chatterjee, N. Diversity of Lawesson’s Reagent: Advances and Scope. *Asian J. Org. Chem.* **2020**, *9* (4), 508–528. <https://doi.org/10.1002/ajoc.202000032>.
- (19) Ozturk, T.; Ertas, E.; Mert, O. Use of Lawesson’s Reagent in Organic Syntheses. *Chem. Rev.* **2007**, *107* (11), 5210–5278. <https://doi.org/10.1021/cr040650b>.
- (20) Kayukova, L. A.; Praliyev, K. D.; Gut’yar, V. G.; Baitursynova, G. P. Modification of Organic Compounds with Lawesson’s Reagent. *Russ. J. Org. Chem.* **2015**, *51* (2), 148–160.

Supplementary information

List of Supplementary Figures

Figure S 5.1: ^{13}C NMR spectrum of compound T1 in CDCl_3	246
Figure S 5.2: ^1H NMR spectrum of compound T1 in DMSO.	246
Figure S 5.3: ^{13}C NMR spectrum of compound T1 in DMSO.	246
Figure S 5.4: FT-IR spectrum of compound T1	247
Figure S 5.5: ^1H NMR spectrum of the compound from the first fraction from reaction a, identified as T1 , in DMSO.	247
Figure S 5.6: ^{13}C NMR spectrum of the compound from the first fraction from reaction a, identified as T1 , in DMSO.	248
Figure S 5.7: ^{13}C NMR spectra of a) the first isolated fraction from reaction a overlayed with T1 in DMSO.	248
Figure S 5.8: ^1H NMR spectrum of the compound from the second fraction from reaction a, identified as T2 , in DMSO.	248
Figure S 5.9: ^{13}C NMR spectrum of the compound from the second fraction from reaction a, identified as T2 , in DMSO.	249
Figure S 5.10: ^1H NMR spectrum of the compound from the fraction isolated from reaction b, identified as T2 , in DMSO.	249
Figure S 5.11: ^{13}C NMR spectrum of the compound from the fraction isolated from reaction b, identified as T2 , in DMSO.	249
Figure S 5.12: ^1H NMR spectra overlay of a) T2 from reaction b and b) T2 from reaction a	250
Figure S 5.13: ^{13}C NMR spectra overlay of a) T2 from reaction b and b) T2 from reaction a.	250

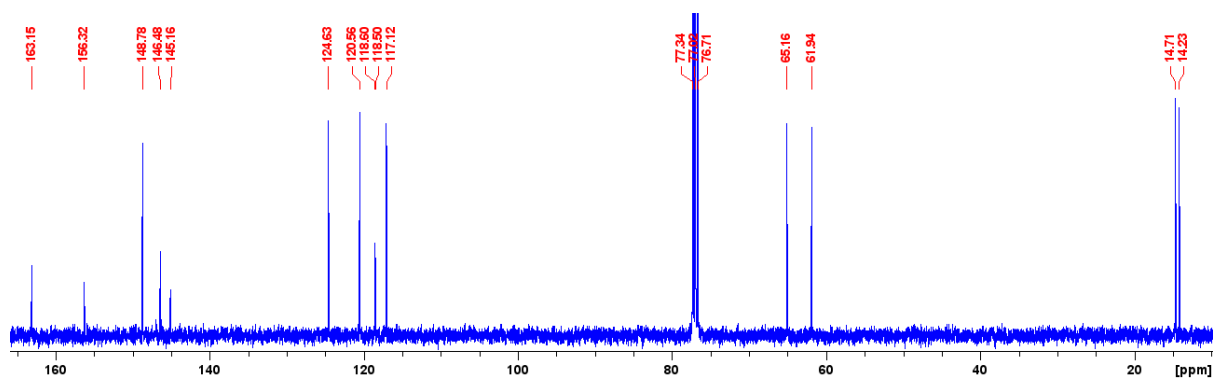


Figure S 5.1: ^{13}C NMR spectrum of compound **T1** in CDCl_3 .

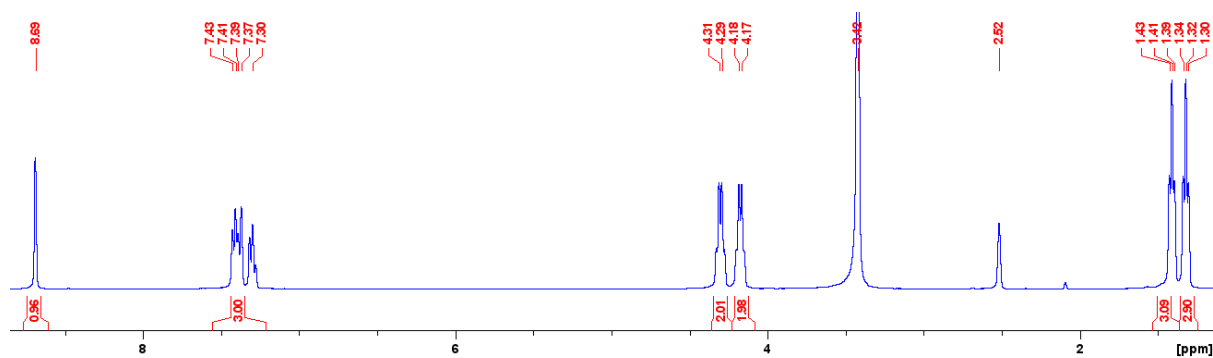


Figure S 5.2: ^1H NMR spectrum of compound **T1** in DMSO .

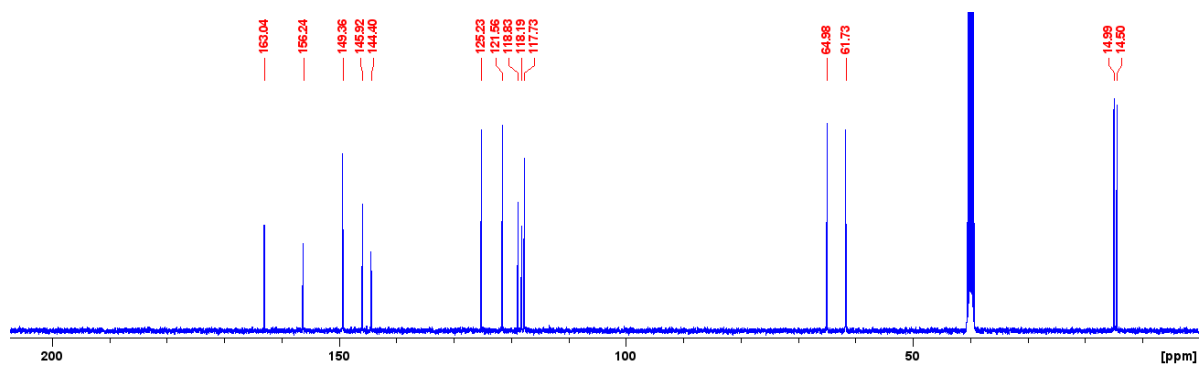


Figure S 5.3: ^{13}C NMR spectrum of compound **T1** in DMSO .

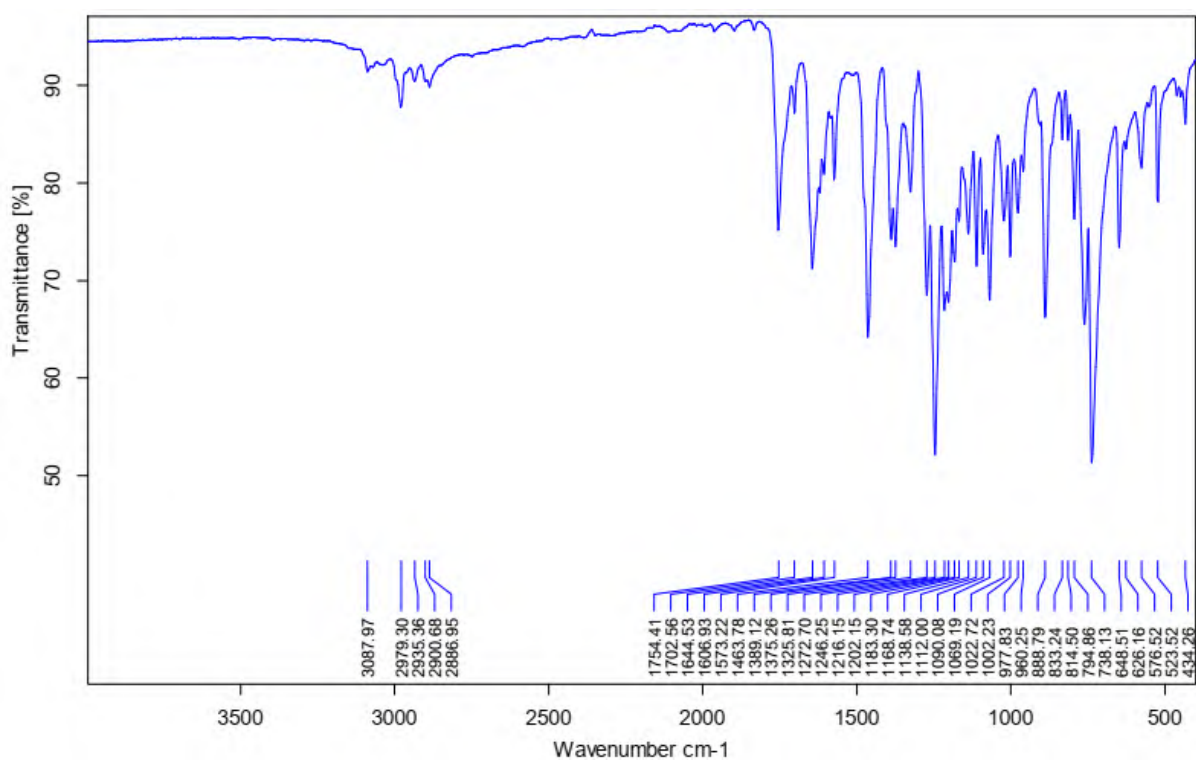


Figure S 5.4: FT-IR spectrum of compound **T1**.

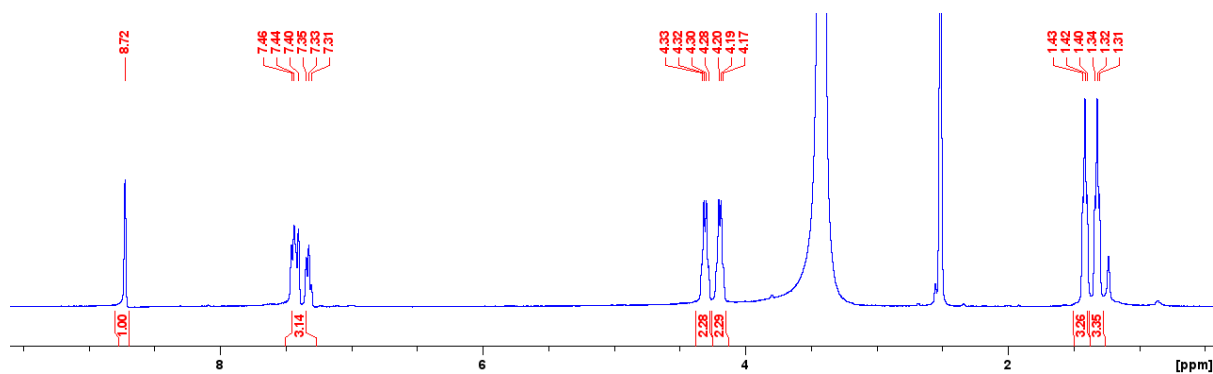


Figure S 5.5: ^1H NMR spectrum of the compound from the first fraction from reaction *a*, identified as **T1**, in DMSO.

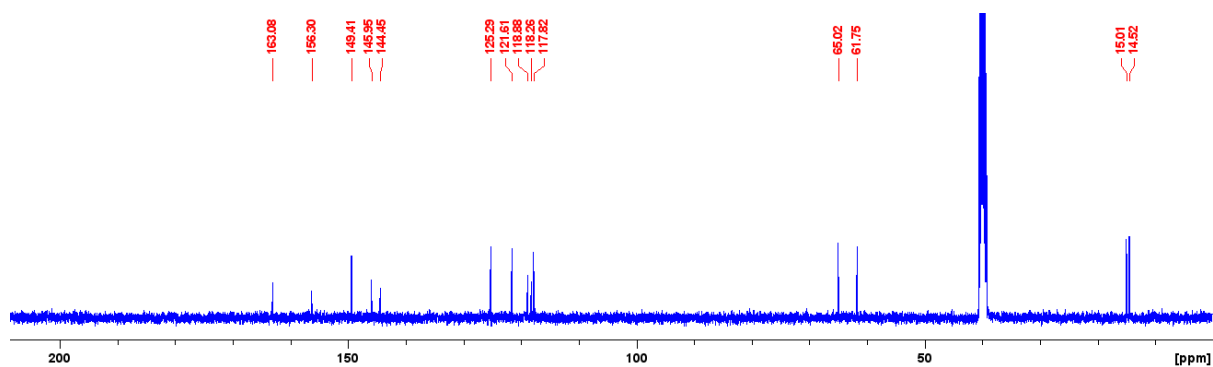


Figure S 5.6: ^{13}C NMR spectrum of the compound from the first fraction from reaction a, identified as **T1**, in DMSO.

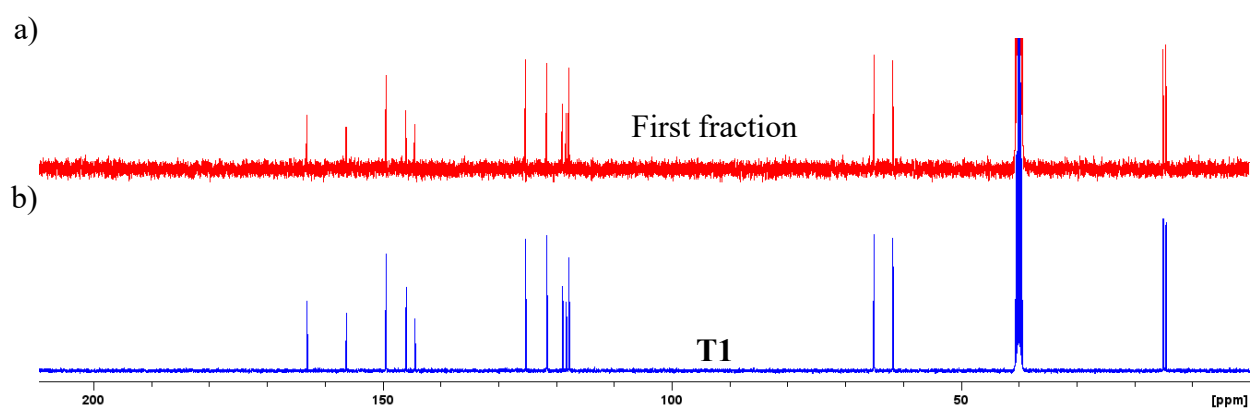


Figure S 5.7: ^{13}C NMR spectra of a) the first isolated fraction from reaction a overlaid with **T1** in DMSO.

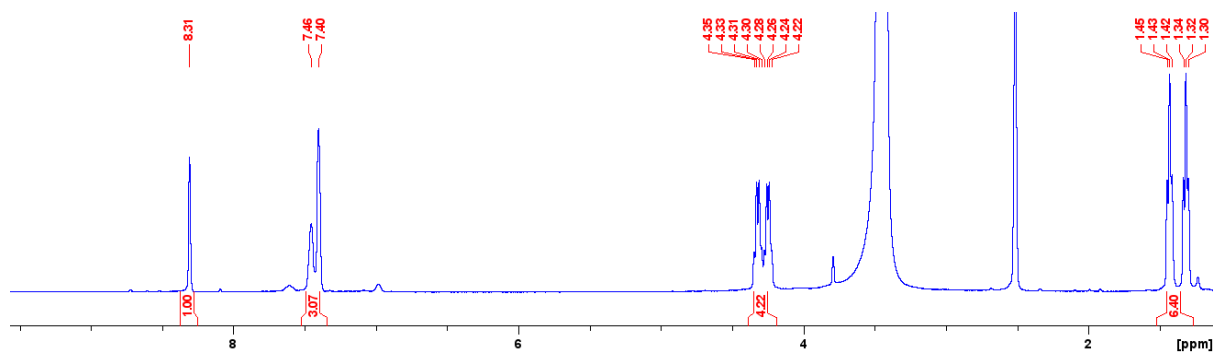


Figure S 5.8: ^1H NMR spectrum of the compound from the second fraction from reaction a, identified as **T2**, in DMSO.

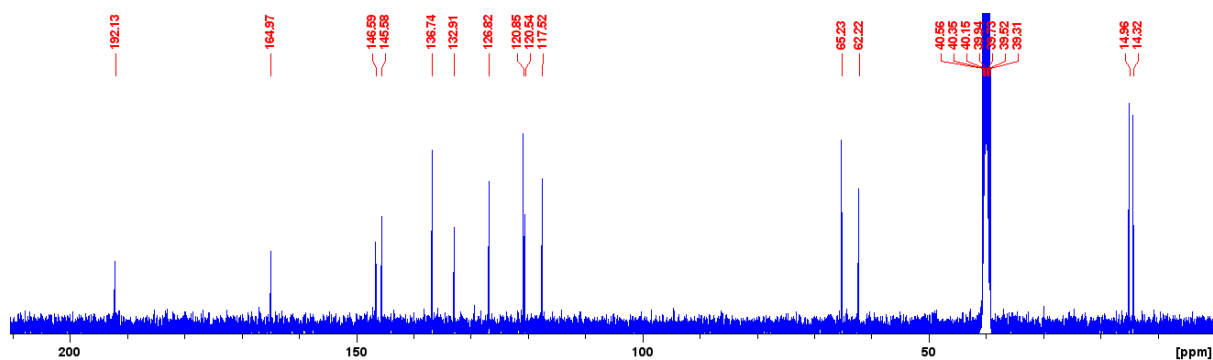


Figure S 5.9: ^{13}C NMR spectrum of the compound from the second fraction from reaction a, identified as **T2**, in DMSO.

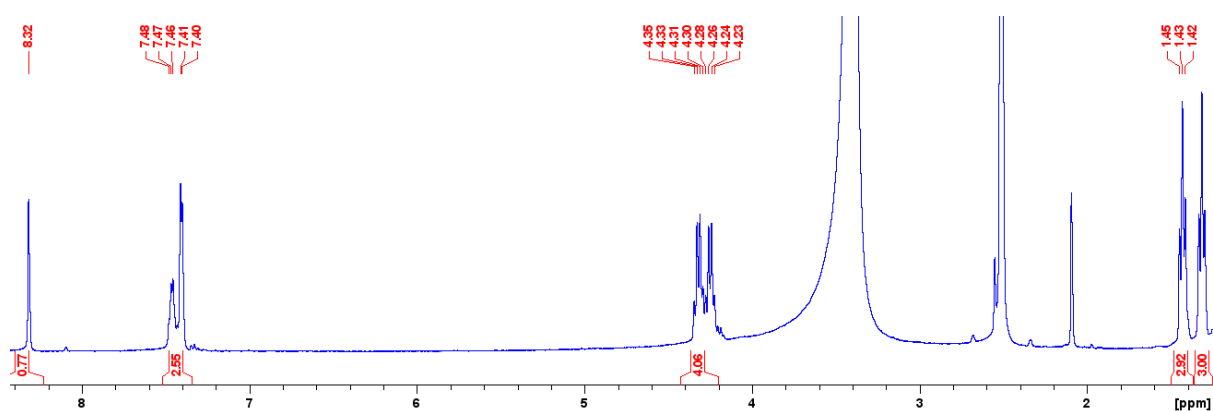


Figure S 5.10: ^1H NMR spectrum of the compound from the fraction isolated from reaction b, identified as **T2**, in DMSO.

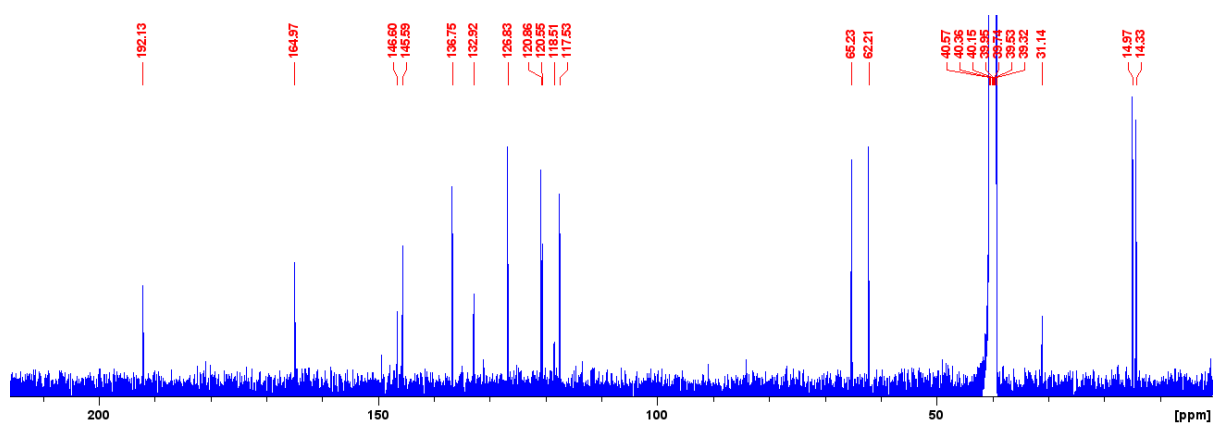


Figure S 5.11: ^{13}C NMR spectrum of the compound from the fraction isolated from reaction b, identified as **T2**, in DMSO.

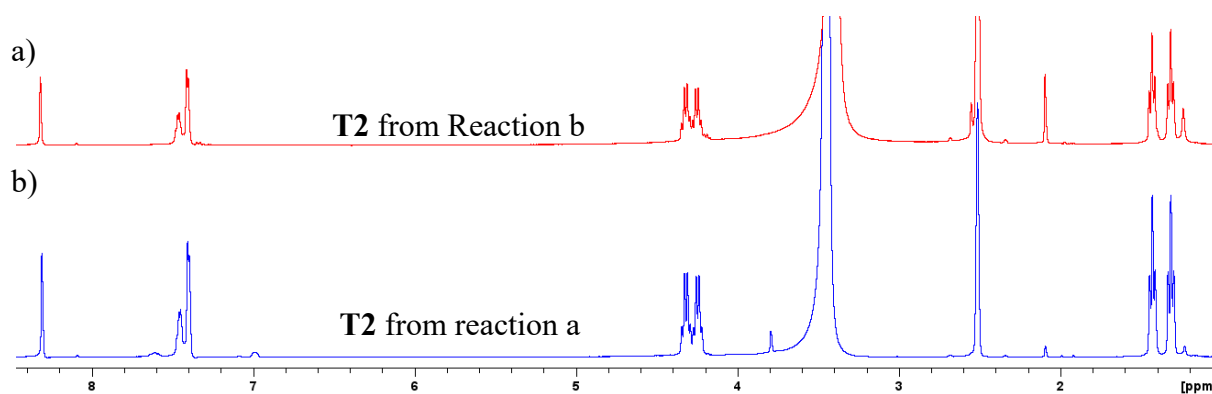


Figure S 5.12: ^1H NMR spectra overlay of a) T2 from reaction b and b) T2 from reaction a.

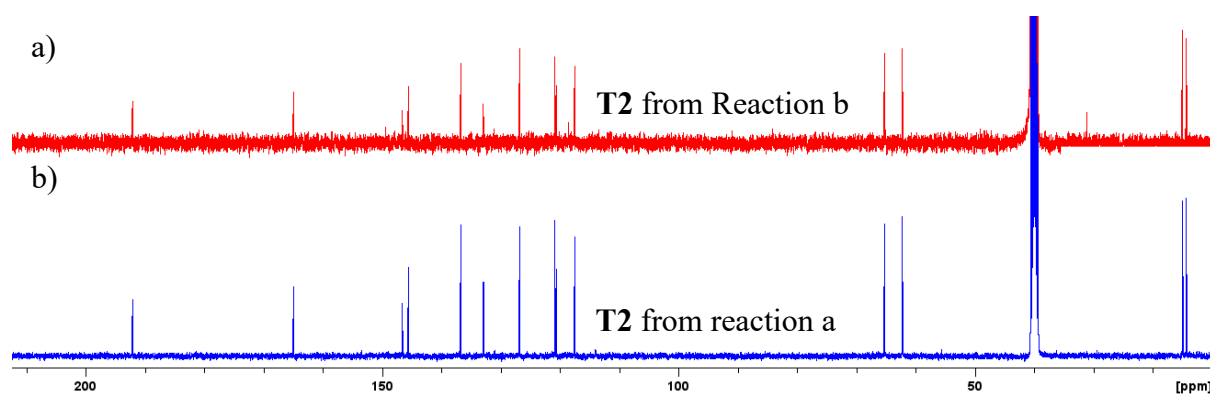


Figure S 5.13: ^{13}C NMR spectra overlay of a) T2 from reaction b and b) T2 from reaction a.

Chapter 6

Hydrazide Chemosensors

Summary

Two hydrazide derivatives, **H1** and **H2**, were successfully synthesised and characterised using ^1H NMR, ^{13}C NMR and FT-IR. **H1** and **H2** were tested for their fluorometric and colourimetric detection of various cations and anions in acetonitrile. It was observed that no fluorometric properties were observed for these chemosensors. However, both compounds showed great promise as colourimetric chemosensors for cations and anions. **H1** and **H2** showed a colour change from clear to bright yellow in the presence of Cu^{2+} . Additionally, **H2** also changed to a red colour in the presence of Fe^{2+} . It was observed that F^- , NC^- , and NCO^- induced an orange colour change in **H1**, whereas, AcO^- caused a yellow colour change. Finally, it was observed that **H2** changed from a clear to a yellow solution for F^- , NC^- , and NCO^- .

Table of Contents

Summary	251
List of Figures	253
List of Schemes.....	253
List of selected Abbreviations	253
6 Hydrazide chemosensors	254
6.1 Introduction	254
6.2 Aim of chapter.....	254
6.3 Synthesis.....	255
6.4 Application studies of H1 and H2 as cationic and anionic chemosensors.....	257
6.4.1 Screening of metal ions.....	257
6.4.2 Screening of anions.....	258
6.5 Conclusion.....	260
6.6 Experimental	261
6.6.1 Synthesis of compounds	261
References.....	263
Supplementary information	264
List of Supplementary Figures.....	264

List of Figures

Figure 6.1: Structures of compounds H1 and H2	254
Figure 6.2: ^1H NMR spectrum of H1 in DMSO.....	255
Figure 6.3: ^1H NMR spectrum of H2 in CDCl_3	256
Figure 6.4: ^1H NMR spectrum of the isolated solid in the attempted synthesis of H3	257
Figure 6.5: a) colourimetric and b) fluorometric cationic chemosensor properties of compound H1	258
Figure 6.6: a) colourimetric and b) fluorometric cationic chemosensor properties of compound H2	258
Figure 6.7: a) colourimetric and b) fluorometric anionic chemosensor properties of compound H1	259
Figure 6.8: a) colourimetric and b) fluorometric anionic chemosensor properties of compound H2	259

List of Schemes

Scheme 6.1: Generalised reaction between an ester (1) and hydrazine (2) to synthesise the hydrazide moiety (3).	254
Scheme 6.2: Synthesis route for H1 . a) Ethanol, benzoic hydrazide, reflux 24h.....	255
Scheme 6.3: Synthesis route for H2 . a) Ethanol, hydrazine hydrate, reflux 24h.	256
Scheme 6.4: Synthesis route for H3 . a) Ethanol, phenylhydrazine, reflux 24h.	257

List of selected Abbreviations

eq. – Equivalence

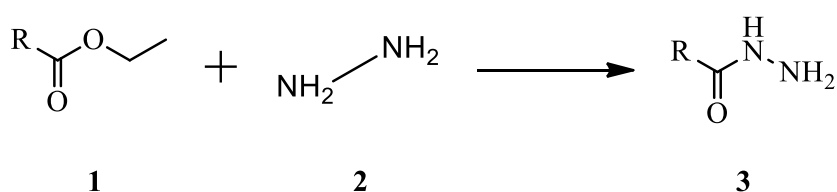
FT-IR – Fourier Transform Infrared

NMR – Nuclear Magnetic Resonance

6 Hydrazide chemosensors

6.1 Introduction

Hydrazide is an amide derivative shown in **Scheme 6.1**. This general synthesis can yield a hydrazide moiety by reacting an ester group with hydrazine hydrate.¹

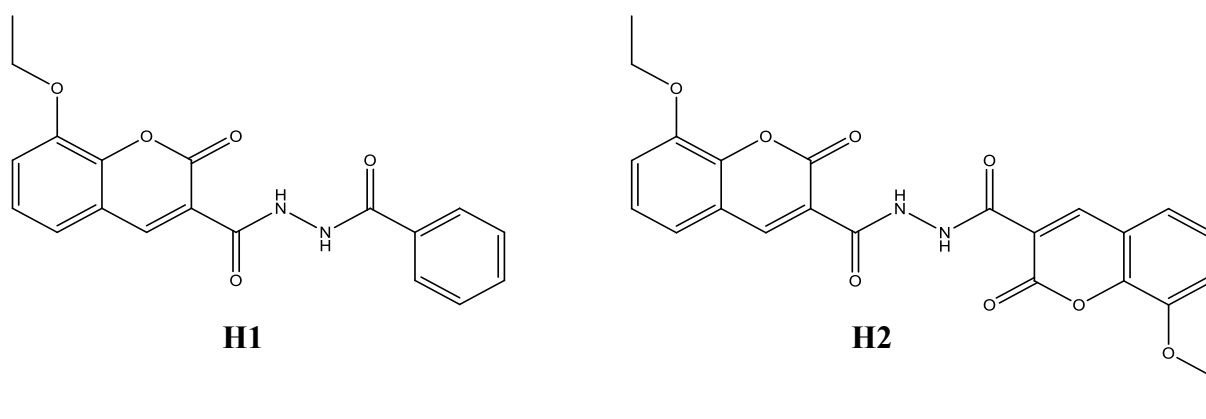


***Scheme 6.1:** Generalised reaction between an ester (1) and hydrazine (2) to form the hydrazide moiety (3).*

Hydrazide chemosensors have shown great promise as colourimetric sensors for detecting various cations and anions. These compounds display a remarkable capacity to form complexes with metals such as iron, nickel, copper and zinc, to name a few.^{2–4} The hydrazide moiety possesses labile protons, which have shown remarkable anion-sensing properties due to the ability for hydrogen bonding or deprotonation interactions.⁵

6.2 Aim of chapter

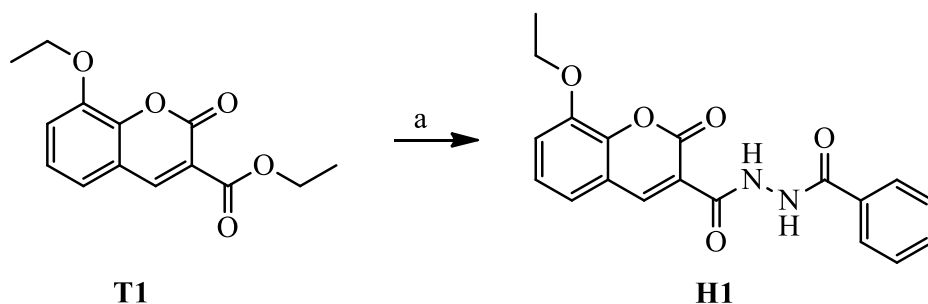
This chapter incorporates hydrazide moieties into a coumarin backbone, at position three, to yield compounds **H1** and **H2**, as shown in **Figure 6.1**. Preliminary cationic and anionic detection tests will be performed on these compounds to investigate their potential application as chemosensors for cations and anions.



***Figure 6.1:** Structures of compounds **H1** and **H2**.*

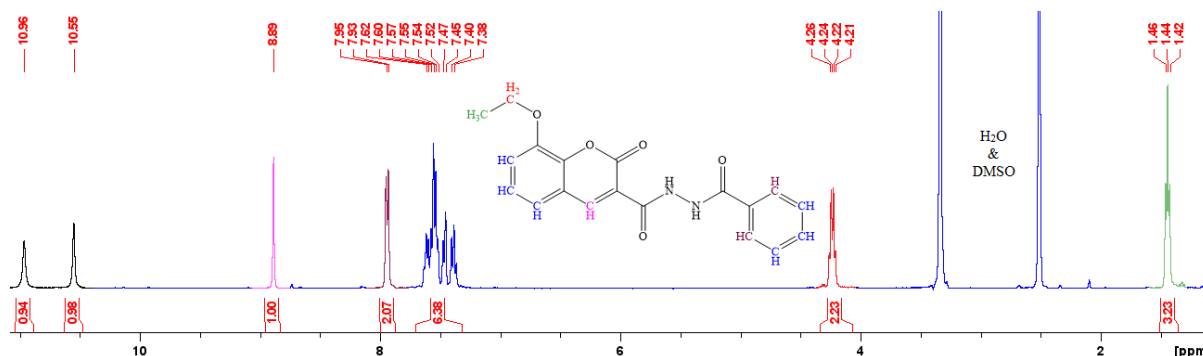
6.3 Synthesis

Two hydrazide compounds, **H1** and **H2**, were synthesised using **T1** from **Chapter 5**. **H1** was synthesised by refluxing **T1** with benzoic hydrazide in ethanol (**Scheme 6.2**), whereas **H2** was synthesised by refluxing **T1** with hydrazine hydrate in a 2:1 molar ratio (**Scheme 6.3**).



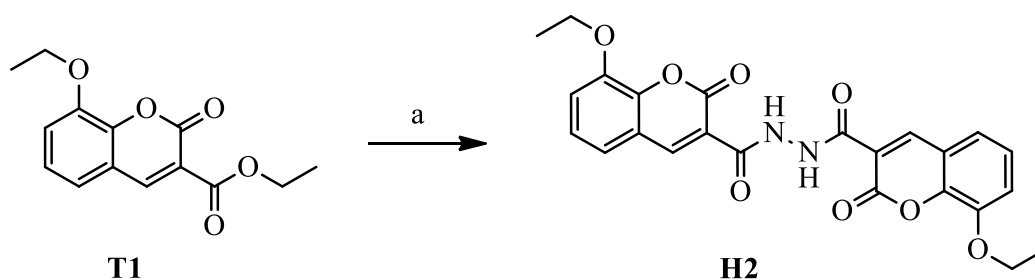
*Scheme 6.2: Synthesis route for **H1**. a) Ethanol, benzoic hydrazide, reflux 24h.*

H1 was successfully synthesised and characterised using ^1H NMR (**Figure 6.2**), ^{13}C NMR (**Figure S 6.1**), and FT-IR (**Figure S 6.3**). The formation of the hydrazide moiety can be seen as two singlets at 10.55 and 10.96 ppm in the ^1H NMR (**Figure 6.2**). Additionally, the absence of the ethyl and methyl protons of **T1** further supports the successful synthesis of **H1**.



*Figure 6.2: ^1H NMR spectrum of **H1** in DMSO.*

Subsequently, **H2** was synthesised by dimerisation via hydrazine hydrate, forming the hydrazide linker between the two coumarin backbones at position three, as shown in **Scheme 6.3**. Two molar equivalence (eq.) of **T1** was reacted with one molar eq. of hydrazine hydrate.



Scheme 6.3: Synthesis route for **H2**. a) Ethanol, hydrazine hydrate, reflux 24h.

The ester functionality of **T1** reacted with hydrazine hydrate forming the hydrazide moiety in **H2**, which was also characterised using ^1H NMR (**Figure 6.3**), ^{13}C NMR (**Figure S 6.2**) and FT-IR (**Figure S 6.4**). The symmetrical **H2** resulted in the labile protons resonating together at 11.58 ppm. In addition, the amide moiety was confirmed in the FT-IR spectra of **H1** and **H2** at 3232 and 3278 cm^{-1} , respectively.

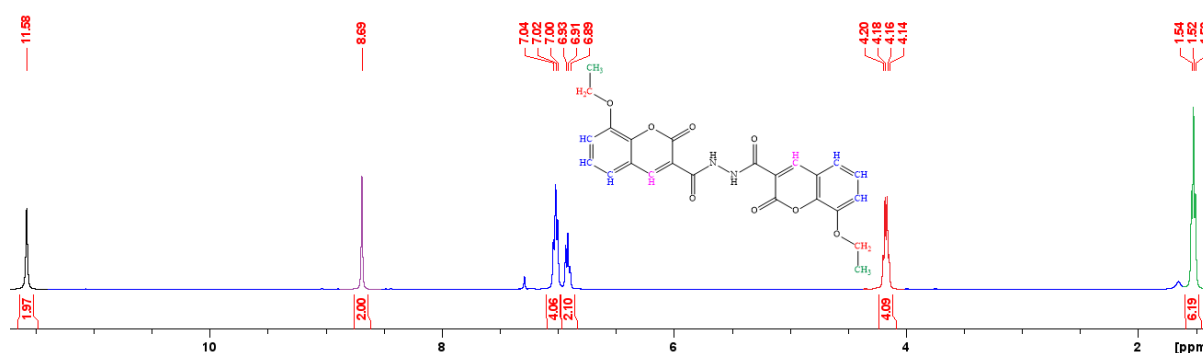
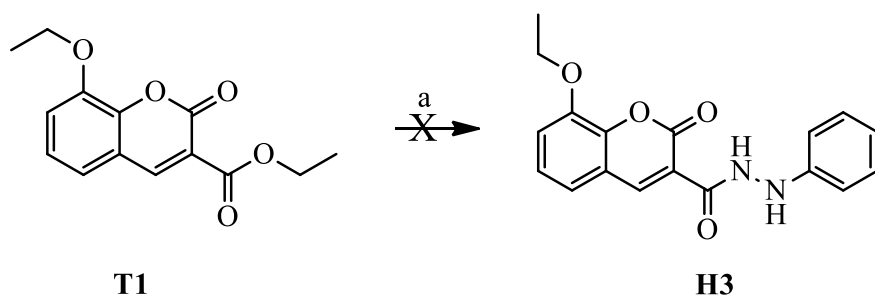
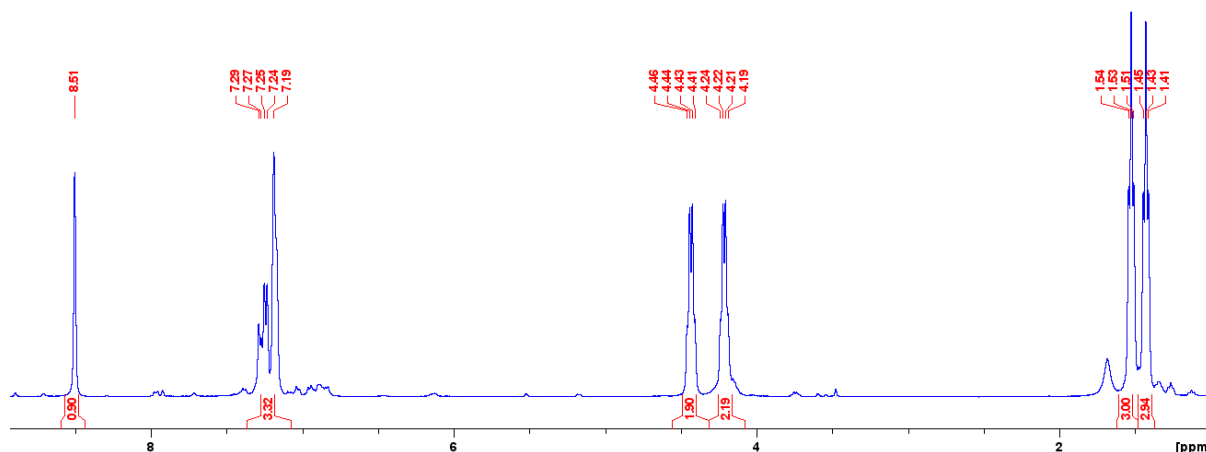


Figure 6.3: ^1H NMR spectrum of **H2** in CDCl_3 .

The synthesis of compound **H3** (**Scheme 6.4**) was also attempted with no success. The same reaction conditions were maintained for both **H1** and **H3**. However, phenylhydrazine was used instead of benzoic hydrazide. The product isolated was identified as unreacted **T1**, as observed in **Figure 6.4**, by the presence of the ethyl quartet at 4.41 – 4.46 ppm and the methyl triplet at 1.51 – 1.54 ppm.



*Scheme 6.4: Synthesis route for **H3**. a) Ethanol, phenylhydrazine, reflux 24h.*



*Figure 6.4: ¹H NMR spectrum of the isolated solid in the attempted synthesis of **H3**.*

6.4 Application studies of **H1** and **H2** as cationic and anionic chemosensors

Screening of various metal cations and anions was done for **H1** and **H2** (in acetonitrile) to test these compounds' usability as chemosensors. These experiments were conducted only with the naked eye with and without UV light (365 nm). The metal ions that were tested include Na⁺, Mg²⁺, Al³⁺, K⁺, Ca²⁺, Cr³⁺, Mn²⁺, Fe²⁺, Fe³⁺, Co³⁺, Ni²⁺, Cu²⁺, Zn²⁺, Pb²⁺, Ag⁺, Cd²⁺, Ba²⁺, and Hg²⁺. Furthermore, the anions that were tested include F⁻, Cl⁻, Br⁻, I⁻, AcO⁻, NC⁻, NCS⁻, NCO⁻, H₂PO₄⁻ and HSO₄⁻.

6.4.1 Screening of metal ions

Figure 6.5 shows the cation screening for chemosensor **H1**, and only Cu²⁺ induced a significant colour change from clear to bright yellow. The coloured solutions observed (Fe²⁺, Fe³⁺ and Ba²⁺) were caused by the cation solution and not by the complex. Furthermore, **Figure 6.5 b**) shows **H1** does not have fluorescent properties.

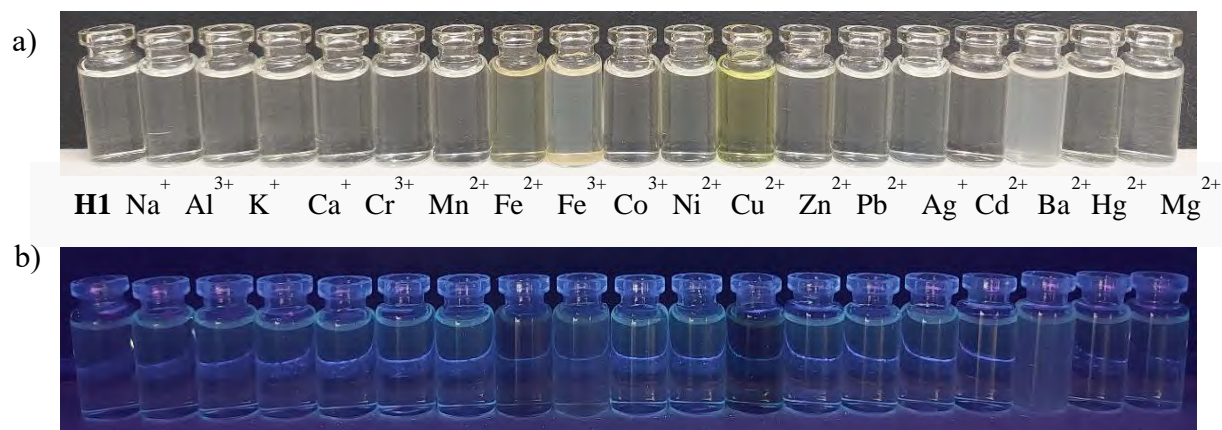


Figure 6.5: a) colourimetric and b) fluorometric cationic chemosensor properties of compound **H1**.

The experiments were done using **H2**. A solution of chemosensor **H2** changed from a clear solution to a dark red in the presence of Fe²⁺ and bright yellow for Cu²⁺. These observations indicate the formation of the expected complexes between the **H2** with these cations.

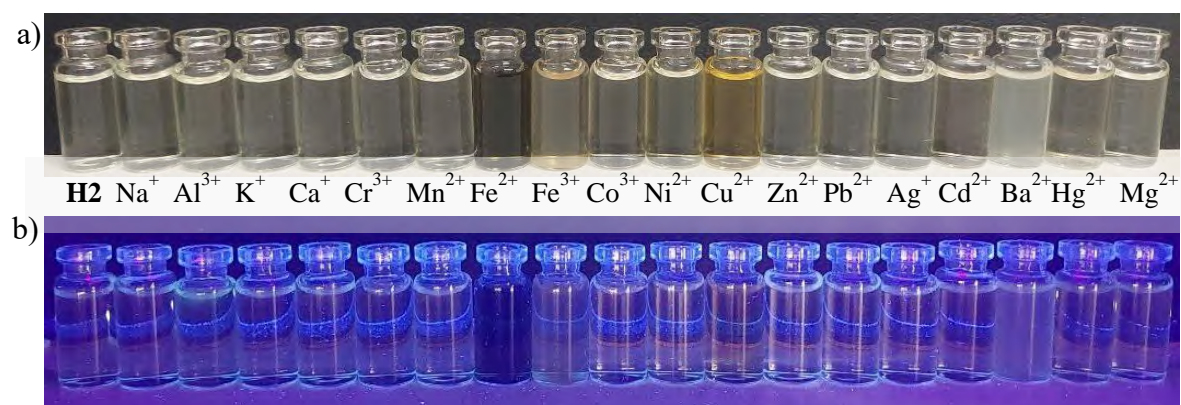


Figure 6.6: a) colourimetric and b) fluorometric cationic chemosensor properties of compound **H2**.

6.4.2 Screening of anions

The anionic chemosensor abilities of **H1** showed colourimetric changes for F⁻, AcO⁻, NC⁻, and NCO⁻, as seen in **Figure 6.7 a**). In the literature, many hydrazide compounds show affinities towards F⁻ and AcO⁻ ions via hydrogen bonding.^{6,7} Moreover, the fluorescent test of **H1** (**Figure 6.7 b**) indicated that none of these anions induced emission properties in **H1**.

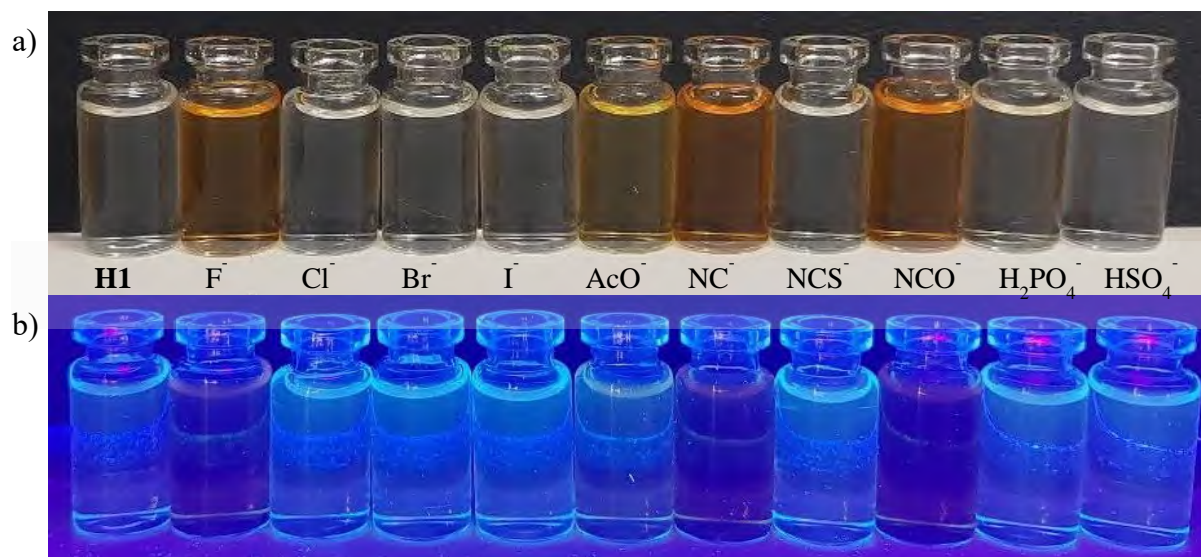


Figure 6.7: a) colourimetric and b) fluorometric anionic chemosensor properties of compound **H1**.

Lastly, the anionic chemosensor abilities of **H2** (Figure 6.8 a) displayed no interactions with most of the tested anions except for F^- , NC^- , and NCO^- as the solution turned yellowish in the presence of these anions. Once again, these observations indicate a potential application of **H2** as a chemosensor for these anions. Furthermore, Figure 6.8 b) shows that the presence of anions also does not induce emission properties in **H2**.

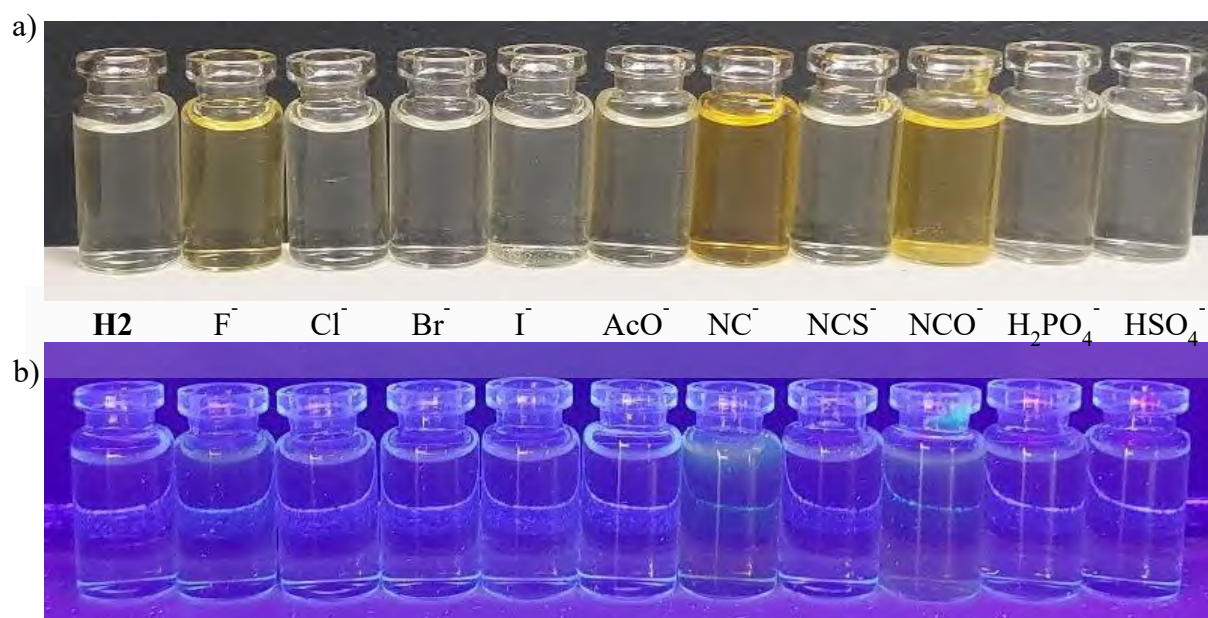


Figure 6.8: a) colourimetric and b) fluorometric anionic chemosensor properties of compound **H2**.

6.5 Conclusion

Herein two hydrazide compounds, **H1** and **H2**, were successfully synthesised and characterised using ^1H NMR, ^{13}C NMR and FT-IR.

H1 and **H2** were tested for their fluorometric, and colourimetric detection of various cations and anions were investigated. Both **H1** and **H2** displayed no fluorometric properties in the presence of the selected cations and anions. However, these compounds showed great promise as colourimetric chemosensors for both cations and anions.

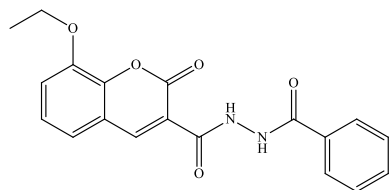
As colourimetric cationic chemosensors, **H1** (Figure 6.5) and **H2** (Figure 6.6) showed a colour change from clear to bright yellow in the presence of Cu^{2+} . Additionally, **H2** also changed to a red colour in the presence of Fe^{2+} . Thus, further studies are encouraged into the colourimetric cationic chemosensors **H1** and **H2**.

The anionic chemosensor tests of **H1** and **H2** were also investigated. It was observed in Figure 6.7 a) that F^- , NC^- , and NCO^- induced an orange colour in **H1** whereas, AcO^- resulted in a yellow solution. Thus, further studies can be done to determine if **H1** can be used to differentiate between the halogens (F^- , Cl^- , Br^- , and I^-) and the different cyanides (NC^- , NCO^- , and NCS^-). It was observed that **H2** changed from a clear to a yellow solution for F^- , NC^- , and NCO^- . Thus, further studies can be done to investigate the use of **H2** in detecting F^- in the presence of other halide ions and NCS^- from NC^- and NCO^- .

6.6 Experimental

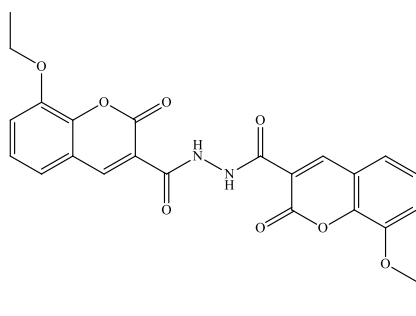
6.6.1 Synthesis of compounds

6.6.1.1 N'-benzoyl-8-ethoxy-2-oxo-2H-chromene-3-carbohydrazide – **H1**



T1 (2.01 g, 7.66 mmol) and benzoic hydrazide (1.26 g, 9.25 mmol) was dissolved in ethanol (20 ml) and refluxed for 24 hours. The solvent was reduced by evaporation, to which the solution was cooled by placing it on crushed ice, and a yellow powder was filtered.⁸ **Yield: 82%.** IR ν_{\max} (cm⁻¹): 3232.72 (>N-H stretching), 3049.41-2885.60 (C-H stretching), 1706.97 (C=O stretching, Lactone ring), 1609.07 (C=O stretching, carbonyl). ¹H NMR (DMSO): $\delta_{\text{H/ppm}}$ = 10.96 (1H, s, >NH), 10.55 (1H, s, >NH), 8.89 (1H, s, Aromatic H), 7.95-7.93 (2H, m, Aromatic H), 7.62-7.38 (6H, m, Aromatic H), 4.26-4.21 (2H, q, -CH₂), 1.46-1.42 (3H, s, -CH₃). ¹³C NMR (DMSO) $\delta_{\text{C/ppm}}$ = 165.32, 160.62, 160.03, 148.81, 146.05, 143.90, 132.61, 132.44, 128.96, 128.07, 125.66, 121.71, 119.44, 118.99, 117.74, 65.08, 15.04.

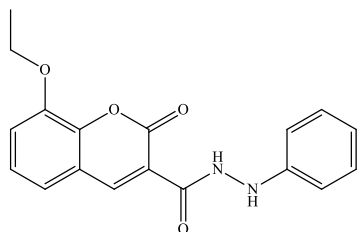
6.6.1.2 8-ethoxy-N'-(8-ethoxy-2-oxo-2H-chromene-3-carbonyl)-2-oxo-2H-chromene-3-carbohydrazide – **H2**



T1 (4.05 g, 15.44 mmol) and hydrazine hydrate 99% (0.4 g, 7.99 mmol) were dissolved in ethanol (20 ml) and refluxed for 24 hours. The solvent was reduced by evaporation, to which the solution was cooled by placing it on crushed ice, and a fine cream powder was filtered.⁸ **Yield: 74%.** IR ν_{\max} (cm⁻¹): 3278.18-3180.29 (>N-H stretching), 3099.47-2873.33 (C-H

stretching), 1721.29 (C=O stretching, Lactone ring), 1673.81-1612.83 (C=O stretching, carbonyl). ^1H NMR (DMSO): $\delta_{\text{H}}/\text{ppm}$ = 11.58 (2H, s, >NH), 8.69 (2H, s, Aromatic H), 7.04-7.00 (4H, m, Aromatic H), 6.93-6.89 (2H, m, Aromatic H), 4.20-4.14 (4H, q, -CH₂), 1.54-1.50 (6H, s, -CH₃). ^{13}C NMR (DMSO) $\delta_{\text{C}}/\text{ppm}$ = 164.70, 150.02, 147.62, 124.11, 119.38, 117.50, 116.75, 64.76, 14.88.

6.6.1.3 8-ethoxy-2-oxo-N'-phenyl-2H-chromene-3-carbohydrazide– **H3**



T1 (2.0 g, 7.64 mmol) and phenylhydrazine (0.85 g, 7.86 mmol) were dissolved in ethanol (20 ml) and refluxed for 24 hours. The solvent was reduced by evaporation, to which the solution was cooled by placing it on crushed ice, and a fine pale yellow powder was filtered and determined, using ^1H NMR, to be the unreacted starting compound.⁸

References

- (1) Abdel-Aziz, H.; Elsaman, T.; Attia, M.; Alanazi, A. The Reaction of Ethyl 2-Oxo-2H-Chromene-3-Carboxylate with Hydrazine Hydrate. *Molecules* **2013**, *18* (2), 2084–2095. <https://doi.org/10.3390/molecules18022084>.
- (2) Tian, F. F.; Jiang, F. L.; Han, X. Le; Xiang, C.; Ge, Y. S.; Li, J. H.; Zhang, Y.; Li, R.; Ding, X. L.; Liu, Y. Synthesis of a Novel Hydrazone Derivative and Biophysical Studies of Its Interactions with Bovine Serum Albumin by Spectroscopic, Electrochemical, and Molecular Docking Methods. *J. Phys. Chem. B* **2010**, *114* (46), 14842–14853. <https://doi.org/10.1021/jp105766n>.
- (3) Anbu, S.; Ravishankaran, R.; Guedes Da Silva, M. F. C.; Karande, A. A.; Pombeiro, A. J. L. Differentially Selective Chemosensor with Fluorescence Off-on Responses on Cu²⁺ and Zn²⁺ Ions in Aqueous Media and Applications in Pyrophosphate Sensing, Live Cell Imaging, and Cytotoxicity. *Inorg. Chem.* **2014**, *53* (13), 6655–6664. <https://doi.org/10.1021/ic500313m>.
- (4) Liu, Y. J.; Tian, F. F.; Fan, X. Y.; Jiang, F. L.; Liu, Y. Fabrication of an Acylhydrazone Based Fluorescence Probe for Al³⁺. *Sensors Actuators, B Chem.* **2017**, *240*, 916–925. <https://doi.org/10.1016/j.snb.2016.09.051>.
- (5) Georgiev, N. I.; Dimitrova, M. D.; Krasteva, P. V.; Bojinov, V. B. A Novel Water-Soluble 1,8-Naphthalimide as a Fluorescent PH-Probe and a Molecular Logic Circuit. *J. Lumin.* **2017**, *187*, 383–391. <https://doi.org/10.1016/j.jlumin.2017.03.049>.
- (6) Naimhwaka, J.; Uahengo, V. A Naphthoquinone Based Colorimetric Probe for Real-Time Naked Eye Detection of Biologically Important Anions Including Cyanide Ions in Tap Water: Experimental and Theoretical Studies. *RSC Adv.* **2019**, *9* (65), 37926–37938. <https://doi.org/10.1039/C9RA06116A>.
- (7) Kim, Y. H.; Choi, M. G.; Im, H. G.; Ahn, S.; Shim, I. W.; Chang, S. K. Chromogenic Signalling of Water Content in Organic Solvents by Hydrazone-Acetate Complexes. *Dye. Pigment.* **2012**, *92* (3), 1199–1203. <https://doi.org/10.1016/j.dyepig.2011.07.019>.
- (8) Patil, S. A.; Unki, S. N.; Kulkarni, A. D.; Naik, V. H.; Badami, P. S. Synthesis, Characterization, in Vitro Antimicrobial and DNA Cleavage Studies of Co(II), Ni(II) and Cu(II) Complexes with ONOO Donor Coumarin Schiff Bases. *J. Mol. Struct.* **2011**, *985* (2–3), 330–338. <https://doi.org/10.1016/j.molstruc.2010.11.016>.

Supplementary information

List of Supplementary Figures

Figure S 6.1: ^{13}C NMR spectrum of **H1** in DMSO. 264

Figure S 6.2: ^{13}C NMR spectrum of **H2** in CDCl_3 264

Figure S 6.3: FT-IR spectrum of **H1**. 265

Figure S 6.4: FT-IR spectrum of **H2**. 265

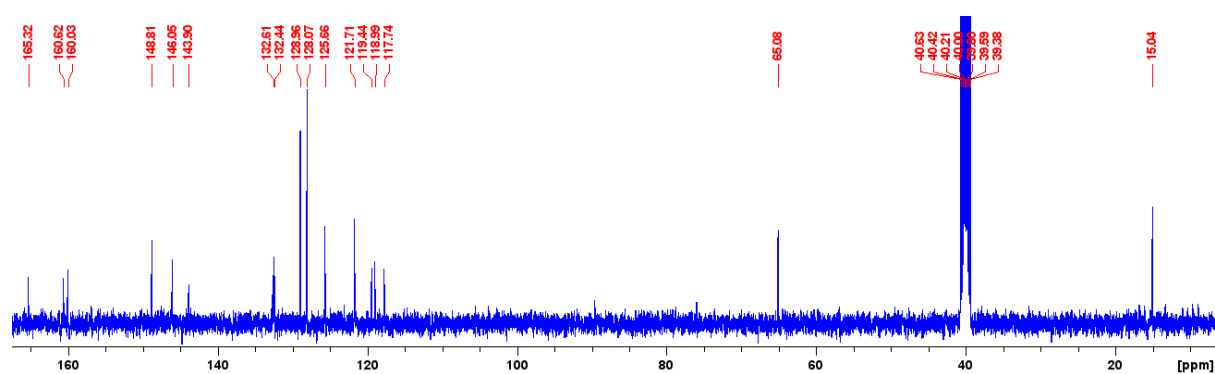


Figure S 6.1: ^{13}C NMR spectrum of **H1** in DMSO.

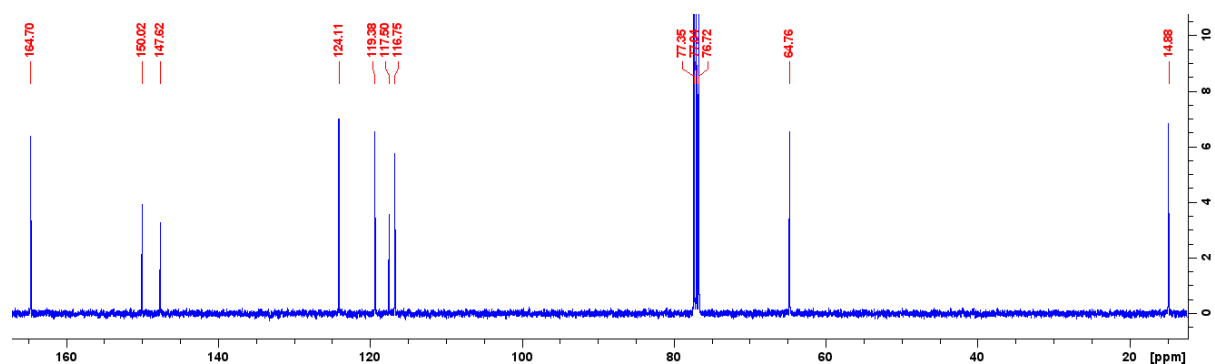


Figure S 6.2: ^{13}C NMR spectrum of **H2** in CDCl_3 .

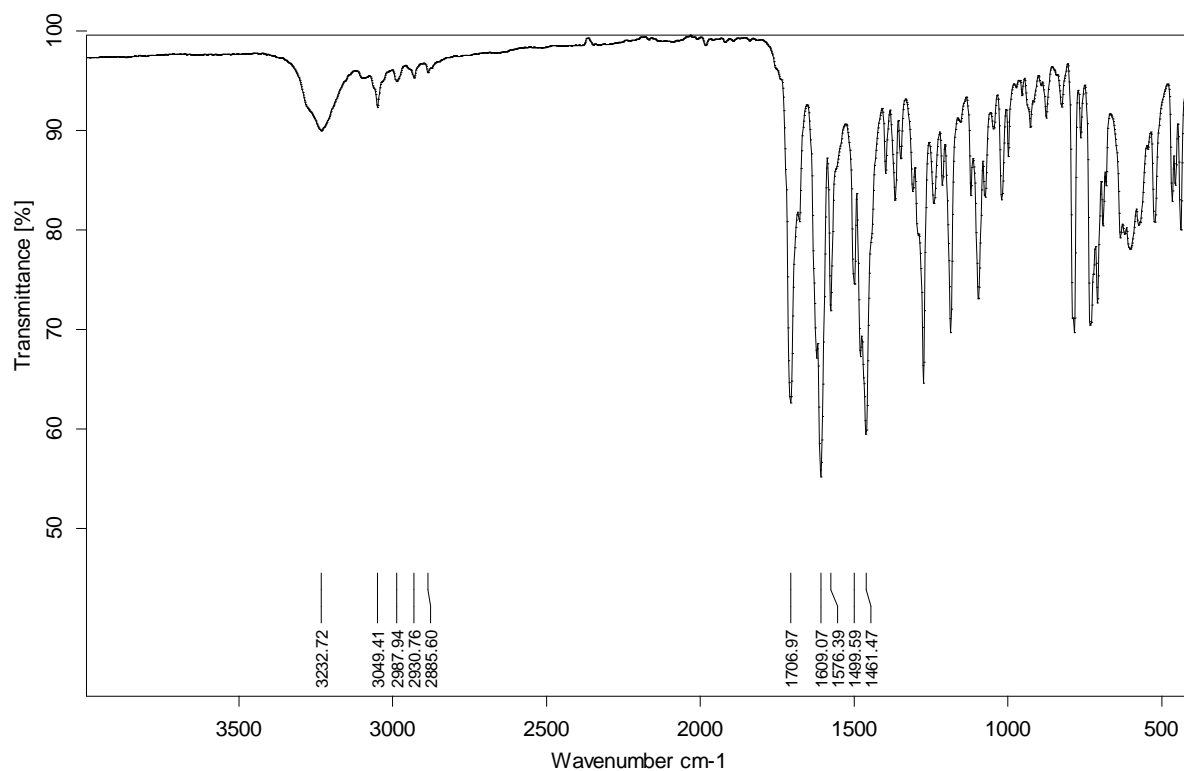


Figure S 6.3: FT-IR spectrum of *H1*.

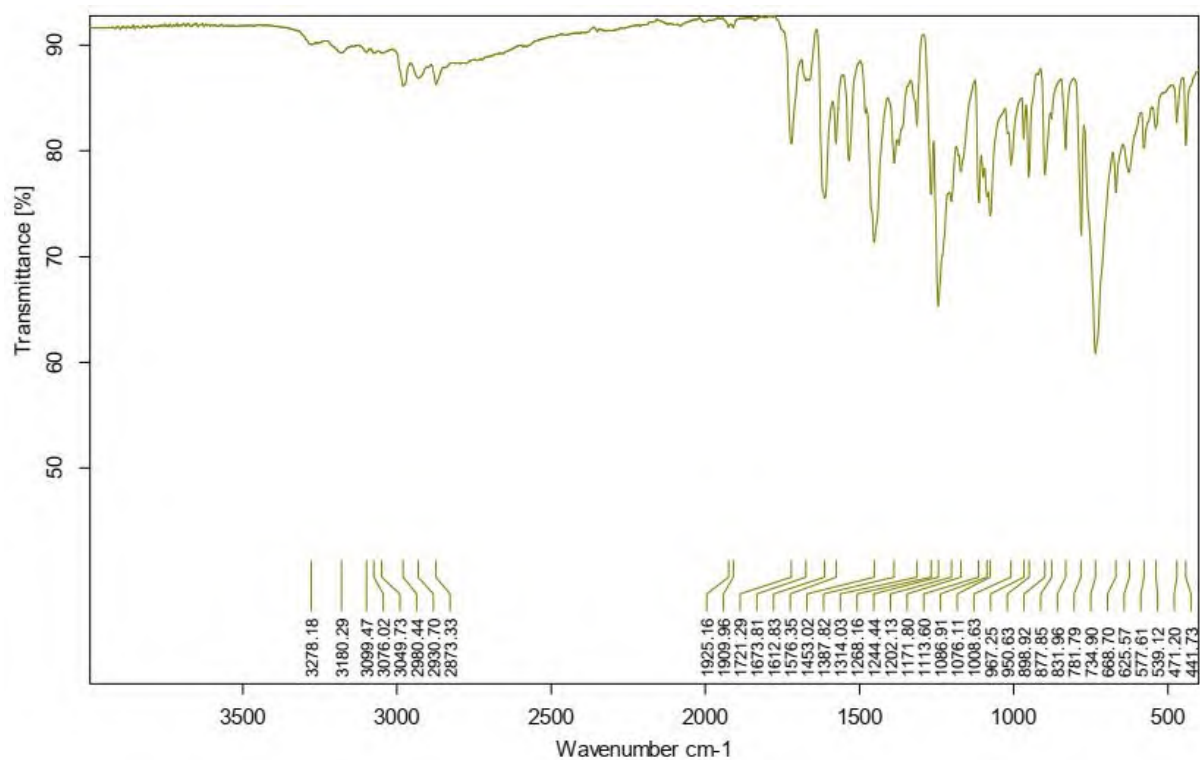


Figure S 6.4: FT-IR spectrum of *H2*.

Chapter 7

Application Studies

Table of Contents

List of Figures	268
List of Tables	268
7 Application studies.....	269
7.1 Sea and river water.....	269
7.2 Lake water	270
7.3 Borehole water	271
7.4 Real-world applications of S10 , E2 and D1	272
7.4.1 Qualitative studies of chemosensor S10	272
7.4.2 Quantitative studies of chemosensors E2 and D1	274
7.5 Experimental	277
7.5.1 General information	277
References.....	278

List of Figures

Figure 7.1: Sampling sites A and B along the Swartkops river in the Eastern Cape, South Africa.	269
Figure 7.2: Sampling site C at the North End Lake in Gqeberha, South Africa.....	271
Figure 7.3: Paper strip spiked with S10 , qualitative tests for a) Ni^{2+} , b) Cu^{2+} , and c) Fe^{2+} in various water samples.	273
Figure 7.4: S10 (500 μM) solution-based qualitative test for a) Ni^{2+} (1.193 μM), b) Cu^{2+} (31 μM) and c) Fe^{2+} (179 μM) in various water samples.	274

List of Tables

Table 7.1: Mean heavy metal concentrations (ug/g) in the sediment of Swartkops estuary in 2001. ²	270
Table 7.2: Fe^{2+} (mM) detection in various real-world water samples using E2	275
Table 7.3: Detection of Cu^{2+} (μM) in various real-world water samples using D1	276

7 Application studies

7.1 Sea and river water

The Swartkops river (**Figure 7.1**) is located in the Eastern Cape region of South Africa. This river has a catchment area stretching through Kariega (formerly named Uitenhage), Kwanobuhle, Despatch, Ibhayi, Redhouse, Bluewater Bay and most of Gqeberha section (formerly named Port Elizabeth). In addition, the Swartkops river flows through highly urbanised, agricultural and industrialised regions.^{1,2} It has been estimated that in 2001 approximately one million people lived and worked in the catchment region of Swartkops river.²

Human activity has severely impacted the water quality of the Swartkops river. These activities include wastewater treatment works (The Kelvin Jones, Despatch, and KwaNobuhle plants)³, salt pans (Marina Sea Salt), Sand and clay mining, brickworks, tanneries, the motor industry, wool industry, railway yards and depots, and domestic and industrial stormwater outlets reaching the estuary and river system.³⁻⁶



Figure 7.1: Sampling sites A and B along the Swartkops river in the Eastern Cape, South Africa.

A study done in 2001 by K. Binning et al. revealed that the sediment in the Swartkops estuary (point SE in **Figure 7.1**) and Swartkops river (point SR in **Figure 7.1**) contained many different heavy metals from which strontium (Sr) and tin (Sn) were of the highest concentrations observed. It was further stated that these sediment pollutants could periodically be released into the water, which can cause serious health concerns.

Table 7.1: Mean heavy metal concentrations (ug/g) in the sediment of Swartkops estuary in 2001.²

	Cr	Pb	Zn	Ti	Mn	Sr	Cu	Sn
SE	7.8	9.6	7.0	58.7	33.4	615.2	1.0	591.3
SR	19.8	90.7	27.9	136.7	51.4	359.6	7.8	1361.8

The Swartkops river and estuary was classified with a “very high” pollution rating based on the pollution load observed.⁶⁻⁸ In the years that followed, numerous clean-up projects were implemented.

7.2 Lake water

The North End Lake is the only freshwater lake located in Gqeberha.⁹ This low-lying Lake is exposed to contamination from runoff and possible wastewater from the industrial area north and west area and contamination from the residential area from the east.¹⁰ The industrial area houses pharmaceutical companies such as Aspen Pharmacare and Fresenius Kabi and various manufacturing factories such as Cadbury, Coca Cola and Rhino plastics.

North End Lake has been classified as a polluted and eutrophic freshwater system. A rehabilitation program was designed and implemented to clean the Lake by 2010 for the Soccer World Cup held in South Africa in 2010.⁹

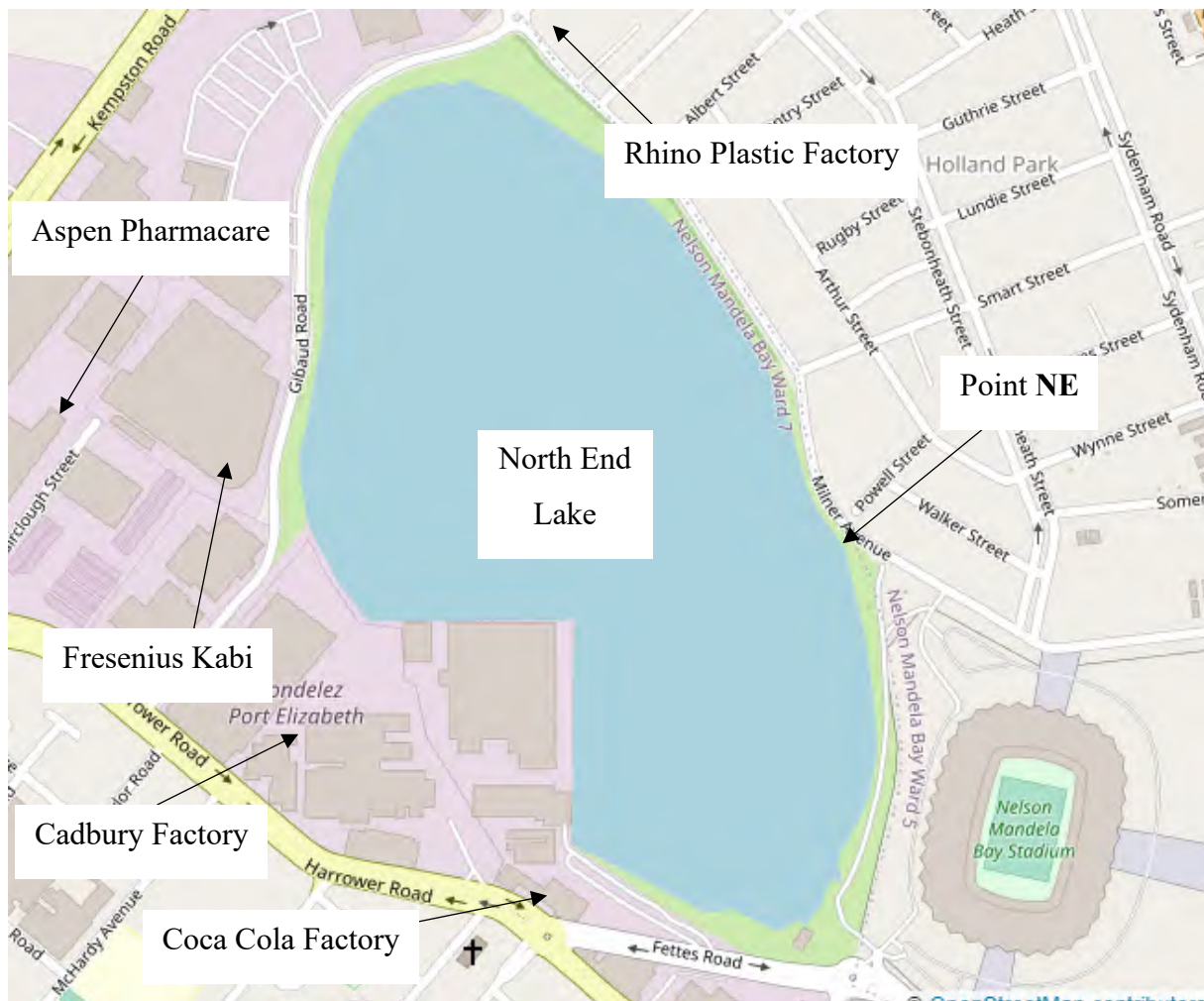


Figure 7.2: Sampling site C at the North End Lake in Gqeberha, South Africa.

7.3 Borehole water

The Walmer and Summerstrand suburbs have the highest number of boreholes in Gqeberha, which accounts for 65% of the boreholes in the Nelson Mandela Metropolitan. The Nelson Mandela Metropolitan area boreholes are generally 60 – 120 m deep.^{11,12}

The boreholes in the Summerstrand suburb contain medium chloride and high nitrate concentrations, and iron has been found in concentrations of less than 1 mg/L.¹¹

However, seawater has been found to contaminate these freshwater boreholes in times of drought due to its proximity to the ocean.¹¹ Other sources of contamination have been identified as leaking sewers, septic tanks, fertiliser application and stormwater. In addition, the surrounding lime-rich coastal sands have introduced more significant calcium and magnesium bicarbonate concentrations.¹²

7.4 Real-world applications of **S10**, **E2** and **D1**

Water samples around Gqeberha, namely Summerstrand borehole (BH), Swartkops estuary (SE) **Figure 7.1**, Swartkops river (SR) **Figure 7.1**, and North End Lake (NE) **Figure 7.2**, were collected and subsequently filtered to remove solid materials. These water samples were used to prepare the metal cation solution to determine the viability of using the chemosensors in real-world samples.

7.4.1 Qualitative studies of chemosensor **S10**

Paper strips are commonly used as paper-based analytical devices to detect heavy metals in fields such as colourimetry.¹³ Hence paper is used with chemosensors for this application. Paper is mainly made from cellulose which contains numerous hydroxyl and carbonyl groups functioning as negatively charged adsorption sites with which heavy metals can interact. These captured heavy metals can therefore interact with the colourimetric chemosensor resulting in a visual colour change. In addition, paper is an economical and environmentally friendly medium on which the chemosensor can be coated. The world health organisation approved using these paper-based devices due to their physical and chemical properties.¹³

Qualitative studies were done using chemosensor **S10** to determine if it can be used to test for the presence of Ni^{2+} , Cu^{2+} , and Fe^{2+} at their respective limits set by the World Health Organisation. The concentrations of these metal ions were $1.193\ \mu\text{M}$ for Ni^{2+} , $31\ \mu\text{M}$ for Cu^{2+} , and $179\ \mu\text{M}$ for Fe^{2+} .¹⁴ Paper test strips were laced on both sides with chemosensor **S10**, and the metal cation solution from each water source was added to the left-hand side, as seen in **Figure 7.3**. In **Chapter 2**, it was observed that nickel induced a bright yellow colour, copper produced a blue colouration and iron(II) resulted in a red-coloured solution in the presence of **S10**. As seen in **Figure 7.3** below, the **S10** chemosensor has a yellow colouration in the paper strips, preventing the detection of nickels. Conversely, both the copper and the iron(II) induced a significant change, the copper changed to a blue-green spot, and the iron(II) consisted of a red dot which is consistent with observations in **Chapter 2**.

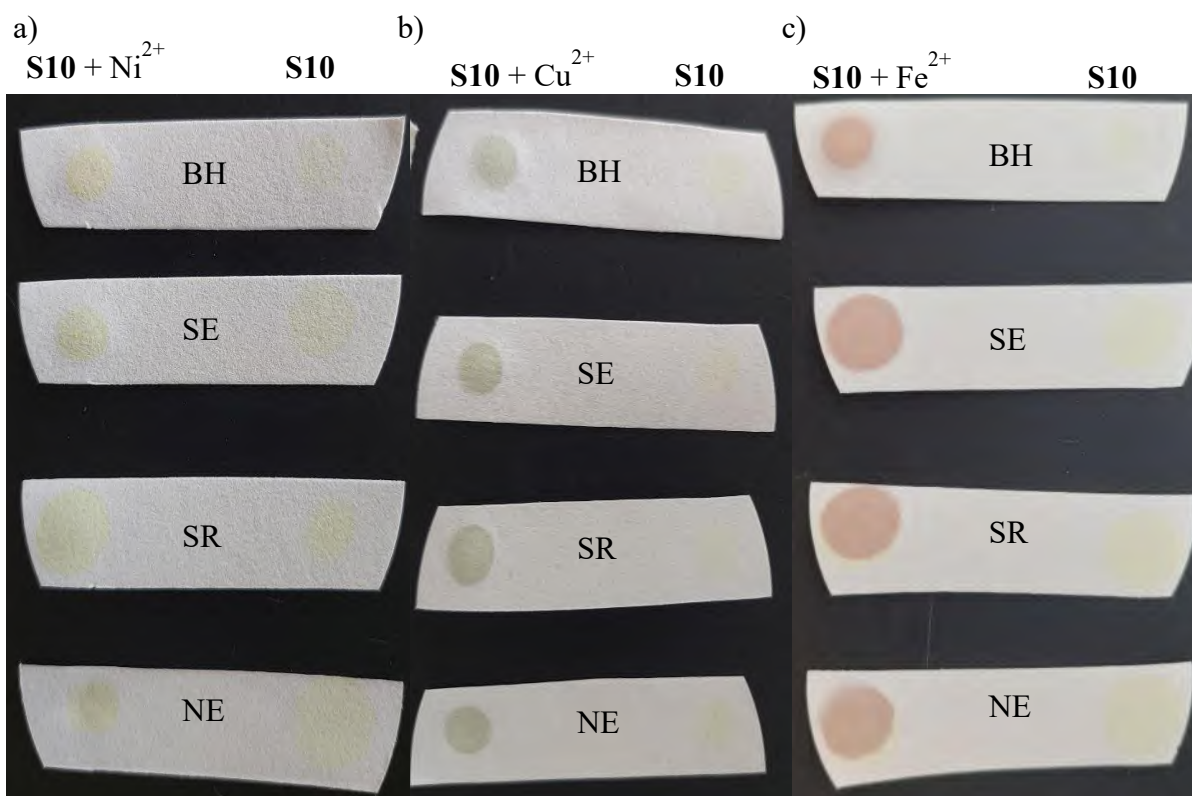


Figure 7.3: Paper strip spiked with **S10**, qualitative tests for a) Ni^{2+} , b) Cu^{2+} , and c) Fe^{2+} in various water samples.

The same test was performed in solution form. As in **Chapter 2**, the solutions were prepared in acetonitrile. The metal solutions were prepared as stated earlier with the addition of a baseline sample consisting of clean Millipore-grade water. As seen in **Figure 7.4 a)** below, nickel induced a significant colour change in **S10** for the water samples obtained from a Summerstrand borehole and the North End Lake but only a slight colour change for the water samples from the salty Swartkops estuary and the freshwater Swartkops river. **Figure 7.4 b)** shows that the solutions containing Cu^{2+} did not result in the expected colour change. This indicates that the World Health Organisation recommended concentration of Cu^{2+} is below the detection limit of **S10**. The solutions containing Fe^{2+} are shown in **Figure 7.4 c)**. The sample in the baseline solution (far right) is the colour observed in **Chapter 2**. However, the real-world water samples induce a range of colour changes which does not correlate to the baseline sample. Hence, this sample was concluded to contain other impurities that interfered with the Fe^{2+} complexation with **S10**.

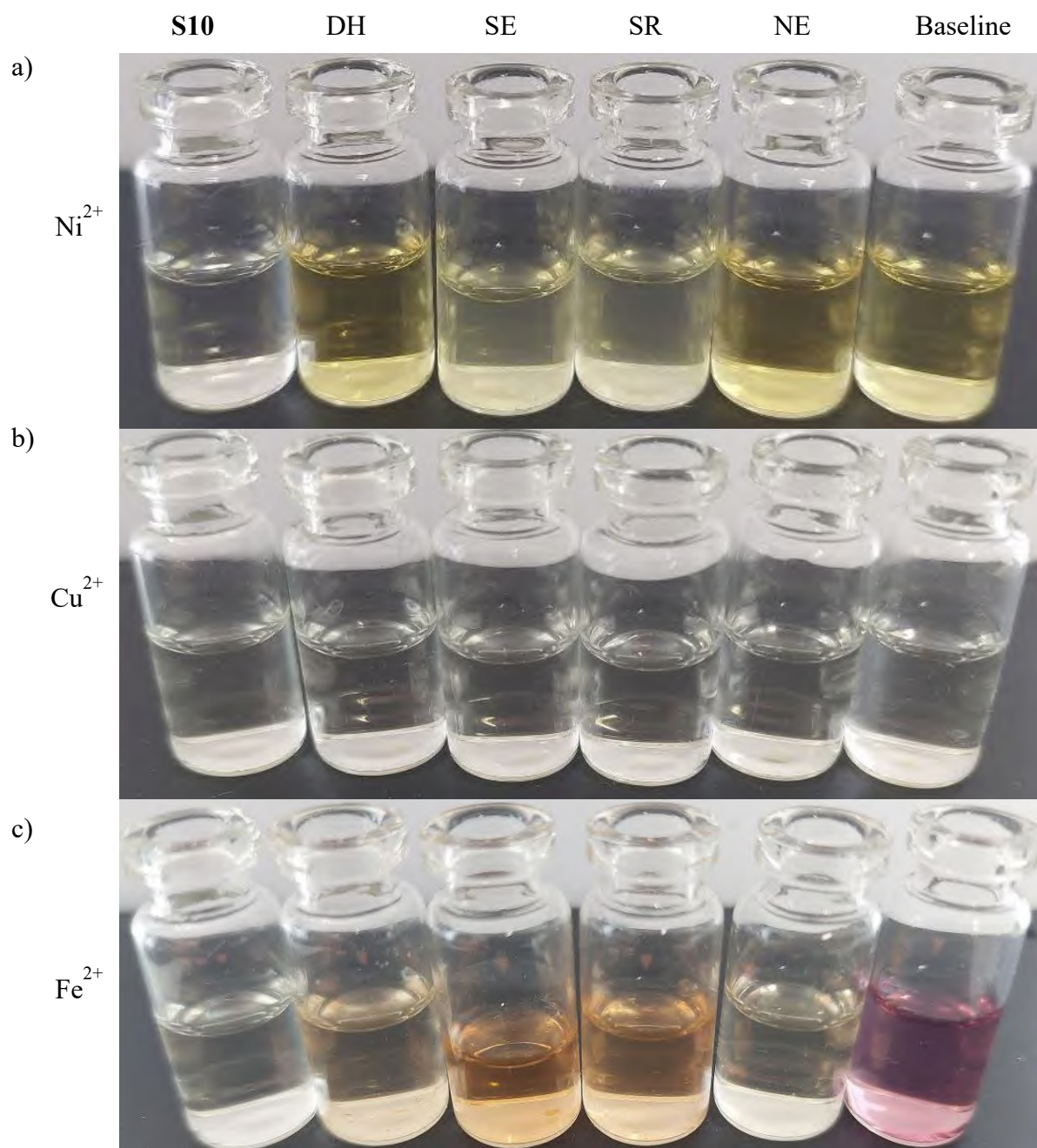


Figure 7.4: S10 (500 μM) solution-based qualitative test for a) Ni^{2+} (1.193 μM), b) Cu^{2+} (31 μM) and c) Fe^{2+} (179 μM) in various water samples.

7.4.2 Quantitative studies of chemosensors **E2** and **D1**

Chemosensors **E2** and **D1** have a linear region in which these chemosensors can be used to determine the concentration of Fe^{2+} and Cu^{2+} , respectively. As discussed in **Chapter 3**, **E2** has a LOQ of 0.074 mM and starts to plateau at 0.833 mM, thus as a quantitative range of 0.074 –

0.833 mM. Furthermore, the linear **Equation 1** can be used to determine the concentration of unknown Fe^{2+} samples.

$$y = 1.22 \times 10^6 x + 612.24 \quad (1)$$

The water samples, spiked with Fe^{2+} , were added at different concentrations to **E2**, and the fluorescence was measured (**Table 7.2**). Evidentially, **E2** could not determine the concentration of Fe^{2+} in the water samples, and as seen by the high standard deviation, the concentrations obtained were inconsistent. Fe^{2+} has a quenching effect on **E2**, and as seen in **Table 7.2**, the fluorescence was enhanced with an increased concentration of Fe^{2+} . Thus it was again concluded that this sample contained other impurities, which interfered with the selectivity of **E2**, resulting in fluorescence enhancement. However, in **Chapter 3**, it was observed that **E2** was highly selective for Fe^{2+} , even in the presence of other metal cations. Thus, other metal cations or anions not tested for could be present in the water samples.

Table 7.2: Fe^{2+} (mM) detection in various real-world water samples using **E2**.

Spiked Concentration	BH	SE	SR	NE
0.167	$0,010 \pm 0.012$	$0,018 \pm 0.021$	$0,081 \pm 0.055$	$0,033 \pm 0.017$
0.333	$-0,017 \pm 0.006$	$-0,015 \pm 0.019$	$0,048 \pm 0.053$	$0,043 \pm 0.014$
0.500	$-0,051 \pm 0.003$	$-0,054 \pm 0.014$	$0,006 \pm 0.045$	$0,048 \pm 0.017$
0.667	$-0,085 \pm 0.003$	$-0,116 \pm 0.016$	$-0,024 \pm 0.046$	$0,038 \pm 0.008$

As discussed in **Chapter 4**, **D1** has a LOQ of $0.249 \mu\text{M}$ and starts to deviate at $0.795 \mu\text{M}$. Thus **D1** has a quantitative range between $0.249 - 0.795 \mu\text{M}$. Furthermore, the linear **Equation 2** can be used to determine the concentration of unknown Cu^{2+} samples.

$$y = -437,57x + 401,85 \quad (2)$$

The fluorescence of **D1**-Cu²⁺ complexes in all the water samples at different concentrations was measured and is shown in **Table 7.3**. None of the concentrations in the real-world water samples could be determined. The fluorescence of **D1** was quenched to an extent but not as significantly as in pure water samples, as done in **Chapter 4**. This was not surprising as chemosensor **D1** was not very selective in the presence of competing metals, as determined by the competition studies in **Chapter 4**.

Table 7.3: Detection of Cu²⁺ (μM) in various real-world water samples using D1.

SPIKED CONCENTRATION	BH	SE	SR	NE
0,399	0,247 ± 0,022	0,205 ± 0,033	0,212 ± 0,002	0,228 ± 0,001
0,498	0,270 ± 0,027	0,231 ± 0,031	0,237 ± 0,001	0,255 ± 0,004
0,598	0,296 ± 0,021	0,248 ± 0,029	0,261 ± 0,002	0,282 ± 0,007
0,697	0,312 ± 0,023	0,264 ± 0,025	0,279 ± 0,004	0,302 ± 0,002

7.5 Experimental

7.5.1 General information

Stock solutions of the sensors (0.05 M) were prepared by dissolving the samples in acetonitrile and diluting them to the desired concentrations. Metal cations (0.05 M) solutions were prepared using the nitrate salts and dissolved in Millipore water.

References

- (1) Gyedu-Ababio, T. K. Pollution Status of Two River Estuaries in the Eastern Cape, South Africa, Based on Benthic Meiofauna Analyses. *J. Water Resour. Prot.* **2011**, *03* (07), 473–486. <https://doi.org/10.4236/jwarp.2011.37057>.
- (2) Binning, K.; Baird, D. Survey of Heavy Metals in the Sediments of the Swartkops River Estuary, Port Elizabeth, South Africa. *Water SA* **2001**, *27* (4), 461–466. <https://doi.org/10.4314/wsa.v27i4.4958>.
- (3) Lemley, D. A.; Human, L. R. D.; Rishworth, G. M.; Whitfield, E.; Adams, J. B. Managing the Seemingly Unmanageable: Water Quality and Phytoplankton Dynamics in a Heavily Urbanised Low-Inflow Estuary. *Estuaries and Coasts* **2022**, No. 0123456789. <https://doi.org/10.1007/s12237-022-01128-z>.
- (4) Adams, J. B.; Pretorius, L.; Snow, G. C. Deterioration in the Water Quality of an Urbanised Estuary with Recommendations for Improvement. *Water SA* **2019**, *45* (1), 86–96. <https://doi.org/10.4314/wsa.v45i1.10>.
- (5) Bate, G.; Smailes, P.; Adams, J. A Water Quality Index for Use with Diatoms in the Assessment of Rivers. *Water SA* **2004**, *30* (4), 493–498. <https://doi.org/10.4314/wsa.v30i4.5101>.
- (6) Olisah, C.; Rubidge, G.; Human, L. R. D.; Adams, J. B. Organophosphate Pesticides in South African Eutrophic Estuaries: Spatial Distribution, Seasonal Variation, and Ecological Risk Assessment. *Environ. Pollut.* **2022**, *306* (November 2021), 119446. <https://doi.org/10.1016/j.envpol.2022.119446>.
- (7) Olisah, C.; Human, L. R. D.; Rubidge, G.; Adams, J. B. Organophosphate Pesticides Sequestered in Tissues of a Seagrass Species - *Zostera Capensis* from a Polluted Watershed. *J. Environ. Manage.* **2021**, *300* (September), 113657. <https://doi.org/10.1016/j.jenvman.2021.113657>.
- (8) Olisah, C.; Adams, J. B.; Rubidge, G. The State of Persistent Organic Pollutants in South African Estuaries: A Review of Environmental Exposure and Sources. *Ecotoxicol. Environ. Saf.* **2021**, *219*, 112316. <https://doi.org/10.1016/j.ecoenv.2021.112316>.
- (9) García-Rodríguez, F.; Anderson, C. R.; Adams, J. B. Paleolimnological Assessment of Human Impacts on an Urban South African Lake. *J. Paleolimnol.* **2007**, *38* (3), 297–308. <https://doi.org/10.1007/s10933-006-9076-8>.
- (10) Kampire, E.; Rubidge, G.; Adams, J. B. Characterization of Polychlorinated Biphenyls in Surface Sediments of the North End Lake, Port Elizabeth, South Africa. *Water SA* **2017**, *43* (4), 646–654. <https://doi.org/10.4314/wsa.v43i4.12>.
- (11) Lomberg, C.; Rosewarne, P.; Raymer, D.; Devey, D. *Research into Groundwater Abstraction in the Port Elizabeth Municipal Area*; 1996.
- (12) Rosewarne, P. *A Synthesis of the Hydrogeology of the Table Mountain Group*; 2002; pp 205–208.

- (13) Ding, R.; Cheong, Y. H.; Ahamed, A.; Lisak, G. Heavy Metals Detection with Paper-Based Electrochemical Sensors. *Anal. Chem.* **2021**, 93 (4), 1880–1888. <https://doi.org/10.1021/acs.analchem.0c04247>.
- (14) World Health Organization. Guidelines for Drinking-Water Quality, 4th Edition, Incorporating the 1st Addendum. **2017**.

Chapter 8

Conclusion and Future work

8 Conclusion and Future work

8.1 Overall conclusion

In this study, several chemosensors were developed for the detection of metal ions and anions in organic solvents. These compounds were designed in such a way that they contained different functional groups that could interact with the analytes. The chemosensing abilities of these novel compounds were investigated in both polar protic and aprotic solvents. Functional groups such as Schiff bases (**Chapter 2**), enones (**Chapters 3 and 4**), and esters and the 2-thiocoumarin (**Chapter 5**) were incorporated onto the coumarin base. The application of selected compounds as chemosensors was extended to real-world application studies (**Chapter 7**). Water samples from the Swartkops estuary, Swartkops river, North End Lake, and a borehole in Summerstrand were obtained and spiked with the required metals to determine the accuracy of these chemosensors.

As shown in **Chapter 1**, Schiff bases chemosensors showed a high dependence on the solvent used. Chemosensor **S10**, for example, showed colourimetric changes towards Cu^{2+} (green), Ni^{2+} (yellow), and Fe^{2+} (red) in acetonitrile, while, in methanol, only iron induced spectral changes. The trend was extended to chemosensors **E2** and **E6** in **Chapter 3**, which turned into a green solution (overnight) in acetonitrile, but the complexes turned red in methanol.

In this study, some of the compounds demonstrated colourimetric properties in the presence of cations or anions. In **Chapter 2**, **S4** and **S10** produced a colour change in the presence of different cations. **E2** and **E6** in **Chapter 3** also resulted in colour changes in the presence of iron. Lastly, **H1** and **H2** in **Chapter 6** also presented colourimetric properties when tested for cations. **S4**, **E2** and **E6** had a delayed response time, from 30 min for **S4** to 12 hours for **E2** and **E6**. However, **S10**, **H1** and **H2** presented distinctive colour changes for their respective cations. Chemosensor **S10** complexed with Cu^{2+} to form a green solution, Ni^{2+} to develop a yellow solution, and in the presence of Fe^{2+} , a red solution was formed. The hydrazide-coumarin derivative **H1** illustrated unique colouration from clear to yellow in the presence of Cu^{2+} . In contrast, the coumarin-hydrazide-coumarin derivative **H2** displayed a significant colour change in the presence of Fe^{2+} (clear to red). Thus, it could differentiate between Fe^{2+} and Fe^{3+} , and Cu^{2+} , which induced a yellow colour change. These novel hydrazide chemosensors, **H1** and **H2**, also show great promise as anionic chemosensors and can differentiate fluoride

(yellow) from other halogens and NCS^- (clear) from NC^- and NCO^- (both displaying a yellow solution).

Fluorescent spectroscopy was also used in this project as a tool to investigate the interactions between the chemosensor and the analytes. In **Chapter 3**, an enone linker was used as a binding site which interacted strongly with Fe^{2+} . The presence of iron(II) induced a static quenching effect on the fluorescence of **E2** due to the formation of the 1:1 **E2**- Fe^{2+} complex. In **Chapter 4**, two novel dimer compounds (**D1** and **D2**) were successfully synthesised. **D1** had an inherent emission band at 573 nm, which could be quenched completely in the presence of Cu^{2+} , resulting in an “on-off” type chemosensor. The Stern-Volmer plot indicated the presence of both static and dynamic quenching in the 1:1 **D1**- Cu^{2+} complex. Furthermore, **D2** displayed no fluorescent properties in various solvents. However, the possibility of an “off-on” type chemosensor was investigated for **D2**. Unfortunately, no significant changes in its fluorescent properties were observed in the presence of numerous cations and anions tested.

In **Chapter 5**, a novel 2-thiocoumarin analogue, **T2**, of the chemosensor **T1** was synthesised through a thionation reaction utilising Lawesson’s reagent. The effect of the thionation was investigated using absorbance studies. Not only were the absorbance spectra significantly altered due to the thionation, but the selectivity towards the metal cations shifted. **T1** characteristically interacted with Fe^{2+} , whereas **T2** characteristically interacted with both Fe^{2+} and Hg^{2+} .

Real-world application studies were performed on selective chemosensors, **S10**, **E2** and **D1**. The applicability of **S10** was tested using paper strips, and the concentration at which each metal of interest in the water samples was $31\ \mu\text{M}\ \text{Cu}^{2+}$, $1.193\ \mu\text{M}\ \text{Ni}^{2+}$, and $179\ \mu\text{M}\ \text{Fe}^{2+}$. As shown in **Chapter 7**, copper(II) and iron(II) could be qualitatively identified by **S10** at these concentrations using the paper strips. Nickel(II), however, could not be definitively identified as the chemosensor **S10** has a yellow colour (same as the **S10**- Ni^{2+} complex). It was observed that the metals could be identified at low concentrations by the naked-eye using paper strips but not in solution.

E2 was tested for the ability to determine the concentration of Fe^{2+} quantificationally. Unfortunately, **E2** could not determine the concentration of Fe^{2+} in any of the water samples. This was surprising since **E2** showed high selectivity towards Fe^{2+} in the presence of competing cations, and the complex was partially reversible. Thus, the water sample contained various

analytes, which were not tested in **Chapter 3** but influenced the complexation. **D1** was also tested for quantitative abilities using fluorescence spectroscopy. In **Chapter 4**, it was observed that **D1** did not show excellent selectivity towards Cu^{2+} in the presence of competing metal cations. However, as seen during application studies in **Chapter 7**, the fluorescence of **D1** was quenched as the concentration of Cu^{2+} was increased; nevertheless, the concentration, using the calibration curve in **Chapter 4**, could not be accurately determined.

8.2 Future work

Schiff base chemosensors show great promise as colourimetric-type chemosensors, which have the great benefit of visually observing the presence of the metal. Thus, more conjugated systems can be designed and synthesised to increase the colourimetric properties.

In this work, it has been observed that the o-anisaldehyde was a poor co-ligand; however, other co-ligands containing functional groups such as $-\text{OH}$, $-\text{NO}_2$, $-\text{CO}_2\text{H}$ can be used.

In future, thionation reactions can be modified by increasing the reaction times, the concentration of Lawesson's reagent and the temperature to substitute the carbonyl oxygens with sulphur for the synthesis of **T3** and **T4** derivatives. **T4** can also be screened for its cationic chemosensor abilities, which could be more selective towards Hg^{2+} as **T2** interacted with both Fe^{2+} and Hg^{2+} , thus, determining if **T4** will only interact with Hg^{2+} . In addition, competition studies need to be done on **T1** and **T2** to determine if they are selective towards each respective cation. In addition, selenium analogues can also be investigated.

Further research into detecting metal ions in sediment should also be considered due to the slow and continuous release of toxic metals back into river systems. Moreover, ground pollution has resulted in vegetables bioaccumulating toxic metals. Thus, further studies into chemosensor applications are required. Lastly, chemosensors can be employed to detect pesticides such as organophosphate and organochlorine pesticides due to their toxicity.